

2019
QCD
and
High Energy Interactions

Sponsored by

- CNRS (Centre National de la Recherche Scientifique)
- CEA (Commissariat à l'Énergie Atomique et aux Énergies Alternatives)
- FNRS (Fond National de la Recherche Scientifique)
- BSP (Belgian Science Policy)

54th Rencontres de Moriond

La Thuile, Aosta Valley, Italy - March 23 - 30, 2019

2019 QCD and High Energy Interactions

©Published by ARISF, 2019

ISBN : 979-10-96879-11-3



All rights reserved. This book, or parts thereof, may not be reproduced in any form or by any means, electronic or mechanical, including photocopying, recording or any information storage and retrieval system now known or to be invented, without written permission from the publisher.

Proceedings of the 54th RENCONTRES DE MORIOND

QCD and High Energy Interactions

La Thuile, Aosta Valley, Italy

March 23-30, 2019

2019
QCD
and
High Energy Interactions

edited by

Étienne Augé

Jacques Dumarchez

and

Jean Trân Thanh Vân

The 54th Rencontres de Moriond

2019 QCD and High Energy Interactions

was organized by

Étienne Augé (LAL, Orsay)

Jacques Dumarchez (LPNHE, Paris)

with the active collaboration of:

- E. Berger (A.N.L. Argonne)
- S. Bethke (M.P.I. Munich)
- A. Capella (L.P.T. Orsay)
- A. Czarnecki (U. Alberta)
- D. Denegri (C.E.A. Saclay)
- N. Glover (Durham)
- B. Klima (Fermilab)
- N. Mahmoudi (University of Lyon)
- L. McLerran (Brookhaven Nat. Lab.)
- B. Pietrzyk (L.A.P.P. Annecy)
- L. Schoeffel (CEA - IRFU/SPP - Saclay)
- Chung-I Tan (Brown University)
- J. Trân Thanh Vân (L.P.T. Orsay)
- U. Wiedemann (CERN)

2019 RENCONTRES DE MORIOND

The 54th Rencontres de Moriond were held in La Thuile, Valle d'Aosta, Italy.

The first meeting took place at Moriond in the French Alps in 1966. There, experimental as well as theoretical physicists not only shared their scientific preoccupations, but also the household chores. The participants in the first meeting were mainly french physicists interested in electromagnetic interactions. In subsequent years, a session on high energy strong interactions was added.

The main purpose of these meetings is to discuss recent developments in contemporary physics and also to promote effective collaboration between experimentalists and theorists in the field of elementary particle physics. By bringing together a relatively small number of participants, the meeting helps develop better human relations as well as more thorough and detailed discussion of the contributions.

Our wish to develop and to experiment with new channels of communication and dialogue, which was the driving force behind the original Moriond meetings, led us to organize a parallel meeting of biologists on Cell Differentiation (1980) and to create the Moriond Astrophysics Meeting (1981). In the same spirit, we started a new series on Condensed Matter physics in January 1994. Meetings between biologists, astrophysicists, condensed matter physicists and high energy physicists are organized to study how the progress in one field can lead to new developments in the others. We trust that these conferences and lively discussions will lead to new analytical methods and new mathematical languages.

The 54th Rencontres de Moriond in 2019 comprised four physics sessions:

- March 16 - 23: “Electroweak Interactions and Unified Theories”
- March 16 - 23: “Quantum Mesoscopic Physics”
- March 23 - 30: “QCD and High Energy Hadronic Interactions”
- March 23 - 30: “Gravitation”

We thank the organizers of the 54th Rencontres de Moriond:

- A. Abada, E. Armengaud, J. Conrad, P. Fayet, J.-M. Frère, P. Hernandez, L. Iconomidou-Fayard, P. Janot, M. Knecht, J. P. Lees, S. Loucatos, F. Montanet, J. Orloff, A. Pich, S. Pokorski, V. Tisserand and D. Wood for the “Electroweak Interactions and Unified Theories” session,
- E. Andrei, A. Blais, H. Bouchiat, P. Delsing, M. Devoret, K. Ensslin, A. Geim, L. Glazman, B. Huard, L. Molenkamp, H. Pothier, P. Roche, G. Steele, C. Schonenberger, C. Stampfer, S. Tarucha, X. Waintal for the “Quantum Mesoscopic Physics” session,
- E. Augé, E. Berger, S. Bethke, A. Capella, A. Czarnecki, D. Denegri, N. Glover, B. Klima, N. Mahmoudi, L. McLerran, B. Pietrzyk, L. Schoeffel, Chung-I Tan, J. Trân Thanh Vân and U. Wiedemann for the “QCD and High Energy Hadronic Interactions” session,
- B. Barish, M. A. Bizouard, L. Blanchet, J.-M. Le Goff, E. Rasel, S. Reynaud, F. Ricci, T. Sumner, J.-Y. Vinet, P. Wolf for the “Gravitation” session

and the conference secretariat and technical staff:

V. de Sá-Varanda and C. Bareille, I. Cossin, G. Dreneau, F. Legrand, G. Perrin, S. Vydelingum

We are also grateful to Giorgio Palmucci, Mimmo De Pisa, Cipriano Deiana, Francesco Quinto, Fulvia Feraco, Laura Basile and the Planibel Hotel staff who contributed through their hospitality and cooperation to the well-being of the participants, enabling them to work in a relaxed atmosphere.

The Rencontres were sponsored by the Centre National de la Recherche Scientifique, the Commissariat à l’Energie Atomique (CEA-Irfu), the Programme National GRAM du CNRS, the European Gravitational Observatory, the Fonds de la Recherche Scientifique (FRS-FNRS) and the Belgium Science Policy. We would like to express our thanks for their encouraging support.

It is our sincere hope that a fruitful exchange and an efficient collaboration between the physicists and the astrophysicists will arise from these Rencontres as from previous ones.

E. Augé, J. Dumarchez and J. Trân Thanh Vân

Table of Contents

1. Higgs

ATLAS Higgs physics results	Kurt Brendlinger	3
CMS Higgs physics results	Martin Flechl	7
The transverse momentum subtraction method at N ³ LO applied to Higgs boson production at the LHC	Leandro Javier Cieri	11
LHC Higgs CP sensitive observables in $H \rightarrow \tau^+\tau^-; \tau^\pm \rightarrow (3\pi)^\pm\nu$ and machine learning benefits	Zbigniew Was	15
Constraining the MSSM Higgs sector using precise Higgs mass predictions	Henning Bahl	21
Higgs boson production in partonic and electromagnetic interactions with heavy ions	David d’Enterria	25

2. Heavy Flavour

2.1 Top

$t\bar{t} + X$ production at ATLAS and CMS	Imma Riu	35
Associated top-pair production with a heavy boson through NLO + NNLL accuracy at the LHC	Anna Kulesza	39
Single top quark and rare top quark production at ATLAS and CMS	Willem Verbeke	43

2.2 Search for New Physics

Flavour physics in vogue	Jernej F. Kamenik	49
Rare, radiative, and electroweak penguin decays of heavy flavour hadrons at LHCb	Clara Remon Alepuz	55
Search for new physics signals via doubly weak B decays	Cai Dian Lu	59
Impact of polarization observables and $B_c \rightarrow \tau\nu$ on new physics explanations of the $b \rightarrow c\tau\nu$ anomaly	Ivan Nišandžić	63
V_{cb} from inclusive $b \rightarrow c$ decays: an alternative method	Matteo Fael	69
Search for production of an invisible dark photon from π^0 decays at NA62	Marco Mirra	73
Lepton Flavour Universality tests with heavy flavour decays at LHCb	Rudolf Oldeman	77
The trouble with $R_{K^{(*)}}$ – updated global fits and future directions	Sébastien Descotes-Genon	81
Explaining the flavor anomalies with a vector leptoquark	Andreas Crivellin	85
Connecting neutral current B anomalies with the heaviness of the third family	Joseph Davighi	91
Confronting B anomalies with low energy parity violation experiments	Abhishek Iyer	95

2.3 Spectroscopy

XYZ particles at BESIII	Riccardo Farinelli	101
Baryon number fluctuation of preconfinement clusters and transverse momentum dependence of bottom baryon production	Shi-Yuan Li	107
Hadron spectroscopy and exotic states at LHCb	Tomasz Skwarnicki	111

2.4 New Phenomena

CMS search highlights	Stéphanie Beauceron	121
Strong SUSY at ATLAS and CMS	Nadja Strobbe	125
LHC constraints on extended SUSY	Sabine Kraml	129
Searches for new resonances (lepton, jets) at ATLAS and CMS	Yiming Abulaiti	133
Searches for new physics with unconventional signatures at ATLAS and CMS	Kevin Pedro	137
Searches for dark matter at CMS and ATLAS	Deborah Pinna	141
Exploring light supersymmetry with GAMBIT	Anders Kvellestad	145
Neutrino dark matter - status and perspectives	Suchita Kulkarni	149
Effective field theory after a new-physics discovery	Matthias König	153

3. Electroweak

Inclusive and differential W and Z at CMS and ATLAS	Emanuele Di Marco	159
The status and prospects of the muon $g - 2$ experiment at Fermilab	Aaron Fienberg	163
Recent results from the VEPP2000 e+e- collider	Evgeny Solodov	167
News on the CLIC physics potential	Rickard Ström	171

4. QCD

Soft QCD at CMS and ATLAS	Merijn van de Klundert	177
QCD with jets and photons at ATLAS and CMS	Jonathan D. Bossio Sola	181
Isolated photon and photon+jet production at NNLO QCD accuracy and the ratio $R_{13/8}^\gamma$	Marius Höfer	185
Analytic form of the planar two-loop five-parton scattering amplitudes in QCD	Samuel Abreu	189
Elliptic polylogarithms and pure functions	Lorenzo Tancredi	193
Power corrections to TMD factorization	Ian Balitsky	197
Angular ordering effects in TMD parton distribution functions and Drell-Yan q_\perp spectra	Aleksandra Lelek	203
Determination of Parton Distribution Functions in pion using xFitter	Ivan Novikov	207
Forward-backward Drell-Yan asymmetry and PDF determination	Francesco Hautmann	211

5. Heavy Ion

Collectivity in RHIC geometry scan as seen by PHENIX	Tamas Novák	215
Studying parton dynamics via single-spin asymmetries and two-particle correlations at PHENIX	Nicole Lewis	221
Results from proton-lead and fixed-target collisions at LHCb	Daniele Marangotto	225
Heavy ion physics at CMS and ATLAS: hard probes	Gábor Veres	229
Heavy ion physics at ATLAS and CMS: flow harmonics across systems (pp , $p+Pb$, $Xe+Xe$, $Pb+Pb$)	Krzysztof Woźniak	233
Probing of multiquark structure in hadron and heavy ion collisions	Mikhail Barabanov	237
Transport anomalies near the QCD phase transition at finite density	Boris Kerbikov	241
Radiative quark p_\perp -broadening in a quark-gluon plasma at RHIC and LHC energies	Bronislav Zakharov	245
Particle production in high energy p-p collisions	Andrew Koshelkin	249
Hadron interactions at ultra-high energies measured by the Pierre Auger Observatory	Ralf Ulrich	253

6. Closing

6.1 Summaries

QCD and high energy interactions: experimental summary	Vincenzo Vagnoni	261
QCD and high energy interactions: Moriond 2019 theory summary	Doreen Wackerroth	275

6.2 Common Session with the Gravitation Conference

Searching for new physics with precision low temperature experiments	Michael Tobar	291
--	---------------	-----

Authors Index		301
----------------------	--	-----

List of participants		305
-----------------------------	--	-----

1. Higgs

ATLAS Higgs Physics Results

Kurt Brendlinger, on behalf of the ATLAS Collaboration

*DESY, Notkestraße 85,
22607 Hamburg, Germany*

Recent measurements of Higgs boson properties are presented using up to 139 fb^{-1} of proton-proton collision data delivered by the Large Hadron Collider and recorded by the ATLAS detector. Three measurements are discussed: first, cross sections of a Higgs boson produced in association with a vector boson are measured using the $H \rightarrow b\bar{b}$ decay channel. These cross section measurements, performed in dedicated phase space regions, are called simplified template cross sections. A measurement of the associated Higgs boson production is also performed in the $H \rightarrow WW$ decay channel. Finally, the production of a Higgs boson in association with a $t\bar{t}$ pair is measured in the diphoton decay channel. The results presented here are compatible with Standard Model predictions.

1 Introduction

The Large Hadron Collider (LHC) [1] has delivered about 155 fb^{-1} of proton-proton collisions at a center-of-mass energy of $\sqrt{s} = 13 \text{ TeV}$ during its Run 2 data taking program between 2015 and 2018. With this data, the ATLAS experiment [2, 3] is able to probe the nature of the Higgs boson with unprecedented precision. The most recent measurements of Higgs boson production, using up to 139 fb^{-1} of high-quality data, are summarized in the following. These measurements are performed in the $b\bar{b}$, WW ($\rightarrow \ell\nu\ell'\nu'$) and diphoton ($\gamma\gamma$) decay channels, and specifically target Higgs boson production in association with a W or Z boson (collectively called VH) or in association with a top quark pair ($t\bar{t}H$).

2 Measurement of the VH production mode in the $b\bar{b}$ decay channel

The observation of Higgs boson production in association with a W or Z boson, reported in Ref. [6], was achieved by combining measurements in the $H \rightarrow b\bar{b}$, $H \rightarrow ZZ^* \rightarrow 4\ell$ and $H \rightarrow \gamma\gamma$ decay channels using 80 fb^{-1} of data collected in Run 2. Following the observation, the VH production mode is studied in further detail using Higgs bosons decaying to a pair of b -jets, the most sensitive decay channel for this production mode, using the same analysis strategy and integrated luminosity [7].

The cross section is measured in bins of the transverse momentum of the associated gauge boson, p_{T}^V . The measurement is performed in the context of the simplified template cross section (STXS) framework [4, 5], which is designed to measure cross sections of production modes as well as kinematic phase space regions, while reducing the model dependence of the measurements. Advanced machine learning techniques are used in this analysis to isolate the signal and enhance the experimental sensitivity of the cross section measurements.

The analysis considers events with 2 b -tagged jets and 0, 1 or 2 reconstructed leptons consistent with vector boson signatures. To extract the signal, eight separate boosted decision trees (BDTs) are trained, one for each signal region considered. The correlation between p_T^V and the BDT output score is exploited to extract the cross section in several regions of p_T^V . Figure 1a compares the BDT output of the background and the inclusive signal, as well as two different p_T^V STXS regions, in a signal region targeting WH production with the W boson decaying leptonically. The clear shape differences between the STXS regions can be used to extract both cross sections simultaneously in the fit to data.

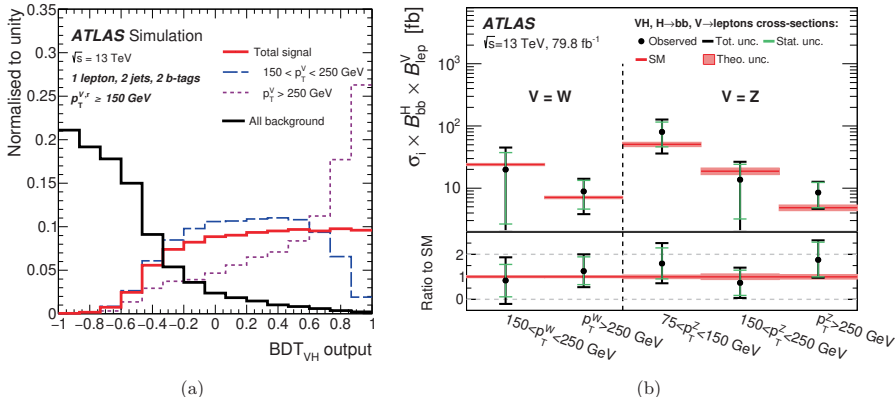


Figure 1: Results from the measurement of VH production in the $H \rightarrow b\bar{b}$ decay channel [7]. (a) The BDT shape of the signal and background distributions in the 1-lepton, 2-jet reconstructed event category targeting WH production. The shape of two STXS signal regions featuring different p_T^V is also shown, highlighting the correlation between p_T^V and the BDT response. (b) The Higgs boson cross sections, binned in the p_T of the associated gauge boson, and compared to the Standard Model prediction.

Figure 1b reports the measured cross sections in several fiducial regions of the STXS framework. The measurements presented here are also used to constrain parameters in an effective Lagrangian framework, whose deviation from predictions would indicate interactions beyond the Standard Model (SM). The results are consistent with the SM prediction. The simplified template cross sections measured in this analysis can be readily combined with those measured in other decay channels, allowing each decay channel to contribute toward reaching the ultimate precision of the full Higgs boson fiducial phase space.

3 Measurement of the VH production mode in the WW decay channel

The VH production of Higgs bosons is also studied in the $H \rightarrow WW$ decay channel, with all vector bosons decaying leptonically, using 36.1 fb^{-1} of data collected in 2015 and 2016 [8]. To gain sensitivity to the WH process, events with three reconstructed leptons are separated into a region depleted in contributions from events with Z bosons by requiring that events have no same-flavor, opposite-charge lepton pair. Two BDTs, one designed to reject $t\bar{t}$ events ($\text{BDT}_{t\bar{t}}$) and one for reducing the WZ background (BDT_{WZ}), are trained for this region. The signal region is composed of six bins in the two-dimensional space defined by the two BDTs: three bins of $\text{BDT}_{t\bar{t}}$, each of which is subdivided into two BDT_{WZ} bins.

A separate signal region targeting WH production is constructed using the remaining three-lepton events, and an additional BDT is used to separate signal events from $WZ/W\gamma^*$ and ZZ^*

backgrounds. Finally, the ZH selection is optimized by separating the signal region into events with one or two same-flavor, opposite-charge lepton pairs.

The WH and ZH cross sections are extracted using a simultaneous fit of the signal regions as well as control regions enhanced in the main analysis backgrounds. Figure 2a depicts the fitted WH signal and background in the 6 bins of the Z -depleted signal region. Figure 2b compares the measured cross section times branching ratio for ZH and WH production to the SM prediction. A mild excess is seen in both cases, though the measured values are consistent with the SM expectation.

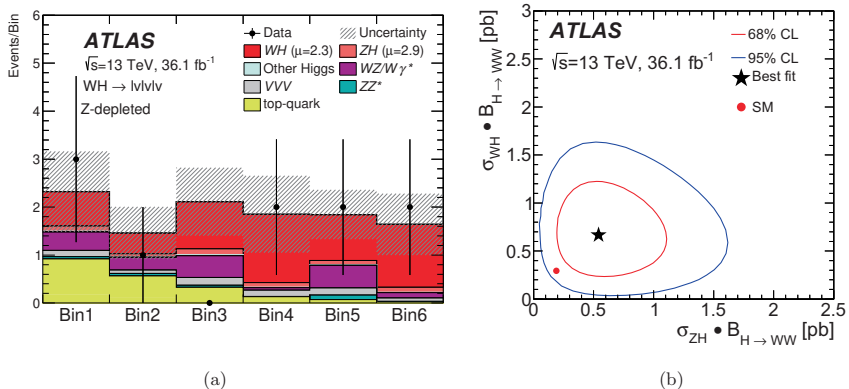


Figure 2: Results from the measurement of VH production in the $H \rightarrow WW$ decay channel [8]. (a) The data and fitted signal and backgrounds in the Z -depleted WH signal region, composed of 6 bins in a two-dimensional space defined by the BDT_{WZ} and $BDT_{t\bar{t}}$ scores—see the text. The shaded band includes statistical and systematic uncertainties on both signal and background as estimated by the fit. (b) The best-fit cross section times branching ratio for WH and ZH production and the 68% and 95% confidence-level contours, compared to the SM prediction.

4 Measurement of Higgs boson production in association with a $t\bar{t}$ pair in the diphoton decay channel

The measurement of Higgs boson production with an associated $t\bar{t}$ pair ($t\bar{t}H$ production) and decay to two photons has been updated to include the full Run 2 dataset [9]. In this analysis, reconstructed events are sorted into two regions: one targeting *hadronic* decays of the $t\bar{t}$ pair and one for *leptonic* decays of at least one of the top quarks. Two BDTs are developed, one for hadronic and one for leptonic events, which give discrimination against both non-resonant background and $H \rightarrow \gamma\gamma$ events from other (non- $t\bar{t}H$) production modes. Seven categories are defined based on the BDT scores (3 BDT bins in the leptonic events and 4 BDT bins in the hadronic events), and a simultaneous fit of the invariant diphoton mass spectra in every category is used to extract the $t\bar{t}H$ signal. Figure 3a shows the sum of the signal and background fits in all 7 categories, where the contribution from each channel is weighted by an approximate measure of its expected significance. In Figure 3b, the contribution of $t\bar{t}H$ signal, other Higgs boson production processes, and continuum background is shown for each category.

The measured $t\bar{t}H$ production cross section times branching ratio is:

$$\sigma_{t\bar{t}H} \times B_{\gamma\gamma} = 1.59^{+0.38}_{-0.36} \text{ (stat.) }^{+0.15}_{-0.12} \text{ (exp.) }^{+0.15}_{-0.11} \text{ (th.) fb,} \quad (1)$$

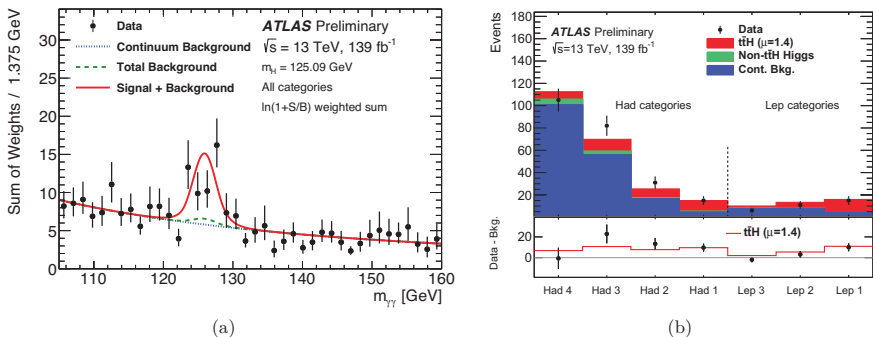


Figure 3: Results from the measurement of $t\bar{t}H$ production in the diphoton decay channel [9]. (a) The invariant mass spectrum of the diphoton system for the sum of all signal regions, weighted by the approximate expected significance of each region. The fitted total background includes non-resonant backgrounds as well as other (non- $t\bar{t}H$) Higgs boson production modes. (b) The number of data events in the diphoton invariant mass window containing 90% of the expected $t\bar{t}H$ signal, in each BDT bin of the hadronic and leptonic categories. The fitted $t\bar{t}H$ signal, continuum background, and non- $t\bar{t}H$ Higgs boson production are shown in each bin.

which is 1.4 times the SM prediction. The measurement has an observed significance of 4.9σ (4.2σ expected), highlighting the importance of the diphoton decay channel in the study of $t\bar{t}H$ production.

5 Summary

The LHC has delivered an unprecedented amount of proton-proton collision data in Run 2, which ATLAS has begun to fully exploit. The results presented here, using up to 139 fb^{-1} of collision data, represent a continuing effort to fully characterize Higgs boson production, as we move into the precision era of Higgs physics.

Copyright 2019 CERN for the benefit of the ATLAS Collaboration. CC-BY-4.0 license.

References

- [1] L. Evans and P. Bryant, *JINST*, 3:S08001, 2008.
- [2] ATLAS Collaboration, *JINST*, 3:S08003, 2008.
- [3] ATLAS Collaboration, ATLAS-TDR-19, <http://cds.cern.ch/record/1291633>, 2010.
- [4] D. de Florian et al., CERN-2017-002-M, <http://cds.cern.ch/record/2227475>, 2017.
- [5] J. R. Andersen et al., arXiv:1605.04692, 2016.
- [6] ATLAS Collaboration, *Phys. Lett.* B786:59, 2018.
- [7] ATLAS Collaboration, *JHEP*, 05:141, 2019.
- [8] ATLAS Collaboration, CERN-EP-2019-038, submitted to *Phys. Lett. B*, 2019.
- [9] ATLAS Collaboration, ATLAS-CONF-2019-004, <http://cds.cern.ch/record/2668103>, 2019.

CMS Higgs physics results

M. Flechl *on behalf of the CMS collaboration*
Institute of High-Energy Physics, Austrian Academy of Sciences,
Nikolsdorfer Gasse 18, 1220 Vienna, Austria



Recent results of searches for Higgs bosons by the CMS collaboration are presented. These consist of searches for rare Higgs boson decays, searches for additional neutral Higgs bosons, and searches for charged Higgs bosons.

1 Introduction

A Higgs boson with a mass of about 125 GeV has been discovered by the ATLAS and CMS collaborations in 2012^{1,2,3}. Since then, the amount of analyzed data has significantly increased and the analysis methods have been adapted, either for measuring Higgs boson properties or for searching for additional Higgs bosons considering the information we have about the discovered Higgs boson, H-125, in particular its mass. So far, all measurements are in agreement with the standard model (SM) hypothesis; however, the sensitivity to many beyond-the-SM (BSM) scenarios is still very patchy and the analysis of the full LHC Run 2 data as well as of following run periods will be needed to test them. In addition to collecting more data, new final states are being probed and provide additional handles on BSM physics. Those include adding measurements of rare H-125 boson decay modes and adding searches for additional neutral and charged Higgs bosons in decay modes not investigated previously.

This articles summarizes the results of CMS⁴ searches for rare Higgs boson decay modes, including Higgs boson decays to invisible particles, Higgs boson decays to mesons and to light pseudoscalars; searches for additional neutral Higgs bosons (scalar H or pseudoscalar A) in decays to a top quark pair or to ZH, and charged Higgs boson decays to $\tau\nu$, tb, and AW.

2 Rare Higgs decays

2.1 Higgs boson production with a top quark pair and decay to invisible particles

First bounds on Higgs boson decays to invisible particles in a topology with two top quarks (ttH) are obtained by reinterpreting searches for scalar top quarks in the 0-lepton (0L), 1-lepton (1L) and 2-lepton (2L) channels. The final state in all cases consists of a varying amount of leptons,

jets and missing transverse momentum. A combined limit of $B(H \rightarrow \text{inv}) < 0.46$ is measured (expected: 0.48)⁵, see Figure 1. This is comparable to the sensitivity in other topologies.

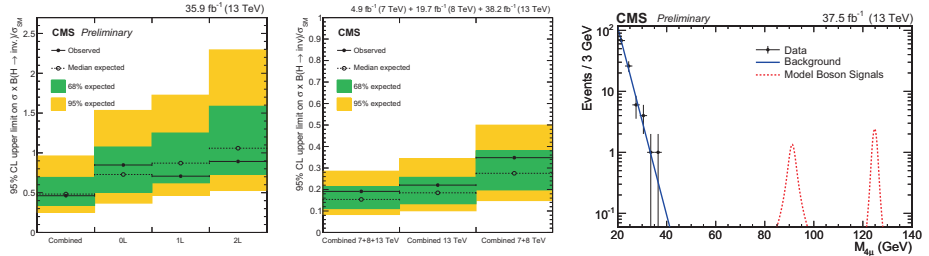


Figure 1 – Limit on the branching ratio $H \rightarrow \text{inv}$ measured in a ttH topology⁵ (left), limit on the branching ratio $H \rightarrow \text{inv}$ combining measurements in gF , VBF and VH topologies⁶ (center) and four-muon-mass distribution in the search for Higgs boson decays to $\Upsilon\Upsilon$ ⁷ (right).

2.2 Combined results for Higgs boson decays to invisible particles

The current best limit on invisible Higgs boson decays is obtained by a combination of analyses using CMS data taken during LHC Run 1 as well as in 2015 and 2016⁶. These analyses investigate the gluon fusion (gF), vector boson fusion (VBF) and V -associated production (VH). The limit is measured as $B(H \rightarrow \text{inv}) < 0.19$ (expected: 0.15) and is shown in Figure 1. Adding the LHC Run 1 data improves the sensitivity by about 5 per cent points. The results are also interpreted in the context of dark-portal models and are competitive to direct dark matter searches for dark matter masses below about 10 GeV.

2.3 Higgs boson decays to mesons

Searches for Higgs boson decays to pairs of J/Ψ or Υ mesons are almost background-free and hence their sensitivity will increase quickly with additional data. Since the SM prediction for the branching ratio to these mesons is very small (about $10^{-9} - 10^{-10}$), any beyond-the-SM enhancement like new amplitudes would be immediately discernible if it is sufficiently large. For the analyses⁷, dedicated 2- and 3-muon triggers with meson mass windows for the muon systems are used. Muons with transverse momenta above 3 GeV are considered. The four-muon mass distribution for the $\Upsilon\Upsilon$ analysis is shown in Figure 1. The measured limits are $B(H \rightarrow J\Psi J\Psi) < 1.8 \times 10^{-3}$ (expected: 1.8×10^{-3}) and $B(H \rightarrow \Upsilon\Upsilon) < 1.4 \times 10^{-3}$ (expected: 1.4×10^{-3}).

2.4 Higgs boson decays to light pseudoscalars

Searches for H -125 decays to a pair of light pseudoscalars, a_1 , are mainly motivated by scenarios with a 2-Higgs-doublet model (2HDM) and an additional singlet, for example the next-to-minimal supersymmetric extension of the SM (NMSSM). The analysis presented here⁸ studies the a_1 mass range from 4 GeV to 15 GeV and a_1 decays to a pair of tau leptons or muons which can have a sizable branching ratio in this mass range. One of the challenges is that such light a_1 mesons would be highly boosted and hence its decay products likely to geometrically overlap. The resulting limit as a function of the a_1 mass is shown in Figure 2 and improves previous CMS limits significantly beyond pure luminosity scaling, e.g. for $m_A = 8$ GeV the branching ratio limits improves from about 25% to about 3%.

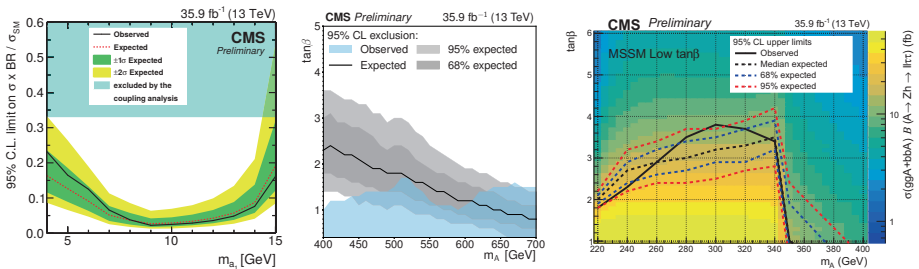


Figure 2 – Limit on Higgs boson decays to a pair of pseudoscalars⁸ (left), interpretation of the search for A/H decays to a top quark pair⁹ in the hMSSM scenario (center) and exclusion region of the A→Zh analysis in the MSSM-low-tan β scenario¹¹ (right).

3 Heavy neutral Higgs boson searches

3.1 Heavy Higgs boson decays to a top quark pair

In the minimal supersymmetric extension of the SM (MSSM), for a low value of $\tan\beta$ (the ratio of the Higgs vacuum expectation values) and a heavy Higgs boson A or H with a mass of at least twice the top quark mass, the search for Higgs boson decays to a pair of top quarks might be the only way to see additional Higgs bosons at the LHC since the branching ratio can approach unity. The main challenge for this search is the interference of the signal with SM top quark pair production which leads to a peak-dip structure of the generated Higgs boson mass spectrum (instead of just a peak at the Higgs boson mass) and requires a non-linear signal model for the interpretation. The analysis sees a slight excess/deficit combination with a local significance of 3.8σ which would be compatible with a Higgs boson of a mass of 400 GeV⁹. However, the global significance is only 2σ . This also manifests itself as a difference between expected and observed exclusion region in the interpretation of the result in the hMSSM¹⁰ scenario, see Fig. 2.

3.2 Heavy Higgs boson decays to Zh

If $\tan\beta$ is small but the pseudoscalar A is too light to decay to a pair of top quarks then the decay mode A→Zh could be dominant with a branching ratio close to unity. The analysis in the $\ell\ell\tau\tau$ final state targets primarily gluon fusion production and the 125-GeV Higgs boson in the final state¹¹. The A boson mass is estimated using a matrix-element-based estimator (SVFi¹²) which also exploits the 125-GeV constraint. The observed distributions agree well with the SM-only hypothesis and MSSM limits are set in the expected low $\tan\beta$ mass region from 220 GeV to 350 GeV, see Figure 2.

4 Charged Higgs boson searches

4.1 Charged Higgs boson decays to $\tau\nu$

Decays to $\tau\nu$ are the flagship LHC channel for the search for charged Higgs bosons, showing the highest sensitivity in the mid- and high- $\tan\beta$ regions. Three channels are combined: $\tau_{\text{had}} + \text{jets}$, $\tau_{\text{had}} + 1\ell$ and $\tau_{\text{had}} + 0\ell$ and the analysis covers the low-mass region (where $t \rightarrow bH^+$ dominates), the high-mass region ($gb \rightarrow tH^+$) and, for the first time in CMS, the intermediate region where none of the two contributions can be neglected¹³. Cross section limits for the charged Higgs boson mass range of 80 GeV – 3000 GeV are set and also interpreted in the context of the MSSM, see Figure 3.

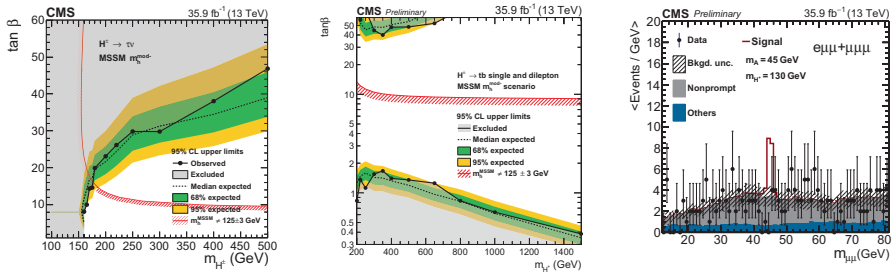


Figure 3 – For the MSSM $m_{H^\pm}^{\text{mod-}}$ scenario, the $H^+ \rightarrow \tau\nu$ exclusion region¹³ (left) and the $H^+ \rightarrow tb$ exclusion region¹⁴ (center). Dimuon mass distribution for the $H^+ \rightarrow AW$ analysis¹⁵ (right).

4.2 Charged Higgs boson decays to tb

Complementary to $\tau\nu$ decays, studying $H^+ \rightarrow tb$ is mainly motivated by MSSM scenarios with low $\tan\beta$. The analysis¹⁴ requires one or two leptons and then categorizes events by the number of jets and b-tagged jets. Machine-learning algorithms help to cover the H^+ mass range from 200 GeV to 3000 GeV. The result interpreted in the context of the MSSM is shown in Fig. 3.

4.3 Charged Higgs boson decays to AW

If $\tan\beta$ is low but H^+ are light then $H^+ \rightarrow AW$ may dominate with branching ratios close to unity. In this study¹⁵ final states with three muons or two muons and an electron are investigated, aiming at $A \rightarrow \mu\mu$ decays. The $m_{\mu\mu}$ distribution is shown in Fig. 3. Limits on the branching ratio $t \rightarrow bH^+$ from 0.6% to 2.9% are set for A boson masses from 15 GeV to 75 GeV.

5 Summary

A wealth of CMS Higgs physics results has been made public in the month prior to the workshop, tackling the SM Higgs hypothesis from two directions: precision measurements and searches for additional Higgs bosons. All results are compatible with the SM but watch out for the full LHC Run 2 results expected this year and the LHC Run 3 to follow in 2021 which will lead to sensitivities allowing to cut deeply into the parameter space of many popular BSM scenarios.

References

1. ATLAS Collaboration, *Phys. Lett. B* **716**, 1 (2012).
2. CMS Collaboration, *Phys. Lett. B* **716**, 30 (2012).
3. CMS Collaboration, *JHEP* **06**, 081 (2013).
4. CMS Collaboration, *JINST* **3** S08004 (2008).
5. CMS Collaboration, CMS-PAS-HIG-18-008, <http://cds.cern.ch/record/2668677>.
6. CMS Collaboration, arXiv:1809.05937, submitted to *Phys. Lett. B*.
7. CMS Collaboration, CMS-PAS-HIG-18-025, <http://cds.cern.ch/record/2667198>.
8. CMS Collaboration, CMS-PAS-HIG-18-006, <http://cds.cern.ch/record/2667402>.
9. CMS Collaboration, CMS-PAS-HIG-17-027, <http://cds.cern.ch/record/2668686>.
10. A. Djouadi et al, *Eur. Phys. J. C* **73**, 2650 (2013).
11. CMS Collaboration, CMS-PAS-HIG-18-023, <http://cds.cern.ch/record/2667215>.
12. L. Bianchini, *Nucl. Instrum. Methods A* **862**, 54 (2017).
13. CMS Collaboration, arXiv:1903.04560, submitted to *JHEP*.
14. CMS Collaboration, CMS-PAS-HIG-18-004, <http://cds.cern.ch/record/2667222>.
15. CMS Collaboration, CMS-PAS-HIG-18-020, <http://cds.cern.ch/record/2667217>.

THE TRANSVERSE MOMENTUM SUBTRACTION METHOD AT N³LO APPLIED TO HIGGS BOSON PRODUCTION AT THE LHC

L. CIERI

INFN, Sezione di Milano-Bicocca, Piazza della Scienza 3, I-20126 Milano, Italy



We consider the extension of the transverse-momentum (q_T) subtraction method at next-to-next-to-next-to-leading order (N³LO) in perturbative QCD. While all the q_T -subtraction ingredients at $q_T \neq 0$ are known in analytical form, the third-order collinear functions and helicity-flip functions, which contribute only at $q_T = 0$, are approximated using a prescription which uses the known result for the total Higgs boson cross section at this order. As a first application of the third-order q_T -subtraction method, we present the N³LO rapidity distribution of the Higgs boson at the LHC.

1 Introduction

Measurements at the LHC present an impressive and continuously improving quality, making even the next-to-next-to-leading order (NNLO) QCD perturbative accuracy not sufficient to match the demands of the LHC data. Processes which manifest such necessity to be computed beyond NNLO, exhibit next-to-leading order (NLO) corrections comparable in size with the leading order (LO), and where the NNLO corrections still exhibit large effects such that the size of the theoretical uncertainties remains larger than the experimental uncertainties.

This motivated a new theoretical effort to go beyond NNLO to include the next perturbative order: the next-to-next-to-next-to-leading order (N³LO). Sum rules, branching fractions¹ and deep inelastic structure functions² have been known to this order for quite some time. At present, the only hadron collider observables for which N³LO QCD corrections have been calculated are the total cross section for Higgs boson production in gluon fusion^{3,4}, $b\bar{b}$ fusion⁵, in vector boson fusion⁶ and Higgs boson pair production⁷ in vector boson fusion. Recently, first steps have been taken towards more differential observables by computing several N³LO threshold expansion terms to the Higgs boson rapidity distribution in gluon fusion^{8,9}. In addition, the projection-to-Born method has been recently extended to N³LO¹⁰ for jet production in deep inelastic scattering.

In this proceeding we present the first extension of the q_T -subtraction method¹¹ at N³LO¹² and we will apply it, to compute Higgs boson production differentially in the Higgs boson rapidity at N³LO accuracy. The proceeding is organized as follows: in Sec. 2 we recall briefly

the main ideas of the q_T -subtraction formalism and we present the necessary ingredients up to $N^3\text{LO}$, specifying which elements are known analytically and identifying the missing coefficients at $N^3\text{LO}$. Results for the $N^3\text{LO}$ Higgs boson rapidity distribution and the associated theoretical uncertainty is presented in Sec. 3. Finally, in Sec. 4 we summarize our results.

2 The q_T -subtraction formalism at $N^3\text{LO}$

We consider the inclusive hard scattering reaction

$$h_1(p_1) + h_2(p_2) \rightarrow F(\{q_i\}) + X, \quad (1)$$

where h_1 and h_2 denote the two hadrons which collide with momenta p_1 and p_2 producing the identified colourless final-state system F , accompanied by an arbitrary and undetected final state X . The colliding hadrons have centre-of-mass energy \sqrt{s} , and are treated as massless particles $s = (p_1 + p_2)^2 = 2p_1 \cdot p_2$. The observed final state F consists of a generic system of non-QCD partons composed of *one or more* colour singlet particles (such as vector bosons, photons, Higgs bosons, Drell–Yan (DY) lepton pairs and so forth) with total invariant mass M ($M^2 = q^2$), transverse momentum q_T with respect to the direction of the colliding hadrons, and rapidity in the centre-of-mass system of the hadronic collision, Y ($Y = \frac{1}{2} \ln \left(\frac{p_2 \cdot q}{p_1 \cdot q} \right)$).

Our strategy is based on the following steps: we first note that, at LO, the transverse momentum $\mathbf{q}_T = \sum_i \mathbf{q}_{Ti}$ of the triggered final state F is exactly zero. As a consequence, as long as $q_T \neq 0$, the $N^i\text{LO}$ contributions^a are actually given by the $N^{i-1}\text{LO}$ contributions to the triggered final state $F + \text{jet}(s)$.

Therefore, the cross section can be written as $d\sigma_{N^i\text{LO}}^F|_{q_T \neq 0} = d\sigma_{N^{i-1}\text{LO}}^{F+\text{jets}}$, implying that, in the limit $q_T \neq 0$, the infrared (IR) divergences in our $N^i\text{LO}$ calculation are those in $d\sigma_{N^{i-1}\text{LO}}^{F+\text{jets}}$. Since we are interested in $N^3\text{LO}$ cross sections, NNLO IR singularities can be handled and cancelled by using available NNLO formulations of subtraction methods (in our case, antenna subtraction¹³).

The only remaining singularities of $N^3\text{LO}$ type are associated to the limit $q_T \rightarrow 0$, and we treat them by an additional subtraction (q_T -subtraction method at $N^3\text{LO}$) presented in Ref. ¹².

The following sketchy presentation is illustrative; for more details, we recommend the foundational papers^{11,14,12}. We use a shorthand notation that mimics the notation of Ref. ¹⁴. We define our counter term^b as

$$d\sigma^{CT} = d\sigma_{LO}^F \otimes \Sigma^F(q_T/Q) d^2\mathbf{q}_T \quad , \quad \Sigma^F(q_T/Q) \rightarrow \sum_{n=1}^{\infty} \left(\frac{\alpha_s}{\pi} \right)^n \sum_{k=1}^{2n} \Sigma^{F(n;k)} \frac{Q^2}{q_T^2} \ln^{k-1} \frac{Q^2}{q_T^2} . \quad (2)$$

The function $\Sigma^F(q_T/Q)$ reproduces the singular behaviour of $d\sigma^{F+\text{jets}}$ in the small q_T regime. In this limit it can be expressed in terms of q_T -independent coefficients $\Sigma^{F(n;k)}$. All the single coefficient functions which are taking part in the counter term up to $N^3\text{LO}$ are known analytically, which ensures a correct and precise numerical cancellation of the IR divergencies (from real contributions) associated to the small- q_T limit. Considering the contribution at $q_T = 0$, which restores unitarity regarding total cross section, the master formula of the q_T -subtraction method is finally:

$$d\sigma_{N^i\text{LO}}^F = \mathcal{H}_{N^i\text{LO}}^F \otimes d\sigma_{LO}^F + \left[d\sigma_{N^{i-1}\text{LO}}^{F+\text{jets}} - d\sigma_{N^i\text{LO}}^{CT} \right] . \quad (3)$$

The coefficient $\mathcal{H}_{N^i\text{LO}}^F$ does not depend on q_T and it is obtained by the $N^i\text{LO}$ truncation of the perturbative function

$$\mathcal{H}^F = 1 + \frac{\alpha_s}{\pi} \mathcal{H}^{F(1)} + \left(\frac{\alpha_s}{\pi} \right)^2 \mathcal{H}^{F(2)} + \left(\frac{\alpha_s}{\pi} \right)^3 \mathcal{H}^{F(3)} + \dots . \quad (4)$$

^a $N^i\text{LO}$ stands for LO if $i = 0$, NLO if $i = 1$, NNLO for $i = 2$ and finally, $N^3\text{LO}$ for $i = 3$ obviously.

^bThe symbol \otimes understands convolutions over momentum fractions and sum over flavour indexes of partons.

At N³LO the hard–virtual functions $\mathcal{H}^{F(i)}$, with $i = 1, 2, 3$ are required by the q_T -subtraction method. The general structure of $\mathcal{H}^{F(1)}$ and $\mathcal{H}^{F(2)}$ (and their specific coefficient functions which are part of them) is explicitly known^{15,16,17,18,19}. The general structure of $\mathcal{H}^{F(3)}$ is known¹² but some of its ingredients are still missing. Nevertheless, within the q_T -subtraction formalism, all these missing coefficients can be inferred for any hard scattering process whose corresponding total cross section is known at N³LO. This point is discussed in detail in Sec. 3 of Ref.¹².

3 The rapidity distribution of the Higgs boson at N³LO

In this section we present our predictions for the Higgs boson rapidity distribution at the LHC, applying the N³LO q_T -subtraction method presented in Sec. 2 for $F = H$.

We consider Higgs boson production ($M \equiv M_H = 125$ GeV) in proton–proton collisions at a centre-of-mass energy of $\sqrt{s} = 13$ TeV in the large- m_t limit ($m_t \rightarrow \infty$). In this limit, the production of the Higgs boson is described through an effective gluon-gluon-Higgs boson vertex. Note that we systematically employ the same order in the PDFs (in particular the set PDF4LHC15_nnlo_mc²⁰) for the LO, NLO, NNLO and N³LO results presented in this proceeding. The central factorization and renormalization scale is chosen as $\mu \equiv \mu_R = \mu_F = M_H/2$. The theoretical uncertainty is estimated by varying the default scale choice independently for μ_R and μ_F by factors of $\{1/2, 2\}$ while omitting combinations with $\mu_R/\mu_F = 4$ or $1/4$, resulting in the common seven-point variation of scale combinations. The contributions $d\sigma^{H+\text{jets}}$ in Eq. 3

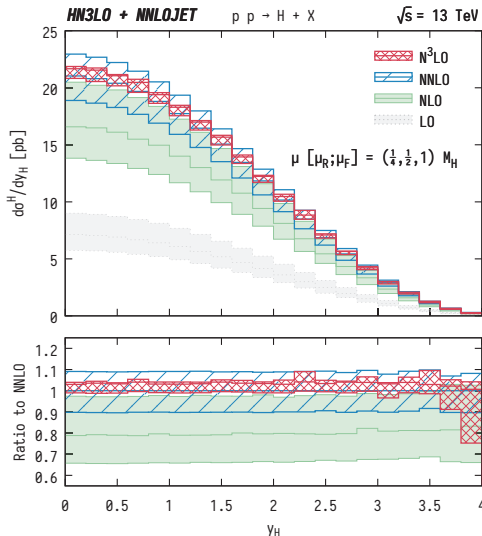


Figure 1 – Rapidity distribution of the Higgs boson computed using the q_T -subtraction formalism up to N³LO. The seven-point scale variation bands of the LO, NLO, NNLO and N³LO results are as follows: LO (pale grey fill), NLO (green fill), NNLO (blue hatched) and N³LO (red cross-hatched). The central scale ($\mu = M_H/2$) at each perturbative order (except LO) is shown with solid lines. In the lower panel, the ratio to the NNLO prediction is shown. While the bands for the predictions at LO, NLO and NNLO are computed with the seven scales as detailed in the text, the N³LO band is obtained after considering also the uncertainties due to the variation of the q_T^{int} and the $\mathcal{H}^{H(3)}$ coefficient in the N³LO-only contribution.

are computed with the parton-level event generator NNLOJET,²¹ which provides the necessary infrastructure for the antenna subtraction method up to NNLO.¹³ The contributions \mathcal{H}^H and $d\sigma^{CT}$ (in Eq. 3) are calculated using a new Monte Carlo generator HN3LO.²²

Figure 1 shows the rapidity distribution of the Higgs boson at LO (pale grey fill), NLO (green fill), NNLO (blue hatched) and N³LO (red cross-hatched). The central scale ($\mu = M_H/2$) is shown as a solid line while the bands correspond to the envelope of seven-point scale variation. At N³LO, the band additionally includes the uncertainties due to q_T^{cut} and $\mathcal{H}^{H(3)}$ as described in Sec. 4.2 of Ref. ¹² Going from LO to NNLO, the scale $\mu = M_H/2$ is always at the center of the respective scale variation band in Fig. 1. The central prediction at N³LO, on the other hand, almost coincides with the upper edge of the band, as was already observed for the total cross section ^{3,4}, see Table 2 and Fig. 3 of Ref. ¹² Figure 1 shows a substantial reduction in the size of the scale variation band at N³LO, both in the total cross section and in differential distributions. Comparing Fig. 1 with the results obtained in Ref. ⁹ we observe very good agreement between the two calculations.

4 Conclusions and outlook

In this proceeding we have presented the extension of the q_T -subtraction method at N³LO applied (for first time) to the rapidity distribution of the Higgs boson at the LHC. We calculate the y_H distribution at N³LO employing a seven-point scale variation and carefully assess systematic errors arising from different q_T^{cut} and the approximation made on $\mathcal{H}^{H(3)}$. Compared to the NNLO y_H distributions, we observe a large reduction of theory uncertainties by more than 50% at N³LO. The scale variation band at N³LO stays within the NNLO band with a flat K -factor of about 1.034 in the central rapidity region ($|y_H| \leq 3.6$). Both the systematic error analysis and the phenomenological predictions confirm that our calculations at N³LO using q_T -subtraction formalism are well under control. The approximation related to some of the coefficients functions of $\mathcal{H}^{H(3)}$ in our approach, can be easily replaced by the full analytical results once available.

References

1. K. G. Chetyrkin, J. H. Kuhn and A. Kwiatkowski, Phys. Rept. **277** (1996) 189.
2. J. A. M. Vermaseren, A. Vogt and S. Moch, Nucl. Phys. B **724** (2005) 3.
3. C. Anastasiou *et al.*, Phys. Rev. Lett. **114** (2015) 212001.
4. B. Mistlberger, JHEP **1805** (2018) 028.
5. C. Duhr, F. Dulat and B. Mistlberger, arXiv:1904.09990.
6. F. A. Dreyer and A. Karlberg, Phys. Rev. Lett. **117** (2016) 072001.
7. F. A. Dreyer and A. Karlberg, Phys. Rev. D **98** (2018) 114016 .
8. F. Dulat, B. Mistlberger and A. Pelloni, JHEP **1801** (2018) 145.
9. F. Dulat, B. Mistlberger and A. Pelloni, Phys. Rev. D **99** (2019) no.3, 034004.
10. J. Currie *et al.*, JHEP **1805** (2018) 209.
11. S. Catani and M. Grazzini, Phys. Rev. Lett. **98** (2007) 222002.
12. L. Cieri *et al.*, JHEP **1902** (2019) 096.
13. A. Gehrmann-De Ridder *et al.*, JHEP **0509** (2005) 056; A. Daleo *et al.*, JHEP **0704** (2007) 016; J. Currie *et al.*, JHEP **1304** (2013) 066.
14. G. Bozzi, S. Catani, D. de Florian and M. Grazzini, Nucl. Phys. B **737** (2006) 73.
15. D. de Florian and M. Grazzini, Nucl. Phys. B **616** (2001) 247.
16. S. Catani, D. de Florian and M. Grazzini, Nucl. Phys. B **596** (2001) 299.
17. S. Catani *et al.*, Eur. Phys. J. C **72** (2012) 2013 [Erratum-ibid. C **72** (2012) 2132].
18. S. Catani *et al.*, Eur. Phys. J. C **72** (2012) 2195.
19. S. Catani *et al.*, Nucl. Phys. B **881** (2014) 414.
20. R. D. Ball *et al.* [NNPDF Collaboration], JHEP **1504** (2015) 040.
21. X. Chen *et al.*, JHEP **1610** (2016) 066.
22. L. Cieri, In preparation.

LHC HIGGS CP SENSITIVE OBSERVABLES IN $H \rightarrow \tau^+\tau^-; \tau^\pm \rightarrow (3\pi)^\pm\nu$ AND MACHINE LEARNING BENEFITS

E. Richter-Was¹ and Z. Was²

¹ *Institute of Physics, Jagiellonian University, 30-348 Kraków, Lojasiewicza 11, Poland*

² *Speaker, Institute of Nuclear Physics, Polish Academy of Sciences, 31-342 Kraków, Radzikowskiego 152, Poland*



In phenomenological preparation for new measurements one searches for the carriers of quality signatures. Often, the first approach quantities may be difficult to measure or to provide sufficiently precise predictions for comparisons. Complexity of necessary details grow with precision. To achieve the goal one can not break the theory principles, and take into account effects which could be ignored earlier. Mixed approach where dominant effects are taken into account with intuitive even simplistic approach was developed. Non dominant corrections were controlled with the help of Monte Carlo simulations. Concept of *Optimal variables* was successfully applied for many measurements.

New techniques, like Machine Learning, offer solutions to exploit multidimensional signatures. Complementarity of these new and old approaches is studied for the example of Higgs Boson CP-parity measurements in $H \rightarrow \tau^+\tau^-$, $\tau^\pm \rightarrow \nu(3\pi)^\pm$ cascade decays.

1 Introduction

Despite multidimensional nature of high energy measurements, where big samples of events consisting of observed particles sets are analyzed, it was generally believed¹ that the best for phenomenology purposes is to construct single, one dimensional distribution which is sensitive to particular quantity of physics interest, such as coupling constants, masses or widths of the investigated particles. Very successful high precision LEP measurements² were following this approach.

Also for Higgs boson CP parity measurement such one dimensional *Optimal Variable* could have been constructed for $H \rightarrow \tau^+\tau^-$, $\tau^\pm\rho^\pm\nu$, $\rho^\pm\pi^\pm\pi^0$ cascade decay³. Simulations necessary to evaluate experimental conditions were performed with the help of τ decay Monte Carlo program TAUOLA⁶ and its **universal interface**⁷. Such measurements are feasible, but suffer because small branching fraction, the $\tau^\pm\rho^\pm\nu$ contributes only 6.5% of $H \rightarrow \tau^+\tau^-$ final states.

For this observable, there was no need to rely on reconstruction of difficult to constraint with the measurements neutrino momenta. Each τ lepton decay channel has different decay products and distinct detector response. In⁸ it was pointed, that every τ decay channel has the same

τ spin sensitivity. This requires non-detectable neutrinos to be reconstructed. What are the possible ways out? Steps in that directions were attempted already long time ago^{4,5}, but were successful only in part.

1.1 Basic formulation

Let us explain very briefly the physics context of the problem. Higgs boson Yukawa coupling expressed with the help of the scalar-pseudoscalar mixing angle ϕ reads as

$$\mathcal{L}_Y = N \bar{\tau} h (\cos \phi + i \sin \phi \gamma_5) \tau \quad (1)$$

where N denotes normalization and $\bar{\tau}$, τ spinors of the τ^+ and τ^- . The decay probability of the scalar/pseudoscalar Higgs

$$\Gamma(H/A \rightarrow \tau^+ \tau^-) \sim 1 - s_{\parallel}^{\tau^+} s_{\parallel}^{\tau^-} \pm s_{\perp}^{\tau^+} s_{\perp}^{\tau^-}, \quad (2)$$

is sensitive to the τ^{\pm} polarization vectors $s^{\tau^{\pm}}$ (defined in their rest frames). The symbols \parallel, \perp denote components parallel/transverse to the Higgs boson momentum as seen from the respective frames. When decay into $\tau^+ \tau^-$ pair is taken into account, polarization vectors s^{τ^-} are replaced with polarimetric vectors h_{\pm} representing τ^{\pm} decay matrix elements. The R matrix depicts spin state of the τ lepton pair. Formula for the most general mixed parity of $H \rightarrow \tau^+ \tau^-$ and τ^{\pm} decays can be thus expressed as

$$|M|^2 \sim 1 + h_{+}^i \cdot h_{-}^j R_{i,j}; \quad i, j = \{x, y, z\}. \quad (3)$$

In notation of Ref.⁹, the corresponding CP sensitive spin weight wt is rather simple:

$$wt = 1 - h_{+}^z h_{-}^z + h_{+}^{\perp} R(2\phi) h_{-}^{\perp}. \quad (4)$$

The formula is valid for h_{\pm} defined in τ^{\pm} rest-frames. The $R(2\phi)$ denote the 2ϕ angle rotation matrix around the z direction: $R_{xx} = R_{yy} = \cos 2\phi$, $R_{xy} = -R_{yx} = \sin 2\phi$. The τ^{\pm} decay polarimetric vectors h_{+}^i, h_{-}^j , in the simplest case of $\tau^{\pm} \rightarrow \pi^{\pm} \pi^0 \nu$ decay read

$$h_{\pm}^i = \mathcal{N} \left(2(q \cdot p_{\nu}) q^i - q^2 p_{\nu}^i \right), \quad (5)$$

where 4-momenta of τ decay products π^{\pm}, π^0 and ν_{τ} are denoted respectively as $p_{\pi^{\pm}}, p_{\pi^0}, p_{\nu}$. The $q = p_{\pi^{\pm}} - p_{\pi^0}$. Obviously, complete CP sensitivity can be extracted only if p_{ν} is controlled.

1.2 The τ decay channel independent features.

Note that spin weight (4), is a simple trigonometric polynomial in Higgs CP parity mixing angle ϕ . This observation is valid for all τ decay channels and that opens possibility for studies, where all effort on experimental reconstruction is concentrated on measurement of the polarimetric vectors h_i . Final analysis of observable significance rely on (4). Such a path was already followed, for CMS experiment. Preliminary effort was presented already at 2018 τ -lepton conference¹⁰. The general principle is of course much older, see eg.⁴ and was revisited in¹¹.

1.3 Multi dimensional nature of the signatures.

In³ to control parity of the Higgs boson use of the acoplanarity angle was proposed. Such a definition for $\tau^{\pm} \rightarrow \nu \pi^{\pm} \pi^0$ rely on directly observable four-momenta, see Fig. 1, only. The distributions were clearly distinct for scalar and mixed parity Higgs, see Fig. 2. To achieve sensitivity the events had to be separated to two groups accordingly to the sign of the product $y_1 y_2$, where

$$y_1 = \frac{E_{\pi^+} - E_{\pi^0}}{E_{\pi^+} + E_{\pi^0}}, \quad y_2 = \frac{E_{\pi^-} - E_{\pi^0}}{E_{\pi^-} + E_{\pi^0}}. \quad (6)$$

All pion energies could be taken in laboratory frame. The reason for $y_{1,2}$ choice were the τ decay matrix element properties.

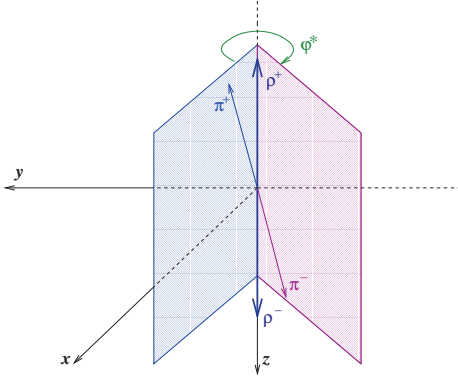


Figure 1 – Definition of acoplanarity angle φ^* in $\rho^+\rho^-$ pair rest-frame by galf-planes spanned over momenta of each ρ visible decay products. In case of $\tau^\pm \rightarrow (3\pi)^\pm\nu$ four such planes can be defined and thus number of possible acoplanarity angles increases to four (or sixteen if both τ^\pm decay to 3π).

1.4 Toward other decay modes

Even though formally distributions of Fig. 2 are one dimensional they require selection with sign of the $y_1 \cdot y_2$ product. In fact, already in the presented above case, minor improvement can be achieved if the statistical analysis of the 3-dimensional distribution over acoplanarity supplemented with y_1 and y_2 is studied. This necessity to study multidimensional distribution

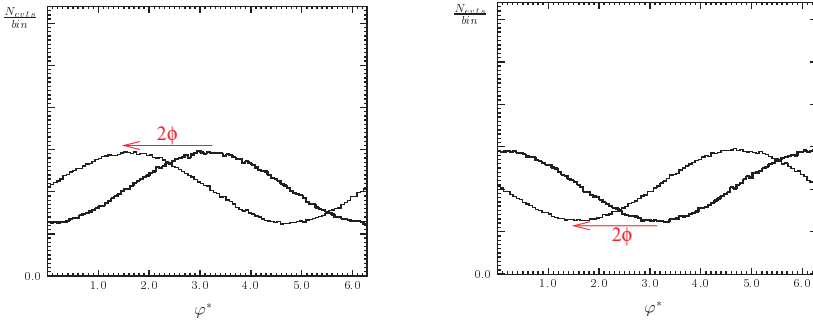


Figure 2 – Distribution of acoplanarity angle φ^* for ρ^+ and ρ^- decay products planes, defined in $\rho^+\rho^-$ pair rest frame, selection on the sign of $y_1 \cdot y_2$ is used, cases of scalar and mixed scalar-pseudoscalar cases are compared.

become even more profound if one turn attention to τ decays with 3 pions in final state. Then not only one plane can be span over the visible decay products, but four, corresponding to intermediate a_1 or ρ decays. Indeed, each of such planes provide some sensitivity to Higgs CP, as it can be seen from Fig. 3, taken from Ref. ¹³. For each plane pair analogous to eq. (6) selections would need to be studied. Each such distribution is of rather minor sensitivity to CP and also because of correlations, such an approach become challenging from the point of view of statistical analysis.

We have used Machine Learning (ML) techniques available as explained in ¹². Results of Table 1 taken from Ref. ¹³ are encouraging, they were stable with respect to inclusion of some approximated detector smearing ¹⁴ see Table 2. Statistical uncertainties were derived from a bootstrap method. Systematic uncertainty was calculated with the method also described in ¹⁴. We played later, in Ref. ¹⁵ with several options of inputs, where so called expert variables, like our acoplanarity angles were used or not. Depending on the ML variants, the performance varied. Sometimes sensitivity was completely absent. In general, structures present in the

Table 1: The ML performance for discrimination between scalar and pseudoscalar Higgs CP state. The 4-momenta of hadronic decay products are used only.

Line content	Channel: $\rho^\pm - \rho^\mp$ $\rho^\pm \rightarrow \pi^\pm \pi^0$	Channel: $a_1^\pm - \rho^\mp$ $a_1^\pm \rightarrow \rho^0 \pi^\pm, \rho^0 \rightarrow \pi^+ \pi^-$ $\rho^0 \rightarrow \pi^+ \pi^-$	Channel: $a_1^\pm - a_1^\mp$ $a_1^\pm \rightarrow \rho^0 \pi^\pm, \rho^0 \rightarrow \pi^+ \pi^-$
Fraction of $H \rightarrow \tau\tau$	6.5%	4.6%	0.8%
Number of features	24	32	48
True (oracle) classification	0.782	0.782	0.782
ML classification	0.638	0.590	0.557

Table 2: Area Under Curve for Neural Network (NN) trained to separate scalar and pseudoscalar hypotheses with combinations of input features marked with a \checkmark . Results in the column labeled “Exact” are from NNs trained with exact data. The results in column labeled “Smearred” are from NNs trained with smeared data.

Features				Exact \pm (stat)	Smearred \pm (stat) \pm (syst)	From Ref. ¹³
ϕ^*	4-vec	y_i	m_i			
$a_1 - \rho$ Decays						
\checkmark	\checkmark	\checkmark	\checkmark	0.6035 ± 0.0005	$0.5923 \pm 0.0005 \pm 0.0002$	0.596
\checkmark	\checkmark	\checkmark	-	0.5965 ± 0.0005	$0.5889 \pm 0.0005 \pm 0.0002$	-
\checkmark	\checkmark	-	\checkmark	0.6037 ± 0.0005	$0.5933 \pm 0.0005 \pm 0.0003$	-
-	\checkmark	-	-	0.5971 ± 0.0005	$0.5892 \pm 0.0005 \pm 0.0002$	0.590
\checkmark	\checkmark	-	-	0.5971 ± 0.0005	$0.5893 \pm 0.0005 \pm 0.0002$	0.594
\checkmark	-	\checkmark	\checkmark	0.5927 ± 0.0005	$0.5847 \pm 0.0005 \pm 0.0002$	0.578
\checkmark	-	\checkmark	-	0.5819 ± 0.0005	$0.5746 \pm 0.0005 \pm 0.0002$	0.569
$a_1 - a_1$ Decays						
\checkmark	\checkmark	\checkmark	\checkmark	0.5669 ± 0.0004	$0.5657 \pm 0.0004 \pm 0.0001$	0.573
\checkmark	\checkmark	\checkmark	-	0.5596 ± 0.0004	$0.5599 \pm 0.0004 \pm 0.0001$	-
\checkmark	\checkmark	-	\checkmark	0.5677 ± 0.0004	$0.5661 \pm 0.0004 \pm 0.0001$	-
-	\checkmark	-	-	0.5654 ± 0.0004	$0.5641 \pm 0.0004 \pm 0.0001$	0.553
\checkmark	\checkmark	-	-	0.5623 ± 0.0004	$0.5615 \pm 0.0004 \pm 0.0001$	0.573
\checkmark	-	\checkmark	\checkmark	0.5469 ± 0.0004	$0.5466 \pm 0.0004 \pm 0.0001$	0.548
\checkmark	-	\checkmark	-	0.5369 ± 0.0004	$0.5374 \pm 0.0004 \pm 0.0001$	0.536

data, which were of polynomial nature were easy to recognize, but the one related to boosts, especially strongly relativistic boosts, especially when rotatory symmetries had to be identified where challenging for the ML algorithms.

2 Conclusions

In our studies we could observe that ML solutions were helpful for significance evaluation in case of Higgs CP signatures in $H \rightarrow \tau\tau$ channel. Massively multi-dimensional signatures could have been controlled. We have identified that features which are related to multi-scale nature of resonance decays of masses ranging from Higgs of 125 GeV to ρ meson of 0.7 GeV were a challenge for ML. General purpose algorithms such as of Refs. ^{16,17,18} required such adjustment. It was enough to boost and rotate input four momenta to appropriate frames, then use of expert variables was not necessary. On the other hand, solutions, like studied and developed in ¹⁹ which are Lorentz group structure savvy may not need such pre-conditioning. ML techniques were useful for phenomenology of Higgs CP in $\tau\tau$ decay channel. For the reversed perspective, the signatures offered good investigation ground for ML algorithms. The case was suitable for such studies, because Matrix Elements are available for event weight calculation. Analytic dependence of weights for Higgs CP dependent part is clear. Studies may be thus of broader than just Higgs CP interest.

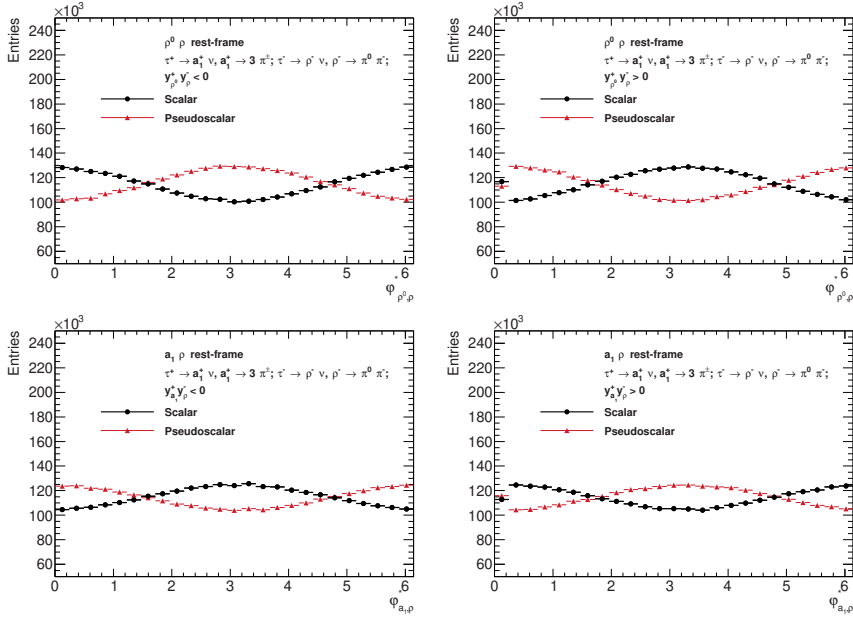


Figure 3 – Acoplanarity angles of oriented half decay planes: $\varphi_{\rho^0\rho}^*$ (top), $\varphi_{a_1\rho}^*$ (bottom), for events grouped by the sign of $y_{\rho^0}^+ y_{\rho^0}^-$ and $y_{a_1}^+ y_{\rho^0}^-$ respectively.

On the other hand, even though ML solutions may seem as panacea for all optimization, one should not ignore Optimal Variables approach, which is not only useful to indicate which experimental features are most important for future sensitivity improvements but also provide essential benchmarks. For example, if ML improvements are surprisingly promising, this may indicate that some technical imperfections of Monte Carlo simulations differ e.g. between simulations for signal and background, thus contributing inappropriately to classification.

Acknowledgments

This project was supported in part from funds of Polish National Science Centre under decision DEC-2017/27/B/ST2/01391.

References

1. M. Davier, L. Dufnot, F. Le Diberder and A. Rouge, *Phys. Lett. B* **306**, 411 (1993).
2. S. Schael *et al.* [ALEPH and DELPHI and L3 and OPAL and SLD Collaborations and LEP Electroweak Working Group and SLD Electroweak Group and SLD Heavy Flavour Group], *Phys. Rept.* **427** (2006) 257
3. G. R. Bower, T. Pierzchala, Z. Was and M. Worek, *Phys. Lett. B* **543** (2002) 227.
4. A. Rouge, *Phys. Lett.* **B619** (2005) 43–49, [hep-ex/0505014](#).
5. K. Desch, Z. Was, and M. Worek, *Eur. Phys. J.* **C29** (2003) 491–496, [hep-ph/0302046](#).
6. S. Jadach, Z. Was, R. Decker and J. H. Kuhn, *Comput. Phys. Commun.* **76** (1993) 361.
7. N. Davidson, G. Nanava, T. Przedzinski, E. Richter-Was and Z. Was, *Comput. Phys. Commun.* **183** (2012) 821 doi:10.1016/j.cpc.2011.12.009 [arXiv:1002.0543 [hep-ph]].

8. J. H. Kuhn, *Phys. Rev. D* **52** (1995) 3128 doi:10.1103/PhysRevD.52.3128.
9. K. Desch, A. Imhof, Z. Was and M. Worek, *Phys. Lett. B* **579** (2004) 157.
10. V. Cherepanov, E. Richter-Was and Z. Was, *SciPost Phys. Proc.* **1** (2019) 018 doi:10.21468/SciPostPhysProc.1.018 [arXiv:1811.03969 [hep-ph]].
11. S. Berge, W. Bernreuther and S. Kirchner, *Phys. Rev. D* **92** (2015) 096012.
12. I. Goodfellow, Y. Bengio, and A. Courville, *Deep learning*. MIT Press, Cambridge, MA, 2017.
13. R. Jozefowicz, E. Richter-Was and Z. Was, *Phys. Rev. D* **94** (2016) no.9, 093001 doi:10.1103/PhysRevD.94.093001 [arXiv:1608.02609 [hep-ph]].
14. E. Barberio, B. Le, E. Richter-Was, Z. Was, D. Zanzi and J. Zaremba, *Phys. Rev. D* **96** (2017) 073002,
15. K. Lasocha, E. Richter-Was, D. Tracz, Z. Was and P. Winkowska, arXiv:1812.08140.
16. T. Chen and C. Guestrin, 1603.02754.
17. L. Breiman, *Machine Learning* **45** (2001), no. 1 5-32.
18. A. Bevan, R. Goni, and T. Stevenson, *J. Phys. Conf. Ser.* **898** (2017), no. 7 072021, 1702.04686.
19. M. Erdmann, E. Geiser, Y. Rath and M. Rieger, arXiv:1812.09722 [hep-ex].

Constraining the MSSM Higgs sector using precise Higgs mass predictions

Henning Bahl

*DESY, Notkestraße 85,
D-22607 Hamburg, Germany*

Different approaches are used for the calculation of the SM-like Higgs boson mass in the MSSM: the fixed-order diagrammatic approach is accurate for low SUSY scales; the EFT approach, for high SUSY scales. Hybrid approaches, combining fixed-order and EFT calculations, allow to obtain a precise prediction also for intermediary SUSY scales. Here, we briefly discuss the hybrid approach implemented into the code `FeynHiggs`. In addition, we show how the refined Higgs mass prediction was used to define new MSSM Higgs benchmark scenarios.

1 Introduction

It is a special feature of the MSSM that it allows to predict the mass of the SM-like Higgs boson, M_h , in terms of the model parameters. At the tree-level, it is determined by only two non-SM parameters, conventionally chosen to be the mass of the \mathcal{CP} -odd Higgs boson A , M_A , and the ratio of the vacuum expectation values of the two Higgs doublets, $\tan\beta$. Loop corrections, depending also on the parameters of other sectors, lead to a significant upwards shift of the tree-level value.

Currently, there are three different approaches for the calculation of the quantum corrections. In the most straightforward fixed-order approach, corrections to the Higgs self-energies are evaluated by calculating Feynman diagrams at a specific order in the full MSSM. This approach has the advantage that all terms at a specific order are incorporated. In case of a large hierarchy between the electroweak and the SUSY scale, however, large logarithms appear in the calculation exacerbating the convergence of the perturbative series. These logarithms can be resummed in the effective field theory (EFT) approach. In its simplest form all SUSY particles are integrated out at a single scale such that below this SUSY scale the SM is recovered as EFT. Matching conditions at the SUSY scale fix the SM Higgs self-coupling. RGE running down to the electroweak scale, where the physical Higgs mass is calculated, corresponds to a resummation of large logarithms. Due to this resummation, the EFT approach is precise for high SUSY scales. Typically, no higher dimensional operators are included in the EFT below the SUSY scale. Therefore, terms suppressed by the SUSY scale are neglected. Thus, the EFT calculation loses its accuracy in case of a low SUSY scale.

To obtain a precise prediction also for intermediary SUSY scales, the diagrammatic and the EFT approach can be combined.^{1–8} Here, we will discuss the hybrid approach implemented into the publicly available code `FeynHiggs`.^{1,2,5,9–14} Afterwards, we show how this calculation has been used to define new MSSM Higgs benchmark scenarios.^{15,16}

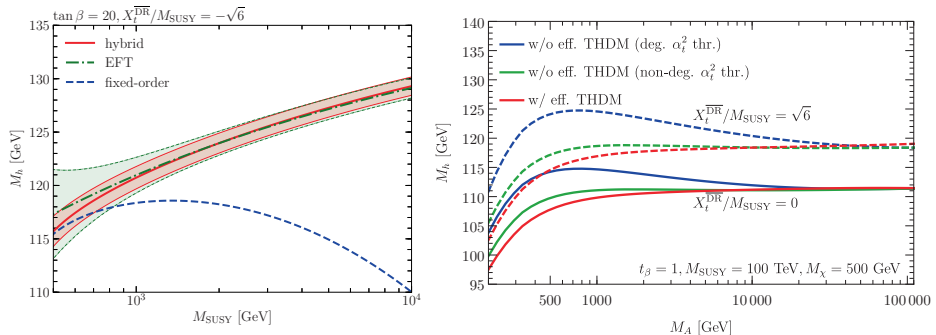


Figure 1 – Left: Results of the hybrid approach (red solid), the EFT approach (green dot-dashed) and the fixed-order approach (blue dashed) for the mass of the SM-like Higgs boson, M_h , in dependence of the SUSY scale, M_{SUSY} . The colored bands depict the associated estimate of the remaining theoretical uncertainties. Right: Results of the hybrid approach for M_h in dependence of M_A . As EFT below the SUSY scale, we use either the THDM (red) or the SM, employing degenerate (blue) or non-degenerate (green) threshold corrections. The results are shown for $X_t^{\text{DR}}/M_{\text{SUSY}} = 0$ (solid) and $X_t^{\text{DR}}/M_{\text{SUSY}} = \sqrt{6}$ (solid).

2 Calculating the SM-like Higgs boson mass

The result of the fixed-order (FO) approach are the renormalized Higgs self-energies in the full MSSM. We denote the self-energy of the SM-like Higgs boson by $\hat{\Sigma}_{hh}^{\text{FO}}(p^2)$, where p^2 is the external momentum. The result of the EFT approach is encoded in the SM Higgs tree-level mass, $2\lambda(M_t)v^2$, which is obtained in terms of the SM Higgs self-coupling λ evaluated at the electroweak scale multiplied with the SM Higgs vacuum expectation value, v .

The basic idea of the hybrid approach implemented in `FeynHiggs` is to add the non-logarithmic terms of the fixed-order result (including all terms suppressed by the SUSY scale) and the resummed logarithms obtained in the EFT approach,

$$\hat{\Sigma}_{hh}^{\text{hybrid}}(p^2) = \hat{\Sigma}_{hh}^{\text{FO}}(p^2) \Big|_{\text{non-log}} - 2\lambda(M_t)v^2 \Big|_{\text{log}}. \quad (1)$$

We obtain the non-logarithmic terms of the Higgs self-energy by subtracting all contained logarithms; and the logarithmic terms of the EFT result, by subtracting all contained non-logarithmic terms. This improved self-energy is then used to obtain the physical Higgs mass by solving the Higgs pole equation within the full MSSM.

In this way, the final result for the physical result for the SM-like Higgs boson mass includes all logarithms resummed in the EFT approach as well as all suppressed terms contained in the fixed-order approach. Therefore, the result of the hybrid approach should approach the fixed-order result for low SUSY scales and the EFT result for high SUSY scales. This is shown in the left plot of Fig. 1 depicting a simplified scenario with the masses of all non-SM particles fixed to the SUSY scale setting the stop mixing parameter $X_t^{\text{DR}} = -\sqrt{6}M_{\text{SUSY}}$ and $\tan\beta = 20$. For low SUSY scales, where terms suppressed by the SUSY scale are relevant, the hybrid approach is in good agreement with the fixed-order result, whereas the EFT result, which does not include suppressed terms, yields a larger result for M_h . For large SUSY scales, where the EFT approach is precise, the hybrid approach and the EFT approach are in good agreement, whereas the fixed-order calculation yields a much lower result. The theoretical uncertainty estimate for the hybrid result¹⁷ is smaller or equal in size as the estimate for the EFT calculation.

So far, we have only considered the simple case of the SM as EFT below the SUSY scale. This choice is not appropriate if some of the non-SM particles are much lighter than the SUSY scale. We study the case of light non-SM like Higgs bosons in the right plot of Fig. 1 choosing

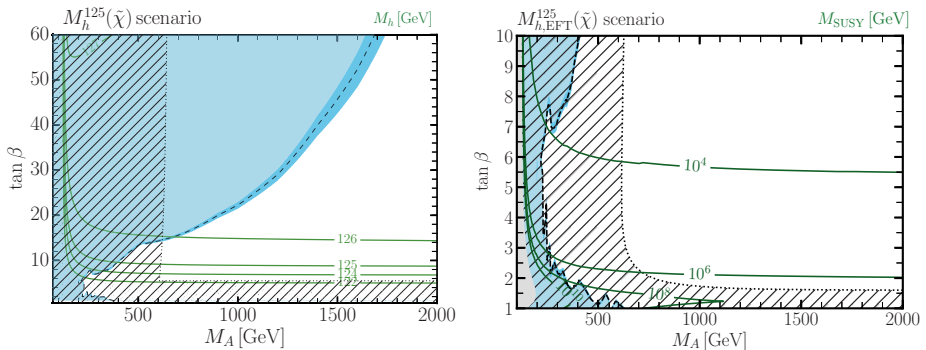


Figure 2 – Left: The $M_h^{125}(\tilde{\chi})$ scenario shown in the $(M_A, \tan\beta)$ plane. The blue region indicates the area excluded by searches for additional Higgs bosons; the hashed region, the area excluded by measuring the properties of the SM-like Higgs boson. The green contours indicate the mass of the SM-like Higgs boson. Right: Same as left plot for the $M_{h,\text{EFT}}^{125}(\tilde{\chi})$ scenario, but the green contours indicate the required SUSY scale. In the grey area, $M_h \sim 125$ GeV can not be reached without raising M_{SUSY} above the upper limit of 10^{16} GeV.

$M_{\text{SUSY}} = 100$ TeV, $\tan\beta = 1$ (the electroweakino mass scale, $M_{\tilde{\chi}}$, is set to 500 GeV). For both considered values of the stop mixing parameter, the use of the THDM, with added electroweakinos,⁷ amounts to a downwards shift of ~ 2 GeV in comparison to the calculation employing the SM as EFT if $M_A \ll M_{\text{SUSY}}$. If in the SM case, M_A is set equal to M_{SUSY} in the two-loop threshold correction for λ controlled by the top Yukawa coupling, this shift is enlarged to up to 8 GeV. If $M_A \sim M_{\text{SUSY}}$, the different calculations are as expected in good agreement.

3 Higgs benchmark scenarios

The large number of free parameters in the MSSM prevents an easy interpretation of the measured properties of the SM-like Higgs boson as well as searches for additional Higgs bosons. Therefore, Higgs benchmark scenarios have been developed. In these scenarios, only two parameters are varied, typically chosen to be M_A and $\tan\beta$. The other parameters are fixed such that one of the Higgs bosons is SM-like with each scenario featuring a distinct Higgs phenomenology. The progress achieved in the calculation of the SM-like Higgs boson mass, including the methods presented in Section 2, ruled out almost the whole parameter space of the original benchmark scenarios.^{18–22} Therefore, new benchmark scenarios were proposed^{15,16} using the most recent version of **FeynHiggs** (Higgs masses and branching ratios), **SusHi**^{23,24} (Higgs production cross-sections), **HiggsBounds**^{25–28} (searches for additional Higgs boson) and **HiggsSignals**²⁹ (properties of the SM-like Higgs boson).

In Fig. 2, we show the $M_h^{125}(\tilde{\chi})$ (left plot) and the $M_{h,\text{EFT}}^{125}(\tilde{\chi})$ (right plot) scenarios as examples. Both scenarios feature light electroweakinos with masses ~ 200 GeV. The masses of the other SUSY particles are chosen above the TeV scale. In the $M_h^{125}(\tilde{\chi})$ scenario the stop mass scale is fixed to 1.5 TeV. Therefore, the mass of the SM-like Higgs boson is too low for $\tan\beta \lesssim 6$. This parameter space is reopened in the $M_{h,\text{EFT}}^{125}(\tilde{\chi})$ scenario by adjusting M_{SUSY} at every point in the plane such that $M_h \sim 125$ GeV (with an upper limit of 10^{16} GeV).

In both scenarios, the measurements of the Higgs signal strengths lead to a lower limit for M_A of ~ 600 GeV. In the $M_h^{125}(\tilde{\chi})$ scenario the lower limit on M_A increase with raising $\tan\beta$ due to constraints from direct searches for neutral heavy Higgs bosons decaying to a pair of tau leptons. This decay mode is irrelevant in the $M_{h,\text{EFT}}^{125}(\tilde{\chi})$ scenario. In this scenario, however, the presence of light charginos leads to an enhancement of the SM-like Higgs to $\gamma\gamma$ decay for low $\tan\beta$ allowing to exclude the region of $\tan\beta \lesssim 1.5$.

4 Conclusion

We discussed how the fixed-order and EFT approaches for the calculation of the SM-like MSSM Higgs boson mass can be combined. The resulting hybrid approach allows a precise prediction of the Higgs boson mass for low, intermediary and high SUSY scales. In addition, we showed how the improved calculation was used as an important constrain for the definition of new MSSM Higgs benchmark scenarios.

References

1. T. Hahn, S. Heinemeyer, W. Hollik, H. Rzehak and G. Weiglein, *Phys. Rev. Lett.* **112** (2014) no.14, 141801
2. H. Bahl and W. Hollik, *Eur. Phys. J. C* **76** (2016) no.9, 499
3. P. Athron, J. h. Park, T. Steudtner, D. Stöckinger and A. Voigt, *JHEP* **1701** (2017) 079
4. F. Staub and W. Porod, *Eur. Phys. J. C* **77** (2017) no.5, 338
5. H. Bahl, S. Heinemeyer, W. Hollik and G. Weiglein, *Eur. Phys. J. C* **78** (2018) no.1, 57
6. P. Athron, M. Bach, D. Harries, T. Kwasnitza, J. h. Park, D. Stöckinger, A. Voigt and J. Ziebell, *Comput. Phys. Commun.* **230** (2018) 145
7. H. Bahl and W. Hollik, *JHEP* **1807** (2018) 182
8. H. Bahl, *JHEP* **1902** (2019) 121
9. S. Heinemeyer, W. Hollik and G. Weiglein, *Comput. Phys. Commun.* **124** (2000) 76
10. S. Heinemeyer, W. Hollik and G. Weiglein, *Eur. Phys. J. C* **9** (1999) 343
11. G. Degrassi, S. Heinemeyer, W. Hollik, P. Slavich and G. Weiglein, *Eur. Phys. J. C* **28** (2003) 133
12. M. Frank, T. Hahn, S. Heinemeyer, W. Hollik, H. Rzehak and G. Weiglein, *JHEP* **0702** (2007) 047
13. T. Hahn, S. Heinemeyer, W. Hollik, H. Rzehak and G. Weiglein, *Comput. Phys. Commun.* **180** (2009) 1426 *Eur. Phys. J. C* **76** (2016) no.9, 499
14. H. Bahl, T. Hahn, S. Heinemeyer, W. Hollik, S. Paßehr, H. Rzehak and G. Weiglein, [arXiv:1811.09073 \[hep-ph\]](https://arxiv.org/abs/1811.09073)
15. H. Bahl *et al.*, [arXiv:1808.07542 \[hep-ph\]](https://arxiv.org/abs/1808.07542).
16. H. Bahl, S. Liebler and T. Stefaniak, *Eur. Phys. J. C* **79** (2019) no.3, 279
17. H. Bahl, S. Heinemeyer, W. Hollik and G. Weiglein, DESY-19-083
18. M. Carena, S. Heinemeyer, C. E. M. Wagner and G. Weiglein, [hep-ph/9912223](https://arxiv.org/abs/hep-ph/9912223)
19. M. Carena, S. Heinemeyer, C. E. M. Wagner and G. Weiglein, *Eur. Phys. J. C* **26** (2003) 601
20. M. Carena, J. R. Ellis, A. Pilaftsis and C. E. M. Wagner, *Phys. Lett. B* **495** (2000) 155
21. M. Carena, S. Heinemeyer, O. Stål, C. E. M. Wagner and G. Weiglein, *Eur. Phys. J. C* **73** (2013) no.9, 2552
22. M. Carena, J. Ellis, J. S. Lee, A. Pilaftsis and C. E. M. Wagner, *JHEP* **1602** (2016) 123
23. R. V. Harlander, S. Liebler and H. Mantler, *Comput. Phys. Commun.* **184** (2013) 1605
24. R. V. Harlander, S. Liebler and H. Mantler, *Comput. Phys. Commun.* **212** (2017) 239
25. P. Bechtle, O. Brein, S. Heinemeyer, G. Weiglein and K. E. Williams, *Comput. Phys. Commun.* **181** (2010) 138
26. P. Bechtle, O. Brein, S. Heinemeyer, G. Weiglein and K. E. Williams, *Comput. Phys. Commun.* **182** (2011) 2605
27. P. Bechtle, O. Brein, S. Heinemeyer, O. Stål, T. Stefaniak, G. Weiglein and K. E. Williams, *Eur. Phys. J. C* **74** (2014) no.3, 2693
28. P. Bechtle, S. Heinemeyer, O. Stal, T. Stefaniak and G. Weiglein, *Eur. Phys. J. C* **75** (2015) no.9, 421
29. P. Bechtle, S. Heinemeyer, O. Stål, T. Stefaniak and G. Weiglein, *Eur. Phys. J. C* **74** (2014) no.2, 2711

Higgs boson production in partonic and electromagnetic interactions with heavy ions

David d'Enterria

CERN, EP Department, CH-1211 Geneva 23, Switzerland



Higgs boson production in partonic and electromagnetic (photon-photon) interactions of light- and heavy-ions (A-A) at the LHC and future colliders is summarized. Parton-induced cross sections –including gluon-gluon, vector-boson fusion, and associated W, Z, t processes– are computed at NNLO with MCFM 8.0 using nuclear parton distribution functions. Photon-photon cross sections are computed with MADGRAPH 5.0 for ultraperipheral A-A interactions with both ions surviving the collision. In the center-of-mass energy range $\sqrt{s_{NN}} \approx 5\text{--}100$ TeV, the ratio of electromagnetic-to-partonic Higgs cross sections, $R_{\text{e.m./parton}} \approx 10^{-5}\text{--}10^{-4}$, is 10–100 larger than in p-p collisions thanks to the strong nuclear coherent γ fluxes. The feasibility of Higgs boson measurements at LHC, HE-LHC, and FCC, in the most-favourable $H \rightarrow \gamma\gamma, b\bar{b}$ decay channels in partonic and e.m. interactions respectively, is determined taking into account standard acceptance and efficiency losses on the final states, plus selection criteria to minimize the respective continuum backgrounds. Whereas 3σ evidence for partonic and e.m. Higgs production require about $\times 35$ and $\times 200$ ($\times 7$ and $\times 30$) larger integrated luminosities than those expected for a nominal 1-month run at the LHC (HE-LHC), a 5σ observation of both production modes is warranted in just one month at the FCC.

1 Introduction

The Higgs boson remains unobserved in heavy-ion collisions at the LHC due to the lower center-of-mass (c.m.) energies, as well as integrated luminosities (\mathcal{L}_{int}), in A-A compared to p-p collisions. Three planned or proposed CERN future hadron colliders: the high-luminosity LHC (HL-LHC)¹, high-energy LHC (HE-LHC)^{1,2}, and Future Circular Collider (FCC)³, will noticeably increase the available c.m. energies and \mathcal{L}_{int} values, thereby making the observation of the scalar boson potentially feasible in nuclear collisions. The motivations for such a measurement are twofold. First, when produced in standard parton-induced processes, the H boson can be used to probe the properties of the quark-gluon plasma produced in A-A collisions⁴ (although this possibility has been challenged in Ref.⁵). Secondly, the Higgs boson can also be exclusively produced via $A\text{-}A \xrightarrow{\gamma\gamma} (A)H(A)$ in ultraperipheral heavy-ion collisions (UPCs) where the ions survive their electromagnetic (e.m.) interaction. This latter unique production mode exploits the huge e.m. fields generated by the collective action of Z individual proton charges, leading to photon-photon cross sections enhanced by up to factors $Z^4 \approx 5 \cdot 10^7$, for Pb-Pb, compared to

proton or e^\pm beams⁶. The UPC production provides an independent measurement of (i) the $H\text{-}\gamma$ coupling not based on Higgs decays but on s -channel production, and (ii) the total Higgs width by combining it with the LHC diphoton decay branching ratio, via $\Gamma_H^{\text{tot}} = \Gamma(H \rightarrow \gamma\gamma)/\mathcal{B}(H \rightarrow \gamma\gamma)$ ⁷.

The parton-initiated cross sections –including gluon-gluon, vector-boson fusion, and associated W, Z, t processes– have been studied for A-A collisions at the LHC and FCC in Ref.⁸, including their expected yields after analysis cuts in the cleanest $H \rightarrow \gamma\gamma$ decay. The Higgs UPC-production was first considered 30 years ago⁹, and detailed studies of the dominant $H \rightarrow b\bar{b}$ decay channel, including realistic acceptance and efficiencies for signal and $\gamma\gamma \rightarrow b\bar{b}$ continuum background presented in Refs.¹⁰ for LHC, HE-LHC, and FCC. This work here extends previous studies by including also light-ion collisions, and compares the results of both production modes.

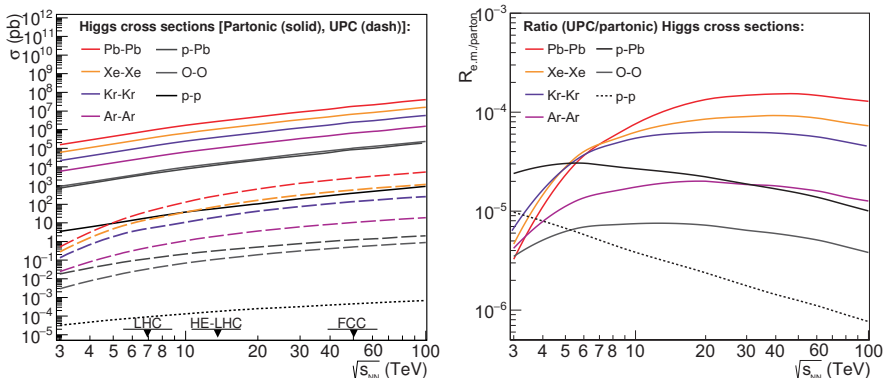


Figure 1 – Partonic (solid) and e.m. (dashed) Higgs cross sections (left) and their ratio (right) in Pb-Pb, Xe-Xe, Kr-Kr, Ar-Ar, O-O, p-Pb, and p-p collisions as a function of c.m. energy over $\sqrt{s_{\text{NN}}} = 3\text{--}100$ TeV.

2 Higgs boson in partonic A-A collisions

The Higgs cross sections in p-Pb and Pb-Pb collisions over $\sqrt{s_{\text{NN}}} \approx 3\text{--}100$ TeV have been computed at NNLO accuracy in Ref.⁸ with MCFM (v.8.0)¹¹, using the CT10 proton PDFs¹² and EPS09 nuclear PDFs (nPDFs, including its 30 eigenvalues sets)¹³, and fixing the default renormalization and factorization scales at $\mu_R = \mu_F = m_H/2$. The PDF uncertainties, obtained adding in quadrature the CT10 and EPS09 uncertainties, are $\sim 10\%$. The computed nucleon-nucleon cross sections are scaled by the mass number A or A^2 to obtain the corresponding p-A or A-A cross sections respectively, including those for future runs with lighter-ions (Xe-Xe, Kr-Kr, Ar-Ar, and O-O), not considered so far. Compared to the corresponding p-p results at a given c.m. energy, antishadowing nPDF modifications slightly enhance (deplete) the yields by $\sim 3\%$ at the LHC (FCC). The $\mathcal{O}(5\text{--}10\%)$ theoretical $\mu_{R,F}$ scale uncertainties cancel out in the ratios of (p-Pb,Pb-Pb)/(p-p) cross sections at the same colliding energy. The collision energy dependence of the parton-induced Higgs cross sections for all colliding systems is shown Fig. 1 (left, solid curves). The cross sections increase by about a factor of $\times 4$ and $\times 20$ between LHC ($\sigma_{\text{PbPb} \rightarrow \text{H}+\text{X}} \approx 500$ nb), and HE-LHC (~ 2 μb) and FCC (~ 11.5 μb) respectively.

A first Higgs measurement in nuclear collisions will use the clean diphoton and 4-lepton final-state channels as done in p-p¹⁴, with very low branching ratios but small and/or controllable backgrounds. After branching ratios ($\mathcal{B} = 0.23\%$ for $\gamma\gamma$, 0.012% for 4ℓ), and taking into account typical ATLAS/CMS analysis cuts^a that result in $\sim 50\%$ acceptance and efficiency signal losses, one expects about 10, 50, and 1500 Higgs bosons per month in Pb-Pb at the LHC (5.5 TeV),

^a $p_T^\gamma > 30, 40$ GeV, $|\eta^\gamma| < 2.5, 5$ (LHC, FCC); $p_T^\ell > 20, 15, 10, 10$ GeV, $|\eta^\ell| < 2.5, 5$ (LHC, FCC); $R_{\text{isol}}^{\gamma,\ell} = 0.3$.

HE-LHC (10.6 TeV), and FCC (39 TeV) with $\mathcal{L}_{\text{int}} = 10, 10, \text{ and } 110 \text{ nb}^{-1}$ respectively, on top of the corresponding $\gamma\gamma$ and 4ℓ non-resonant backgrounds. In the $\gamma\gamma$ case, the backgrounds include the irreducible QCD diphoton continuum plus 30% of events coming from misidentified γ -jet and jet-jet processes. For the nominal HL-LHC and HE-LHC luminosities, the significances of the diphoton signal (S) over the background (B), computed via S/\sqrt{B} at the Higgs peak, are 0.5, 1.2σ , and thus one would need a factor of $\times 35$ and $\times 7$ larger integrated luminosities to reach 3σ evidence at both machines. A straightforward way to gain a factor of ~ 10 in \mathcal{L}_{int} would be to run one full-year, instead of one heavy-ion month, but even in this case evidence at the HL-LHC would require an extra $\times 3$ increase in the instantaneous luminosity. The situation is much more favourable at HE-LHC and FCC. Figure 2 shows the expected diphoton invariant mass distributions for Pb-Pb at HE-LHC ($\times 7$ the nominal 1-month luminosity, left) and FCC (nominal luminosity, right). The significances of the $H(\gamma\gamma)$ peaks are 3σ and 5.5σ respectively.

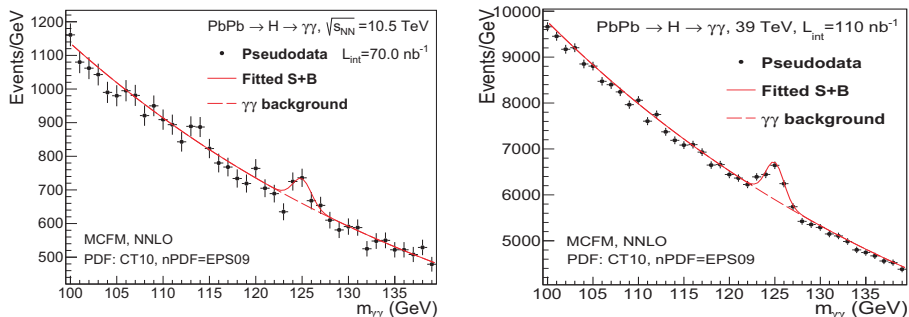


Figure 2 – Expected diphoton invariant mass distributions in Pb-Pb at HE-LHC ($\mathcal{L}_{\text{int}} = 70 \text{ nb}^{-1}$, left) and FCC (nominal 1-month $\mathcal{L}_{\text{int}} = 110 \text{ nb}^{-1}$, right) for a Higgs boson signal on top of the $\gamma\gamma$ backgrounds after cuts.

3 Higgs boson in electromagnetic A-A collisions

The MADGRAPH 5 (v.2.6.5) Monte Carlo event generator¹⁵ is employed to compute the UPC cross sections for Higgs boson and diquark continuum ($b\bar{b}$, as well as misidentified $c\bar{c}$ and light-quark $q\bar{q}$, pairs)¹⁰, by convolving the Weizsäcker-Williams equivalent γ fluxes for the ions (as a function of impact parameter b)¹⁶ and/or protons¹⁷ with the elementary $\gamma\gamma \rightarrow H$ cross section (with H - γ coupling parametrized in the Higgs effective field theory). We exclude nuclear overlap by imposing $b_1 > R_{A_1}$ and $b_2 > R_{A_2}$ for each γ flux (where R_A is the radius of nucleus A), and applying a correcting factor¹⁸ on the final cross section that depends on the ratio of Higgs mass over $\sqrt{s_{\text{NN}}}$. The computed exclusive $\gamma\gamma \rightarrow H$ cross sections are shown in Fig. 1 as a function of $\sqrt{s_{\text{NN}}}$ for all colliding systems (left, dashed curves). The larger the charge of the ions, the larger the UPC cross sections. In the Pb-Pb case, the Higgs cross sections increase by about a factor of $\times 10$ and $\times 100$ between LHC ($\sigma_{\text{Pb-Pb} \rightarrow \gamma\gamma \rightarrow H} \approx 15 \text{ pb}$), and HE-LHC ($\sim 150 \text{ pb}$) and FCC ($\sim 1.8 \text{ nb}$) respectively. We note that, below $\sqrt{s_{\text{NN}}} \approx 5 \text{ TeV}$, the e.m. Higgs production cross section in Pb-Pb is larger than the *partonic* one in p-p collisions. The ratio of parton-to-photon-initiated Higgs cross section is shown in Fig. 1 (right). For A-A collisions, one finds $R_{\text{e.m./parton}} \approx 10^{-5} - 10^{-4}$, which is 10–100 larger than for p-p collisions thanks to the strong nuclear coherent γ fluxes. This ratio in practice increases to $R_{\text{e.m./parton}} \approx 0.01 - 0.03$ when one further accounts for the $\mathcal{B} = 0.27\%$, 56% branching fractions of the most-favourable $H \rightarrow \gamma\gamma, b\bar{b}$ decay channels for a measurement in partonic and e.m. interactions respectively.

The feasibility of measuring UPC Higgs production is carried out in its dominant $H \rightarrow b\bar{b}$ decay. Taking into account the expected beam luminosities, the most competitive system to try a measurement is Ar-Ar (Kr-Kr) at HL-LHC (HE-LHC). At the FCC, the combination of

$\times 100$ larger cross sections and $\times 10$ larger \mathcal{L}_{int} yield ~ 200 Higgs produced per month (~ 110 in the $b\bar{b}$ channel). The following acceptance and reconstruction performances are assumed: jet reconstruction over $|\eta| < 2$ (5 for FCC), 7% b-jet energy resolution (resulting in ~ 6 GeV dijet mass resolution at the Higgs peak), 70% b-jet tagging efficiency, and 5% (1.5%) b-jet mistagging probability for a c (q) quark. These selection criteria lead to a $\sim 50\%$ signal loss, and a total reduction of the misidentified $c\bar{c}$ and $q\bar{q}$ non-resonant backgrounds by factors of ~ 400 and ~ 4500 respectively. The remaining irreducible $b\bar{b}$ continuum is further suppressed through kinematical cuts on the jet $p_T^{\text{jet}} \approx 55\text{--}67$ GeV, invariant dijet mass $m_{b\bar{b}} \approx 116\text{--}134$ GeV, and dijet angular distribution $|\cos\theta_{j_1j_2}| < 0.5$. The final signal significance is derived from the number of counts around the Gaussian Higgs peak over the dijet continuum. Evidence for UPC Higgs at the HL-LHC requires $\times 200$ times larger-than-nominal \mathcal{L}_{int} values in Ar-Ar(6.3 TeV), in order to reach $S/\sqrt{B} \approx 10/\sqrt{12} \approx 3$ (Fig. 3, left). The same analysis for Kr-Kr(12.5 TeV) at the HE-LHC indicates that $\times 30$ larger \mathcal{L}_{int} values are needed than currently designed. On the other hand, Pb-Pb collisions at $\sqrt{s_{\text{NN}}} = 39$ GeV with the FCC nominal $\mathcal{L}_{\text{int}} = 110 \text{ nb}^{-1}$ per month, yield ~ 20 signal counts over about the same number for the sum of backgrounds. Reaching a 5σ statistical significance would just require to combine the measurements of the first run from two different experiments or accumulating two 1-month runs in a single one (Fig. 3, right).

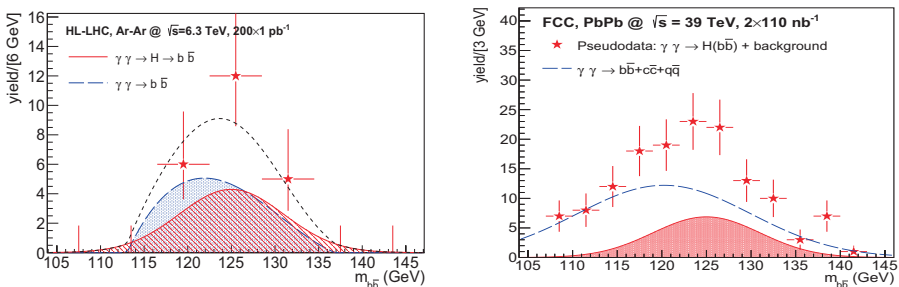


Figure 3 – Expected invariant mass distributions for b-jet pairs from $\gamma\gamma \rightarrow H(b\bar{b})$ signal (hatched red Gaussian) and $b\bar{b} + c\bar{c} + q\bar{q}$ continuum (blue curve) in ultraperipheral Ar-Ar (HL-LHC, left) and Pb-Pb (FCC, right) collisions¹⁰.

4 Conclusions

The production cross sections and expected yields of the Higgs boson in parton-induced and exclusive photon-photon processes using heavy- and light-ion collisions have been studied in the diphoton and $b\bar{b}$ final states respectively at the HL-LHC, HE-LHC, and FCC. Evidence for the scalar boson, over the expected continuum backgrounds, seems out of reach at the HL-LHC with the currently expected integrated luminosities, but can be possible in the partonic mode at HE-LHC. Full observation in both production modes requires a future hadron collider such as the FCC.

References

1. Z. Citron *et al.*, arXiv:1812.06772 [hep-ph].
2. A. Abada *et al.* [FCC Collaboration], CERN-ACC-2018-0059.
3. A. Dainese *et al.*, CERN Yellow Report **3** (2017) 635, D. d’Enterria *et al.*, Nucl. Phys. A **967** (2017) 888; and A. Abada *et al.* [FCC Collaboration], CERN-ACC-2018-0058.
4. D. d’Enterria and C. Loizides, arXiv:1809.06832 [hep-ph].
5. J. Ghiglieri and U. A. Wiedemann, Phys. Rev. D **99** (2019) 054002.
6. A. J. Baltz *et al.*, Phys. Rept. **458** (2008) 1.

7. D. L. Borden, D. A. Bauer and D. O. Caldwell, Phys. Rev. D **48** (1993) 4018.
8. D. d'Enterria, Nucl. Part. Phys. Proc. **289-290** (2017) 237.
9. M. Grabiak *et al.*, J. Phys. G **15** (1989) L25; E. Papageorgiu, Phys. Rev. D **40** (1989) 92; M. Drees *et al.*, Phys. Lett. B **223** (1989) 454; K. J. Abraham *et al.*, *ibid.* **251** (1990) 186.
10. D. d'Enterria and J. P. Lansberg, Phys. Rev. D **81** (2010) 014004; D. d'Enterria, D. E. Martins and P. Rebello Teles, arXiv:1904.11936 [hep-ph].
11. R. Boughezal *et al.*, Eur. Phys. J. C **77** (1) (2017) 7.
12. H.-L. Lai *et al.*, Phys. Rev. D **82** (2010) 074024.
13. K. J. Eskola, H. Paukkunen, C. A. Salgado, JHEP 04 (2009) 065.
14. ATLAS Collaboration, Phys. Lett. B **716** (2012) 1; CMS Collaboration *ibid.* 716 (2012) 30.
15. J. Alwall *et al.*, JHEP **07** (2014) 079.
16. J.D. Jackson, *Classical Electrodynamics*, 2nd edition, John Wiley & Sons (1975).
17. V. M. Budnev, I. F. Ginzburg, G. V. Meledin, V. G. Serbo, Phys. Rept. **15** (1975) 181.
18. R. N. Cahn and J. D. Jackson, Phys. Rev. D **42** (1990) 3690.



2. **Heavy Flavours**

2.1
Top

$t\bar{t} + X$ PRODUCTION AT ATLAS AND CMS

Imma Riu on behalf of the ATLAS and CMS Collaborations
*Institut de Física d'Altes Energies (IFAE), The Barcelona Institute of Science and Technology (BIST),
Universitat Autònoma de Barcelona, Bellaterra, Spain*



Recent measurements of top-quark pair production in association with W -bosons, Z -bosons, photons and b -tagged jets are reported. The measurements are based on ATLAS and CMS analyses of proton–proton collisions at the Large Hadron Collider of 13 TeV center-of-mass energy. Inclusive and differential cross-sections of these rare processes are compared to Standard Model theory predictions. They provide stringent tests of QCD predictions and serve as a probe for new physics beyond the Standard Model.

1 Introduction

The expected cross-sections of the production of a top-quark pair in association with massive vector bosons, photons or b -tagged jets are about three orders of magnitude smaller than top-quark pair production and constitute rare Standard Model (SM) processes. Inclusive and differential cross-sections are measured by the ATLAS¹ and CMS² collaborations at the Large Hadron Collider (LHC) using data taken at 13 TeV center-of-mass energy. The measurements of these rare processes provide tests of QCD predictions and are important backgrounds in the measurement of the associated production of a top-quark pair with the Higgs boson for example, or in searches of physics beyond the SM. The measurements serve as a probe for the presence of new physics like vector-like quarks, strongly coupled Higgs bosons or anomalous couplings of the top quark.

2 $t\bar{t}W$ and $t\bar{t}Z$ production at $\sqrt{s}=13$ TeV

Simultaneous measurements of the inclusive $t\bar{t}W$ and $t\bar{t}Z$ production cross-sections are performed by ATLAS³ using 36.1 fb^{-1} of 13 TeV proton–proton collision data taken in 2015 and 2016 and by CMS⁴ using 35.9 fb^{-1} of data taken in 2016. CMS recently published a new $t\bar{t}Z$ analysis using 77.5 fb^{-1} , which additionally includes data taken in 2017⁵. Events where either one or both top quarks decay leptonically are the most sensitive channels and are classified according to the number of leptons, their flavour and charge, and the numbers of jets and b -tagged jets.

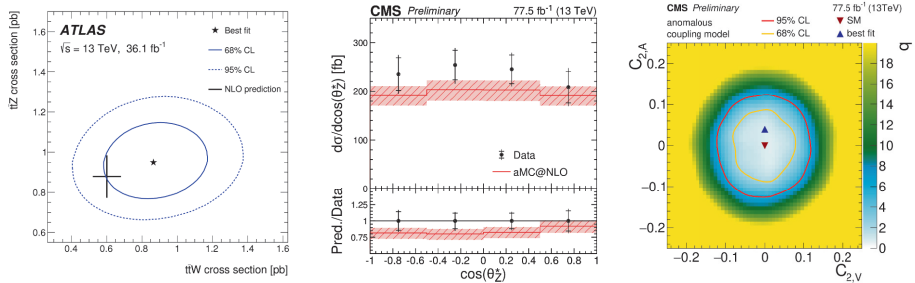


Figure 1 – The left plot shows the ATLAS $t\bar{t}Z$ and $t\bar{t}W$ cross-section measurements³. The middle plot shows the CMS absolute $t\bar{t}Z$ cross-section measurement with respect to the $\cos(\theta_Z^*)$ ⁵. The right plot shows the CMS log-likelihood scan in the two-dimensional plane of the weak magnetic and electric dipole interaction couplings⁵.

In the $t\bar{t}W$ analysis, ATLAS uses the di-lepton same-sign and tri-lepton channels where leptons are required to be isolated in order to reduce background from non-prompt leptons from hadron decays or jets misidentified as leptons. A multivariate discriminant is built to distinguish prompt leptons from leptons arising from heavy-hadron decays inside jets, and another one is created to suppress background from electrons with misidentified charge, which represent an important background in the same-sign di-lepton channel. Control regions are defined to estimate the lepton efficiencies using an orthogonal selection. A total of twelve and four signal regions are used in the di-lepton and tri-lepton channels, respectively, separated by flavour, the sum of charges of the leptons, and the number of b -tagged jets. CMS uses only the di-lepton same-sign channel. A final discriminant is used to categorise events in a total of 20 signal regions depending on the leptons charge, discriminant value and numbers of jets and b -tagged jets.

In the $t\bar{t}Z$ analysis, ATLAS uses three different signal regions in the opposite-sign di-lepton channel, four in the tri-lepton, and another four in the four-lepton channel, categorised by the numbers of jets and b -tagged jets, and separated by lepton flavour. Two control regions are used to determine the normalisation of the WZ +jets and ZZ background. CMS uses four-lepton and tri-lepton opposite-sign same flavour channels, summing up a total of eleven signal regions.

Both ATLAS and CMS measure the $t\bar{t}Z$ and $t\bar{t}W$ production cross-sections simultaneously using a combined fit based on the expected and observed number of events in all control and signal regions. The left plot in Figure 1 shows the ATLAS $t\bar{t}W$ and $t\bar{t}Z$ cross-section measurements, with their precision dominated by systematic uncertainties. They are in good agreement with next-to-leading order (NLO) calculations in QCD. A similar precision is obtained by CMS, with results also compatible with theory.

In addition, CMS measures the $t\bar{t}Z$ absolute and differential cross-sections using 77.5 fb^{-1} . Using an improved lepton selection with respect to the previous analysis, the inclusive cross-section is measured with a 10% precision, representing a 40% uncertainty reduction with respect to the previous result. Absolute differential distributions are also measured with respect to both the transverse momentum of the Z system and the cosine of the angle between the Z and the negatively charged lepton from the Z decay in the Z -rest frame, the latter shown in the middle plot of Figure 1. These are interpreted in models with modified tZ interactions and used to set constraints to anomalous couplings like weak magnetic and electric dipole moments, as shown in the right plot of Figure 1.

3 $t\bar{t}\gamma$ production at ATLAS at $\sqrt{s}=13 \text{ TeV}$

The measurement of the $t\bar{t}\gamma$ production cross-section can be used to probe the top to photon electroweak coupling and provide insight on the $t\bar{t}$ spin correlation and charge asymmetry. The

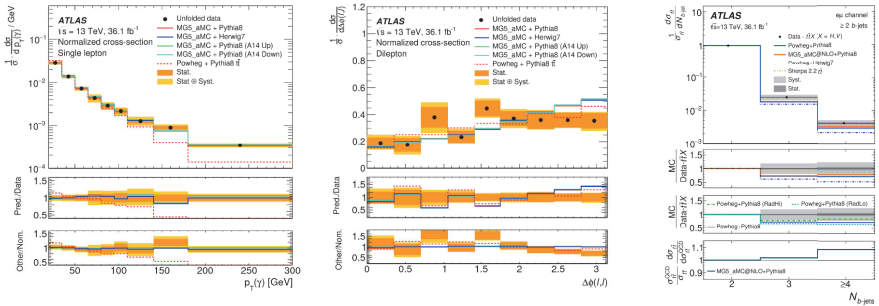


Figure 2 – The left and middle plots show the normalised differential distributions of the transverse momentum of the photon in the single-lepton channel and the azimuthal opening angle between the two leptons measured by ATLAS, respectively⁸. The right plot shows the normalised differential distribution of the b -jet multiplicity measured by ATLAS in the $t\bar{t} + b\bar{b}$ analysis¹⁰.

inclusive and differential fiducial $t\bar{t}\gamma$ production cross-sections were measured by ATLAS⁶ and CMS⁷ using data taken at 8 TeV center-of-mass energy. A more recent measurement was done by ATLAS using 36.1 fb^{-1} of data taken at 13 TeV⁸. Both the $t\bar{t}$ lepton+jets and dilepton channels are used. At least one b -tagged jet is required. A neural network trained to distinguish signal from background separately for the single and di-lepton channels is used. The main backgrounds are events with a misidentified lepton, photon or b -jet. A dedicated neural network is trained to discriminate between prompt photons and hadronic-fake photons. This tagger is one of the inputs to the discriminator. Various control regions are used to measure the fake-lepton efficiency and electron-to-photon fake rate. Finally, a profile likelihood fit to an event-level discriminator is performed.

The absolute fiducial cross-section results obtained for the single and di-lepton channels are more precise than the NLO predictions and in good agreement with them. Only the dilepton measurement is limited by statistics. ATLAS also measures differential cross-section distributions. The kinematic properties of the photon are sensitive to the top to photon coupling, while the di-lepton azimuthal opening angle is sensitive to $t\bar{t}$ spin correlation. For the single-lepton channel, differential distributions of the transverse momentum of the photon, the absolute value of the η coordinate of the photon and the radial distance between the photon and the lepton, are provided. In the di-lepton channel, both the distance in η and azimuthal opening angle between the two leptons are measured in addition to the previous ones. All differential distributions are unfolded to particle level and normalised to unity such that shape discrepancies can be observed. Distributions as predicted by different Monte Carlo (MC) tunes and various parton shower models are compared. All simulations predict very similar shapes and in general describe the data well. The left plot of Figure 2 shows the normalised differential distribution of the transverse momentum of the photon. Data show a harder transverse momentum spectrum than the Pythia 8 prediction. A small deviation from the prediction is observed in the azimuthal opening angle between the two leptons, where the leptons in the prediction are more back-to-back than observed in data, as shown in the middle plot of the same figure.

4 $t\bar{t} + b\bar{b}$ production at ATLAS and CMS at $\sqrt{s} = 13 \text{ TeV}$

The measurement of the $t\bar{t}$ production with additional b -tagged jets provide important tests of QCD predictions. State-of-the-art QCD calculations give predictions for the $t\bar{t}$ production cross-section with up to two additional massless partons at NLO in perturbation theory matched to a parton shower, and the QCD production of $t\bar{t}b\bar{b}$ with massive b -quarks is calculated at NLO

matched to a parton shower.

CMS published a first analysis using 2.3 fb^{-1} of data at 13 TeV^9 . Only the di-lepton electron-muon channel is included. A two-dimensional b -tagging discriminant for the third versus fourth jets is used in a likelihood function to measure the total cross-section and the ratio of $t\bar{t} + b\bar{b}$ and $t\bar{t} + 2$ additional jets irrespective of its type. The results are dominated by systematic uncertainties.

ATLAS recently published results¹⁰ using a total of 36.1 fb^{-1} . The lepton+jets channel is used in addition to the di-lepton electron-muon channel. Templates of b -tagging discriminants categorising the events as $t\bar{t} + b$, $t\bar{t} + c$, $t\bar{t}$ +light jet or non- $t\bar{t}$ are built. For the di-lepton channel, a one-dimensional template is built with three bins corresponding to different b -tagging efficiencies for the jet with the third-highest b -tagging discriminant value. For the lepton+jets channel, two-dimensional templates with five bins are built using the discriminant values of the two jets with the third- and fourth-highest b -tagging discriminant values. The fiducial cross-section is extracted using a binned maximum likelihood fit together with data-driven corrections to the predictions of $t\bar{t} + c$ and $t\bar{t}$ +light jets. The number of events with more than two b -tagged jets is found to be slightly underestimated. The fiducial cross-sections obtained for the various channels are found a bit higher than the predictions but still compatible.

ATLAS also measures normalised fiducial differential cross-sections as a function of several kinematic variables and compares them with various predictions. The precision of the observables ranges between 10 to 30% at the edge of the phase space. The right plot in Figure 2 shows the differential cross-section as a function of the number of b -tagged jets for data and various MC predictions, including POWHEG-BOX $t\bar{t}$ at NLO in the matrix element calculation interfaced with PYTHIA parton shower to predict additional b -jets and Sherpa, modelling zero and one additional-parton process at NLO accuracy and up to four additional partons at leading-order accuracy. Sherpa shows the best agreement with data in most observables.

5 Summary

The measurements of $t\bar{t}$ production in association with vector bosons, photons or additional b -tagged jets provide tests of the SM QCD predictions. The cross-section of the $t\bar{t}$ production in association with a Z boson is measured with a precision of 10% by CMS. Both ATLAS and CMS measure the $t\bar{t}$ production with a W boson with a precision of ~ 12 -14% and are in agreement with theoretical predictions. Various normalised differential cross-sections of $t\bar{t} + \gamma$ production are measured by ATLAS, showing good agreement with NLO predictions. A small deviation from the prediction of the di-lepton azimuthal angle separation distribution is observed in data. The $t\bar{t} + b\bar{b}$ fiducial cross-section is measured by ATLAS and normalised fiducial differential distributions of different kinematic variables are compared to various MC predictions.

References

1. ATLAS Collaboration, JINST **3**, S08003 (2008).
2. CMS Collaboration, JINST **3**, S08004 (2008).
3. ATLAS Collaboration, Phys. Rev. D **99**, 072009 (2019).
4. CMS Collaboration, JHEP **08**, 011 (2018).
5. CMS Collaboration, CMS-PAS-TOP-18-009 (2019).
6. ATLAS Collaboration, JHEP **11**, 086 (2017).
7. CMS Collaboration, JHEP **10**, 006 (2017).
8. ATLAS Collaboration, Eur. Phys. J. C **79**, 382 (2019).
9. CMS Collaboration, Phys. Lett. B **776**, 355 (2018).
10. ATLAS Collaboration, JHEP **04**, 046 (2019).

ASSOCIATED TOP-PAIR PRODUCTION WITH A HEAVY BOSON PRODUCTION THROUGH NLO+NNLL ACCURACY AT THE LHC

A. Kulesza ^a, L. Motyka ^b, D. Schwartländer ^a, T. Stebel ^c and V. Theeuwes ^d

^a*Institute for Theoretical Physics, WWU Münster, D-48149 Münster, Germany*

^b*Institute of Physics, Jagiellonian University, S.Łojasiewicza 11, 30-348 Kraków, Poland*

^c*Institute of Nuclear Physics PAN, Radzikowskiego 152, 31-342 Kraków, Poland*

^d*Institute for Theoretical Physics, Georg-August-University Göttingen, Friedrich-Hund-Platz 1, 37077 Göttingen, Germany*

In this talk we present results of our recent calculations of cross sections and distributions for the associate production of top-antitop quark pairs with a heavy boson (Higgs, W, Z) at the LHC, obtained using threshold resummation in direct QCD, i.e. in the Mellin-space approach.

The measurements¹⁻³ of associated production of a Higgs or a heavy electroweak (EW) boson (H, W, Z) with a top-antitop quark pair provide an important test for the Standard Model at the LHC, in particular the top quark couplings. For example, the associated $t\bar{t}H$ production directly probes the top Yukawa coupling without making any assumptions on its nature. Fixed order cross sections up to next-to-leading order in α_s have been known for some time both for the associated Higgs boson^{4,5} and W and Z boson production.^{6,7} They were recalculated and matched to parton showers in.⁸⁻¹⁴ Furthermore, next-to-leading order (NLO) QCD-EW corrections are also known.^{15,16} For the $t\bar{t}H$ process, the NLO EW and QCD corrections to production with off-shell top quarks were also obtained.^{17,18} While next-to-next-to-leading order (NNLO) calculations for this particular type of 2 to 3 processes are currently out of reach, a class of corrections beyond NLO from the emission of soft and/or collinear gluons can be taken into account with the help of resummation methods. Such methods allow to account for effects of soft gluon emission to all orders in perturbation theory. Two approaches to perform soft gluon resummation are either a direct calculation in QCD or in an effective field theory, in this case soft-collinear effective theory (SCET).

For the associated $t\bar{t}H$ production, the first calculations of the resummed cross section at the next-to-leading logarithmic (NLL) accuracy, matched to the NLO result were presented in.¹⁹ The calculation relied on application of the traditional Mellin-space resummation formalism in the absolute threshold limit, i.e. in the limit of the partonic energy $\sqrt{\hat{s}}$ approaching the production threshold $M = 2m_t + m_H$. Subsequently, resummation of NLL corrections arising in the limit of $\sqrt{\hat{s}}$ approaching the invariant mass threshold Q , with $Q^2 = (p_t + p_{\bar{t}} + p_H)^2$, was performed in²⁰ and later extended to the next-to-next-to-leading-logarithmic (NNLL) accuracy.²¹ Calculations in the SCET framework for the $t\bar{t}H$ process led first to obtaining approximate NNLO²² and later full NLO+NNLL predictions.²³ SCET results at the NLO+ NNLL accuracy for the $t\bar{t}W/Z$ production have been also obtained.^{24,25}

In this proceedings we report on our predictions for the threshold-resummed cross sections $pp \rightarrow t\bar{t}B$, $B = H, W, Z$, obtained using the Mellin-space approach at the NNLL accuracy. We treat the soft gluon corrections in the invariant mass kinematics, i.e. we consider the limit

$\hat{\rho} = \frac{Q^2}{\hat{s}} \rightarrow 1$ with $Q^2 = (p_t + p_{\bar{t}} + p_B)^2$ and \hat{s} the partonic center of mass energy. The resummation of large logarithms of $1 - \hat{\rho}$ takes place in the space of Mellin moments N , taken w.r.t. $\hat{\rho}$. At the NNLL accuracy, our key formula for the resummed cross section for the partonic process $ij \rightarrow t\bar{t}B$ reads^{26–30}

$$\begin{aligned} \frac{d\hat{\sigma}_{ij \rightarrow t\bar{t}B}^{(\text{NNLL})}}{dQ^2}(N, Q^2, \{m^2\}, \mu_F^2, \mu_R^2) = & \text{Tr} \left[\mathbf{H}_R(Q^2, \{m^2\}, \mu_F^2, \mu_R^2) \bar{\mathbf{U}}_R(N+1, Q^2, \{m^2\}, Q^2) \right. \\ & \times \tilde{\mathbf{S}}_R(N+1, Q^2, \{m^2\}) \mathbf{U}_R(N+1, Q^2, \{m^2\}, Q^2) \left. \right] \\ & \times \Delta^i(N+1, Q^2, \mu_F^2, \mu_R^2) \Delta^j(N+1, Q^2, \mu_F^2, \mu_R^2), \end{aligned}$$

where $\{m^2\}$ denotes all masses entering the calculations and μ_F, μ_R are the factorization and renormalization scales. The jet functions Δ_i and Δ_j account for (soft-)collinear logarithmic contributions from the initial state partons and are well known at NNLL.³¹ $\mathbf{H}_R, \bar{\mathbf{U}}_R, \mathbf{U}_R$ and \mathbf{S}_R are matrices in colour space over which the trace is taken. The term $\bar{\mathbf{U}}_R \tilde{\mathbf{S}}_R \mathbf{U}_R$ originates from a solution of the renormalization group equation for the soft function and consists of the evolution matrices $\bar{\mathbf{U}}_R, \mathbf{U}_R$, as well as the function $\tilde{\mathbf{S}}_R$ which plays the role of a boundary condition of the renormalization group equation. In general the evolution matrices are given by path-ordered exponentials of the soft anomalous dimension matrix $\mathbf{\Gamma}_{ij \rightarrow t\bar{t}B}(\alpha_s) = (\frac{\alpha_s}{\pi}) \mathbf{\Gamma}_{ij \rightarrow t\bar{t}B}^{(1)} + (\frac{\alpha_s}{\pi})^2 \mathbf{\Gamma}_{ij \rightarrow t\bar{t}B}^{(2)} + \dots$. At NLL, the path-ordered exponentials collapse to standard exponential factors in the colour space \mathbf{R} where $\mathbf{\Gamma}_R^{(1)}$ is diagonal. At NNLL, the path-ordered exponentials are eliminated by treating \mathbf{U}_R and $\bar{\mathbf{U}}_R$ perturbatively.^{32,33} The function \mathbf{H}_R accounts for the hard scattering contributions projected on the \mathbf{R} color basis. At NNLL, the $\mathcal{O}(\alpha_s)$ terms in the perturbative expansion of \mathbf{H}_R and $\tilde{\mathbf{S}}_R$, as well as $\mathbf{\Gamma}_R^{(2)}$ are needed. While the latter is known,³⁴ the virtual corrections which enter $\mathbf{H}_R^{(1)}$ are extracted numerically from the NLO calculations provided by PowHel^{10,11} and MadGraph5_aMC@NLO.¹³ For more information on the theoretical framework, we refer the reader to our earlier publications.²¹

The results for the resummed cross sections are matched the NLO cross sections calculated with MadGraph5_aMC@NLO.¹³ In the numerical calculations we use the PDF4LHC15_30 parton distribution function sets³⁵ and the same input parameters as in the HXSWG Yellow Report 4,³⁶ i.e. $m_H = 125$ GeV, $m_t = 172.5$ GeV, $m_W = 80.385$ GeV, $m_Z = 91.188$ GeV, $G_F = 1.1663787 \times 10^{-5}$ GeV⁻², so that we reproduce the NLO values of the $t\bar{t}B$ cross sections listed there. The NNLO sets are employed for the NLO+NNLL predictions, whereas the NLO+NLL predictions are calculated with NLO sets.

In Fig. 1 we show numerical predictions for the total cross sections at 13 TeV with three choices of the central value of the renormalization and factorization scales, $\mu_0 = \mu_{F,0} = \mu_{R,0}$, i.e. $\mu_0 = Q$, $\mu_0 = M/2 = m_t + m_B/2$ and $\mu_0 = Q/2$. The theoretical error due to scale variation is calculated using the so called 7-point method, where the minimum and maximum values obtained with $(\mu_F/\mu_0, \mu_R/\mu_0) = (0.5, 0.5), (0.5, 1), (1, 0.5), (1, 1), (1, 2), (2, 1), (2, 2)$ are considered.

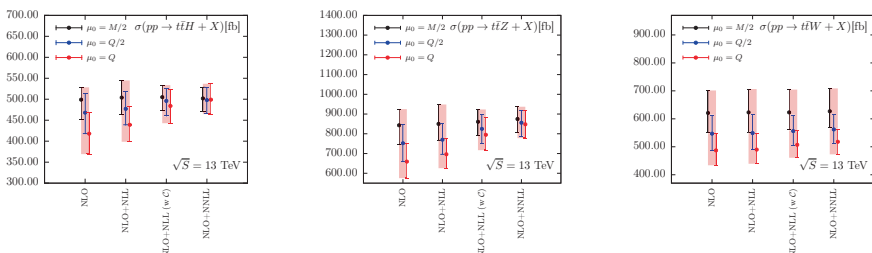


Figure 1 – Total cross sections for the $t\bar{t}H$ (left), $t\bar{t}Z$ (center) and $t\bar{t}W$ (right) production at $\sqrt{S} = 13$ TeV, as described in text.

Total cross section results were obtained by integrating the resummed differential cross section. Apart from results at the NLO+NNLL accuracy, we also shown predictions at lower logarithmic accuracy i.e. at NLO+NLL and NLO+NLL w \mathcal{C} as defined and discussed in our latest work.²¹ Compared to NLO, the NLO+NNLL results demonstrate remarkable stability w.r.t. the scale choice, indicating the importance of resummed calculations. The stability increases as the accuracy of resummation improves from NLL to NNLL. In general, resummation leads to positive corrections, bringing the theoretical predictions for the $t\bar{t}Z$ and, to a lesser extent, $t\bar{t}W$ total cross sections closer to experimental measurements.²¹ The relative size of the NNLL corrections w.r.t. NLO results differs from 1% to 19% (for $t\bar{t}H$) or 4% to 24% (for $t\bar{t}Z$), depending on the scale choice. All the trends discussed here are much stronger for the $t\bar{t}H$ and $t\bar{t}Z$ than for the $t\bar{t}W$ production due to the gg channel contributing to the LO and, correspondingly, to the resummed cross section. Another feature of the resummed predictions is a decrease of the scale uncertainties calculated for each specific scale choice, which is also progressing with increasing precision of the theoretical predictions. For example, for the $t\bar{t}H/Z$ production and $\mu_0 = Q$ scale choice, the relative size of the scale error is reduced by about 40%.²¹ For the other two scale choices the effect is smaller but still sizeable, bringing the value of the scale error down to 5–7% and 7–8% for the $t\bar{t}H$ and $t\bar{t}Z$ production, respectively. Thus, while at NLO the accuracy of the $t\bar{t}Z$ predictions is worse than the experimental precision, the accuracy of the NLO+NNLL calculations matches the latest experimental precision.³

Resummation also leads to an improvement of theoretical predictions for the invariant mass distributions²¹ and transverse momentum (p_T) distributions of the EW boson. In Fig. 2 we show the $p_T(Z)$ distributions for the $t\bar{t}Z$ production. The predictions also include the EW corrections,¹⁵ added³⁶ to the NLO and NLO+NNLL results in QCD. By comparing the left and center plots, it is clear that the spread in the NLO predictions due to scale variation is reduced greatly if the NNLL corrections are included in the predictions. In the right plot in Fig. 2 we compare the NLO(QCD+EW)+NNLL distribution, calculated with $\mu_0 = H_T/2$, to the recent measurement of $p_T(Z)$ by the CMS collaboration³. The NNLL corrections increase the NLO predictions by about 10% and bring the theory predictions in full agreement with data.

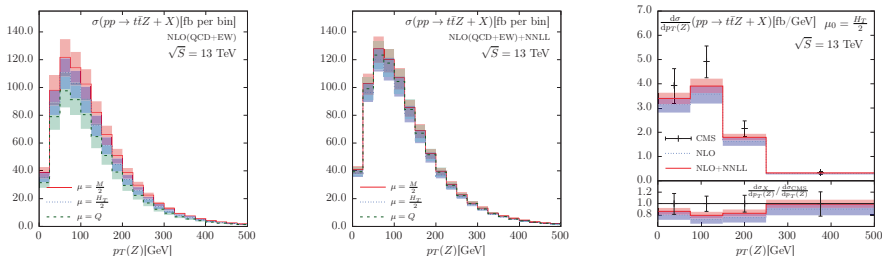


Figure 2 – Dependence of the transverse momentum distribution of the Z boson in $t\bar{t}Z$ production at the NLO(QCD+EW) accuracy (left) and NLO(QCD+EW)+NNLL accuracy (center) on the scale choice. (Right) comparison of the NLO(QCD+EW) and NLO(QCD+EW)+NNLL predictions at $\mu_0 = H_T/2$ with data.³

Acknowledgments

The authors acknowledge financial support by the DFG Grant KU 3103/1 (AK, DS), NCN grant No. 2017/27/B/ST2/02755 (LM, TS), and by the DAAD with funds from the BMBF and the European Union (FP7-PEOPLE-2013-COFUND - grant agreement n° 605728) (VT).

References

1. M. Aaboud *et al.*, *Phys. Lett. B* **784** (2018) 173; *Eur. Phys. J. C* **77** (2017) no.1, 40; *Phys. Rev. D* **99** (2019) no.7, 072009; G. Aad *et al.*, *JHEP* **1511** (2015) 172.
2. A. M. Sirunyan *et al.*, *Phys. Rev. Lett.* **120** (2018) no.23, 231801; *JHEP* **1808** (2018) 011; V. Khachatryan *et al.*, *JHEP* **1601** (2016) 096; *Eur. Phys. J. C* **74** (2014) no.9, 3060; S. Chatrchyan *et al.*, *Phys. Rev. Lett.* **110** (2013) 172002.
3. CMS Collaboration, CMS-PAS-TOP-18-009.
4. W. Beenakker *et al.*, *Phys. Rev. Lett.* **87** (2001) 201805; *Nucl. Phys. B* **653** (2003) 151.
5. L. Reina and S. Dawson, *Phys. Rev. Lett.* **87** (2001) 201804; L. Reina, S. Dawson and D. Wackerroth, *Phys. Rev. D* **65** (2002) 053017; S. Dawson *et al.*, *Phys. Rev. D* **67** (2003) 071503; S. Dawson *et al.*, *Phys. Rev. D* **68** (2003) 034022.
6. A. Lazopoulos, T. McElmurry, K. Melnikov and F. Petriello, *Phys. Lett. B* **666** (2008) 62.
7. A. Lazopoulos, K. Melnikov and F. J. Petriello, *Phys. Rev. D* **77** (2008) 034021
8. V. Hirschi *et al.* *JHEP* **1105** (2011) 044.
9. R. Frederix *et al.* *Phys. Lett. B* **701** (2011) 427.
10. M. V. Garzelli *et al.*, *EPL* **96** (2011) no.1, 11001; *Phys. Rev. D* **85** (2012) 074022; *JHEP* **1211** (2012) 056;
11. A. Kardos, Z. Trocsanyi and C. Papadopoulos, *Phys. Rev. D* **85** (2012) 054015.
12. J. M. Campbell and R. K. Ellis, *JHEP* **1207** (2012) 052.
13. J. Alwall *et al.*, *JHEP* **1407** (2014) 079.
14. H. B. Hartanto, B. Jäger, L. Reina and D. Wackerroth, *Phys. Rev. D* **91** (2015) 9, 094003.
15. S. Frixione *et al.* *JHEP* **1409** (2014) 065; *JHEP* **1506** (2015) 184.
16. Y. Zhang, W. G. Ma, R. Y. Zhang, C. Chen and L. Guo, *Phys. Lett. B* **738** (2014) 1.
17. A. Denner and R. Feger, *JHEP* **1511** (2015) 209.
18. A. Denner, J. N. Lang, M. Pellen and S. Uccirati, *JHEP* **1702** (2017) 053.
19. A. Kulesza, L. Motyka, T. Stebel and V. Theeuwes, *JHEP* 1603 (2016) 065.
20. A. Kulesza, L. Motyka, T. Stebel and V. Theeuwes, *PoS LHCP 2016* (2016) 084.
21. A. Kulesza, L. Motyka, T. Stebel and V. Theeuwes, *Phys. Rev. D* **97** (2018) no.11, 114007; *Eur. Phys. J. C* **79** (2019) no.3, 249.
22. A. Broggio, A. Ferroglia, B. D. Pecjak, A. Signer and L. L. Yang, *JHEP* **1603** (2016) 124.
23. A. Broggio, A. Ferroglia, B. D. Pecjak and L. L. Yang, *JHEP* **1702** (2017) 126.
24. H. T. Li, C. S. Li and S. A. Li, *Phys. Rev. D* **90** (2014) no.9, 094009.
25. A. Broggio *et al.* *JHEP* **1609** (2016) 089; *JHEP* **1704** (2017) 105.
26. H. Contopanagos, E. Laenen and G. F. Sterman, *Nucl. Phys. B* **484** (1997) 303 .
27. N. Kidonakis, G. Oderda and G. Sterman, *Nucl. Phys. B* **525**, 299 (1998); *Nucl. Phys. B* **531** (1998) 365;
28. N. Kidonakis and G. Sterman, *Nucl. Phys. B* **505** (1997) 321.
29. R. Bonciani, S. Catani, M. L. Mangano and P. Nason, *Nucl. Phys. B* **529** 424 (1998).
30. M. Czakon, A. Mitov and G. F. Sterman, *Phys. Rev. D* **80** (2009) 074017.
31. S. Catani, D. de Florian, M. Grazzini and P. Nason, *JHEP* **0307** (2003) 028.
32. A. J. Buras, *Rev. Mod. Phys.* **52** (1980) 199.
33. V. Ahrens *et al.* *JHEP* **1009** (2010) 097.
34. A. Ferroglia *et al.*, *Phys. Rev. Lett.* **103** (2009) 201601; *JHEP* **0911** (2009) 062.
35. J. Butterworth *et al.*, *J. Phys. G* **43** (2016) 023001; S. Dulat *et al.*, *Phys. Rev. D* **93** (2016) no.3, 033006; L. A. Harland-Lang *et al.*, *Eur. Phys. J. C* **75** (2015) no.5, 204; R. D. Ball *et al.*, *JHEP* **1504** (2015) 040; J. Gao and P. Nadolsky, *JHEP* **1407** (2014) 035; S. Carrazza *et al.*, *Eur. Phys. J. C* **75** (2015) no.8, 369.
36. D. de Florian *et al.* [LHC Higgs Cross Section Working Group], arXiv:1610.07922 [hep-ph].

Single top quark and rare top quark production at ATLAS and CMS

Willem Verbeke

*On behalf of the ATLAS and CMS Collaborations
Department of Physics and Astronomy,
Universiteit Gent, Gent, Belgium*



The latest results from ATLAS and CMS on single top quark production and rare production channels of top quarks at the LHC are presented.

1 Introduction

The dominant production mechanism of top quarks at the LHC is pair production through the strong interaction ($t\bar{t}$). Electroweak production of single top quarks is more rare, but provides essential complementary information for furthering our understanding of the SM. Being the heaviest particle in the SM, the top quark plays an important role in many new physics models. Measurements of rare processes involving top quarks are therefore essential tests of the SM.

The latest results on single top quark production and rare production channels of top quarks from ATLAS¹ and CMS² are presented below. The majority of these results are based on data from proton-proton (pp) collisions at a center of mass energy of 13 TeV, and unless otherwise specified, these conditions are assumed. Analyses discussed in this document generally use events with electrons and muons in the final state, and therefore ‘leptons’ will only refer to electrons and muons unless otherwise stated.

2 Single top quark production

Production of single top quarks in the t -channel is highly sensitive to the proton’s parton distribution functions (PDF) since the flavor of the incoming quark determines the charge of the top quark. Through this process one can additionally measure the CKM matrix element V_{tb} . Using events with a single isolated lepton and several jets in 35.9 fb^{-1} of pp collision data, CMS measured $|f_{LV} V_{tb}| = 1.00 \pm 0.08 \text{ (exp)} \pm 0.02 \text{ (theo)}$, where f_{LV} is a modification factor, and the charge ratio $\sigma_{t\text{-ch},t}/\sigma_{t\text{-ch},\bar{t}} = 1.66 \pm 0.02 \text{ (stat)} \pm 0.05 \text{ (syst)}$.³

2019 CERN for the benefit of the ATLAS and CMS Collaborations. CC-BY-4.0 license.

Combinations of all 7 TeV and 8 TeV measurements of single top quark production in the t - and s -channels and in association with a W boson, from ATLAS and CMS, were recently performed. These result in more precise measurements of each of the production cross sections, and the most precise direct determination of V_{tb} to date. ⁴ The combined value is $|f_{LV}V_{tb}| = 1.02 \pm 0.04$ (exp) ± 0.02 (theo), with a relative uncertainty of about 3.7%, markedly smaller than in the best single measurement where the uncertainty is 4.7%. ⁵

The cross section and charge-ratio of t -channel single top quark production are measured differentially in the top quark transverse momentum (p_T) and rapidity, the charged lepton p_T and rapidity, and the p_T of the W boson from the top quark decay, by CMS using 35.9 fb^{-1} of data. The results are in agreement with predictions from several NLO event generators using multiple sets of PDFs. The cross section is additionally measured as a function of the top quark polarization angle, shown in Fig. 1, which can be used to probe the structure of the tbW vertex. This is quantified by the so-called top quark spin asymmetry, which is found to be $A = 0.439 \pm 0.032$ (stat + exp) ± 0.053 (syst), in excellent agreement with the SM value of $A = 0.436$ as predicted by POWHEG. ⁶

Associated production of a single top quark with a W boson and b quark (tWb) interferes with $t\bar{t}$ because both processes have the same final state of two W bosons and two b quarks. The first probe of these interference effects is done by ATLAS in events with exactly two b jets and two leptons in 36.1 fb^{-1} of pp collision data. To attain sensitivity to the interference effects a differential cross section measurement of $t\bar{t} + tWb$ is done as a function of $m_{b\bar{b}}^{\text{minimax}}$ ($= \min\{\max(m_{b_1\ell_1}, m_{b_2\ell_2}), \max(m_{b_1\ell_2}, m_{b_2\ell_1})\}$), which is always smaller than $\sqrt{m_t^2 - m_W^2}$ for $t\bar{t}$ at parton level. Different modeling schemes of the interference effects are then compared to the unfolded $m_{b\bar{b}}^{\text{minimax}}$ distribution. The best modeling is found to be given by a POWHEG-BOX-RES simulation of the $\ell^+\ell^-\nu\bar{\nu}b\bar{b}$ final state which takes off-shell and interference effects into account, as shown in Fig. 2. ⁷

3 Rare top quark production

Production of a single top quark and a photon ($t\gamma q$) is sensitive to the top quark's charge, and its electric- and magnetic dipole moments. A search for this process is performed by CMS in events with a muon, a photon, and jets in 35.9 fb^{-1} of data. A boosted decision tree (BDT) is used to separate the signal from the background, and a fit to the BDT distribution results in a cross section measurement $\sigma(\text{pp} \rightarrow t\gamma q)\mathcal{B}(t \rightarrow \mu\nu b) = 115 \pm 17$ (stat) ± 30 (syst) fb, in a fiducial volume characterized by $p_T^\gamma > 25 \text{ GeV}$, $|\eta^\gamma| < 1.44$, and $\Delta R(X, \gamma) > 0.5$, where X signifies a muon or parton. The signal has an observed (expected) significance of 4.4 (3.0) standard deviations (s.d.) over the background only hypothesis, the first evidence for $t\gamma q$. ⁸

Single top quark production in association with a Z boson (tZq) is a rare process that until recently remained unobserved. It depends on the tZ and WWZ couplings, and is highly sensitive to the presence of new physics because of unitary cancellations in the SM. A new search for this process is done by CMS, using events with three leptons in 77.4 fb^{-1} of pp collision data. A crucial improvement is the usage of a BDT-based lepton identification, which increases the signal efficiency while lowering the background from nonprompt muons (electrons) by a factor 8 (2) compared to the lepton identification used in the previous CMS search for tZq . The tZq cross section is extracted from a fit to BDT distributions in three event categories based on the number of jets and b jets. The result is $\sigma(\text{pp} \rightarrow tZq \rightarrow t\ell\ell q) = 111 \pm 13$ (stat) $_{-9}^{+11}$ (syst) fb, for dilepton invariant masses above 30 GeV with $\ell = e, \mu, \tau$, in agreement with the SM expectation. The observed (expected) significance of the signal is 8.2 (7.7) s.d. above the background only hypothesis, marking the first observation of this process. The distribution of the BDT discriminant for events with 2 or 3 jets, one of them b-tagged, the most important event category, is shown in Fig. 1. ⁹

An extremely rare and unobserved process is the production of four top quarks ($t\bar{t}t\bar{t}$), which

The comparison of the measured and expected cross sections as a function of $|y_t/y_t^{\text{SM}}|$, results in a 95% C.L. upper limit $|y_t/y_t^{\text{SM}}| < 1.7$.¹⁴

Charged lepton flavor violation (cFLV) can occur in the SM by means of neutrino oscillations, but it is so rare that it is far beyond our current experimental reach. As such, the observation of cFLV would be a clear sign of the presence of new physics. The first direct search for cFLV in top quark decays is carried out by ATLAS in 79.8 fb^{-1} of pp collision data. The search targets the decay $t \rightarrow \ell^\pm \ell'^\mp q$, and uses events with three leptons and several jets out of which there is at most one that is b-tagged. A BDT discriminant, plotted in Fig. 2, is used to separate the signal from the background. The data are found to be consistent with the SM, and the resulting 95% C.L. upper limits on the cFLV branching fraction are $\mathcal{B}(t \rightarrow \ell \ell' q) < 1.86 (1.36^{+0.61}_{-0.37}) \cdot 10^{-5}$ if $\ell = e, \mu, \tau$, and $\mathcal{B}(t \rightarrow e \mu q) < 6.6 (4.8^{+2.1}_{-1.4}) \cdot 10^{-6}$ if $\ell = e, \mu$. This represents an improvement of several orders of magnitude compared to the previous best limits from indirect searches which are of the order of 10^{-3} .¹⁵

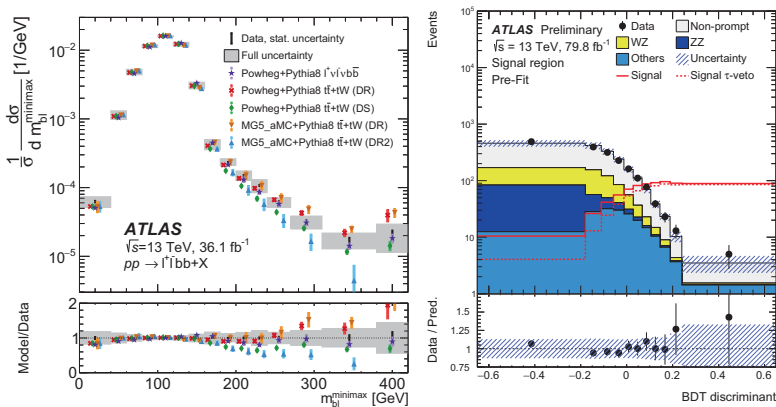


Figure 2 – Normalized cross section of $t\bar{t} + tWb$ as a function of $m_{b\ell}^{\text{minimax}}$ (left)⁷, BDT distribution of the cFLV search (right)¹⁵.

References

1. ATLAS Collaboration, JINST **3**, S08003 (2008)
2. CMS Collaboration, JINST **3**, S08004 (2008)
3. CMS Collaboration, arXiv:1812.10514
4. ATLAS and CMS Collaborations, arXiv:1902.07158
5. ATLAS Collaboration, Eur. Phys. J. **C77**, 2017 (531)
6. CMS Collaboration, CMS-PAS-TOP-17-023 (2019), <https://cds.cern.ch/record/2667180>
7. ATLAS Collaboration, Phys. Rev. Lett. **121**, 152002 (2018)
8. CMS Collaboration, Phys. Rev. Lett. **121**, 221802 (2018)
9. CMS Collaboration, Phys. Rev. Lett. **122**, 132003 (2019)
10. ATLAS Collaboration, Phys. Rev. D **99**, 052009 (2019)
11. ATLAS Collaboration, JHEP **1812**, 039 (2018)
12. CMS Collaboration, CMS-PAS-TOP-17-019 (2019), <https://cds.cern.ch/record/2666712>
13. CMS Collaboration, Eur. Phys. J. **C78**, 140 (2018)
14. CMS Collaboration, CMS-PAS-TOP-18-003 (2019), <https://cds.cern.ch/record/2668710>
15. ATLAS Collaboration, ATLAS-CONF-2018-044 (2018), <https://cds.cern.ch/record/2638305>

2.2 Search for New Physics

FLAVOUR PHYSICS IN VOGUE

J. F. KAMENIK

*Faculty of Mathematics and Physics, University of Ljubljana, Jadranska 19, 1000 Ljubljana, Slovenia
Jožef Stefan Institute, Jamova 39, 1000 Ljubljana, Slovenia*



A brief overview of the status of flavour physics within and beyond the standard model is presented with an emphasis on the near future experimental prospects. The topics covered include precision determination of the CKM parameters and constraints on new physics from neutral meson oscillation measurements. Some perspective on the recent intriguing experimental results concerning direct CP violation in charm decays as well as lepton flavor universality in (rare) semileptonic B decays is also given.

1 Introduction

Over the past few decades, the standard model (SM) structure of (quark) flavour has been fully and firmly established. This was made possible through a remarkable interplay of continuing theoretical and experimental advances. Today, the precision achieved in flavour observables allows us to probe possible new physics (NP) beyond the standard model (BSM) up to energy scales which can span orders of magnitude above the direct reach of collider experiments.

Recently, several cracks have appeared in the simple coherent picture of SM flavour physics, thrusting flavour physics back into the spotlight of BSM searches. These possible early signs of NP, if confirmed, would have far reaching implications for high p_T measurements at the LHC as well as for BSM model building. Fortunately, there are exciting prospects for a timely resolution or confirmation of the so called B -anomalies by the upcoming Belle-II and LHCb-II experiments. One needs to keep in mind though that fully leveraging the power of these new experimental facilities will require some crucial progress on the theory side as well.

2 Flavour in Standard Model

In the SM, flavour physics is intrinsically connected to the phenomenon on electroweak symmetry breaking via the Higgs mechanism. In particular, in the quark sector, the Y_u and Y_d Yukawa matrices, parametrizing the couplings of quark fields to the Higgs are the only breaking sources of the large global flavour symmetry, respected by the SM gauge interactions. The 10 physical quark flavour parameters can thus all be traced back to the Yukawa sector of the SM. In particular,

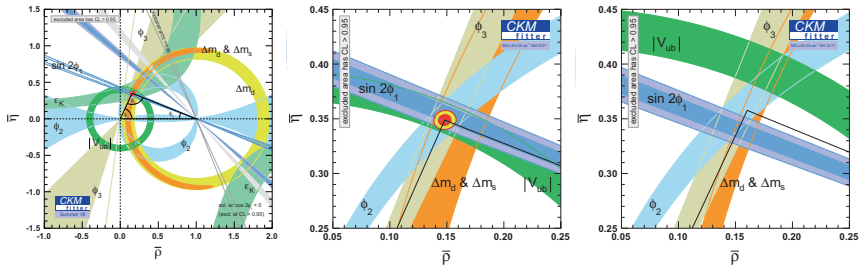


Figure 1 – The global CKM fit projected onto the $(\bar{\rho}, \bar{\eta})$ plane. The current world average is shown on left hand side. The central and right hand side plots demonstrate projected future precision assuming (fixing) the central values of observables either as predicted by the current SM global CKM fit, or to current individual observable measurements themselves, respectively.

the six quark masses can be written as $m_u = vV_L^u Y_u V_R^{u\dagger}$ and $m_d = vV_L^d Y_d V_R^{d\dagger}$, where $v \simeq 246$ GeV is the Higgs condensate and $V_{L,R}^{u,d}$ are unitary matrices diagonalizing the Yukawas. More importantly, all flavour phenomena in the SM quark sector are determined by the four (three angles and a CP-odd phase) parameters of the unitary CKM matrix, given by $V_{\text{CKM}} \equiv V_L^u V_L^{d\dagger}$. While the SM parametrization of flavour is quite economical, the observed hierarchical structures of both $m_{u,d}$ (where the quark masses span five orders of magnitude) as well as V_{CKM} (being almost diagonal) are very suggestive of a deeper flavour structure. This so called *origin of flavour puzzle* is one of the most important open problems in fundamental physics today.

The consistency of the SM description of flavour, in particular, the unitarity of the CKM as well as a single source of CP violation (CPV) contributing to all measured flavor transitions has been well tested experimentally. This main legacy of the B-factories Belle and Babar¹ is perhaps best represented by the so-called CKM unitarity triangle plot in Figure 1 (left hand side plot) representing the projection of measurements sensitive to CKM parameters onto the $(\bar{\rho}, \bar{\eta})$ plane.^{2,3} Quantitatively, the apex of the triangle is currently known to around 6% relative precision,²

$$\bar{\rho} = 0.1577_{-0.0074}^{+0.0096}, \quad \bar{\eta} = 0.3493_{-0.0071}^{+0.0095}. \quad (1)$$

More importantly, there are now good experimental prospects to improving this precision further in the near future. In particular, several key observables entering the CKM determination (including all the three unitarity triangle angles as well as the modulus $|V_{ub}/V_{cb}|$) are expected to be measured more precisely by the Belle II³ and LHCb-II⁴ experiments in the coming decade. To bring the power of these upcoming measurements into perspective, one can try to extrapolate the current experimental results to the projected future precision assuming (fixing) the central values of observables either (a) as predicted by the current SM global CKM fit, or (b) to current individual observable measurements themselves. Comparing the left hand side and central plots in Figure 1, we can conclude that in the SM consistent projection (a) the CKM triangle apex precision would improve by a factor of a few. On the other hand, an extrapolation of current measurements (b) would result in significant tensions within the CKM fit signaling possible BSM contributions to flavour observables, as illustrated by the right hand side plot in Figure 1.

In order to leverage the projected increased precision of the new experiments, several outstanding theoretical challenges need to be met. In particular, several key CKM fit inputs like $|V_{ub,cb}|$, as well as neutral $B_{d,s}$ meson oscillation frequencies given by $\Delta m_{d,s}$, are currently limited by theoretical uncertainties. Taking a closer look at the CKM moduli $|V_{ub,cb}|$, these are determined from (semi)leptonic decay rates of b -flavoured hadrons. The current treatments of these observables can be divided into two classes of studies: (1) exclusive decays to a single par-

ticular final state, and (2) inclusive decays where one sums over a certain range of final states (for example all single and multi-hadron final states of a given net flavor). Theoretical and experimental approaches with their resulting uncertainties are very different for both classes of observables and can thus serve as an important internal consistency check. In fact, over the past few years, several tensions have appeared between the various inclusive and exclusive $|V_{ub,cb}|$ determinations.⁵ The origins of these discrepancies have to be well understood and overcome at the expected Belle II and LHCb-II precision.

3 Constraining NP with Flavour: $\Delta F = 2$

Determining SM flavour parameters becomes more involved in presence of possible NP. The key challenge is to disentangle the SM from NP contributions to key flavour observables. A common working assumption, based on the apparent good consistency of the global CKM fit, is that NP predominantly contributes to observables, which are (loop, helicity) suppressed in the SM. This allows to use unsuppressed (tree-level) SM processes (allowing the extraction of ϕ_2, ϕ_3 angles as well as $|V_{ub}/V_{cb}|$) to fully determine the CKM and thus predict SM contributions to other (loop) suppressed observables.

Often it makes sense to parameterize NP effects relative to (known) SM contributions in a model independent way. A well studied example is the neutral meson dispersive mixing amplitude, which can be written in full generality as $M_{12} = M_{12}^{\text{SM}}(1 + h_{\text{NP}}e^{i\theta_{\text{NP}}})^2$, where h_{NP} and θ_{NP} parametrize the NP modulus and phase modifications relative to the SM reference point ($h_{\text{NP}} = \theta_{\text{NP}} = 0$). With such a parametrization, NP deviations with respect to the SM can be predicted in all physical observables affected by B meson oscillations. This in turn allows to extract tight constraints on h_{NP} and θ_{NP} , given sufficiently precise knowledge of M_{12}^{SM} . Fortunately, the continuous improvements in CKM parameter determinations, perturbative electroweak and QCD calculations of short distance SM contributions, as well as non-perturbative Lattice QCD simulations of the required long distance hadronic matrix elements over the past few decades, today allow us to predict M_{12}^{SM} to better than 10% for the $B_{d,s}$ meson systems and also $\text{Im}(M_{12}^{\text{SM}})$ for neutral kaons.⁶ And given good consistency with current relevant experimental results, we can conclude that NP in neutral meson mixing is at most comparable to the SM.

Conversely, the resulting severe constraints on BSM effects in $\Delta F = 2$ processes induce the so called *NP flavour problem*. In particular, we can parameterize contributions of heavy NP degrees of freedom to low energy (flavour) observables in terms of a Wilsonian expansion

$$\mathcal{L}_{\text{BSM}} = \mathcal{L}_{\text{SM}} + \sum_{i,(d>4)} \frac{\mathcal{Q}_i^{(d)}}{\Lambda^{d-4}}, \quad (2)$$

where \mathcal{L}_{SM} is the SM Lagrangian, and the sum runs over all possible (consistent with the SM gauge symmetry) local operators $\mathcal{Q}_i^{(d)}$ of a given canonical dimension d containing SM fields only. Then, Λ parametrizes the effective NP scale. Consistency of flavour observables with SM expectations can be cast in terms of lower bounds on Λ . For generic NP operator flavour structures contributing to $\Delta F = 2$ processes, e.g. $\mathcal{Q}_{AB}^{(6)} \sim [\bar{q}_i \Gamma^A q_j] \times [\bar{q}_i \Gamma^B q_j]$, where $\Gamma^{A,B}$ are elements from the Clifford algebra, the current bounds on Λ are starting to reach $\mathcal{O}(\text{EeV})$.⁷ This is seemingly at odds with expectations of $\mathcal{O}(\text{TeV})$ NP based on the EW hierarchy problem or the WIMP dark matter paradigm. It is however important to stress, that future improvements in $\Delta F = 2$ sensitivity to heavy NP will crucially depend on improved theory (in particular Lattice QCD) inputs.

4 CP Violation in Charm Decays

Very recently, direct CP violation in decays of charmed mesons has been observed (again) by the LHCb collaboration.⁸ The relevant observables here are the time integrated CP violating

decay asymmetries to CP eigenstates

$$a_f \equiv \frac{\Gamma(D^0 \rightarrow f) - \Gamma(\bar{D}^0 \rightarrow f)}{\Gamma(D^0 \rightarrow f) + \Gamma(\bar{D}^0 \rightarrow f)}, \quad (3)$$

which in principle receive contributions from both direct and indirect CP violation $a_f = a_f^{\text{dir.}} + \frac{\langle \tau \rangle}{\tau_D} a_{CP}^{\text{indir.}}$, in practice however the smallness of the effective lifetime window cut ($\langle \tau \rangle$) at LHCb severely suppresses indirect CP violating effects (from interference between mixing and decay amplitudes). Direct CP violation arises from interference between decay amplitudes. In particular, LHCb observed a non-vanishing difference between CP asymmetries in D decays to pairs of charged kaons and pions $\Delta a_{CP} \equiv a_{K^+K^-} - a_{\pi^+\pi^-} = (-15.4 \pm 2.9) \times 10^{-4}$.⁸

The result poses an important question: can the observed CP violation be accounted for within the SM or does it signal the presence of NP? The SM contributions to the relevant direct CP asymmetries can be conveniently parametrized as $a_f^{\text{dir.}} \simeq 2r_f \sin \phi_f \sin \delta_f$, $f = K, \pi$ where r_f denotes the absolute ratio of the two dominant interfering decay amplitudes, while ϕ_f and δ_f stand for the relative weak (CP odd) and strong (CP even) phase differences, respectively. Written in terms of the relevant weak decay amplitudes

$$A_K = \lambda_s A_K^{(1)} + \lambda_b A_K^{(2)}, \quad A_\pi = \lambda_d A_\pi^{(1)} + \lambda_b A_\pi^{(2)}, \quad (4)$$

where $\lambda_q = V_{cq}^* V_{uq}$, one deduces that $r_f \propto \xi = |\lambda_b/\lambda_s| \simeq |\lambda_b/\lambda_d| \approx 0.0007$ while $\phi_K^{\text{SM}} = \arg(\lambda_b/\lambda_s) \simeq -\arg(\lambda_b/\lambda_d) = -\phi_\pi^{\text{SM}} \approx 70^\circ$. Consequently, one can write⁹

$$\Delta a_{CP}^{\text{SM}} \approx (0.13\%) \text{Im}(\Delta R^{\text{SM}}), \quad \text{where} \quad \Delta R^{\text{SM}} \equiv \frac{A_K^{(2)}}{A_K^{(1)}} + \frac{A_\pi^{(2)}}{A_\pi^{(1)}}. \quad (5)$$

At leading order the the perturbative α_s expansion in the heavy charm quark ($m_c \gg \Lambda_{\text{QCD}}$) limit yields for the relevant ratio of amplitudes $A_f^{(2)}/A_f^{(1)} \sim \alpha_s(m_c)/\pi$.¹⁰ However values of ΔR^{SM} of order one cannot be excluded from first principles with current approaches.¹¹ The resolution of this questions will thus possibly require considerable progress in Lattice QCD techniques, especially in light of the ongoing efforts to resolve a similar puzzle of direct CP violation in neutral kaon decays (ϵ'/ϵ).⁶

5 NP Sensitivity of $\Delta F = 1$ Processes

In general, (semi)leptonic flavour changing neutral current (FCNC) decays offer BSM probes, complementary to those of $\Delta F = 2$. For example, the rare leptonic decays $B_{d,s} \rightarrow \mu^+ \mu^-$ are both electroweak loop and helicity suppressed in the SM and theoretically well under control,¹² again using a combination of CKM inputs, perturbative QCD calculations and Lattice QCD evaluation of non-perturbative hadronic matrix elements of the relevant quark currents (decay constants). In the model-independent effective field theory extension of the SM in Eq. (2) they probe the so called ‘Z-penguin’ and semileptonic four-fermion operators which modify the SM expectations for the relevant branching ratios as $\mathcal{B}^{s,d} \simeq \mathcal{B}_{\text{SM}}^{s,d} (1 \pm 4\pi v^2/g^2 |V_{tb} V_{ts,d}^*|^2 \Lambda^2)$, where g is the SM weak coupling.¹³ The current experimental precision and consistency with SM expectations at the level of 30% allows to probe NP scales up to $\Lambda \gtrsim \mathcal{O}(40)$ TeV.¹⁴

More information than just the total rate is available in semileptonic decays in the form of kinematical distributions of the decay products. A notable example is the decay $B^0 \rightarrow (K^{*0} \rightarrow K^+ \pi^-) \mu^+ \mu^-$, whose triple differential decay rate can be fully parametrized in terms of eight helicity amplitudes and is sensitive to several effective operator structures. Unfortunately, a straightforward extraction of short distance contributions is obscured by the challenging theoretical uncertainties due to the hadronic substructure of the photon. A number optimized observables with reduced long distance contamination in certain regions of phase space has been

proposed and implemented into experimental analyses with intriguing yet somewhat inconclusive results.¹⁵

Another way to go beyond hadronic uncertainties is to consider lepton flavor universality (LFU) ratios like $R_K = \Gamma(B^+ \rightarrow K^+ \mu^+ \mu^-) / \Gamma(B^+ \rightarrow K^+ e^+ e^-)$. In the SM the decays to different lepton flavors only differ by phase space. In particular, the hadronic uncertainties predominantly cancel in LFU ratios and the dominant contributions come from electromagnetic radiative effects. Consequently, away from thresholds $R_K = 1 + \mathcal{O}(10^{-3})$.¹⁶ Intriguingly, the most precise LHCb results for the LFU ratios in both $B \rightarrow K$ and $B \rightarrow K^*$ decays have been consistently *below* one at the level of 20%!¹⁷ This has to be contrasted with LFU tests in Z and W decays performed at LEP, which have probed and confirmed LFU at the sub-percent level.¹⁸ Another venue to test LFU are however charged current mediated (semi)leptonic B decays.

6 LFU Tests in Semileptonic B Decays

As discussed in Sec. 2, semileptonic B decays are usually considered to be dominated by SM contributions and thus suitable for a clean extraction of $|V_{cb,ub}|$. Recently, the Belle collaboration tested for LFU violations in $B \rightarrow D^* \mu / e \nu$ decays and found agreement with LFU at the percent level.¹⁹ Alternatively, one can consider the taonic ratio²⁰

$$R(D^{(*)}) \equiv \frac{\mathcal{B}(B \rightarrow D^{(*)} \tau \nu)}{\mathcal{B}(B \rightarrow D^{(*)} \ell \nu)}, \quad (\ell = e, \mu). \quad (6)$$

In these ratios, phase space effects are much more significant than in R_K , and additional m_τ/m_B suppressed helicity amplitude contributions cannot be neglected. Nonetheless, a combination of heavy quark effective theory estimates, lattice QCD results and kinematical distribution fits to data presently allows to control the theoretical uncertainties at the few percent level. Since a few years the experimental results for $R(D^{(*)})$ from BaBar, Belle and LHCb have consistently exhibited *upward* tensions with respect to the SM expectations, and after the latest Belle update are at the 20% level.²¹

7 Perspective on the LFU B -anomalies

There are a number of reasons why apparent departures from LFU in B decays are interesting and deserve thorough scrutiny: The SM gauge sector respects a large accidental flavor symmetry $G_F^{\text{SM}} = U(3)^5$, where each $U(3)$ refers to the generational flavour symmetry of one fermionic SM gauge representation. G_F^{SM} is broken only by the Higgs Yukawas down to $G_{\text{acc}}^{\text{SM}} = U(1)^4$, the $U(1)$ factors referring to baryon number and the three lepton numbers, respectively. Thus, charged lepton masses are the unique source of LFU breaking in the SM. Consequently, any LFU violation beyond lepton mass effects would be a clear sign of NP. Secondly, any prospective BSM physics aiming to address the LFU anomalies, needs to face the NP flavor problem. In particular, as we have briefly discussed in Sec. 3 new sources of (a) flavor breaking, (b) CP violation or (c) new chiral structures (with respect to the SM) are severely constrained by existing measurements. At the same time, and somewhat surprisingly, none of these are actually required or implied by the current LFU violation hints. BSM models should thus be non-generic – with either suppressed or vanishing new sources of (a,b,c) features. This raises the question whether we can keep ignoring the SM ‘origin of flavor’ puzzle in NP model building?

8 Conclusions

We live in interesting and exciting times for flavor physics. Several apparent flavour anomalies are currently awaiting resolution, and with good experimental prospects! New experiments like Belle II, and LHCb-II are starting, and an order of magnitude improvement in statistics is expected

in the next decade. The experimental front will be further broadened by several upcoming Kaon experiments like NA62²² and KOTO²³, measuring rare kaon decays like $K \rightarrow \pi\nu\bar{\nu}$ at unprecedented precision.

Thus, while there is cautious excitement at the prospect of possible NP discoveries, we nonetheless need to keep in mind the lessons from the persistent $V_{ub,cb}$ discrepancies. There are also other eagerly awaited developments, like the Lattice QCD progress in the resolution of the ϵ'/ϵ status and possibly Δa_{CP} , as well as news from Fermilab regarding the improved measurement of the anomalous magnetic moment of the muon $-(g-2)_\mu$.²⁴ All of these guarantee that flavour physics will remain vibrant and in vogue in the years to come.

Acknowledgments

The author would like to thank the organizers for the generous support, hospitality and excellent organization and acknowledges the financial support from the Slovenian Research Agency (research core funding No. P1-0035 and J1-8137).

References

1. A. J. Bevan *et al.* [BaBar and Belle Collaborations], *Eur. Phys. J. C* **74** (2014) 3026.
2. CKMfitter collaboration, Summer 2018 update available on <http://ckmfitter.in2p3.fr/>.
3. E. Kou *et al.* [Belle-II Collaboration], arXiv:1808.10567 [hep-ex].
4. R. Aaij *et al.* [LHCb Collaboration], arXiv:1808.08865.
5. M. Fael, these proceedings.
6. S. Aoki *et al.* [Flavour Lattice Averaging Group], arXiv:1902.08191 [hep-lat].
7. M. Gonz alez-Alonso, these proceedings.
8. R. Aaij *et al.* [LHCb Collaboration], arXiv:1903.08726 [hep-ex].
9. G. Isidori, J. F. Kamenik, Z. Ligeti and G. Perez, *Phys. Lett. B* **711** (2012) 46.
10. Y. Grossman, A. L. Kagan and Y. Nir, *Phys. Rev. D* **75** (2007) 036008.
11. J. Brod, A. L. Kagan and J. Zupan, *Phys. Rev. D* **86** (2012) 014023.
12. C. Bobeth, M. Gorbahn, T. Hermann, M. Misiak, E. Stamou and M. Steinhauser, *Phys. Rev. Lett.* **112** (2014) 101801.
13. U. Haisch, Heavy Flavour physics at HL-LHC, 31 August 2016, CERN.
14. A. Cerri, these proceedings.
15. R. Alepuz, these proceedings.
16. M. Bordone, G. Isidori and A. Pattori, *Eur. Phys. J. C* **76** (2016) no.8, 440.
17. R. Oldeman, these proceedings.
18. S. Schael *et al.* [ALEPH and DELPHI and L3 and OPAL and SLD Collaborations and LEP Electroweak Working Group and SLD Electroweak Group and SLD Heavy Flavour Group], *Phys. Rept.* **427** (2006) 257.
19. A. Abdesselam *et al.* [Belle Collaboration], arXiv:1809.03290 [hep-ex].
20. J. F. Kamenik and F. Mescia, *Phys. Rev. D* **78** (2008) 014003. S. Fajfer, J. F. Kamenik and I. Nisandzic, *Phys. Rev. D* **85** (2012) 094025.
21. G. Caria, proceedings of the Moriond EW 2019.
22. E. Cortina Gil *et al.* [NA62 Collaboration], *Phys. Lett. B* **791** (2019) 156.
23. J. K. Ahn *et al.* [KOTO Collaboration], *PTEP* **2017** (2017) no.2, 021C01.
24. F. Jegerlehner, *Acta Phys. Polon. B* **49** (2018) 1157.

RARE, RADIATIVE, AND ELECTROWEAK PENGUIN DECAYS OF HEAVY FLAVOUR HADRONS AT LHCb

CLARA REMON ALEPUZ, ON BEHALF OF THE LHCb COLLABORATION
Instituto de Física Corpuscular (Universidad de Valencia - CSIC), Spain

Rare b -decays allow to probe large energy scales through indirect measurements. Over recent years an interesting pattern of deviations has emerged in $b \rightarrow s\ell\ell$ transitions. These proceedings review the experimental status of rare b -decays (excluding Lepton Flavour Universality tests), focusing on recent results by the LHCb collaboration involving a $b \rightarrow s\gamma$ transition. The newest measurements from the LHCb collaboration that will be discussed here are the first observation of $\Lambda_b \rightarrow \Lambda\gamma^1$ and the time-dependent analysis of $B_s^0 \rightarrow \phi\gamma^2$, which provides constraints on right-handed current contributions which are suppressed in the SM.

1 Introduction

Rare b -decays involve Flavour Changing Neutral Currents (FCNC), thus they can only occur via loop diagrams in the Standard Model (SM). Therefore, new heavy particles can enter the loop inducing quantum effects in different observables. That makes rare b -decays a perfect probe of New Physics (NP) as they allow to explore much larger energy scales than direct searches. Figure 1 shows the three different transition types that can be involved in rare b -decays, each of them sensitive to different NP effects. Within a model-independent description the effective Hamiltonian can be written as a combination of effective couplings ($C_i^{(\prime)}$, also referred to as Wilson coefficients) and local operators ($O_i^{(\prime)}$): $\mathcal{H}_{eff} = -\frac{4G_F}{\sqrt{2}} V_{tb} V_{ts}^* \frac{\alpha}{4\pi} \sum_i \{C_i O_i + C_i' O_i'\}$, where the primed (C_i' and O_i') refers to right-handed currents. The radiative penguin is ruled by the electromagnetic operator ($O_7^{(\prime)}$), thus $b \rightarrow s\gamma$ is sensitive to $C_7^{(\prime)}$. The $b \rightarrow \ell\ell$ transitions are sensitive to $C_{10,S,P}^{(\prime)}$, which are the effective couplings for vector-axial, scalar and pseudoscalar operators, respectively. And $b \rightarrow s\ell\ell$ processes are sensitive to $C_{7,9,10}^{(\prime)}$, where $C_9^{(\prime)}$ is the purely vector Wilson coefficient.

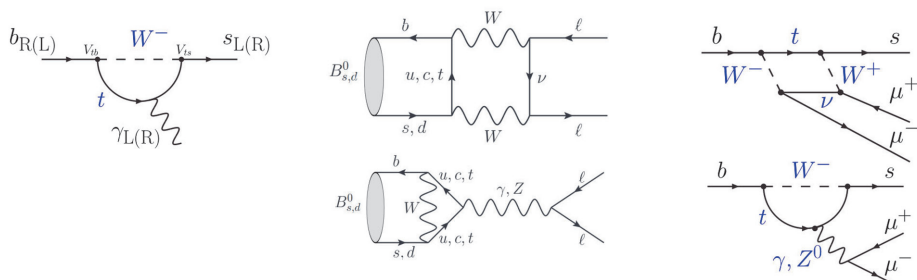


Figure 1 – Rare b -decays transitions at quark level: $b \rightarrow s\gamma$, $b \rightarrow \ell\ell$ and $b \rightarrow s\ell\ell$.

In recent years some tensions with respect to the SM predictions have appeared in measurements of experimental observables involving $b \rightarrow s\ell\ell$ transitions. These are present in branching

ratio measurements of different decay modes at the low q^2 region^{3 4 5}, and also in comparatively clean angular observables, such as the P'_n basis used in the angular analysis of $B^0 \rightarrow K^{*0} \mu^+ \mu^-$ decay⁶. These combined with LFUV measurements give rise to sizeable deviations with respect to the SM in the global fits⁷. These tensions could be driven by statistical fluctuations or the possibility of underestimated hadronic uncertainties. On the other hand, if this effect points to NP, it is compatible with lepto-quarks or Z' models. In order to confirm and understand this pattern, it is crucial to exploit all the data collected during Run II of LHC and explore new modes which can provide complementary measurements.

Moreover, there are two very recent results at LHCb involving $b \rightarrow s \gamma$ transitions that are presented in the following sections (Sec. 3 and 2). Radiative decays proceed via the electroweak penguin diagram described in Fig.1. Due to the chiral structure of the W boson, the photon polarization is predominantly left-handed in the SM, with a small right-handed component of the order $\mathcal{O}\left(\frac{m_s}{m_b}\right)$. However, there is an enhancement of the right-handed component predicted by some extensions of the SM (e.g LRMS)⁸, where A_L/A_R can be up to 1/2.

2 First observation of $\Lambda_b \rightarrow \Lambda \gamma$

The measurement of the $\mathcal{B}(\Lambda_b \rightarrow \Lambda \gamma)$ represents the first observation of a radiative b-baryon decay. Given the large amount of Λ_b^0 baryons produced at the LHC, it gives the perfect opportunity to study this process at the LHCb detector, which was optimized to reconstruct b-hadron decays. The best limit, set by the CDF experiment, is $\mathcal{B}(\Lambda_b \rightarrow \Lambda \gamma) < 1.9 \times 10^{-3}$ at 95% CL⁹, being this measurement still far from the SM prediction ($6 - 100 \times 10^{-7}$)⁹. Moreover, thanks to the Λ_b non-zero spin, it is possible to access the photon polarization through an angular analysis¹⁰.

From the experimental point of view this is a very challenging decay process, since the Λ_b vertex cannot be reconstructed. This is due to the long flight of the Λ^0 before decaying, along with the unknown photon direction as it is measured as a cluster in the electromagnetic calorimeter. Therefore a high performance BDT is used to separate signal from background. The data sample

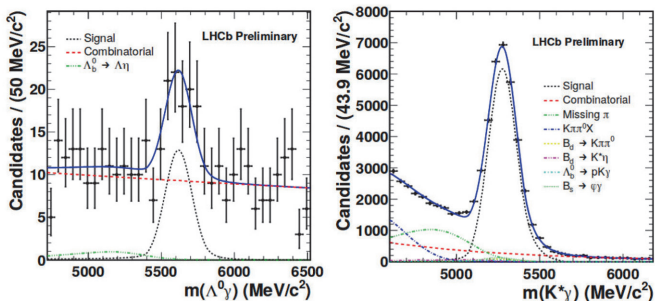


Figure 2 – Simultaneous fit to the invariant mass of $\Lambda_b \rightarrow \Lambda \gamma$ (left) and $B^0 \rightarrow K^{*0} \gamma$ (right). Black dots corresponds to the data and the blue curve represents the fit, while dashed lines are the individual contributions.

used to perform the measurement corresponds to an integrated luminosity of 1.7 fb^{-1} , collected by the LHCb experiment in p-p collisions at $\sqrt{13} \text{ TeV}$. In Fig 2, the simultaneous fit of the reconstructed invariant mass of signal and normalization modes is shown, the latter being the well known $B^0 \rightarrow K^{*0} \gamma$ decay. A signal excess of 65 ± 13 candidates is observed with a significance of 5.6σ , including systematic uncertainties. The branching fraction is found to be:

$$\mathcal{B}(\Lambda_b \rightarrow \Lambda \gamma) = (7.1 \pm 1.5 \pm 0.7 \pm 0.6) \times 10^{-6}$$

where the first uncertainty is statistical, the second systematic and the third comes from the ratio

of hadronization fractions. This represents the first time the rare radiative $\Lambda_b \rightarrow \Lambda \gamma$ decay is observed, opening the possibility of photon polarization measurements in b-baryons.

3 Measurement of CP-violating observables in $B_s^0 \rightarrow \phi \gamma$

The B_s^0 is a neutral meson which presents the mixing induced interference phenomenon giving access to the photon polarization, via the exploitation of the time evolution of $B_s^0 \rightarrow \phi \gamma$:

$$\Gamma(t) \propto e^{-\Gamma_s t} \left[\cosh\left(\frac{\Delta\Gamma_s t}{2}\right) - \mathcal{A}_{\phi\gamma}^{\Delta} \sinh\left(\frac{\Delta\Gamma_s t}{2}\right) \pm C_{\phi\gamma} \cos(\Delta m_s t) \mp S_{\phi\gamma} \sin(\Delta m_s t) \right] \quad (1)$$

where $\mathcal{A}_{\phi\gamma}^{\Delta}$ and $S_{\phi\gamma}$ are sensitive to photon polarization (and weak phases), while $C_{\phi\gamma}$ is related to direct CP violation. The SM predicts these three parameters to be very close to zero¹¹, therefore any sizeable value may be a sign of NP. The LHCb experiment measured $\mathcal{A}_{\phi\gamma}^{\Delta}$ parameter for the first time, using the complete Run I dataset corresponding to 3 fb^{-1} , obtaining a result compatible with the SM expectation within two standard deviations¹²: $\mathcal{A}_{\phi\gamma}^{\Delta} = -0.98^{+0.46}_{-0.52} +0.23_{-0.20}$. This result is dominated by the statistical uncertainty, and the main systematic contribution comes from the background modelling.

Furthermore, if we know the flavour of the initial B_s meson we can also access $C_{\phi\gamma}$ and $S_{\phi\gamma}$, which have been never measured before in B_s decays. The flavour information of the B_s is obtained from two classes of flavour-tagging algorithms at LHCb: same-side (SS)¹³ and opposite-side (OS)¹⁴ taggers. In a further analysis the LHCb experiment measured for the first time these parameters, using a sample of more than 5000 $B_s^0 \rightarrow \phi \gamma$ signal candidates reconstructed in the full Run I data sample. $\mathcal{A}_{\phi\gamma}^{\Delta}$ result is also updated with respect the aforementioned analysis¹², as the reconstruction has been improved. The $B^0 \rightarrow K^{*0} \gamma$ decay, with very similar topology to the signal, is used to control the acceptance, since it has six times larger branching and the decay rate is not affected by NP. Figure 3 shows the mass-fit of the signal and control modes, which is used to subtract the background with the sPlot technique¹⁵. Mixing-induced CP-violating observables

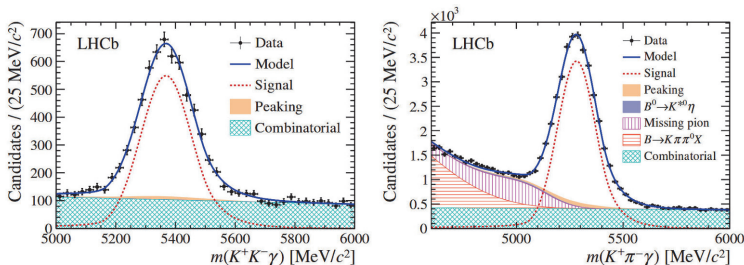


Figure 3 – Fits to the invariant mass distributions of the B_s^0 (top) and B^0 (bottom) candidates.

are extracted from a simultaneous unbinned fit to the decay-time distributions of $B_s^0 \rightarrow \phi \gamma$ and $B^0 \rightarrow K^{*0} \gamma$, using the weighted data. The decay-time distributions and the corresponding fit projections are shown in Figure 4, and the measured values are:

$$\begin{aligned} S_{\phi\gamma} &= 0.43 \pm 0.30 \pm 0.11, \\ C_{\phi\gamma} &= 0.11 \pm 0.29 \pm 0.11, \\ \mathcal{A}_{\phi\gamma}^{\Delta} &= -0.67^{+0.37}_{-0.41} \pm 0.17 \end{aligned}$$

which are compatible with the SM within 1.3, 0.3 and 1.7 σ . The first uncertainty is statistical (including the external parameters), and the second corresponds to the systematic. In the case of $S_{\phi\gamma}$ and $C_{\phi\gamma}$ the main source of the systematic is the control of the resolution using simulation, and the calibration of the flavour tagging, while the $\mathcal{A}_{\phi\gamma}^{\Delta}$ measurement is dominated by the background modelling.

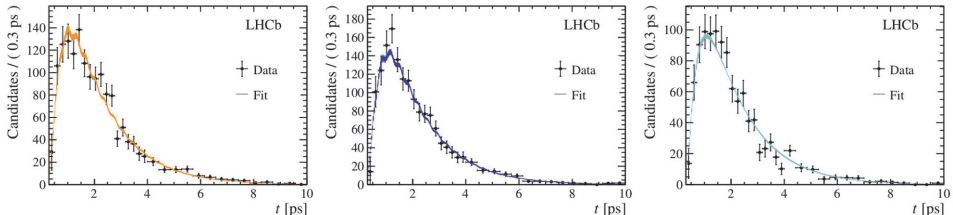


Figure 4 – Decay-time fit projections for $B_s^0 \rightarrow \phi\gamma$ decays where the candidate is tagged as B_s (left), as \bar{B}_s^0 (middle) and (right) untagged candidates.

This is the first measurement of $S_{\phi\gamma}$ and $C_{\phi\gamma}$ in B_s^0 decays, competitive with previous B -factories measurements done in B^0 decays, all compatible with the SM. Considering that $S_{\phi\gamma}$ and $\mathcal{A}_{\phi\gamma}^{\Delta}$ are sensitive to the imaginary and real parts of C'_7 respectively, this result gives complementary constraints on the C'_7 complex plane and thus provides further constraints on the right-handed current contributions in $b \rightarrow s\gamma$ transitions.

4 Summary

Rare b-decays occurs via FCNC's allowing to probe large energy scales through indirect measurements. In recent years an interesting pattern of deviations has emerged in $b \rightarrow s\ell\ell$. Even so, no evidence of NP has been found, therefore exploiting more data and new modes is crucial to shed light on this subject.

There has been two very recent results in LHCb involving $b \rightarrow s\gamma$ transitions. $\Lambda_b \rightarrow \Lambda\gamma$ has been observed for the first time, opening the possibility of photon polarization measurements in b-baryons. Moreover the first measurement of $S_{\phi\gamma}$ and $C_{\phi\gamma}$ in B_s^0 through the time-dependent analysis of $B_s^0 \rightarrow \phi\gamma$ gives constraints on $\text{Re}(C'_7)$ and $\text{Im}(C'_7)$.

References

1. R. Aaij *et al*, First observation of the rare radiative $\Lambda_b \rightarrow \Lambda\gamma$ decay. (2019 in preparation)
2. R. Aaij *et al*, Measurement of the mixing-induced and CP-violating observables in $B_s^0 \rightarrow \phi\gamma$ decays at LHCb. (2019 in preparation)
3. R. Aaij *et al*. [LHCb Collaboration], JHEP **1406** (2014) 133, arXiv:1403.8044 [hep-ex]
4. R. Aaij *et al*. [LHCb Collaboration], JHEP **1506** (2015) 115, arXiv:1503.07138 [hep-ex]
5. R. Aaij *et al*. [LHCb Collaboration], JHEP, 09:179, 2015.
6. R. Aaij *et al*. JHEP, 02:104, 2016.
7. S. Descotes-Genon *et al*., JHEP 06 (2016) 092, arXiv:1510.04239v3 [hep-ph]
8. Fu-Sheng Yu *et al.*, JHEP12 (2013), 102, arXiv:1305.3173 [hep-ph]
9. D. Acosta *et al.*, Phys. Rev., D66:112002, 2002.
10. L.M Garcia *et al.*, (2019) arXiv:1902.04870v2 .
11. F. Muheim, Y. Xie, and R. Zwicky, Physics Letters B 664 (2008) 174
12. R. Aaij *et al*. [LHCb Collaboration], Phys. Rev. Lett. 118, 109901 (2017)
13. R. Aaij *et al*. [LHCb Collaboration], JINST 11 (2016) P05010, arXiv:1602.07252
14. R. Aaij *et al*. [LHCb Collaboration], Eur. Phys. J.C72 (2012) 2022, arXiv:1202.4979
15. M. Pivk *et al.*, Nucl. Instrum. Meth. A555 (2005) 356, arXiv:physics/0402083

SEARCH FOR NEW PHYSICS SIGNALS VIA DOUBLY WEAK B DECAYS

FAISAL MUNIR BHUTTA^{1,3}, CAI DIAN LÜ^{1,2},

¹*Institute of High Energy Physics, Chinese Academy of Sciences, Beijing 100049, China*

²*University of Chinese Academy of Sciences, Beijing 100049, China*

³*Institute of Theoretical Physics, College of Applied Sciences, Beijing University of Technology, Beijing 100124, China*

The doubly weak $b \rightarrow dd\bar{s}$ and $b \rightarrow ss\bar{d}$ processes are highly suppressed in the standard model that offer the unique opportunity to explore new physics signals. The wrong sign decay $\bar{B}^0 \rightarrow K^+\pi^-$ mediated by the $b \rightarrow dd\bar{s}$ transition can be distinguished from the penguin decay $B^0 \rightarrow K^+\pi^-$, through time dependent measurement in experiments. We consider a model independent analysis of $\bar{B}^0 \rightarrow K^+\pi^-$ decay, within the perturbative QCD approach and explore various effective dimension-6 operators, in which large effects are possible. We also study the doubly weak exclusive process in two example models namely Randall-Sundrum model with custodial protection and the bulk-Higgs Randall-Sundrum model. A large and significant enhancement of the branching ratio, in comparison to the standard model, is observed after satisfying all the relevant constraints on the parameter spaces of these models, which requires to be searched in future experiments.

1 Introduction

Rare B decays induced by flavor-changing neutral-current (FCNC) transitions come with an interesting possibility of exploring the virtual effects from new physics (NP) beyond the standard model (SM). Compared to radiative, leptonic and semi-leptonic rare B decays, NP investigations through purely hadronic B decays pose added difficulty because of relatively much larger theoretical hadronic uncertainties, which hinder to make any definite conclusion for the presence of NP signals in the hadronic rare decays. Therefore we focus on an alternate strategy proposed by Huitu *et al.*¹, which is to search for the rare b decay channels which have extremely small rates in the SM, so that mere detection of such processes will be a clear signal of NP.

The doubly weak transitions, $b \rightarrow dd\bar{s}$ and $b \rightarrow ss\bar{d}$ are prototype processes which occur via box diagrams and are highly suppressed in the SM, with branching ratios of approximately $\mathcal{O}(10^{-14})$ and $\mathcal{O}(10^{-12})$, respectively. Both inclusive and exclusive $B \rightarrow PP, PV, VV$ channels based on $b \rightarrow dd\bar{s}$ and $b \rightarrow ss\bar{d}$ transitions have been investigated in several examples of NP models^{2,3}. However, measuring these two body doubly weak decays in experiments, is challenging, since in most cases they mix with the ordinary weak decays through $B_{d,s}^0$ - $\bar{B}_{d,s}^0$ mixing or K^0 - \bar{K}^0 mixing. In the case of $b \rightarrow dd\bar{s}$ transition, only three-body decay $B^+ \rightarrow \pi^+\pi^+K^-$ is searched experimentally and the LHCb collaboration has provided the upper limit⁴ $\mathcal{B}(B^+ \rightarrow \pi^+\pi^+K^-) < 4.6 \times 10^{-8}$.

We calculate the exclusive two body pure annihilation decay $\bar{B}^0 \rightarrow K^+\pi^-$ induced by $b \rightarrow dd\bar{s}$ transition, within the perturbative QCD factorization approach (PQCD) and propose to look for this wrong sign decay by performing a flavour-tagged time-dependent analysis of the right sign decay $B^0 \rightarrow K^+\pi^-$ with a large data sample, following reference⁵. For detail discussion, we refer the reader to⁶.

2 $\bar{B}^0 \rightarrow K^+ \pi^-$ decay in the standard model

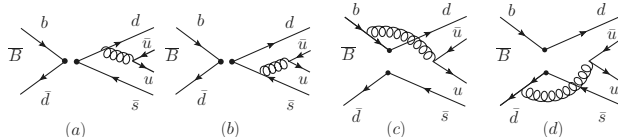


Figure 1 – Leading order Feynman diagrams contributing to $\bar{B}^0 \rightarrow K^+ \pi^-$ decay, (a) and (b) are the factorizable diagrams, (c) and (d) are the nonfactorizable diagrams.

In the SM, $b \rightarrow dd\bar{s}$ transition is both loop and CKM suppressed. The local effective Hamiltonian for $b \rightarrow dd\bar{s}$ transition is given by:

$$\mathcal{H}^{\text{SM}} = C^{\text{SM}} [(\bar{d}_L^\alpha \gamma^\mu b_L^\alpha)(\bar{d}_L^\beta \gamma_\mu s_L^\beta)] \quad (1)$$

with C^{SM} involving the CKM matrix elements and the loops functions given in⁶. The exclusive $\bar{B}^0 \rightarrow K^+ \pi^-$ decay, mediated by $b \rightarrow dd\bar{s}$ transition, proceeds through the annihilation type Feynman diagrams which can be calculated in PQCD formalism⁷. Figure 1 shows four lowest order annihilation Feynman diagrams for $\bar{B}^0 \rightarrow K^+ \pi^-$ decay. By solving these diagrams in PQCD factorization approach, we estimate the branching fraction in the SM:

$$\mathcal{B}(\bar{B}^0 \rightarrow K^+ \pi^-)^{\text{SM}} = 1.0 \times 10^{-19}. \quad (2)$$

3 Model independent analysis of the $\bar{B}^0 \rightarrow K^+ \pi^-$ Decay

To perform model independent analysis, we consider the most general local effective Hamiltonian with all possible dimension-6 operators⁸:

$$\mathcal{H}_{\text{eff}}^{\text{NP}} = \sum_{j=1}^5 [C_j \mathcal{O}_j + \tilde{C}_j \tilde{\mathcal{O}}_j], \quad (3)$$

where

$$\begin{aligned} \mathcal{O}_1 &= (\bar{d}_L \gamma_\mu b_L)(\bar{d}_L \gamma^\mu s_L), & \mathcal{O}_2 &= (\bar{d}_R b_L)(\bar{d}_R s_L), & \mathcal{O}_3 &= (\bar{d}_R^\alpha b_L^\beta)(\bar{d}_R^\beta s_L^\alpha), \\ \mathcal{O}_4 &= (\bar{d}_R b_L)(\bar{d}_L s_R), & \mathcal{O}_5 &= (\bar{d}_R^\alpha b_L^\beta)(\bar{d}_L^\beta s_R^\alpha). \end{aligned} \quad (4)$$

The chirality flipped $\tilde{\mathcal{O}}_j$ operators can be written from \mathcal{O}_j by $L \leftrightarrow R$ exchange. The NP beyond the SM can change the Wilson coefficient of operator \mathcal{O}_1 and it can also provide non zero Wilson coefficients for other new operators. These Wilson coefficients are not free parameters and are constrained by $K^0 - \bar{K}^0$ and $B^0 - \bar{B}^0$ mixing parameters. In the case, where NP only contributes to the local operator \mathcal{O}_1 , similar to the SM, NP contributions are not allowed much room due to a good agreement of the SM results for mixing observables with the experimental data. Among the remaining nine non-standard operators, we consider each operator individually and calculate the corresponding decay width of the $\bar{B}^0 \rightarrow K^+ \pi^-$ decay given in case of \mathcal{O}_{2-5} and $\tilde{\mathcal{O}}_{1-5}$:

$$\Gamma_j = \frac{m_B^3}{64\pi} \left| F_{aj} \left[\frac{4}{3} C_j^{dd\bar{s}} \right] + \mathcal{M}_{aj} \left[C_j^{dd\bar{s}} \right] \right|^2, \quad \tilde{\Gamma}_j = \frac{m_B^3}{64\pi} \left| F_{aj} \left[\frac{4}{3} \tilde{C}_j^{dd\bar{s}} \right] + \mathcal{M}_{aj} \left[-\tilde{C}_j^{dd\bar{s}} \right] \right|^2, \quad (5)$$

respectively. Index “ j ” corresponds to the operator number. The explicit expressions of F_{aj} and \mathcal{M}_{aj} are given in⁶. Further, we define the ratio R between the branching fraction of the wrong sign decay and the branching fraction of the right sign decay:

$$R \equiv \frac{\mathcal{B}(\bar{B}^0 \rightarrow K^+ \pi^-)}{\mathcal{B}(\bar{B}^0 \rightarrow K^- \pi^+)}. \quad (6)$$

Table 1: Upper bounds on the Wilson coefficients of NP operators for experimental precision $R < 0.001$.

Parameter	Allowed range (GeV^{-2})	Parameter	Allowed range (GeV^{-2})
C_2	$< 6.3 \times 10^{-9}$	\tilde{C}_1	$< 1.1 \times 10^{-7}$
C_3	$< 5.1 \times 10^{-8}$	\tilde{C}_2	$< 6.8 \times 10^{-9}$
C_4	$< 4.9 \times 10^{-9}$	\tilde{C}_3	$< 5.3 \times 10^{-8}$
C_5	$< 1.6 \times 10^{-6}$	\tilde{C}_4	$< 4.2 \times 10^{-9}$
		\tilde{C}_5	$< 7.3 \times 10^{-7}$

Ratio R can be directly measured in experiments. Assuming that the current experimental precision can probe R to less than 10^{-3} , we obtain the upper bound on the Wilson coefficient of each non-standard NP operator, presented in Table 1.

Next, we consider a NP scenario involving NP field X , with mass M_X , that carries a conserved quantum number. In this NP example, it is possible to trivially satisfy mixing constraints through hierarchies among the NP couplings, so that $b \rightarrow dd\bar{s}$ transition remains unbounded³. We consider four scenarios of NP such that in S1 and S2, we suppose that NP matches onto the local operators \mathcal{O}_1 and $\tilde{\mathcal{O}}_1$, respectively, while in S3 (S4), NP involves the linear combination of local operators \mathcal{O}_4 (\mathcal{O}_5) and $\tilde{\mathcal{O}}_4$ ($\tilde{\mathcal{O}}_5$). As $K^0 - \bar{K}^0$ and $B^0 - \bar{B}^0$ mixing bounds do not constrain M_X in this case, we assume two cases of NP scale with $M_X = 1$ TeV and $M_X = 10$ TeV, respectively, and obtain the resulting PQCD prediction for the ratio R_X in each scenario. The results for both cases along with R_{SM} are listed in Table 2.

Table 2: Ratio R_X in case of NP carrying conserved charge along with R_{SM} .

Scenarios	R_X				R_{SM}
	M_X (TeV)	Case-I	M_X (TeV)	Case-II	
S1	1	0.085	10	8.5×10^{-6}	6.8×10^{-15}
S2		0.074		7.3×10^{-6}	
S3		55		0.005	
S4		0.002		1.9×10^{-7}	

4 $\bar{B}^0 \rightarrow K^+\pi^-$ in Randall-Sundrum Models

$\bar{B}^0 \rightarrow K^+\pi^-$ decay in the custodial Randall-Sundrum (RS_c) model^{9,10} receives tree level contributions from the lightest Kaluza-Klein (KK) gluons $\mathcal{G}^{(1)}$, KK photon $A^{(1)}$ and new heavy electroweak (EW) gauge bosons (Z_H, Z'). Z contributions protected through discrete P_{LR} symmetry and $\Delta F = 2$ contributions from Higgs boson exchanges are negligible. In the bulk-Higgs Randall-Sundrum (RS) model, $\bar{B}^0 \rightarrow K^+\pi^-$ decay results from the tree-level exchanges of KK gluons, KK photons, Z and the Higgs boson including their KK excitations and from the extended scalar fields $\phi^{Z(n)}$. Starting with the local effective Hamiltonian of Eq. (3) and assigning a common name $M_{g^{(1)}}$ to the masses of the lightest KK gauge bosons, we calculate the Wilson coefficients in both the RS models at $\mu = \mathcal{O}(M_{g^{(1)}})$. For explicit expressions we refer to⁶. The dominant contribution, in both RS models, comes from the KK gluons, while in RS_c model Z_H, Z' bosons try to compete with KK gluons contributions.

Two sets of data points are generated, by using the strategy employed in^{10,11,12}, which belong to anarchic 5D Yukawa coupling matrices with $y_\star = 1.5$ and 3. y_\star defines the maximum allowed value for the elements of the 5D Yukawa matrices. In the bulk-Higgs RS model, we use two different values of parameter β , which belong to different localization of the Higgs field along the extra dimension. Figure 2 shows a range of PQCD predictions for the branching ratio of the $\bar{B}^0 \rightarrow K^+\pi^-$ decay as a function of $M_{g^{(1)}}$ with two different values of y_\star , in both the RS models, after simultaneously incorporating the $\Delta m_K, \epsilon_K$ and Δm_{B_d} constraints. $y_\star = 1.5$

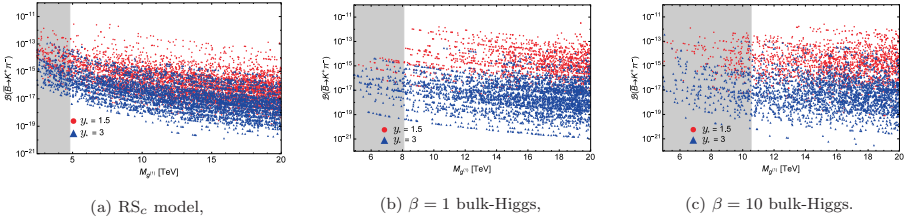


Figure 2 – $\overline{B}^0 \rightarrow K^+\pi^-$ branching fraction vs. the KK gluon mass $M_{g(1)}$ with two different values of y_* , (a) in the RS_c model and (b), (c) in the bulk-Higgs RS model with $\beta = 1$ and $\beta = 10$. The gray regions are excluded by the analysis of electroweak precision experiments.

and $y_* = 3$ cases are shown as red and blue scatter points, respectively. The gray shaded areas are excluded by the EW precision data. It is evident from Figure 2(a) that in the RS_c model, a maximum increase of six orders of magnitude in the branching ratio, compared to SM result, is achievable for $y_* = 1.5$ case. While from Figure 2(b) and 2(c), in the bulk-Higgs RS model, $\overline{B}^0 \rightarrow K^+\pi^-$ decay can get a maximum enhancement of five and six orders of magnitude for $y_* = 3$ and $y_* = 1.5$ value, respectively with both values of $\beta = 1$ and $\beta = 10$.

5 Conclusions

Doubly weak $\overline{B}^0 \rightarrow K^+\pi^-$ decay, mediated by $b \rightarrow dd\bar{s}$ transition, is studied in detail within the PQCD framework and a method is proposed to distinguish it from the right sign decay $B^0 \rightarrow K^+\pi^-$, by the time-dependent measurement of neutral B decays in $B^0 - \overline{B}^0$ mixing. In the model independent analysis, constraints on the Wilson coefficients of the new physics dimension-6 operators are derived for a specific experimental precision of the ratio R , while very large predictions for the ratio R_χ in different NP scenarios involving NP with a conserved charge are obtained due to the hierarchies among the NP couplings. In two variants of the RS model, after satisfying all the relevant constraints, a maximum enhancement of five to six orders of magnitude, in the decay rate of $\overline{B}^0 \rightarrow K^+\pi^-$, is possible for different parameter values, which leaves this decay free for the search of NP in future experiments.

Acknowledgments

We thank Ying Li and Yue-Hong Xie for collaboration on this topic. The work is partly supported by National Science Foundation of China (11521505 and 11621131001).

References

1. K. Huitu, C.-D. Lü, P. Singer and D.-X. Zhang, *Phys. Rev. Lett.* **81**, 4313 (1998).
2. S. Fajfer, J. F. Kamenik and N. Kosnik, *Phys. Rev. D* **74**, 034027 (2006).
3. D. Pirjol and J. Zupan, *JHEP* **02**, 028 (2010).
4. R. Aaij *et al.* [LHCb Collaboration], *Phys. Lett. B* **765**, 307 (2017).
5. B. Aubert *et al.* [BaBar Collaboration], *Phys. Rev. Lett.* **93**, 081801 (2004).
6. F. M. Bhutta, Y. Li, C.-D. Lü and Y.-H. Xie, [arXiv:1807.05350].
7. C. D. Lu, K. Ukai and M. Z. Yang, *Phys. Rev. D* **63**, 074009 (2001).
8. Y. Grossman, M. Neubert and A. L. Kagan, *JHEP* **10**, 029 (1999).
9. L. Randall and R. Sundrum, *Phys. Rev. Lett.* **83**, 3370 (1999).
10. M. Blanke, A. J. Buras, B. Duling, S. Gori and A. Weiler, *JHEP* **03**, 001 (2009).
11. C.-D. Lü, F. Munir and Q. Qin, *Chin. Phys. C* **41**, 053106 (2017).
12. A. Nasrullah, F. M. Bhutta and M. J. Aslam, *J. Phys. G* **45**, 095007 (2018).

Impact of polarization observables and $B_c \rightarrow \tau\nu$ on new physics explanations of the $b \rightarrow c\tau\nu$ anomaly

Ivan Nišandžić

Institut für Theoretische Teilchenphysik (TTP), Karlsruher Institut für Technologie (KIT), 76131 Karlsruhe, Germany

The combined analysis of the data on $B \rightarrow D^{(*)}\tau\nu$ decay observables shows some hints for the physics beyond the standard model (SM). In this talk we discuss the one- and two-dimensional fit scenarios which can be generated by adding a single new particle to the SM. We put an emphasis on model-discriminating power of $F_L(D^*)$, τ -polarizations, and an interplay with constraints from $BR(B_c \rightarrow \tau\nu)$.

1 Introduction

The tauonic decays of B mesons provide an interesting avenue for searches of beyond the standard model (SM) sources of violation of the lepton flavor universality (LFU).¹ An original motivation for closer study of these processes was provided by a possibility of revealing new physics (NP) effects of a charged Higgs.²⁻⁴ While the theoretical predictions for the individual semileptonic rates still involve sizeable hadronic uncertainties related to the form factors, normalizing the branching ratios $BR(B \rightarrow D^{(*)}\tau\nu)$ to $BR(B \rightarrow D^{(*)}e(\mu)\nu)$ yields the observables with theoretical uncertainties at the level of only a few percent.

The measurements of the corresponding ratios $\mathcal{R}(D)$ and $\mathcal{R}(D^*)$ by the BaBar, LHCb and Belle collaborations⁷⁻¹⁴ revealed the tension with respect to the average of the SM expectations¹⁵ given by: $\mathcal{R}_{\text{SM}}(D) = 0.299 \pm 0.003$ and $\mathcal{R}_{\text{SM}}(D^*) = 0.258 \pm 0.005$. This discrepancy has been extensively investigated in the literature for the last several years from the point of view of NP scenarios.

While the recent new measurement result presented by the Belle collaboration⁶ $\mathcal{R}(D)_{\text{Belle}} = 0.307 \pm 0.037 \pm 0.016$ and $\mathcal{R}(D^*)_{\text{Belle}} = 0.283 \pm 0.018 \pm 0.014$ turns out consistent with the SM expectation, the new world average¹⁵ of the measurements:

$$\mathcal{R}(D) = 0.340 \pm 0.027 \pm 0.013, \quad \mathcal{R}(D^*) = 0.295 \pm 0.011 \pm 0.008, \quad \rho = -0.38, \quad (1)$$

remains at the tension with respect to the SM at the level of 3.1σ in the $\mathcal{R}(D)$ - $\mathcal{R}(D^*)$ plane. The comparison between the measurements and the theory expectations is shown in figure 1.

2 Effective description

Accommodating the above experimental results requires NP that can compete with the tree-level exchange of W-boson in $b \rightarrow c\tau\nu$ transitions at a scale of at most $\Lambda_{NP} \sim 1 - 2$ TeV. Since new mediators are necessarily electrically charged and thus required to be heavy for phenomenological reasons, they can be integrated out, producing the following low energy effective description:

$$\mathcal{H}_{\text{eff}} = 2\sqrt{2}G_F V_{cb} [(1 + C_V^L)O_V^L + C_S^R O_S^R + C_S^L O_S^L + C_T O_T], \quad (2)$$

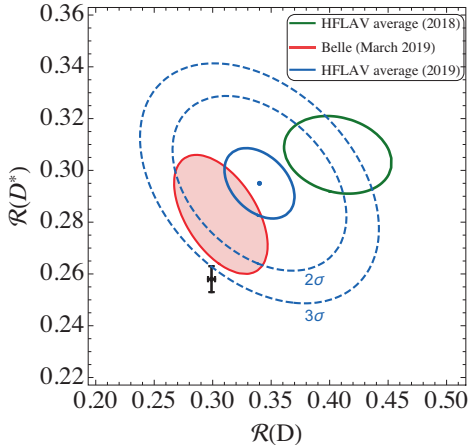


Figure 1 – The red (filled) ellipse shows the result of the new measurement by the Belle collaboration, while the blue ellipse shows the new world average. The SM predictions are represented by the black bars.

with the four-fermion operators:

$$\begin{aligned}
 O_V^L &= (\bar{c}\gamma^\mu P_L b)(\bar{\tau}\gamma_\mu P_L \nu_\tau), \quad O_S^R = (\bar{c}P_R b)(\bar{\tau}P_L \nu_\tau), \\
 O_S^L &= (\bar{c}P_L b)(\bar{\tau}P_L \nu_\tau), \quad O_T = (\bar{c}\sigma^{\mu\nu} P_L b)(\bar{\tau}\sigma_{\mu\nu} P_L \nu_\tau).
 \end{aligned}
 \tag{3}$$

Here we assume that NP can affect only the third lepton generation, and the absence of the right-handed neutrinos in the final states.

We consider the following combinations of Wilson coefficients that can result from integrating out of a single heavy mediator: a) real-valued ($C_V^L, C_S^L = -4C_T$) - motivated by leptoquark $S_1(3, 1, -1/3)$, b) real-valued (C_S^R, C_S^L) from a charged Higgs, c) real-valued (C_V^L, C_S^R) motivated by spin one leptoquark $U_1(3, 1, 2/3)$ and d) $Re[C_S^L = 4C_T], Im[C_S^L = 4C_T]$ from scalar leptoquark $S_2(3, 2, 7/6)$.

We perform the fits for the Wilson coefficients of the four scenarios using the measured values of the relevant observables, as follows. In addition to $\mathcal{R}(D^*)$, we include τ -polarization asymmetry in $B \rightarrow D^* \tau \nu$ with the measured value¹¹ $P_\tau(D^*) = -0.38 \pm 0.51_{-0.16}^{+0.21}$ and the result of the recent first measurement of the longitudinal D^* -polarization fraction,¹⁶ $F_L(D^*)_{\text{Belle}} = 0.60 \pm 0.08 \pm 0.035$. The latter is presently consistent with SM prediction $F_L(D^*)_{SM} = 0.46 \pm 0.04$ at 1.5σ , but nonetheless helps to favor some of the NP scenarios over the others. We use the fit results to predict the yet unmeasured baryonic ratio $R(\Lambda_c)$ which is an analogue of $\mathcal{R}(D)$ for the decays of the bottom baryons $\Lambda_b \rightarrow \Lambda_c \ell \nu$.

3 On the $B_c \rightarrow \tau \nu$ constraints

Charged Higgs explanation of the discrepancy has been found to be under a pressure from the B_c -lifetime that constrains yet unmeasured branching fraction $BR(B_c \rightarrow \tau \nu)$. This decay process is affected by the pseudoscalar Wilson coefficient combination $C_S^R - C_S^L$, the same combination that is able to enhance the $\mathcal{R}(D^*)$. Within charged Higgs scenarios one finds that the $\mathcal{R}(D^*)$ is compatible with the data only with an excessive enhancement of $BR(B_c \rightarrow \tau \nu)$ over its SM-value $BR(B_c \rightarrow \tau \nu)_{SM} \sim 2\%$. Since this branching fraction has not been measured yet, one could attempt to obtain some indirect constrains thereof. An upper bound $BR(B_c \rightarrow \tau \nu) < 10\%$ was inferred¹⁷ from non-observation of $Z \rightarrow b\bar{b}[B_c \rightarrow \tau \nu]$ at the LEP experiment. In order to extract this bound, the authors¹⁷ used the estimate of the ratio f_c/f_u of $b \rightarrow B_c$

and $b \rightarrow B_u$ fragmentation probabilities from pp -data using the ratios $R \equiv f_c/f_u BR(B_c^- \rightarrow J/\psi\pi^-)/BR(B_c^- \rightarrow J/\psi K^-)$ for $p_T > 15$ GeV by the CMS¹⁸ and for $0 < p_T < 20$ GeV by the LHCb¹⁹ collaboration. In ref.⁵ we critically reexamined this bound. Note that pp -collisions produce B_c through mechanisms that have no counterpart in Z -decays and that fragmentation functions depend on kinematics, thus casting a doubt on the 10% constraint.

The total width $\Gamma(B_c)$ is known from the measured lifetime of B_c meson. In order to use this information for the extraction of the bound on $BR(B_c \rightarrow \tau\nu)$, one requires the theoretical prediction for $\Gamma(B_c)$ within the SM. This is a challenging task at present, for the latter is governed by non-perturbative QCD effects. The 30%-bound²⁰ was obtained using the theoretical predictions of $\Gamma(B_c)$ within the theoretical framework of expansion in inverse powers of the heavy-quark masses combined with nonrelativistic QCD.²¹ In our view, the applicability of this method to this case has not been completely understood; the dominant contribution to the width comes from the decays of constituent charm quark and involves strong sensitivity to its mass.

In the light of the above discussion we chose to compare our fit results for the three constraints: $BR(B_c \rightarrow \tau\nu) < 10\%$, $BR(B_c \rightarrow \tau\nu) < 30\%$, $BR(B_c \rightarrow \tau\nu) < 60\%$.

4 Fits

Concerning one-dimensional fit scenarios motivated by a single particle mediators, only C_V^L produces a good fit with the best-fit point $C_V^L \sim 0.07$ (with p-value $p_{val} \sim 40\%$) and $F_L(D^*) = F_{L,SM}(D^*)$. Impact of the choice of the limit of $BR(B_c \rightarrow \tau\nu)$ on one-dimensional scenarios is currently limited and we therefore focus on two-dimensional fit scenarios.

The summary of the results are shown in tables 1 and 2. For the details of our definitions and the fit methodology we refer the reader to the original article.² As an illustration, in table

Table 1: Comparison of the fit results for the two NP scenarios, distinguished by the colors. The last three columns show the predictions of the fit.

2D hyp.	best-fit	p-value percent	pull _{SM}	$\mathcal{R}(D)$	$\mathcal{R}(D^*)$	$F_L(D^*)$	$P_\tau(D^*)$	$P_\tau(D)$	$\mathcal{R}(\Lambda_c)$
$(C_V^L, C_S^L = -4C_T)$	(0.10, -0.04)	30	3.6	0.333 -0.2 σ	0.297 +0.2 σ	0.47 -1.5 σ	-0.48 -0.2 σ	0.25	0.38
$(C_S^R, C_S^L)_{60\%}$	(0.29, -0.25) (-0.16, -0.69)	76	3.9	0.338 +0.1 σ	0.297 +0.1 σ	0.54 -0.7 σ	-0.27 +0.2 σ	0.39	0.38
$(C_S^R, C_S^L)_{30\%}$	(0.21, -0.15) (-0.26, -0.61)	31	3.6	0.353 +0.4 σ	0.280 -1.1 σ	0.51 -1.0 σ	-0.35 0.0 σ	0.42	0.37
$(C_S^R, C_S^L)_{10\%}$	(0.11, -0.04) (-0.37, -0.51)	2.6	2.9	0.366 +0.9 σ	0.263 -2.3 σ	0.48 -1.4 σ	-0.44 -0.1 σ	0.44	0.36

1 we compare the two scenarios: $(C_V^L, C_S^L = -4C_T)$ inspired by a leptoquark S_1 and (C_S^L, C_S^R) inspired by a charged Higgs scenario. The former possibility performs well in the fit, and leads to SM-like values of F_L and $P_\tau(D^*)$. The current value of F_L favors a scenario involving a charged Higgs. If this scenario is true, then either $\mathcal{R}(D^*)$ will go down towards the SM value or $BR(B_c \rightarrow \tau\nu) \gtrsim 30\%$, as can be read from the table: the corresponding p-value decreases once the B_c -bound is strengthened. In table 2 we present the results for the scenarios (C_V^L, C_S^R) and complex-valued $(C_S^L = 4C_T)$. In both scenarios the F_L turns out SM-like. In the case of future bound $BR(B_c \rightarrow \tau\nu) \lesssim 10\%$, the latter scenario would be in tension with current value of $\mathcal{R}(D^*)$. This scenario is further meaningfully probed by high p_T -data from ATLAS and CMS.²²

In figure 3. we show an example of the pairwise correlations between observables for different NP scenarios. The predicted 1σ regions in the four two-dimensional scenarios, assuming $BR(B_c \rightarrow \tau\nu) < 60\%$ are shown. Note that in some cases the preferred regions are essentially lines, revealing the tight correlations between two observables in a given scenario. However, note that these correlations are obtained in the limit of vanishing form-factor uncertainties, thus representing idealized situation which can in principle be obtained in a given scenario assuming

Table 2: Continuation of the table 1.

2D hyp.	best-fit	p-value percent	pull _{SM}	$\mathcal{R}(D)$	$\mathcal{R}(D^*)$	$F_L(D^*)$	$P_\tau(D^*)$	$P_\tau(D)$	$\mathcal{R}(\Lambda_c)$
(C_V^L, C_S^R)	(0.08, -0.01)	27	3.6	0.343 +0.1 σ	0.294 -0.1 σ	0.46 -1.6 σ	-0.49 -0.2 σ	0.31	0.38
$(\text{Re}[C_S^L = 4C_T], \text{Im}[C_S^L = 4C_T]) _{60,30\%}$	(-0.06, ±0.31)	25	3.6	0.339 0.0 σ	0.295 0.0 σ	0.45 -1.7 σ	-0.41 0.1 σ	0.41	0.38
$(\text{Re}[C_S^L = 4C_T], \text{Im}[C_S^L = 4C_T]) _{10\%}$	(-0.03, ±0.24)	6	3.2	0.330 -0.3 σ	0.275 -1.4 σ	0.46 -1.6 σ	-0.45 -0.1 σ	0.38	0.36

the current experimental data. In order to fully use the complementarity of the polarization observables to the LFU ratios, the further improvements of the theory predictions of the form factor would be beneficial.

We find an interesting correlation with the observable $\mathcal{R}(\Lambda_c)$; in fact, in all scenarios with good p-values the $\mathcal{R}(\Lambda_c)$ has essentially the same value (with a current data):

$$\begin{aligned} \mathcal{R}(\Lambda_c) &= \mathcal{R}_{\text{SM}}(\Lambda_c) (1.15 \pm 0.04) \\ &= 0.38 \pm 0.01|_{\text{exp.}} \pm 0.01|_{\text{th.}}, \end{aligned} \quad (4)$$

where the first error reflects the current experimental errors from $\mathcal{R}(D^{(*)})$ and the second error reflects the form factor uncertainties within $\mathcal{R}(\Lambda_c)$. The above enhancement of $\mathcal{R}(\Lambda_c)$ can be understood as a result of the certain sum-rule, see Eq. (28) in the original paper.⁵ The $\mathcal{R}(\Lambda_c)$ is an important "redundant" observable whose measurement could provide a crosscheck of the $\mathcal{R}(D)$ - $\mathcal{R}(D^*)$ anomaly.

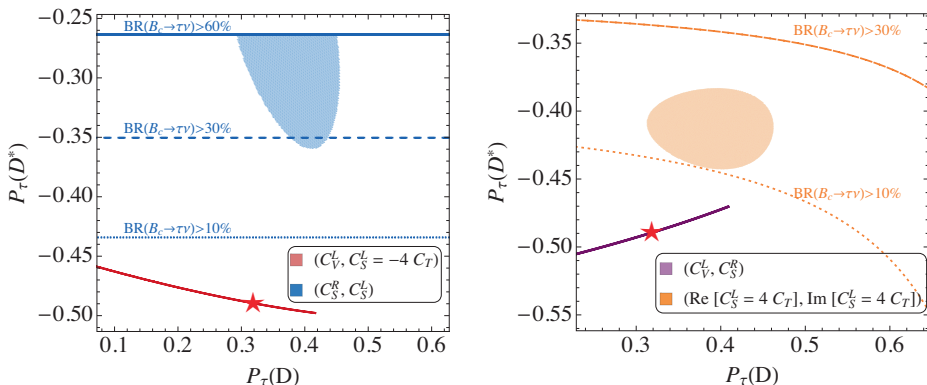


Figure 2 – Pairwise correlations between the observables $P_\tau(D)$, $P_\tau(D^*)$, for the bound $BR(B_c \rightarrow \tau\nu) < 60\%$. Boundaries that correspond to different B_c constraints are denoted by the lines.

Acknowledgments

I would like to thank my coauthors in ref.⁵ for pleasant collaboration and the organizers of this inspiring conference for an opportunity to present the results. My work is supported by BMBF under grant no. 05H18VKKB1.

References

1. S. Fajfer, J. F. Kamenik, I. Nisandzic and J. Zupan, Phys. Rev. Lett. **109** (2012) 161801 [arXiv:1206.1872 [hep-ph]].
2. U. Nierste, S. Trine and S. Westhoff, Phys. Rev. D **78** (2008) 015006 [arXiv:0801.4938 [hep-ph]].

3. J. F. Kamenik and F. Mescia, Phys. Rev. D **78** (2008) 014003 [arXiv:0802.3790 [hep-ph]].
4. S. Fajfer, J. F. Kamenik and I. Nisandzic, Phys. Rev. D **85** (2012) 094025 [arXiv:1203.2654 [hep-ph]].
5. M. Blanke, A. Crivellin, S. de Boer, M. Moscati, U. Nierste, I. Nišandžić and T. Kitahara, Phys. Rev. D **99** (2019) no.7, 075006 [arXiv:1811.09603 [hep-ph]].
6. A. Abdesselam *et al.* [Belle Collaboration], arXiv:1904.08794 [hep-ex].
7. J. P. Lees *et al.* [BaBar Collaboration], Phys. Rev. Lett. **109** (2012) 101802 [arXiv:1205.5442 [hep-ex]].
8. M. Huschle *et al.* [Belle Collaboration], Phys. Rev. D **92** (2015) no.7, 072014 [arXiv:1507.03233 [hep-ex]].
9. Y. Sato *et al.* [Belle Collaboration], Phys. Rev. D **94** (2016) no.7, 072007 [arXiv:1607.07923 [hep-ex]].
10. S. Hirose *et al.* [Belle Collaboration], Phys. Rev. Lett. **118** (2017) no.21, 211801 [arXiv:1612.00529 [hep-ex]].
11. S. Hirose *et al.* [Belle Collaboration], Phys. Rev. D **97** (2018) no.1, 012004 [arXiv:1709.00129 [hep-ex]].
12. R. Aaij *et al.* [LHCb Collaboration], Phys. Rev. Lett. **115** (2015) no.11, 111803 Erratum: [Phys. Rev. Lett. **115** (2015) no.15, 159901] [arXiv:1506.08614 [hep-ex]].
13. R. Aaij *et al.* [LHCb Collaboration], Phys. Rev. Lett. **120** (2018) no.17, 171802 [arXiv:1708.08856 [hep-ex]].
14. R. Aaij *et al.* [LHCb Collaboration], Phys. Rev. D **97** (2018) no.7, 072013 [arXiv:1711.02505 [hep-ex]].
15. Y. Amhis *et al.* [HFLAV Collaboration], Eur. Phys. J. C **77** (2017) no.12, 895, <https://hflav-eos.web.cern.ch/hflav-eos/semi/spring19/html/RDsDsstar/RDRDs.html>, [arXiv:1612.07233 [hep-ex]].
16. A. Abdesselam *et al.* [Belle Collaboration], arXiv:1903.03102 [hep-ex].
17. A. G. Akeroyd and C. H. Chen, Phys. Rev. D **96** (2017) no.7, 075011 [arXiv:1708.04072 [hep-ph]].
18. V. Khachatryan *et al.* [CMS Collaboration], JHEP **1501** (2015) 063 [arXiv:1410.5729 [hep-ex]].
19. R. Aaij *et al.* [LHCb Collaboration], Phys. Rev. Lett. **114** (2015) 132001 [arXiv:1411.2943 [hep-ex]].
20. R. Alonso, B. Grinstein and J. Martin Camalich, Phys. Rev. Lett. **118** (2017) no.8, 081802 [arXiv:1611.06676 [hep-ph]].
21. M. Beneke and G. Buchalla, Phys. Rev. D **53** (1996) 4991 [hep-ph/9601249].
22. A. Greljo, J. Martin Camalich and J. D. Ruiz-Alvarez, Phys. Rev. Lett. **122** (2019) no.13, 131803 [arXiv:1811.07920 [hep-ph]].
23. S. Iguro, T. Kitahara, Y. Omura, R. Watanabe and K. Yamamoto, JHEP **1902** (2019) 194 [arXiv:1811.08899 [hep-ph]].



V_{cb} FROM INCLUSIVE $b \rightarrow c$ DECAYS: AN ALTERNATIVE METHOD ^a

MATTEO FAEL

Theoretische Physik I, Universität Siegen, Walter-Flex-Strasse 3, 57068 Siegen, Germany



These proceedings review how reparametrization invariance, a symmetry within the heavy quark expansion (HQE) reflecting Lorentz invariance of the underlying QCD, reduces the number of independent HQE parameters necessary to predict total rate and q^2 moments in inclusive semileptonic B decays. An alternative extraction of V_{cb} based on q^2 -moment measurements at B factories is proposed. This novel method could push the V_{cb} determination up to order $1/m_b^4$ without prior estimates of the higher order terms in the $1/m_b$ expansion and access their size in a model independent way.

1 Introduction

The current extraction of V_{cb} from inclusive semileptonic B decays ($B \rightarrow X_c \ell \nu$) is based on the possibility to predict the total rate and the spectral moments as a double series in Λ_{QCD}/m_b and α_s . The moments of the electron energy spectrum and the hadronic invariant mass were measured by BABAR ^{1,2} and Belle ^{3,4} and previously by CDF, ⁵ CLEO ⁶ and DELPHI. ⁷

Using moments of the semileptonic b decay spectra, Gambino *et al.* ^{8,9,10} performed global fits of V_{cb} , the heavy quark masses and the non perturbative parameters of the heavy quark expansion (HQE), obtaining ¹⁰

$$|V_{cb}| = (42.11 \pm 0.74) \times 10^{-3}, \quad (1)$$

whose fractional uncertainty is about 1.8%. They relayed on NNLO perturbative corrections to the partonic rate, as well as NLO corrections to the $1/m_b^2$ terms. They also included at tree-level the HQE parameters up to $1/m_b^5$. Up to $1/m_b^3$ there are only four HQE parameters, starting at $1/m_b^4$ their number grows factorially and increases up to 32 when $1/m_b^5$ corrections are considered. This constitutes a theoretical challenge as the extraction of all HQE parameters in a fully data driven way becomes complicated. Therefore, one has to rely on *a priori* estimates of the expectation value of the parameters at order $1/m_b^4$ and $1/m_b^5$.

The V_{cb} value in (1) was determined estimating local operators of the form $\bar{b}_v i D_{\mu_1} \dots i D_{\mu_N} b_v$ using the lowest-lying state saturation approximation (LLSA), that splits chains of covariant

^aSI-HEP-2019-06

derivatives into shorter ones,^{11,12}

$$\langle B | \bar{b}_v X_1^k X_k^N b_v | B \rangle = \frac{1}{2m_B} \sum_n \langle B | \bar{b}_v X_1^k b_v | H_n \rangle \langle H_n | \bar{b}_v X_k^N b_v | B \rangle, \quad (2)$$

where H_n are hadronic states and $X_i^j = iD_{\mu_i} \dots iD_{\mu_j}$. The LLSA assumes that the sum is saturated by the ground state multiplets B or B^* . The fit was performed starting with the LLSA central values (2) and assigning 60% gaussian priors. A sub-percent reduction in V_{cb} was found.

It is thus desirable to confirm the smallness of the higher order terms in the $1/m_b$ expansion in a model-independent approach, also in light of the future experimental precision at the Belle II experiment which might allow a measurement of V_{cb} below 1%. In these proceedings we review the alternative method for the determination of V_{cb} proposed by Fael, Mannel & Vos.¹³ The method is based on the measurement of the leptonic invariant mass (q^2) moments and the fractional branching ratio as a function of a lower cut on q^2 . These observables are invariant under reparametrization, a symmetry within the HQE reflecting Lorenz invariance of the underlying QCD, and therefore they depend on a reduced set of HQE parameters, as it was shown for the total rate by Mannel & Vos.¹⁴ The smaller set of parameters necessary in a global fit of these observables (eight instead of 13 up to $1/m_b^4$) opens the possibility to extract V_{cb} in a completely data-driven way, without making use of the LLSA, and thus to independently check and validate the finding of Gambino *et al.*¹⁰ about the size of the higher order terms in the HQE.

2 Reparametrization invariance in HQE

The semileptonic decays of a b quark to final states with a charm are due to the weak Hamiltonian

$$\mathcal{H}_W = \frac{4G_F}{\sqrt{2}} V_{cb} (\bar{c}\gamma^\mu P_L b) (\bar{\ell}\gamma^\mu P_L \nu) + \text{h.c.} = \frac{4G_F}{\sqrt{2}} V_{cb} J_q^\mu J_{\ell\mu} + \text{h.c.}, \quad (3)$$

where P_L is the left-handed projector, J_q^μ and J_ℓ^μ are the hadronic and the leptonic currents, respectively. The rate for the inclusive decay $B(p_B) \rightarrow X_c(p_X)\ell(p_\ell)\nu(p_\nu)$ is determined by the hadronic tensor

$$W^{\mu\nu} = (2\pi)^4 \sum_X \delta^4(p_B - q - p_X) \langle B | J_q^\mu | X \rangle \langle X | J_\ell^\nu | B \rangle, \quad (4)$$

where $q = p_e + p_\nu$. The differential rate can be written as $d\Gamma \propto L_{\mu\nu}(p_e, p_\nu) W^{\mu\nu}(q^2, q \cdot v)$, where $v = p_B/m_B$ is the B meson velocity and $L_{\mu\nu}$ is the lepton tensor. The non-perturbative hadronic tensor $W^{\mu\nu}$ is related via the optical theorem to the imaginary part of the forward scattering amplitude

$$W^{\mu\nu} = 2 \text{Im} \langle B | R(S) | B \rangle = 2 \text{Im} \langle B | i \int d^4x e^{-im_b S \cdot x} T \{ \bar{b}_v(x) \gamma^\mu P_L c(x) \bar{c}(0) \gamma_\nu P_L b_v(0) \} | B \rangle, \quad (5)$$

where $S = v - q/m_b$ and $b_v(x) = \exp(im_b v \cdot x) b(x)$ is the re-phased b -quark field. Then, we perform an operator product expansion (OPE) for the time-ordered product:

$$R(S) = \sum_{n=0}^{\infty} \frac{C_{\mu_1 \dots \mu_n}^{(n)}(S)}{m_b^{n+3}} \otimes \bar{b}_v(iD^{\mu_1} \dots iD^{\mu_n}) b_v, \quad (6)$$

where the symbol \otimes is a shorthand notation for contraction of spinor indices. Taking the forward matrix element $\langle \bar{b}_v \dots b_v \rangle \equiv \langle B(p) | \bar{b}_v \dots b_v | B(p) \rangle$, we obtain the hadronic tensor for the inclusive transition $B \rightarrow X_c \ell \bar{\nu}$:

$$W(p, q) = 2 \text{Im} \sum_{n=0}^{\infty} C_{\mu_1 \dots \mu_n}^{(n)}(S) \otimes \langle \bar{b}_v(iD^{\mu_1} \dots iD^{\mu_n}) b_v \rangle, \quad (7)$$

where we suppressed the Lorentz indices for simplicity.

The hadronic tensor (4), as well as its OPE in (6), do not depend on v as long as all orders in the OPE are taken into account. This means that both are invariant under the reparametrization (RP) transformation δ_{RP} that shifts $v_\mu \rightarrow v_\mu + \delta v_\mu$. One can show that the invariance under reparametrization (RPI), which dictates $\delta_{\text{RP}} R(S) = 0$, connects subsequent orders in the $1/m_b$ series of Eq. (6). This generates relations between the coefficients C at order n and $n+1$:¹⁴

$$\delta_{\text{RP}} C_{\mu_1 \dots \mu_n}^{(n)}(S) = m_b \delta v^\alpha \left[C_{\alpha \mu_1 \dots \mu_n}^{(n+1)}(S) + C_{\mu_1 \alpha \dots \mu_n}^{(n+1)}(S) + \dots + C_{\mu_1 \dots \mu_n \alpha}^{(n+1)}(S) \right]. \quad (8)$$

The hadronic matrix elements $\langle \bar{b}_v(iD_{\mu_1} \dots iD_{\mu_n})b_v \rangle$ can be expressed in terms of scalar matrix elements, such as the kinetic energy parameter μ_π^2 and the chromomagnetic parameter μ_G^2 at $n=2$. However the number of independent parameters grows factorially in the $1/m_b$ expansion (at tree level there are nine and 18 at order $1/m_b^4$ and $1/m_b^5$, respectively^{11,15}) and therefore their extraction from data becomes challenging already at order $1/m_b^4$. Because of RPI the total rate depends only on a reduced set of HQE parameters, which are given by fixed linear combination of the matrix elements defined for the general case.¹⁴ Up to order $1/m_b^4$ there are only eight independent parameters at tree level (for their explicit definitions see Mannel *et al.*^{13,14}).

3 Observables invariant under reparametrization

The e^+e^- colliders measure moments of decay spectra rather than differential rates. We can define them in a generic way as the phase-space integration of the differential rate multiplied by an appropriate weight function w to some power n :

$$\langle M^k[w] \rangle = \int d\Phi w^k(v, p_e, p_\nu) W^{\mu\nu} L_{\mu\nu}. \quad (9)$$

Spectral moments of the charged lepton energy E_ℓ and the hadronic invariant mass M_X^2 are obtained by setting $w(v, p_e, p_\nu) = v \cdot p_e$ and $w(v, p_e, p_\nu) = (m_B v - q)^2$, while the moments of the leptonic invariant mass q^2 correspond to the weight function $w(v, p_e, p_\nu) = q^2$. In analogy to $R(S)$, we assume that the moment M has an OPE of the form:

$$M^k[w] = \sum_{n=0}^{\infty} \frac{a_{\mu_1 \dots \mu_n}^{(n)}}{m_b^{n+3}} \otimes \bar{b}_v(iD^{\mu_1} \dots iD^{\mu_n})b_v. \quad (10)$$

Performing a RP transformation in (10), we obtain a similar tower of relations between the coefficients at order n and at order $n+1$, as for the total rate. The key observation is that for RPI weight functions $\delta_{\text{RP}} w(v, p_e, p_\nu) = 0$. In this case the relations among the coefficients $a^{(n)}$ are the same relations as for the total rate. Therefore observables that are invariant under reparametrization can be expressed in terms of the reduced set of HQE parameters. For the semileptonic decays the moments of the leptonic invariant mass (q^2) have this property, since the corresponding weight function is independent on the velocity v . On the contrary electron energy moments and moments of the hadronic invariant mass are not RPI and so they depend on the full set of operators.

4 Extracting V_{cb} from q^2 moments

Given that q^2 moments depend on the reduced set of HQE parameters, we propose a novel strategy for the determination of V_{cb} from inclusive semileptonic B decays. The method is identical to the approach of Gambino *et al.* however it is based only on the measurement of q^2 moments,

$$\langle (q^2)^n \rangle_{q_{\text{cut}}^2} \equiv \int_{q_{\text{cut}}^2}^{(m_b - m_c)^2} dq^2 (q^2)^n \frac{d\Gamma}{dq^2} \bigg/ \int_{q_{\text{cut}}^2}^{(m_b - m_c)^2} dq^2 \frac{d\Gamma}{dq^2}, \quad (11)$$

and also on the fractional branching ratio $R^* = \Gamma_{q^2 > q_{\text{cut}}^2} / \Gamma_{\text{tot}}$. Their lengthy expressions are attached to the arXiv version of our original paper,¹³ where we computed them and verified explicitly that indeed they depend on the reduced set of operators since the redundant ones cancel out in the final results. A cut on E_e in (11) would have broken explicitly the RPI of the q^2 moments, with the consequence of reintroducing the complete set of parameters. For this reason, we introduced in the definition (11) a lower cut on q^2 instead of E_e because in this way we preserve the RPI property of these observables.

The V_{cb} fits performed by Gambino *et al.*^{16,8,9} make use of the electron energy and the hadronic mass moments, including a cut on the electron energy. In fact, the moments up to $n = 4$ and their computable cut-dependence allow for a fully data-driven analysis up to $1/m_b^3$, which means that V_{cb} , the quark masses as well as the HQE parameters $\mu_\pi^2, \mu_G^2, \rho_D^3$ and ρ_{LS}^3 can be fitted from data. Accessing higher orders in the $1/m_b$ expansion requires to model the HQE parameters of order $1/m_b^4$ and $1/m_b^5$ with the LLSA.^{11,12}

We therefore propose to determine V_{cb} from the q^2 moments with a possible additional dependence on a lower q^2 cut. Since we need eight HQE parameters up to $1/m_b^4$ instead of 13, precise inputs from the q^2 spectrum measured at Belle/Belle II would allow us to perform a fully data driven analysis, i.e. an extraction of V_{cb} up to $1/m_b^4$ entirely data based.

5 Conclusions

We proposed to measure at B factories the moments of the q^2 semileptonic- B -decay spectrum with a lower cut q_{cut}^2 . Since these observables depend on a smaller set of HQE parameters as they are invariant under reparametrization, we suggested the possibility for a novel fit of V_{cb} , the heavy quark masses and the non-perturbative parameters up to $1/m_b^4$ in a fully data-driven way based entirely on these kind of observables. This analysis would represent a crucial independent check of the results of Gambino *et al.*¹⁰ about the smallness of the higher order terms in the HQE. It is thus an indispensable ingredient in order to push the V_{cb} uncertainty below the 1% level, given the upcoming precise data of Belle II, and to correctly access the theoretical uncertainty in the V_{cb} extraction.

Acknowledgments

This review is based on the work presented in Ref. 13 and I would like to thank T. Mannel and K. K. Vos for the super nice collaboration. This work was supported by DFG through the Research Unit FOR 1873 “Quark Flavour Physics and Effective Field Theories” (QFET).

References

1. B. Aubert *et al.* [BaBar Collaboration], Phys. Rev. D **69** (2004) 111104 [hep-ex/0403030].
2. B. Aubert *et al.* [BaBar Collaboration], Phys. Rev. D **81** (2010) 032003 [arXiv:0908.0415 [hep-ex]].
3. P. Urquijo *et al.* [Belle Collaboration], Phys. Rev. D **75** (2007) 032001 [hep-ex/0610012].
4. C. Schwanda *et al.* [Belle Collaboration], Phys. Rev. D **75** (2007) 032005 [hep-ex/0611044].
5. D. Acosta *et al.* [CDF Collaboration], Phys. Rev. D **71** (2005) 051103 [hep-ex/0502003].
6. S. E. Csorna *et al.* [CLEO Collaboration], Phys. Rev. D **70** (2004) 032002 [hep-ex/0403052].
7. J. Abdallah *et al.* [DELPHI Collaboration], Eur. Phys. J. C **45** (2006) 35 [hep-ex/0510024].
8. P. Gambino and C. Schwanda, Phys. Rev. D **89** (2014) no.1, 014022 [arXiv:1307.4551 [hep-ph]].
9. A. Alberti *et al.*, Phys. Rev. Lett. **114** (2015) no.6, 061802 [arXiv:1411.6560 [hep-ph]].
10. P. Gambino, K. J. Healey and S. Turczyk, Phys. Lett. B **763** (2016) 60 [arXiv:1606.06174 [hep-ph]].
11. T. Mannel, S. Turczyk and N. Uraltsev, JHEP **1011** (2010) 109 [arXiv:1009.4622 [hep-ph]].
12. J. Heinonen and T. Mannel, Nucl. Phys. B **889** (2014) 46 [arXiv:1407.4384 [hep-ph]].
13. M. Fael, T. Mannel and K. Keri Vos, JHEP **1902**, 177 (2019) [arXiv:1812.07472 [hep-ph]].
14. T. Mannel and K. K. Vos, JHEP **1806** (2018) 115 [arXiv:1802.09409 [hep-ph]].
15. B. M. Dassinger, T. Mannel and S. Turczyk, JHEP **0703**, 087 (2007) [hep-ph/0611168].
16. P. Gambino and N. Uraltsev, Eur. Phys. J. C **34** (2004) 181 [hep-ph/0401063].

SEARCH FOR PRODUCTION OF AN INVISIBLE DARK PHOTON FROM π^0 DECAYS AT NA62

Marco Mirra^a

INFN - Sezione di Napoli, Complesso Universitario di Monte Sant'Angelo, Cintia street, I-80126, Napoli, Italy

A search for an invisible dark photon A' has been performed, exploiting the efficient photon-veto capability and high resolution tracking of the NA62 detector at CERN. The signal stems from the chain $K^+ \rightarrow \pi^+ \pi^0$ followed by $\pi^0 \rightarrow A' \gamma$. No significant statistical excess has been identified. Upper limits on the dark photon coupling to the ordinary photon as a function of the dark photon mass have been set, improving on the previous limits over the mass range 60–110 MeV/ c^2 .

1 Introduction

The standard model of elementary particle physics (SM) was largely completed in the early 1970s and its last missing piece, the Higgs boson, revealed itself at the LHC. But LHC also explored a large new territory and no unambiguous signal of new physics (NP) has been found. However some yet unknown particles or interactions are required to explain a number of observed phenomena in particle physics like the neutrino masses and oscillations, the baryon asymmetry of the universe, the dark matter and energy. Complementary approaches to LHC in the intensity

^aOn behalf of the NA62 Collaboration: R. Aliberti, F. Ambrosino, R. Ammendola, B. Angelucci, A. Antonelli, G. Anzivino, R. Arcidiacono, T. Bache, M. Barbanera, J. Bernhard, A. Biagioni, L. Bician, C. Biino, A. Bizzeti, T. Blazek, B. Bloch-Devaux, V. Bonaiuto, M. Boretto, M. Bragadireanu, D. Britton, F. Brizioli, M.B. Brunetti, D. Bryman, F. Bucci, T. Capussela, J. Carmignani, A. Ceccucci, P. Cenci, V. Cerny, C. Cerri, B. Checcucci, A. Conovaloff, P. Cooper, E. Cortina Gil, M. Corvino, F. Costantini, A. Cotta Ramusino, D. Coward, G. D'Agostini, J. Dainton, P. Dalpiaz, H. Daniels-son, N. De Simone, D. Di Filippo, L. Di Lella, N. Doble, B. Dobrich, F. Duval, V. Duk, J. Engelfried, T. Enik, N. Estrada-Tristan, V. Falaleev, R. Fantechi, V. Fascianelli, L. Federici, S. Fedotov, A. Filippi, M. Fiorini, J. Fry, J. Fu, A. Fucci, L. Fulton, E. Gamberini, L. Gatignon, G. Georgiev, S. Ghinescu, A. Gianoli, M. Giorgi, S. Giudici, F. Gonnella, E. Goudzovski, C. Graham, R. Guida, E. Gushchin, F. Hahn, H. Heath, E.B. Holzer, T. Husek, O. Hutanu, D. Hutchcroft, L. Iacobuzio, E. Iacopini, E. Imbergamo, B. Jenninger, J. Jerhot, R.W. Jones, K. Kampf, V. Kekelidze, S. Kholodenko, G. Khoriauli, A. Khotyantsev, A. Kleimenova, A. Korotkova, M. Koval, V. Kozuharov, Z. Kucerova, Y. Kudenko, J. Kunze, V. Kurochka, V. Kurshtsov, G. Lanfranchi, G. Lamanna, E. Lari, G. Latino, P. Laycock, C. Lazzeroni, M. Lenti, G. Lehmann Miotto, E. Leonardi, P. Lichard, L. Litov, R. Lollini, D. Lomidze, A. Lonardo, P. Lubrano, M. Lupi, N. Lurkin, D. Madigozhin, I. Mannelli, G. Mannocchi, A. Mapelli, F. Marchetto, R. Marchevski, S. Martellotti, P. Massarotti, K. Massri, E. Maurice, M. Medvedeva, A. Mefodev, E. Menichetti, E. Migliore, E. Minucci, M. Mirra, M. Misheva, N. Molokanova, M. Moulson, S. Movchan, M. Napolitano, I. Neri, F. Newson, A. Norton, M. Noy, T. Numao, V. Obratsov, A. Ostankov, S. Padolski, R. Page, V. Palladino, A. Parenti, C. Parkinson, E. Pedreschi, M. Pepe, M. Perrin-Terrin, L. Peruzzo, P. Petrov, Y. Petrov, F. Petrucci, R. Piandani, M. Piccini, J. Pinzino, I. Polenkevich, L. Pontisso, Yu. Potrebenikov, D. Protopopescu, M. Raggi, A. Romano, P. Rubin, G. Ruggiero, V. Ryjov, A. Salamon, C. San-toni, G. Saracino, F. Sargeni, S. Schuchmann, V. Semenov, A. Sergi, A. Shaikhiev, S. Shkarovskiy, D. Soldi, V. Sugonyaev, M. Sozzi, T. Spadaro, F. Spinella, A. Sturgess, J. Swallow, S. Trilov, P. Valente, B. Velghe, S. Venditti, P. Vicini, R. Volpe, M. Vormstein, H. Wahl, R. Wanke, B. Wrona, O. Yushchenko, M. Zamkovsky, A. Zinchenko.

frontier field allow us to explore NP effects using high-rate environment and looking for very rare processes.

To explain the abundance of dark matter in our universe, SM can be extended using a new $U(1)$ gauge-symmetry sector, with a vector mediator field A' named as “dark photon” with mass $M_{A'}$. In a simple realization of such a scenario^{1,2}, the A' field would feebly interact with the SM photon through a kinetic mixing lagrangian with a coupling parameter ϵ . The above lagrangian might be accompanied by additional interactions, both with SM matter fields and with a hidden sector of possible dark-matter candidate fields. If these are lighter than the A' , the dark photon would decay mostly invisibly, so that a missing-energy signature might reveal its presence. In this study³, an A' search is performed, with A' escaping detection from the decay chain

$$K^+ \rightarrow \pi^+ \pi^0 \text{ with } \pi^0 \rightarrow A' \gamma, \quad (1)$$

where

$$\text{BR}(\pi^0 \rightarrow A' \gamma) = 2\epsilon^2 \left(1 - \frac{M_{A'}^2}{M_{\pi^0}^2}\right)^3 \times \text{BR}(\pi^0 \rightarrow \gamma \gamma) \quad (2)$$

The high-energy unseparated hadron beam from the CERN Super Proton Synchrotron (SPS) provides an abundant flux of K^+ mesons useful to this purpose. The search is performed using the NA62 experiment, which has the main goal of measuring the branching ratio (BR) of the rare decay $K^+ \rightarrow \pi^+ \nu \bar{\nu}$ with 10% precision⁴. The A' search exploits the extreme photon-veto capability and high resolution tracking of the NA62 detector in a high-rate environment⁵.

2 Analysis strategy

If the A' decays into some invisible mode, the experimental signature for the events described in Eq. 1 is given by a charged kaon decaying into a charged pion and a photon hitting the liquid Krypton calorimeter (LKr), with missing energy and momentum. The kaon and pion momenta are measured with a silicon and straw spectrometers, respectively, and the corresponding 4-momenta are denoted P_K and P_π . The measurement of the position of impact and the energy released in the LKr calorimeter allow the determination of the photon 4-momentum P_γ , assuming emission from the kaon decay vertex. The squared missing mass

$$M_{\text{miss}}^2 = (P_K - P_\pi - P_\gamma)^2 \quad (3)$$

is expected to peak at $M_{A'}^2$ for the decay chain in Eq. 1 and at zero for the most abundant background, $\pi^0 \rightarrow \gamma \gamma$ with one photon undetected.

A high-purity kinematic identification of the $K^+ \rightarrow \pi^+ \pi^0$ decays is performed by identifying and reconstructing the K^+ and π^+ particles and requiring $(P_K - P_\pi)^2$ to be consistent with the squared π^0 mass. The number n_{π^0} of $K^+ \rightarrow \pi^+ \pi^0$ decays defines the statistics of tagged π^0 mesons used for this analysis. In order to enforce the sole presence of a π^+ and one photon in the final state, further conditions are required and the most relevant are:

- No in-time signals from the photon veto system must be present, except for the ones related to the single photon and to the π^+ detected by the LKr.
- No in-time hits in the hodoscope (NA48-CHOD) before the LKr calorimeter must be found except for those geometrically associated with the π^+ . This condition is referred to as the *NA48-CHOD Extra-activity cut* and it is useful to reject events in which one photon is lost because of conversion upstream of the hodoscope.

A peak search in the positive tail of the M_{miss}^2 background distribution is performed by comparing the number of events in a sliding M_{miss}^2 window to the background expectation for different $M_{A'}$ hypothesis in the range 30-130 MeV/ c^2 .

For example, Fig. 1 shows the distributions of M_{miss}^2 from a Monte Carlo (MC) simulation of the NA62 apparatus when injecting A' signals with masses of 60, 90, and 120 MeV/c^2 and a coupling strength $\epsilon^2 = 2.5 \times 10^{-4}$ (see Eq. 2). These are superimposed on the expected contribution from a data sample with fully reconstructed $\pi^0 \rightarrow \gamma\gamma$ in which one of the two photon hitting the LKr calorimeter, randomly chosen, is artificially excluded.

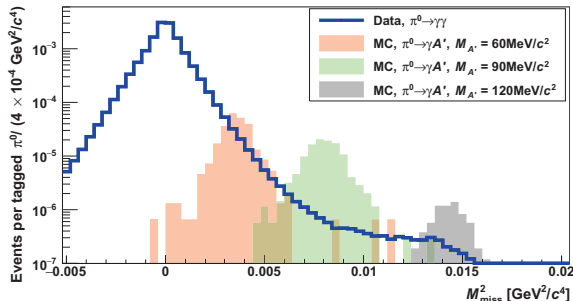


Figure 1 – Distributions of the squared missing mass evaluated from K^+ decays with one photon and one π^+ reconstructed (Eq. 3). Data from $\pi^0 \rightarrow \gamma\gamma$ with one photon, randomly chosen, assumed to be undetected are shown by the blue line. The expected spectra from MC simulations of $\pi^0 \rightarrow A'\gamma$ with a coupling strength $\epsilon^2 = 2.5 \times 10^{-4}$ and A' masses of 60 (red), 90 (green) and 120 MeV/c^2 (grey) are also shown. The data distribution is scaled to n_{π^0} . Each MC distribution is scaled to the equivalent number of tagged π^0 mesons corresponding to the generated statistics.

To evaluate the expected background, a data-driven approach is used. The same data selection used for the signal search is applied but the *NA48-CHOD Extra activity cut* is partially inverted: events with in-time NA48-CHOD signals geometrically associated with the detected photon are rejected, while the presence of signals far from both the π^+ and photon impact points to the NA48-CHOD hodoscope is required. This allows the selection of a data control sample of $\pi^0 \rightarrow \gamma\gamma$ events with one photon detected by the LKr calorimeter and the other lost because of conversion upstream of the NA48-CHOD. Since there is no overlap with the signal sample, the control sample can be used to evaluate the expected M_{miss}^2 background distribution. The control sample is scaled to the signal sample in a side-band region adjacent to but not overlapping with the A' search region.

3 Results

The observed data and the expected background counts are evaluated by integrating the corresponding M_{miss}^2 spectrum in the sliding window for each $M_{A'}$ hypothesis. The width of the sliding window is $\pm 1\sigma_{M_{\text{miss}}^2}$ around the expected M_{miss}^2 peak value, where $\sigma_{M_{\text{miss}}^2}$ is the resolution evaluated with MC simulations and checked with $K^+ \rightarrow \pi^+\pi^0$, $\pi^0 \rightarrow \gamma e^+e^-$ data sample.

Using the CL_s algorithm, frequentist 90% confidence intervals are determined for the number of signal events. The upper limits are compatible within two standard deviations with the fluctuation expected in the background-only hypothesis. The 90% CL upper limits obtained on the coupling parameter ϵ^2 as a function of $M_{A'}$ are shown in Fig. 2. The limit from the number of observed events (solid curve) is compared to the bands with 68% and 95% coverage in the absence of signal and no statistically significant excess is detected. This NA62 result improves on the previous limits over the mass range 60–110 MeV/c^2 (Fig. 3). It has to be underlined that the experimental technique used by NA62 is totally different than the one of the other recent results.

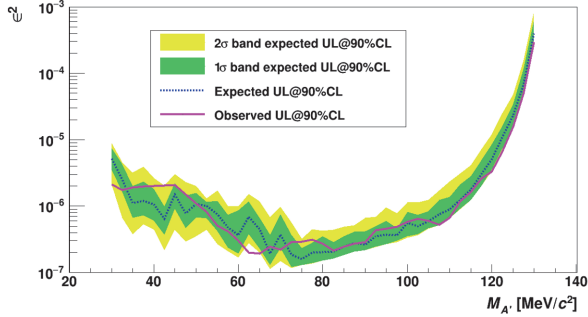


Figure 2 – Upper limits at 90% CL on the dark photon coupling strength (ϵ^2) as a function of the mass ($M_{A'}$). The limit obtained from data (solid line) should be compared to that expected in the absence of signal: the median of the upper-limit distribution in the background-only hypothesis is shown by the dashed line and the corresponding fluctuation bands with 68% and 95% coverage are shown by the shaded areas.

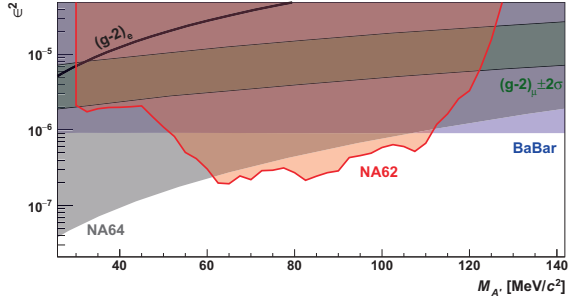


Figure 3 – Upper limit at 90% CL from NA62 (red region) in the ϵ^2 vs $M_{A'}$ plane with A' decaying into invisible final states. The limits from the BaBar⁶ (blue) and NA64⁷ (light grey) experiments are shown. The green band shows the region of the parameter space corresponding to an explanation of the discrepancy between the measured and expected values of the anomalous muon magnetic moment $(g-2)_\mu$ in terms of a contribution from the A' in the quantum loops^{8,9}. The region above the black line is excluded by the agreement of the anomalous magnetic moment of the electron $(g-2)_e$ with its expected value^{10,11,12}.

References

1. L. Okun, Sov. Phys. JETP 56 (1982) 502.
2. B. Holdom, Phys. Lett. B 166 (1986) 196.
3. E. Cortina Gil, et al. [The NA62 Collaboration], accepted for publication by the Journal of High Energy Physics, arxiv:1903.08767
4. E. Cortina Gil, et al. [The NA62 Collaboration], Phys. Lett. B 791 (2019) 156.
5. E. Cortina Gil, et al. [The NA62 Collaboration], J. Instrum. 12 (2017) P05025.
6. J. P. Lees, et al. [The BaBar Collaboration], Phys. Rev. Lett. 119 (2017) 131804.
7. D. Banerjee, et al. [The NA64 Collaboration] Phys. Rev. D 97 (2018) 072002.
8. P. Fayet, Phys. Rev. D 75 (2007) 115017.
9. M. Pospelov, Phys. Rev. D 80 (2009) 095002.
10. D. Hanneke, S. Fogwell and G. Gabrielse, Phys. Rev. Lett. 100 (2008) 120801.
11. R. Bouchendir, et al., Phys. Rev. Lett. 106 (2011) 080801.
12. T. Aoyama, M. Hayakawa, T. Kinoshita and M. Nio, Phys. Rev. Lett. 109 (2012) 111807.

Lepton Flavour Universality tests with heavy flavour decays at LHCb

R.G.C. Oldeman, for the LHCb collaboration

INFN Sezione di Cagliari and Università di Cagliari, Monserrato, Italy.



Several recent measurements of semileptonic charged-current and neutral-current B decays differ somewhat from theoretical predictions. While none of the individual measurements is statistically compelling, taken together they present a picture that hints to possible signs of new physics. An updated measurement of $R_K \equiv \frac{BF(B^+ \rightarrow K^+ \mu^+ \mu^-)}{BF(B^+ \rightarrow K^+ e^+ e^-)}$ is presented, based on a combination of 3 fb^{-1} of LHCb Run 1 data and 2 fb^{-1} of Run 2 data. For the dilepton invariant mass range $1.1 \leq q^2 \leq 6.0 \text{ GeV}^2$, we measure $R_K = 0.846^{+0.060+0.016}_{-0.054-0.014}$, where the first uncertainty is statistical and the second systematic. This measurement is consistent with the Standard Model prediction of $R_K = 1.0$ at the level of 2.5σ .

1 Introduction

Recent measurements of the Flavour-Changing Neutral Current (FCNC) decays $b \rightarrow s \mu^+ \mu^-$ show decay rates that are somewhat below the theoretical expectations^{1,2}. Measurements of angular distributions in $B^0 \rightarrow K^{*0} \mu^+ \mu^-$ decays, where the theoretical uncertainties are smaller, also differ notably from the predictions^{3,4,5,6}.

In the Standard Model (SM), coupling to the charged leptons is universal, and the decay rate of b hadrons to final states with one or more leptons are expected to differ only due to the mass differences between the e^\pm , μ^\pm and τ^\pm leptons, and can be determined with very small theoretical uncertainties. However, the experimental measurements of these ratios are challenging, since the signature in a typical particle detector differs strongly between the three leptons: muons leave long tracks that can be efficiently identified due to their high penetration power; electrons, when passing through matter, quickly lose momentum through emission of high-energy Bremsstrahlung photons; taus are very short-lived and decay to an electron, a muon or hadrons, in addition to one or more neutrinos.

In charged-current $B^0 \rightarrow D^{(*)-} \ell^+ \nu_\ell$ decays, the ratios $R_{D^{(*)+}} \equiv \frac{BF(B^0 \rightarrow D^{(*)-} \tau^+ \nu_\tau)}{BF(B^0 \rightarrow D^{(*)-} \mu^+ \nu_\mu)}$ have been found to be higher than expected with a combined significance of 3.8σ ⁷. However, a preliminary new measurement from Belle reduces this to 3.1σ ⁸.

In neutral-current $b \rightarrow s \ell^+ \ell^-$ decays, measurements of the ratios $R_K \equiv \frac{BF(B^+ \rightarrow K^+ \mu^+ \mu^-)}{BF(B^+ \rightarrow K^+ e^+ e^-)}$ ^{9,10,11} and $R_{K^*} \equiv \frac{BF(B^0 \rightarrow K^{*0} \mu^+ \mu^-)}{BF(B^0 \rightarrow K^{*0} e^+ e^-)}$ ^{12,13} are below the expected value of 1.0.

These so-called flavour anomalies are particularly tantalising since they may be due to new particles with very high masses. Models that involve a Z' boson or a leptoquark are able to give sizable deviations from the SM even if their masses are larger than what can be produced directly at the LHC.

2 New LHCb result on R_K

In a previous analysis, based on 3fb^{-1} of pp collision data at centre-of-mass energies of 7 and 8 TeV, LHCb measured for the dilepton invariant mass squared range $1.0 < q^2 < 6.0\text{GeV}^2$, $R_K = 0.745^{+0.090}_{-0.074} \pm 0.036$, where the first uncertainty is statistical and the second systematic. An updated measurement performed on an extended data set which includes 2fb^{-1} of pp collision data at a centre-of-mass energy of 13 TeV is presented here. Moreover, the reconstruction techniques have been improved and the analysis strategy has been reoptimised. The range in q^2 has also been slightly reduced to $1.1 < q^2 < 6.0\text{GeV}^2$, to avoid the region near the $\phi(1020)$ resonance.

Since the detector signature differs so strongly between electrons and muons, the measurement is performed as a double ratio, using the clean and abundant $B^+ \rightarrow J/\psi K^+$ decay as a normalisation:

$$R_K = \frac{BF(B^+ \rightarrow K^+\mu^+\mu^-)/BF(B^+ \rightarrow J/\psi(\rightarrow \mu^+\mu^-)K^+)}{BF(B^+ \rightarrow K^+e^+e^-)/BF(B^+ \rightarrow J/\psi(\rightarrow e^+e^-)K^+)} \quad (1)$$

This approach is valid because lepton universality has been experimentally verified in $J/\psi \rightarrow \ell^+\ell^-$ decays at the 0.4% level.

Candidate B^+ decays are selected by combining an identified charged kaon candidate with two opposite-sign lepton candidates. Single-charm decays $B \rightarrow DX$ with one misidentified track form a large background, and are rejected by requiring $m(K^+\ell^-) > m(D^0)$. Loose selections are then applied on the transverse momenta and impact parameters of the final-state tracks, and on the vertex quality, the vertex displacement and the pointing angle of the B candidate. The same 13 variables are also used for a multivariate selection based on a Boosted Decision Tree (BDT). The BDT is trained on simulated events for signal and on data candidates with $m(K^+\ell^+\ell^-) > 5.4\text{GeV}$ for background. A k -folding technique with $k = 10$ is used to separate the training and the testing samples. Finally, the selection is optimised for the highest expected significance. Figure 1 shows the 2-dimensional invariant-mass distributions for the B candidates based on muons and on electrons. The deterioration of the momentum resolution with electrons is clearly visible from the much wider radiative tail.

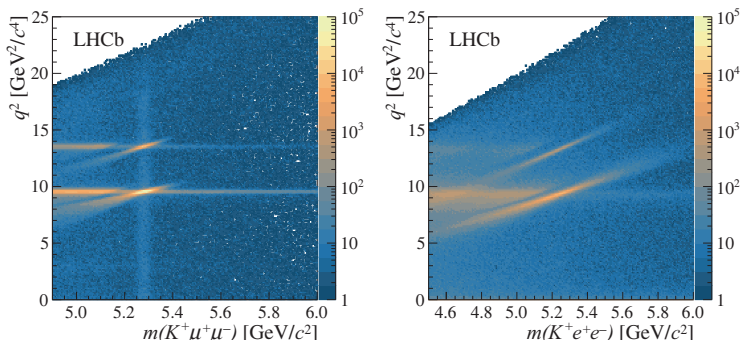


Figure 1 – Two-dimensional invariant-mass distributions of (left) $B^+ \rightarrow K^+\mu^+\mu^-$ and (right) $B^+ \rightarrow K^+e^+e^-$ candidates after preselection.

The mass distributions after the multivariate selection are shown in Fig. 2. The signals are modelled by Gaussian cores with power-law tails, with the shape parameters determined from simulation. The combinatoric background is modelled by an exponential, and the shape of the partially reconstructed background is obtained from simulated $B^0 \rightarrow K^{*0} \ell^+ \ell^-$ decays.

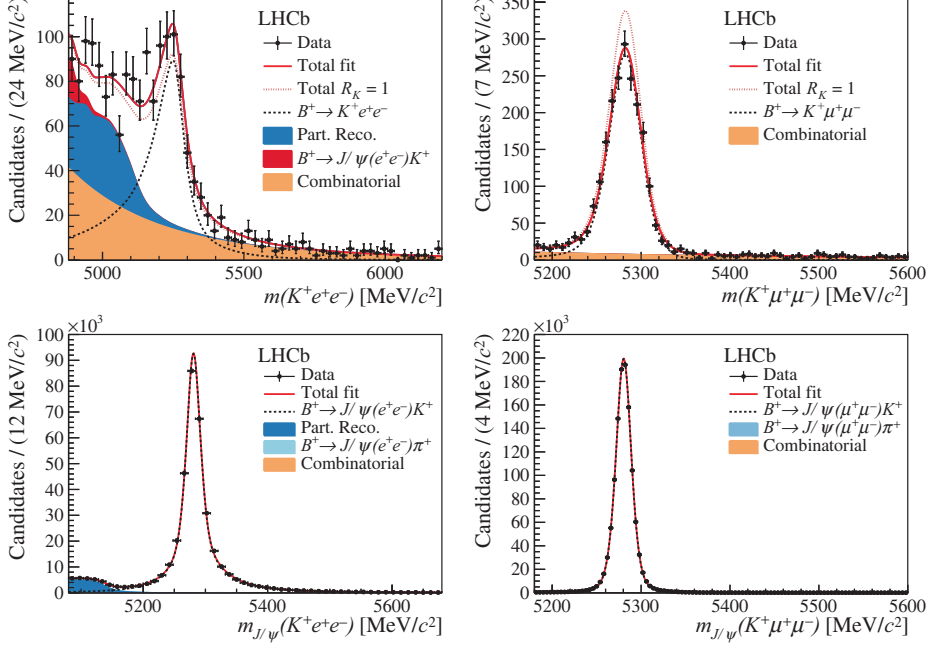


Figure 2 – Invariant-mass distributions of (top left) $B^+ \rightarrow K^+ e^+ e^-$, (top right) $B^+ \rightarrow K^+ \mu^+ \mu^-$, (bottom left) $B^+ \rightarrow J/\psi(\rightarrow e^+ e^-) K^+$ and (bottom right) $B^+ \rightarrow J/\psi(\rightarrow \mu^+ \mu^-) K^+$ candidates after the multivariate selection. Fits to the data are described in the text.

Even with the use of the double ratio for the determination of R_K , efficiencies do not fully cancel and simulation is used to account for the remaining differences. The simulation is extensively tested on high-statistics data, and corrections are made to the simulation where it does not describe the data well. The $p_T(B^+)$ spectrum is adjusted based on the $B^+ \rightarrow J/\psi(\rightarrow \mu^+ \mu^-) K^+$ data. The trigger efficiency is measured with a tag-and-probe method using $B^+ \rightarrow J/\psi(\rightarrow \ell^+ \ell^-) K^+$ data. Particle identification efficiencies are calibrated using a variety of high-statistics data samples¹⁵. The resolution on the q^2 variable is tuned to match the large peak in $B^+ \rightarrow J/\psi(\rightarrow \ell^+ \ell^-) K^+$ decays. The overall effect of these corrections on the measurement of R_K is small at ≈ 0.02 .

As a cross-check, we measure the ratio

$$r_{J/\psi} \equiv \frac{BF(B^+ \rightarrow J/\psi(\rightarrow \mu^+ \mu^-) K^+)}{BF(B^+ \rightarrow J/\psi(\rightarrow e^+ e^-) K^+)} = 1.014 \pm 0.035, \quad (2)$$

where the uncertainty comprises both statistical and systematic uncertainties. It is also verified that the value of $r_{J/\psi}$ has no dependence on a large number of lab-frame variables, such as the dilepton opening angle and the transverse momentum of the leptons. The double ratio of branching fractions

$$R_{\psi(2S)} \equiv \frac{BF(B^+ \rightarrow \psi(2S)(\rightarrow \mu^+ \mu^-) K^+)/BF(B^+ \rightarrow J/\psi(\rightarrow \mu^+ \mu^-) K^+)}{BF(B^+ \rightarrow \psi(2S)(\rightarrow e^+ e^-) K^+)/BF(B^+ \rightarrow J/\psi(\rightarrow e^+ e^-) K^+)}, \quad (3)$$

is also found to be compatible with 1.0.

Systematic uncertainties are evaluated by varying the methods used for the efficiency calibration: variations in the trigger tag-and-probe method, in the PID calibration, the modelling of the q^2 resolution and the material description of the detector all result in uncertainties on R_K of less than 1%. The statistical uncertainty on the simulation and calibration samples accounts for 1.0% uncertainty. Variations in the shape of the signal and the partially reconstructed background account for another 1.1% uncertainty. Added in quadrature, the total systematic uncertainty on R_K is 1.7%.

The result of the updated measurement is $R_K = 0.846_{-0.054}^{+0.060+0.016}$. It is consistent with the SM expectation at the level of 2.5σ . The Run1 and Run2 data are consistent with each other at the 1.9 σ level: $R_K^{\text{and8TeV}} = 0.717_{-0.071}^{+0.083+0.017}$ and $R_K^{13\text{TeV}} = 0.928_{-0.076}^{+0.089+0.020}$. The new Run1-only result is also consistent at the level of 1σ with the previous Run1 analysis, where the large overlap has been taken into account.

To conclude, a new LHCb measurement of R_K has been presented, based on approximately twice the statistics as the previous analysis. While the central value has come closer to the SM expectation, the smaller uncertainty implies that the agreement remains at the same level. In the short term, analysis of the full Run2 data sample is expected to result in a further improvement in precision. The LHCb detector is presently undergoing a major upgrade, and new data amounting to five times the integrated luminosity and collected with more efficient triggers are expected to provide a more precise measurement of R_K .

References

1. R. Aaij *et al.* [LHCb Collaboration], JHEP **1406** (2014) 133
2. R. Aaij *et al.* [LHCb Collaboration], JHEP **1509** (2015) 179
3. R. Aaij *et al.* [LHCb Collaboration], JHEP **1602** (2016) 104
4. S. Wehle *et al.* [Belle Collaboration], Phys. Rev. Lett. **118** (2017) no.11, 111801
5. M. Aaboud *et al.* [ATLAS Collaboration], JHEP **1810** (2018) 047
6. A. M. Sirunyan *et al.* [CMS Collaboration], Phys. Lett. B **781** (2018) 517
7. Y. Amhis *et al.* [HFLAV Collaboration], Eur. Phys. J. C **77** (2017) no.12, 895
8. G. Caria [Belle Collaboration], Proceedings of the Recontres de Moriond 2019, EW session
9. R. Aaij *et al.* [LHCb Collaboration], Phys. Rev. Lett. **113**, 151601 (2014)
10. J.-T. Wei *et al.* [Belle Collaboration], Phys. Rev. Lett. **103** (2009) 171801
11. J. P. Lees *et al.* [BaBar Collaboration], Phys. Rev. D **86** (2012) 032012
12. R. Aaij *et al.* [LHCb Collaboration], JHEP **1708** (2017) 055
13. A. Abdesselam *et al.* [Belle Collaboration], arXiv:1904.02440 [hep-ex].
14. R. Aaij *et al.* [LHCb Collaboration], arXiv:1903.09252 [hep-ex].
15. R. Aaij *et al.*, arXiv:1812.10790 [hep-ex].

The trouble with $R_{K^{(*)}}$ – updated global fits and future directions

S. DESCOTES-GENON

*Laboratoire de Physique Théorique (UMR 8627),
CNRS, Univ. Paris-Sud, Université Paris-Saclay, 91405 Orsay Cedex, France*

I review the interpretation of the available data on $b \rightarrow s\ell\ell$ transitions, including recent updates from LHCb and Belle collaborations on the ratios R_K and R_{K^*} assessing Lepton-Flavour Universality in these decays.

The flavour-changing neutral current (FCNC) transition $b \rightarrow s\ell^+\ell^-$ are studied in detail in the LHC experiments (LHCb, CMS and ATLAS experiments) as well as at Belle, showing interesting deviations from the SM. The appearance of several tensions in different $b \rightarrow s\ell^+\ell^-$ channels is interesting since all these observables are sensitive (in different ways) to the same short-distance Wilson Coefficients, in particular $\mathcal{C}_{7,9,10}^{(\prime)}$, in the effective Hamiltonian approach. One can perform global fits to all these data, leading to consistent New Physics (NP) scenarios where some or all of these short-distance couplings are affected by NP. One can assess the success of these NP scenarios to explain the anomalies by considering their goodness-of-fit and their pulls with respect to the SM hypothesis (in some cases above the 5σ level).

During the Moriond 2019 conference, there have been several updates concerning the two lepton-flavour universality (LFU) ratios:

$$R_{K^{(*)}} = \frac{\mathcal{B}(B \rightarrow K^{(*)}\mu^+\mu^-)}{\mathcal{B}(B \rightarrow K^{(*)}e^+e^-)} \quad (1)$$

R_K was updated in the bin [1.1,6] by the LHCb collaboration¹, whereas results on R_{K^*} were presented by the Belle collaboration in three bins². We have updated our results^{3,4} taking these new measurements into account⁵ as well as the new ATLAS value for $\mathcal{B}(B_s \rightarrow \mu\mu)$ ⁶.

1 Model-independent approach

First we consider scenarios where NP occurs only in $b \rightarrow s\mu\mu$, performing fits to the full set of data (“All”) or restricted to quantities measuring Lepton Flavour Universality Violation (LFUV). While we do not observe any significant difference in the 1D scenarios with “All” data compared to³, some of the pulls with respect to the SM for the LFUV 1D fits get reduced by half a sigma. A few other comments are in order: 1) the scenario $\mathcal{C}_{9\mu}^{\text{NP}} = -\mathcal{C}_{9'\mu}$ which favours a SM-like value of $R_K^{[1.1,6]}$ ^{4,7} has an increased significance in the “All” fit, 2) the scenario $\mathcal{C}_{9\mu}^{\text{NP}}$ is favoured in the “All” fit while $\mathcal{C}_{10\mu}^{\text{NP}} = -\mathcal{C}_{10\mu}^{\text{NP}}$ is favoured in the LFUV fit, a difference which can be solved through the introduction of Lepton Flavour Universal (LFU) New Physics, as shown in^{4,5} the best-fit point for the scenario $\mathcal{C}_{9\mu}^{\text{NP}}$ coincides now in the “All” and LFUV fits and 4) the scenario with only $\mathcal{C}_{10\mu}^{\text{NP}}$ has a significance in the “All” fit of only 4.0σ level and 3.9σ for the LFUV fit.

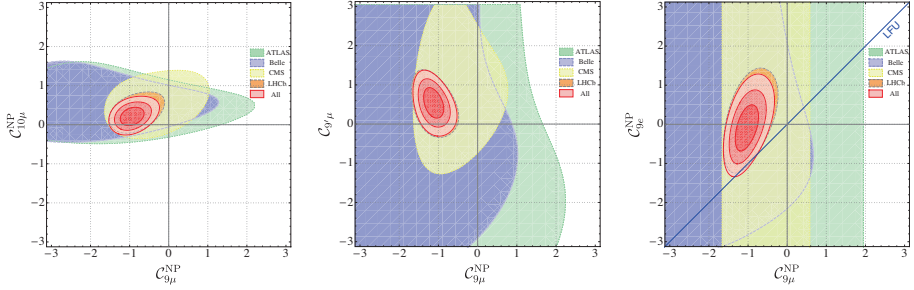


Figure 1 – From left to right: Allowed regions in the $(C_{9\mu}^{\text{NP}}, C_{10\mu}^{\text{NP}})$, $(C_{9\mu}^{\text{NP}}, C_{9'\mu})$ and $(C_{9\mu}^{\text{NP}}, C_{9e}^{\text{NP}})$ planes for the corresponding 2D hypotheses discussed in ², using all available data (fit “All”).

Concerning 2D scenarios, the same picture arises as in ³, except that C_{9e}^{NP} is now centered around zero and small contributions to right-handed currents (RHCs) seem slightly favoured ($C_{9'\mu} > 0, C_{10'\mu} < 0$). The scenario $C_{9'\mu} = -C_{10'\mu}$ (left-handed lepton coupling for right-handed quarks) prefers to be associated with $C_{9\mu}^{\text{NP}}$ (vector lepton coupling for left-handed quarks) rather than $C_{9\mu}^{\text{NP}} = -C_{10\mu}^{\text{NP}}$ (left-handed lepton coupling for left-handed quarks). Fig. 1 show the results of some favoured NP scenarios. Finally, no significant changes are observed in the 6D fit, except for the slight increase in the Pull_{SM} .

We also update the scenarios considered in ⁴ that allow for the presence of Lepton Flavour Universal NP, leading to the separation $C_{ie} = C_i^{\text{U}}, C_{i\mu} = C_i^{\text{U}} + C_{i\mu}^{\text{V}}$. Favoured scenarios are show in Fig. 2. Such a situation may occur rather naturally in various NP models, for instance through the evolution of charged-current operators that mix into $\mathcal{O}_{9\ell}$ through LFU radiative corrections⁸, or in the context of models with vector-like quark models where the induced couplings to Z (and Z') may generate $C_{9(\ell)}^{\text{V}}$ and $C_{10(\ell)}^{\text{V}}$ ⁹. We observe a slight decrease in significance for the scenarios already considered in ⁴. We also consider a new set of scenarios (9-13) allowing for LFU NP in C_{10} in both left-hand currents (LHC) and right-hand currents (RHC) providing also good descriptions of the data⁵.

More information (goodness-of-fit, SM pulls, best-fit points, confidence intervals, illustrative plots) on both types of scenarios can be found in ⁵.

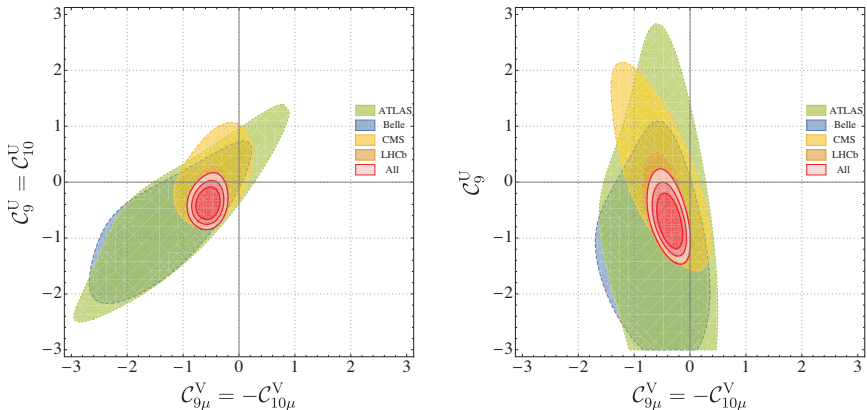


Figure 2 – Allowed regions for scenarios 6 and 8 discussed in ³.

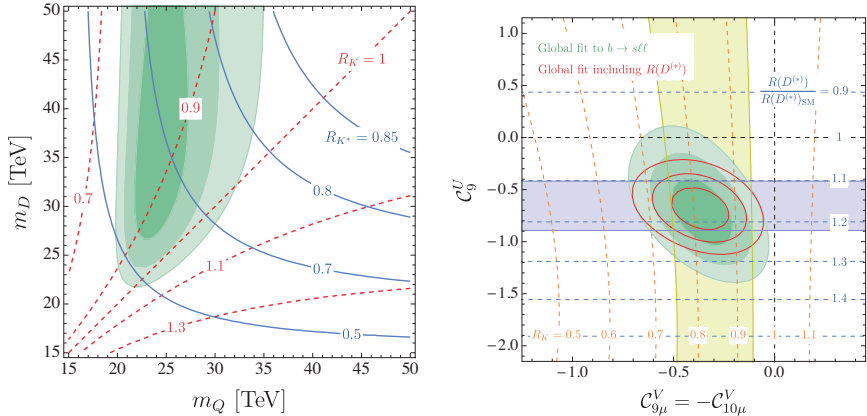


Figure 3 – Left: Preferred regions (at the 1, 2 and 3 σ level) for the $L_\mu - L_\tau$ model in ¹⁰ from $b \rightarrow s\ell^+\ell^-$ data (green) in the (m_Q, m_D) plane with $Y^{D,Q} = 1$. The contour lines denote the predicted values for $R_K^{[1,1,6]}$ (red, dashed) and $R_{K^*}^{[1,1,6]}$ (blue, solid). Right: Preferred regions at the 1, 2 and 3 σ level (green) in the $(C_{9\mu}^V = -C_{10\mu}^V, C_9^U)$ plane from $b \rightarrow s\ell^+\ell^-$ data. The red contour lines show the corresponding regions once $R_{D^{(*)}}$ is included in the fit (for $\Lambda = 2$ TeV). The horizontal blue (vertical yellow) band is consistent with $R_{D^{(*)}}$ (R_K) at the 2 σ level and the contour lines show the predicted values for these ratios. More information can be found in ^{2,3}.

2 Impact on specific NP models

Some of the scenarios discussed above find a natural explanation in simplified NP models discussed recently in the literature. The $(C_{9\mu}, C_{9'\mu})$ scenario is naturally generated in a Z' model with opposite couplings to right-handed and left-handed quarks. This setup was already proposed in ¹⁰ within the context of a gauged $L_\mu - L_\tau$ symmetry with vector-like quarks. We show the update of Fig. 2 in ¹⁰ in the left panel of Fig. 3.

Scenario 8 in ⁴ allows for a model-independent connection between the anomalies in $b \rightarrow s\ell^+\ell^-$ and $b \rightarrow c\tau\nu$, which are also at the 4 σ level ¹¹. Such a correlation arises in the $C^{(1)} = C^{(3)}$ scenario as expressed in terms of gauge-invariant dimension-6 operators. The operator involving third generation leptons explains $R_{D^{(*)}}$ and the one with second generation ones give a LFUV effect in $b \rightarrow s\mu^+\mu^-$. The constraint from $b \rightarrow c\tau\nu$ and $SU(2)_L$ invariance leads generally to large contributions to the operator $\bar{s}\gamma^\mu P_L b \bar{\tau}\gamma_\mu P_L \tau$, which enhances $b \rightarrow s\tau^+\tau^-$ processes ¹², but also mixes into \mathcal{O}_9 and generates C_9^U at $\mu = m_b$ ⁸. Therefore, one of our scenarios (scenario 8) is reproduced in this setup with an additional correlation between C_9^U and $R_{D^{(*)}}$, leading to the right plot of Fig. 3. Note that this scenario has a pull of 7.0 σ due to the inclusion of $R_{D^{(*)}}$.

In both cases, more information can be found in ⁵.

Acknowledgments

This project has received funding from the EU Horizon 2020 research and innovation programme under the Marie Skłodowska-Curie grant agreements No 690575 and No 674896.

References

1. R. Aaij *et al.* [LHCb Collaboration], arXiv:1903.09252 [hep-ex].
2. A. Abdesselam *et al.* [Belle Collaboration], arXiv:1904.02440 [hep-ex].
3. B. Capdevila *et al.*, JHEP **1801** (2018) 093
4. M. Algueró *et al.*, Phys. Rev. D **99** (2019) no.7, 075017

5. M. Algueró *et al.*, arXiv:1903.09578 [hep-ph].
6. M. Aaboud *et al.* [ATLAS Collaboration], JHEP **1904** (2019) 098
7. M. Algueró *et al.*, arXiv:1902.04900 [hep-ph].
8. A. Crivellin *et al.*, Phys. Rev. Lett. **122** (2019) no.1, 011805
9. C. Bobeth *et al.*, JHEP **1704** (2017) 079
10. W. Altmannshofer *et al.*, Phys. Rev. D **89** (2014) 095033
11. Y. Amhis *et al.* [HFLAV Collaboration], Eur. Phys. J. C **77** (2017) no.12, 895
12. B. Capdevila *et al.*, Phys. Rev. Lett. **120** (2018) no.18, 181802

Explaining the Flavor Anomalies with a Vector Leptoquark

ANDREAS CRIVELLIN

Paul Scherrer Institut, CH-5232 Villigen PSI, Switzerland

Physik-Institut, Universität Zürich, Winterthurerstrasse 190, CH-8057 Zürich, Switzerland



Several experiments revealed intriguing hints for lepton flavor universality (LFU) violating new physics (NP) in semi-leptonic B meson decays, mainly in $b \rightarrow c\tau\nu$ and $b \rightarrow s\ell^+\ell^-$ transitions at the $3-5\sigma$ level. Leptoquarks (LQ) are prime candidates to address these anomalies as they contribute to semi-leptonic decays already at tree level while effects in other flavor observables, agreeing with the standard model (SM), are loop suppressed.

In these proceedings we review the vector leptoquark $SU(2)_L$ singlet, contained in the famous Pati-Salam model, which is able to address both $b \rightarrow c\tau\nu$ and $b \rightarrow s\mu^+\mu^-$ data simultaneously. Due to the large couplings to tau leptons needed to account for the $b \rightarrow c\tau\nu$ data, sizable loop effects arise which we include in our phenomenological analysis. Updating our result of Ref.¹ with the recent measurements of LHCb² and BELLE^{3,4} we find an even better fit to data than before.

1 Introduction

While so far the LHC has not detected any particles beyond the ones present in the Standard Model (SM), intriguing hints for LFU violation in semi-leptonic B -meson decays were accumulated in several (classes of) observables:

$$b \rightarrow s\ell^+\ell^-$$

In these flavor changing neutral current transitions, measurements of the ratios

$$R(K^{(*)}) = \frac{\text{Br}[B \rightarrow K\mu^+\mu^-]}{\text{Br}[B \rightarrow Ke^+e^-]}$$

show sizable deviations from their respective SM prediction. While the newest measurement of $R(K)$ by the LHCb collaboration² shows a deviation of 2.5σ from the SM, the Belle result for $R(K^{(*)})$ is consistent with the SM.³ However, due to the larger errors, this result also agrees with previous LHCb measurement of $R(K^{(*)})$ which deviate from the SM⁵ in the same direction as $R(K)$. Taking into account all other $b \rightarrow s\mu^+\mu^-$ observables (like the lepton flavor universal

observable $P_5^{\prime 6}$), the global fit prefers various NP scenarios above the 5σ level⁷ compared to the SM, also when the newest measurements are taken into account.^{8–11}

In order to resolve the discrepancy in the neutral current transitions, an effect of $\mathcal{O}(10\%)$ is required at the amplitude level. Since this flavor changing neutral current (FCNC) is suppressed in the SM as it is only induced at one loop level, a small NP contribution is already sufficient. In a global fit one finds a preference for scenarios like $C_9^{\mu\mu} = -C_{10}^{\mu\mu}$ (i.e. a left-handed current coupling to muons only).⁸ Such an effect is naturally obtained at tree-level with the vector LQ $SU(2)$ singlet.^{1,12–32} However, a $C_9^{\mu\mu} = -C_{10}^{\mu\mu}$ effect complemented by a flavor universal effect in C_9 gives an even better fit to data.^{8,33} As we will see, this is exactly the pattern that arises in our model.

$b \rightarrow c\tau\nu$

There are also indications for LFU violation in charged current transitions, namely in the ratios

$$R(D^{(*)}) = \frac{\text{Br}[B \rightarrow D^{(*)}\tau\nu]}{\text{Br}[B \rightarrow D^{(*)}\ell\nu]}$$

where $\ell = \{e, \mu\}$. While the newest measurements from Belle⁴ agree with the SM prediction, including previous measurements by BaBar, Belle and LHCb still yield a deviation of 3.1σ ³⁴ from the SM prediction. Furthermore there is also a measurement of the ratio $R(J/\Psi) = \frac{\text{Br}[B_c \rightarrow J/\Psi\tau\nu]}{\text{Br}[B_c \rightarrow J/\Psi\mu\nu]}$ exceeding its SM prediction.³⁵

Also here a NP effect of $\mathcal{O}(10\%)$ is needed at the amplitude level. However, since $b \rightarrow c\tau\nu$ transitions are mediated at tree level by the exchange of a W boson in the SM, the NP effect needs to be large. This means that NP should contribute at tree level with sizable couplings and at a not too high NP scale. Here, the best single particle solution is the vector LQ $SU(2)$ singlet^{1,12–32} since it does not give a tree-level effect in $b \rightarrow s\nu\nu$ processes and provides a common rescaling of $R(D)$ and $R(D^*)$ with respect to the SM prediction.

2 The Pati Salam vector leptoquark as combined solution to the anomalies

The vector Leptoquark $SU(2)_L$ singlet with hypercharge $-4/3$, arising in the famous Pati-Salam model,³⁶ is a prime candidate to explain both the anomalies in charged current and neutral current B decays simultaneously.^{12–14,17–20} It gives a $C_9 = -C_{10}$ effect in $b \rightarrow s\ell^+\ell^-$ at tree level and at the same time a sizable effect in $b \rightarrow c\tau\nu$ without violating bounds from $b \rightarrow s\nu\nu$ and/or direct searches and does not lead to proton decay. Note that this LQ by itself is not UV complete, however several UV complete models for this LQ have been proposed.^{15,16,21–29,37}

For the purpose of our phenomenological analysis, let us consider a model where we simply extend the SM by this LQ. Its interaction with the SM particles is given by the Lagrangian

$$\mathcal{L}_{V_1} = \kappa_{fi}^L \overline{Q}_f \gamma_\mu L_i V_\mu^{1\dagger} + h.c. ,$$

where $Q(L)$ is the quark (lepton) $SU(2)_L$ doublet, κ_{fi}^L represents the couplings of the LQ to the left handed quarks (leptons) and f and i are flavor indices. Note that in principle couplings to right-handed SM particles are also allowed, they are however not relevant for this discussion. After electro-weak symmetry breaking, we work in the down basis, meaning that no CKM matrix elements appear in FCNC processes.

We start by taking κ_{23}^L and κ_{33}^L as the only non-zero couplings, as they are necessary to explain $b \rightarrow c\tau\nu$ data. Here, strong effects in $b \rightarrow s\tau^+\tau^-$ transitions³⁹ are generated which at the 1-loop level affect $b \rightarrow s\ell^+\ell^-$ via the Wilson coefficients $C_{9, sb}^{\ell\ell}$ and C_7^{sb} , as is depicted to the

left in Fig. 1. Due to the correlation with $b \rightarrow c\tau\nu$, these Wilson coefficients can be expressed as functions of $R(D^{(*)})/R(D^{(*)})_{\text{SM}}$. The Wilson coefficients' dependency on these ratios is shown in the right plot of Fig. 1, where the RGE evolution of C_7^{sb} from the NP scale down to the b quark scale is also taken into account (see Ref.⁴⁰). Interestingly, assuming an explanation of $b \rightarrow c\tau\nu$ data, the effects generated in $C_{9,sb}^{\ell\ell}$ and C_7^{sb} agree with the 1σ ranges of the model independent fit to $b \rightarrow s\mu^+\mu^-$ data excluding LFU violating observables.^{38,41}

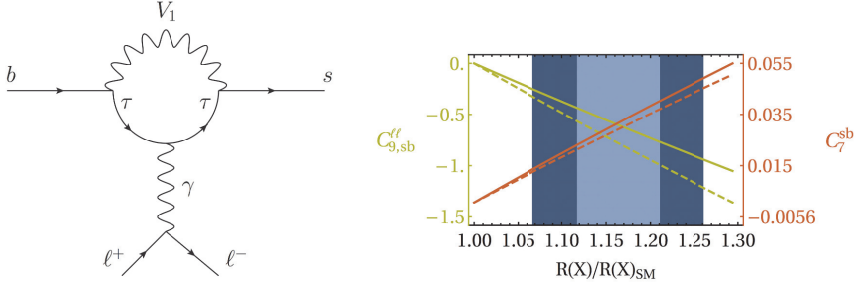


Figure 1 – Left: Feynman diagram depicting the loop effects induced by the $bc\tau\nu$ operator from $SU(2)$ invariance. Right: $C_{9,sb}^{\ell\ell}$ and $C_7^{sb}(\mu_b)$, generated by these loop effects, as functions of $R(D^{(*)})/R(D^{(*)})_{\text{SM}}$. The solid (dashed) lines correspond to $M = 1$ TeV (5 TeV) while the (dark blue) region is preferred by $b \rightarrow c\tau\nu$ data at the 1σ (2σ) level, taking into account the most recent measurements. From the global fit, taking into account only lepton flavor conserving observables, we have $-1.29 < C_{9,sb}^{\ell\ell} < -0.87$ and $-0.01 < C_7^{sb}(\mu_b) < 0.05$ at the 1σ level. Assuming an explanation of $b \rightarrow c\tau\nu$, our model predicts the right size and sign of the effect in $C_{9,sb}^{\ell\ell}$ and $C_7^{sb}(\mu_b)$ needed to explain $b \rightarrow s\ell^+\ell^-$ data.

Now we also allow κ_{32}^L and κ_{22}^L to be non-zero, generating a tree level effect in $b \rightarrow s\mu^+\mu^-$ which is necessary to account for the LFU violating observables as well. In Fig. 2 we show the allowed (colored) regions from $b \rightarrow s\mu^+\mu^-$ and $b \rightarrow c\tau\nu$ as well as the exclusions from $b \rightarrow s\tau\mu$ and $\tau \rightarrow \phi\mu$. A simultaneous explanation of the anomalies is perfectly possible since the colored regions overlap and do not extend to the parameter space excluded by $b \rightarrow s\tau\mu$ and $\tau \rightarrow \phi\mu$. Interestingly, we predict a lepton flavor universal effect in $C_{9,sb}^{\ell\ell}$ and C_7^{sb} in addition to a LFU violating tree-level effect of the form $C_{9,sb}^{\mu\mu} = -C_{10,sb}^{\mu\mu}$ in muonic channels only. This means that the effect of NP compared to the SM is expected to be larger in lepton flavor universal observables like $P5'$ relative to LFU violation observables as $R(K^{(*)})$, which is in perfect agreement with global fit scenarios.⁸ In fact, the agreement is even better after the inclusion of the new measurements of BELLE and LHCb.

Note added

These proceedings match the ones of Francesco Saturnino for "XXVII International Workshop on Deep-Inelastic Scattering and Related Subjects - DIS2019" and are submitted as a common arxiv version.

References

1. A. Crivellin, C. Greub, D. Mller and F. Saturnino, "Importance of Loop Effects in Explaining the Accumulated Evidence for New Physics in B Decays with a Vector Leptoquark," Phys. Rev. Lett. **122**, no. 1, 011805 (2019) doi:10.1103/PhysRevLett.122.011805 [arXiv:1807.02068 [hep-ph]].
2. R. Aaij *et al.* [LHCb Collaboration], "Search for lepton-universality violation in $B^+ \rightarrow K^+\ell^+\ell^-$ decays," Phys. Rev. Lett. **122**, no. 19, 191801 (2019) doi:10.1103/PhysRevLett.122.191801 [arXiv:1903.09252 [hep-ex]].

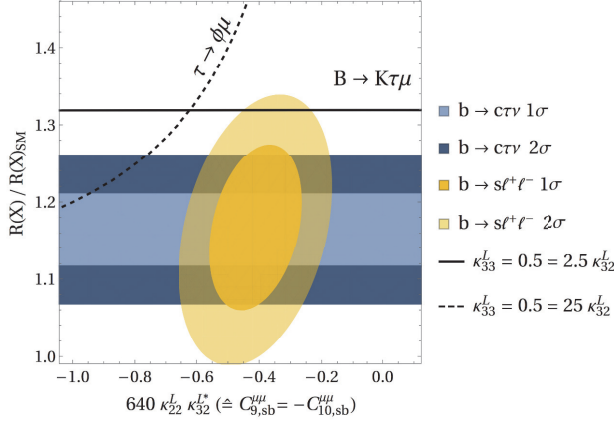


Figure 2 – Allowed (colored) regions in the $C_{9, sb}^{\mu\mu} = -C_{10, sb}^{\mu\mu}$ ($\hat{=} 640\kappa_{22}^L\kappa_{32}^{L*}$) – $R(X)/R(X)_{\text{SM}}$ plane for $M = 1$ TeV and $X = \{D, D^*\}$ at the 1σ and 2σ level. The region above the black dashed (solid) line is excluded by $\tau \rightarrow \phi\mu$ ($B \rightarrow K\tau\mu$) for $\kappa_{33}^L = 0.5 = 25\kappa_{32}^L$ ($\kappa_{33}^L = 0.5 = 2.5\kappa_{32}^L$). The bound from $\tau \rightarrow \phi\mu$ ($B \rightarrow K\tau\mu$) depends on κ_{33}^L and κ_{32}^L and gets stronger if κ_{32}^L gets smaller (larger). That is, for $\kappa_{33}^L = 0.5$ and $2.7 < \kappa_{33}^L/\kappa_{32}^L < 27$, the whole 2σ region preferred by $b \rightarrow c\tau\nu$ and $b \rightarrow s\ell^+\ell^-$ data is consistent with these bounds. Note that we used the most recent experimental results for both the $b \rightarrow c\tau\nu$ and $b \rightarrow s\ell^+\ell^-$ transitions, therefore updating our analysis.

3. A. Abdesselam *et al.* [Belle Collaboration], “Test of lepton flavor universality in $B \rightarrow K^*\ell^+\ell^-$ decays at Belle,” arXiv:1904.02440 [hep-ex].
4. A. Abdesselam *et al.* [Belle Collaboration], “Measurement of $\mathcal{R}(D)$ and $\mathcal{R}(D^*)$ with a semileptonic tagging method,” arXiv:1904.08794 [hep-ex].
5. R. Aaij *et al.* [LHCb Collaboration], “Test of lepton universality with $B^0 \rightarrow K^{*0}\ell^+\ell^-$ decays,” JHEP **1708**, 055 (2017) doi:10.1007/JHEP08(2017)055 [arXiv:1705.05802 [hep-ex]].
6. R. Aaij *et al.* [LHCb Collaboration], “Angular analysis of the $B^0 \rightarrow K^{*0}\mu^+\mu^-$ decay using 3 fb^{-1} of integrated luminosity,” JHEP **1602**, 104 (2016) doi:10.1007/JHEP02(2016)104 [arXiv:1512.04442 [hep-ex]].
7. B. Capdevila, A. Crivellin, S. Descotes-Genon, J. Matias and J. Virto, “Patterns of New Physics in $b \rightarrow s\ell^+\ell^-$ transitions in the light of recent data,” JHEP **1801**, 093 (2018) doi:10.1007/JHEP01(2018)093 [arXiv:1704.05340 [hep-ph]].
8. M. Alguer, B. Capdevila, A. Crivellin, S. Descotes-Genon, P. Masjuan, J. Matias and J. Virto, “Emerging patterns of New Physics with and without Lepton Flavour Universal contributions,” arXiv:1903.09578 [hep-ph].
9. J. Aebischer, W. Altmannshofer, D. Guadagnoli, M. Reboud, P. Stangl and D. M. Straub, “ B -decay discrepancies after Moriond 2019,” arXiv:1903.10434 [hep-ph].
10. M. Ciuchini, A. M. Coutinho, M. Fedele, E. Franco, A. Paul, L. Silvestrini and M. Valli, “New Physics in $b \rightarrow s\ell^+\ell^-$ confronts new data on Lepton Universality,” arXiv:1903.09632 [hep-ph].
11. A. Arbey, T. Hurth, F. Mahmoudi, D. M. Santos and S. Neshatpour, “Update on the $b \rightarrow s$ anomalies,” arXiv:1904.08399 [hep-ph].
12. R. Alonso, B. Grinstein and J. Martin Camalich, “Lepton universality violation and lepton flavor conservation in B -meson decays,” JHEP **1510**, 184 (2015) doi:10.1007/JHEP10(2015)184 [arXiv:1505.05164 [hep-ph]].
13. L. Calibbi, A. Crivellin and T. Ota, “Effective Field Theory Approach to $bs(\prime)$, $BK(\prime)$ and $BD(\prime)$ with Third Generation Couplings,” Phys. Rev. Lett. **115**, 181801 (2015)

- doi:10.1103/PhysRevLett.115.181801 [arXiv:1506.02661 [hep-ph]].
14. S. Fajfer and N. Konik, “Vector leptoquark resolution of R_K and $R_{D^{(*)}}$ puzzles,” Phys. Lett. B **755**, 270 (2016) doi:10.1016/j.physletb.2016.02.018 [arXiv:1511.06024 [hep-ph]].
 15. R. Barbieri, G. Isidori, A. Pattori and F. Senia, “Anomalies in B -decays and $U(2)$ flavour symmetry,” Eur. Phys. J. C **76**, no. 2, 67 (2016) doi:10.1140/epjc/s10052-016-3905-3 [arXiv:1512.01560 [hep-ph]].
 16. R. Barbieri, C. W. Murphy and F. Senia, “B-decay Anomalies in a Composite Leptoquark Model,” Eur. Phys. J. C **77**, no. 1, 8 (2017) doi:10.1140/epjc/s10052-016-4578-7 [arXiv:1611.04930 [hep-ph]].
 17. G. Hiller, D. Loose and K. Schnwald, “Leptoquark Flavor Patterns & B Decay Anomalies,” JHEP **1612**, 027 (2016) doi:10.1007/JHEP12(2016)027 [arXiv:1609.08895 [hep-ph]].
 18. B. Bhattacharya, A. Datta, J. P. Guvin, D. London and R. Watanabe, “Simultaneous Explanation of the R_K and $R_{D^{(*)}}$ Puzzles: a Model Analysis,” JHEP **1701**, 015 (2017) doi:10.1007/JHEP01(2017)015 [arXiv:1609.09078 [hep-ph]].
 19. D. Buttazzo, A. Greljo, G. Isidori and D. Marzocca, “B-physics anomalies: a guide to combined explanations,” JHEP **1711**, 044 (2017) doi:10.1007/JHEP11(2017)044 [arXiv:1706.07808 [hep-ph]].
 20. J. Kumar, D. London and R. Watanabe, “Combined Explanations of the $b \rightarrow s\mu^+\mu^-$ and $b \rightarrow c\tau^-\bar{\nu}$ Anomalies: a General Model Analysis,” Phys. Rev. D **99**, no. 1, 015007 (2019) doi:10.1103/PhysRevD.99.015007 [arXiv:1806.07403 [hep-ph]].
 21. N. Assad, B. Fornal and B. Grinstein, “Baryon Number and Lepton Universality Violation in Leptoquark and Diquark Models,” Phys. Lett. B **777**, 324 (2018) doi:10.1016/j.physletb.2017.12.042 [arXiv:1708.06350 [hep-ph]].
 22. L. Di Luzio, A. Greljo and M. Nardecchia, “Gauge leptoquark as the origin of B-physics anomalies,” Phys. Rev. D **96**, no. 11, 115011 (2017) doi:10.1103/PhysRevD.96.115011 [arXiv:1708.08450 [hep-ph]].
 23. L. Calibbi, A. Crivellin and T. Li, “Model of vector leptoquarks in view of the B -physics anomalies,” Phys. Rev. D **98**, no. 11, 115002 (2018) doi:10.1103/PhysRevD.98.115002 [arXiv:1709.00692 [hep-ph]].
 24. M. Bordone, C. Cornella, J. Fuentes-Martin and G. Isidori, “A three-site gauge model for flavor hierarchies and flavor anomalies,” Phys. Lett. B **779**, 317 (2018) doi:10.1016/j.physletb.2018.02.011 [arXiv:1712.01368 [hep-ph]].
 25. R. Barbieri and A. Tesi, “ B -decay anomalies in Pati-Salam $SU(4)$,” Eur. Phys. J. C **78**, no. 3, 193 (2018) doi:10.1140/epjc/s10052-018-5680-9 [arXiv:1712.06844 [hep-ph]].
 26. M. Blanke and A. Crivellin, “ B Meson Anomalies in a Pati-Salam Model within the Randall-Sundrum Background,” Phys. Rev. Lett. **121**, no. 1, 011801 (2018) doi:10.1103/PhysRevLett.121.011801 [arXiv:1801.07256 [hep-ph]].
 27. A. Greljo and B. A. Stefanek, “Third family quarklepton unification at the TeV scale,” Phys. Lett. B **782**, 131 (2018) doi:10.1016/j.physletb.2018.05.033 [arXiv:1802.04274 [hep-ph]].
 28. M. Bordone, C. Cornella, J. Fuentes-Martin and G. Isidori, “Low-energy signatures of the PS^3 model: from B -physics anomalies to LFV,” JHEP **1810**, 148 (2018) doi:10.1007/JHEP10(2018)148 [arXiv:1805.09328 [hep-ph]].
 29. S. Matsuzaki, K. Nishiwaki and K. Yamamoto, “Simultaneous interpretation of K and B anomalies in terms of chiral-flavorful vectors,” JHEP **1811**, 164 (2018) doi:10.1007/JHEP11(2018)164 [arXiv:1806.02312 [hep-ph]].
 30. L. Di Luzio, J. Fuentes-Martin, A. Greljo, M. Nardecchia and S. Renner, “Maximal Flavour Violation: a Cabibbo mechanism for leptoquarks,” JHEP **1811**, 081 (2018) doi:10.1007/JHEP11(2018)081 [arXiv:1808.00942 [hep-ph]].
 31. A. Biswas, D. Kumar Ghosh, N. Ghosh, A. Shaw and A. K. Swain, “Novel collider signature of U_1 Leptoquark and $B \rightarrow \pi$ observables,” arXiv:1808.04169 [hep-ph].

32. A. Angelescu, D. Beirevi, D. A. Faroughy and O. Sumensari, “Closing the window on single leptoquark solutions to the B -physics anomalies,” *JHEP* **1810**, 183 (2018) doi:10.1007/JHEP10(2018)183 [arXiv:1808.08179 [hep-ph]].
33. M. Alguer, B. Capdevila, S. Descotes-Genon, P. Masjuan and J. Matias, “Are we over-looking lepton flavour universal new physics in $b \rightarrow s\ell\ell$?,” *Phys. Rev. D* **99**, no. 7, 075017 (2019) doi:10.1103/PhysRevD.99.075017 [arXiv:1809.08447 [hep-ph]].
34. Y. Amhis *et al.* [HFLAV Collaboration], “Averages of b -hadron, c -hadron, and τ -lepton properties as of summer 2016,” *Eur. Phys. J. C* **77**, no. 12, 895 (2017) doi:10.1140/epjc/s10052-017-5058-4 [arXiv:1612.07233 [hep-ex]].
35. R. Aaij *et al.* [LHCb Collaboration], “Measurement of the ratio of branching fractions $\mathcal{B}(B_c^+ \rightarrow J/\psi\tau^+\nu_\tau)/\mathcal{B}(B_c^+ \rightarrow J/\psi\mu^+\nu_\mu)$,” *Phys. Rev. Lett.* **120**, no. 12, 121801 (2018) doi:10.1103/PhysRevLett.120.121801 [arXiv:1711.05623 [hep-ex]].
36. J. C. Pati and A. Salam, “Lepton Number as the Fourth Color,” *Phys. Rev. D* **10**, 275 (1974) Erratum: [*Phys. Rev. D* **11**, 703 (1975)]. doi:10.1103/PhysRevD.10.275, 10.1103/PhysRevD.11.703.2
37. C. Cornella, J. Fuentes-Martin and G. Isidori, “Revisiting the vector leptoquark explanation of the B-physics anomalies,” arXiv:1903.11517 [hep-ph].
38. S. Descotes-Genon, L. Hofer, J. Matias and J. Virto, “Global analysis of $b \rightarrow s\ell\ell$ anomalies,” *JHEP* **1606**, 092 (2016) doi:10.1007/JHEP06(2016)092 [arXiv:1510.04239 [hep-ph]].
39. B. Capdevila, A. Crivellin, S. Descotes-Genon, L. Hofer and J. Matias, “Searching for New Physics with $b \rightarrow s\tau^+\tau^-$ processes,” *Phys. Rev. Lett.* **120**, no. 18, 181802 (2018) doi:10.1103/PhysRevLett.120.181802 [arXiv:1712.01919 [hep-ph]].
40. A. Crivellin and F. Saturnino, “Correlating Tauonic B Decays to the Neutron EDM via a Scalar Leptoquark,” arXiv:1905.08257 [hep-ph].
41. W. Altmannshofer and D. M. Straub, “New physics in $b \rightarrow s$ transitions after LHC run 1,” *Eur. Phys. J. C* **75**, no. 8, 382 (2015) doi:10.1140/epjc/s10052-015-3602-7 [arXiv:1411.3161 [hep-ph]].

Connecting neutral current B anomalies with the heaviness of the third family

Joe Davighi

DAMTP, University of Cambridge, United Kingdom

It is possible, and for several reasons attractive, to explain a collection of recent anomalies involving $b \rightarrow s\mu\mu$ processes with a Z' gauge boson coupled only to the third family in the weak eigenbasis. From this premise, requiring cancellation of all gauge anomalies (including mixed and gravitational anomalies) fixes a unique charge assignment for the third family Standard Model fermions, which is simply proportional to hypercharge. After a brief discussion of some general features of anomaly cancellation in Z' theories, we discuss the phenomenology of such a ‘Third Family Hypercharge Model’, which is subject to a trio of important constraints: (i) $B_s - \bar{B}_s$ mixing, (ii) lepton universality of the Z boson couplings, and (iii) constraints from direct searches for the Z' boson at the LHC. Finally, in gauging third family hypercharge, this model forbids all Yukawa couplings (at the renormalisable level) save those of the third family, leading to a possible explanation of the heaviness of the third family.

1 Introduction

There is a tension between Standard Model (SM) predictions and experimental measurements involving $b \rightarrow s\mu\mu$ transitions, for example in LHCb’s measurements of the lepton flavour universality (LFU) ratios $R_{K^{(*)}} = BR(B \rightarrow K^{(*)}\mu^+\mu^-)/BR(B \rightarrow K^{(*)}e^+e^-)$. For the di-lepton invariant mass-squared bin $q^2 \in [1.1, 6] \text{ GeV}^2$, in which the SM predicts $R_{K^{(*)}}$ equal to unity at the percent level, the new measurement of R_K (which includes Run-1 data and 2 fb^{-1} of Run-2 data) is $R_K = 0.846_{-0.054-0.014}^{+0.060+0.016}$, where the first (second) uncertainty is statistical (systematic).¹ LHCb has also measured $R_{K^*} = 0.69_{-0.07}^{+0.11} \pm 0.05$ in the same q^2 bin, and $R_{K^*} = 0.66_{-0.07}^{+0.11} \pm 0.03$ for $q^2 \in [0.045, 1.1] \text{ GeV}^2$, both using Run-1 data only.² Furthermore, there are notable deviations between the SM prediction and the measurements of $BR(B_s \rightarrow \mu\mu)$ by LHCb & CMS,³ and (as of Moriond 2019) ATLAS,⁴ and in $B \rightarrow K^*\mu^+\mu^-$ angular observables such as P'_5 .^{5,6} This collection of discrepancies, which we shall henceforth refer to as the ‘neutral current B -anomalies’ (NCBAs), all point consistently towards a common new physics explanation in which LFU is violated, favouring (for example) a reduction in the effective coupling of the left-handed $b\bar{s}$ current to muons.⁷ The absence of similar anomalies in semileptonic decays of lighter mesons, such as kaons, pions, or charm-mesons, hints that whatever new physics underlies the NCBAs couples primarily to the third-family quarks. Taking this hint seriously, we here outline a simple model in which a heavy Z' boson is coupled to the third family.

2 Third family Z' models

Let us suppose that the NCBAs are mediated by a heavy Z' boson, deriving from a spontaneously broken $U(1)'$ gauge symmetry by which we extend the SM, under which only the third family will be charged in the weak eigenbasis. In addition to the Z' , we require a scalar which is charged only under $U(1)'$, responsible for breaking $U(1)'$ at the TeV scale. In the spirit of bottom-up

model building, we shall not introduce any further fields beyond those of the SM. We nonetheless need additional input to constrain the third family charges.

When building such a low-energy effective field theory (EFT), it is prudent to insist on gauge anomaly cancellation. This avoids the complication of including appropriate Wess-Zumino (WZ) terms to cancel anomalies in an otherwise anomalous low-energy EFT. Moreover, even if a specific set of anomalies can be cancelled by new UV physics, such as a set of heavy chiral fermions, it will be difficult to give these chiral fermions heavy enough masses in a consistent framework. Thus, we shall require that our charge assignment is anomaly-free.

2.1 Anomaly cancellation in $SM \times U(1)'$ theories

The space of anomaly-free $SM \times U(1)'$ theories has been explored in detail recently.⁸ The interest in such flavoured Z' models goes beyond the NCBA's; for example, in modelling dark matter⁹ or fermion masses.¹⁰ Thus, before we define our third family Z' model, we shall briefly discuss anomaly cancellation in Z' model building more generally.

Given only the chiral fermions of the SM, there are fifteen rational $U(1)'$ charges F_{X_i} to assign in a $SM \times U(1)'$ theory, where $X \in \{Q, L, e, u, d\}$, and $i \in \{1, 2, 3\}$ labels the family. After rescaling the gauge coupling, anomaly cancellation implies a system of Diophantine equations over fifteen integer variables. These equations are non-linear, due to the $U(1)_Y \times U(1)'^2$ and $U(1)'^3$ anomalies, which makes parametrizing its solution space a challenging arithmetic problem. Nonetheless, if we restrict to just two families of the SM, we can parametrize all solutions analytically using Diophantine methods.⁸ To wit, the sums of charges $F_{X_+} \equiv F_{X_1} + F_{X_2}$ must be proportional to hypercharge, *viz.* $F_{u_+} = 4F_{Q_+}$, $F_{d_+} = -2F_{Q_+}$, $F_{e_+} = -6F_{Q_+}$, and $F_{L_+} = -3F_{Q_+}$, where $F_{Q_+} \in \mathbb{Z}$, and the differences of charges $F_{X_-} \equiv F_{X_1} - F_{X_2}$ are fixed by the quadratic equation $F_{Q_-}^2 + F_{d_-}^2 + F_{e_-}^2 - F_{L_-}^2 - 2F_{u_-}^2 = 0$. All integer solutions to this equation are parametrized by four positive integers $\{a, a_e, a_d, a_u\}$, explicitly $F_{Q_-} = a^2 - a_d^2 - a_e^2 + 2a_u^2$, $F_{L_-} = a^2 + a_d^2 + a_e^2 - 2a_u^2$, $F_{d_-} = 2aa_d$, $F_{e_-} = 2aa_e$, and $F_{u_-} = 2aa_u$.

In the full three-family SM, we find a vast ‘atlas’ of anomaly-free $SM \times U(1)'$ theories,⁸ some small fraction of which have been explored in the literature,^a by finding all solutions with integer charges of magnitude up to some pre-defined maximum Q_{\max} using a numerical scan. We find that, for example with $Q_{\max} = 6$, there are more than 10^5 inequivalent (up to rescalings and permuting families) charge assignments if three right-handed neutrinos are included. On the other side of the coin, anomaly cancellation is a stringent constraint on $U(1)'$ charges; with $Q_{\max} = 6$, including right-handed neutrinos, only about one in every billion possible charge assignments happens to be anomaly-free. This unexplored solution space only opens up in the full three-family SM. We now return to the special case with only the third family charged under $U(1)'$. It turns out that in this case, there is a unique anomaly-free charge assignment, and that is simply hypercharge.

2.2 Third Family Hypercharge Model and the heaviness of the third family

In the Third Family Hypercharge Model (TFHM),¹² the charges of the third family fields in the weak eigenbasis equal their hypercharges, with the first two families being uncharged under $U(1)'$. If we assign the Higgs a $U(1)'$ charge also equal to its hypercharge, then the only gauge invariant Yukawa couplings are those of the third family. In the spirit of EFT, we nonetheless expect a perturbation around this renormalizable Yukawa sector due to higher-dimension operators. While an explanation of the precise hierarchies observed in the quark and lepton masses, and in the mixing angles of the CKM and PMNS matrices, would require more detailed model building of the UV physics, the zeroth-order predictions of such a setup are that (i) the third family is hierarchically heavier than the first two, and (ii) quark mixing angles are small,^b thus

^aFor example, gauging $L_\mu - L_\tau$ has been extensively explored phenomenologically.¹¹

^bNote that lepton mixing is not expected to be small, because we have not specified a mass sector for neutrinos.

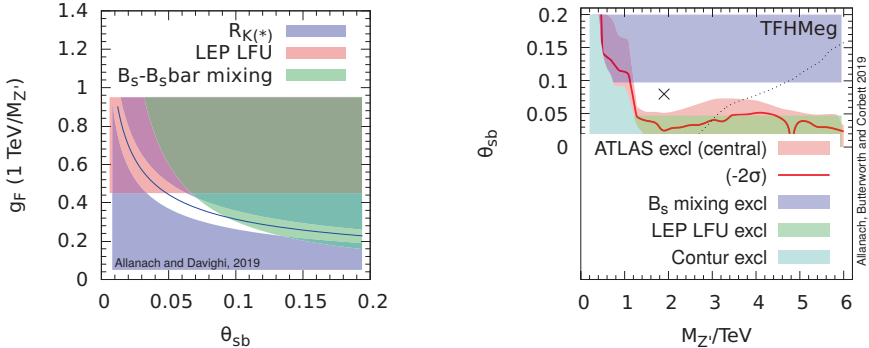


Figure 1 – Bounds on the TFHMeg; in both plots, the white region is allowed parameter space. Left - the bounds on $g_F/M_{Z'}$ versus θ_{sb} from fitting the (post Moriond 2019) NCBA’s (blue), including constraints from LEP LFU (red) and $B_s - \bar{B}_s$ mixing (green). Right - we also include the constraint from direct $Z' \rightarrow \mu\mu$ searches at the ATLAS, in the θ_{sb} vs. $M_{Z'}$ plane.¹³ Here, the value of the coupling g_F is fixed to the central value from the fit to the NCBA’s. Also, we include constraints from other LHC searches using the CONTUR tool (turquoise).^{13,14}

shedding light on the coarsest features of the SM flavour problem.

In order to compare the model with experimental bounds, one must specify the mixing between the mass and weak eigenbases. Consider the limiting case defined by the mixing matrices:

$$V_{dL} = \begin{pmatrix} 1 & 0 & 0 \\ 0 & \cos \theta_{sb} & -\sin \theta_{sb} \\ 0 & \sin \theta_{sb} & \cos \theta_{sb} \end{pmatrix}, \quad V_{eL} = \begin{pmatrix} 1 & 0 & 0 \\ 0 & 0 & 1 \\ 0 & 1 & 0 \end{pmatrix}, \quad (1)$$

together with $V_{uL} = V_{dL}V^\dagger$, $V_{uR} = V_{dR} = 1$, $V_{\nu L} = V_{eL}U^\dagger$, and $V_{eR} = 1$, where V is the CKM matrix and U is the PMNS matrix.^c We shall refer to this particular one-parameter (θ_{sb}) family of example cases of the Third Family Hypercharge Model as the ‘TFHMeg’.

3 Phenomenology of the TFHM example case

3.1 Constraints

The TFHMeg lagrangian contains the operators $g_{sb}\bar{s}\not{Z}'P_L b + g_{\mu\mu}\bar{\mu}\not{Z}'P_L\mu + H.c.$, where $g_{sb} = g_F(\sin 2\theta_{sb})/12$ and $g_{\mu\mu} = -g_F/2$, which, after integrating out the Z' , generate effective operators that can provide a good fit to the NCBA’s. Using the post-Moriond 2019 global fit to the NCBA data,⁷ the bound on the TFHMeg is $g_F = (M_{Z'}/36 \text{ TeV})\sqrt{24x/\sin(2\theta_{sb})}$, where $x = 1.06 \pm 0.16$, at the 95% CL.¹³

The other important constraints on this model are threefold. Firstly, the g_{sb} coupling of the Z' leads to a tree-level contribution to $B_s - \bar{B}_s$ mixing, which is loop-suppressed in the SM. While there are a number of different calculations, the most recent constraint, which incorporates lattice data and sum rules¹⁵ with experimental measurements,¹⁶ yields the bound $|g_{sb}| \leq M_{Z'}/(194 \text{ TeV})$.¹³ Secondly, in this model there is mass-mixing between the Z and Z' , because the Higgs has $U(1)'$ charge. While this mixing is small, the resulting flavour-dependent couplings inherited by the Z boson are tightly constrained by LEP data. In particular, the LEP measurement of $R \equiv \Gamma(Z \rightarrow e^+e^-)/\Gamma(Z \rightarrow \mu^+\mu^-)$ results in the bound $g_F < M_{Z'}/(2.2 \text{ TeV})$, at the 95% CL.¹² Finally, there is a constraint coming from direct searches for the Z' at colliders, for example in the dimuon decay channel. This constraint is obtained by recasting the most recent $Z' \rightarrow \mu^+\mu^-$ search constraints from ATLAS,¹⁷ which uses 139 fb^{-1} of 13 TeV pp collisions at the LHC.¹³ These constraints leave a viable region of parameter space in the TFHMeg (Fig. 1).

^cNote that this choice of V_{eL} implies that the tauon Yukawa must in fact be suppressed relative to the naïve order one expectation. We will address this issue in a future work.

3.2 Predictions

In addition to direct $Z' \rightarrow \mu^+ \mu^-$ searches, there are other distinct predictions of the TFHMeg (and the TFHM in general). Firstly, the Z' decays predominantly to third family fermions, with the largest branching ratios to $t\bar{t}$ (42%) and $\tau^+ \tau^-$ (30%). Nevertheless, the bounds from dimuon searches (branching ratio of 8%) provide the strongest constraint at present.¹³ With the nominal integrated luminosity expected at the HL-LHC being 3000 fb^{-1} , we expect the parameter space of the TFHMeg to be fully covered by the HL-LHC.¹³ In addition to these exciting prospects from direct searches at the LHC, the TFHM also predicts rare top decays, $t \rightarrow Zu$ and $t \rightarrow Zc$, as a result of flavour-changing Z' couplings to up-type quarks and the $Z - Z'$ mixing.¹² The current constraints from LHC bounds on $BR(t \rightarrow u, c)$ are weak, but likely to become important in the HL-LHC. Finally, the TFHMeg predicts a deficit in $BR(B \rightarrow K^{(*)} \tau^+ \tau^-)$.¹² Advances in τ identification and measurements of, for example, the LFU-probing ratio $BR(B \rightarrow K \tau^+ \tau^-) / BR(B \rightarrow K e^+ e^-)$ are much anticipated at both LHCb and Belle II.

4 Conclusion

We have discussed the possibility that the NCBA might be mediated by a Z' boson coupled only to the third family in the weak eigenbasis, with charges set to hypercharge by anomaly cancellation. We saw how gauging third family hypercharge might explain the heaviness of the third family. Finally, such a model leads to a distinctive and testable phenomenology, with resonances predicted in top, bottom, and tauon pairs.

Acknowledgments

JD thanks his collaborators Ben Allanach and Scott Melville for their contributions to this work, and for their permission to present the figures used in this talk. JD is supported by The Cambridge Trust and by the STFC consolidated grant ST/P000681/1.

References

1. R. Aaij *et al.*, arXiv:1903.09252 (2019).
2. R. Aaij *et al.*, JHEP **1708**, 055 (2017).
3. V. Khachatryan *et al.*, Nature **522**, 68 (2015).
4. M. Aaboud *et al.*, JHEP **1904**, 098 (2019).
5. R. Aaij *et al.*, JHEP **1602**, 104 (2016).
6. V. Khachatryan *et al.*, Phys. Lett. B **753**, 424 (2016).
7. J. Aebischer, W. Altmannshofer, D. Guadagnoli, M. Reboud, P. Stangl, and D. M. Straub, arXiv:1903.10434 (2019).
8. B. C. Allanach, J. Davighi, and S. Melville, JHEP **1902**, 082 (2019).
9. W. Altmannshofer, S. Gori, S. Profumo, and F. S. Queiroz, JHEP **1612**, 106 (2016).
10. C. D. Froggatt and H. B. Nielsen, Nucl. Phys. B **147**, 277 (1979).
11. W. Altmannshofer and I. Yavin, Phys. Rev. D **92**, no. 7 075022 (2015).
12. B. C. Allanach and J. Davighi, JHEP **1812**, 075 (2018).
13. B. C. Allanach, J. M. Butterworth, and T. Corbett, arXiv:1904.10954 (2019).
14. J. M. Butterworth, D. Grellscheid, M. Krämer, B. Sarrazin, and D. Yallup, JHEP **1703**, 078 (2017).
15. D. King, A. Lenz, and T. Rauh, arXiv:1904.00940 (2019).
16. Y. Amhis *et al.*, Eur. Phys. J. C **77**, 895 (2017).
17. G. Aad *et al.*, arXiv:1903.06248 (2019).

Confronting B anomalies with low energy parity violation experiments

Abhishek M. Iyer

INFN Sezine di Napoli, Via Cintia, Complesso Monte Sant Angelo, 80126 Napoli Italia



Low energy precision experiments play an important role in constraining several new physics extensions to the SM. In this talk we explore correlations between solutions to the lepton flavour universality violations and low energy parity violation experiments. The correlation is facilitated by considering a minimal model with an additional heavy neutral vector (Z'). Assuming electron only solutions to the anomalies, we explore to what extent can they be accommodated after the imposition of parity violating data. The conclusion is characterized by different limiting behavior depending on the chirality of the lepton current. Such a synergy between the different low energy experiments could shed light on the underlying nature of the anomalies in the event of their confirmation.

1 Introduction

Lepton flavour universality violations in the semi-leptonic decays of B mesons constitute one of the strongest hints for BSM physics. The measurement of $R_K = 0.846_{-0.054-0.014}^{+0.06+0.016}$ signals a $\sim 2.5 \sigma$ deviation from the standard model (SM) prediction of $R_K^{SM} = 1.0003 \pm 0.0001$ ². The reported deviations in the measurement of these ratios can be understood in terms of additional contributions to the Wilson coefficients of the following effective operators:

$$\mathcal{H}_{eff} = -\frac{G_f \alpha}{\sqrt{2}\pi} V_{tb} V_{ts}^* \sum_i \mathcal{O}_{XY} C_{XY} \quad (1)$$

where $C_{XY} = C_{XY}^{SM} + C_{XY}^{NP}$ and where X, Y denote the chirality of the quark(lepton) current. Different patterns of solutions for the combination of Wilson coefficients (C_{XY}^l) are possible and may involve either electrons or muons or both. In this talk we consider the extreme possibility involving only the electron contribution and confront the solutions to the anomalies with the following two measurements: weak charge of the proton Q_W^p ³ and the Caesium atom (Q_W^{Cs})⁴. It receives contribution in the SM from the following axial-electron-vector-quark current current Lagrangian:

$$\mathcal{L}_{Q_W, Q_P} = \frac{\bar{e} \gamma_\mu \gamma_5 e}{2v^2} \sum_{q=u,d} C_{1q} \bar{q} \gamma^\mu q \quad (2)$$

where the tree-level expressions for C_{1q} are given as: $C_{1u} = -\frac{1}{2} + \frac{4}{3} \sin^2 \theta_W$, $C_{1d} = \frac{1}{2} - \frac{2}{3} \sin^2 \theta_W$. The SM values for C_{1q} are: $C_{1u}^{SM} = -0.1887 \pm 0.0022$ and $C_{1d}^{SM} = 0.3419 \pm 0.0025$. In terms

of C_{1q} , the expressions for the weak charge of the proton and Caesium atom then are given as: $Q_W^p = -2[2C_{1u} + C_{1d}]$ $Q_W^{Cs} = -2[55(2C_{1u} + C_{1d}) + 78(C_{1u} + 2C_{1d})]$. From independent measurements of Q_W^p of the proton³ and the Caesium atom (Q_{Cs}^p)⁴, the allowed ranges at 1σ are: $Q_W^p = 0.0719 \pm 0.0045$; $Q_W^{Cs} = -72.58(29)_{expt}(32)_{theory}$. Fig. 1 illustrates the simultaneous compatibility of both these measurements showing the 2σ ranges allowed by the measurement of weak charge of proton (gray) and Caesium (brown) in the $C_{1u} - C_{1d}$ plane.

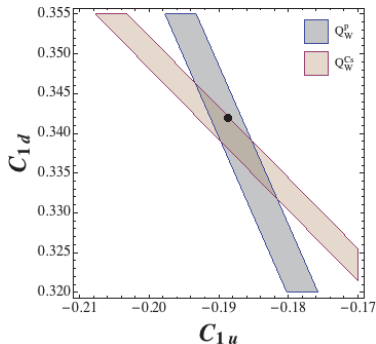


Figure 1 – Allowed regions in the $C_{1u}C_{1d}$ plane due to measurements of weak charge of proton (gray) and Caesium (brown). The central value in the SM is represented by the black point.

1.1 New Physics

The coefficients C_{1q} in Eq. 2 can receive corrections due to different extensions of the SM. To quantify this, we consider a generic NP contribution to Eq. 1 as:

$$\mathcal{L} = \frac{\bar{e}\gamma_\mu\gamma_5 e}{2v^2} \sum_{q=u,d} C_{1q}^{eff} \bar{q}\gamma^\mu q$$

where $C_{1q}^{eff} = C_{1q}^{SM} + C_{1q}^{NP}$ and correspondingly lead to corrections to Eq. 1. Similar to the SM, the C_{1q}^{NP} can be factored into the NP axial vector coupling to electrons (g_e^{AV}) and the vector coupling to light quarks (g_q^V)

2 Correlating B anomalies and low energy parity violation

While the anomalies correspond to a flavour changing observable, $Q_W^{Cs,p}$ is characterized by the flavour diagonal transition. Furthermore, the former predominantly involves third generation quarks ($b \rightarrow s$ transitions) while the latter corresponds to first generation vector quark currents. A priori there is no relation between the two sectors. To facilitate a correlation, we consider model with an additional heavy neutral vector and characterized by a flavour symmetry ($U(2)$). This correlation between the couplings g_q, g_e is then used to compute its effects on the C_{1q} which are determined at $q^2 = 0$. The most general Lagrangian, after electroweak symmetry breaking, responsible for $b \rightarrow s$ transitions in a Z' model can be parametrized as:

$$\begin{aligned} \mathcal{L} = & \frac{Z'^\mu}{2 \cos \theta_w} \left[g_e(g'_e)\bar{e}\gamma_\mu P_{L(R)}e + g_\mu(g'_\mu)\bar{\mu}\gamma_\mu P_{L(R)}\mu + \sum_q (g_q\bar{q}\gamma_\mu P_{Lq} + g'_q\bar{q}\gamma_\mu P_{Rq}) \right. \\ & \left. + (g_t - g_q)V_{ts}^* V_{tb}\bar{s}\gamma_\mu P_{L,R}b + \dots \right] \end{aligned} \quad (3)$$

Assuming the contribution to the Wilson coefficients due to the muon to be negligible, we set $g_\mu \lll g_e$ in Eq. 3. Fits involving only the electrons were considered in⁵ for different

Table 1: 2σ ranges used for the fits to Wilson coefficients in the case where only electron couples to New Physics.

	operator	Best fit	2σ	$\sqrt{\chi^2 - \chi_{SM}^2}$
Case A	$(\bar{s}_L\gamma^\mu b_L)(\bar{e}_L\gamma_\mu e_L)$	0.79	[0.29,1.29]	3.5
Case B	$(\bar{s}_L\gamma^\mu b_L)(\bar{e}_R\gamma_\mu e_R)$	-3.31	[-4.41,-2.21]	3.8
Case C	$(\bar{s}_R\gamma^\mu b_R)(\bar{e}_R\gamma_\mu e_R)$	-3.32	[-4.72,-1.92]	2.7

combinations of chirality of the quark and the lepton current. The best fit point and the corresponding 2σ ranges for the Wilson coefficients are given in Table 1.

Corresponding to Table 1 we discuss Case A and Case B below (Case C is similar to that of B and is discussed in⁶:

Case A $g'_e = 0$: In this case the right handed lepton current in Eq. 3 vanishes. Additionally, assuming a $U(3)$ symmetry in the coupling of the singlets to the Z' results in the absence of tree level FCNC for the down type singlets. Comparing Eq. 1 and Eq. 3 we can extract the Wilson coefficient C_{LL} contributing to $b \rightarrow sll$ and is given as:

$$C_{LL} = \frac{\sqrt{2}\pi g_e(g_t - g_q)}{4 \cos^2 \theta_W m_{Z'}^2 G_F \alpha} \quad (4)$$

In the first instance, we assume a $L \leftrightarrow R$ symmetry in the coupling of the first two generations, to Z' resulting in $g_V^q = g_q$. For the electron the axial vector coupling is simply $g_e^{AV} = g_e/2$. Using this, the coefficients C_{1q} get corrected with contributions proportional to g_V^q and g_e^{AV} as:

$$C_{1q}^{eff} = C_{1q}^{SM} + \frac{2v^2 g_e g_q}{8 \cos^2 \theta_W m_{Z'}^2} \quad (5)$$

The following ranges are chosen for the fermion couplings: $g_e \in [0.02, 2]$ $g_t \in [0.02, 2]$ $g_q \in [0.02, 2]$. Left plot of Fig. 2 gives the overlap of the region satisfying the anomaly (blue) superimposed on Fig. 1. The black point denotes the SM prediction. The length of the blue band satisfying the anomalies is determined by scanning the allowed ranges for the coupling parameters. Irrespective of the length, Fig. 2 illustrates that there exists only a marginal region common to fit involving Eq. 4 and the anomalies. The left plot of Fig.2 gives the change in the light quark coupling before and after the imposition of low energy parity violation data.

Case B $g_e = 0$: This corresponds to the case where the NP contribution to the Wilson coefficients is only due to the right handed electron (C_{LR}). The Wilson coefficient in this case is given as:

$$C_{LR} = \frac{\sqrt{2}\pi g'_e(g_t - g_q)}{4 \cos^2 \theta_W m_{Z'}^2 G_F \alpha} \quad (6)$$

Since only the right handed electron current couples to new physics, the corresponding axial vector current is simply $g_e^{AV} = -g'_e/2$. For the light quark case we first begin with the assumption of $L \leftrightarrow R$ symmetry: $g_q = g'_q$. In this case, the coefficients C_{1q} get corrected as

$$C_{1q} = C_{1q}^{SM} - \frac{2v^2 g'_e g_q}{8 \cos^2 \theta_W m_{Z'}^2} \quad (7)$$

The results are illustrated in the left plot of Fig. 3. Unlike Case A, the limiting case does not reduce to the SM. This is a consequence of the fact that for the solutions to the anomalies, the Wilson coefficients are negative implying $g_q > g_t$ and $g_q \rightarrow 0$ is not permitted. However, these solutions are not compatible with the constraints from low energy parity violation data. One possible solution is to break the $L \leftrightarrow R$ symmetry in the light quark coupling *i.e* $g_q \gg g'_q$,

resulting in the corrections to C_{1q} being reduced by a factor of 2: $C_{1q} = C_{1q}^{SM} - \frac{2v^2 g_e' g_q}{16 \cos^2 \theta_W m_{Z'}^2}$ and the corresponding results are shown in right plot of Fig. 3

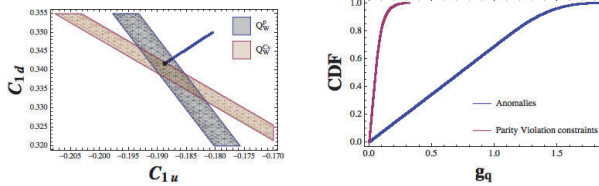


Figure 2 – Results with electron only fits for Case A. Left plot gives the projection on the $C_{1u} - C_{1d}$ plane, while the right plot represents the changes in the range for g_q . The blue (red) curve represents the CDF before (after) the imposition of parity violating constraints.

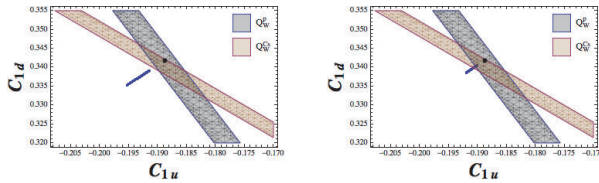


Figure 3 – Results with electron only fits for Case B. Left plot corresponds to the case $g_q = g'_q$ while the right corresponds to $g_q \gg g'_q$ i.e where $L \leftrightarrow R$ in the coupling of light quarks is no longer valid.

3 Conclusions

We discussed two possibilities of fits to the anomalies using only the electron contribution to the Wilson coefficients. The goodness of fits is not different between the two when only anomalies are taken into account. However, the difference in the chiral structure lead to drastically different limiting behaviour in the context of their corrections to the weak charges. Such complementarity between different measurements can have implications for direct searches⁶ in addition to throwing light on the nature of the solutions to the anomalies.

Acknowledgments

AI were supported in part by MIUR under Project No. 2015P5SBHT and by the INFN research initiative ENP. A.I. would also like to thank the organizers of Rencontres de Moriond QCD for the opportunity to present the work.

References

1. R. Aaij *et al.* [LHCb Collaboration], arXiv:1903.09252 [hep-ex].
2. C. Bobeth, G. Hiller and G. Piranishvili, JHEP **0712**, 040 (2007) doi:10.1088/1126-6708/2007/12/040 [arXiv:0709.4174 [hep-ph]].
3. D. Androi *et al.* [Qweak Collaboration], Nature **557**, no. 7704, 207 (2018). doi:10.1038/s41586-018-0096-0
4. V. A. Dzuba, J. C. Berengut, V. V. Flambaum and B. Roberts, Phys. Rev. Lett. **109**, 203003 (2012) doi:10.1103/PhysRevLett.109.203003 [arXiv:1207.5864 [hep-ph]].
5. G. D’Amico, M. Nardecchia, P. Panci, F. Sannino, A. Strumia, R. Torre and A. Urbano, JHEP **1709**, 010 (2017) doi:10.1007/JHEP09(2017)010 [arXiv:1704.05438 [hep-ph]].
6. G. D’Ambrosio, A. M. Iyer, F. Piccinini and A. D. Polosa, arXiv:1902.00893 [hep-ph].

2.3 Spectroscopy

XYZ particles at BESIII

R. Farinelli ^{a,1,2}, on behalf of BESIII collaboration

¹ INFN Sezione di Ferrara, I-44122, Ferrara, Italy

² University of Ferrara, I-44122, Ferrara, Italy

XYZ states are resonances connected to the charmonium and observed by many experiments. The abundance of discoveries of those particles and the accumulation of some properties determined a common pattern that is able to answer to some questions inherit to the XYZ nature. BESIII is exploring the energy region between 3.9 and 4.6 GeV/c² in order to collect more information about the composition of those resonances and to identify the theoretical papers matching the experimental observations. In this proceeding, recent results on the measurements of the line-shape of $e^+e^- \rightarrow \gamma(\pi^+\pi^- J/\psi)$ and $e^+e^- \rightarrow \gamma(\omega J/\psi)$ which address a connection between X and Y states will be presented. An abundance of Z will be reported beside the preliminary measurement of $Z_c \rightarrow \rho\eta_c$ and the rejection of two possible models. Finally the present BESIII data above the $e^+e^- \rightarrow \Lambda_c \bar{\Lambda}_c$ will be discussed because they are connected to the Y(4660), a candidate charmed baryonium state.

1 Introduction

Elementary particles such as quarks and leptons are the constituent pieces of the nature. The strong interaction is one of the four fundamental forces and it bounds quarks together into *hadrons* following the rules given by Quantum-Chromo-Dynamics (QCD). Today only certain combinations are known and well defined: *baryons*, bound states with three quarks, and *mesons* with a quark and anti-quark. Different bound states are not forbidden by QCD and physicists are looking for new kinds of structures that bound together quarks. In the 10s two discoveries of interest have to be reported: the $Z_c(3900)$ ¹ discovered by BESIII and the P_c^+ ² discovered by LHCb. These states have been claimed as possible tetraquark (Z_c) and pentaquark (P_c^+).

The Z_c showed connection to the charmonium, an heavy meson built up a charm and anti-charm quark. The potential model describes the bound state and it can predict its mass and mean life as a function of the quantum number, *e.g.* η_c , ψ and χ_c mesons. Charmonium masses range from less than 3 GeV/c² to above 4.4 GeV/c². The production threshold of the $D\bar{D}$ at 3.74 GeV/c² is a value of interest for the potential model. Below it the charmonium masses predicted and the measured ones agree while above the $D\bar{D}$ threshold many expected states have not been discovered but many unexpected others have been seen³.

These unpredicted states are connected to the charmonium but they do not fit the potential model. The first unconventional state is the $X(3872)$ ⁴ discovered by Belle in the invariant mass spectrum of $J/\psi\pi^+\pi^-$. Its nature is clearly exotic due to its width smaller than 1.2 MeV and isospin-violating decays^{5,6}. An abundance of vector states connected to the charmonium has been observed, first of all the $Y(4260)$ ⁷ by BaBar collaboration in 2005. Later in 2013 BESIII reported the first evidence of a new kind of bound state, the $Z(3900)$ ¹, that decays in charmonium and a charged pion.

^aCorresponding author email: rfarinelli@fe.infn.it

Many other resonances were discovered in the past years and a common pattern is showing up: many states have been observed to decay in charged and neutral mode then they have been grouped under the label “Z states”; similarly to the vectorial resonances as “Y states”. Everything leftover is a “X state”. All of them show connection to the charmed mesons but moreover a connection between them has been reported and discussed in this proceeding.

2 BESIII experiment

The Beijing Spectrometer (BESIII)⁸ is an experiment of high energy physics built around the interaction point of the Beijing Electron Positron Collider (BEPCII)⁹. The leptonic beams can interact at an energy in the center of mass between 2 and 4.6 GeV and guarantee a low background environment and a precise measurement of the collision energy. The spectrometer has a cylindrical shape on the barrel and two end-caps. A main drift chamber (MDC) surrounds the beam pipe and performs tracking reconstruction and dE/dx measurements. Particle identification is given by the MDC together with a time of flight detector. An electromagnetic calorimeter measures the photon energy above 20 MeV with crystals of CsI(Tl). The geometrical coverage is 93 % of the solid angle.

3 Heavy X state

X(3872) is a resonance with quantum numbers $J^{PC} = 1^{++}$ observed for the first time in the B decays by Belle⁴. It has a width smaller than 1.2 MeV, its mass is consistent with the $D^0\bar{D}^{0*}$ threshold and it has isospin-violating decays since it decays to both $\rho J/\psi$ ⁵ and $\omega J/\psi$ ⁶. No isospin partner is known. BESIII can produce this resonance through radiative decay such as $e^+e^- \rightarrow \gamma(\pi^+\pi^- J/\psi)$ ¹⁰ and $e^+e^- \rightarrow \gamma(\omega J/\psi)$ ¹¹. These are measures of interest to explain the nature of this bound state. A cross section smaller than few pb has been reported in both decay channels and a simultaneous fit has been performed with a Breit-Wigner as shown in Fig. 1. A resonance with a mass of $4200_{13.3}^{+7.9} \pm 3.0$ MeV/ c^2 and width $115_{26}^{+38} \pm 12$ MeV can describe the lineshape of the two cross sections. This suggests a possible connection like $e^+e^- \rightarrow R \rightarrow \gamma X$, where R could be a Y state or $\psi(4140)$.

The hunting for the X(3872) has been extended to the $e^+e^- \rightarrow \pi^0\eta_{cJ}$ channel. The measurement has been proposed¹² to understand if it is a conventional $c\bar{c}$ state or not. The transition has been observed with more than 5σ significance in the mode J=1. No observations have been observed for J=0,2. Being $\Gamma(X(3872) \rightarrow \pi^0\chi_{c1}) > 0.06$ keV then the pure $c\bar{c}$ interpretation is disfavored¹³.

Another channel used to discern the possible explanation about this state is $e^+e^- \rightarrow D\bar{D}$. If X(3872) was a $D\bar{D}^*$ molecule then a X(4013) state would be expected as heavy quark spin-

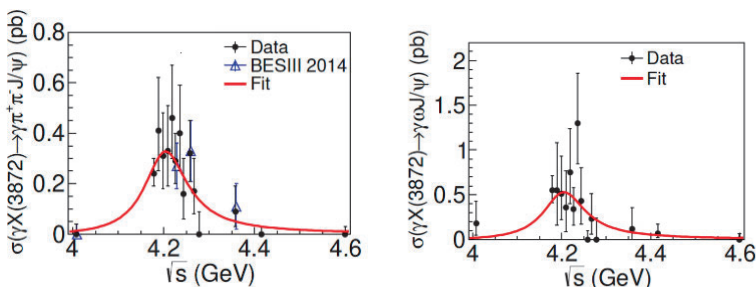


Figure 1 – Cross section lineshape from the two processes: $e^+e^- \rightarrow \gamma(\pi^+\pi^- J/\psi)$ on the left and $e^+e^- \rightarrow \gamma(\omega J/\psi)$ on the right.

symmetry partner with $J^{PC} = 2^{++}$. The $X(4013)$, if it exists, would decay dominantly in $D\bar{D}$. No observation has been reported by BESIII¹⁴.

4 Charmed Z states

A new field of research has been opened by BESIII after the discovery of the $Z(3900)$. The resonance has been observed in the decay channel $e^+e^- \rightarrow (J/\psi\pi^+)\pi^-$ and since it decays in charmonium plus a charged pion it should contain at least four quarks. The resonance has been confirmed by Cleo-c and Belle. In 2015 a resonance with a compatible mass and width and same quantum numbers has been observed in the neutral channel mode $e^+e^- \rightarrow (J/\psi\pi^0)\pi^0$ ¹⁵, this established the isospin triplet for this state. Moreover many other decay modes have been reported and they accumulate around two points, labelled $Z_c(3900)$ and $Z'_c(4020)$. The Z_c and Z'_c decay in pion plus a charmonium state as: J/ψ , h_c and $\psi(2S)$ ^{16,17,18,19}. Moreover decays into D mesons have been observed^{21,22}. A summary is presented in Table. Each channel has been observed both in charged and neutral mode.

Particle	$I^G J^{PC}$	Mass [MeV]	Width [MeV]	Production and Decay
$Z(3900)$	$1^+ 1^{+-}$	3886.6 ± 2.4	28.1 ± 2.6	$\pi J/\psi$ $D\bar{D}^*$
$Z(4020)$	$1^+ ?^{2-}$	4024.1 ± 1.9	13 ± 5	$\pi\psi$ πh_c $D^*\bar{D}^*$

Another decay mode is under study by BESIII: $e^+e^- \rightarrow \pi^0\rho\eta_c$. The hunting for Z_c and Z'_c into $\rho\eta_c$ has been performed at 5 different energy values. No clear signal has been reported for Z'_c among all the points. The measurement is important to define the Z_c composition. Looking at the ratio $R = Br(Z_c \rightarrow \rho\eta_c)/Br(Z_c \rightarrow \pi J/\psi)$ BESIII would be able to discern between the dynamical tetraquark model and the molecular state assumption²³. A preliminary measurement of R returns a value not compatible for both theories.

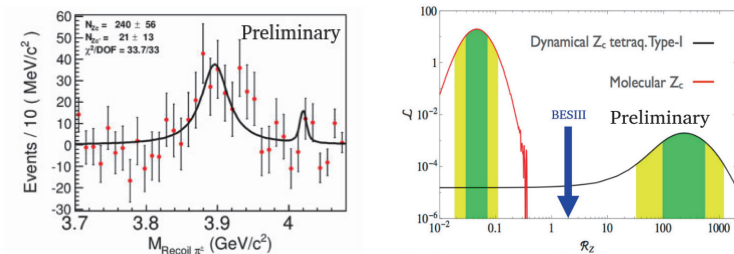


Figure 2 – Recoil mass of the π^0 in the process $e^+e^- \rightarrow \pi^0\rho\eta_c$ on the left, on the right the BESIII measurement of the ratio $R = Br(Z_c \rightarrow \rho\eta_c)/Br(Z_c \rightarrow \pi J/\psi)$ with respect to the theoretical value evaluated by A. Esposito defined in bibliography.

5 Vector Y states

Charmonium vector states above the $D\bar{D}$ threshold decay mainly in $D\bar{D}$ while the $Y(4260)$ observed by BaBar⁷ decays also into charmonium. The resonance has been confirmed by Belle²⁴ and BESIII²⁵. After the $Y(4260)$ many others have been discovered such $Y(4360)$ and $Y(4660)$. BESIII used its large statistic collected in this energy range to study the $Y(4260)$ and to resolve the strange lineshape in the $\pi^+\pi^-J/\psi$ invariant mass that BaBar was not able to describe properly. Two different resonances with masses of about 4220 and 4360 GeV/c^2

has been discovered instead of the single peak description. To support this discovery BESIII studied other decay channels: $e^+e^- \rightarrow \pi^+\pi^-\psi(2S)$, $e^+e^- \rightarrow \pi^+\pi^-h_c$, $e^+e^- \rightarrow \pi^+D^0\bar{D}^{*-}$ and $e^+e^- \rightarrow \omega\chi_{c0}$ ^{26,27,28,29}. Each one of those decay channels shows two resonances in the energy range between 4.2 and 4.4 GeV. The current studies fit the two resonances with two Breit-Wigner without any interference term. This affects the mass and width precision. The latest measurement to be reported is the observation of the Y(4220) in $e^+e^- \rightarrow \omega\chi_{c0}$. The values reported are in agreement with the other measurements as reported in Fig. 3. Despite the fact that the resonances Y(4220) and Y(4360) have been determined, a partial wave analysis is still needed for a more precise measurement of their properties. No evidence about their nature has been reported but it is interesting to notice the connection of the other two kinds of particles with this one: a radiative decay seems to connect the X(3872) to the Y(4220) while a pionic decay defines the transitions from the vector states in this region to the Z_c and Z'_c .

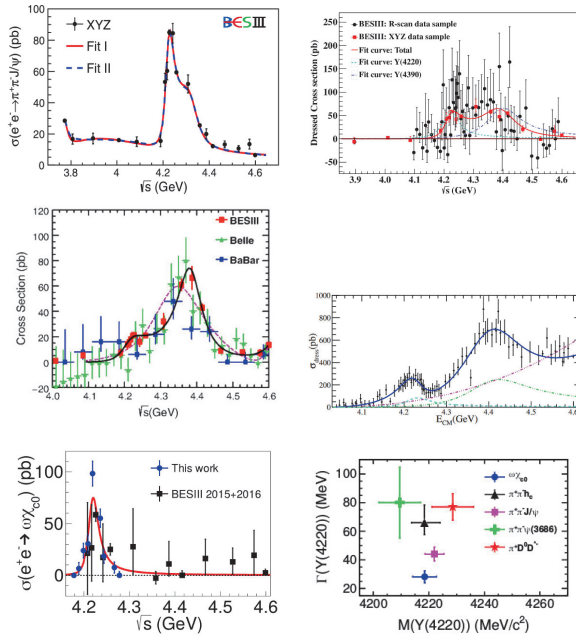


Figure 3 – Cross section lineshape for the processes e^+e^- going to $\pi^+\pi^-J/\psi$ (top left), $\pi^+\pi^-h_c$ (top right), $\pi^+\pi^-\psi(2S)$ (middle left), $\pi^+D^0\bar{D}^{*-}$ (middle right) and $\omega\chi_{c0}$ (bottom left). On the bottom right the values of mass and width of the Y(4220) as a function of the decay channel is shown.

A totally different behavior has been observed in the Y(4660) resonance. This particle has been seen by Belle²⁴ and BaBar³⁰ in the decay channel $e^+e^- \rightarrow \pi^+\pi^-\psi(2S)$ but unseen in $e^+e^- \rightarrow \pi^+\pi^-J/\psi$ while this would be expected to show a strong evidence for the Y(4660), if it was a $c\bar{c}$ state. A compatible resonance has been observed in the invariant mass spectrum of $\Lambda_c\bar{\Lambda}_c$ by Belle³¹. BESIII can not measure the entire cross section lineshape due to energy limitation but up to now the results show a slightly different trend³² as shown in Fig 4. This resonance is interesting to understand the nature of the Y(4660) and possibly any connection to the other vector state. The cross section at peak in the baryonic decay is 10 times larger than the mesonic case and this supports the thesis of the Y(4660) as a hidden-charmed baryonium, as described by Rossi-Veneziano-Chew paradigm^{33,34}. BESIII is planning to increase the beam energy in order to study this resonance and its nature.

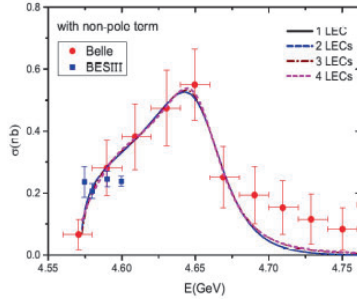


Figure 4 – Cross section lineshape of $e^+e^- \rightarrow \Lambda_c \bar{\Lambda}_c$.

6 Conclusion

A large set of resonances connected to the charmonium has been observed by the BESIII experiment. Many measures have been performed to shed light on their nature: from the narrow $X(3872)$ to the tetra-quark candidate Z_c , both connected to the Y states and to the charmonium. The cross section of two different radiative decays from $J^{PC}=1^{--}$ to $X(3872)$ has been measured and they suggest a connection to the $Y(4220)$. The seen decay $X(3872) \rightarrow \pi^0 \chi_{c1}$ and the unseen $X(4013) \rightarrow D\bar{D}^*$ reject the hypothesis of the $X(3872)$ as a $c\bar{c}$ state and a DD molecule assumption. Concerning the Z_c and Z'_c , many decay modes show their connection to charmonium and open charm meson. The measurements in the decay channel $Z_c \rightarrow \rho\eta_c$ do not confirm the dynamic tetra-quark assumption, neither the molecule one. Two resonances have been measured in five different decay channels with similar mass values and quantum numbers but different widths labelled as $Y(4220)$ and $Y(4360)$. A more puzzling behavior has been observed for the $Y(4660)$.

References

1. M. Ablikim *et al.*, [BESIII Collaboration] Phys. Rev. Lett. **110**, 252001 (2013)
2. R. Aaij *et al.*, [LHCb Collaboration] Phys. Rev. Lett. **115**, 072001 (2015)
3. R. F. Lebed *et al.*, Nucl. Phys. **93**, 143-194 (2017)
4. S. K. Choi *et al.*, [Belle Collaboration] Phys. Rev. Lett. **91**, 262001 (2003)
5. S. K. Choi *et al.*, Phys. Rev. **D 84**, 052004 (2011)
6. P. del Amo Sanchez *et al.*, [BaBar Collaboration] Phys. Rev. **D 82**, 011101 (2010)
7. B. Aubert *et al.*, [BaBar Collaboration] Phys. Rev. Lett. **95**, 142001 (2005)
8. M. Ablikim *et al.*, [BESIII Collaboration] Nucl. Instr. A **614**, Issue 3 (2010)
9. C. Zhang, G.X. Pei for BEPCII Team, Proc. of 2005 Particle Accelerator Conference, Knoxville, Tennessee 131-135 (2005)
10. M. Ablikim *et al.*, [BESIII Collaboration] Phys. Rev. Lett. **112**, 092001 (2014)
11. M. Ablikim *et al.*, [BESIII Collaboration] arXiv:1903.04695 (2019) - Submitted PRL
12. S. Dubynskiy, Phys. Rev. **D 77**, 014013 (2008)
13. M. Ablikim *et al.*, [BESIII Collaboration] arXiv:1901.03992 (2019) - Submitted PRL
14. M. Ablikim *et al.*, [BESIII Collaboration] arXiv:1903.08126 (2019) - Submitted PRD
15. M. Ablikim *et al.*, [BESIII Collaboration] Phys. Rev. Lett. **115**, 112003 (2015)
16. M. Ablikim *et al.*, [BESIII Collaboration] Phys. Rev. Lett. **111**, 242001 (2013)
17. M. Ablikim *et al.*, [BESIII Collaboration] Phys. Rev. Lett. **97**, 052001 (2018)
18. M. Ablikim *et al.*, [BESIII Collaboration] Phys. Rev. Lett. **96**, 032004 (2017)
19. M. Ablikim *et al.*, [BESIII Collaboration] Phys. Rev. Lett. **97**, 052001 (2018)

20. M. Ablikim *et al.*, [BESIII Collaboration] Phys. Rev. Lett. **115**, 222002 (2015)
21. M. Ablikim *et al.*, [BESIII Collaboration] Phys. Rev. Lett. **112**, 132001 (2013)
22. M. Ablikim *et al.*, [BESIII Collaboration] Phys. Rev. Lett. **115**, 182002 (2015)
23. A. Esposito, Phys. Rev. Lett. **746**, 194 (2015)
24. G. Pakhlova *et al.*, [Belle Collaboration] Phys. Rev. D **91**, 112007 (2015)
25. M. Ablikim *et al.*, [BESIII Collaboration] Phys. Rev. Lett. **118**, 092001 (2017)
26. M. Ablikim *et al.*, [BESIII Collaboration] Phys. Rev. Lett. **118**, 092002 (2017)
27. M. Ablikim *et al.*, [BESIII Collaboration] Phys. Rev. Lett. **96**, 032004 (2017)
28. M. Ablikim *et al.*, [BESIII Collaboration] Phys. Rev. Lett. **122**, 102002 (2019)
29. M. Ablikim *et al.*, [BESIII Collaboration] Phys. Rev. Lett. **112**, 092001 (2015)
30. B. Aubert *et al.*, [BaBar Collaboration] Phys. Rev. D **86**, 051102 (R) (2012)
31. G. Pakhlova *et al.*, [Belle Collaboration] Phys. Rev. Lett. **101**, 172001 (2008)
32. M. Ablikim *et al.*, [BESIII Collaboration] Phys. Rev. Lett. **120**, 132001 (2018)
33. G. C. Rossi and G. Veneziano, Nucl. Phys. B **123**, 507 (1977)
34. G. F. Chew, Nucl. Phys. B **79**, 365 (1974)

Baryon Number Fluctuation of Preconfinement Clusters and Transverse Momentum Dependence of Bottom Baryon Production

LI Shi-Yuan

Institute of Theoretical Physics, Shandong University, Jinan, 250100, P.R. China



We point out the existence and make the investigation of the baryon number fluctuation of the preconfinement colour-singlet clusters, which are constructed at the end of the QCD evolution from the hard interaction in the high energy collisions. This fluctuation is one of the aspects of the baryon production mechanism in strong interaction. It leads to, e.g., the transverse momentum dependence of the baryon over meson ratio, since it is enhanced by the number of and suppressed by the average mass of the clusters. The cluster mass, within the non-Abelian gauge theory QCD, is much smaller than the initial large hard scale. Here we take bottom baryon production as an example for the study.

In high energy strong interactions, especially those with hard subprocess(es), e.g., production of the hard jet, heavy quark, quark gluon matter with high temperature and/or density, etc., the basic coloured quanta, quarks and gluons, explicitly play the key rôle. However, these coloured partons have to be confined into the colour singlet (colourless) hadrons at last. This 'blanching' process in QCD is complex. The hard part of this blanching process can be described by the perturbative QCD evolution^{1,2,3}, until to the end, which is named as preconfinement by Amati and Veneziano forty years ago⁴. This preconfinement constructs colour-singlet clusters, each of which transfers into several hadrons. The latter soft process is described by various hadronization models^{5,6,7}. According to Amati and Veneziano⁴, it is the non-Abelian gauge theory, QCD, which dictates that the average mass of the color-singlet clusters, Q_0 , though could be significantly larger than the lightest hadron mass m_π , is much smaller than the large initial hard scale Q . So Q_0 can be considered as the characteristic scale which separating the hard and soft interactions in QCD. The concept of local parton hadron duality (see,⁸ and ref. therein) is the result of the formation of the preconfinement cluster and its characteristic scale Q_0 , hence the corresponding phenomenology is the evidence of it. All these are consistent with the characteristics of the nonperturbative QCD — no large momentum transfer. If we adopt such a physical picture, the global property in momentum space can be fixed. Once we introduce the infrared safe quantities, they can be calculated by perturbative QCD (see, e.g,⁹). A perturbative QCD based parton shower model can give the momentum space configuration of the preconfinement clusters or other corresponding structure (such as in Phythia¹⁰). But things like the distribution and fluctuation of the colour structure and other U(1) quantum numbers (global symmetries of QCD) like baryon number,

strangeness, etc., are yet not possible to be determined by perturbative QCD. So these details of the interface between the hard and soft QCD are necessary information for the study of the hadron productions, as input for any practical hadronization models.

Another of the subtleties is that the above perturbative QCD investigation on preconfinement is in the large N_c limit. In this limit or approximation, the preconfinement structure can get more definiteness. However, it can not describe the whole story of the real world. One of the simple examples is the existence of baryon. Since its wave function with explicit colour degree of freedom is $\sum_{i_1 i_2 \dots i_{N_c}} \epsilon_{i_1 i_2 \dots i_{N_c}} q^{i_1} q^{i_2} \dots q^{i_{N_c}}$. This means that when N_c is very large, the baryon can not exist, *SINCE the very preconfinement scale Q_0 can not be very large, and valence quark is massive*. For the real world $N_c = 3$, the baryon production is in general suppressed comparing to meson, seemingly demonstrating that the Chinese ancient wisdom that three means many really works. But one immediately finds that the colour structure becomes complex. Among all of the uncertainties of the preconfinement structure, the colour structure is the most widely studied. Rich evidences on the colour structure beyond the large N_c approximation have been obtained ^{11,12,13,14,15,16,17}. Moreover, in the consideration of colour structure, sometimes named alternatively colour 're-connection, some certain cases can enhance the possibility of the production of baryon, such as string/cluster junction (see, e.g.,¹⁸) and special colour connection¹⁷ that the cluster must have a non zero baryon number. In principle, the 'standard Lund' popcorn and diquark mechanism can also be considered as colour fluctuation.

However, here we would like to emphasize:

1) In general, these above baryon production/enhancement considerations are assigned *within* the preconfinement cluster. Until now, one has not yet made any general investigation on the question what about the baryon number of the preconfinement cluster, is it fixed to be zero or can be of some non zero integer (to be colour singlet)? If it could be non zero, what is the distribution of such value?

2) Some crucial experimental results related with baryon production can not be understood from the traditional models which take the baryon number of preconfinement cluster to be exactly zero.

So in this paper we want to initialize such an investigation. It of course can shed light on the confinement dynamics and nonperturbative QCD. Furthermore, the preconfinement scale Q_0 puts a natural cutoff for multi-quark states. The study of baryon number distribution leads to more detailed information on the clusters hence helpful for the multi-quark state production mechanism complementary to the unitarity consideration (see my 2011, 2017 moriond talks and refs. therein).

Let's first see one possible example that will lead to preconfinement clusters with non zero baryon number. For the case of heavy quark with considerable momentum, as well as the light quark produced from the hard scattering, it is *not* distributed together with the corresponding anti-particle partner in production *locally in momentum space*, e.g., quark antiquark pair produced from a heavy short-lived particle decay are back to back and in the two extremes in momentum space in the center of mass frame (Here we emphasize all the discussions in the whole paper are in momentum space, not referring to the coordinate one. So the discussions are all quantum, not semiclassical). On the other hand, the preconfinement cluster mass must be moderate, so that the hard quark and anti quark are with large probability *not* in the same colour singlet cluster. At the same time, quark carries baryon number, which is of course the origin of any baryon number. It is these kind of *hard* baryonic partons who can make the cluster not neutral in baryon number (Other U(1) quantum number fluctuation can be analyzed in the similar way). The baryon number fluctuation of the clusters is thus enhanced. This is never considered before, by whatsoever the case 'colour-neutral flow', 'colour rearrangement' or 'colour separate states', to directly study the baryon number fluctuation of the preconfinement clusters and its phenomenology consequent relating with baryon production. Here we take the heavy quarks to study, because they can be predicted by perturbative calculation, and can be tracked for its behaviour afterward in the constructing of the preconfinement cluster and even hadronization. Moreover the mass of the heavy quark can affect the value of Q_0 , which will be discussed following.

The above examples make clear that the expanding on the range/scale of the momentum space by the coloured baryonic partons to much larger than that of the pre-confinement scale Q_0 , is one of the key points of the baryon number fluctuation. A more complex case is the quark gluon plasma production, though it may not happen through hard scattering. The Bjorken expansion of the system gives the large range of the QGP parton momentum space. So in the case of QGP, the baryon number fluctuation of clusters can happen at the time of freeze out.

As a matter of fact, the corresponding phenomenology in heavy ion collision is one breakthrough for the study of baryon production mechanism, though it is long and well known that the baryon production is an ambiguity. In RHIC it is observed that the baryon over meson ratio is transverse momentum dependent and can be significantly enhanced at intermediate transverse momentum, contrary to the prediction of the fragmentation function. Soon these data are explained by combination models in various versions. Combination models can naturally give the baryon. It just combines quark and antiquark to get meson while combining three quarks to get baryon. However, one must introduce a combination rule/function to tune the production rate of the baryon. Furthermore, with the recognition of multi-quark states, one encounters the challenge for the production of the exotic particles in combination models, since a unitarity constraint exists.

Even ignoring these problems, one is still in doubt about why the fragmentation function becomes non-universal. Since there is no large momentum transfer for the non-perturbative/confinement phase, hence the dynamical process must happen locally in the momentum space, likely pre-confinement structure should emerge. But the clusters from QGP can be different from those from e^+e^- annihilation (where the fragmentation function is obtained) on the baryon number fluctuation. In e^+e^- annihilation evolution, the development of the parton shower leads to very tiny baryon number fluctuation. However, the fluctuation will be large because of underlying events, rescattering, finite temperature effects etc. These explain the tension. The difference between the in-jet clusters and underlying event clusters has been investigated, and got solid results. See talk by Livio Bianchi in this proceeding.

The key fact of the combination models is in fact try to make a 'better'/'advanced' arrangement on the quarks for the favour of producing baryons *when the quark number is large*. However, anytime one encounters a large bulk (momentum space!) of partons so that inevitably their whole mass and energy corresponding to a large $Q \gg Q_0$, one will have to deal with the question of the pre-confinement cluster formation and the fluctuation of the clusters.

From the above introduction of the pre-confinement clusters and the phenomenology requirements on the cluster baryon number fluctuation, especially its dependence on transverse momentum, we here list the qualitative/semi-quantitative property for this fluctuation:

* The pre-confined singlet cluster can form with baryon number = 0, 1, 2...(integers). * So one may address that the production mechanisms of baryons are mainly two folds: One is the 'fluctuation' (popcorn/diquark, special combination way, etc.) *within* the pre-confined cluster; the other is the pure baryon number of the cluster because of the fluctuation when the cluster is constructed, and the baryon number conservation forces it transferring into hadrons under strong interaction (rather, all kinds of SM interactions respect this conservation).

* By the above consideration, one can deduce the conjecture that $\langle |B| \rangle$ (expected value of the colour singlet bulk of quarks and gluons) increases with the cluster number N for a certain local bulk of momentum space. but it must reach a limit because of the Q_0 , and mass of 1 baryon number $\geq m_{proton}$ seen from the hadron level. Thus one can say that this saturation is typical of the QCD theory (Amati and Veneziano). However, it could be that the average mass of the cluster takes different values, especially when there is bottom quark, $Q(b)_0 > Q(c, s, u, d)_0$ since bottom quark is much more heavy. It could probe different ranges of scales during the hadronization.

For the experimental aspect, the saturation has been observed for the light quark and charm sectors by comparing the data from LHC and RHIC respectively. The average number of clusters is proportional to the average number of quarks, while the latter can be deduced from the multiplicity. However, since the b sector may have a larger Q_b , it seems that the saturation has not yet been reached. First of all, one sees from data that the baryon over meson ratio for the bottom sector, the larger

the lower transverse momentum, since the lower the transverse momentum, the more number of quarks and hence more clusters. One also sees that this value increase with collision energy, since the higher the collision energy, the more number of quarks (multiplicity). So it is necessary to measure the case for even larger number of quarks hence clusters. The good opportunity is to do the measurement in the heavy ion collisions of the highest available energy at LHC. A prediction by the scaling of multiplicity has been made. We see that two data sets corresponding different multiplicity can be re-scaled and consistent, so we can employ the similar scaling to predict. See Figure 1.

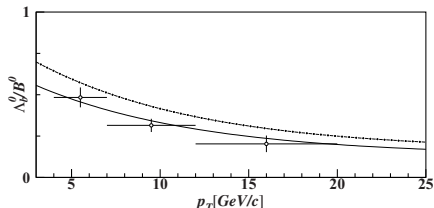


Figure 1 – The solid line is a parametrization and rescaling by multiplicity on the pp collision and the data dots are for pA collision^{20,19}, respectively. The dash-dotted line are prediction for AA collision by the scaling of the multiplicity.

Acknowledgments

This work is in Collaboration with Y. Jin, Z.G.Si, T. Yao and F.S. Yu, and is supported by National Natural Science Foundation of China (grant Nos. 11635009, 11775130) and the Natural Science Foundation of Shandong Province (grant No. ZR2017MA002)

References

1. G. Altarelli and G. Parisi, Nucl. Phys. B **126** (1977) 298.
2. Y. L. Dokshitzer, Sov. Phys. JETP **46** (1977) 641.
3. V. N. Gribov and L. N. Lipatov, Sov. J. Nucl. Phys. **15** (1972) 438.
4. D. Amati and G. Veneziano, Phys. Lett. **83B** (1979) 87.
5. T. Sjostrand, Int. J. Mod. Phys. A **3**, 751 (1988).
6. G. Marchesini and B. R. Webber, Nucl. Phys. B **238**, 1 (1984); B. R. Webber, Nucl. Phys. B **238**, 492 (1984).
7. Y. Jin, Z. Si, Q. Xie and T. Yao, Sci. China Phys. Mech. Astron., **53**, 1998 (2010) , and refs. therein.
8. Y. L. Dokshitzer, V. A. Khoze and S. I. Troian, J. Phys. G **17** (1991) 1585.
9. K. Konishi, A. Ukawa and G. Veneziano, Phys. Lett. B **78** (1978) 243; *ibid.* B **80** (1979) 259.
10. T. Sjöstrand *et al.*, Comp. Phys. Commun., **135**, 238 (2001).
11. G. Gustafson, Z. Phys. C **15** (1982) 155.
12. T. Sjostrand and V. A. Khoze, Z. Phys. C **62** (1994) 281.
13. S. Gieseke, C. Rohr and A. Siodmok, Eur. Phys. J. C **72** (2012) 2225.
14. S. y. Li, F. I. Shao, Q. b. Xie and Q. Wang, Phys. Rev. D **65**, 077503 (2002).
15. Z. G. Si, Q. Wang and Q. B. Xie, Phys. Lett. B **401**, 107 (1997).
16. W. Han, S. -Y. Li, Z. -G. Si and Z. -J. Yang, Phys. Lett. B **642**, 62 (2006).
17. Y. Jin, S. -Y. Li, Z. -G. Si, Z. -J. Yang and T. Yao, Phys. Lett. B **727**, 468 (2013).
18. S. Gieseke, P. Kirchgaer and S. Platzer, Eur. Phys. J. C **78** (2018) no.2, 99.
19. R. Aaij *et al.* [LHCb Collaboration], Phys. Rev. D **99**, no. 5, 052011 (2019).
20. R. Aaij *et al.* [LHCb Collaboration], arXiv:1902.06794 [hep-ex].

HADRON SPECTROSCOPY AND EXOTIC STATES AT LHCb

Tomasz Skwarnicki
on behalf of the LHCb collaboration

Department of Physics, Syracuse University,
Syracuse, NY 13244, USA



Three analyses of the combined Run 1 and Run 2 proton-proton collisions data set collected with the LHCb detector are presented. A new narrow charmonium state is observed in decays to $D\bar{D}$. Two excited B_c^+ states are observed in $\pi^+\pi^-$ transitions to the lighter B_c^+ states, confirming the CMS results. New narrow pentaquarks states decaying to $J/\psi p$ are discovered and reported at this conference for the first time.

1 Near-threshold $D\bar{D}$ Spectroscopy (LHCb-PAPER-2019-005)

Thanks to its ability to trigger on purely hadronic final states, the LHCb experiment accumulated a large samples of the inclusively reconstructed $D^0\bar{D}^0 \rightarrow (K^-\pi^+)(K^+\pi^-)$ and $D^+D^- \rightarrow (K^-\pi^+\pi^+)(K^+\pi^-\pi^-)$ pairs¹. Their invariant mass distributions (Fig. 1) reveal a peaking structure near the $D^0\bar{D}^0$ threshold, dominated by the feeddown from $X(3872) \rightarrow D^0\bar{D}^{*0}$ decays, the $\psi(3770)$ and $\chi_{c2}(3930)$ states (observed in prompt hadroproduction for the first time, predominantly 1^3D_1 and 2^3P_2 excitations of the $c\bar{c}$ system), and a new narrow, $\Gamma = 2.79 \pm 0.51 \pm 0.35$ MeV, state at $3842.71 \pm 0.16 \pm 0.12$ MeV. The latter fits the expectations for the 1^3D_3 charmonium state, for which the small width is expected from the angular momentum

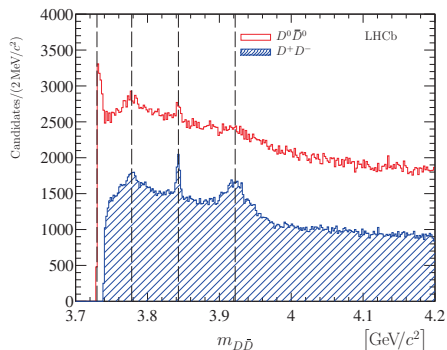


Figure 1 – The mass spectra for selected $D\bar{D}$ combinations from Ref. 1. The open red histogram corresponds to $D^0\bar{D}^0$ pairs, while the hatched blue histogram corresponds to D^+D^- pairs. Vertical black dashed lines help to identify the peaks from (left to right) partially reconstructed $X(3872) \rightarrow D^0\bar{D}^{*0}$ decay, $\psi(3770)$, $X(3842)$ and $\chi_{c2}(3930)$ decays to $D\bar{D}$.

barrier and phase-space suppression². The measurements of the mass ($3921.90 \pm 0.55 \pm 0.19$ MeV) and width ($36.64 \pm 1.88 \pm 0.85$ MeV) of the $\chi_{c2}(3930)$ state are improved over the previous determinations^{3,4}. It is interesting to see that while the mass of the 1^3D_3 state was predicted by the relativized potential model with about 6 MeV accuracy, the mass of the 2^3P_2 state was overestimated by about 52 MeV by the same model². This likely reflects an impact of the couplings to the decay channels, neglected in such calculations, which are more important for wider states.

2 Excited B_c^+ States (LHCb-PAPER-2019-007)

Decays of the B_c^+ (1^1S_0 $b\bar{c}$ state) to $J/\psi\pi^+$, with $J/\psi \rightarrow \mu^+\mu^-$, are easier to trigger on at the LHC. When combined with the $\pi^+\pi^-$ pairs stemming from the pp collision point, the $B_c^+\pi^+\pi^-$ mass distribution observed by the LHCb⁵ exhibits two peaks (Fig. 2), which fit the mass expectations for the radially excited triplet (2^3S_1) and singlet (2^1S_0) states, emitting $\pi^+\pi^-$ pair in transitions to the corresponding 1^3S_1 and 1^1S_0 states (the photon from the subsequent $1^3S_1 \rightarrow \gamma 1^1S_0$ transition is undetected). These results confirm the recent analysis by the CMS Collaboration⁶. The ATLAS Collaboration earlier observed the $B_c^+\pi^+\pi^-$ mass structure in this region, but did not resolve the two peaks⁷.

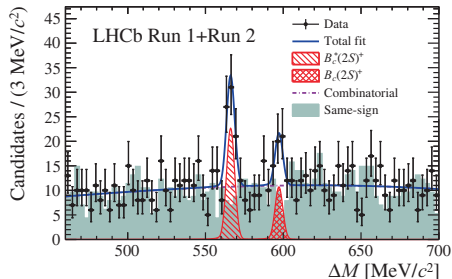


Figure 2 – Distribution of $\Delta M = m_{B_c^+\pi^+\pi^-} - m_{B_c^+}$ with the fit results overlaid. See Ref.5 for more detailed description.

3 Pentaquark P_c^+ States (LHCb-PAPER-2019-014)

From an analysis of Run 1 data, the LHCb collaboration reported significant $J/\psi p$ structures in $A_b^0 \rightarrow J/\psi p K^-$ decays⁸. The exotic character of these structures, with the minimal quark content of $uudc\bar{c}$, was demonstrated in a nearly model-independent way in Ref.9, where it was shown that the $J/\psi p$ structure near 4450 MeV was too narrow to be accounted for by $\Lambda^* \rightarrow p K^-$ reflections (Λ^* denotes a generic Λ excitation), reinforcing the results from the earlier model-dependent six-dimensional amplitude analysis of invariant masses and decay angles describing the A_b^0 decay in the same data⁸, in which the $P_c(4450)^+$ structure was determined to peak at $4449.8 \pm 1.7 \pm 2.5$ MeV, have a width of $39 \pm 5 \pm 19$ MeV and a fit fraction of $(4.1 \pm 0.5 \pm 1.1)\%$. Even though not apparent from the $m_{J/\psi p}$ distribution, the amplitude analysis also required a second broad $J/\psi p$ state to obtain a good description of the data, which peaks at $4380 \pm 8 \pm 29$ MeV with a width of $205 \pm 18 \pm 86$ MeV and a fit fraction of $(8.4 \pm 0.7 \pm 4.2)\%$.

The two leading interpretations of these structures were either tightly or loosely-bound pentaquarks states. In the tightly-bound model all quarks are confined in the same volume, likely with a diaquark, or even triquark (i.e. diaquark-antiquark) substructures. The main challenge for this model was to explain the narrowness of the $P_c(4450)^+$ structure, given that its mass is about 400 MeV above the threshold for the decay to $J/\psi p$. It was hypothesized that the c and \bar{c} are spatially separated by the P -wave angular momentum barrier between the diaquark and the antiquark, suppressing the fast desintegration of the state¹⁰. The lower mass $P_c(4380)^+$ would be an S -wave state, thus much broader. This model predicts existence of a large number of excitations of such quark system, corresponding to various radial, angular momentum and quark spin configurations in the confining color potential.

In the loosely-bound model quarks are subdivided into two confining volumes, corresponding

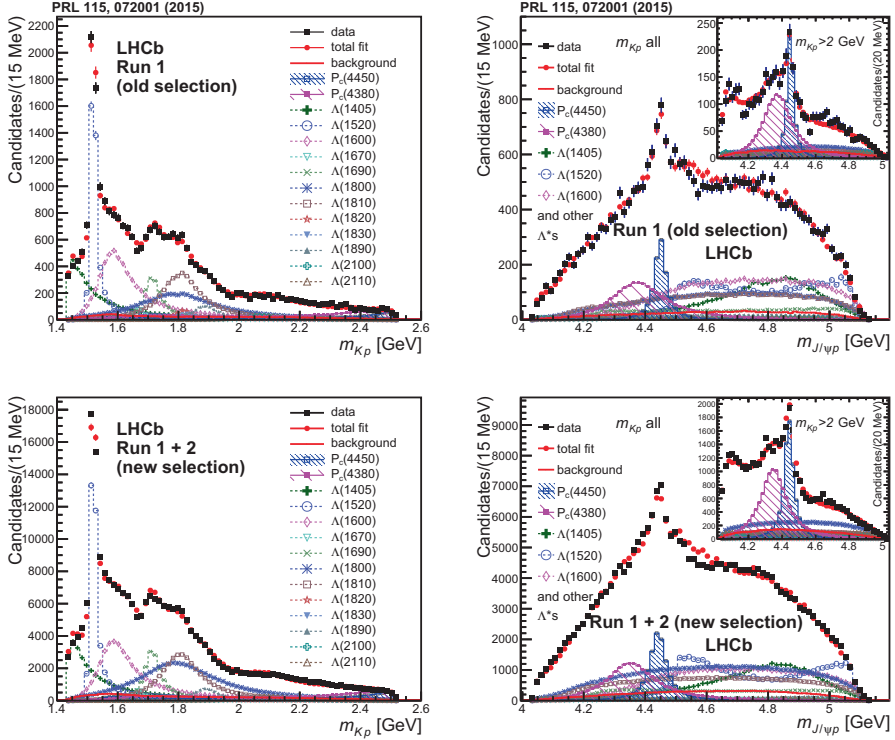


Figure 3 – Distributions of (left column) m_{Kp} and (right column) $m_{J/\psi p}$, together with the projections of the six-dimensional amplitude model [the nominal “reduced” cFit model], (top row) taken from Ref.8 and (bottom row) fit to the new $\Lambda_b^0 \rightarrow J/\psi p K^-$ sample. The plots illustrate consistency of the old and new Λ_b^0 data samples.

to a baryon and a meson, bound together by interactions similar to thus between nucleons in nuclei. With the c and \bar{c} spatially separated into a baryon and a meson, such states are expected to be narrow. The mass of $P_c(4450)^+$ was only about 10 MeV below the $\Sigma_c^+ \bar{D}^{*0}$ mass threshold - a plausible binding energy for such interactions^{11,12,13}. The wide $P_c(4380)^+$ state does not find a natural explanation in such “molecular” model. Bound by a shallow nuclear potential well, no radial or angular momentum excitations are expected between the baryon and the meson. Thus, very few states are expected in loosely-bound models, corresponding to a limited ways the spins of the constituent hadrons can be added.

The mass of the $P_c(4450)^+$ coincided with the $\chi_{c1} p$ mass threshold. While no attractive forces between such hadron pair are expected⁴, this coincidence fueled the suggestions that this structure could come from the triangle diagram process¹⁵, in which Λ_b^0 decays weakly to χ_{c1} and an excited Λ state, which quickly desintegrates into K^- and p . The latter rescatters with χ_{c1} to $J/\psi p$. Such processes are expected to peak at the rescattering threshold.

At this conference, we present for the first time the analysis of the combined Run 1 and Run 2 data set of 246,000 $\Lambda_b^0 \rightarrow J/\psi p K^-$ decays¹⁶. This is a nine-fold increase over the number of Λ_b^0 decays reconstructed in the previous Run 1 analyses^{8,9}. Improvements in the data selection yielded a factor of 2 increase, while keeping non- Λ_b^0 background small (6.4% of the analyzed sample). The increase in the integrated luminosity gave a factor of 3 increase, and the rest came from the increased Λ_b^0 production cross-section due to the higher pp collision energies in Run 2 (13 TeV vs. 7-8 TeV). When the same six-dimensional amplitude model as used previously is fit to the masses and decay angles, the new data sample gives the $P_c(4450)^+$ and $P_c(4380)^+$

Table 1: Summary of P_c^+ properties. The central values are based on the fit displayed in Fig. 5.

State	M [MeV]	Γ [MeV]	(95% CL)	\mathcal{R} [%]
$P_c(4312)^+$	$4311.9 \pm 0.7_{-0.6}^{+6.8}$	$9.8 \pm 2.7_{-4.5}^{+3.7}$	(< 27)	$0.30 \pm 0.07_{-0.09}^{+0.34}$
$P_c(4440)^+$	$4440.3 \pm 1.3_{-4.7}^{+4.1}$	$20.6 \pm 4.9_{-10.1}^{+8.7}$	(< 49)	$1.11 \pm 0.33_{-0.10}^{+0.22}$
$P_c(4457)^+$	$4457.3 \pm 0.6_{-1.7}^{+4.1}$	$6.4 \pm 2.0_{-1.9}^{+5.7}$	(< 20)	$0.53 \pm 0.16_{-0.13}^{+0.15}$

parameters consistent with the previous results, as illustrated in Fig. 3. However, this should be considered only as a cross check, since analysis of this much larger data sample reveals additional peaking structures in the $J/\psi p$ mass spectrum, which are too small to have been significant before. A narrow peak is observed near 4312 MeV with a width comparable to the mass resolution (Figs. 4-5). The structure at 4450 MeV is now resolved into two narrow peaks at 4440 and 4457 MeV.

Performing a rigorous amplitude analysis of this new data sample is computationally challenging. Fortunately, the newly observed peaks are so narrow that it is not necessary to construct an amplitude model to prove that these states are not artifacts of interfering Λ^* resonances⁹. We perform one-dimensional fits to $m_{J/\psi p}$ distributions to characterize the narrow peaks. Such analysis is not sensitive to any broad $J/\psi p$ contributions like $P_c(4380)^+$. We fit three narrow Breit-Wigner (BW) resonances, smeared with the mass resolution which is about 2 – 3 MeV (RMS) in the relevant mass range, plus high-order polynomial to represent any other contributions, predominantly from the Λ^* reflections. Alternatively, we use low-order polynomial plus a broad P_c^+ state as the background parameterization. The two approaches give similar fit qualities (Fig. 4). To account for the systematic uncertainties we also fit three different $m_{J/\psi p}$ distribution: inclusive, after the $m_{Kp} > 1.9$ GeV requirement to suppress the Λ^* reflections, and optimally weighted sample to enhance the narrow P_c^+ contributions over the backgrounds. The event weights are dependent on $\cos\theta_{P_c}$, which is correlated with the m_{Kp} values (θ_{P_c} is the P_c^+ helicity angle). In the nominal approach we add the BW contributions incoherently. Possible interferences are allowed when exploring the systematic uncertainties. The results for the masses (M), widths (Γ) and relative production rates (\mathcal{R}) are given in Table 1.

The fit chosen for the central mass and width values is displayed in Fig. 5. The $P_c(4312)^+$ state peaks right below the $\Sigma_c^+ \bar{D}^0$ threshold and has statistical significance over 7.6σ . The significance of the two-peak versus one-peak hypothesis for the 4450 MeV structure is over 5.4σ , rendering the single peak interpretation of this region obsolete. The $P_c(4457)^+$ state peaks right below the $\Sigma_c^+ \bar{D}^{*0}$ threshold. The mass coincidence with the two, rather than one, related thresholds, as well as the very narrow widths of these states,

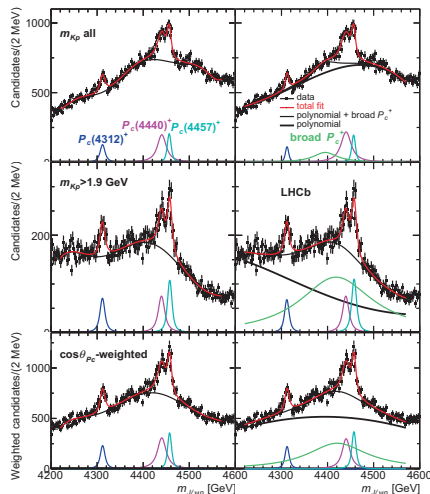


Figure 4 – Fits to the $m_{J/\psi p}$ distributions of the (top row) inclusive, (middle row) $m_{Kp} > 1.9$ GeV, and (bottom row) $\cos\theta_{P_c}$ -weighted samples¹⁶ with three incoherently summed BW amplitudes representing the narrow P_c^+ signals on top of a (left column) high-order polynomial function or (right column) lower-order polynomial plus a broad P_c^+ state represented by a fourth BW amplitude.

favor the loosely-bound pentaquark model. Given how close these peaks are to the thresholds, they might be virtual rather than bound states of these baryon-meson combinations. Since the spins of Σ_c^+ and of \bar{D}^{*0} can be combined in two different ways, the third narrow $P_c(4440)^+$ peak, which is about 20 MeV below the $\Sigma_c^+ \bar{D}^{*0}$ threshold, also finds the natural explanation in this model^{2,11,17,18}, which was studied well before the first LHCb results on this subject¹⁶. Since a pion cannot be exchanged in the $\Sigma_c^+ \bar{D}^0$ bound state³, the existence of the $P_c(4312)^+$ state points to the importance of exchange of vector mesons (ρ, ω) in binding hadrons, if the “molecular” interpretation is correct. This calls for more sensitive searches for, so far undetected, $D\bar{D}$ and $B\bar{B}$ states. Good candidates for $D\bar{D}^*$, $D^* \bar{D}^*$ and $B\bar{B}^*$, $B^* \bar{B}^*$ states have been known for a while (see e.g. Refs.19,20).

It would be premature to consider the loosely-bound model to be firmly established. This model comes with the definite predictions for the spin and parity (J^P) of the observed states ($1/2^-$ for $P_c(4312)^+$, $1/2^-$ and $3/2^-$ for $P_c(4440)^+$ and $P_c(4457)^+$, in either order), which must be verified by the data. The present analysis is insensitive to the J^P values. The full six-dimensional amplitude analysis is in progress. This model also predicts isospin partners and other decay modes. Related $\Sigma_c^{*+} \bar{D}$ and $\Sigma_c^{*+} \bar{D}^*$ states, decaying to $J/\psi p$, are also expected (they may be wider due to the larger Σ_c^{*+} width²¹).

The tightly bound models now face additional challenges. If the higher mass states are P -states and the $P_c(4312)^+$ is an S -state, why is it so narrow? One would need a different type of potential barrier between diquarks than the centrifugal one²². Rather precise alignment of the P_c^+ masses with the baryon-meson thresholds is unlikely to be random, though some mechanisms for synchronisation of quark structures with “molecular” thresholds have been suggested before^{23,24,25,26,27}. If there is a change in the orbital angular momentum between the quarks in the $P_c(4312)^+$ structure and the two higher mass states, this necessarily implies the change of parity, in contrast with the loosely-bound model. Thus, J^P determinations are very important. Even if the narrow states are loosely-bound systems, this does not exclude a possibility of many, perhaps broad, tightly-bound pentaquark structures in the same $m_{J/\psi p}$ mass spectrum. It should be noted that the amplitude analyses of the B decays to a charmonium and $\pi^+ K^-$ produced a number of broad $Z_c^+ \rightarrow (c\bar{c})\pi^+$ tetraquark candidates, which do not find a good explanation in loosely-bound models^{19,20}. Probing for broad P_c^+ contributions is among the goals of the ongoing full amplitude analysis of the $\Lambda_b^0 \rightarrow J/\psi p K^-$ decays.

Can the observed narrow P_c^+ states be due to the triangle diagram processes? Such processes cannot produce peaking below the corresponding rescattering thresholds, thus triangles involving rescattering of $\Sigma_c^+ \bar{D}^{(*)0}$ can be ruled out. The explicit fit of triangle diagram model to the LHCb data with an exchange of excited D_s^- (Λ), followed by $\Lambda_c^+ \bar{D}^{*0}$ ($\chi_{c0} D$) rescattering to $J/\psi p$ fails to account for the $P_c(4312)^+$ ($P_c(4440)^+$) peaks when a realistic width of the exchanged particle is assumed (see the left-bottom plot in Fig. 6). The $P_c(4457)^+$ is in more favorable situation to be explained by the triangle diagram with an exchange of an excited D_s^- followed by the $\Lambda_c^+ \bar{D}^{*0}$ rescattering, since it peaks right at such threshold, rather than above it. However, the triangle

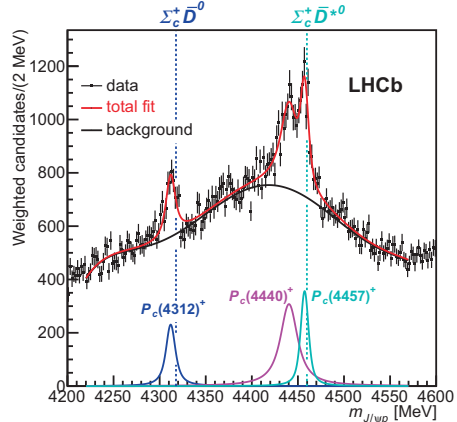


Figure 5 – Fit to the $\cos\theta_{P_c}$ -weighted $m_{J/\psi p}$ distribution with three BW amplitudes and a sixth-order polynomial background. This fit is used to determine the central values of the masses and widths of the P_c^+ states. The mass thresholds for the $\Sigma_c^+ \bar{D}^0$ and $\Sigma_c^+ \bar{D}^{*0}$ final states are superimposed.

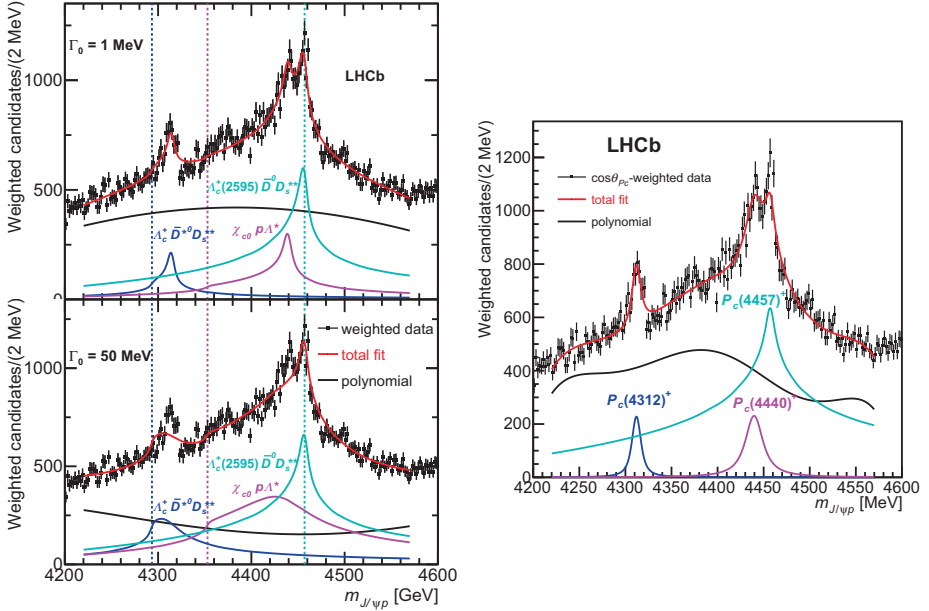


Figure 6 – (left) Fit of three triangle-diagram amplitudes and a quadratic background to the $\cos\theta_{P_c}$ -weighted distribution. The widths of the excited particles exchanged in the triangles is (top) an unrealistic value of 1 MeV or (bottom) a more plausible value of 50 MeV. Individual triangle diagram contributions are also shown. The dashed vertical lines are the $\Lambda_c^+ \bar{D}^{*0}$, $\chi_{c0} p$ and $\Lambda_c^+ (2595) \bar{D}^0$ thresholds. (right) Fit of two BW amplitudes, one triangle-diagram amplitude, and a sixth-order polynomial background to the $\cos\theta_{P_c}$ -weighted distribution. The width of the excited D_s^- state exchanged in the triangle loop is set to $\Gamma(D_{s1}(2860)^-) = 159$ MeV^{21,28}. The predicted width for this state, interpreted as the 1^3D_1 $s\bar{c}$ excitation in the quark model, is 197 MeV²⁹.

diagram model does not fit the $P_c(4457)^+$ peak as well as the BW model when the measured width of the $D_{s1}(2860)^-$ is assumed (the right plot in Fig. 6). More detailed discussion of these fits can be found in the Supplementary Material to Ref.16.

4 Summary

The first analyses of the combined Run 1 and Run 2 LHCb data have yielded interesting, some even astonishing, results:

- The observation of a very narrow $X(3842)$ state decaying to $D\bar{D}$, likely spin-3 1^3D_3 excitation of the $c\bar{c}$ system.
- In addition, the $\psi(3770)$ and $\chi_{c2}(3930)$ states have been observed in prompt hadroproduction for the first time.
- The two B_c^+ excitations, likely 2^1S_0 and 2^3S_1 states of $b\bar{c}$ system, are confirmed.
- The observation of the three narrow pentaquark states, $P_c(4312)^+$, $P_c(4440)^+$ and $P_c(4457)^+$, shedding more light into the nature of the $J/\psi p$ structures in $\Lambda_b^0 \rightarrow J/\psi p K^-$ decays. Their proximity to the $\Sigma_c^+ \bar{D}^0$ and $\Sigma_c^+ \bar{D}^{*0}$ thresholds suggests that these thresholds play an important role in the dynamics of these states.

The LHCb detector is now being replaced by its upgraded version to accumulate even much larger data samples over the next decade.

References

1. R. Aaij et al. Near-threshold $D\bar{D}$ spectroscopy and observation of a new charmonium state. 2019. arXiv:1903.12240, submitted to JHEP.
2. T. Barnes, S. Godfrey, and E. S. Swanson. Higher charmonia. *Phys. Rev.*, D72:054026, 2005.
3. S. Uehara et al. Observation of a χ'_{c2} candidate in $\gamma\gamma \rightarrow D\bar{D}$ production at Belle. *Phys. Rev. Lett.*, 96:082003, 2006.
4. B. Aubert et al. Observation of the $\chi_{c2}(2P)$ meson in the reaction $\gamma\gamma \rightarrow D\bar{D}$ at BaBar. *Phys. Rev.*, D81:092003, 2010.
5. R. Aaij et al. Observation of an excited B_c^+ state. 2019. arXiv:1904.00081, submitted to Phys. Rev. Lett.
6. A. M. Sirunyan et al. Observation of two excited B_c^+ states and measurement of the $B_c^+(2S)$ mass in pp collisions at $\sqrt{s} = 13$ TeV. *Phys. Rev. Lett.*, 122(13):132001, 2019.
7. G. Aad et al. Observation of an excited B_c^\pm meson state with the ATLAS Detector. *Phys. Rev. Lett.*, 113(21):212004, 2014.
8. R. Aaij et al. Observation of $J/\psi p$ resonances consistent with pentaquark states in $\Lambda_b^0 \rightarrow J/\psi p K^-$ decays. *Phys. Rev. Lett.*, 115:072001, 2015.
9. R. Aaij et al. Model-independent evidence for $J/\psi p$ contributions to $\Lambda_b^0 \rightarrow J/\psi p K^-$ decays. *Phys. Rev. Lett.*, 117:082002, 2016.
10. L. Maiani, A. D. Polosa, and V. Riquer. The new pentaquarks in the diquark model. *Phys. Lett.*, B749:289–291, 2015.
11. W. L. Wang, F. Huang, Z. Y. Zhang, and B. S. Zou. $\Sigma_c \bar{D}$ and $\Lambda_c^+ \bar{D}$ states in a chiral quark model. *Phys. Rev.*, C84:015203, 2011.
12. Jia-Jun Wu, R. Molina, E. Oset, and B. S. Zou. Prediction of narrow N^* and Λ^* resonances with hidden charm above 4 GeV. *Phys. Rev. Lett.*, 105:232001, 2010.
13. M. Karliner and J. L. Rosner. New exotic meson and baryon resonances from doubly-heavy hadronic molecules. *Phys. Rev. Lett.*, 115(12):122001, 2015.
14. T. J. Burns. Phenomenology of $P_c(4380)^+$, $P_c(4450)^+$ and related states. *Eur. Phys. J.*, A51(11):152, 2015.
15. F.-K. Guo, Ulf-G. Meißner, W. Wang, and Z. Yang. How to reveal the exotic nature of the $P_c(4450)$. *Phys. Rev.*, D92(7):071502, 2015.
16. R. Aaij et al. Observation of a narrow $P_c(4312)^+$ state and of two-peak structure of the $P_c(4450)^+$. 2019. arXiv:1904.03947, accepted by Phys. Rev. Lett.
17. Zhong-Cheng Yang, Zhi-Feng Sun, Jun He, Xiang Liu, and Shi-Lin Zhu. Possible hidden-charm molecular baryons composed of anti-charmed meson and charmed baryon. *Chin. Phys.*, C36:6–13, 2012.
18. Jia-Jun Wu, T. S. H. Lee, and B. S. Zou. Nucleon resonances with hidden charm in coupled-channel models. *Phys. Rev.*, C85:044002, 2012.
19. S. L. Olsen, T. Skwarnicki, and D. Zieminska. Nonstandard heavy mesons and baryons: Experimental evidence. *Rev. Mod. Phys.*, 90(1):015003, 2018.
20. M. Karliner, J. L. Rosner, and T. Skwarnicki. Multiquark states. *Ann. Rev. Nucl. Part. Sci.*, 68:17–44, 2018.
21. M. Tanabashi et al. Review of particle physics. *Phys. Rev.*, D98(3):030001, 2018.
22. L. Maiani, A. D. Polosa, and V. Riquer. A theory of X and Z multi-quark resonances. *Phys. Lett.*, B778:247–251, 2018.
23. D. V. Bugg. How resonances can synchronise with thresholds. *J. Phys.*, G35:075005, 2008.
24. A. P. Szczepaniak. Triangle singularities and XYZ quarkonium peaks. *Phys. Lett.*, B747:410–416, 2015.
25. S. H. Blitz and R. F. Lebed. Tetraquark cusp effects from diquark pair production. *Phys. Rev.*, D91(9):094025, 2015.

26. F. K. Guo, C. Hanhart, Yu. S. Kalashnikova, P. Matuschek, R. V. Mizuk, A. V. Nefediev, Q. Wang, and J. L. Wynen. Interplay of quark and meson degrees of freedom in near-threshold states: A practical parametrization for line shapes. *Phys. Rev.*, D93(7):074031, 2016.
27. A. Pilloni, C. Fernandez-Ramirez, A. Jackura, V. Mathieu, M. Mikhasenko, J. Nys, and A. P. Szczepaniak. Amplitude analysis and the nature of the $Z_c(3900)$. *Phys. Lett.*, B772:200–209, 2017.
28. R. Aaij et al. Observation of overlapping spin-1 and spin-3 $\bar{D}^0 K^-$ resonances at mass $2.86 \text{ GeV}/c^2$. *Phys. Rev. Lett.*, 113:162001, 2014.
29. S. Godfrey and K.h Moats. Properties of excited charm and charm-strange mesons. *Phys. Rev.*, D93(3):034035, 2016.

2.4 New Phenomena

CMS Search Highlights

S. BEUCERON

on behalf of the CMS Collaboration

*Institut de Physique Nucléaire de Lyon, 4 rue Enrico Fermi,
69622 Villeurbanne Cedex, France*

The most recent results of CMS¹ in term of searches are presented. The focus is given to searches with added interpretation and analysis improvements.

1 Introduction

CMS has between 20 to 30 new results on searches depending on what we define as searches since January. Only a few results are highlighted here. Five results of CMS on searches are using the total run 2 statistics so far, only one of them is presented below, the others are covered by other speakers over the conference. The selected results have either an added theory interpretation or a significant analysis improvement.

2 Enriched understanding

In this section, the analyses described below present either new interpretation, improved description of the signal/background or better defined categorisation for searches.

2.1 Search for heavy fermions or light (-pseudo) scalar

The search is an extension of a type III seesaw mechanism which was produced with 2016 data² and which is extended here with the run 2 dataset adding also an interpretation in terms of light (-pseudo) scalar³. The search for heavy fermions is performed in the flavour democratic scenario looking at pair production. The heavy fermions decay either via a $W + \text{neutrino}$, via $Z + \text{lepton}$ or via $H + \text{neutrino}$. In the case of the search of light (-pseudo) scalar extension, the light (-pseudo) scalar is produced in association with a pair of top quarks. Moreover the branching fraction of the decay of the light (-pseudo) scalar to leptons is let as a free parameter.

The searches are performed in a multilepton final state. At least 3 electrons or muons are requested in the final state. The data are split in categories depending on the lepton flavour (electron/muon) and their multiplicity, the presence or not of a Z candidate, the opposite sign same flavour component, missing transverse momentum and the number of b tagged jets observed.

Two main variables are defined depending on the search: for the heavy fermions search, the sum of the transverse momentum of the leptons and the missing transverse momentum divided by the transverse mass is used. For the search of light (-pseudo) scalar, the attractor mass is used. The attractor mass is defined as the two same flavour opposite sign leptons mass closest to the target mass being either 20 GeV or 300 GeV.

No excess is observed above the background, so limits are established. In the case of the heavy fermions search they improved by 50 GeV the mass excluded with the 2016 analysis. For the light (-pseudo) scalar search, this is the first limit established as a function of the branching fraction of the decay of the light (-pseudo) scalar to leptons.

2.2 Search for heavy Higgs decaying into a pair of W bosons

The search looks for heavy Higgs decaying into a pair of W bosons⁴. It uses 2016 data and it improves the signal understanding by taking into account the signal and background interference and considering also the Vector Boson Fusion (VBF) production mode. The interference of the signal with the Higgs Standard Model or diboson production nearly cancel. The analysis has a broad range of mass from 200 GeV up to 3 TeV.

The search is using two decay channel: the lepton+jets channel and the dilepton one. The VBF production mode requests two additional jets. A tagging based on angular distribution of the decay is made to distinguish gluon fusion and VBF production. For the search in the dilepton channel, at least two opposite sign leptons (electron or muon) are requested together with a large missing transverse momentum. The events are categorised depending on the lepton flavour, the missing transverse momentum, the number of jets and the VBF channel. In the case of the lepton+jets channel, a b tag veto is in place to reject top quark pair production and the search is performed with either the hadronic W boson being boosted or resolved. Some missing transverse momentum is required. A cut on the transverse momentum of the W boson over the invariant mass of the two W bosons is applied and it depends on the boost or not of the hadronic W .

The variable used to distinguish signal from background depends on the final state. For the dilepton channel the transverse visible mass is used which is defined as the transverse mass of the quadrivector of the two leptons and the missing transverse momentum. In the lepton+jets channel, both W mass are determined, the main variable is simply the invariant mass of the two boson system.

The data is in agreement with the expected background so limits are set. The limits consider the fraction of VBF production floating and some interpretation in 2 Higgs Doublet Models (2HDM).

2.3 Search for pair produced gluinos/stops and neutralinos with gauge mediated SUSY

The final state of a search for pair produced gluinos/stops and neutralinos with gauge mediated SUSY, is very rich thanks to the various decays⁵. It consists of photons, jets which can be b tagged and missing transverse momentum. The search is performed using 2016 data only and it develops dedicated regions to emphasise the decays of gluino/stop via top or bottom quarks.

The analysis selection relies on the presence of the high transverse momentum photon and a large hadronic energy, 2 jets, large missing transverse momentum and various angular separation. A veto on lepton is imposed. The search is binned in various categories based on the value of the missing transverse momentum, the number of jets and the number of b jets. No excess is observed with respect to the expected background in each bins so limits are established in the plane of the neutralino mass versus the stop/gluino mass.

3 Enriched technics

In this section, searches using dedicated analysis technics are presented. These technics use a better understanding of the data and improve the searches.

3.1 Specific reconstruction

One of the improved technics is the specific interpretation of the electronic signal to particles for difficult searches. Mainly, the searches for long-lived particle request an adjustment of the reconstruction and the background determination. For example, in the case of delayed jets and missing transverse momentum used to look for gauge mediated supersymmetry breaking⁶, it relies on a high timing precision of the CMS electromagnetic calorimeter in order to select 'late' jets with respect to collision time but also in order to remove jets coming from satellite bunches. Another example is the searches in the context of compressed SUSY with tiny mass difference between the chargino and the neutralino⁷. For such a search, the chargino would decay inside the tracker volume and the neutralino has too low energy to reach the electromagnetic calorimeter. The signal is then a disappearing track accompanying a few jets in the final state. The tracker reconstruction has to adapt to keep disappearing tracks.

3.2 Multiple identification of boosted jets

This technics consists in trying to identify simultaneous all the boosted jets in an event. It is based on a Neural Network named BEST (Boosted Event Shape Tagger⁸). It is used in the context of pair produced vector like quark in the all hadronic channel⁹ (T or B) which would decay into Wb/Zt or Ht for the T case (and into Wt/Zb/Hb in the B case). The analysis requests 4 boosted jets in the final state with transverse momentum greater than 400 GeV and uses 2016 data. The events are pushed through BEST and analysis categories are made depending on the final state looked at. In parallel to the analysis using BEST algorithm, a cut based analysis is made. Clearly the BEST algorithm improves the limits in channel with complex jets (Top/Higgs) and also improve the previous limits on pair produced vector like quarks.

3.3 Multi dimensional fit

A 3D fit is developed in the context of search for a resonance of a mass larger than 1 TeV decaying into two boosted bosons (W/Z) in all hadronic final state¹⁰. As the bosons are boosted they present only one jet which shows a resonance at the invariant mass of the boson. Using such information, a 3D fit is made looking for a resonance for the first/second jet mass and a third resonance in the invariant mass of the two jets as illustrated in figure 1.

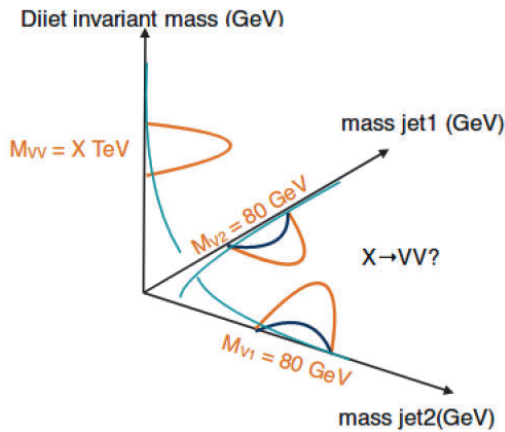


Figure 1 – 3D representation of the 3D multi dimensional fit.

The analysis uses 2016 and 2017 data and selects events with 2 boosted jets with transverse momentum larger than 200 GeV. A large separation in eta is requested between the two jets. Events are categorised based on a decorrelation of τ_{21} variable indicating the likelihood for a jets to come from the merging of two subjets. The interpretation of the search is in bulk gravitons model and heavy vector triplet (W' and Z'). Limits are derived for each case and the multi dimensional fit improves the previous results by 20 to 30%.

4 Conclusion

With the run 2 data becoming available, CMS is pursuing searches not simply via an increased statistics and also by improving the models/technics. Additional models are introduced, new categories or even dedicated reconstruction are used. In parallel, new analysis technics are exploited via Neural Network or multi dimensional fit. This goes together with the Run 3 preparation where all the narrow corners will need to be used. The searches are far to be over. They request improvements to go in narrow corner of phase space of models or simply pushing further down the cross section.

References

1. CMS Collaboration, *Journal of Instrumentation* **3**, S08004 (2008)
2. CMS Collaboration, *Phys. Rev. Lett.* **119**, 221802 (2017)
3. CMS Collaboration, CMS-PAS-EXO-19-002, <http://cds.cern.ch/record/2668721>
4. CMS Collaboration, CMS-PAS-HIG-17-033, <http://cds.cern.ch/record/2668687>
5. CMS Collaboration, arXiv:1901.06726 [hep-ex], <https://arxiv.org/abs/1901.06726>
6. CMS Collaboration, CMS-PAS-EXO-19-001, <http://cds.cern.ch/record/2667508>
7. CMS Collaboration, CMS-PAS-SUS-19-005, <http://cds.cern.ch/record/2668105>
8. J. S. Conway, R. Bhaskar, R. D. Erbacher, and J. Pilot, *Phys. Rev. D* **94**, 090427 (2016)
9. CMS Collaboration, CMS-PAS-B2G-18-005, <http://cds.cern.ch/record/2667230>
10. CMS Collaboration, CMS-PAS-B2G-18-002, <http://cds.cern.ch/record/2668755>

Strong SUSY at ATLAS and CMS

Nadja Strobbe on behalf of the ATLAS and CMS Collaborations
*Fermi National Accelerator Laboratory,
PO Box 500, Batavia, IL 60510, USA*

Supersymmetry (SUSY) remains one of the most elegant theories of new physics. The experiments at the LHC are able to put stringent constraints on strongly produced SUSY particles. Several of the most recent results by the CMS and ATLAS Collaborations in searches for gluinos and squarks are presented. The results use between 36 and 139 fb⁻¹ of proton-proton collision data at 13 TeV, and the background predictions agree with the observed data. For a variety of SUSY models, new limits on sparticle masses are set that surpass previous results.

1 Introduction

Supersymmetry (SUSY) is a well-motivated extension of the standard model (SM) in which a new symmetry between fermions and bosons is postulated. SUSY introduces a superpartner for every existing SM particle that has the same quantum numbers except for its spin, which differs by one-half. In models of R-parity conserving SUSY, the lightest SUSY particle (LSP) is stable and can be a dark matter candidate. In nearly all models considered here the LSP is assumed to be the lightest neutralino, $\tilde{\chi}_1^0$. This particle is weakly interacting and neutral, and does not leave any hits in the detector, resulting into potentially large missing transverse momentum, p_T^{miss} . This characteristic is exploited by many searches for SUSY.

Run 2 of the LHC was very successful, with over 150 fb⁻¹ of proton-proton collisions at a center-of-mass energy of 13 TeV delivered to the ATLAS¹ and CMS² detectors during the years 2015–2018. These proceedings present the results of three searches for supersymmetry using the full Run 2 data set, as well as several more that use a partial data set. In general, SUSY searches are expanding, and the large inclusive analyses with many search regions are complemented by dedicated searches that aim to close gaps in our search coverage. In many cases, analysis techniques have been improved and machine learning techniques are used to identify charm, bottom, or top quarks, and even Higgs bosons. All searches presented find good agreement between the observed data and the background prediction. Limits on gluino and squark masses are several hundred GeV stronger than those obtained by previous analyses.

2 Jets + M_{T2} search (CMS)

The jets + M_{T2} search³ performed by the CMS Collaboration is an inclusive search using 137 fb⁻¹ of data targeting a wide range of strong SUSY models. There are 282 signal regions defined using kinematic variables such as the number of jets, the number of b-tagged jets, H_T , and M_{T2} . The main backgrounds are the lost lepton background, in which p_T^{miss} arises from a leptonic W boson decay where the lepton is not reconstructed or identified, the $Z \rightarrow \nu\bar{\nu}$ background which has genuine p_T^{miss} from the neutrinos, and the multijet background where p_T^{miss} arises from jet mismeasurements. All these backgrounds are estimated using data control

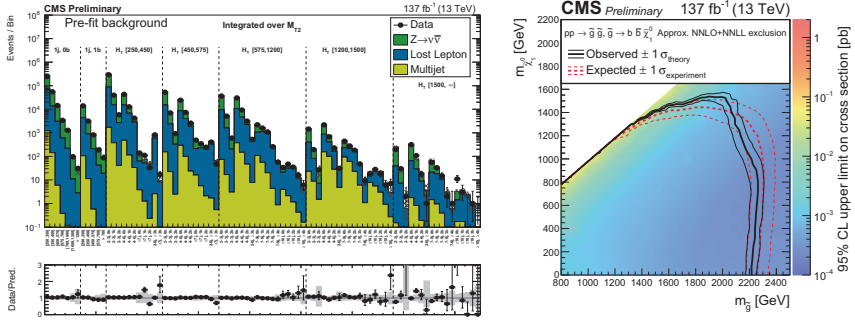


Figure 1 – (left)³ Observed data counts and corresponding background prediction for all signal regions integrated over M_{T2} ; (right)³ Expected and observed upper limit on the cross section as a function of gluino and LSP mass for the signal model with $\tilde{g} \rightarrow b\bar{b}\tilde{\chi}_1^0$.

regions and transfer factors that relate the control to the signal regions. No evidence for an excess above the expected background event yields is observed. The results are interpreted using simplified models of squark and gluino pair production, and the reach is extended by 150–350 GeV compared to the previous 36 fb^{-1} results. Figure 1 shows the observed data and background prediction for all signal regions integrated over M_{T2} , as well as the limit on the gluino and LSP mass for the signal model in which the gluino decays into two b quarks and the LSP. Gluino masses up to 2.2 TeV can be excluded.

3 B-tagged jets + Higgs boson + p_T^{miss} search (ATLAS)

The discovery of the Higgs boson opens up new ways of probing new physics. This analysis⁴ by the ATLAS Collaboration using 139 fb^{-1} of data exploits the large branching fraction of $h \rightarrow b\bar{b}$ to target sbottom squarks that decay into a bottom quark, a Higgs boson, and the LSP via the $\tilde{\chi}_2^0$. Higgs candidates are identified using the invariant mass and angular separation of b-tagged jet pairs. Several search regions are defined requiring many b-tagged jets and large p_T^{miss} , and are optimized to target different regions of phase space. The main backgrounds are $t\bar{t}$ or Z+jets production, and are estimated using 1- and 2-lepton data control regions. Good agreement is found between observed data counts and the background prediction. As shown in Fig. 2, sbottom quarks are excluded up to 1400 GeV for $m(\tilde{\chi}_1^0) = 60\text{ GeV}$, with reduced sensitivity when the Higgs boson is just barely on shell.

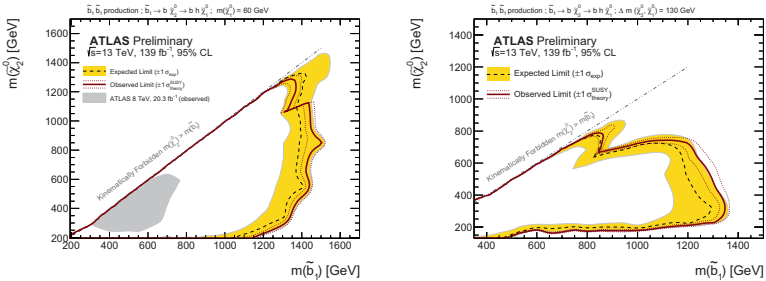


Figure 2 – Exclusion contours⁴ in the $m(\tilde{b}, \tilde{\chi}_2^0)$ plane for (left) the $m(\tilde{\chi}_1^0) = 60\text{ GeV}$ signal scenario, and (right) the $\Delta m(\tilde{\chi}_2^0, \tilde{\chi}_1^0) = 130\text{ GeV}$ signal scenario.

4 Same-sign dilepton + multilepton search (CMS)

Processes producing 2 same-sign or ≥ 3 leptons are very rare in the SM. This makes for a low-background environment to do searches. This CMS search⁵ for supersymmetry in events with 2 same-sign or 3 or more leptons using 137 fb^{-1} of data targets gluinos, top squarks, and bottom squarks. There are 168 search regions, which are defined using a variety of kinematic variables including lepton p_T , number of (b-tagged) jets, H_T , and p_T^{miss} . This search also includes signal regions at low p_T^{miss} resulting in good sensitivity to certain SUSY models with R-parity violation (RPV). The dominant backgrounds come from rare SM processes such as WZ or $t\bar{t}W$, nonprompt leptons, and electron charge flip. Good agreement between data and prediction is observed, and the limits are extended by 150–200 GeV compared to the previous 36 fb^{-1} results. Figure 3 shows the data and predicted background for a subset of the signal regions, as well as the upper limit on the cross section for an example RPV SUSY model as a function of the gluino mass.

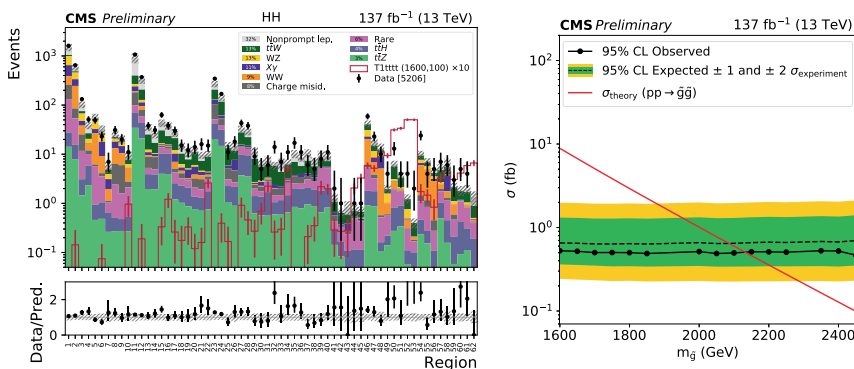


Figure 3 – (left)⁵ Observed data and expected background in a selection of search bins. An example signal model is overlaid. (right)⁵ Upper limit on the cross section as a function of gluino mass for the RPV model in which the gluino decays to four quarks and a lepton.

5 Top squark searches

The recent results in searches for top squarks focus on tricky corners of phase space and use the partial Run 2 data set. The ATLAS search for top squarks with charm tagging⁶ targets models with so-called compressed spectra, in which the mass difference Δm between the top squark and the LSP is very small, and the loop-induced decay $\tilde{t} \rightarrow c\tilde{\chi}_1^0$ can dominate. To improve sensitivity to these compressed mass spectrum scenarios, the analysis relies on initial-state radiation to provide large p_T^{miss} . As shown in Fig 4, top squarks can be excluded up to 500 GeV depending on Δm . This analysis is also sensitive to charm squark production, and can exclude charm squarks up to 800 GeV.

Two other analyses focus instead on the “top corridor” region, in which Δm is about the top quark mass. In this case, top quarks from the $\tilde{t} \rightarrow t\tilde{\chi}_1^0$ decay will be produced almost at rest, and resemble SM $t\bar{t}$ production. To target these models, a precision approach is needed, and both analyses use the clean $e\mu$ final state. The ATLAS analysis exploits $t\bar{t}$ spin correlations⁷, in particular the effects on the double-differential distributions of lepton $\Delta\phi$ and $\Delta\eta$. Top squarks are scalar particles, and are produced more central in the detector. In addition, the top quarks from top squark decays are uncorrelated. The CMS search⁸ relies on a precise estimate of the $t\bar{t}$ background in addition to extra discrimination power from the M_{T2} variable. Top squark masses up to 225 GeV can be excluded in this “top corridor” scenario.

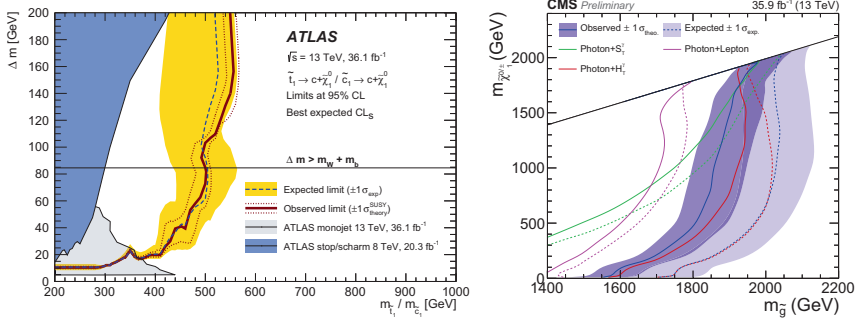


Figure 4 – (left)⁶ Exclusion contour as a function of the top/charm squark mass and Δm for the search with charm tagging; (right)⁹ Limits on the gluino and LSP masses for the combined photon analysis as well as the individual analyses.

6 SUSY searches with photons

SUSY searches with photons are motivated by gauge-mediated SUSY breaking, in which the lightest neutralino decays into a gravitino and a photon. A combination of four separate CMS analyses with photons was performed⁹. The searches included are (i) Photon + lepton + p_T^{miss} , (ii) Photon + S_T + p_T^{miss} , (iii) Photon + H_T + p_T^{miss} , (iv) Diphoton + p_T^{miss} . Special consideration was given to remove overlaps between these analyses so that they could be fully combined. The strong SUSY model considered in this analysis is gluino pair production, with the gluino decaying to two quarks and the $\tilde{\chi}_1^0$, and the $\tilde{\chi}_1^0$ decaying to the gravitino and either a W boson or a photon. Gluino masses up to about 2 TeV can be excluded for this model, and the combination improved the sensitivity especially in the compressed region, as illustrated in Fig. 4.

7 Summary

The very successful Run 2 of the LHC finished at the end of 2018, and we have now entered LS2, with preparations for Run 3 in full swing. The first full Run 2 results for searches for strongly produced SUSY particles by the ATLAS and CMS Collaborations were presented. Gluinos are excluded up to 2.2 TeV and sbottoms up to 1.4 TeV in simplified models. In addition, several analyses that are targeting difficult corners of phase space using the partial Run 2 data set, such as searches for top squarks in the top corridor, were presented.

References

1. ATLAS Collaboration, *JINST* **3** (2008) S08003.
2. CMS Collaboration, *JINST* **3** (2008) S08004.
3. CMS Collaboration, [CMS-PAS-SUS-19-005](#) (2019).
4. ATLAS Collaboration, [ATLAS-CONF-2019-011](#) (2019).
5. CMS Collaboration, [CMS-PAS-SUS-19-008](#) (2019).
6. ATLAS Collaboration, *JHEP* **09** (2018) 050.
7. ATLAS Collaboration, [arXiv:1903.07570\[hep-ex\]](#) (2019), Submitted to *Eur. Phys. J. C*.
8. CMS Collaboration, *JHEP* **03** (2019) 101.
9. CMS Collaboration, [CMS-PAS-SUS-18-005](#) (2019).

LHC constraints on extended SUSY

S. KRAML

*Laboratoire de Physique Subatomique et de Cosmologie, Université Grenoble-Alpes, CNRS/IN2P3,
53 Avenue des Martyrs, F-38026 Grenoble, France*

A characteristic feature of extended SUSY is the presence of Dirac gauginos. In this talk, we discuss some of the phenomenological consequences and how the impact the LHC constraints.

1 Introduction

Most supersymmetry (SUSY) searches at the LHC have the Minimal Supersymmetric Standard Model (MSSM) as their paradigm; analyses are designed and optimised with (often simplified) MSSM scenarios in mind. Non-minimal realisations of SUSY can however have quite distinct phenomenological features. It is therefore highly valid to ask how the current LHC searches constrain them.

In the MSSM, gauginos are Majorana particles. A theoretically very appealing extension is to introduce instead Dirac gauginos (DGs): DG models are linked to $N = 2$ supersymmetry, have a softer UV behaviour (super-softness), can preserve R-symmetry, offer simpler SUSY breaking, and provide a natural scenario for neutralino dark matter as well as a tree-level boost to the Higgs mass — see¹ for a concise, yet comprehensive overview and list of references.

Table 1: Chiral and gauge multiplet fields in the minimal DG model; the upper part contains the usual MSSM fields, the lower one the new chiral multiplets necessary to form Dirac gaugino masses.

Names		Spin 0	Spin 1/2	Spin 1	$SU(3)_c, SU(2)_L, U(1)_Y$
Quarks	Q	$\tilde{Q} = (\tilde{u}_L, \tilde{d}_L)$	(u_L, d_L)		(3, 2, 1/6)
($\times 3$ families)	u^c d^c	\tilde{u}_L^c \tilde{d}_L^c	u_L^c u_L^c		($\bar{3}, 1, -2/3$) ($\bar{3}, 1, 1/3$)
Leptons	L	$(\tilde{\nu}_{eL}, \tilde{e}_L)$	(ν_{eL}, e_L)		(1, 2, -1/2)
($\times 3$ families)	e^c	\tilde{e}_L^c	e_L^c		(1, 1, 1)
Higgs	H_u H_d	(H_u^+, H_u^0) (H_d^0, H_d^-)	$(\tilde{H}_u^+, \tilde{H}_u^0)$ $(\tilde{H}_d^0, \tilde{H}_d^-)$		(1, 2, 1/2) (1, 2, -1/2)
Gluons	W_{3α}		$\lambda_{3\alpha} [\equiv \tilde{g}_\alpha]$	g	(8, 1, 0)
W	W_{2α}		$\lambda_{2\alpha} [\equiv \tilde{W}^\pm, \tilde{W}^0]$	W^\pm, W^0	(1, 3, 0)
B	W_{1α}		$\lambda_{1\alpha} [\equiv \tilde{B}]$	B	(1, 1, 0)
DG-octet	O_g	$O_g [\equiv \Sigma_g]$	$\chi_g [\equiv \tilde{g}']$		(8, 1, 0)
DG-triplet	T	$\{T^0, T^\pm\}$ [$\equiv \{\Sigma_W^0, \Sigma_W^\pm\}$]	$\{\chi_T^0, \chi_T^\pm\}$ [$\equiv \{\tilde{W}'^\pm, \tilde{W}'^0\}$]		(1, 3, 0)
DG-singlet	S	$S [\equiv \Sigma_B]$	$\chi_S [\equiv \tilde{B}']$		(1, 1, 0)

To write Majorana masses, one needs just one Weyl fermion λ_i for each gaugino: $\mathcal{L} \supset -\frac{1}{2}M_i\lambda_i\lambda_i$ with $i = 1\dots 3$. Dirac masses, $\mathcal{L} \supset -m_{Di}\chi_i\lambda_i + \text{h.c.}$, require pairing the λ_i with additional Weyl fermions χ_i in the adjoint representation of each gauge group: a singlet \mathbf{S} for $U(1)_Y$, a triplet \mathbf{T} for $SU(2)_L$ and an octet \mathbf{O}_g for $SU(3)_c$. The resulting field content is summarised in Table 1. It leads to a larger electroweak-ino sector with six neutralino and three chargino mass eigenstates, $\tilde{\chi}_{1\dots 6}^0$ and $\tilde{\chi}_{1\dots 3}^\pm$, as compared to four neutralinos and two charginos in the MSSM. The singlet and triplet fields can moreover have new superpotential couplings with the Higgs,

$$W \supset \lambda_S \mathbf{S} \mathbf{H}_u \cdot \mathbf{H}_d + 2\lambda_T \mathbf{H}_d \cdot \mathbf{T} \mathbf{H}_u, \quad (1)$$

which naturally enhance the Higgs mass at tree level, $m_h^2 \simeq M_Z^2 \cos^2 2\beta + \frac{v^2}{2}(\lambda_S^2 + \lambda_T^2) \sin^2 2\beta$. This makes it easier to achieve $m_h = 125$ GeV without the need for multi-TeV stops.

In this contribution, we discuss some consequences for LHC phenomenology and review how current experimental analyses constrain the minimal DG model.

2 Bounds on sgluons from Standard Model four-top analysis

The DG model contains a complex color-octet scalar, which, if CP is conserved, splits into two non-degenerate real components (a scalar and a pseudoscalar) after SUSY breaking. These “sgluons” are R -parity even. The scalar is generally heavier and decays into both, quarks and gluons. It might also decay into pairs of gluinos or squarks if kinematically possible, giving spectacular signatures of, e.g., 8 jets + 4 LSPs, for high enough \sqrt{s} . The pseudoscalar state is generally lighter and decays into a pair of quarks. A generic expectation is that the top-antitop channel dominates, which makes the 4 top signature from pseudoscalar sgluon pair production, see Fig. 1, the golden channel.

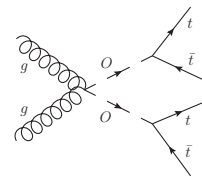


Figure 1 – Representative Feynman diagram for sgluon pair production and decay into a four-top final state.

Reference² implemented the CMS four-top analysis³ for 36 fb^{-1}

at 13 TeV in the `MadAnalysis 5` framework and re-interpreted it to set limits on sgluon-induced four-top signal. It was found that pseudoscalar sgluons of mass up to 1.06 TeV are conservatively excluded at the 95% confidence level (CL), see the left panel of Fig. 2. It will be highly interesting to see how the CMS update for the full Run 2 dataset (137 fb^{-1}), presented at this conference, pushes this limit even higher.

The sensitivity of the analysis could be improved by exploiting differences in the kinematic distributions with respect to Standard Model four-top production. For example, the signal H_T distribution, shown in the right panel of Fig. 2, presents a peak close to the sgluon mass and could hence be used to discriminate between Standard Model and sgluon-induced four-top production.

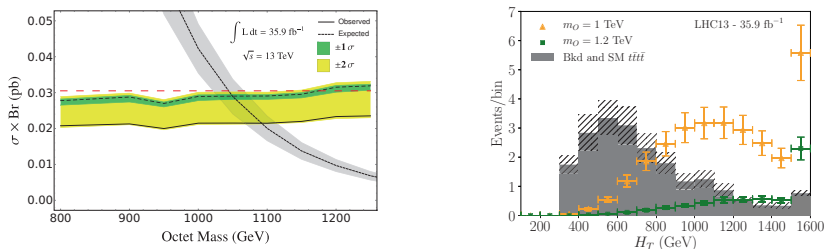


Figure 2 – Left: 95% CL limit on pseudoscalar sgluon production from a recast of the CMS four-top analysis with 36 fb^{-1} . Right: example for a kinematical distribution (H_T), which might be used to improve the reach for sgluon pair production.

3 Constraints on gluinos and squarks

Let us now turn to SUSY searches. The arguably best known consequence of Dirac gauginos is the suppression of light-flavour squark production at the LHC^{4,5}. This is illustrated in Fig. 3, which compares the production cross-sections for 1.5 TeV squarks in the MSSM and the DG model as a function of the gluino mass. As can be seen, in the MSSM squark-squark production (proceeding via t -channel gluino exchange) dominates up to high $m_{\tilde{g}}$. In the DG case, the total squark production cross section is much smaller, and $\tilde{q}\tilde{q}^*$ production starts to dominate over $\tilde{q}\tilde{q}$ production already at $m_{\tilde{g}} \approx 3$ TeV. The reason is that $pp \rightarrow \tilde{q}_{L,R}\tilde{q}_{L,R}$ requires a chirality flip, which is absent in the DG case. Moreover, the other t -channel gluino exchange processes are suppressed by $1/m_{\tilde{g}}^2$.

Gluino-pair production, on the other hand, is enhanced in the DG case because of the larger number of degrees of freedom than in the MSSM. For $g\tilde{g}$ associated production, the cross section is the same as in the MSSM.

In addition one may expect that the more complex electroweak-ino spectrum influences the experimental bounds in scenarios that go beyond simplified models⁶. Taking m_{DY} smaller than m_{D2} and the higgsino mass parameter μ , the lightest neutralinos $\tilde{\chi}_{1,2}^0$ will be a pair of mostly bino/ $U(1)$ -adjoint states with a mass splitting of $m_{\tilde{\chi}_2^0} - m_{\tilde{\chi}_1^0} = \left| 2 \frac{M_Z^2 \sin^2 \theta_W}{\mu} \frac{(2\lambda_S^2 - g_Y^2)}{g_Y^2} \cos \beta \sin \beta \right|$. It is important to note here that every decay that would go into the $\tilde{\chi}_1^0$ in the MSSM is now, in the DG case, shared out almost equally between decays into $\tilde{\chi}_1^0$ and $\tilde{\chi}_2^0$.

In the following we fix $m_{DY} = 200$ GeV, $m_{D2} = 500$ GeV, $\mu = 400$ GeV, $\tan \beta = 2$, and $\lambda_T = 0.2$, which gives a light, but still somewhat hierarchical spectrum of bino-, higgsino- and wino-like states with masses of about 200, 400 and 500 GeV, respectively. The dependence of the $\tilde{\chi}_{1,2}^0$ mass splitting and the $\tilde{\chi}_2^0$ lifetime on λ_S is shown in Fig. 4. We see that for small $|\lambda_S|$ the $\tilde{\chi}_2^0$ is mass-degenerate with the $\tilde{\chi}_1^0$ and quasi-stable; the $\tilde{\chi}_{1,2}^0$ thus appear like just one bino LSP in the MSSM. For large $|\lambda_S|$, the mass difference is tens of GeV and the $\tilde{\chi}_2^0$ decays promptly into $\tilde{\chi}_1^0 + f\bar{f}$ via an off-shell Z boson. In between there is a certain range of $|\lambda_S|$ where the $\tilde{\chi}_2^0$ appears as a neutral long-lived particle, leading to signatures with displaced vertices.

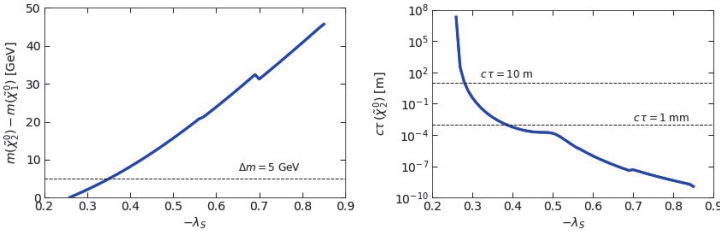


Figure 4 – Influence of λ_S on the mass splitting between the two bino-like mass eigenstates $\tilde{\chi}_{1,2}^0$ (left) and on the lifetime of the $\tilde{\chi}_2^0$ (right); for $m_{DY} = 200$ GeV, $m_{D2} = 500$ GeV, $\mu = 400$ GeV, $\tan \beta = 2$, and $\lambda_T = 0.2$.

To investigate how all this influences the LHC limits on gluinos and squarks, we recasted in⁶ the ATLAS Run 2 search⁷ in final states with 2–6 jets and large E_T^{miss} (for 36 fb^{-1}) with **MadAnalysis 5**. Here we show results for the DG benchmark scenarios DG1, DG2, DG3. They all have the same parameters as in Fig. 4 but are distinguished by different values of λ_S to have either a quasi-stable or a promptly decaying $\tilde{\chi}_2^0$ (the long-lived case will require a separate analysis).

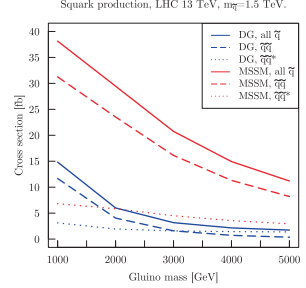


Figure 3 – Squark production cross sections at leading order for the 13 TeV LHC as a function of the gluino mass in the MSSM (in red) and in the DG case (in blue).

Stop masses are adjusted such that $m_h \simeq 125$ GeV. Concretely, DG1 has $\lambda_S = -0.27$ and $m_{\tilde{t}} \sim 3.6$ TeV, while DG2 and DG3 have $\lambda_S = -0.74$ and stops at 2.6 TeV (DG2) or 1.6 TeV (DG3). See⁶ for details. The resulting 95% CL exclusion in the gluino vs. squark mass plane is shown in Fig. 5 and compared to the equivalent MSSM case with Majorana gaugino masses of $M_1 = 200$ GeV and $M_2 = 500$ GeV (and higgsino mass $\mu = 400$ GeV).

As can be seen, for $m_{\tilde{g}} \approx m_{\tilde{q}}$, the mass limit is about 2.1 TeV for both gluinos and squarks in all three DG benchmark scenarios. For 4 TeV gluinos, the squark mass limit is about 1.4 TeV for DG1, decreasing to 1.1–1.15 TeV for DG2 and DG3, where $\tilde{\chi}_2^0 \rightarrow Z^* \tilde{\chi}_1^0$ decays appear in the squark decay chains. The gluino mass limit in the region $m_{\tilde{q}} > m_{\tilde{g}}$ also depends on the assumed DG scenario. While we find a robust limit of $m_{\tilde{g}} \gtrsim 1.65$ TeV for very heavy squarks in all cases, we also observe “dip+peak” features in the exclusion contours which differ for DG1, DG2 and DG3. This comes from the change in the best signal region (from 6j-Meff-1800 to 6j-Meff-2600) happening at different gluino/squark mass combinations and was explained in some detail in the talk, but cannot be elaborated on in this writeup due to page limitations. The differences as compared to the MSSM are obvious from the MSSM1 exclusion line. Before concluding we note that our results were obtained for leading order cross sections. Higher-order corrections will increase the cross sections, and thus the mass limits quoted here, but should not change the overall picture.

4 Conclusions

Dirac gauginos lead to a distinct phenomenology and to LHC limits differing from the MSSM. The differences include enhanced gluino production, strongly suppressed squark production, and more complicated SUSY decay chains due to the extended electroweak-ino spectrum. In particular, the $\tilde{\chi}_2^0$ may be long-lived. In the R-parity even sector, pair-production of pseudoscalar sgluons can give rise to a four-top signal, which can be constrained from the respective Standard Model analysis. Overall, it is interesting and more than worthwhile to explore the experimental consequences of non-standard SUSY realisations in detail.

References

1. K. Benakli. *Fortsch. Phys.*, 59:1079–1082, 2011.
2. L. Darmé, B. Fuks, and M. Goodsell. *Phys. Lett.*, B784:223–228, 2018.
3. A. M. Sirunyan et al. *Eur. Phys. J.*, C78(2):140, 2018.
4. M. Heikinheimo, M. Kellerstein, and V. Sanz, *JHEP*, 04:043, 2012.
5. G. D. Kribs and A. Martin. *Phys. Rev.*, D85:115014, 2012.
6. G. Chalons, M. D. Goodsell, S. Kraml, H. Reyes-Gonzalez, and S. L. Williamson. *JHEP*, 04:113, 2019.
7. M. Aaboud et al. *Phys. Rev.*, D97(11):112001, 2018.

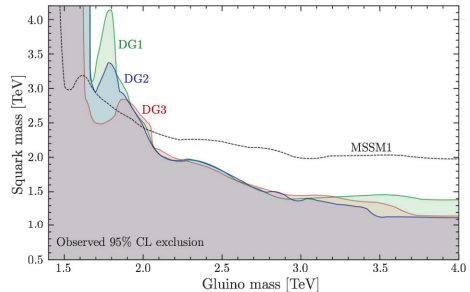


Figure 5 – 95% CL exclusion limits in the gluino vs. squark mass plane for DG1 (green), DG2 (blue), DG3 (red) and the equivalent MSSM case, MSSM1 (black dashed line), derived from the recasting of the ATLAS 2–6 jets + E_T^{miss} analysis for 36 fb^{-1} at $\sqrt{s} = 13$ TeV.

Searches for New Resonances (lepton, jets) at ATLAS and CMS

Yiming (Ablet) Abulaiti

On behalf of the ATLAS and CMS Collaborations
*HEP Division, Argonne National Laboratory,
9700 S. Cass Avenue, Argonne, IL 60439, USA*



This proceeding summarizes recent results from searches for new resonances decaying to a pair of jets or leptons (electrons, muons), from the ATLAS and CMS collaborations, with the Run 2 LHC data collected during the years 2015 to 2018 at center-of-mass energy $\sqrt{s} = 13$ TeV. A search for excited leptons and a search that uses a multilepton signature are also described. The results show no significant deviation from SM expectations. Upper limits are set at the 95% confidence level on the fiducial cross-section times branching ratio of new particles.

1 Introduction

Many beyond standard model (BSM) physics predict the existence of new particles with masses that can be produced in proton-proton (pp) collisions at the Large Hadron Collider¹ (LHC) experiment. This proceeding presents results of search for resonances decaying to a pair of jets or leptons, but also includes a couple of other results, from the ATLAS² and CMS³ collaborations, with either the partial or the full Run 2 LHC dataset.

Resonance searches with dijet and dilepton final states address BSM scenarios in which new heavy particles decay into a pair of leptons or jets. In these scenarios, BSM signal events form a narrow bump structure on top of a smoothly falling invariant mass spectrum of paired jets or leptons (electrons, muons). The main background is multi-jets processes, production of jet pairs in pp collisions primarily results from $2 \rightarrow 2$ parton scattering described by quantum chromodynamics (QCD) in dijet searches; and Drell-Yan (DY), top-quark pair, single-top-quark and diboson productions in dilepton and nonresonance searches. The results of the dijet resonance search are described in Section 2. Results of dijet analyses with an additional lepton or photon described in Section 3. The results of the high mass resonance searches in the dilepton channels are described in Section 4.

The excited leptons and multilepton searches, on the other hand, look for excesses in the invariant mass of two leptons and two jets and the tails of distributions of kinematic variables, respectively. The results of an excited lepton search and an inclusive multilepton search are also presented in Section 5.

© 2019 CERN for the benefit of the ATLAS and CMS Collaborations. CC-BY-4.0 license.

2 Search for dijet resonances

ATLAS searched for heavy resonances in the dijet invariant mass spectrum constructed from two leading jets with radius parameter $\Delta R = 0.4^a$. This analysis⁴ used the full ATLAS Run 2 dataset, corresponding to a luminosity of 139 fb^{-1} . The total background estimation is derived from data using a sliding-window method⁵ in which the shape of the total background is modeled with a parametric function. Results of this analysis show that the observed data are compatible with a smoothly falling background expectation. Therefore model dependent and independent upper limits are set on BSM models. Figure 1 (left) shows the upper limits on the cross section times acceptance times branching ratio ($\sigma \times A \times BR$) on an excited quark (q^*) model. Masses of q^* model below 6.7 TeV are excluded at 95% confidence level (CL).

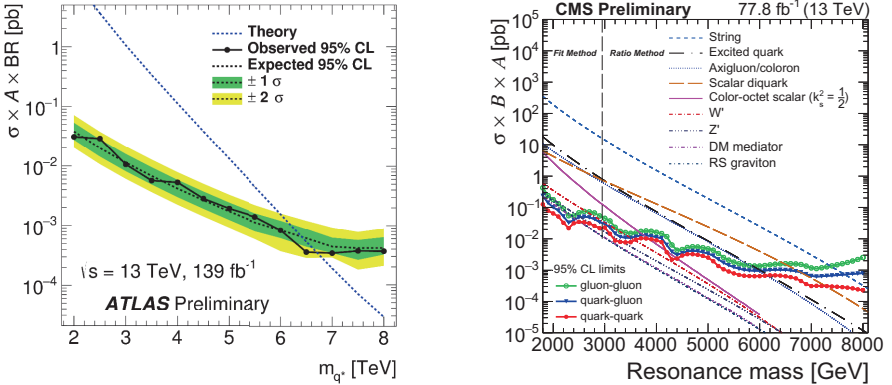


Figure 1 – The 95% CL upper limits on the $\sigma \times A \times BR$ of BSM models. Theory predictions of the cross-sections of BSM models are overlaid. Left: ATLAS dijet results⁴ interpreted on the q^* model. Right: the observed limits from CMS dijet analysis⁶, on the gluon-gluon, quark-gluon, quark-quark type of resonances.

The CMS collaboration also published a results on the dijet invariant mass distribution with 77.8 fb^{-1} of Run 2 data. This analysis uses so-called wide-particle flow jets (wide-jets) to reduce the sensitivity of the analysis to hard gluon radiation from the final state jets. The wide-jets are constructed by adding jets ($\Delta R = 0.4$) to the two leading jets if they are within $\Delta R < 1.1$. The resulting two wide-jets are used to calculate the dijet invariant mass. The total background for $m_{jj} < 2.5 \text{ TeV}$ is estimated with a parametric function while for $m_{jj} > 2.5 \text{ TeV}$ it is extrapolated from a dedicated control region. The observed data agrees with the SM-only background expectation, and upper limits are set for various BMS processes. Figure 1 (right) shows the observed limits on the $\sigma \times A \times BR$. The limits are different for gluon-gluon, quark-gluon, quark-quark type of dijet system due to shape difference between them.

3 Search for dijet resonances with an additional lepton or photon in the final state

The dijet analyses described in the previous section use the lowest unprescaled single jet triggers to collect data. However these triggers require a jet with momentum 420 GeV or higher for ATLAS (550 GeV for CMS) to be fully efficient, which makes the dijet analyses sensitive to only high mass resonances.

The dijet analyses with one associated lepton⁷ or photon⁸ use the single lepton (e or mu) or photon triggers. The single lepton and photon triggers allows for the sensitivity of the analyses to be extended to the mass region well below 1 TeV. Results from these analyses show that the data

^a $\Delta R = \sqrt{(\Delta\eta)^2 + (\Delta\phi)^2}$

is compatible with the SM model background only hypotheses. Therefore, in both analyses, 95% CL model independent and dependent limits are set on BSM models. In the dijet analysis with one associated lepton, the results is interpreted on a technicolor model ($\rho_T \rightarrow W\pi_T$). This model is excluded below a π_T mass of 0.5 TeV.

4 Search for high mass dilepton resonances

The ATLAS collaboration searched for new resonances decaying to dileptons⁹ (electrons or muons) using 139 fb^{-1} of data. Figure 2 shows the reconstructed dilepton mass distributions for the dielectron and dimuon channels. The dilepton invariant mass spectrum is fit above 225 GeV to avoid contamination from Z boson peak. The observed highest mass dilepton event is at $m = 4.06 \text{ TeV}$ and belongs to the electron channel.

Total backgrounds are estimated by fitting a parametric function to the observed data. The results show that the observed data is compatible with the SM expectation. The local maximum deviations from the background-only hypotheses are 2.9σ ($m_{ee} = 774 \text{ GeV}$), 2.4σ ($m_{\mu\mu} = 767 \text{ GeV}$) and 2.3σ ($m_{ll} = 764 \text{ GeV}$) in the dielectron, dimuon and combined dilepton channels, respectively. However the corresponding global significance are 0.1σ , 0.3σ , and zero, respectively. Upper limits are set on the cross section of spin 1 heavy resonances, but the limits are also shown to be applicable to the spin 0 and spin 2 hypotheses.

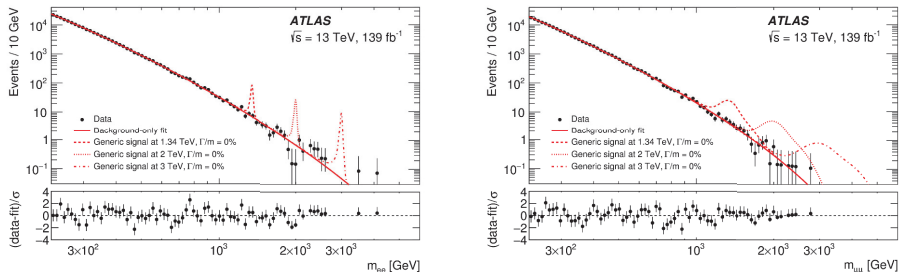


Figure 2 – Results from ATLAS dilepton analysis⁹. Total background compared to data, in the dielectron channel (left) and dimuon channel (right).

5 Other searches involving leptons and jets

The CMS collaboration performed an excited lepton¹⁰ (electron and muon) search with 77.4 fb^{-1} of LHC data. The excited lepton decays via a contact interaction to two leptons and two jets. The analysis is looking for an excess in an invariant mass of two selected leptons and two leading jets, M_{lljj} . Figure 3 (left) shows the upper limits on the $\sigma \times BR$ of the excited electron (the limits for an excited muon is similar). Excited electron (muon) masses below 5.6 (5.7) TeV are excluded.

The type-III seesaw (Σ) and $tt\phi$ (ϕ is new light scalars or pseudoscalars) models predict complex final states including multileptons. These types of models create non-resonance signatures at the LHC. The CMS collaboration published a results from multilepton analysis¹¹ using 137 fb^{-1} the full Run 2 dataset to address such non-resonance signatures in three or more lepton final states. Figure 3 (right) shows heavy fermions in the type-III seesaw model are excluded with masses below 880 GeV.

6 Summary

This proceeding highlighted some searches for resonances decaying to a pair of jets or leptons, and other searches involving leptons and jets, from the ATLAS and CMS collaborations, using Run

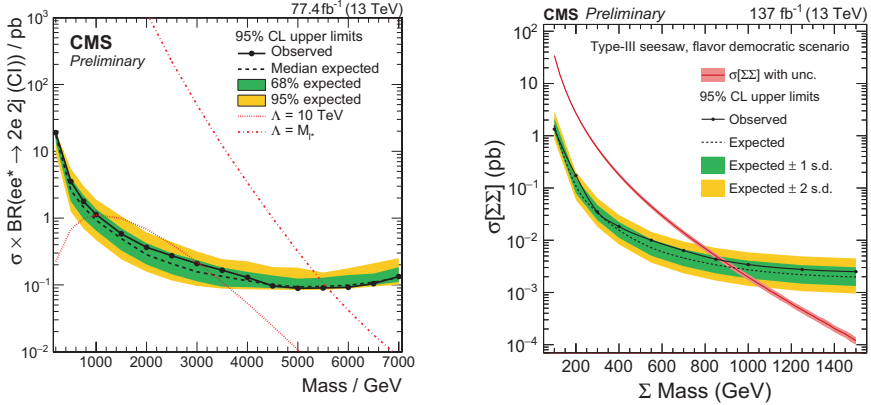


Figure 3 – Left: 95% CL upper limits from CMS excited electron search¹⁰ using M_{eej} . Right: 95% CL upper limits on the Σ model from CMS multilepton analysis¹.

2 LHC data (full or partial data set) at $\sqrt{s} = 13 \text{ TeV}$. The results show no evidence for BSM physics, and 95% CL upper limits are set on the cross-sections of various BSM models. In the dijet searches, q^* with masses below 6.7 TeV⁴ (with full Run2 data) and string resonances with masses below 7.6 TeV⁶ are excluded. The ATLAS dilepton analysis excludes sequential standard model Z' boson masses below $m_{ll} = 5.1 \text{ TeV}$ ⁷ (with full Run2 data), in the combined ee and $\mu\mu$ channel. The CMS multilepton analysis placed a limit, $m_\Sigma < 880 \text{ GeV}$ ¹¹ (with full Run2 data), on the type-III seesaw model.

References

1. L. Evans and P. Bryant, LHC Machine, JINST **3**, 2008 (S08001), DOI: [10.1088/1748-0221/3/08/S08001](https://doi.org/10.1088/1748-0221/3/08/S08001).
2. ATLAS Collaboration, JINST **3**, 2008 (S08003), DOI: [10.1088/1748-0221/3/08/S08003](https://doi.org/10.1088/1748-0221/3/08/S08003).
3. CMS Collaboration, JINST **3**, 2008 (S08004), DOI: [10.1088/1748-0221/3/08/S08004](https://doi.org/10.1088/1748-0221/3/08/S08004).
4. ATLAS Collaboration, Search for New Phenomena in Dijet Events using 139 fb¹ of pp collisions at $\sqrt{s} = 13 \text{ TeV}$ collected with the ATLAS Detector, [ATLAS-CONF-2019-007](https://arxiv.org/abs/1708.03828).
5. ATLAS Collaboration, Search for new phenomena in dijet events using 37 fb¹ of pp collision data collected at $\sqrt{s} = 13 \text{ TeV}$ with the ATLAS detector *Phys. Rev. D* **96**, 052004 (2017), DOI:[10.1103/PhysRevD.96.052004](https://doi.org/10.1103/PhysRevD.96.052004).
6. CMS Collaboration, Searches for dijet resonances in pp collisions at $\sqrt{s} = 13 \text{ TeV}$ using the 2016 and 2017 datasets, [CMS-PAS-EXO-17-026](https://arxiv.org/abs/1708.03828).
7. ATLAS Collaboration, Search for dijet resonances in events with an isolated lepton using $\sqrt{s} = 13 \text{ TeV}$ proton–proton collision data collected by the ATLAS detector, [ATLAS-CONF-2018-015](https://arxiv.org/abs/1808.07514).
8. ATLAS Collaboration, Search for low-mass resonances decaying into two jets and produced in association with a photon using pp collisions at $\sqrt{s} = 13 \text{ TeV}$ with the ATLAS detector, CERN-EP-2018-347, Submitted to: *Phys. Lett. B* (2019), [arXiv: 1901.10917v2 \[hep-ex\]](https://arxiv.org/abs/1901.10917v2)
9. ATLAS Collaboration, Search for high-mass dilepton resonances using 139 fb⁻¹ of pp collision data collected at $\sqrt{s} = 13 \text{ TeV}$ with the ATLAS detector, CERN-EP-2019-030, [arXiv: 1903.06248v2 \[hep-ex\]](https://arxiv.org/abs/1903.06248v2).
10. CMS Collaboration, Search for excited leptons decaying via contact interaction to two leptons and two jets, [CMS-PAS-EXO-18-013](https://arxiv.org/abs/1808.07514).
11. CMS Collaboration, Search for new physics in multilepton final states in pp collisions at $\sqrt{s} = 13 \text{ TeV}$, [CMS-PAS-EXO-19-002](https://arxiv.org/abs/1903.06248v2).

Searches for new physics with unconventional signatures at ATLAS and CMS

Kevin Pedro (on behalf of the ATLAS and CMS Collaborations)
Fermi National Accelerator Laboratory, Batavia, IL 60510, USA

Selected results from searches for new physics with unconventional signatures using the ATLAS and CMS detectors are presented. Such signatures include emerging jets, heavy charged particles, displaced or delayed objects, and disappearing tracks. These signatures may arise from hidden sectors or supersymmetric models. The searches use proton-proton collision data from Run 2 of the LHC with a center-of-mass energy of 13 TeV.

1 Introduction

Searches for physics beyond the standard model (BSM) typically assume that any new particles produced will either decay promptly or, in the case of stable, invisible particles, traverse the detector without depositing any energy. However, unconventional signatures, unlike the previous cases, are also possible. These signatures often involve long-lived particles (LLPs) that decay after some non-negligible lifetime, producing a displaced vertex and an associated displaced object, such as a lepton or a jet. In addition, a disappearing track may occur when a charged BSM particle decays to a neutral particle after traveling some distance. If a charged BSM particle is stable, it may leave an ionization trail through the detector, rather than a decay signature. One class of BSM models that may produce these signatures is hidden sectors, with new particles and/or new forces that have a very small coupling to the SM. Another class of models is supersymmetry (SUSY), with variations such as R -parity violating (RPV), split, stealth, and gauge- or anomaly-mediated SUSY breaking (GMSB or AMSB, respectively). These searches face challenges in reconstruction, triggering, and estimating instrumental backgrounds, often requiring low-level subdetector information. A number of searches for new physics with unconventional signatures have been performed using the ATLAS¹ and CMS² experiments.

2 Search for Emerging Jets

In a hidden sector model with a dark QCD force and dark quarks, the dark quarks will form mesons and baryons, generically labeled π_{DK} , that decay back to SM hadrons after a non-negligible lifetime³. These decays form emerging jets, which are jets that contain a large number of different displaced vertices: one vertex per dark meson or baryon. A search for emerging jets was conducted in 16.1 fb^{-1} of proton-proton (pp) collision data collected with the CMS detector at a center-of-mass energy of 13 TeV⁴. In particular, this search considered the pair production of a complex scalar mediator X_{DK} , with each mediator decaying to a dark quark and an SM quark. The final signature, therefore, contains two SM jets and two emerging jets, or just one emerging jet and missing energy if $c\tau_{\pi_{\text{DK}}}$ is large, so one of the emerging jets forms outside of the detector. Track impact parameter variables, such as the median 2D impact parameter considering all tracks associated with the jet, are used to tag the emerging jets, distinguishing them from SM jets. The background arises from SM jets that are mistakenly identified as emerging jets by the tagging algorithm. The misidentification rate for the tagging algorithm is

measured in a γ +jets control region, and applied to the yield of a QCD-enriched, signal-depleted control region to predict the background yield in the signal region. The observed data are found to agree with the background prediction, within uncertainties, for all signal regions. Limits are set at 95% confidence level (CL) in the plane of $m_{X_{\text{DK}}}$ and $c\tau_{\text{DK}}$, as shown in Fig. 1 (left). The search excludes $400 < m_{X_{\text{DK}}} < 1250$ GeV for $5 < c\tau_{\text{DK}} < 225$ mm, with less stringent limits outside of that range.

3 Search for Heavy Charged Long-Lived Particles

There are several SUSY models that may produce heavy charged LLPs. If strong SUSY particles are produced and have a non-negligible lifetime, they may form R -hadron bound states with SM particles. This can occur for gluinos (\tilde{g}) in split SUSY models or for top squarks (\tilde{t}) in models motivated by electroweak baryogenesis. Alternatively, electroweak production of SUSY particles may also lead to heavy charged LLPs, including staus ($\tilde{\tau}$) in GMSB models or charginos ($\tilde{\chi}_1^\pm$) in AMSB models. Searches for these signatures were conducted using 36.1 fb^{-1} of pp collision data collected with the ATLAS detector at $\sqrt{s} = 13 \text{ TeV}$ ⁵. The search for \tilde{g} and \tilde{t} uses two approaches: “full-detector” and “MS-agnostic”, with the latter approach ignoring the muon spectrometer (MS) to provide model-independent sensitivity. The search for $\tilde{\tau}$ and $\tilde{\chi}_1^\pm$ uses both the inner detector and the MS to require consistent ionization deposits. The particle candidate velocity β is measured using dE/dx from ionization or time of flight, from which the candidate mass $m = p/\beta\gamma$ can be derived. No significant excess is observed in the data, compared to the background prediction. Assuming the LLPs are stable on the scale of the detector volume, 95% CL limits are placed on the cross sections for the production of the various SUSY particles. These limits translate into bounds on the particle masses: $m_{\tilde{g}} < 2.0$ TeV shown in Fig. 1 (center), $m_{\tilde{t}} < 1.34$ TeV, $m_{\tilde{\tau}} < 430$ GeV, and $m_{\tilde{\chi}_1^\pm} < 1.09$ TeV.

4 Search for Delayed Jets

Delayed jets may be produced in GMSB models with pair-produced gluinos, each of which forms an R -hadron and then decays to a gluon and a gravitino. The gravitino is stable and invisible, serving as the lightest SUSY particle (LSP), and induces missing energy in the event. Such jets are likely to be displaced beyond the tracker volume, reducing the sensitivity of existing searches for displaced vertices. A search for such events was performed with the CMS detector, using 137.4 fb^{-1} of 13 TeV pp collision data, comprising the full LHC Run 2 dataset ⁶. This is the first use of the electromagnetic calorimeter (ECAL) timing measurement to distinguish displaced jets from SM jets, with the signal region defined to include events with at least one jet having $t_{\text{jet}} > 3$ ns. The backgrounds arise mainly from instrumental sources. These backgrounds are rejected using selections on information from different subdetectors. To estimate the remaining background in the signal region, the efficiencies of the various selections are measured in data control regions. The total background, including contributions from beam halo, core and satellite bunches, and cosmic rays, is predicted to be $1_{-1}^{+2.5}$ event, in agreement with the observation of 0 events. Based on this measurement, the search excludes $m_{\tilde{g}} < 2.5$ TeV for $c\tau_0 \approx 1$ m, or $m_{\tilde{g}} < 2.0$ TeV for $c\tau_0 \approx 10$ m. As shown in Fig. 1 (right), these limits significantly improve on previous tracker-based searches for displaced jets when considering $c\tau_0 > 1$ m.

5 Search for Displaced Hadronic Jets

In a simplified hidden sector model with a heavy neutral boson Φ that decays to light scalars s as $\Phi \rightarrow ss \rightarrow ff'f'$, displaced hadronic jets will be produced if the scalars are long-lived. A search was conducted for this signature using the ATLAS experiment, with custom triggers to select events of interest in the observed data ⁷. These triggers use the quantity $CalRatio$, which is

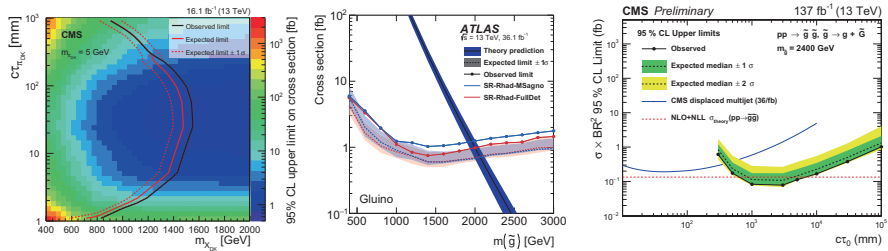


Figure 1 – Left: 95% CL limits on emerging jets in the plane of $m_{\pi_{DK}}$ and $c\tau_{\pi_{DK}}$, for $m_{\pi_{DK}} = 5 \text{ GeV}^4$. Center: 95% CL limits on stable gluino R -hadrons from the search for heavy charged LLPs⁵. Right: 95% CL limits on gluino R -hadrons with $m_{\tilde{g}} = 2400 \text{ GeV}$ versus $c\tau_0$, comparing a previous tracker-based displaced search to the new ECAL-based delayed jet search⁶.

defined as $E_{\text{HCAL}}/E_{\text{ECAL}}$. There are separate high- E_T and low- E_T criteria; the former processed 33.0 fb^{-1} of 13 TeV data, while the latter was introduced later in the run and processed 10.8 fb^{-1} of data. Separate data streams for cosmic and beam-induced background (BIB) were collected in addition in order to characterize these backgrounds. A multilayer perceptron (MLP) is trained to predict the jet decay position. The result from this MLP and various jet- and track-related quantities are provided as input to a boosted decision tree (BDT) that classifies jets as signal, QCD, or BIB. This classification and several event-level variables are provided as input to event BDTs that are optimized for the high- E_T and low- E_T cases. These event BDTs are able to reject all of the cosmic and BIB events in the signal region. The remaining background from QCD multijet events is estimated using control regions defined by $\sum \Delta R_{\text{min}}(\text{jets}, \text{track})$ and the event BDT score. A simultaneous fit to signal and background in the signal region and control regions is performed, finding agreement between the observation and the background prediction. 95% CL upper limits are set on the product of the cross section and branching fraction for various models, shown in Fig. 2 (left).

6 Search for Supersymmetry with Disappearing Tracks

Disappearing tracks may occur in highly compressed models of strong SUSY production, with $\Delta m(\tilde{\chi}_1^\pm, \tilde{\chi}_1^0) \approx 100 \text{ GeV}$ and $c\tau(\tilde{\chi}_1^\pm) \approx 50 \text{ cm}$. The $\tilde{\chi}_1^\pm$ decays to a $\tilde{\chi}_1^0$ and a π^\pm with momentum too low to be detected. A search for strong SUSY with disappearing tracks was conducted using 137.4 fb^{-1} of data collected with the CMS experiment⁸. The search requires at least two jets, the transverse mass $M_{T2} > 200 \text{ GeV}$, and at least one short track (ST). 68 search regions are defined, based on intervals in the number of jets, H_T , the ST length, and the ST p_T . To predict the SM background, the misidentification rate for STs is applied to ST candidates with relaxed quality and isolation requirements. Figure 2 (center) shows the exclusion of $m_{\tilde{g}} < 2.46 \text{ TeV}$ and $m_{\tilde{\chi}_1^0} < 2.0 \text{ TeV}$, an improvement of 210 GeV and 525 GeV, respectively, compared to the traditional SUSY search without any disappearing tracks.

7 Search for Displaced Vertex and Muon

Displaced vertices and muons may be produced in RPV supersymmetry if the RPV coupling is small, leading to suppressed decays and the formation of R -hadrons. In particular, this search considers a model in which the top squark is the LSP and the λ'_{23k} coupling is active, coupling the top squark to a muon and any quark. The search is performed with the full Run 2 dataset of 136 fb^{-1} collected with the ATLAS experiment⁹. Two orthogonal signal regions are defined based on the triggers: the first requires $p_T^{\text{miss}} > 180 \text{ GeV}$, while the second requires $p_T(\mu) > 60 \text{ GeV}$, $|\eta(\mu)| < 2.5$, and $p_T^{\text{miss}} < 180 \text{ GeV}$. A large-radius tracking algorithm

is used to reconstruct tracks with large impact parameters, and displaced vertices (DV) are reconstructed with a custom secondary vertex algorithm. To predict the backgrounds from cosmic rays, misidentified muons, and heavy flavor, transfer factors are computed in data control regions with different DV requirements and applied to data control regions with different muon selections. In the p_T^{miss} signal region, 0 events are observed, in agreement with the predicted background of $0.43 \pm 0.16 \pm 0.16$ events. In the muon signal region, 1 event is observed, in agreement with the predicted background of $1.88 \pm 0.20 \pm 0.28$ events. The search excludes $m_{\tilde{\tau}} < 1.7$ TeV for $\tau_{\tilde{\tau}} = 0.1$ ns, or $m_{\tilde{\tau}} < 1.3$ TeV for a wider range $0.01 < \tau_{\tilde{\tau}} < 30$ ns, as shown in Fig. 2 (right). These are the strictest limits to date for a metastable \tilde{t} decaying via an RPV coupling λ'_{ijk} . Model-independent limits on the number of signal events S_{obs}^{95} and the visible cross section σ_{vis} are also derived: $S_{\text{obs}}^{95} = 3.1$ and $\sigma_{\text{vis}} = 0.023$ fb in the p_T^{miss} signal region, and $S_{\text{obs}}^{95} = 3.7$ and $\sigma_{\text{vis}} = 0.027$ fb in the muon signal region.

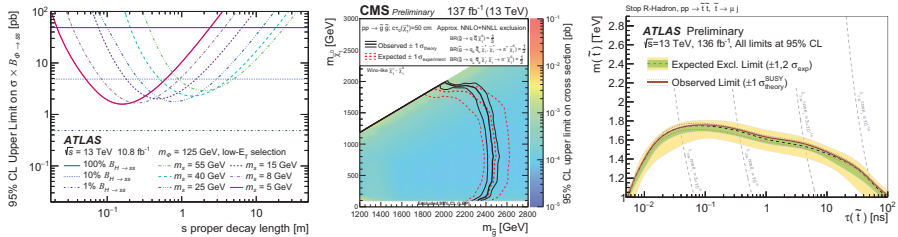


Figure 2 – Left: 95% CL limits from the displaced hadronic jet search on the product of the cross section and branching fraction for models with low-mass Φ , versus the proper decay length⁷. Center: 95% CL limits in the plane of $m_{\tilde{g}}$ versus $m_{\tilde{\chi}_0^0}$ for the disappearing track search⁸. Right: 95% CL limits on $m_{\tilde{\tau}}$ as a function of $\tau_{\tilde{\tau}}$ for the displaced muon search⁹.

8 Conclusions

There is a growing interest in collider searches for new physics with unconventional signatures. This proceeding surveys a wide variety of recent searches for emerging jets, heavy charged long-lived particles, delayed jets, displaced hadronic jets, disappearing tracks, and displaced muons. These searches include results from both the ATLAS and CMS experiments using the full LHC Run 2 dataset at a center-of-mass energy of 13 TeV. In general, the searches are sensitive to decay lengths from 1 mm to 100 m and beyond, and exclude many new particles with masses up to ≈ 1 –2 TeV. Future possibilities for these searches are addressed in the recent white paper, Ref.¹⁰.

© CERN for the benefit of the ATLAS and CMS Collaborations. CC-BY-4.0 license.

References

1. ATLAS Collaboration, *JINST* **3** (2008) S08003.
2. CMS Collaboration, *JINST* **3** (2008) S08004.
3. P. Schwaller, D. Stolarski, and A. Weiler, *JHEP* **05** (2015) 059, [arXiv:1502.05409](#).
4. CMS Collaboration, *JHEP* **02** (2019) 179, [arXiv:1810.10069](#).
5. ATLAS Collaboration, [arXiv:1902.01636](#).
6. CMS Collaboration, CMS Physics Analysis Summary CMS-PAS-EXO-19-001, 2019.
7. ATLAS Collaboration, [arXiv:1902.03094](#).
8. CMS Collaboration, CMS Physics Analysis Summary CMS-PAS-SUS-19-005, 2019.
9. ATLAS Collaboration, ATLAS Conference Note ATLAS-CONF-2019-006, 2019.
10. J. Alimena et al., [arXiv:1903.04497](#).

SEARCHES FOR DARK MATTER AT ATLAS AND CMS

DEBORAH PINNA, on behalf of the ATLAS and CMS Collaborations
Boston University

Evidence of the existence of dark matter is provided by astrophysical observations, but its nature or non-gravitational interactions still remain elusive. Dark matter might be produced at the LHC if it consists of weakly interacting massive particles. A selection of the most recent ATLAS and CMS dark matter searches is presented.

1 Introduction

Proof of the existence of dark matter (DM) in our universe is provided by various astrophysical observations^{1,2,3}, but the DM nature or its non-gravitational interactions still remain elusive.

One of the most studied scenarios assumes DM to be a stable, weakly interacting massive particle, which can be produced in high energy collisions at the LHC⁴. If produced, the DM will leave no direct traces in the detector but its presence can be inferred by a large transverse momentum imbalance (MET) when produced in association with a detectable physics object. Such searches are usually referred as mono-X searches, where X identifies the visible object.

A convenient framework to interpret mono-X results is provided by simplified models⁵, where the DM particles are produced via new mediators that couple both to DM and standard model (SM) particles. These models are appealing benchmarks for DM searches due to the limited number of parameters (DM mass, mediator mass and couplings) that enclose the relevant physics process features, and because kinematically distinct set of parameters can be identified⁵.

Mono-X searches share a common analysis strategy, which exploits the presence of a high p_T object X produced in association with the DM particles. Signal events will then appear as an excess of events in the tail of the MET distribution over SM expectations, making DM searches very challenging due to the absence of a striking signature. In addition, a precise modeling and evaluation of SM processes in the signal region (SR) is essential, which is achieved through dedicated control regions (CR) enriched in the background of interest. The results are then extracted comparing the SM predictions to data and if no significant excess is found the results are interpreted in terms of benchmark models. Other experimental challenges associated with mono-X searches include the need of an accurate energy calibration and resolution of the visible objects as well as a precise particle reconstruction and identification.

2 Spin-1 mediator: simplified and extended sectors

Assuming Dirac fermion DM particles produced via a spin-1 mediator Z' , the vector and axial-vector interactions are described by the interaction Lagrangians:

Copyright 2019 CERN for the benefit of the ATLAS and CMS Collaborations. CC-BY-4.0 license.

$$\mathcal{L}_{\text{vector}} \supset g_q \sum_q Z'_\mu \bar{q} \gamma^\mu q, \quad \mathcal{L}_{\text{axial-vector}} \supset g_q \sum_q Z'_\mu \bar{q} \gamma^\mu \gamma^5 q \quad (1)$$

where the coupling g_q is assumed to be equal for all quarks. Mono-X signatures that increase the cross section, as mono-jet, or that despite the lower cross section achieve a higher background rejection, as mono-photon or mono- V/Z' ($V=W, Z$), are the most sensitive to these interactions.

The ATLAS collaboration⁶ considers hadronically-decaying high- p_T V/Z' bosons recoiling against large MET⁸. The number of jets in the final state depends on the V/Z' Lorentz boost: for a large boost ($p_T > 200$ GeV) the vector boson is reconstructed as a single large-radius jet, otherwise as two separate small-radius jets. Consistency with hadronic V/Z' decays is guaranteed by requirements on the large-radius jet invariant mass and substructure quantities. The main backgrounds consist of $t\bar{t}$, $Z(\nu\nu)$, and $W(l\nu)$ +jets events, which are estimated from data in dedicated CRs. The results are then extracted by a simultaneous fit in SRs and CRs to the MET distributions. No significant excess above SM expectation is observed and the results are interpreted in terms of models where the interaction is mediated by a Z' boson (simplified vector model), or an additional heavier fermion (dark-fermion model) or Higgs boson (dark-Higgs model) is also assumed in the dark sector. The corresponding 95% confidence level limits are presented in Fig. 1. This is the first search for DM associated production with a Z' boson.

The CMS⁷ mono-photon analysis⁹ follows a similar strategy, selecting events with a high- p_T photon and large MET. Energy deposits in the calorimeter produced by mechanisms other than proton-proton collisions can be misidentified as photons. This challenging background is reduced to negligible amounts with dedicated requirements on the shape and time of the electromagnetic shower. The remaining background are from $Z(\nu\nu) + \gamma$, and $W(l\nu) + \gamma$ events. No significant excess above SM expectation is observed and the results are interpreted in terms of spin-1 benchmark models. The results for the vector hypothesis are shown in Fig. 1 left.

Simplified models also predict mediator decays back to SM particles. For this reason, at the LHC signatures beyond mono-X can also provide important constraints on DM models parameters, as shown in Fig. 1 where ATLAS dijet searches are compared to mono-X results for a spin-1 vector mediator¹⁰. It can be seen that their interplay highly depends on the g_q value and that both type of signatures are essential in the hunt for DM.

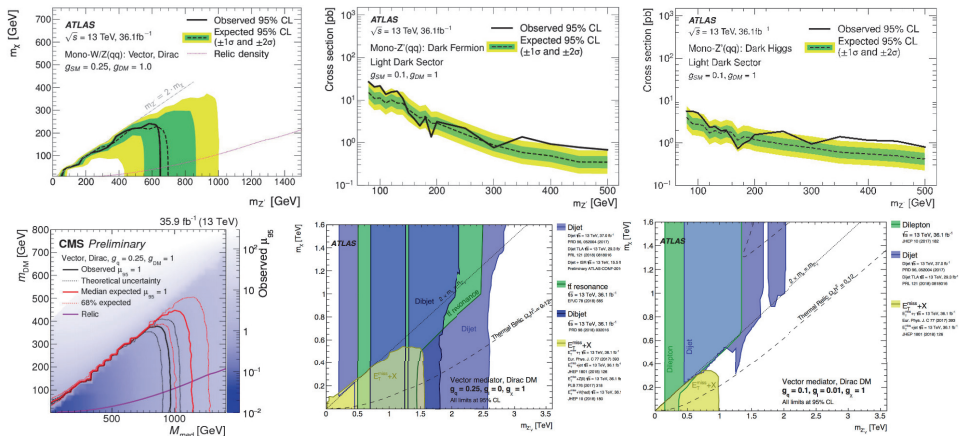


Figure 1 – Exclusion limits at 95% confidence level on DM produced in association with V/Z' ⁸, assuming a simplified vector (upper left), dark-fermion (upper center), a dark-Higgs (upper right) model. The DM interpretation for vector interactions is presented for the mono-photon search⁹ (lower left) and for the comparison of mono-X and dijet searches¹⁰ assuming $g_q = 0.25$ (lower center) or $g_q = 0.1$ (lower right).

3 Spin-0 mediator: simplified and extended sectors

Assuming the DM particles to be Dirac fermions, the interaction Lagrangian terms for the production of a scalar or pseudoscalar mediator particle can be expressed as:

$$\mathcal{L}_{\text{scalar}} \supset \frac{\phi}{\sqrt{2}} \sum_q (g_v y_q \bar{q} q), \quad \mathcal{L}_{\text{pseudoscalar}} \supset \frac{iA}{\sqrt{2}} \sum_q (g_v y_f \bar{q} \gamma^5 q) \quad (2)$$

where y_q are the Yukawa couplings. Spin-0 interactions present a cross-section proportionality on the quark mass, hence the mediator couples preferentially to top quarks. The CMS search¹¹ for the associated production of DM with a single top quark (DM+t) or a top quark pair (DM+tt) is performed with a similar strategy to the previously mentioned results. Final states with zero or one lepton from the top quark decay are considered and events are categorized based on the number of b-tagged and forward jets ($|\eta| > 2.4$). The main backgrounds consist of $t\bar{t}$ and V+jets events, which are estimated from data in dedicated CRs. The results are then extracted by a simultaneous fit in SRs and CRs to the MET distribution. No significant excess above SM expectation is observed and the results are interpreted in terms of spin-0 benchmark models, as presented in Fig. 2. This is the first search looking for DM+t as well as DM+tt events.

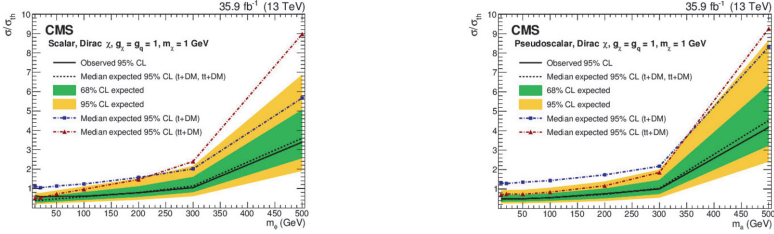


Figure 2 – Exclusion limits on DM production cross section normalized by the theoretical value for the associated production with one or two top quarks, assuming a scalar (left) or pseudoscalar (right) interaction¹¹.

4 Higgs boson: extended sectors and invisible decays

The Higgs boson can also be considered as a detectable physics object in DM searches, and this mono-H signature is considered by ATLAS and CMS for different H decay modes. The CMS collaboration considers H decays to WW or ZZ in final states with two or four leptons¹², respectively. This signatures, despite the low branching ratio, allow an effective background rejection. A similar strategy to the previous analyses is adopted and no significant excess above SM expectation is observed in either decay mode. ATLAS and CMS searches also target the mono-H(bb) signature^{10,15,12,13,14}, which provides the highest sensitivity given the large statistics. Events where the Higgs candidate is reconstructed as a single large-radius jet or as two separate small-radius jets are considered. The major backgrounds are from $t\bar{t}$ and V+jets processes which are estimated from dedicated CRs. The results are extracted by a simultaneous fit in SRs and CRs to distributions associated to the MET or the Higgs boson kinematic. No significant excess above SM expectations is observed and the results are interpreted in terms of benchmark models where the H boson is radiated by a Z' mediator (Z' baryonic), or in extended 2HDM scenarios where a Z' boson or a light pseudoscalar particle are also considered (Z' -2HDM and 2HDM+a respectively), as shown in Fig. 3. CMS mono-H(VV) and mono-H(bb) results are also combined (Fig. 3 left), showing their complementarity as a function of the mediator mass.

The Higgs boson might mediate the interaction between the DM and SM sectors. Decays of the H boson into DM will cause an enhancement of the H to invisible branching ratio over the SM predictions. Assuming SM-like H boson production, the vector-boson fusion mode has

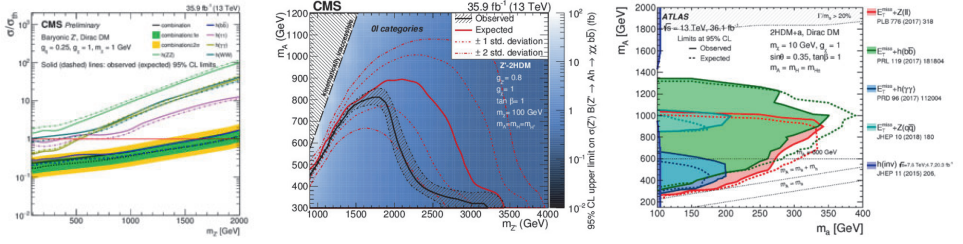


Figure 3 – Expected and observed exclusion 95% confidence level limits on DM produced in association with a H bosons assuming a Z' baryonic¹² (left), a Z' -2HDM¹⁴ (center), or a 2HDM+a¹⁰ (right) model.

the highest sensitivity and events are required to have high MET and two forward jets. It is therefore essential for experiments to have an excellent calorimetry in the forward region. ATLAS and CMS exclude H to invisible branching ratios below 0.26 and 0.19 respectively, when combining results from data collected at different center-of-mass energies^{16,17}. These results are also translated in terms of spin-independent DM-nucleon scattering cross section limits and compared to the most recent direct detection results, as shown in Fig. 4.

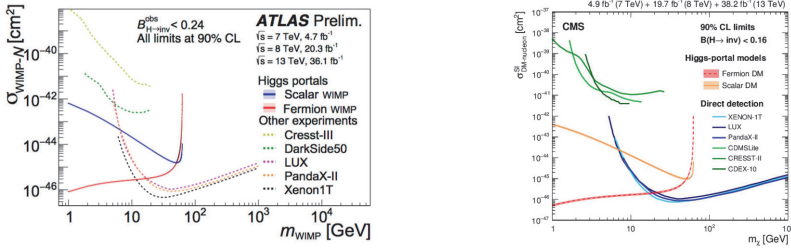


Figure 4 – Inferred 90% confidence level limits on spin-independent DM-nucleon scattering cross section for Higgs decays to invisible performed by ATLAS¹⁶ (left) and CMS¹⁷ (right), compared with the most recent results from direct-detection experiments.

References

1. F. Zwicky, *Helv. Phys. Acta* **6**, 110 (1933).
2. V. C. Rubin and W. K. Ford, Jr., *Astrophys. J.* **159**, 379 (1970)
3. D. Clowe *et al*, *Astrophys. J.* **648**, L109 (2006)
4. G. Bertone *et al*, *JCAP* **03**, 026 (2018)
5. D. Abercrombie *et al*, *arXiv* **1507.00966**, (2015)
6. ATLAS Collaboration, *JINST* **3**, S08003 (2008)
7. CMS Collaboration, *JINST* **3**, S08004 (2008)
8. ATLAS Collaboration, *JHEP* **10**, 180 (2018)
9. CMS Collaboration, *JHEP* **02**, 074 (2019)
10. ATLAS Collaboration, *arXiv* **1903.01400**, (2019)
11. CMS Collaboration, *JHEP* **03**, 141 (2019)
12. CMS Collaboration, *CMS-PAS-EXO-18-011*, <http://cds.cern.ch/record/2665233>
13. CMS Collaboration, *Eur. Phys. J* **C79**, 280 (2019)
14. CMS Collaboration, *JHEP* **11**, 172 (2018)
15. ATLAS Collaboration, *ATLAS-CONF-2018-039*, <https://cds.cern.ch/record/2632344>
16. ATLAS Collaboration, *ATLAS-CONF-2018-054*, <https://cds.cern.ch/record/2649407>
17. CMS Collaboration, *arXiv* **1809.05937**, (2018)

EXPLORING LIGHT SUPERSYMMETRY WITH GAMBIT

A. KVELLESTAD, on behalf of the GAMBIT Collaboration
*Department of Physics, Imperial College London, Blackett Laboratory,
Prince Consort Road, London SW7 2AZ, United Kingdom*

I summarize a recent study by the GAMBIT Collaboration in which we investigated the combined collider constraints on the chargino and neutralino sector of the Minimal Supersymmetric Standard Model. Through a large fit using GAMBIT we found that current ATLAS and CMS results with 36 fb^{-1} of 13 TeV LHC collision data do not provide a general constraint on the lightest neutralino and chargino masses. Further, we found that a pattern of excesses in some of the LHC analyses can be fit in a subset of the model parameter space. The excess has an estimated local significance of 3.3σ based on the 13 TeV results alone, and 2.9σ when 13 TeV and 8 TeV results are combined.

Due to its potential for solving problems such as the hierarchy problem and dark matter, weak-scale supersymmetry (SUSY) has long been among the best motivated scenarios for experimentally accessible physics beyond the Standard Model (SM). A commonly studied realisation of SUSY is the Minimal Supersymmetric Standard Model (MSSM), in which large parametric freedom is used to express ignorance about what mechanism is responsible for breaking SUSY. As a consequence the MSSM parameter space encompasses a wide range phenomenological scenarios, making it both a useful and challenging target for experiments.

Searches for SUSY particles by the ATLAS and CMS experiments at the LHC are typically optimised on so-called “simplified models”. In these models only the few lightest SUSY particles are assumed to contribute to the targeted signal. This assumption reduces the size of the relevant parameter space to a manageable size for experimental optimisation—typically two or three masses and/or branching ratios. A downside of this approach, however, is that it is not clear to what extent the resulting experimental constraints on the simplified models also apply in more realistic SUSY realisations such as the MSSM. This question motivated a recent study by the GAMBIT Collaboration, in which we investigated the constraints on the full neutralino and chargino sector (the *electroweakino* sector) of the MSSM resulting from a combination of 13 TeV LHC results and other collider constraints.¹

For this study we assumed that all sparticles except the neutralinos and charginos are too heavy to impact current LHC searches. This assumption limits the relevant electroweak MSSM parameter space to only four free parameters: the bino mass parameter M_1 , the wino mass parameter M_2 , the Higgsino mass parameter μ , and the ratio of the vevs for the two Higgs doublets $\tan\beta$. We name this four-parameter model EWMSSM.

Using GAMBIT,² and in particular the SpecBit, DecayBit and ColliderBit modules,^{3,4} we performed a fit of the EWMSSM to recent results from 13 TeV ATLAS and CMS searches for charginos and neutralinos. See Ref. 1 for details of the included analyses. At each sampled EWMSSM parameter point we ran full Monte Carlo simulations of the LHC searches and used the predicted signal rates to formulate a proper joint likelihood for our fit. In this likelihood function we also included other relevant collider observables, namely the Z and Higgs invari-

ble decay widths and SUSY cross-section limits from LEP. To efficiently explore the parameter space we used the Diver differential evolution sampler in ScannerBit.⁵ After the parameter scan we repeated our LHC simulations with higher event statistics for all parameter samples within the identified best-fit parameter regions, going up to 64 million events per point for the 500 highest-likelihood points.

The main results of our analysis are displayed in Fig. 1, which shows the profile likelihood ratio in different planes of neutralino and chargino masses. The star indicates the best-fit point while the white contours outline the 1σ and 2σ confidence regions. We see that, when combined, the current collider data prefers a specific pattern of low-mass solutions in the EWMSSM, with the lightest neutralino below ~ 200 GeV (top left panel) and the heaviest neutralino below ~ 700 GeV (bottom right panel) at the 2σ level. In these scenarios the lightest neutralino is dominantly bino, but with a non-negligible Higgsino or wino component. Another characteristic of the best-fit region is the presence of two $\gtrsim m_Z$ gaps in the electroweakino mass spectrum.

There are a number of small data excesses in some of the LHC searches, most importantly the ATLAS SUSY searches for 2-, 3- and 4-lepton final states.^{6,7,8} We found that these excesses can be simultaneously fit in the EWMSSM, explaining the preference for low-mass solutions in our result. The excesses are seen in signal regions that target leptons coming from decays of on-shell SM gauge bosons. This is why our fit favours spectra with mass differences large enough to produce on-shell Z's and W's in the sparticle decays. The LHC search displaying the strongest tension with our best-fit scenario is the CMS search for multi-lepton final states,⁹ as further discussed in Ref. 1. Through dedicated Monte Carlo simulations of our likelihood ratio test statistic, we estimated the local significance of the combined excess to be 3.3σ when using our best-fit EWMSSM point as the signal hypothesis.

Our original fit did not include simulations of 8 TeV SUSY searches, as this would essentially have doubled the computational expense of our study. To investigate the impact of 8 TeV results on the EWMSSM scenarios preferred by our fit we therefore post-processed the parameter samples in the 1σ region with simulations of several 8 TeV ATLAS and CMS analyses. The result was a small shift of the best-fit point towards higher masses—the best-fit value for the lightest neutralino mass moved from 49.4 GeV to 67.3 GeV—accompanied by a reduction in the local significance, from 3.3σ to 2.9σ .

Regardless of whether the current excess turns out to be an early hint of new physics or not, our result highlights a caveat regarding the interpretation of constraints derived for simplified SUSY models: A mass hypothesis for the lighter electroweakinos that is excluded in a simplified model, may still be perfectly viable—and even preferred—within the more general MSSM electroweakino sector. There are several reasons for this. First, the additional signal processes introduced by the heavier neutralinos and charginos can provide improved fits to other analyses/signal regions, which in a proper statistical combination can compensate for the bad fit to the analysis/signal region that excluded the simplified model scenario. Second, for LHC analyses that only make use of the signal region with the best expected exclusion sensitivity, the heavier electroweakino states can affect which signal region is identified as the most sensitive one. Third, even though a simplified model scenario and an MSSM scenario may have identical masses for the lighter electroweakinos, the bino/wino/Higgsino admixture of these states may differ, affecting the production cross-sections and branching ratios. All these effects are at play in our fit.

Acknowledgments

I thank my colleagues in the GAMBIT community for collaboration on the work presented here, and acknowledge PRACE for granting GAMBIT access to the Marconi supercomputer at CINECA, Italy.

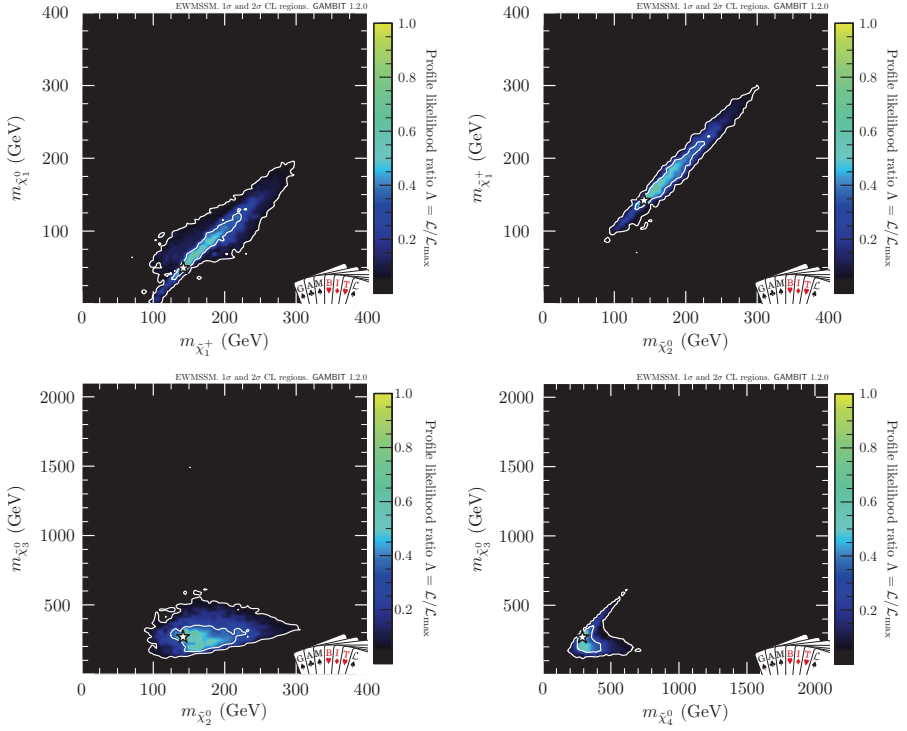


Figure 1 – The profile likelihood ratio shown for the following planes of neutralino and chargino masses: $(m_{\tilde{\chi}_1^\pm}, m_{\tilde{\chi}_1^0})$, $(m_{\tilde{\chi}_2^0}, m_{\tilde{\chi}_1^\pm})$, $(m_{\tilde{\chi}_2^0}, m_{\tilde{\chi}_3^0})$ and $(m_{\tilde{\chi}_4^0}, m_{\tilde{\chi}_3^0})$. The white contours outline the 1 σ and 2 σ confidence regions and the best-fit point is indicated by the white star.

References

1. GAMBIT Collaboration: P. Athron, C. Balázs, *et. al.*, *Combined collider constraints on neutralinos and charginos*, arXiv:1809.02097.
2. GAMBIT Collaboration: P. Athron, C. Balázs, *et. al.*, *GAMBIT: The Global and Modular Beyond-the-Standard-Model Inference Tool*, *Eur. Phys. J. C* **77** (2017) 784, [arXiv:1705.07908].
3. GAMBIT Models Workgroup: P. Athron, C. Balázs, *et. al.*, *SpecBit, DecayBit and PrecisionBit: GAMBIT modules for computing mass spectra, particle decay rates and precision observables*, *Eur. Phys. J. C* **78** (2018) 22, [arXiv:1705.07936].
4. GAMBIT Collider Workgroup: C. Balázs, A. Buckley, *et. al.*, *ColliderBit: a GAMBIT module for the calculation of high-energy collider observables and likelihoods*, *Eur. Phys. J. C* **77** (2017) 795, [arXiv:1705.07919].
5. GAMBIT Scanner Workgroup: G. D. Martinez, J. McKay, *et. al.*, *Comparison of statistical sampling methods with ScannerBit, the GAMBIT scanning module*, *Eur. Phys. J. C* **77** (2017) 761, [arXiv:1705.07959].
6. ATLAS Collaboration: M. Aaboud *et. al.*, *Search for electroweak production of supersymmetric particles in final states with two or three leptons at $\sqrt{s} = 13$ TeV with the ATLAS detector*, *Eur. Phys. J. C* **78** (2018) 995, [arXiv:1803.02762].
7. ATLAS Collaboration: M. Aaboud *et. al.*, *Search for chargino-neutralino production using recursive jigsaw reconstruction in final states with two or three charged leptons in proton-proton collisions at $\sqrt{s} = 13$ TeV with the ATLAS detector*, *Phys. Rev. D* **98** (2018) 092012, [arXiv:1806.02293].
8. ATLAS Collaboration: M. Aaboud *et. al.*, *Search for supersymmetry in events with four or more leptons in $\sqrt{s} = 13$ TeV pp collisions with ATLAS*, *Phys. Rev. D* **98** (2018) 032009, [arXiv:1804.03602].
9. CMS Collaboration, *Search for electroweak production of charginos and neutralinos in multilepton final states in pp collision data at $\sqrt{s} = 13$ TeV*, Tech. Rep. CMS-PAS-SUS-16-039, CERN, Geneva, 2017.

Sneutrino dark matter - status and perspectives

Suchita Kulkarni

*Institut für Hochenergiephysik, Österreichische Akademie der Wissenschaften, Nikolsdorfer Gasse 18, 1050
Wien, Austria*



The existence of neutrino masses is one of the strongest reasons for searching for beyond the Standard Model physics. Extension of the Standard Model to accommodate neutrino masses often gives rise to right handed neutrinos. Supersymmetric versions such extensions, come equipped with the right handed sneutrino dark matter and give rise to either right handed or left right mixed sneutrino dark matter candidates. We review two of such models and their associated LHC phenomenology. We also present a wishlist to go beyond the existing status of such sneutrino dark matter scenarios.

1 Introduction

While there is plenty of evidence that the existing knowledge of elementary particle physics in the form of the Standard Model of particle physics is incomplete, the searches for beyond the Standard Model (BSM) signals at several ongoing experiments have provided little conclusive evidence so far. In this light, it has become important to analyse and understand the impact of experimental searches for a variety of BSM scenarios in unbiased attitude. Within the context of supersymmetry, this approach implies exploring supersymmetric scenarios beyond those featuring well studied neutralino dark matter. Plenty of viable alternative supersymmetric scenarios exists and one such alternative is that of sneutrino dark matter. The exiting understanding of particle physics properties of dark matter is consistent with a charge and color neutral, stable particle. Within the so called Minimal Supersymmetric Standard Model (MSSM) it is possible to realise both the neutralino and sneutrino dark matter candidates, however the sneutrino dark matter being the superpartner of the SM neutrino, can only be left handed and has been ruled out by the dark matter direct detection constraints in combination with the invisible Z decay width.

The observational evidence of neutrino masses on the other hand points to the existence of right handed neutrinos and is also a strong evidence for BSM physics. Supersymmetric versions of extensions of the SM containing right handed neutrinos lead to right handed sneutrino. The resulting sneutrino dark matter is a mixture of left and right handed sneutrino. Such scenario will henceforth be referred to as mixed sneutrino dark matter. From the point of view of early Universe phenomenology such mixed sneutrino dark matter presents interesting scenarios. Depending on the amount of left - right mixing, such sneutrino dark matter candidate can feature a thermal or

non-thermal relic density generation. If the sneutrino dark matter is completely right handed it can not achieve thermal equilibrium with the SM bath and the relic density must be generated non-thermally e.g. from the decay of a heavier supersymmetric particle. In the literature, both the thermal and non-thermal sneutrino dark matter candidate has been explored. Here, we will focus on thermal sneutrino dark matter. A generic feature of sneutrino dark matter is existence of both left and right handed sneutrino. However, the actual model building and possible couplings of sneutrino to SM particles depend on the exact neutrino mass generation mechanism used. Here we take the example of two different sneutrino dark matter models and illustrate their phenomenology. It is however important to notice that this does not exhaust the sneutrino dark matter model space.

2 Minimal sneutrino dark matter model MSSM + RN

To begin with, it is an appealing possibility to extend the MSSM with right handed sneutrino component which comes about as a superpartner of the right handed neutrino component. Such model was considered e.g. in ^{1,2,3,4}. Here we take a specific example of Dirac right handed neutrino superfield, with lepton number violating terms absent.

The superpotential for Dirac RH neutrino superfield is given by

$$W = \epsilon_{ij}(\mu \hat{H}_i^u \hat{H}_j^d - Y_i^{IJ} \hat{H}_i^d \hat{L}_j^I \hat{R}^J + Y_\nu^{IJ} \hat{H}_i^u \hat{L}_j^I \hat{N}^J), \quad (1)$$

where Y_ν^{IJ} is a matrix in flavor space (which we choose to be real and diagonal), from which the mass of neutrinos are obtained as $m_D^I = v_u Y_\nu^{II}$. Note that lepton-number violating terms are absent in this scheme. The additional scalar fields contribute with new terms in the soft-breaking potential

$$V_{\text{soft}} = (M_L^2)^{IJ} \tilde{L}_i^* \tilde{L}_j^I + (M_N^2)^{IJ} \tilde{N}^{I*} \tilde{N}^J - [\epsilon_{ij}(\Lambda_i^{IJ} H_i^d \tilde{L}_j^I \tilde{R}^J + \Lambda_\nu^{IJ} H_i^u \tilde{L}_j^I \tilde{N}^J) + \text{h.c.}], \quad (2)$$

where both matrices M_N^2 and Λ_ν^{IJ} are real and diagonal, $M_N^2 = \text{diag}(m_{N^k}^2)$ and $\Lambda_\nu^{IJ} = \text{diag}(A_\nu^k)$, with $k = e, \mu, \tau$ being the flavor index. In the sneutrino interaction basis, defined by the vector $\Phi^\dagger = (\tilde{\nu}_L^*, \tilde{N}^*)$, the sneutrino mass potential is

$$V_{\text{mass}}^k = \frac{1}{2} \Phi_{LR}^\dagger \mathcal{M}_{LR}^2 \Phi_{LR}, \quad (3)$$

with the squared-mass matrix \mathcal{M}_{LR}^2

$$\mathcal{M}_{LR}^2 = \begin{pmatrix} m_{L^k}^2 + \frac{1}{2} m_D^2 \cos(2\beta) + m_D^2 & \frac{1}{\sqrt{2}} A_\nu^k v \sin \beta - \mu m_D / \tan \beta \\ \frac{1}{\sqrt{2}} A_\nu^k v \sin \beta - \mu m_D / \tan \beta & m_{N^k}^2 + m_D^2 \end{pmatrix}. \quad (4)$$

Here, $m_{L^k}^2$ are the soft mass terms for the three SU(2) leptonic doublets, $\tan \beta = v_u / v_d$ and $v^2 = v_u^2 + v_d^2 = (246 \text{ GeV})^2$, with $v_{u,d}$ the usual Higgs vacuum expectation values (vevs). The Dirac neutrino mass m_D is small and can be safely neglected.

The off-diagonal term determines the mixing of the LH and RH fields. If $A_\nu^k = \eta Y_\nu$, that is if the trilinear term is aligned to the neutrino Yukawa, this term is certainly small compared to the diagonal entries and is therefore negligible. However, A_ν^k can in general be a free parameter and may naturally be of the order of the other entries of the matrix^{5,6}, thus inducing a sizeable mixing among the interaction eigenstates. The sneutrino mass eigenstates are then given by

$$\begin{pmatrix} \tilde{\nu}_{k_1} \\ \tilde{\nu}_{k_2} \end{pmatrix} = \begin{pmatrix} -\sin \theta_\nu^k & \cos \theta_\nu^k \\ \cos \theta_\nu^k & \sin \theta_\nu^k \end{pmatrix} \begin{pmatrix} \tilde{\nu}_L^k \\ \tilde{N}^k \end{pmatrix}. \quad (5)$$

The relevant parameters at the electroweak (EW) scale for the sneutrino sector are the two mass eigenvalues $m_{\tilde{\nu}_{k_1}}$ and $m_{\tilde{\nu}_{k_2}}$ and the mixing angle θ_ν^k , related to the A_ν^k term via

$$\sin 2\theta_\nu^k = \sqrt{2} \frac{A_\nu^k v \sin \beta}{(m_{\tilde{\nu}_{k_2}}^2 - m_{\tilde{\nu}_{k_1}}^2)}. \quad (6)$$

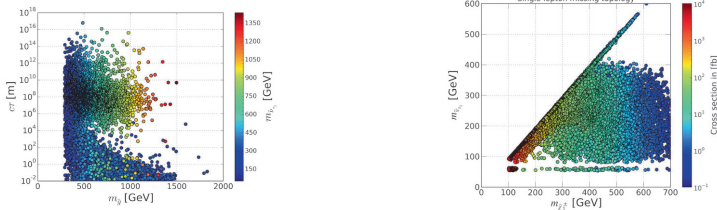


Figure 1 – MSSM+RN sneutrino dark matter parameter space leading to long lived gluinos (left) and single lepton + missing energy final state (right). In the left panel, color code shows the mass of the sneutrino while in the right panel the color code corresponds to the cross section of the final state.

The sneutrino coupling to the Z boson, which does not couple to $SU(2)_L$ singlets, is largely reduced by a sizeable mixing. This has a relevant impact on the sneutrino phenomenology, as discussed in, *e.g.*, Refs. ^{6,7,1,2}.

It is furthermore important to note that due to the Renormalization Group Equation (RGE) running of the new singlet superfield, treated by neglecting all lepton Yukawa couplings except the tau, will lead to light tau sneutrino compared to light electron or muon sneutrino. While the electron and muon sneutrino masses are degenerate, the mass difference between tau and other two sneutrino species is often less than 5 GeV.

In such scenario, the sneutrino is a mixture of left and right component and is a thermal dark matter. The relic density is obtained by annihilations either via the Higgs/ Z mediated diagrams or by coannihilation with the stau. Among others, existence of light sneutrino dark matter (< 10 GeV) prior to Higgs discovery was demonstrated ⁴, for the light sneutrino region constraints from indirect detection due to capture in the Sun were also studied ². Post Higgs discovery, it was shown that the light sneutrino region is no longer viable ⁸. This work also concentrated on the LHC phenomenology and analysed multilepton signatures, in particular also showing the possibility of long lived staus. Following on this work a global analysis of the mixed sneutrino dark matter parameter space was performed ⁹, in particular demonstrating the applicability of LHC simplified model results derived for neutralino dark matter used for sneutrino dark matter. It further showed the complementarity between direct detection and LHC results showing that distinct and complimentary regions of parameter space are within reach by these two approaches. Figure 1 ⁹ shows the parameter space consistent with the 8 TeV LHC and phenomenological constraints which leads to long lived gluinos (left) and single leptons plus missing energy final state (right). The long lived gluinos appear as an outcome of suppressed couplings between gluinos and sneutrino and can thus have a large mass gap between progenitor and the outgoing sneutinos. The single lepton plus missing energy final state is on the other hand outcome of pair production of chargino - neutralino, where the chargino decays to sneutrino via a lepton and the neutralino decays invisibly via a SM neutrino. Such final state has a significant cross section at LHC and should be explored in more details, possibly via an addition of an initial state radiation to help control the backgrounds. Possibility of constraining sneutrino dark matter at neutrino telescopes was further studied in ¹⁰.

3 GUT scale sneutrino dark matter model BLMSSM

The model construction of such a BLMSSM scenario relies on extension of the Standard Model by $U(1)_{B-L}$ gauge symmetry. This symmetry provides with an additional gauge boson Z' , which by construction is an anomalous model. Addition of three fermionic species which can be identified with the right handed neutrinos, is necessary in order to cancel this anomaly. Among other, ¹¹ studied the dark matter phenomenology of such a scenario. They demonstrated that with the GUT scale realisations of this model, the strongest constraints arise from the resonance searches for the Z' to dilepton final states pushing the mass limits on Z' to multi-TeV and the searches for gluino at the LHC. These two combined, push the scale of soft parameters to multi-TeV scales and

therefore leading to overall heavy spectrum. It is however demonstrated that within such scenarios the dark matter phenomenology is curious, in which one does not have to rely on SM sector or heavy Higgs mediators for dark matter thermalisation to take place but it can rather be achieved by additional gauge or the Higgs bosons coming from the extended gauge groups.

The LHC phenomenology of such GUT scale model presents alternative challenges. For one thing, the existing constraints on gluino and Z' searches do not help for keeping an overall light particle spectrum, on the other hand, suppressed couplings between the SM and the sneutrino due to left right mixing lead to small direct sneutrino production cross sections at the LHC. Among possible processes are, sneutrino pair production via the SM Higgs boson, which necessitates an off-shell Higgs boson for most parameter space and is suppressed. Alternatively, one could hope to produce supersymmetric particles via the decays of the Z' gauge boson, such a gauge boson could create a pair of sneutrino LSP-NLSP and the NLSP could decay leading to a $Z + \text{LSP}$. Such mono- Z final state however will require higher center-of-mass energy and is best explored at future colliders. Finally, it is still possible to produce light sleptons at the LHC and study their subsequent decays to sneutrino LSP. An interesting observation here is that the Z' can possibly have large decay width due to its potential decays to multiple susy particles¹². Such large width Z' do not appear in minimal $B - L$ scenarios and hence are a distinct feature of supersymmetric versions.

Sneutrino dark matter, thus offer a rich phenomenology, model building and can potentially lead to new LHC analyses. It however remains to be seen, which areas of parameter space are uncovered by the current constraints from LHC, flavour as well as astrophysical constraints. Global fits to sneutrino dark matter will thus prove to be a crucial step in this direction. To this extent it is also imperative to perform a reinterpretation of the Long Lived Particle searches from ATLAS/CMS collaborations for the sneutrino dark matter scenarios, in particular to constrain the long lived gluinos which are abundant, further analysis of this parameter space can lead to so far unidentified search opportunities at the LHC. Finally, it is equally important to analyse sneutrino dark matter at future colliders. At their formative stages the designs of future colliders can this be influenced to cover the differences between sneutrino and neutralino dark matter.

References

1. C. Arina and N. Fornengo, *Sneutrino cold dark matter, a new analysis: Relic abundance and detection rates*, *JHEP* **11** (2007) 029, [0709.4477].
2. G. Belanger, M. Kakizaki, E. K. Park, S. Kraml and A. Pukhov, *Light mixed sneutrinos as thermal dark matter*, *JCAP* **1011** (2010) 017, [1008.0580].
3. G. Belanger, S. Kraml and A. Lessa, *Light Sneutrino Dark Matter at the LHC*, *JHEP* **07** (2011) 083, [1105.4878].
4. B. Dumont, G. Belanger, S. Fichet, S. Kraml and T. Schwetz, *Mixed sneutrino dark matter in light of the 2011 XENON and LHC results*, *JCAP* **1209** (2012) 013, [1206.1521].
5. F. Borzumati and Y. Nomura, *Low scale seesaw mechanisms for light neutrinos*, *Phys. Rev.* **D64** (2001) 053005, [hep-ph/0007018].
6. N. Arkani-Hamed, L. J. Hall, H. Murayama, D. Tucker-Smith and N. Weiner, *Small neutrino masses from supersymmetry breaking*, *Phys. Rev.* **D64** (2001) 115011, [hep-ph/0006312].
7. Y. Grossman and H. E. Haber, *Sneutrino mixing phenomena*, *Phys. Rev. Lett.* **78** (1997) 3438–3441, [hep-ph/9702421].
8. C. Arina and M. E. Cabrera, *Multi-lepton signatures at LHC from sneutrino dark matter*, *JHEP* **04** (2014) 100, [1311.6549].
9. C. Arina, M. E. C. Catalan, S. Kraml, S. Kulkarni and U. Laa, *Constraints on sneutrino dark matter from LHC Run 1*, *JHEP* **05** (2015) 142, [1503.02960].
10. C. Arina, S. Kulkarni and J. Silk, *Monochromatic neutrino lines from sneutrino dark matter*, *Phys. Rev.* **D92** (2015) 083519, [1506.08202].
11. L. Delle Rose, S. Khalil, S. J. D. King, S. Kulkarni, C. Marzo, S. Moretti et al., *Sneutrino Dark Matter in the BLSSM*, *JHEP* **07** (2018) 100, [1712.05232].
12. W. Abdallah, J. Fiaschi, S. Khalil and S. Moretti, *Mono-jet, -photon and -Z signals of a supersymmetric ($B \neq L$) model at the Large Hadron Collider*, *JHEP* **02** (2016) 157, [1510.06475].

Effective Field Theory after a New-Physics Discovery

Matthias König

Physik Institut, Universität Zürich, CH-8057 Zürich, Switzerland



After the discovery of a new resonance, its couplings to the Standard Model (SM) need to be described by the means of an effective theory, appropriately constructed to separate its mass scale from the mass scales associated with the SM decay products. At the example of a scalar resonance transforming as a singlet under the SM gauge group, we construct the operator basis for such a theory using the language of Soft-Collinear Effective Theory (SCET) and perform the resummation of the leading Sudakov logarithms.

1 Introduction

To describe interactions between possible high-scale new-physics (NP) effects and the SM, one needs to account for the large scale gap between the NP scale and the scale of the observable under consideration. For example, it is well-known that large QCD logarithms $\alpha_s \log(q^2/\Lambda_{\text{NP}}^2)$ can spoil the convergence of the perturbation expansion for hadronic low-energy observables, where $q^2 \sim \mathcal{O}(\Lambda_{\text{QCD}}^2)$. By describing the process in terms of an effective field theory (EFT), these large logarithms can be resummed using renormalization group methods. For decays of a NP resonance, $q^2 \sim \Lambda_{\text{NP}}^2$ is of the high scale and one might suspect the absence of large logarithms. However, the scale hierarchy between q^2 and the masses in the final state introduces large Sudakov logarithms, which need to be resummed just as well.

The appropriate effective theory of a heavy-to-light transition is the Soft-Collinear Effective Theory^{1,2,3,4}, in which the low-energy degrees of freedom are comprised of fields with low virtualities $k^2 \sim 0$. In contrast to traditional EFTs, individual components of k^μ can still be large, as long as k^μ is light-like, and consequently operators can be non-local along the directions of these large momentum components. The interested reader is referred to the literature for more details on the construction and the resulting field-theory implications⁵.

Here we show an excerpt of the operator basis of the recently developed SCET_{BSM}, constructed for a singlet scalar resonance decaying to SM fields. Furthermore, we comment on the matching procedure to a concrete UV completion and the size of the resummation effects. The full operator basis along with the anomalous dimensions up to next-to-next-to-leading order in the EFT power-counting can be found in the original paper⁶, whereas the in-depth treatment of the UV completion was presented in a later work⁷.



Figure 1 – Validity regions and matching thresholds for the various effective theories depending on the scale hierarchy between the resonance mass m_S and the scale of the additional NP sector m_Ψ .

2 Effective Lagrangian

To construct the operator basis, one writes down all possible interactions between the resonance and the SM degrees of freedom allowed by the symmetries of the theory, just like one does in any EFT like for example the SMEFT^{8,9,10,11,12}. One could now envision supplementing the SMEFT operator basis by local operators coupling the scalar resonance S to various SM singlet currents to describe the S couplings to the SM fields^{13,14}. Such a “SMEFT+ S ” would separate the scale of the resonance mass m_S from the scale m_Ψ of the UV completion that generates these couplings, but not the resonance mass from the SM mass scales $\mu_{\text{SM}} \sim v$. Furthermore, there is no reason to believe that $m_\Psi \gg m_S$ should hold. In fact, it is very plausible that a new resonance is simply the first discovered particle out of a larger (undiscovered) NP sector.

By constructing the operator basis in the language of SCET, one obtains an effective theory that can deal with both cases $m_\Psi \sim m_S$ and $m_\Psi \gg m_S$. In the latter case, one simply integrates out the UV completion at m_Ψ and matches the “SMEFT+ S ” to the SCET at the matching scale m_S . If the sectors are at similar scales, $m_\Psi \sim m_S$, one integrates out the full NP sector at m_S and matches it to the SCET, as depicted in Fig. 1.

In the SCET_{BSM}, operators are organized in powers of the scale ratio $\lambda = \mu_{\text{SM}}/m_S$. Instead of discussing the full basis, we will focus on three operators for brevity:

$$O_{AA} = S g_{\mu\nu}^\perp \mathcal{A}_{n_1}^{\mu,a} \mathcal{A}_{n_2}^{\nu,a} \quad O_{\phi\phi} = S \left(\Phi_{n_1}^\dagger \Phi_{n_2} + \Phi_{n_2}^\dagger \Phi_{n_1} \right), \quad O_{F_L \bar{F}_R}^{ij} = S \bar{E}_{L,n_1}^i \Phi_0 f_{R,n_2}^j, \quad (1)$$

where the first two are of $\mathcal{O}(\lambda^2)$ and the third one is of $\mathcal{O}(\lambda^3)$ in SCET power-counting. The subscripts n_i denote the directions of large momentum in which the particle is moving, described by light-like reference vectors, satisfying^a $n^2 = 0$ and $\bar{n} \cdot n = 2$. Each field operator can be displaced along this direction $\psi_n \equiv \psi_n(x + t\bar{n})$. The Lagrangian is then a convolution over the parameters t with the Wilson coefficients:

$$\mathcal{L} \sim \int dt_1 dt_2 C(t_1, t_2, \mu) S(x) \phi_{n_1}^\dagger(x + t_1 \bar{n}_1) \phi_{n_2}(x + t_2 \bar{n}_2). \quad (2)$$

Field operators are dressed with Wilson lines, defined by:

$$W_n^{(A)}(x) = P \exp \left[ig_A \int_{-\infty}^0 ds \bar{n}_i \cdot A_{n_i}(x + s \bar{n}_i) \right], \quad (3)$$

to ensure gauge invariance. For scalars, fermions and gauge fields, the field operators are related to the SM fields via^{15,16}:

$$\Phi_n(x) = W_n^\dagger(x) \phi(x), \quad \Psi_n(x) = \frac{\not{n} \not{\bar{n}}}{4} W_n^\dagger(x) \psi(x), \quad \mathcal{A}_n^\mu(x) = W_n^{(A)\dagger}(x) [iD_n^\mu W_n^{(A)}(x)]. \quad (4)$$

The field Φ_0 denotes a Higgs doublet carrying no momentum, which will be replaced by the Higgs vacuum expectation value after electroweak symmetry breaking. The operator O_{AA} generates the decays $S \rightarrow jj, \gamma\gamma, W^+W^-$ and ZZ whereas the operator $O_{\phi\phi}$ is responsible for the di-Higgs decay as well as the decay into longitudinal electroweak bosons. The operators $O_{F_L \bar{F}_R}^{ij}$ generate the various difermion decays.

^aThe standard choice for a two-body decay would be $n_1 = (1, 0, 0, 1)$, $n_2 = (1, 0, 0, -1)$, $\bar{n}_1 = n_2$, $\bar{n}_2 = n_1$.

When performing the matching to the SCET_{BSM}, one expands amplitudes in the mass ratio λ . If another NP scale $m_\Psi \sim m_S$ is present, one keeps the full dependence on it. As an example, the decay $S \rightarrow gg$, generated through a loop of vectorlike fermions of mass m_Ψ leads to the Wilson coefficient

$$C_{GG}(q^2) = \frac{T_F}{\pi^2} \left[\left(\frac{4m_\Psi^2}{q^2} - 1 \right) \arcsin^2 \left(\sqrt{\frac{q^2}{4m_\Psi^2}} \right) - 1 \right], \quad (5)$$

where the non-polynomial dependence of the coefficient on the momentum transfer $q^2 = m_S^2$ is a consequence of the non-locality of the operator and a feature typical of SCET.

3 Resummation of large logarithms

The motivation for describing the decays $S \rightarrow \text{SM}$ in the framework of the SCET_{BSM} is the systematic resummation of large (double) logarithms of the form $\alpha \log^2 \lambda$. This is achieved by solving the renormalization group equations of the couplings in the effective theory. We will demonstrate this by showing the numerical coefficients $U_i(\mu_0, M) = C_i(\mu_0)/C_i(M)$, assuming a NP-scale $M = 2.5$ TeV. We will also show the ratio between the resummed and the fixed-order decay rates $R_i = \Gamma_i^{\text{res}}/\Gamma_i^{\text{fo}}$ for the modes $S \rightarrow \gamma\gamma$, $S \rightarrow jj$, $S \rightarrow t\bar{t}$ and $S \rightarrow hh$. Only numerical results will be shown here and none of the ingredients necessary to obtain them. They are detailed in the original papers and references therein^{6,7}, including analytical solutions to the RG equations governing the scaling behavior of the various Wilson coefficients.

Two operators contribute to the diphoton decay, O_{BB} and O_{WW} . Their running is described by the coefficients $U_{WW}(m_W, M) = 0.80 e^{23i}$, and $U_{BB}(m_W, M) = 1$. Neglecting an interaction of the form $S\phi^\dagger\phi$, the resummation leads to a suppression of the decay rate by a factor of:

$$R_{S \rightarrow \gamma\gamma} = |0.9U_{WW}(m_W, M) + 0.1|^2 \approx 0.67, \quad (6)$$

which is a sizeable effect, originating solely from electroweak corrections.

The leading contribution to the decay of $S \rightarrow jj$ is given by the operator O_{GG} . The Wilson coefficient of this operator needs to be scale-evolved to μ_j , which is an energy scale associated with the definition of the jets. Assuming $\mu_j = 100$ GeV, we find $U_{GG} \approx 0.38 e^{0.98i}$. This leads to a suppression of the dijet rate by:

$$R_{S \rightarrow gg} = |U_{GG}(\mu_j, M)|^2 \approx 0.15. \quad (7)$$

Neglecting resummation effects would thus vastly overestimate the decay rate due to large QCD corrections.

As an example of a difermion decay, the operator $C_{Q_L \bar{u} R}^{33}$ generates the decay $S \rightarrow t\bar{t}$. The RG evolution from M to the top-quark mass is given by $U_{q\bar{q}}(m_t, M) = 0.90 e^{0.31i}$. This is a relatively mild correction, leading only to a suppression of:

$$R_{S \rightarrow t\bar{t}} = |U_{q\bar{q}}(m_t, M)|^2 \approx 0.81. \quad (8)$$

Finally, the di-Higgs decay of the S is described by the operator $O_{\phi\phi}$. Solving its evolution equation yields the correction factor $U_{\phi\phi}(m_h, M) \approx 0.79 e^{0.08i}$. Consequently, the di-Higgs decay rate is suppressed by:

$$R_{S \rightarrow hh} = |U_{\phi\phi}(m_h, M)|^2 \approx 0.62, \quad (9)$$

which is again a large correction, despite the fact that the final state does not contain any color-charged particles.

4 Conclusions

We have developed an effective theory to describe the decays of a hypothetical scalar new-physics resonance into SM fields, the SCET_{BSM}. Since the mass of the resonance injects large energies into the light final states, radiative corrections are bound to generate Sudakov logarithms of the form $\alpha \log^2(\mu_{\text{SM}}^2/m_S^2)$, which can spoil the convergence of the perturbation expansion and need to be resummed to all orders. Since the light final state particles travel with large momenta, the appropriate effective theory is SCET, which can separate the scales m_S and μ_{SM} .

The construction of the SCET_{BSM} does not make any assumptions about how the couplings between S and the SM are generated in a UV-complete model, especially about the masses of a possible larger NP sector. Traditional EFT constructions, akin to the SMEFT supplemented by the scalar S are only valid in the case in which all other NP degrees of freedom are much heavier than the resonance itself - an assumption that is not automatically justified. Furthermore, even if the assumption is valid, the “SMEFT+ S ” can only separate the scale m_S from the heavier NP-scale and not m_S from μ_{SM} . Therefore, in either case of the NP scale hierarchy, the result has to be matched onto the SCET_{BSM} to resum the large double logarithms.

The size of the resummation effects on the decay rates of the resonance were found to be large - ranging from $\sim 20\%$ in the mildest case up to a suppression factor of $\sim 85\%$ for the most extreme scenario and assuming a resonance mass of $m_S \approx 2.5$ TeV. The impact on predictions for and constraints on beyond-the-SM constructions is therefore significant and should be taken into account. Our framework provides a straightforward way of doing so, albeit at the time of writing only for a spin-0, gauge-singlet resonance. In future work, we will extend the approach to more complicated cases of non-singlet resonances and ones with non-zero spin, to cover the interesting cases like leptoquarks, Z' bosons and heavy gluon excitations.

Acknowledgments

MK gratefully acknowledges support by the Swiss National Science Foundation (SNF) under contract 200021-159720 and would like to thank the organizers for keeping up the spirit of Moriond by organizing a fantastic conference.

References

1. C. W. Bauer, S. Fleming, D. Pirjol and I. W. Stewart, Phys. Rev. D **63** (2001) 114020
2. C. W. Bauer and I. W. Stewart, Phys. Lett. B **516** (2001) 134
3. C. W. Bauer, D. Pirjol and I. W. Stewart, Phys. Rev. D **65** (2002) 054022
4. M. Beneke, A. P. Chapovsky, M. Diehl and T. Feldmann, Nucl. Phys. B **643** (2002) 431
5. T. Becher, A. Broggio and A. Ferroglia, Lect. Notes Phys. **896** (2015)
6. S. Alte, M. König and M. Neubert, JHEP **1808** (2018) 095
7. S. Alte, M. König and M. Neubert, Eur. Phys. J. C **79** (2019) no.4, 352
8. S. Weinberg, Phys. Rev. Lett. **43**, 1566 (1979).
9. F. Wilczek and A. Zee, Phys. Rev. Lett. **43**, 1571 (1979).
10. W. Buchmüller and D. Wyler, Nucl. Phys. B **268**, 621 (1986).
11. C. N. Leung, S. T. Love and S. Rao, Z. Phys. C **31**, 433 (1986).
12. B. Grzadkowski, M. Iskrzynski, M. Misiak and J. Rosiek, JHEP **1010**, 085 (2010)
13. B. Gripaios and D. Sutherland, JHEP **1608**, 103 (2016)
14. R. Franceschini, G. F. Giudice, J. F. Kamenik, M. McCullough, F. Riva, A. Strumia and R. Torre, JHEP **1607**, 150 (2016)
15. C. W. Bauer, S. Fleming, D. Pirjol, I. Z. Rothstein and I. W. Stewart, Phys. Rev. D **66** (2002) 014017
16. R. J. Hill and M. Neubert, Nucl. Phys. B **657** (2003) 229

3. **Electroweak**

Inclusive and differential W and Z at CMS and ATLAS

E. Di Marco

*Istituto Nazionale di Fisica Nucleare, p.le Aldo Moro 2,
Roma 00185, Italy*

Several electroweak precision measurements are performed by the ATLAS and CMS collaborations at the LHC. The main ones are carried out using Drell-Yan production of single W and Z boson. They regard the measurement of the production cross sections of W and Z bosons, the mass of the W boson, and $\sin^2 \theta_W$. The results of the $\sin^2 \theta_W$ measurements have an accuracy of approximately twice that reached at LEP and SLD. Other measurements reported are about the Drell-Yan differential production cross section.

1 Introduction

The LHC and other hadron colliders measure many parameters of the Standard Model (SM) and they give very important inputs to the global SM fits¹. One relevant SM parameter is the W boson mass m_W , measured at the Tevatron and at the LHC. This can be compared to the SM prediction obtained using the measurement of the top quark mass m_t , which is precisely measured at the LHC and Tevatron, and the Higgs boson mass m_H , which is precisely measured at the LHC. In this respect, a global electroweak fit to SM parameters yields an indirect estimate of $m_W = 80358 \pm 8$ MeV¹, thus with a precision of 10^{-4} .

Other SM parameters which are discussed in this presentation are the measurements of the weak mixing angle ($\sin^2 \theta_W$) and the measurement of differential cross sections of the Z boson. These studies are based on large samples of γ^*/Z decays to electrons and muons, collected during the Run 1 or Run 2 of the LHC. The measurement of $\sin^2 \theta_W$ provides an indirect measurement of m_W , through the relation:

$$\sin^2 \theta_W = 1 - \frac{m_W^2}{m_Z^2} \quad (1)$$

Different experiments use Z boson decays into muon pairs and, whenever possible, also into electron pairs. The standard selection of Z decays requires both leptons to have a pseudorapidity $|\eta| < 2.4$ (or 2.5), but ATLAS also uses electron pairs with a forward electron which does not traverse the tracker and is identified and measured in the calorimeters.

2 Measurement of $\sin^2 \theta_W$

The most precise measurement of $\sin^2 \theta_W$ at hadron colliders is based on the forward-backward asymmetry A_{FB} in Drell-Yan $qq \rightarrow \ell^+ \ell^-$ events, where ℓ stands for muon (μ) or electron (e). The forward-backward asymmetry is defined using the angle θ^* between the outgoing lepton and the incoming quark in the Collins-Soper reference frame. A needed ingredient to define θ^* is the direction of the incoming quark. At the LHC, which is a pp collider, the direction of the quark is not known event-by-event, but can be approximated to be the same as the longitudinal component

of the Z boson momentum because antiquarks originate from the sea and tend to have lower momentum than quarks which are predominantly valence quarks. Given the uncertainties in the quark assignment at the LHC, which are largest for central events, the observed asymmetry is reduced, compared to the true one and this effect is referred as dilution. When the Z boson has no longitudinal momentum, the observed asymmetry becomes 0 as it becomes impossible to identify the quark direction. The differential cross section at leading order is:

$$\frac{d\sigma}{d(\cos\theta^*)} \propto 1 + \cos^2\theta^* + A_4 \cos\theta^* \quad (2)$$

where θ^* is the polar angle of the negative lepton in the CollinsSoper frame of the dilepton system and A_{FB} is defined as:

$$A_{FB} = \frac{3}{8} A_4 = \frac{\sigma_F - \sigma_B}{\sigma_F + \sigma_B} \quad (3)$$

where σ_F and σ_B are the cross sections for leptons in the forward and backward hemispheres in terms of θ^* . The weak mixing angle, $\sin^2\theta_W$, is related to the masses of the W and Z bosons through the relation in Eq. 1. In the improved Born approximation the effective mixing angle, $\sin^2\theta_{\text{eff}}^\ell$, is defined, which absorbs some of the higher-order corrections.

2.1 Measurement of $\sin^2\theta_{\text{eff}}^\ell$ at CMS

CMS measured $\sin^2\theta_{\text{eff}}^\ell$, using Z decays into electrons and muons collected at 8 TeV during Run 1. The CMS measurement is based on a template fit of the $\cos\theta^*$ distributions. An event weighting² is used to build $\cos\theta^*$ templates, and weights are used for parton distribution function (PDF) replicas to also constrain PDFs with data.

The asymmetry measurement is carried out in 6 bins for the dilepton rapidity $y_{\ell\ell}$ and in 12 bins for the dilepton invariant mass $m_{\ell\ell}$. The measured data and the results of the fit are shown in Fig. 1. The PDF uncertainties mainly affect AFB far from the Z boson peak while $\sin^2\theta_{\text{eff}}^\ell$ has the largest effect on the peak. By eff using weights proportional to $\exp(-\chi^2/2)$, which is equivalent to profiling over the PDF replicas, the uncertainty due to PDF decreases from 0.00057 to 0.00030. The final CMS results⁴ is:

$$\sin^2\theta_{\text{eff}}^\ell = 0.23101 \pm 0.00053 = 0.23101 \pm 0.00036(\text{stat}) \pm 0.00018(\text{syst}) \pm 0.00016(\text{theory}) \pm 0.00031(\text{PDF}).$$

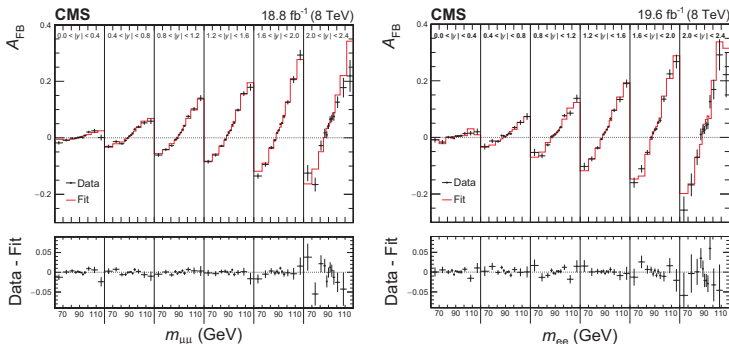


Figure 1 – CMS measurement of A_{FB} . Left for $Z \rightarrow \mu\mu$. Right for $Z \rightarrow ee$.

2.2 Measurement of $\sin^2 \theta_{\text{eff}}^\ell$ and triple differential distributions at ATLAS

The ATLAS collaboration previously carried out a measurement of $\sin^2 \theta_{\text{eff}}^\ell$ using data collected at 7 TeV. The result is:

$$\sin^2 \theta_{\text{eff}}^\ell = 0.23140 \pm 0.00036 = 0.23140 \pm 0.00021(\text{stat}) \pm 0.00016(\text{syst}) \pm 0.00024(\text{PDF}).$$

The most recent analysis consists in a triple differential cross section measurement, differential in $m_{\ell\ell}$, $\cos \theta^*$ and $y_{\ell\ell}$ ³. The analysis is carried out using 8 TeV data in the $Z/\gamma \rightarrow \mu\mu$ and $Z/\gamma \rightarrow ee$ channels, where both leptons are central, and also in $Z/\gamma \rightarrow ee$ channel with one central and one forward electron. The analysis is performed in a total of 504+504+104 bins. Figure 2 shows the measurement as function of $y_{\ell\ell}$ in various $\cos \theta^*$ bins, positive and negative and for three different $m_{\ell\ell}$ ranges, below, on and above the Z peak. The data show good agreement with the predictions of POWHEG. These measurements can be used to extract the measurement of $\sin^2 \theta_{\text{eff}}^\ell$.

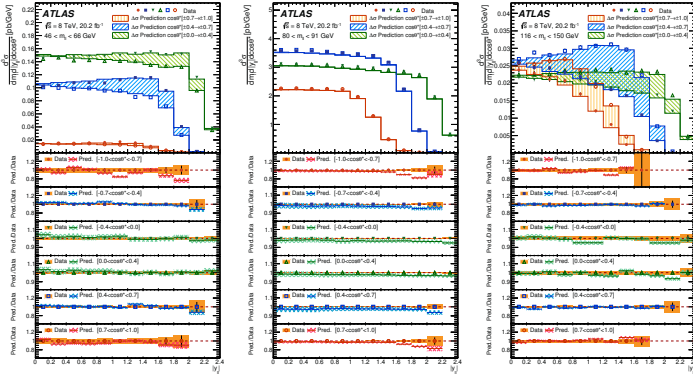


Figure 2 – CMS measurement of AFB. Left for $Z \rightarrow \mu\mu$. Right for $Z \rightarrow ee$.

3 Measurement of W boson mass at ATLAS

The mass of the W boson is measured by ATLAS collaboration using leptonic decays in 4.6 fb^{-1} of data recorded in 2011 at $\sqrt{s} = 7$ TeV⁵. Since it is not possible to fully reconstruct the W boson mass, the measurement relies on mass-sensitive final state variables, the transverse momentum of the charged lepton p_T^ℓ and the W boson transverse mass m_T , defined as $m_T = \sqrt{2p_T^\ell p_T^{\text{miss}}(1 - \cos \phi)}$ where p_T^{miss} is the neutrino missing transverse momentum, estimated with the vector sum of the transverse energy of all clusters reconstructed in the calorimeters excluding the lepton deposits. Templates of these distributions, obtained from simulation with different values of m_W , are compared to the observed distributions and a χ^2 minimisation is performed to extract the W boson mass.

Muon momentum scale and resolution corrections are derived using $Z \rightarrow \mu\mu$ (ee) decays. The combined uncertainty is dominated by the finite size of the Z boson sample. The total muon calibration and efficiency uncertainty in the W boson mass is 9.8 MeV when estimated using the p_T^ℓ distribution and 9.7 MeV using m_T . The hadronic recoil calibration enters the definition of m_T , and it is sensitive to pileup and underlying event description. Resolution mismodelling is estimated with Z boson events in data, and transferred to the W boson sample. The uncertainties from the hadronic recoil calibration affect the W boson mass by 2.6 MeV when fitting the p_T^ℓ distribution and by 13 MeV for m_T .

The simulated samples of inclusive vector-boson production are based on the Powheg MC generator interfaced to Pythia 8, but provide an imperfect modelling of all the observed distributions. Ancillary measurements of DrellYan processes are used to validate (and tune) the model and to assess systematic uncertainties. The W and Z boson samples are reweighted to include the effects of higher-order QCD and EW corrections, as well as the results of fits to measured distributions which improve the agreement of the simulated lepton kinematic distributions with the data.

The QCD parameters of the parton shower model (PYTHIA 8) were determined by fits to the transverse momentum distribution of the Z boson measured at 7 TeV, and it is extrapolated to the W using the ratio:

$$R_{W/Z}(p_T) = \left(\frac{1}{\sigma_W} \frac{d\sigma_W(p_T)}{dp_T} \right) \left(\frac{1}{\sigma_Z} \frac{d\sigma_Z(p_T)}{dp_T} \right)^{-1} \quad (4)$$

the uncertainties propagated in the ratio are the statistical precision of the Z data, c-quark and b-quark variations, factorisation scale variation in the QCD ISR, decorrelating W and Z for the heavy flavour initiated production while correlating for the light quark production, leading order PS PDF variations. The uncertainty from the PDFs on the fixed-order predictions dominate the total uncertainty in the measurement and amounts to 8.0 MeV in the p_T^L fit, and to 8.7 MeV in the m_T fit.

The final combination of all categories gives: $m_W = 80370 \pm 7(stat.) \pm 11(exp.syst.) \pm 14(mod.syst.) MeV$, where the first uncertainty is statistical, the second corresponds to the experimental systematic uncertainty, and the third to the physics modelling systematic uncertainty. The final measurement uncertainty is dominated by modelling uncertainties, mainly the strong interaction uncertainties. Lepton calibration uncertainties are the dominant sources of experimental systematic uncertainty for the extraction of m_W from the p_T^L distribution.

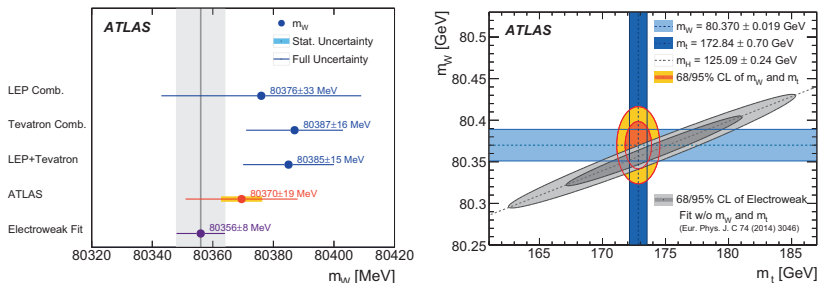


Figure 3 – Left: The measured value of m_W is compared to other published results, including measurements from the LEP experiments, and from the Tevatron collider experiments. Right: confidence-level contours of the m_W and m_t indirect determination from the global electroweak fit are compared to the ATLAS measurements of the top-quark and W-boson masses.

References

1. M. Baak *et al.* [Gfitter Group], *Eur. Phys. J. C* **74**, 3046 (2014)
2. A. Bodek, *Eur. Phys. J. C* **67**, 321 (2010)
3. M. Aaboud *et al.* [ATLAS Collaboration], *JHEP* **1712**, 059 (2017)
4. A. M. Sirunyan *et al.* [CMS Collaboration], *Eur. Phys. J. C* **78**, no. 9, 701 (2018)
5. M. Aaboud *et al.* [ATLAS Collaboration], *Eur. Phys. J. C* **78**, no. 2, 110 (2018)

The Status and Prospects of the Muon $g - 2$ Experiment at Fermilab

A.T. FIENBERG

Department of Physics, University of Washington, Seattle

The E989 Muon $g - 2$ Experiment at Fermilab aims to measure the muon magnetic anomaly, a_μ , to an unprecedented precision of 140 parts per billion (ppb), representing a four-fold improvement over the current best measurement, achieved at Brookhaven National Lab. There stands a greater than 3 standard deviations discrepancy between the Brookhaven measurement of a_μ and the theoretical value predicted using the Standard Model. The Fermilab experiment seeks to either resolve or confirm this discrepancy, which is suggestive of new physics interactions. To achieve the E989 target precision, the anomalous precession frequency of muons in a magnetic storage ring must be determined with a systematic uncertainty below 70 ppb, and the average magnetic field experienced by these stored muons must be known equally well. The muon anomalous precession frequency is imprinted on the time-dependent energy distribution of decay positrons observed by 24 electromagnetic calorimeters. A suite of pulsed NMR probes continually monitors the magnetic field. This document presents the current status of the Fermilab experiment while emphasizing the ongoing analysis of the 2018 Run 1 dataset and the systematic effects that complicate it.

1 Motivation

The magnetic dipole moment, $\vec{\mu}$, of a subatomic particle can be expressed in terms of its dimensionless g factor as follows:

$$\vec{\mu} = \pm g \frac{e}{2m} \vec{S}, \quad (1)$$

where e is the elementary charge, m is the particle's mass, and S is its spin. The Dirac equation and tree-level quantum electrodynamics (QED) predict that $g = 2$ for a structureless spin-1/2 particle such as the electron or the muon. Loop effects yield observable adjustments to the Dirac equation's prediction. These adjustments motivate the definition of the magnetic anomaly, a :

$$a \equiv \frac{g - 2}{2}. \quad (2)$$

While at tree level $a_e = a_\mu = 0$, loop corrections to the electron and muon anomalies are significantly and measurably different. In general, a_μ receives larger contributions from virtual heavy particles than does a_e because of the muon's larger mass. This document and the experiment it describes pertain to the muon magnetic anomaly, a_μ .

The Standard Model (SM) provides a testable prediction of a_μ , with QED accounting for the overwhelming majority of the predicted value. Beyond QED, hadronic and electroweak (EW) effects produce 60 parts-per-million (ppm) and 1 ppm contributions, respectively. Recent comprehensive SM evaluations of a_μ , such as those by Keshavarzi *et al*¹ and Davier *et al*,² have combined uncertainties of 300–400 parts-per-billion (ppb), and these uncertainties are dominated by nonperturbative hadronic interactions. Hadronic corrections are categorized by diagram topology into hadronic vacuum polarization (HVP) diagrams and hadronic light-by-light scattering (HLbL) diagrams. Currently, the HVP diagrams are evaluated using dispersive

approaches and the HLbL diagrams are evaluated using hadronic models. There is active research in the theory community toward reducing the SM hadronic uncertainties through the refinement of traditional techniques and the development of novel approaches.

The SM prediction of a_μ can be confronted with experiment. A measurement of a_μ that differed significantly from the SM prediction would be clear evidence of new phenomena. Conversely, confirmation of the SM prediction within the combined experimental and theoretical uncertainties would place severe constraints on proposed new physics models. Thus, a precision measurement of a_μ is a new physics search and SM test that is complementary to concurrent high-energy approaches.

Numerous experiments to measure a_μ have been conducted in the past decades. The E821 Experiment at Brookhaven National Lab (BNL) achieved a 540 ppb measurement, which is sensitive to all categories of SM effects.³ The BNL result differs from recent theoretical evaluations by $3.5\text{--}3.7\sigma$, hinting at but not guaranteeing the presence of detectable new physics interactions. Despite careful scrutiny of both the experiment and the theory, the muon $g - 2$ discrepancy observed at BNL has only increased in significance since its original publication. To elucidate the nature of the discrepancy, an improved measurement is warranted.

The E989 Experiment is designed to repeat the BNL measurement with a target uncertainty of 140 ppb divided evenly between statistics and systematics.⁴ E989 requires approximately 20 times the number of muons that were in the combined BNL dataset. Together with expected improvements in the theoretical prediction, E989 seeks to either resolve the BNL discrepancy or confirm it with a significance greater than 5σ .

2 Experimental Technique

When placed in a highly uniform dipole magnetic field—and within small, known corrections—the rate of change of the angle between a muon’s spin and its momentum is directly proportional to a_μ . This rate of change is called the anomalous precession frequency, ω_a , and in the case where motion is entirely perpendicular to a perfectly uniform field it is related to a_μ by

$$\omega_a = a_\mu \frac{eB}{m_\mu}. \quad (3)$$

The precision of an a_μ value determined using Eq. 3 is limited by whichever of the anomalous precession frequency, ω_a , the magnetic field magnitude, B , the elementary charge, e , or the muon mass, m_μ , is least precisely known. Introducing the muon-distribution-weighted average proton Larmor precession frequency in the storage ring’s field, $\tilde{\omega}_p$, the proton magnetic moment μ_p , the electron g factor, g_e , the electron mass, m_e , and the electron magnetic moment, μ_e , the above equation can be rearranged into the form

$$a_\mu = \frac{g_e \omega_a m_\mu \mu_p}{2 \tilde{\omega}_p m_e \mu_e}. \quad (4)$$

The ratio $\omega_a/\tilde{\omega}_p$ will be measured in E989 and then combined with the quantities $g_e/2$, m_μ/m_e , and μ_p/μ_e —known to 0.26 parts-per-trillion, 22 ppb, and 3 ppb, respectively—to determine a_μ . (Quoted uncertainties are CODATA’s recommended values.)⁵ The proxy for the storage ring’s magnetic field, $\tilde{\omega}_p$, is measured using a suite of pulsed proton NMR probes: fixed probes that constantly monitor the magnetic field through time, probes mounted on a mobile trolley that intermittently measure the magnetic field in the muon storage region when beam is not present, an absolute calibration probe, and a probe that can be inserted or retracted from the storage ring to transfer the calibration from the absolute probe to the trolley probes.

The quantity ω_a is measured solely through observing the energy spectrum of positrons produced by the decay of polarized μ^+ in the storage ring. This is possible because of parity violation in the weak decay of the muon: in the rest frame of a positive muon, decay positrons

are preferentially emitted in the direction of the muon spin. In the laboratory frame, positrons emitted in the direction of the muon momentum receive the largest possible Lorentz boost and are observed with higher energies than positrons emitted in other directions. Therefore, as the muon spins rotate relative to their momenta, the decay positron energy distribution in the laboratory frame changes. By this mechanism, the observed positron energy spectrum undergoes periodic modulation at ω_a .

Highly polarized 3.1 GeV/c muon bunches are delivered to the storage ring in a series of injections, or fills, at an average rate of 11.4 Hz. The beam is injected with a radial offset relative to the design orbit, which is then corrected by firing a pulsed electromagnetic kicker once during the injected beam's first orbit. Electrostatic quadrupoles focus the beam vertically. Approximately 10,000 muons are stored per fill, and the minimum time separation between fills is 10 ms. Following each injection, muon decays are observed for approximately 700 μ s by 24 electromagnetic calorimeters that are evenly spaced in azimuth around the inside of the storage ring. In-vacuum straw tracking detectors are positioned in front of two of the 24 calorimeters to detect decay positrons in transit to those calorimeters, reconstruct their tracks, and extrapolate their trajectories back to the original decay vertices. In this way, the tracking detectors provide knowledge of the muon beam's physical position in the storage region as a function of time. This information is critical for understanding the stored beam's dynamics and the associated systematic uncertainties present in the ω_a measurement.

3 Run 1 Analysis Status

E989 completed its first commissioning run with beam in the spring of 2017 and its first physics run, Run 1, in the spring of 2018. Before data quality cuts, the final Run 1 dataset contains nearly twice as many observed muon decays as were present in the combined BNL dataset and is sufficient to reach an a_μ uncertainty of approximately 400 ppb. The collaboration is focused both on completing the Run 1 a_μ analysis in a timely fashion and on operating the experiment for Run 2.

The Run 1 analysis efforts were initially limited to a subdataset, called the 60-Hour Dataset, sufficient for a 1.3 ppm ω_a measurement. To ensure the correctness and internal consistency of the ω_a analysis, six separate teams worked in parallel to extract ω_a . Across these six teams there were three separate treatments of the raw data (reconstructions). Each team independently developed the corrections necessary to remove certain undesirable effects from the data and determined the residual systematic uncertainties inherent in these corrections.

A robust method for extracting ω_a from the calorimeter data is to set a fixed energy threshold and then count the number of decay positrons observed above that threshold. As the positron energy spectrum oscillates at ω_a , so too does the probability that a decay positron will be emitted with an energy above any given nonzero threshold. Thus, in an idealized case, the times relative to the beam injection at which decay positrons above a certain energy threshold will be detected should be well described by the function

$$f(t) = Ne^{-t/\tau} [1 + A \cos(\omega_a t - \phi)]. \quad (5)$$

The asymmetry, A , and normalization, N , and the initial phase, ϕ , will depend on the chosen energy threshold. One finds that the statistical uncertainty achieved using this technique is minimized with an energy threshold of 1.7 GeV.

In reality, Eq. 5 does not adequately describe the collected data. Corrections are necessary both for the dynamics of the stored beam and for the nonideal response of the calorimeters. The salient beam dynamics effect is the physical oscillation of the beam position in the storage region. As the muon beam is injected with a radial offset and with a range of momenta, no applied kick will place all injected muons onto their ideal orbits. Each individual muon oscillates about its ideal orbit, and the aggregate effect of all these oscillations is a coherent oscillation of the

moments of the stored beam’s vertical and radial distributions. These oscillations—which occur at known, calculable frequencies—appear in the calorimeter data through acceptance effects. The signals are quite strong and must be addressed by the fit model. Other beam dynamics effects that must be accounted for include stored muon losses, and corrections to Eq. 3 arising from the electrostatic quadrupoles and from beam motion parallel to the magnetic field.

The primary detector-based effects of concern are pileup, or the calorimeter’s inability to resolve arbitrarily close pulse pairs, and calorimeter gain changes. Pileup and gain can both bias ω_a through the energy dependence of the positron drift time. As evident in Eq. 5, a time shift is equivalent to a different phase, ϕ . Time-dependent misinterpretation of the detected positron energies imparts to the observed phase a time dependence that is indistinguishable from a shifted precession frequency. In E989, gain changes are measured in situ with a laser calibration system⁶ and removed in software. The differing reconstruction procedures employed by the six analysis teams have intrinsically different pileup behaviors, and each analysis team developed its own correction procedure to account for the pileup remaining after reconstruction.

The ω_a analyses are blinded; all fits are relative to a secret reference frequency. In February 2019, the six ω_a analysis teams compared their 60-Hour Dataset results using a common reference frequency—a relative unblinding. The numbers were in excellent agreement, and the groups produced similar estimates of the dataset’s systematic uncertainties. This agreement validated the independent approaches taken by the different teams and demonstrated the collaboration’s preparedness to analyze Run 1 in its entirety.

4 Prospects

Analysis efforts have moved beyond the 60-Hour Dataset. A comparison between analysis teams of blinded ω_a values extracted from the majority of the Run 1 data is planned for early summer 2019. Depending on the outcome of this comparison, final internal reviews and systematic uncertainty assessments will occur throughout the summer and a combined Run 1 a_μ result will be announced. Run 2 data collection is expected to continue until early summer 2019. Run 3 will occur in 2019-2020.

Acknowledgments

This work was supported in part by Fermilab and the US DOE, Office of Science, Office of Nuclear Physics under award number DE-FG02-97ER41020.

References

1. A. Keshavarzi *et al*, *Phys. Rev. D* **97**, 114025 (2018).
2. M. Davier *et al*, *Eur. Phys. J. C* **77**, 827 (2017).
3. G.W. Bennet *et al*, *Phys. Rev. D* **73**, 072003 (2006).
4. J. Grange *et al*, Muon (g-2) Technical Design Report (2015).
5. J. Mohr *et al*, *Rev. Mod. Phys.* **88**, 035009 (2016).
6. A. Anastasi *et al*, *Nucl. Instrum. Methods A* **842**, 86 (2017).

RECENT RESULTS FROM THE VEPP2000 e^+e^- COLLIDER

E.P. SOLODOV

On behalf of CMD-3 and SND Collaborations

*Budker Institute of Nuclear Physics, 11 Lavrentieva ave.,
Novosibirsk State University, 3 Pirogova, Novosibirsk, 630090, Russia*

The CMD-3 and SND detectors are taking data at the VEPP-2000 e^+e^- collider (Budker INP, Novosibirsk, Russia). The main goal of experiments is the measurement of the cross-sections and dynamics of the exclusive modes of e^+e^- annihilation to hadrons. In particular, these results provide an important input for calculations of the hadronic contribution to the muon anomalous magnetic moment. Since start operation in 2011 few energy scans have been performed in the center-of-mass (c.m.) energy range from 0.32 to 2.0 GeV. The collected data sample with about 200 pb^{-1} per detector exceeds those in all previous experiments for this region. Here we present the present status of data analysis, including a precise measurement of the $e^+e^- \rightarrow \pi^+\pi^-$ reaction as well as other hadron final states with up to seven pions or states including two kaons or neutral pions.

1 Introduction

The electron-positron collider VEPP-2000¹ has been operating at Budker Institute of Nuclear Physics since December 2010, and has been upgraded to the new injection system in December 2016. The collider is designed to provide luminosity up to $10^{32}cm^{-2}s^{-1}$ at the maximum c.m. energy $\sqrt{s} = 2$ GeV. Two detectors, CMD-3² and SND³, are installed and simultaneously taking data in two interaction regions. The CMD-3 is the general-purpose particle magnetic (1.3 T) detector, equipped with the tracking system, two crystal (CSI and BGO) calorimeters, liquid Xe (LXe) calorimeter, TOF and muon systems. The CMD-3 detector has a high detection efficiency, good energy and angular resolution for charged particles as well as for photons. The SND is a non-magnetic detector based on the NaI crystals, arranged in three spherical layers, surrounding tracking system and Cherenkov aerogel counter: 1.05 and 1.13 refraction indexes can be used. The SND detector has very good energy resolutions for photons, and allows to separate particle types using energy deposition in three calorimeter layers and Cherenkov counter response. The integrated luminosity collected is about 60 pb^{-1} per detector in 2011-2013 runs with additional 160 pb^{-1} in 2017-2019 runs after the upgrade. The luminosity is measured with about 1% accuracy⁴ using Bhabha events. Figure 1 (left) shows the integrated luminosity averaged over 10% of best runs: green points correspond to new 2017-2019 runs. The collected integrated luminosity vs experimental energy is shown in Fig. 1 (right): in addition to few scans of all available energies, luminosity has been collected at $\omega(782)$, $\phi(1020)$ resonances and at the $N\bar{N}$ production threshold. The beam energy was continuously measured concurrently with the data taking using a Compton back scattering system⁵.

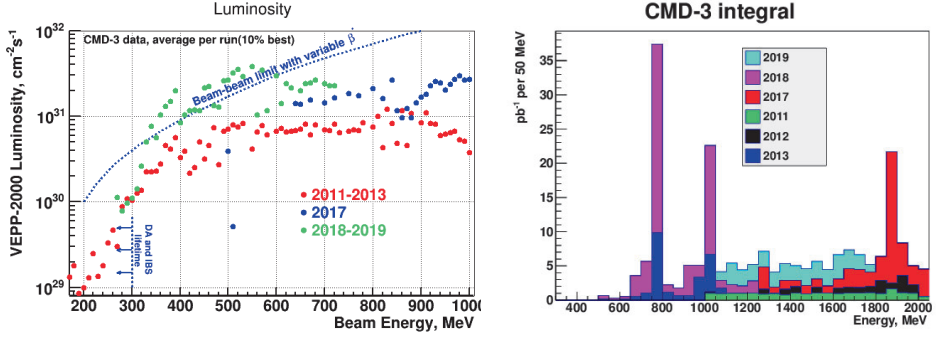


Figure 1 – (left) The integrated luminosity averaged over 10% of the best runs vs beam energy: 2017-2019 improvement is shown by green points. (right) The collected integrated luminosity vs energy at the CMD-3 detector.

2 What we do: available and expected results

We study the $e^+e^- \rightarrow \text{hadrons}$ production in all available energy range, and the measured cross sections are the main input for the calculation of hadronic contribution to $g - 2$ of muon. The analysis of data is in process and a number of results on exclusive cross sections was published by the CMD-3 and SND Collaborations. All major channels are under analysis including channels with up to seven pions or two kaons and two pions in the final state. Here we review the published results and show some of the recent preliminary results.

The CMD-3 collaboration has published several results with a few charged particles in the final state: $e^+e^- \rightarrow 3(\pi^+\pi^-)^6$, $e^+e^- \rightarrow K^+K^-\pi^+\pi^-^7$, $e^+e^- \rightarrow K_S K_L, K_S \rightarrow \pi^+\pi^-^8$, $e^+e^- \rightarrow K^+K^-^9$ and $e^+e^- \rightarrow 2(\pi^+\pi^-)^{10}$ around the ϕ -meson, $e^+e^- \rightarrow \pi^+\pi^-\pi^0\eta^{11}$, $e^+e^- \rightarrow p\bar{p}^{12}$, and most recent publication $e^+e^- \rightarrow 3(\pi^+\pi^-)\pi^0^{13}$.

The SND group uses advantage of well granulated calorimeter and has published many results with only neutral particles in final state: $e^+e^- \rightarrow \pi^0\pi^0\gamma^{14}$, $e^+e^- \rightarrow n\bar{n}^{15}$, $e^+e^- \rightarrow \pi^0\gamma^{16}$, $e^+e^- \rightarrow \eta\eta^{17}$, $e^+e^- \rightarrow \eta(958)^{25}$, $e^+e^- \rightarrow K_S K_L\pi^0, K_S \rightarrow \pi^0\pi^0^{19}$. With the help of tracking system and Cherenkov counter many reactions with charged particles are also studies: $e^+e^- \rightarrow K^+K^-^{18}$, $e^+e^- \rightarrow \omega\eta^{20}$, $e^+e^- \rightarrow \pi^+\pi^-\eta^{21}$.

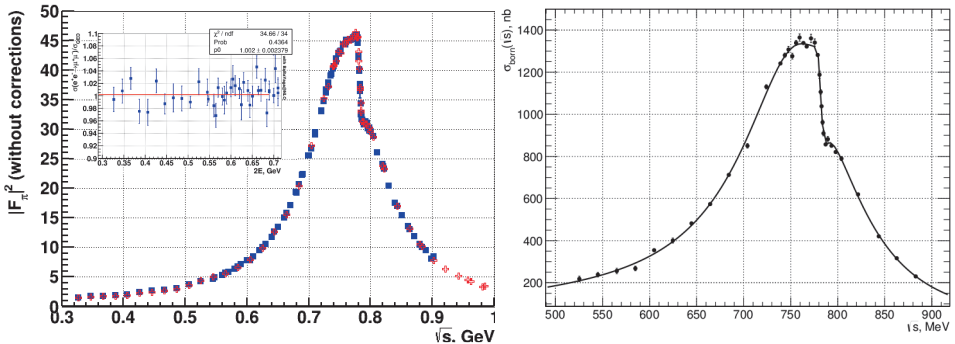


Figure 2 – (left) CMD-3 analysis of the $e^+e^- \rightarrow \pi^+\pi^-$ reaction: squares - particle separation with momenta, points - particle separation with energy deposition in calorimeter. insert box: Results of the measurement of muon pair production in comparison with the QED prediction. (right) SND preliminary results on the $e^+e^- \rightarrow \pi^+\pi^-$ cross section.

Preliminary results for the pion form factor from the $e^+e^- \rightarrow \pi^+\pi^-$ cross section measurement

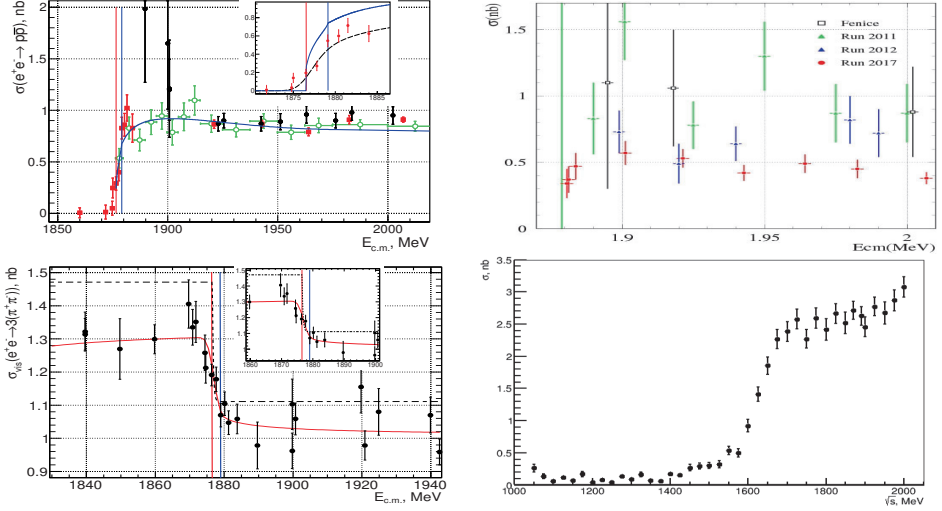


Figure 3 – (left top) The $e^+e^- \rightarrow p\bar{p}$ Born cross section measured with the CMD-3 detector. Solid curve shows result of the model from Ref. ²³. Inset shows expanded view of visible cross section at the threshold with theoretical curve convoluted with radiative effects and 1.2 MeV energy spread. The vertical lines show the $p\bar{p}$ and $n\bar{n}$ thresholds. (left bottom) The $e^+e^- \rightarrow 3(\pi^+\pi^-)$ visible cross section measured with the CMD-3 detector. Solid curve shows fit with Born cross section (dashed curve) convoluted with energy spread and radiation function. The vertical lines show the $p\bar{p}$ and $n\bar{n}$ thresholds. (right top) The $e^+e^- \rightarrow n\bar{n}$ Born cross section measured with the SND detector. (right bottom) the $e^+e^- \rightarrow \pi^+\pi^-4\pi^0$ cross section measured with the SND detector.

are shown in Fig. 2. CMD-3 uses two independent methods for separation of two-pion events from the e^+e^- and $\mu^+\mu^-$ pairs: using only DC information or using only calorimeter response, shown in Fig. 2 (left). We already estimate the DC selection accuracy below or close to 1%, which is cross checked with the cross section of the $e^+e^- \rightarrow \mu^+\mu^-$ process, shown as inserted box with respect to the QED prediction: it provides an important overall systematic test of the measurement. SND detector uses energy deposition in three layers of the calorimeter and response of the Cherenkov counter. The separation also allows to obtain about 1% systematic error and preliminary results are shown in Fig. 2 (right). A study of the systematic uncertainties are in progress, and we plan to “open the box” and present final results in time with the first publication the muon $g - 2$ measurement from FermiLAB.

Many other exclusive cross sections like $e^+e^- \rightarrow \pi^+\pi^-\pi^0$, $e^+e^- \rightarrow \pi^+\pi^-\omega$, $e^+e^- \rightarrow \pi^+\pi^-\phi$, $e^+e^- \rightarrow K^+K^-\pi^0(\eta)$, $e^+e^- \rightarrow K_S^0K_L^0\pi^0(\eta)$, $e^+e^- \rightarrow 2(\pi^+\pi^-)$, $e^+e^- \rightarrow \pi^+\pi^-\pi^0\pi^0$ etc. in the VEPP2000 energy range are under study and results will be published soon.

Because of good operation of the VEPP2000 and large statistics, both, CMD-3 and SND detectors performed the measurements of the reactions, which were never studied before. The examples are the measurement of the $e^+e^- \rightarrow 3(\pi^+\pi^-)\pi^0$ reaction by CMD-3¹³, and the $e^+e^- \rightarrow \omega\pi^0\eta$ reaction by SND²². These two measurements show that our knowledge in this energy range is incomplete, and we should continue search for new reactions, contributed to the total hadronic cross section.

3 Study of the hadron reactions at the $N\bar{N}$ threshold

Another $\approx 19\text{pb}^{-1}$ has been collected in the nucleons $N\bar{N}$ threshold scan with a step comparable with the beam energy spread of 1.2 MeV. Figure 3 (left top) shows CMD-3 result for the $e^+e^- \rightarrow p\bar{p}$ cross section, while Fig. 3 (right top) is for the $e^+e^- \rightarrow n\bar{n}$ cross section from SND detector.

Very sharp cross section behavior has been observed at the threshold, consistent with about 1 MeV exponential rise. Figure 3 (left bottom) shows the CMD-3 result for the $e^+e^- \rightarrow 3(\pi^+\pi^-)$ cross section measurement²⁴. The observed step is consistent with that in the $p\bar{p}$ cross section and also has about 1 MeV width. CMD-3 has observed similar step in the $e^+e^- \rightarrow K^+K^-\pi^+\pi^-$ reaction²⁴. Note, that no indication of the $N\bar{N}$ threshold is observed in the $e^+e^- \rightarrow \pi^+\pi^-4\pi^0$ cross section measured with the SND detector, shown in Fig. 3 (right bottom), or in the $e^+e^- \rightarrow 2(\pi^+\pi^-)$ cross section measured with the CMD-3 detector²⁴.

4 Search for C-even states

We continue to search for the production of C-even states in the e^+e^- annihilation via two-photon interactions, first presented in Ref.²⁵ for the $e^+e^- \rightarrow \eta(958)$ reaction. We have collected 654 nb⁻¹ at the η -mass energy and SND has set four times better limit $BR(\eta \rightarrow e^+e^-) < 7 \times 10^{-7}$ ²⁶ at 90% C.L.. Using 3.4 pb⁻¹ at 1285 MeV an upper limit $BR(f_1(1285) \rightarrow e^+e^-) < 2.5 \times 10^{-9}$ at 90% C.L. has been set, close to the prediction from Ref.²⁷. About 4 pb⁻¹ has been collected at $E_{c.m.}=2007$ MeV to search for a direct production of $D^*(2007)^0$ in the e^+e^- annihilation. The CMD-3 has set first time limit $B(D^{*0} \rightarrow e^+e^-) < 1.7 \times 10^{-6}$ at 90% C.L.. An observation of such production at any level above the SM prediction $B(D^{*0} \rightarrow e^+e^-) \sim O(10^{-19})$ would be a clear signal of physics beyond SM²⁸.

References

1. I. A. Koop, Nucl. Phys. B (Proc. Suppl.) **181-182**, 371 (2008). P. Yu. Shatunov *et al.*, Phys.Part.Nucl.Lett. **13** no.7 (2016). D. Schwartz *et al.*, PoS ICHEP2016 054 (2016).
2. B. I. Khazin *et al.*, Nucl.Phys.B, Proc. Suppl. **181-182**, 376 (2008).
3. M. N. Achasov *et al.*, Nucl.Instrum.Meth. **A598**, 31 (2009).
4. R. R. Akhmetshin *et al.*, JINST **9** C09003 (2014).
5. E. V. Abakumova *et al.*, Phys.Rev.Lett. **110**, 140402 (2013).
6. R. R. Akhmetshin *et al.*, Phys. Lett. B **723**, 82 (2013).
7. D. N. Shemyakin *et al.*, Phys. Lett. B **756**, 153 (2016).
8. E. A. Kozyrev *et al.*, Phys. Lett. B **760**, 314 (2016).
9. E. A. Kozyrev *et al.*, Phys. Lett. B **760**, 314 (2017).
10. R. R. Akhmetshin *et al.*, Phys. Lett. B **768**, 345 (2017).
11. R. R. Akhmetshin *et al.*, Phys. Lett. B **773**, 150 (2017).
12. R. R. Akhmetshin *et al.*, Phys. Lett. B **759**, 634 (2016).
13. R. R. Akhmetshin *et al.*, Phys. Lett. B **792**, 419 (2019).
14. M. N. Achasov *et al.*, Phys. Rev. D **94** 112001 (2016).
15. M. N. Achasov *et al.*, Phys. Rev. D **90** 112007 (2014).
16. M. N. Achasov *et al.*, Phys. Rev. D **93** 092001 (2016).
17. M. N. Achasov *et al.*, Phys. Rev. D **90** 032002 (2014).
18. M. N. Achasov *et al.*, Phys. Rev. D **94** 112006 (2016).
19. M. N. Achasov *et al.*, Phys. Rev. D **97** 032011 (2018).
20. M. N. Achasov *et al.*, Phys. Rev. D **94** 092002 (2016).
21. M. N. Achasov *et al.*, Phys. Rev. D **97** 012008 (2018).
22. M. N. Achasov *et al.*, Phys. Rev. D **94** 092010 (2016).
23. A. I. Milstein and S. G. Salnikov, Nucl. Phys. **A977**, 60 (2018).
24. R. R. Akhmetshin *et al.*, arXiv:1808.00145, Submitted to Phys. Lett. B.
25. M. N. Achasov *et al.*, Phys. Rev. D **91** 092010 (2015).
26. M. N. Achasov *et al.*, Phys. Rev. D **98** 052007 (2018).
27. A. S. Rudenko, Phys. Rev. D **96** 076004 (2017).
28. A. Khodjamirian, T. Mannel, A. Petrov, JHEP **1511** 142 (2015).

News on the CLIC physics potential

R. Ström, on behalf of the CLICdp Collaboration
CERN, Switzerland

The Compact Linear Collider (CLIC) is a proposed TeV-scale high-luminosity electron-positron collider. For an optimal exploitation of its physics potential, CLIC is foreseen to be built and operated in three stages, with centre-of-mass energies ranging from 380 GeV up to 3 TeV. Electron beam polarisation is provided at all energies. The initial energy stage will focus on precision measurements of Higgs-boson and top-quark properties. The subsequent energy stages enhance the reach of many direct and indirect searches for new physics Beyond the Standard Model and give access to the Higgs self-coupling. Higgs and top-quark projections have been evaluated using full detector simulation studies. Many new phenomenology studies have been undertaken to explore the BSM reach of CLIC, from EFT interpretations of precision measurements through to signature-based searches; these include flavour dynamics, and dark matter and heavy neutrino searches. This talk will review some of the latest results that demonstrate the outstanding potential of CLIC in many physics domains.

1 The Compact Linear Collider (CLIC)

CLIC is a proposed TeV-scale high-luminosity e^+e^- collider for the era beyond HL-LHC¹. It occupies a privileged spot between the precision and energy frontiers, reaching unprecedented precision for Standard Model (SM) physics and sensitivities up to tens of TeV for many beyond SM (BSM) physics scenarios. In addition, new physics can be discovered through direct production at the high-energy stages of CLIC. Indeed, many BSM scenarios, such as supersymmetry, have substantial parameter space in regions where CLIC has an advantage over other colliders: for example for models with highly compressed mass spectra or with BSM states that only have electroweak interactions.

CLIC is powered by an innovative two-beam accelerating scheme using a low-energy high-current drive beam to generate high power radiofrequency (RF) waves for efficient acceleration of the main beams of colliding particles. This enables a compact and cost-effective accelerator complex, with a site length ranging between 11 km and 50 km, for collisions at a centre-of-mass energy of 380 GeV and 3 TeV, respectively. The project features an advanced detector concept that matches the challenging physics performance requirements and the CLIC experimental conditions. It includes an ultra low mass tracking system and highly granular sampling calorimetry systems, all enclosed in a 4 T solenoidal magnet.

The main accelerator technologies such as drive beam production, two-beam acceleration, high-gradient X-band accelerating structures, and ultra-low transverse emittance have all been successfully demonstrated in beam experiments, hardware tests, and extensive simulations². Based on purely technological considerations, first beams could be realised by 2035, resulting in a diverse physics programme spanning three decades. The CLIC project is hosted by CERN and consists of around 75 collaborating institutes worldwide. For optimal use of its physics potential, CLIC is foreseen to be built and operated in three stages, providing high-luminosity collisions at centre-of-mass energies 380 GeV (1.0 ab^{-1}), 1.5 TeV (2.5 ab^{-1}), and 3 TeV (5.0 ab^{-1}) with $\pm 80\%$ longitudinal

electron polarisation at all stages.

The project status has been summarised in a series of reports for the European Strategy for Particle Physics Update (ESPPU): <https://clic.cern/european-strategy>.

2 Learning from Standard Model processes

A key element of the CLIC physics programme is the detailed study of the properties of the known SM particles. This section focuses on CLIC’s potential for precision measurements of Higgs and top-quark physics (Drell-Yan and multi-boson production have also been studied³) and present its global sensitivity to BSM effects in the Effective Field Theory (EFT) framework. The predictions for the Higgs and top-quark programme are based on detailed studies including realistic detector simulation, overlay of beam-induced background, and particle-flow reconstruction. In addition, jet substructure methods are used for the reconstruction of boosted top-quarks⁴.

The first CLIC stage at $\sqrt{s} = 380$ GeV gives access to the Higgsstrahlung process, $e^+e^- \rightarrow HZ$, which enables an absolute determination of the Higgs couplings to SM particles. Such model-independent extractions are only possible at lepton colliders. At the higher energy stages large Higgs boson samples are produced through WW fusion. The expected precision on g_{HZZ} from a model-independent global fit of the Higgs programme is 0.6%³. Other couplings reach similar precision and the g_{Hcc} coupling, which is very challenging at hadron colliders, can be probed with percent-level precision. It is also possible to set a model-independent upper limit on the level of invisible Higgs boson decays of 0.69%³ at 90% C.L. For a model-dependent global fit where non-SM Higgs boson decays are assumed to be zero (equivalent to the approach often adapted by hadron colliders) several Higgs couplings are constrained to per mille-level precision. Further, operation at 1.5 and 3 TeV gives access to the Higgs self-coupling at tree level through double-Higgs boson production, reaching an accuracy of about 10%³ for the full CLIC programme.

Top-quark pair production is accessible throughout the CLIC programme. An energy scan around the top-pair production threshold allows for the extraction of the top-quark mass with a total uncertainty of around 50 MeV⁴. High-energy operation also gives access to associated Higgs and top-quark production, enabling extraction of the top Yukawa coupling with a precision of 2.7%⁴, as well as study of top-quark pair production initiated by low-virtuality and highly energetic vector bosons in a vector-boson fusion topology.

In general, the high-energy operation of CLIC enables discovery of new particles almost up to the kinematic limit and provides indirect sensitivity far beyond the collision energy. The global sensitivity of the CLIC physics programme to BSM effects is probed through EFT dim-6 operators, extending the SM Lagrangian by introducing a new physics scale Λ beyond the direct reach of CLIC. Fig. 1 shows the sensitivity of the different CLIC stages through a global fit of universal probes, i.e. direct couplings of heavy BSM particles to the SM gauge and Higgs bosons³. These results use predictions from the full physics programme and illustrate the reach of CLIC compared to and combined with projections for HL-LHC under two assumptions of systematic uncertainty. The

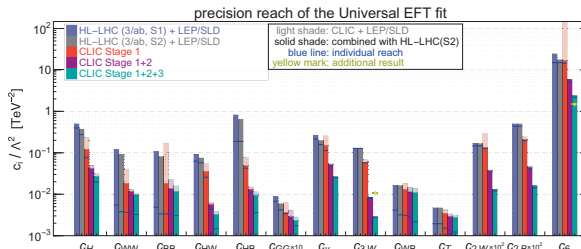


Figure 1 – Sensitivity to universal SM-EFT dim-6 operators from analysis of CLIC’s sensitivities to Higgs couplings, top-quark observables, W^+W^- production, and Drell-Yan processes, for the three CLIC energy stages.

results clearly demonstrate that even the initial stage of CLIC is highly competitive with HL-LHC for many operators. In addition, the high-energy e^+e^- operation that is unique to CLIC, leads to significant improvements for operators that grow quadratically with the centre-of-mass energy, for example c_{HW} , c_{HB} , c_{3W} , c_{2W} , and c_{2B} .

Since universal probes are unavoidable in any BSM scenario that is connected with electroweak (EW) or EW symmetry-breaking physics, they are very robust as BSM probes. They contribute to top-quark physics but are generally probed better by other processes. Relevant operators for the top-quark physics programme are instead so-called “top-philic” non-universal operators that emerge from the direct BSM coupling to the fields of the 3rd generation of quarks. In fact, strong new physics couplings with the top-quark sector, leading to enhanced top-philic operators, are well motivated. In this case top-philic effects can be more effective indirect probes of new physics than the universal ones. Here, the sensitivity to four-fermion operators, which represent a massive new mediator beyond direct reach, rise steeply with energy and improve by more than one order of magnitude at the high-energy stages of CLIC, compared to the initial stage. Overall, CLIC probes the universal and “top-philic” EFT operator coefficients much more precisely than what is possible at the HL-LHC³.

3 Examples of new physics searches

In this section we discuss several concrete new physics phenomena, covering both direct and indirect detection. In general, CLIC can search indirectly for particles with electroweak-sized couplings well above the HL-LHC reach; where they are produced directly, precise measurements of properties such as mass and spin can be made.

3.1 Extended Higgs sector heavy scalar singlets

An extended scalar sector with new states that are not charged under the Standard Model gauge group, appears in many BSM scenarios, for example in the Next-to-Minimal Supersymmetric Standard Model (NMSSM) and in many realisations of Twin Higgs models. Such new “singlet” scalars may interact with the SM through mixing with the Higgs boson portal and can then be probed indirectly through their effects on the Higgs boson couplings and through the direct production of new particle states. For the latter we focus on a case where the extra singlet Φ is at least two times heavier than the Higgs boson, and study Higgs pair production with four b-quarks in the final state. The resulting indirect and direct exclusion contours of CLIC are shown to the left in Fig. 2 and improve dramatically on the predictions for HL-LHC. This illustrates the complementarity of indirect and direct constraints and in addition, the capability of CLIC as a discovery machine. It is found that in the case of the NMSSM, CLIC can exclude a new scalar lighter than 1.5 TeV in the most well-motivated phase space region of the NMSSM³. In conclusion, CLIC is able to test thoroughly the extended Higgs sectors and exclude new scalar states up to multi-TeV masses.

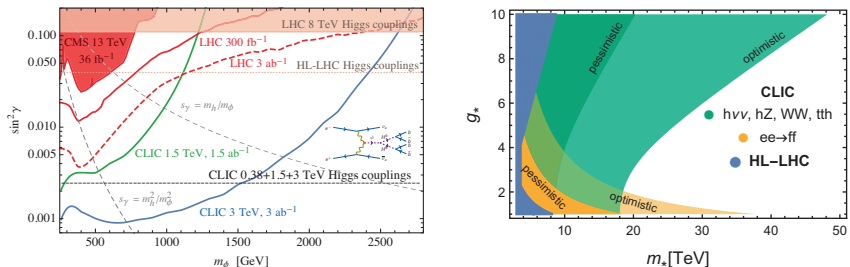


Figure 2 – Exclusion contour at 95% C.L. for heavy scalar singlets (left). Discovery (5σ) reach on composite Higgs region in the (m_*, g_*) plane (right).

3.2 Higgs and top-quark compositeness

A possible composite nature of the Higgs boson is investigated for a canonical scenario where a Higgs bound state arises as the pseudo-Nambu-Goldstone boson of an underlying strongly-interacting composite sector, characterised by the mass scale m_* (above direct reach) and coupling strength g_* . If realised, such scenarios could provide an improved understanding of the microscopic origin of the electroweak symmetry breaking and possibly also the fine-tuning (or Naturalness) problem associated with the SM Higgs mass parameter.

In CLIC, a composite Higgs could be searched for through precision measurements of EFT operators, which are either enhanced or suppressed depending on the characteristics of the composite sector. Constraints from the global fit of observables presented in Fig. 1 are here re-interpreted in terms of compositeness, with the 5σ discovery contours presented to the right in Fig. 2, for optimistic and pessimistic values of the corresponding operator coefficients³. While the measurement of single Higgs boson couplings provide the most stringent constraints at large values of g_* , the precision measurements of c_{HW} , c_{HB} , c_{2W} , and c_{2B} , which are possible at high-energy CLIC, dramatically improve the reach at small and intermediate values. In addition, top-quark compositeness emerges naturally in the composite Higgs framework. The associated flavour-dependent top-philic operator coefficients are best probed in the top-quark sector and are constrained by measuring the top Yukawa coupling and, very effectively, by top-quark pair production at high-energy CLIC. In conclusion, CLIC can discover Higgs and top-quark compositeness if the mass scale is below 8 TeV, and for certain favourable conditions, up to 40 TeV.

3.3 Exotic signatures of new physics Higgsino reach from stub tracks

Exotic signatures of new physics are an important benchmark for future colliders. Such signatures may be realised in models with a small mass splitting between dark sector particles. For example in SUSY models where the charged component of the Minimal Dark Matter multiplet is long-lived, with a macroscopic decay length, giving rise to disappearing/stub tracks. Studies based on detailed tracking performance show that the discovery potential of CLIC reaches Higgsino masses of 1.1 TeV, required for DM relic mass density, even with some level of background.

4 Summary

CLIC is an attractive post-LHC facility for CERN with unprecedented, diverse and guaranteed physics reach. The key accelerator technologies have been demonstrated and the project is ready to proceed towards a Technical Design Report. The CLIC project foresees first beams by 2035, marking the start of a unique physics programme spanning three decades.

References

1. The Compact Linear Collider (CLIC) 2018 Summary Report, edited by P.N. Burrows, N. Catalan Lasheras, L. Linssen, M. Petri, A. Robson, D. Schulte, E. Sicking, S. Stapnes, *CERN Yellow Reports: Monographs*, **Vol. 2**/2018, CERN-2018-005-M (CERN, Geneva, 2018), <https://doi.org/10.23731/CYRM-2018-002>
2. The Compact Linear Collider (CLIC) Project Implementation, edited by M. Aicheler, P.N. Burrows, N. Catalan, R. Corsini, M. Draper, J. Osborne, D. Schulte, S. Stapnes, M.J. Stuart, *CERN Yellow Reports: Monographs*, **Vol. 4**/2018, CERN2018010M (CERN, Geneva, 2018), <https://doi.org/10.23731/CYRM-2018-004>
3. The CLIC Potential for New Physics, edited by J. de Blas, R. Franceschini, F. Riva, P. Roloff, U. Schnoor, M. Spannowsky, J. D. Wells, A. Wulzer and J. Zupan, *CERN Yellow Reports: Monographs*, **Vol. 3**/2018, CERN-2018-009-M (CERN, Geneva, 2018), <https://doi.org/10.23731/CYRM-2018-003>
4. Top-Quark Physics at the CLIC Electron-Positron Linear Collider, H. Abramowicz *et al.* [CLICdp Collaboration], arXiv:1807.02441

4. QCD

SOFT QCD AT ATLAS AND CMS

MERIJN H F VAN DE KLUNDERT on behalf of the the ATLAS and CMS Collaborations

*DESY, Notkestraße 85
22607 Hamburg, Germany*



A subset of results of the ATLAS and CMS experiments at the LHC on soft QCD obtained in 2018 and 2019 is presented. After a brief outline of double parton scattering phenomenology, new results of ATLAS and CMS are presented in p+p collisions at 8 and 13 TeV respectively. The analysis of ATLAS was performed using events containing four charged leptons, while the CMS Collaboration presented the first evidence for double parton scattering in the same-sign WW channel. For both analyses no significant deviations between the measurement and model predictions were observed. Subsequently, two CMS analyses exploiting the very forward CASTOR calorimeter are discussed. After a succinct introduction of CASTOR, an analysis of the forward energy flow in p+p collisions at 13 TeV and the forward jet-energy spectrum in proton-lead collisions at $\sqrt{s_{NN}} = 5.02$ TeV is presented.

1 Introduction

The ATLAS¹ and CMS² Collaborations study soft QCD processes in hadronic interactions for various reasons^a. The unprecedented centre-of-mass energy \sqrt{s} , different beam setups, and luminosities achievable at the LHC allow for intriguing tests of QCD, such as parton dynamics alternative to the conventional DGLAP evolution and the study of rare processes. Besides, in searches for new physics, certain backgrounds can't be obtained in a data-driven manner, and thus it is important that the event generators describe the data correctly. The double parton scattering cross section for example can be a background process for Higgs or new physics searches. Also, a correct description of the data is needed for correct radiation dose estimates, which in turn is vital for the upgrade programs of the LHC experiments for the high-luminosity phase. In this report we review two double parton scattering studies of ATLAS and CMS, in p+p collisions at 8 and 13 TeV respectively. Also, we review results obtained with the very forward CASTOR calorimeter of the CMS experiment on the energy flow in p+p collisions at 13 TeV and jets in p+Pb collisions at 5.02 TeV.

^aCopyright 2019 CERN for the benefit of the ATLAS and CMS Collaborations. CC-BY-4.0 license.

2 Results on Double Parton Scattering

In hadronic interactions at the LHC energies, multiple-parton interactions (MPI) occur simultaneously with the hard scattering. The lowest order MPI interaction is a double parton scattering (DPS) interaction, in which four partons participate in the interaction. Since this process may contribute to the background of Higgs analyses and searches for new physics, a proper estimate of its magnitude is necessary. Besides, an analysis of angular distributions in same sign WW DPS would allow for testing if longitudinal parton correlations occur in hadrons³.

Under the assumption that there is no transversal or longitudinal correlation between the partons, the DPS cross section σ_{AB}^{DPS} factorises to

$$\sigma_{AB}^{DPS} = \frac{k}{2} \cdot \frac{\sigma_A \sigma_B}{\sigma_{eff}}. \quad (1)$$

In this equation, σ_{eff} describes the effective transversal overlap between the spatial distributions. This parameter is predicted to be independent of the process and centre-of-mass energy. This assumption has been tested in many channels at various values of \sqrt{s} .

A measurement of DPS in the four charged lepton final state at 8 TeV⁴ was performed by the ATLAS Collaboration. Only a fraction f_{DPS} of the four charged lepton events comes from actual DPS events: $\sigma_{4l}^{DPS} = f_{DPS} \cdot \sigma_{4l}$. Thus, σ_{eff} can be calculated as:

$$\sigma_{eff} = \frac{2}{k} \cdot \frac{1}{f_{DPS}} \cdot \frac{\sigma_{2l}^A \sigma_{2l}^B}{\sigma_{4l}} \quad (2)$$

To obtaining a precise estimate of f_{DPS} , an elastic neural network (ENN) was trained using 21 kinematic input variables to distinguish the four-jet events originating from a DPS event from the backgrounds. The output distributions of the ENN were successively used to make template fits to the real data. The value found for f_{DPS} for this process is consistent with zero, and a 95% confidence upper limit was determined as $f_{DPS} \leq 0.042$. For this calculation, the inclusive four charged lepton cross section was taken from Ref.⁵.

This number was converted into a lower limit on σ_{eff} , which was determined to be $\sigma_{eff} \geq 1.0$ mb at the 95% confidence level. This limit is compatible with the hypothesis that σ_{eff} is a universal parameter, and displayed together with other σ_{eff} measurements in Fig. 2 (left).

An analysis of DPS in same sign WW production in the leptonic channel at 13 TeV p+p collisions⁶ was performed by the CMS Collaboration. Since the leptonic channel yields a relatively clean experimental signal, this provides a good channel to test DPS hypotheses. Furthermore, the single parton scattering contributions are suppressed at matrix element level. Moreover, these processes result in jets, which are absent for the signal. The dominant background processes (WZ , $W\gamma$, ZZ , fake leptons, and rare processes) can be corrected for, and these backgrounds were weighed to the data.

To select good lepton candidates a boosted decision tree was deployed. Another boosted decision tree was applied to distinguish the signal from the background, using ten input variables.

The final value of the measured cross section is depicted in table 1 and Fig. 2 (right). This is the extrapolated result which includes opposite sign WW pairs as well. The significance of the signal is 3.9σ , and thus the measurement establishes the first evidence for the same-sign WW DPS process. Comparisons with predictions of Pythia8 and a factorised approach are included. For the factorised predictions, NNLO inclusive W production cross sections were combined with $\sigma_{eff} = 20.7$ mb; the latter value was obtained from a previous measurement. It can be seen that the measurement is compatible with both predictions. The consistency between the factorised prediction and the measurement depends on the assumption of the value of σ_{eff} though.

Table 1: The measured value of the DPS cross section in the WW channel. Predictions of Pythia8 and a factorised approach are included⁶

Quantity	Pythia8	factorised	meas.
$\sigma(\text{pb})$	1.92	0.87	$1.41 \pm 0.28(\text{stat}) \pm 0.28(\text{sys})$
sign.	5.4	2.5	3.9
Lim. no signal:	-	20.7	$12.7_{-2.9}^{5.0}$

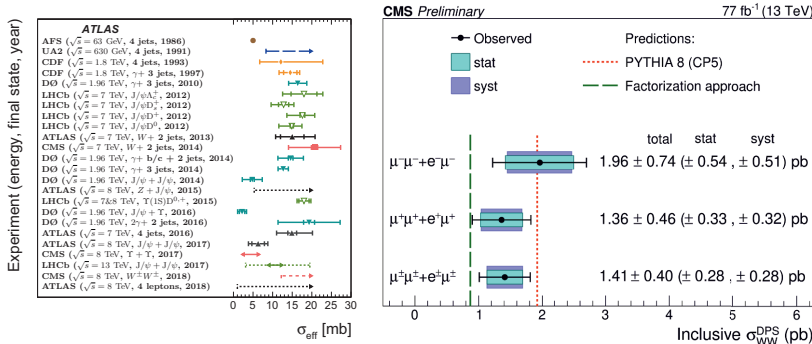


Figure 1 – Left: measurements of σ_{eff} in various channels and centre-of-mass energies, complemented with the limit in the four charged lepton channel found by ATLAS⁴. Right: the DPS cross sections from the same-sign WW analysis⁶ at 13 TeV of CMS

3 Results of CMS with the CASTOR calorimeter

The CMS detector has hermetic calorimetric acceptance within $\eta \leq 5.2$. In the negative η hemisphere, this is complemented by the CASTOR calorimeter, which extends the acceptance to -6.6 , and therefore measures in a kinematic domain that is unique at the LHC. This detector is a tungsten-quartz Cherenkov sampling calorimeter and can measure energy deposits, jets, and rapidity gaps. It has 16-fold transversal segmentation and 14 longitudinal layers. It should be noted that CASTOR has no η segmentation though. The detector successfully collected data at various centre-of-mass energies and beam configurations during LHC Run 1 and 2. Two novel analyses using data from CASTOR are reviewed below.

In Ref.⁷ a measurement of the energy flow in p+p collisions at 13 TeV within $3.5 < |\eta| < 5.2$ is presented. This is complemented at one side with the measurement of CASTOR in $-6.6 < \eta < -5.2$. A key motivation for this measurement is to test various models in a phase space relevant to Cosmic Ray physics, and to review the hypothesis on limiting fragmentation.

The energy flow is defined as:

$$\frac{dE}{d\eta} = \frac{1}{N_{evt.}} \sum_i E_i \frac{C(\eta)}{\Delta\eta}, \quad (3)$$

in which i runs over the calorimeter towers, and C corrects the detector-level measurement to the particle level. The limiting fragmentation hypothesis predicts a longitudinal scaling in terms of a shifted variable $\eta' = \eta - y_{beam}$. This would result in an invariance of E_T w.r.t. the beam energy for $\eta' = 0$. In this, E_T is defined as $E_T = E \cdot \cosh(\eta)$.

In Fig. 2 (left) we display the measurement, together with previous measurements. The results are complemented by predictions of EPOS-LHC and QGSJetII-0.4, which are Cosmic Ray physics oriented event generators. It can be seen that the results support the limiting fragmentation hypothesis, and that the predictions agree well with the data.

An analysis of the inclusive jet energy spectrum in p+Pb collisions at 5.02 TeV in CASTOR was published in Ref. ⁸. In this report we focus on the configuration with the proton towards CASTOR. In this beam configuration, the hard partons of the proton probe the soft gluons of the heavy ion down to very small fractions of the longitudinal momenta x . In this region the gluon density is expected to become very high, resulting in nonlinear fusion reactions between the gluons. This is expected to result in a saturation of the gluon density. The data are compared to predictions of the KATIE linear (depicted in blue) and nonlinear (in green) model in Fig. 2 (middle). It can be seen that at low jet energies, these predictions differ by over an order of magnitude, while converging at high jet energies, confirming that indeed the measurement is very sensitive to the saturation reactions. The shape of KATIE nonlinear appears to describe the data best, while the normalisation of KATIE linear is better. Also predictions of the AAMQS group are included, which are based on calculations in the Coloured Glass Condensate framework. It can be seen that these predictions underestimate the data also by an order of magnitude at low jet energies, where the saturation effects are strongest, while converging at high energies. In Fig. 2 right we compare the measurement to predictions of the EPOS-LHC, QGSJetII-04, and HIJING event generators. The latter is based on conventional DGLAP evolution and incorporates, among many other effects, nuclear shadowing, which is an effect on nucleon rather than on parton level. The HIJING model describes the data with the proton towards CASTOR well, but since many effects are included in the model this doesn't automatically prove that nuclear shadowing is responsible for a correct description of the data. Further, it can be seen that at high jet energies the EPOS-LHC and QGSJetII-04 models underestimate the data by over two orders of magnitude, underlining the importance of a measurement in this part of the phase space.

Concluding, the measurement is remarkably sensitive to gluon saturation effects, and none of the saturation models is currently able to fully describe the data. The data hint that perhaps nuclear shadowing may provide a relevant model of the underlying physics process.

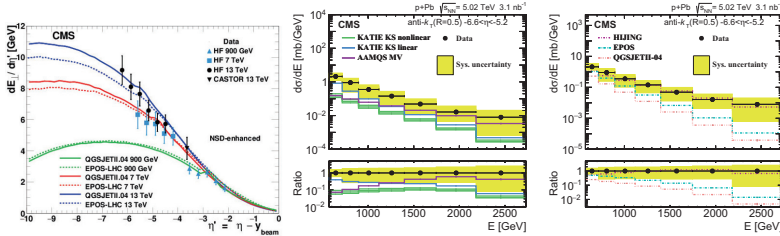


Figure 2 – The DPS cross sections from the same-sign WW analysis ⁶ at 13 TeV

References

1. ATLAS Collaboration, JINST 3 S08003 (2008)
2. CMS Collaboration, JINST 3 S08004 (2008)
3. Giorgio Calucci and Daniele Treleani, arXiv:1009.5881v4
4. ATLAS Collaboration, Phys. Lett. B 790 (2019) 595
5. ATLAS Collaboration, Phys. Lett. B 753 (2016) 552
6. CMS Collaboration, CMS-PAS SMP-18-015 (2018), <http://cds.cern.ch/record/2668320>
7. CMS Collaboration, Eur. Phys. J. C 79 (2019) 391
8. CMS Collaboration, J. High Energ. Phys. (2019) 2019: 43

QCD WITH JETS AND PHOTONS AT ATLAS AND CMS

J.D. BOSSIO SOLA, ON BEHALF OF THE ATLAS AND CMS COLLABORATIONS

Department of Physics, McGill University

The most recent QCD results involving jets and photons in the final state in proton-proton collisions data recorded by the ATLAS and CMS Collaborations at the LHC are summarized.

1 Introduction

The jet and photon cross-section measurements presented here collectively probe Parton Density Functions (PDFs) and next-to-leading-order (NLO) precision Quantum Chromodynamics (pQCD) calculations. Measurements of final states with multiple jets or a photon (plus jets), as well as ratios of cross sections for different centre-of-mass energies, help to test and constrain QCD. The most recent results using proton-proton (pp) collisions data recorded by the ATLAS¹ and CMS² Collaborations at the LHC are discussed.

2 Jet measurements

Inclusive 2- and 3-jet event cross sections are measured in nearly back-to-back topologies using data collected by the CMS detector at $\sqrt{s} = 13$ TeV and corresponding to an integrated luminosity of 35.9 fb^{-1} ³. The unfolded data is compared to different NLO Monte Carlo (MC) simulation samples, as shown in Fig. 1, where the cross sections are depicted as a function of the azimuthal separation of the two leading p_T jets ($\Delta\phi_{12}$) in different bins of the highest jet p_T (p_T^{max}). Concerning the NLO event generators, predictions are obtained using the POWHEG BOX library^{4,5,6} with the NNPDF3.0NLO⁷ PDF set. The event generators PYTHIA⁸ (tune CUETP8M1⁹) and HERWIG++¹⁰ (tune CUETHppS1⁹) are used to simulate the parton shower, hadronization, and multiple parton interactions. The POWHEG generator in dijet mode¹¹ (three-jet mode¹²), referred to as PH-2j (PH-3j), provides an NLO $2 \rightarrow 2$ ($2 \rightarrow 3$) calculation. Discrepancies between the predictions and the data are as large as 15%, mainly in the $177^\circ < \Delta\phi_{12} < 180^\circ$ region. It is suggested that the observed differences are related to the way soft partons are simulated in the parton shower³.

The fraction of dijet events with $\Delta\phi < \Delta\phi_{\text{max}}$ is measured as a function of the half absolute rapidity separation between the two leading p_T jets (y^*) and the event total scalar transverse momentum (H_T) for different $\Delta\phi_{\text{max}}$ values by the ATLAS Collaboration in $\sqrt{s} = 8$ TeV data¹³. Theoretical pQCD predictions from NLOJET++^{14,15}, corrected for non-perturbative effects, describe the unfolded data in the whole kinematic region. The data is used to determine the strong coupling α_S , and to test the pQCD predictions for the dependence of α_S on the momentum transfer Q by the renormalization group equation (RGE)^{16,17}. The results are shown in Fig. 2. The combination of the data at all momentum transfers results in $\alpha_S(m_Z) = 0.1127^{+0.0063}_{-0.0027}$.

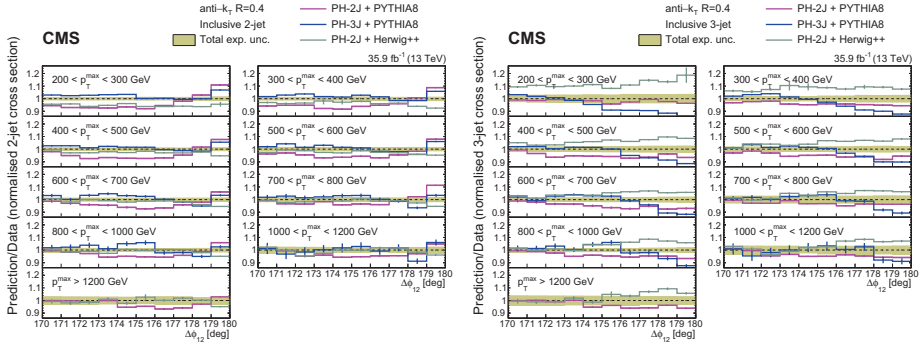


Figure 1 – Ratios of the normalized inclusive 2- (left) and 3-jet (right) distributions for the PH-2j+PYTHIA 8, PH-3j+PYTHIA 8, and PH-2j+HERWIG++ predictions to data as a function of $\Delta\phi_{12}$ for different p_T^{\max} regions. The solid band indicates the total experimental uncertainty and the error bars on the points represent the statistical uncertainties from the MC simulation sample. The PH-3j prediction is not shown for the highest p_T^{\max} bin because of its large statistical uncertainty.

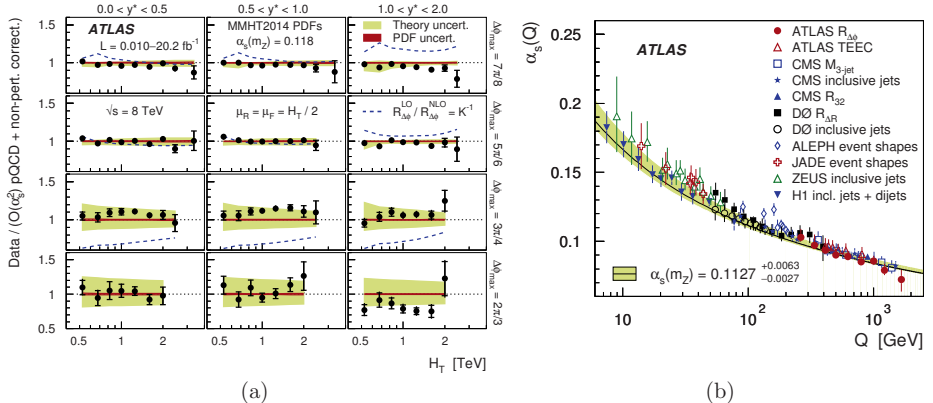


Figure 2 – (a) The ratios of the measured $R_{\Delta\phi}$ cross-sections to the theoretical predictions using the MMHT2014^{18,19} PDF set and $\alpha_S(m_Z) = 0.118$. The ratios are shown as a function of H_T for different y^* (columns) and $\Delta\phi_{\max}$ (rows) regions. The inner error bars indicate the statistical uncertainties, while the total error bars show the sum in quadrature of the statistical and systematic uncertainties. The theoretical uncertainty is the sum in quadrature of uncertainties due to the PDF set and the scale dependence. The ratio of the LO predictions to the NLO predictions is displayed by the dashed line. (b) The extracted $\alpha_S(Q)$ values for the $262 < Q < 1675$ GeV range, compared to results from jet data obtained by other experiments. Also shown is the prediction of the RGE for the $\alpha_S(m_Z)$ result obtained from the measured data.

3 Cross sections for isolated-photon and photon+jets production

Differential cross sections for inclusive isolated-photon and photon+jets production are measured by the CMS Collaboration using $\sqrt{s} = 13$ TeV data corresponding to an integrated luminosity of 2.26 fb^{-1} ²⁰. This analysis allows to test gluon PDF in different Bjorken- x and Q^2 values. The isolated-photon cross sections are measured as a function of E_T^γ in different $|y^\gamma|$ bins, while the γ +jet cross sections are measured as a function of E_T^γ in different $|y^\gamma|$ and $|y^{\text{jet}}|$ bins. Prompt photons are identified with a boosted decision tree algorithm, implemented using the TMVA v4.1.2 toolkit²¹. Figure 3(a) shows a comparison of the unfolded data distributions with NLO pQCD calculations from JETPHOX^{22,23} using the NNPDF3.0NLO PDF set. All measurements

are in agreement with the theoretical predictions.

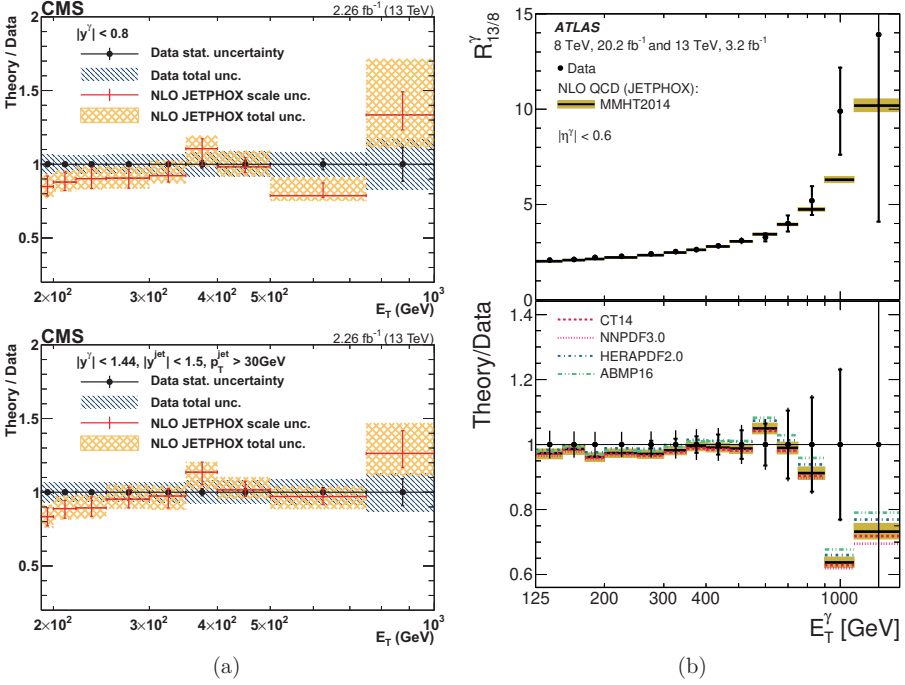


Figure 3 – (a) The ratios of theoretical predictions at NLO to data for the differential cross sections for isolated-photon (photon+jets) production in the $|y^\gamma| < 0.8$ ($|y^\gamma| < 1.44$, $|y^{\text{jet}}| < 1.5$, $p_T^{\text{jet}} > 30 \text{ GeV}$) region are shown in the top (bottom). The error bars on data points represent the statistical uncertainties, while the hatched area shows the total experimental uncertainty. The errors on the ratio represent scale uncertainties, and the shaded regions represent the total theoretical uncertainties. (b) The ratio $R_{13/8}^\gamma$ (dots) as a function of E_T^γ in the $|\eta^\gamma| < 0.6$ region. The NLO pQCD predictions using the MMHT2014 PDF set (black lines) are also shown. The inner (outer) error bars represent the statistical (total) uncertainties, while the shaded band represents the theoretical uncertainty. The bottom panel shows the ratio of the predictions to the measured $R_{13/8}^\gamma$ (black lines). The ratios of the predictions based on alternative PDF sets to the measured $R_{13/8}^\gamma$ are also included.

A ratio of cross sections for inclusive isolated-photon production at $\sqrt{s} = 13$ and 8 TeV ($R_{13/8}^\gamma$) is performed by the ATLAS Collaboration²⁴. The ratio is measured as a function of E_T^γ in different $|\eta^\gamma|$ ranges. Reduced systematic and theoretical uncertainties are achieved by taking into account the correlations between data taken at different centre-of-mass energies. And because of this, the photon energy scale is no longer the dominant uncertainty (with some exceptions at high E_T^γ). A small background contribution still remains after imposing photon identification and isolation requirements and is subtracted using a data-driven method based on background control regions^{25,26}. NLO pQCD predictions calculated with JETPHOX, corrected for non-perturbative effects, and using several PDF sets are compared with the unfolded data, as shown in Fig. 3(b). In addition, ATLAS measured isolated-photon plus jet production cross sections as a function of several observables with $\sqrt{s} = 13$ TeV data corresponding to an integrated luminosity of 3.2 fb^{-1} ²⁷. In both measurements, the NLO theoretical predictions agree with the data within uncertainties.

4 Conclusions

The latest QCD results from ATLAS and CMS Collaborations at the LHC are presented. Cross section measurements for multijet final states in nearly back-to-back topologies show discrepancies with state-of-the-art NLO MC simulation samples, which gives room to improve MC event simulations. The measurement of azimuthal decorrelations shows a remarkable agreement with the NLO pQCD calculations. The ratio of cross-sections at different centre-of-mass energies allows to significantly reduce the experimental and theoretical uncertainties, granting better constrains to QCD. More precise measurements are expected in the coming years using the full data collected by both experiments, foreseeing stronger tests of the QCD theory.

© 2019 CERN for the benefit of the ATLAS and CMS Collaborations. Reproduction of this article or parts of it is allowed as specified in the CC-BY-4.0 license.

References

1. ATLAS Collaboration, 2008 JINST 3 S0800.
2. CMS Collaboration, 2008 JINST 3 S08004.
3. CMS Collaboration, Submitted to EPJC, arXiv:1902.04374.
4. P. Nason, JHEP11(2004) 040.
5. S. Frixione, P. Nason, and C. Oleari, JHEP11(2007) 070.
6. S. Alioli, P. Nason, C. Oleari, and E. Re, JHEP06(2010) 043.
7. NNPDF Collaboration, JHEP04(2015) 040.
8. T. Sjöstrand et al., Comput. Phys. Commun.191(2015)159.
9. NNPDF Collaboration, Nucl. Phys. B855(2012) 153.
10. M. Bähr et al., Eur. Phys. J. C58(2008) 639.
11. S. Alioli et al., JHEP11(2011) 081.
12. A. Kardos, P. Nason, and C. Oleari, JHEP04(2014)043.
13. ATLAS Collaboration, Phys. Rev. D 98 (2018) 092004.
14. Z. Nagy, Phys. Rev. D68(2003) 094002.
15. Z. Nagy, Phys. Rev. Lett.88(2002) 122003.
16. H. D. Politzer, Phys. Rev. Lett.30(1973) 1346.
17. D. J. Gross and F. Wilczek, Phys. Rev. D8(1973) 3633.
18. L. A. Harland-Lang, A. D. Martin, P. Motylinski, and R. S. Thorne, Eur. Phys. J. C75(2015) 204.
19. L. A. Harland-Lang, A. D. Martin, P. Motylinski, and R. S. Thorne, Eur. Phys. J. C75(2015) 435.
20. CMS Collaboration, Eur. Phys. J. C 79 (2019) 20.
21. H. Voss, A. Höcker, J. Stelzer, and F. Tegenfeldt, XIth International Workshop on Advanced Computing and Analysis Techniques in Physics Research (ACAT), p. 40. 2007.
22. S. Catani, M. Fontannaz, J. Ph. Guillet and E. Pilon, JHEP05(2002) 028.
23. P. Aurenche, M. Fontannaz, J. Ph. Guillet, E. Pilon and M. Werlen, Phys. Rev. D73(2006) 094007.
24. ATLAS Collaboration, Submitted to JHEP, arXiv:1901.10075.
25. ATLAS Collaboration, JHEP08(2016) 005.
26. ATLAS Collaboration, Phys. Lett. B770(2017) 473.
27. ATLAS Collaboration, Phys. Lett. B 780 (2018) 578.

ISOLATED PHOTON AND PHOTON+JET PRODUCTION AT NNLO QCD ACCURACY AND THE RATIO $R_{13/8}^\gamma$

X. CHEN,^a T. GEHRMANN,^a N. GLOVER,^b M. HÖFER,^a A. HUSS^c

^a *Physik-Institut, Universität Zürich, Winterthurerstrasse 190, CH-8057 Zürich, Switzerland*

^b *Institute for Particle Physics Phenomenology, Durham University, Durham, DH1 3LE, UK*

^c *Theoretical Physics Department, CERN, CH-1211 Geneva 23, Switzerland*

We discuss different approaches to photon isolation in fixed-order calculations and present a new next-to-next-to-leading order (NNLO) QCD calculation of $R_{13/8}^\gamma$, the ratio of the inclusive isolated photon cross section at 8 TeV and 13 TeV, differential in the photon transverse momentum, which was recently measured by the ATLAS collaboration.

1 Introduction

Both inclusive isolated photon ($\gamma + X$) and photon-plus-jet ($\gamma + j$) production in pp collisions present a means to test QCD dynamics using a colourless probe. Because their Born-level processes are $\bar{q}q \rightarrow g\gamma$ and $qg \rightarrow q\gamma$, related observables are sensitive to the gluon-distribution in the proton already at leading order (LO).

Recent experimental analyses by ATLAS^{1,2} and CMS³ pushed the experimental uncertainties down to a few percent. To match this accuracy also in theory calculations, the inclusion of NNLO QCD corrections is crucial. They have been calculated for $\gamma + X$ and $\gamma + j$ at $\sqrt{s} = 8$ TeV by the MCFM⁴ collaboration. In our recent paper⁵ we present an independent calculation of the NNLO corrections, using the NNLOJET framework. NNLOJET is a parton-level event generator which uses the antenna subtraction method⁶ to subtract the infrared (IR) QCD divergencies. The matrix elements for $\gamma + X$ and $\gamma + j$ are implemented up to NNLO in analytic form.

In the experimental environment it is necessary to separate any photon produced in the hard partonic scattering process from photons of other origin, for example radiation occurring during the hadronization process. One therefore measures the hadronic energy in the vicinity of the photon and defines conditions for its shape and amount. If these are met, the photon is said to be isolated.

When reconstructing the experimental isolation procedure in fixed-order theory calculations, one has to deal with hadronic radiation arbitrarily collinear to the photon. This must be taken care of by either including photon fragmentation functions to the perturbative order under consideration, which to NNLO has not been done so far, or by modifying the isolation prescription to eliminate the collinear configurations. In the latter approach a systematic difference between isolation procedures used in experiment and theory emerges.

2 Photon Isolation

There are several prescriptions for the photon isolation. They mainly differ in how exactly the “vicinity” of the photon is defined and how the hadronic energy therein may be distributed.

The two most common ones are the fixed (hard) cone isolation, and the dynamical cone (Frixione⁷) isolation.

Fixed cone isolation - A cone around the photon axis is defined by the distance $R = \sqrt{\Delta\eta^2 + \Delta\phi^2}$, called the radius of the cone. The integrated hadronic transverse energy within the cone has to be smaller as a certain E_T^{\max} for the photon to be considered as isolated. Often E_T^{\max} is given as a simple linear function of the photon transverse momentum/ energy:

$$E_T^{\max} = \varepsilon E_T^\gamma + E_T^{\text{thres}}. \quad (1)$$

This isolation criterion is used in all experimental analyses so far. It allows, however, for hadronic radiation arbitrarily collinear to the photon, as long as its energy is not too large. This introduces a sensitivity to the photon fragmentation, which is difficult to describe from the theoretical viewpoint. On the other hand it is not possible to simply set $E_T^{\max} = 0$, because this would, while indeed eliminating the fragmentation sensitivity, cut out part of the soft phase space, rendering observables IR unsafe.

Dynamical cone isolation - Instead of a fixed E_T^{\max} one defines a profile $E_T^{\max}(r_d)$ with $E_T^{\max}(r_d) \rightarrow 0$ as $r_d \rightarrow 0$. r_d is again the distance from the photon. For any sub-cone with r_d smaller than some maximal radius R_d the integrated energy within this sub-cone must not exceed $E_T^{\max}(r_d)$. The functional form of the profile conventionally used is

$$E_T^{\max} = \varepsilon_d E_T^\gamma \left(\frac{1 - \cos r_d}{1 - \cos R_d} \right)^n \quad \text{for all } r_d < R_d. \quad (2)$$

This prescription both eliminates the fragmentation sensitivity and ensures IR safety. It can, however, only be approximated in experiments and so one has to tune the parameters of the dynamical isolation to fit the experimental setup as closely as possible.

This difference in the isolation procedures used in experiment and theory is unsatisfactory, as it is a source of uncertainty, which is difficult to quantify. Only the inclusion of the photon fragmentation functions to the same order as the partonic calculation can solve this issue. To NNLO this has not been done so far. But an improvement over the current situation can already be achieved by combining both fixed and dynamical cone in a hybrid approach⁸, as used by ATLAS in their $\gamma + j$ study².

Hybrid cone isolation - A dynamical cone with comparatively small R_d is used to eliminate the fragmentation contribution. In a second stage of the isolation a fixed cone with $R^2 \gg R_d^2$ is applied, the parameters of which are chosen according to any experimental analysis under consideration. In this way observables should retain the correct dependence on the parameters of the outer "physical" isolation cone. A residual dependence on the inner dynamical cone remains, but can in principle be made small for a suitable choice of parameters. In our paper⁵ we present some technical studies on the choice of the inner cone parameters. We calculated the total cross section for $\gamma + X$ at 13 TeV as a function of the outer isolation cone radius R , too. It would be interesting to see this analysis performed also in experiment.

3 The ratio $R_{13/8}^\gamma$

In our paper⁵ we calculated, using the hybrid isolation procedure, several differential distributions for $\gamma + X$ and $\gamma + j$ at 8 TeV and 13 TeV, based on studies by ATLAS^{1,2} and CMS³. We found that the inclusion of NNLO corrections leads to a significant improvement in both the accuracy of the predictions and the description of the data. Amounting to no more than a few percent, the theory uncertainties are now competitive with experimental errors.

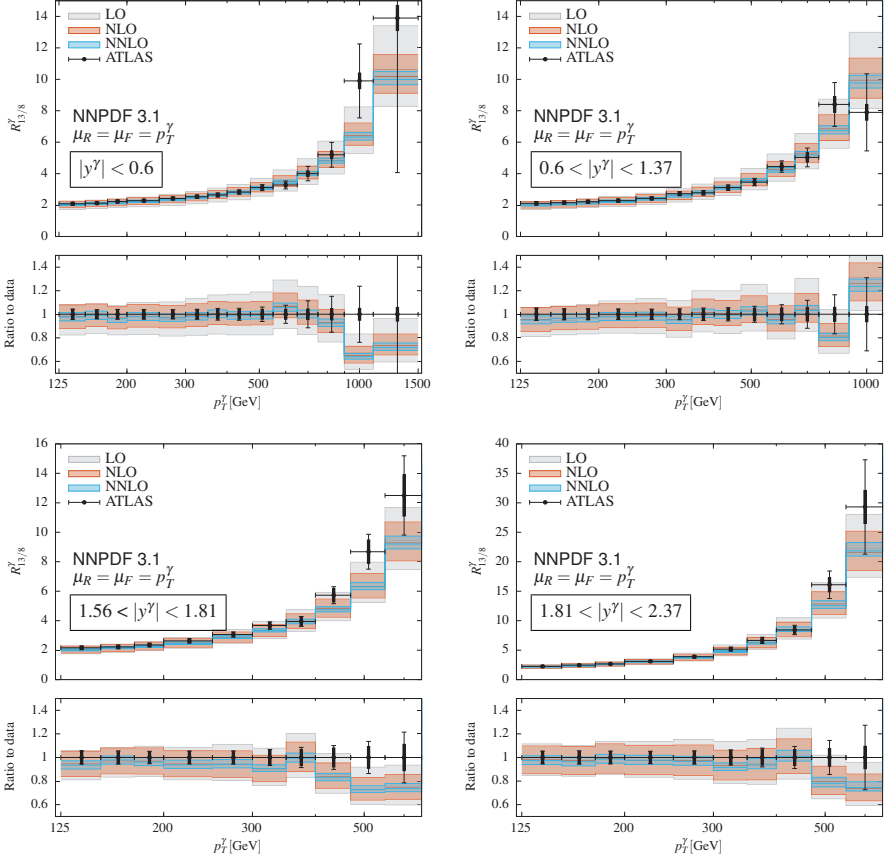
NNLOJET $pp \rightarrow \gamma + X$ $\sqrt{s} = (8, 13) \text{ TeV}$ 

Figure 1 – $R_{13/8}^{\gamma}$ as a function of the transverse energy/momentum of the isolated photon at LO, NLO and NNLO in four different rapidity bins, from central (top left) to most forward (bottom right). The theoretical uncertainty bands are derived by means of an independent variation of factorization and renormalization scales, both in the numerator and the denominator (see text for details). The results are compared to ATLAS data ⁹.

Here we present a NNLO calculation of the ratio $R_{13/8}^\gamma$ of the $\gamma+X$ cross section at 8 TeV and 13 TeV, differential in p_T^γ and presented in four rapidity bins. It is based on a recent measurement of this quantity by ATLAS⁹. Measuring ratios is a means to reduce the experimental systematic uncertainties.

Both the 8 TeV and the 13 TeV measurements of the p_T^γ -distribution in isolated photon production by ATLAS were performed in four different regions in rapidity

$$|y^\gamma| < 0.6, \quad 0.6 < |y^\gamma| < 1.37, \quad 1.56 < |y^\gamma| < 1.81, \quad 1.81 < |y^\gamma| < 2.37, \quad (3)$$

which excludes the region [1.37, 1.56]. The ratio is measured in the same bins, using the overlap of the phase-space regions of both measurements, with $p_T^\gamma > 125$ GeV.

For the NNLOJET prediction we use the NNPDF3.1 PDF set and a hybrid photon isolation with parameters

$$\begin{aligned} R_d = 0.1, & \quad \varepsilon_d = 0.1, & \quad n = 2, \\ R = 0.4, & \quad E_T^{\text{thres}} = 4.8 \text{ GeV}, & \quad \varepsilon = 0.0042, \end{aligned} \quad (4)$$

where the fixed-cone parameters $(R, E_T^{\text{thres}}, \varepsilon)$ correspond to the isolation set-up used by ATLAS.

The theory prediction for $R_{13/8}^\gamma$ has not been performed as an independent calculation, but rather has been derived using the two calculations for 8 TeV and 13 TeV. For both the theoretical uncertainty is estimated by means of a seven-point scale variation, $\mu_F = a p_T^\gamma$, $\mu_R = b p_T^\gamma$ with $a, b \in \{1/2, 1, 2\}$, where we exclude the configurations with $a/b \in \{1/4, 4\}$.

The uncertainty of $R_{13/8}^\gamma$ has now been estimated by forming the ratio for all possible combinations of the seven scale configurations for numerator and denominator, excluding again the combinations where the ratio of any two scales equals 1/4 or 4. This effectively corresponds to a generalisation of the seven-point scale variation for two scales to a 31-point variation for four scales.

In figure 1 we show the result in the four rapidity bins mentioned above and compare to ATLAS data⁹. Except for the highest bins in p_T^γ the description of the data is excellent. Like for the calculations⁵ for individual \sqrt{s} we see a significant reduction in the uncertainty when going from NLO to NNLO: While at NLO the uncertainty lies between (+10, -9)% and (-17, -14)%, only slightly growing with p_T^γ and $|y^\gamma|$, at NNLO it lies between (+3.4, -2.8)% and (+6.5, -4.0)%.

References

1. The ATLAS Collaboration, *JHEP* **08**, 005 (2016), *Phys. Lett.* **B770**, 473-493 (2017)
2. The ATLAS Collaboration, *Phys. Lett.* **B780**, 578-602 (2018)
3. The CMS Collaboration, *JHEP* **10**, 128 (2015), *Eur. Phys. J.* **C79**, 20 (2019)
4. J.M. Campbell *et al*, *Phys. Rev. Lett.* **118**, 222001 (2017), *Phys. Rev.* **D96**, 014037 (2017)
5. X. Chen *et al*, arXiv:1904.01044
6. A. Gehrmann-De Ridder *et al*, *JHEP* **09**, 056 (2005), A. Daleo *et al* *JHEP* **04**, 016 (2007), J. Currie *et al* *JHEP* **04**, 066 (2013)
7. S. Frixione, *Phys. Lett.* **B429**, 369-374 (1998)
8. F. Siegert, *J. Phys.* **G44**, 044007 (2017)
9. The ATLAS Collaboration, *JHEP* **04**, 093 (2019)
10. The NNPDF Collaboration, *Eur. Phys. J.* **C77**, 663 (2017)

ANALYTIC FORM OF PLANAR TWO-LOOP FIVE-PARTON SCATTERING AMPLITUDES IN QCD

S. Abreu,^a J. Dormans,^b F. Febres Cordero,^{b,c} H. Ita,^b B. Page,^d V. Sotnikov^b

^a*Center for Cosmology, Particle Physics and Phenomenology (CP3), Université Catholique de Louvain, 1348 Louvain-La-Neuve, Belgium*

^b*Physikalisches Institut, Albert-Ludwigs Universität Freiburg, D-79104 Freiburg, Germany*

^c*Physics Department, Florida State University, 77 Chieftan Way, Tallahassee, FL 32306, U.S.A.*

^d*Institut de Physique Théorique, CEA, CNRS, Université Paris-Saclay, F-91191 Gif-sur-Yvette cedex, France*

We discuss the recent calculation of the analytic form of the two-loop five-parton amplitudes in QCD. These constitute the full set of amplitudes required for the computation of NNLO QCD corrections to three-jet production at hadron colliders in the leading-color approximation. The calculation is done by combining efficient numerical evaluations and analytic reconstruction techniques. The techniques we present open the door to the evaluation of multi-leg two-loop amplitudes beyond the current state of the art.

After a first phase which culminated in the discovery of the Higgs boson by the ATLAS and CMS collaborations, experiments at the Large Hadron Collider (LHC) have moved towards a phase of high precision QCD measurements that is probing the Standard Model at the percent level for several observables. Maximizing the impact of this new experimental data requires theoretical predictions of similar precision levels. In practice, this means that next-to-next-to leading order (NNLO) QCD results are required. A crucial ingredient in obtaining these theoretical predictions is the evaluation of two-loop amplitudes. In these proceedings we discuss the computation of a complete set of independent planar two-loop five-parton helicity amplitudes, including contributions from closed fermion loops¹. These amplitudes complete the set required for the description of three-jet production at NNLO at hadron colliders in the leading-color approximation². Beyond the results for these particular amplitudes, we present a new approach to the evaluation of scattering amplitudes. This approach combines the two-loop numerical unitarity method with efficient functional reconstruction techniques³: the numerical calculation bypasses the large intermediate expressions that are often the bottleneck in more standard approaches, and the functional reconstruction directly targets the compact final expressions of the amplitudes. Similar techniques have been used recently by other groups to compute five-point two-loop amplitudes^{4,5}.

1 Two-loop amplitudes

We consider all five-parton amplitudes at leading-color. They can be decomposed into partial amplitudes \mathcal{A} ,

$$A(1, 2, 3, 4, 5)|_{\text{leading color}} = \sum_{\sigma \in \mathcal{S}} C_{\sigma} \mathcal{A}(\sigma(1), \sigma(2), \sigma(3), \sigma(4), \sigma(5)), \quad (1)$$

where all properties of each particle (parton type, momentum, helicity, etc.) are kept implicit, S is the set of inequivalent permutations in the color decomposition for each parton type, and C_σ is a color factor. The partial amplitudes have a perturbative expansion in the QCD coupling α_s , and we denote by $\mathcal{A}^{(k)}$ a k -loop partial amplitude. Each $\mathcal{A}^{(k)}$ can be further expanded as a series in powers of N_f/N_c with maximal degree k . We will be interested in the case $k = 2$.

Computing the amplitude means determining the decomposition of the partial amplitudes $\mathcal{A}^{(2)}$ into a linear combination of master integrals,

$$\mathcal{A}^{(2)} = \sum_{\Gamma} \sum_{i \in M_{\Gamma}} c_{\Gamma,i}(\epsilon) \mathcal{I}_{\Gamma,i}(\epsilon), \quad (2)$$

where Γ denotes a set of propagators, M_{Γ} is the corresponding set of master integrals and ϵ is the dimensional regulator (our calculations are done in the 't Hooft-Veltman scheme). The coefficients are functions of the kinematic invariants and specific to each particle type, helicity and power of N_f . The complete set of master integrals is determined by the kinematics only, and thus common to all five-parton amplitudes. For planar five-point massless amplitudes, all master integrals are known^{6,7} and the only task is to determine the coefficients $c_{\Gamma,i}$.

In a standard approach to the calculation of amplitudes, one would first compute the integrand $\mathcal{A}(\ell_i)$ from the Feynman rules of the theory (ℓ_i denotes the loop momenta), and then use integration-by-parts (IBP) identities to reduce the amplitude to a linear combination of master integrals. This approach is very sensitive to the number of variables on which the amplitude depends. Indeed, the intermediate expressions become very large, mainly due to the complexity of the IBP identities, which obscures the relative simplicity of the final expressions. The amplitudes we are interested in depend on four dimensionless variables and the complexity of the required IBP tables makes this approach too inefficient for their calculation.

1.1 Two-loop numerical unitarity

Alternatively, one can perform the reduction to master integrals numerically. This idea, together with a more efficient construction of the integrand that directly implements the reduction to master integrals, is the basis of the two-loop numerical unitarity method^{8,9}. In a nutshell, one first constructs an ansatz for the integrand of the amplitude in terms of a well-chosen set of tensor insertions⁸. The insertions are chosen so that they are separated into terms that integrate to master integrals ($i \in M_{\Gamma}$) and terms that integrate to zero ($i \in S_{\Gamma}$)

$$\mathcal{A}^{(2)}(\ell_i) = \sum_{\Gamma \in \Delta} \sum_{i \in M_{\Gamma} \cup S_{\Gamma}} c_{\Gamma,i} \frac{m_{\Gamma,i}(\ell_i)}{\prod_{j \in P_{\Gamma}} \rho_j}. \quad (3)$$

The coefficients $c_{\Gamma,i}$ (for $i \in M_{\Gamma}$) are determined by solving a large system of linear equations constructed by exploring the factorization properties of the integrand when propagators are put on-shell. The numerical nature of this procedure means that it is susceptible to precision loss, but this can be overcome by performing the calculation in a finite field, which gives exact numerical values for the coefficients $c_{\Gamma,i}$. This procedure was recently implemented to numerically compute the five-parton amplitudes¹⁰ (see also¹¹).

Two-loop numerical unitarity provides a generic approach to amplitude evaluation. Its numerical nature means it behaves well with the number of variables, and one-loop experience suggests that numerical calculations become more efficient than analytic expressions for a large enough number of scales. We thus believe that numerical unitarity will be an important framework when two-loop amplitudes with a very high number of scales become necessary for phenomenological studies. For the purpose of these proceedings, we will use its efficiency and the fact that it is exact when implemented over a finite field to generate the numerical data for our functional reconstruction program.

2 Simplifications for efficient reconstruction

The algorithm for functional reconstruction of rational functions from numerical data is very sensitive to the complexity of the rational functions. For two-loop five-parton amplitudes, the coefficients $c_{\Gamma,i}$ are in general very complex functions. The choice of variables has a large impact¹, but we can also use physical considerations to define simpler objects to reconstruct.

We are interested in the Laurent expansion of the amplitudes around $\epsilon = 0$. Eq. (2) is a decomposition into a linearly independent set of master integrals prior to expansion in ϵ . The coefficients of the Laurent expansion in ϵ of the master integrals $\mathcal{I}_{\Gamma,i}(\epsilon)$ are linear combinations of multiple polylogarithms (MPLs), which are known to satisfy many linear relations. In order to find a minimal decomposition of the Laurent expansion of the amplitude, we use a basis B of the space of MPLs built from so-called pentagon functions⁷, denoted $h_i \in B$, and write

$$\mathcal{A}^{(2)} = \sum_{i \in B} \sum_{k=-4}^0 \epsilon^k \tilde{c}_{k,i} h_i + \mathcal{O}(\epsilon). \quad (4)$$

All linear relations between master integrals that appear after expansion in ϵ are resolved in such a decomposition.

The two-loop amplitude contains a lot of information that is related to lower loop orders. In particular, all the poles in the Laurent expansion are dictated from the corresponding tree and one-loop amplitudes, together with some universal operators denoted $\mathbf{I}^{(1)}$ and $\mathbf{I}^{(2)}$. Using this observation, we can define a finite remainder by subtraction of these contributions:

$$\mathcal{R}^{(2)} = \mathcal{A}^{(2)} - \mathbf{I}_{[n]}^{(2)}(\epsilon) \mathcal{A}^{(0)} - \mathbf{I}_{[n]}^{(1)}(\epsilon) \mathcal{A}^{(1)} + \mathcal{O}(\epsilon). \quad (5)$$

The remainder will be a simpler function with no dependence on ϵ . Since both one-loop amplitudes and the operators $\mathbf{I}^{(1,2)}$ can be written in terms of pentagon functions, the remainder satisfies a decomposition similar to eq. (4):

$$\mathcal{R}^{(2)} = \sum_{i \in B} r_i h_i. \quad (6)$$

The coefficients r_i are rational functions of the Mandelstam invariants and the anti-symmetric contraction $\text{tr}_5 = 4i \varepsilon(p_1, p_2, p_3, p_4)$. These are the coefficients whose form we will reconstruct.

The denominators of the r_i can be determined very easily². Indeed, since the singularity structure of the amplitude is constrained by physical considerations, the denominators must be related to the logarithmic singularities of the pentagon functions. We can thus write an ansatz for the denominators of the r_i which can be fixed by evaluating the amplitude on a so-called ‘univariate slice’. After this step, we end up only needing to reconstruct the numerators of the r_i , which are no longer rational functions but multivariate polynomials.

3 Functional reconstruction of two-loop five-parton amplitudes

We have implemented the two-loop numerical unitarity algorithm in a finite field in a C++ code, which allows us to compute the decomposition (2) with exact numerical coefficients. The handling of fermions has been improved compared to previous implementations¹⁰. After inserting both the expressions for the master integrals and the one-loop amplitudes in terms of pentagon functions, we obtain exact numerical values for the coefficients r_i of eq. (6). This procedure is iterated at enough kinematic points to generate the necessary numerical data for the rational reconstruction. The choice of points is dictated by the functional reconstruction algorithm³, which we have also implemented in C++ and slightly modified to allow a more efficient parallelization. The output of the reconstruction is a rational function with numerical coefficients in a finite field with cardinality of order $O(2^{31})$. We then implement a partial-fraction decomposition

of the rational functions which greatly simplifies the final results. After this simplification, all numerical coefficients can be mapped back to the field of rational numbers from their value in a single finite field. The most complicated amplitude requires evaluation at 95,000 phase-space points. With an evaluation time of 4.5min/point, this is a simple calculation on a modern cluster. Our final analytic expressions for the full set of two-loop five parton amplitudes are very compact, with a total combined size of 10MB, making it suitable to be employed in future phenomenological studies.

4 Outlook

The approach we propose uses two-loop numerical unitarity to bypass the large intermediate analytic expressions and directly targets the simpler final analytic result. We obtain compact analytic expressions, opening the door to phenomenological studies of three-jet production at the LHC. With this approach the planar five-point massless QCD amplitudes which were a bottleneck for many years become a simple calculation. The efficiency of the approach paves the way to other complex calculations of phenomenological relevance, such as the two-loop five-point amplitudes with one external mass for H+2-jet or Z/W+2-jet production at the LHC.

Acknowledgments

The work of S.A. is supported by the Fonds de la Recherche Scientifique–FNRS, Belgium. The work of J.D., F.F.C. and V.S. is supported by the Alexander von Humboldt Foundation, in the framework of the Sofja Kovalevskaja Award 2014, endowed by the German Federal Ministry of Education and Research. The work of B.P. is supported by the French Agence Nationale pour la Recherche, under grant ANR–17–CE31–0001–01. The authors acknowledge support by the state of Baden–Württemberg through bwHPC and the German Research Foundation (DFG) through grant no INST 39/963-1 FUGG.

References

1. S. Abreu, J. Dormans, F. Febres Cordero, H. Ita, B. Page and V. Sotnikov, arXiv:1904.00945 [hep-ph], *to appear in JHEP*.
2. S. Abreu, J. Dormans, F. Febres Cordero, H. Ita and B. Page, Phys. Rev. Lett. **122** (2019) no.8, 082002 doi:10.1103/PhysRevLett.122.082002 [arXiv:1812.04586 [hep-ph]].
3. T. Peraro, JHEP **1612** (2016) 030 doi:10.1007/JHEP12(2016)030 [arXiv:1608.01902 [hep-ph]].
4. S. Badger, C. Brønnum-Hansen, H. B. Hartanto and T. Peraro, JHEP **1901** (2019) 186 doi:10.1007/JHEP01(2019)186 [arXiv:1811.11699 [hep-ph]].
5. S. Badger *et al.*, arXiv:1905.03733 [hep-ph].
6. C. G. Papadopoulos, D. Tommasini and C. Wever, JHEP **1604** (2016) 078 doi:10.1007/JHEP04(2016)078 [arXiv:1511.09404 [hep-ph]].
7. T. Gehrmann, J. M. Henn and N. A. Lo Presti, JHEP **1810** (2018) 103 doi:10.1007/JHEP10(2018)103 [arXiv:1807.09812 [hep-ph]].
8. H. Ita, Phys. Rev. D **94** (2016) no.11, 116015 doi:10.1103/PhysRevD.94.116015 [arXiv:1510.05626 [hep-th]].
9. S. Abreu, F. Febres Cordero, H. Ita, M. Jaquier, B. Page and M. Zeng, Phys. Rev. Lett. **119** (2017) no.14, 142001 doi:10.1103/PhysRevLett.119.142001 [arXiv:1703.05273 [hep-ph]].
10. S. Abreu, F. Febres Cordero, H. Ita, B. Page and V. Sotnikov, JHEP **1811** (2018) 116 doi:10.1007/JHEP11(2018)116 [arXiv:1809.09067 [hep-ph]].
11. S. Badger, C. Brønnum-Hansen, T. Gehrmann, H. B. Hartanto, J. Henn, N. A. Lo Presti and T. Peraro, PoS LL **2018** (2018) 006 doi:10.22323/1.303.0006 [arXiv:1807.09709 [hep-ph]].

ELLIPTIC POLYLOGARITHMS AND PURE FUNCTIONS

Lorenzo Tancredi

*TH Department, CERN, 1 Esplanade des Particules,
Geneva 23, CH-1211, Switzerland*

In this contribution I describe some of the recent developments in our understanding of the class of special functions required to compute multiloop Feynman integrals with massive internal particles.

1 Introduction

The discovery of the Higgs boson at the LHC in July 2012 was a milestone for particle physics. After the Higgs' discovery, the absence of any clear signs on new physics has generated an impressive concerted effort from the theory and experimental community to push the discovery potential of the LHC further, by turning it into an impressive precision machine. In fact, while almost every single measurement carried on at the LHC seems to confirm that the Standard Model is in great shape, we are also very much aware of the many shortcomings of our current understanding of the physical world. As a matter of fact, seeing the Higgs boson not only revealed the presence of a new (apparently) fundamental particle, but it was also provided us with the first evidence for the existence of a new elementary interaction, whose nature remains largely not understood. The dynamics behind the spontaneous symmetry breaking (SSB) mechanism is believed to be tightly intertwined with some of the most pressing questions in fundamental physics, as for example the origin of masses and the strong hierarchy among them, in particular in the lepton and quark sectors. Ultimately, understanding these phenomena could hold the key to answer questions about the existence of stable matter in the universe.

In this scenario, the LHC constitutes a unique opportunity, since it is the very first instrument able to probe *directly* the characteristic energy scale for these phenomena, as it was beautifully demonstrated by the recent observation of the production of a $t\bar{t}$ -pair together with a Higgs boson at the ATLAS and CMS experiments^{1,2}. In order to fully exploit the discovery potential of the LHC and gain as much information as possible from its observations, high-precision measurements of relevant physics observables should be compared to equally precise theoretical calculations for these observables in the Standard Model (or its possible modifications). It is only in this way, in fact, that we can hope to pin-point elusive signs of new physics phenomena that could explain, among the others, the dynamics behind the SSB mechanism. Clearly, precision physics at hadron colliders is complicated by strong pollution due to the underlying non-perturbative dynamics in Quantum Chromodynamics (QCD). Nevertheless, thanks to the existence of factorization theorems that allow us to separate the non-perturbative from the perturbative dynamics, and also thanks to the concerted effort of the community in keeping all ingredients of these factorization theorems under precise theoretical control, in the last years it has become clear that precision physics at the LHC up to the $\mathcal{O}(1\%)$ level could become possible in the near future³. This will require, among the others, having the hard scattering process in

perturbative Quantum Field Theory (pQFT) under control at the same level of precision.

Focussing now on the hard-scattering process, reaching the $\mathcal{O}(\%)$ -level precision in perturbative QCD (and generally in the Standard Model) typically requires the calculation of multiloop corrections to scattering amplitudes for a multitude of $2 \rightarrow 1$, $2 \rightarrow 2$ and $2 \rightarrow 3$ processes. While such calculations constitute in general insurmountable tasks, the last decade has witnessed impressive advancements of our understanding of pQFT and in particular of the recurring mathematical structures hiding behind scattering amplitudes. In the next section I will summarize some of these ideas and elucidate how they are helping us to complete important perturbative calculations that would have been considered impossible until only a few years ago.

2 Scattering amplitudes and special functions

Scattering amplitudes constitute our main instrument to extract quantitative physical predictions from QFT. Scattering amplitudes are often computed in perturbation theory through an expansion in Feynman diagrams. As hinted to in the introduction, in order to match the precision level of present and future experimental measurements at the LHC, typically scattering amplitudes in second- and third-order perturbation theory must be computed, which in turn require the computation of two- and three-loop Feynman diagrams. Since the computation of any loop diagram requires the evaluation of d -dimensional integral^a, the higher the number of loops we are interested in, the more the computations become intractable. Since the dawn of loop-calculation, a considerable effort has been devoted in computing observables at higher and higher loops orders. What has soon become clear is that, more or less independently of the complexity of the intermediate steps required to get to the final results, the latter would always exhibit a much higher degree of simplicity than expected. In particular, the class of mathematical functions and constants required to express loop corrections to scattering amplitude, appeared to be largely self-contained, in the sense that the same kinds of functions would show up over and over again in apparently unrelated calculations.

Indeed, quantum mechanics determines the analytic structure of scattering amplitudes and, in particular, it requires them to be complex functions with poles and branches whose positions are dictated by unitarity. The fact that scattering amplitudes must have branch cuts in the complex hyper-plane spanned by the kinematic invariants, means that the (special) functions required to compute them will have to be in general multivalued complex functions. Indeed, the natural language to describe these functions turns out to be that of *Riemann surfaces* and *algebraic geometry*.

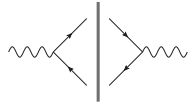
Trying to avoid a technical discussion, let me start with an example. The one-loop corrections to the photon propagator in Quantum ElectroDynamics (QED) require the calculation of the following one-loop Feynman integral

$$\text{Diagram} = \int \frac{d^d k}{(2\pi)^d} \frac{1}{(k^2 - m^2)((k - p)^2 - m^2)}, \quad (1)$$

where in the following I will put $s = p^2$. For simplicity, let me consider the graph in $d = 2$ space-time dimensions.^b In order to see its structure, let me compute its imaginary part (or its discontinuity) by cutting the graph as follows⁵:


^aAt least in dimensional regularization.

^bIt can be shown that it is always possible to recover the $d = 4$ dimensional result from the $d = 2$ one through simple algebraic operations⁴.



$$= \int \frac{d^2 k}{(2\pi)^2} \delta^+(k^2 - m^2) \delta^+((k-p)^2 - m^2) \sim \frac{1}{\sqrt{s(s-4m^2)}}, \quad (2)$$

where I neglected numerical overall prefactors. The result for the Feynman integral can then be computed by use of a dispersion relation and gives



$$\sim \int_{4m^2}^{\infty} \frac{ds'}{s' - s - i\epsilon} \frac{1}{\sqrt{s'(s' - 4m^2)}} = \frac{1}{\sqrt{s(s-4m^2)}} \ln \left(\frac{\sqrt{s-4m^2} + \sqrt{s}}{\sqrt{s-4m^2} - \sqrt{s}} \right). \quad (3)$$

This very simple example is enough to show a quite general structure recurring in loop calculations. As we see, eq. (3) consists in an (iterated) integral over rational functions and algebraic functions of the kinematics (in this case, a square-root). It is easy to convince oneself that, by extending this calculation to higher orders in $(d-2)$, i.e. by computing the Feynman integrals as a Laurent series in ϵ , where $d = 2 - 2\epsilon$, this structure would be preserved to all orders.

The question we want to ask ourselves now is, what is the general geometry where these (iterated) integrals of rational and algebraic functions are defined? If we inspect eq. (3), we could at first imagine that some non-trivial geometry could be generated by the presence of the square-root $y = \sqrt{s(s-4m^2)}$, which can be interpreted as the equation defining an *algebraic curve*. In this case, nevertheless, it turns out that by a suitable change of variables, the square root can be *rationalized*. Indeed, by defining

$$s = m^2 \frac{(1+x)^2}{x} \quad \rightarrow \quad y = m^2 \frac{1-x^2}{x} \quad (4)$$

the square root disappears, leaving into eq. (3) integrals over simple *rational functions* in x .

This simplification is crucial. Indeed, as complex functions, rational functions are *single valued functions* (they do not possess any branch cut) and the corresponding integrals over them can be defined on the standard complex plane with the addition of the point at infinity, also referred to as *Riemann sphere*, \mathbb{C}_∞ . The class of special functions defined as iterated integrals of rational functions on the Riemann sphere has been given the name of *multiple polylogarithms* (MPLs) and their integral representation reads^{6,7}

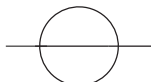
$$G(c_1, c_2, \dots, c_n, x) = \int_0^x \frac{dt_1}{t_1 - c_1} G(c_2, \dots, c_n, t_1), \quad G(\underbrace{0, \dots, 0}_n, x) = \frac{1}{n!} \ln^n x. \quad (5)$$

As the name suggests, their simplest instance is given by the well known *logarithm*

$$\int_0^x \frac{dt_1}{t_1 - c_1} = \ln \left(1 - \frac{x}{c_1} \right), \quad \text{if } c_1 \neq 0.$$

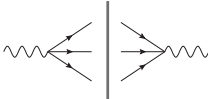
MPLs have found applicability in a large number of problems in high-energy physics; having understood their analytic and algebraic properties, which have at their origin the simplicity of the geometry of \mathbb{C}_∞ , has allowed physicists to perform many multi-loop calculations of fundamental importance for the physics program of the LHC.

Nevertheless, MPLs and their underlying \mathbb{C}_∞ geometry are not the end of the story and more complicated examples can be found already starting at the two-loop order. The first example of this was discovered by A. Sabry in 1961, when he attempted to compute the two-loop corrections to the electron self-energy in QED⁸. Indeed, when computing the relevant Feynman diagrams, Sabry encountered what we refer to today as the *Sunrise graph*:



$$= \int \frac{d^d k}{(2\pi)^d} \frac{d^d l}{(2\pi)^d} \frac{1}{(k^2 - m^2)(l^2 - m^2)((k-l-p)^2 - m^2)}. \quad (6)$$

When trying to repeat the same calculation performed for the one-loop photon self-energy, eq. (3), for the sunrise, one is immediately faced with an entirely new structure. Indeed, the discontinuity of the Sunrise graph in $d = 2$ dimensions reads (up to constant prefactors)



$$\sim \int_{9m^2}^{(\sqrt{s}-m)^2} \frac{dx}{\sqrt{x(x-4m^2)(x-(\sqrt{s}-m)^2)(x-(\sqrt{s}+m)^2)}}. \quad (7)$$

While this looks qualitatively similar to eq. (2), there is a crucial difference. The square root in eq. (7) is the root of a fourth-order polynomial and therefore, as one can rigorously prove, it cannot be removed by a rational transformation. This implies that the new square root intrinsically defines a new kind of algebraic variety, i.e. an *elliptic curve*. Indeed, the fact that the square root cannot be rationalized also implies that, when considering (iterated) integrals of rational functions which involve this square root, the natural complex surface where such functions are well defined cannot be anymore simply \mathbb{C}_∞ . Instead, it is easy to show that, quite in general, the geometry of the *Riemann surface* associated to the square root $y = \sqrt{P_4(x)}$, where $P_4(x)$ is a forth-order polynomial in x , is a *complex torus* T . While a Torus is intrinsically more complicated than the Riemann sphere, this geometrical point of view allows one to rather easily generalize the definition of MPLs in eq. (5) to a new class of functions, originating by *iterated integrations of rational functions on an elliptic curve* (or a torus), dubbed *elliptic multiple polylogarithms* (eMPLs). Their definition reads

$$\mathcal{E}_4(\overset{n_1}{c_1} \cdots \overset{n_k}{c_k}; x, \vec{a}) = \int_0^x dt \Psi_{n_1}(c_1, t, \vec{a}) \mathcal{E}_4(\overset{n_2}{c_2} \cdots \overset{n_k}{c_k}; t, \vec{a}), \quad (8)$$

where the explicit form of the kernels $\Psi_{n_1}(c_1, t, \vec{a})$ is at first rather complicated and I refer to the literature for details⁹. Note that MPLs are trivially contained in eMPLs since one has $\Psi_1(c_1, t, \vec{a}) = 1/(t - c_1)^c$. What is important to stress here is that, thanks to this new class of functions, for the first time it has been possible to find analytical results in closed form for Feynman integrals contributing to different processes of crucial importance for LHC physics and whose analytical calculation was considered to be out of reach until recently. We expect these functions show up in the calculation of multiloop corrections to the Drell-Yan process, to the production of pairs of vector bosons or pairs of heavy quarks and other processes.

Acknowledgments

I would like to thank Johannes Broedel, Claude Duhr, Falko Dulat, Brenda Penante and Ettore Remiddi for a long lasting collaboration and many interesting discussions on all the topics presented in this contribution.

References

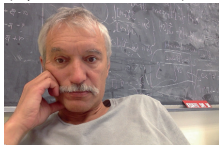
1. F. Hubaut [ATLAS Collaboration], arXiv:1811.10282.
2. K. Skovpen [CMS Collaboration], arXiv:1810.05715.
3. G. P. Salam, PoS LHCP **2018** (2018) 304
4. O. V. Tarasov, Phys. Rev. D **54** (1996) 6479
5. R. E. Cutkosky, J. Math. Phys. **1** (1960) 429.
6. E. Remiddi and J. A. M. Vermaseren, Int. J. Mod. Phys. A **15** (2000) 725
7. A. B. Goncharov, Adv. Math, **114** (1995) 197.
8. A. Sabry, Nucl. Phys. **33** (1962) 401
9. J. Broedel, C. Duhr, F. Dulat, B. Penante and L. Tancredi, JHEP **1901** (2019) 023

⁹Note that the vector $\vec{a} = (a_1, a_2, a_3, a_4)$ specifies the position of the four roots of $P_4(x)$.

POWER CORRECTIONS TO TMD FACTORIZATION

I. BALITSKY

*JLab, 1200 Jefferson Ave, Newport News, VA 23606, USA,
and ODU Phys. Dept., 4600 Elkhorn Ave, Norfolk, VA 23529, USA*



A typical factorization formula for production of a particle with a small transverse momentum in hadron-hadron collisions is given by a convolution of two TMD parton densities with cross section of production of the final particle by the two partons. For practical applications at a given transverse momentum, though, one should estimate at what momenta the power corrections to the TMD factorization formula become essential. In this talk I discuss the results of calculation of the first power corrections to TMD factorization formula for Higgs and Z-boson production in high-energy hadron-hadron collisions.

1 TMD factorization for particle production

A typical analysis of differential cross section of particle production in hadron-hadron collisions at small momentum transfer of the produced particle is performed with the help of TMD factorization^{1,2,3,4}. However, the question of how small should be the momentum transfer in order for leading power TMD analysis to be successful cannot be resolved at the leading-power level. The sketch of the factorization formula for the differential cross section is^{1,5}

$$\frac{d\sigma}{d\eta d^2q_\perp} = \sum_f \int d^2b_\perp e^{i(q,b)_\perp} \mathcal{D}_{f/A}(x_A, b_\perp, \eta) \mathcal{D}_{f/B}(x_B, b_\perp, \eta) \sigma(ff \rightarrow H) + \text{power corrections} + \text{Y-terms}, \quad (1)$$

where η is the rapidity, $\mathcal{D}_{f/A}(x, z_\perp, \eta)$ is the TMD density of a parton f in hadron A , and $\sigma(ff \rightarrow H)$ is the cross section of production of particle H of invariant mass $m_H^2 = Q^2$ in the scattering of two partons. The common wisdom is that when we increase q_\perp^2 of the produced hadron, at first the leading power TMD analysis with (nonperturbative) TMDs applies, then at some point power corrections kick in, and finally at $q_\perp^2 \sim Q^2$ they are transformed into so-called Y-terms making smooth transition to collinear factorization formulas. Here I discuss the question about the first transition, namely at what q_\perp^2 power corrections become significant.

As an example, let us consider production of an (imaginary) scalar particle Φ in proton-proton scattering. This particle is connected to gluons by the vertex

$$\mathcal{L}_\Phi = g_\Phi \int d^4x \Phi(x) g^2 F^2(x), \quad F^2(x) \equiv F_{\mu\nu}^a(x) F^{a\mu\nu}(x) \quad (2)$$

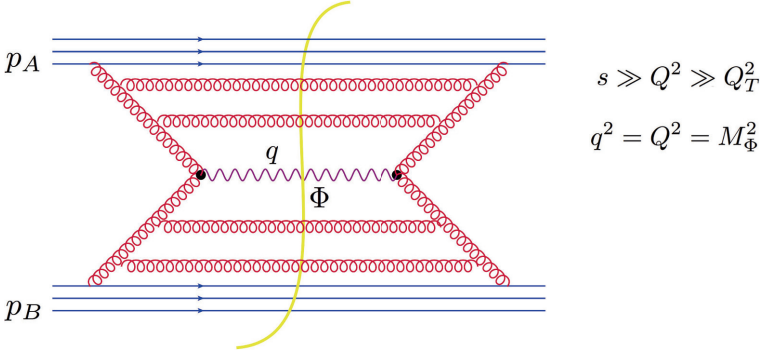


Figure 1 – Particle production by gluon-gluon fusion

This is a $\frac{m_H}{m_t} \ll 1$ approximation for Higgs production via gluon fusion at LHC with

$$g_H = \frac{1}{48\pi^2 v} \left(1 + \frac{11}{4\pi} \alpha_s + \dots\right)$$

where $\alpha_s = \frac{g^2}{4\pi}$ as usual. The differential cross section of Φ production has the form

$$d\sigma = \frac{d^3q}{2E_q (2\pi)^3} \frac{g_\Phi^2}{2s} W(p_A, p_B, q) \quad (3)$$

where we defined the “hadronic tensor” $W(p_A, p_B, q)$ as

$$\begin{aligned} W(p_A, p_B, q) &\stackrel{\text{def}}{=} \sum_X \int d^4x e^{-iqx} \langle p_A, p_B | g^2 F^2(x) | X \rangle \langle X | g^2 F^2(0) | p_A, p_B \rangle \\ &= \int d^4x e^{-iqx} \langle p_A, p_B | g^4 F^2(x) F^2(0) | p_A, p_B \rangle \end{aligned} \quad (4)$$

As usual, \sum_X denotes the sum over full set of “out” states.

2 Power corrections to Higgs production

We use Sudakov variables $p = \alpha p_1 + \beta p_2 + p_\perp$ and the notations $x_\bullet \equiv x_\mu p_1^\mu$ and $x_* \equiv x_\mu p_2^\mu$ for the dimensionless light-cone coordinates ($x_* = \sqrt{\frac{s}{2}} x_+$ and $x_\bullet = \sqrt{\frac{s}{2}} x_-$). Our metric is $g^{\mu\nu} = (1, -1, -1, -1)$ so that $p \cdot q = (\alpha_p \beta_q + \alpha_q \beta_p) \frac{s}{2} - (p, q)_\perp$ where $(p, q)_\perp \equiv -p_i q^i$.

The hadronic tensor can be formally written as a double functional integral, over the fields A and ψ to the right of the cut and fields \tilde{A} and $\tilde{\psi}$ to the left of the cut. The boundary condition is that the fields A and \tilde{A} coincide at time infinity reflecting the sum over all intermediate states in Eq. (4). To derive the factorization formula, we separate the gluon (and quark) fields into three sectors: “projectile” fields A_μ, ψ_a with $|\beta| < \sigma_a$, “target” fields with $|\alpha| < \sigma_b$ and “central rapidity” fields C_μ, ψ with $|\alpha| > \sigma_b$ and $|\beta| > \sigma_a$.^a

Our approximation at the tree level is that $\beta = 0$ for A, \tilde{A} fields and $\alpha = 0$ for B, \tilde{B} fields which corresponds to $A = A(x_\bullet, x_\perp)$, $\tilde{A} = \tilde{A}(x_\bullet, x_\perp)$ and $B = B(x_*, x_\perp)$, $\tilde{B} = \tilde{B}(x_*, x_\perp)$.

^aThe standard factorization scheme for particle production in hadron-hadron scattering is splitting the diagrams in collinear to projectile part, collinear to target part, hard factor, and soft factor¹. Here we factorize only in rapidity. For our purpose of calculation of power corrections in the tree approximation this is sufficient.

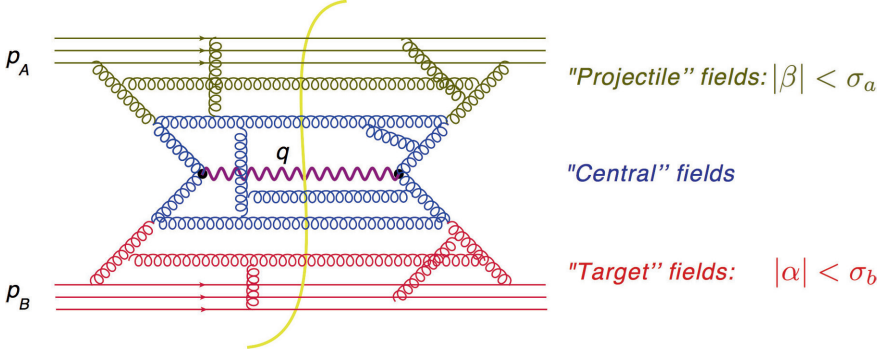


Figure 2 – Rapidity factorization for particle production

Because of boundary conditions, for the purpose of calculating the diagrams with central fields one can set

$$\begin{aligned}
 A(x_\bullet, x_\perp) &= \tilde{A}(x_\bullet, x_\perp), & \psi_a(x_\bullet, x_\perp) &= \tilde{\psi}_a(x_\bullet, x_\perp) \\
 \text{and} \\
 B(x_*, x_\perp) &= \tilde{B}(x_*, x_\perp), & \psi_b(x_*, x_\perp) &= \tilde{\psi}_b(x_*, x_\perp)
 \end{aligned}
 \tag{5}$$

Indeed, because A, ψ and $\tilde{A}, \tilde{\psi}$ do not depend on x_* , if they coincide at $x_* = \infty$ they should coincide everywhere. Next, it is well known that for equal sources to the left and to the right of the cut in the diagrams 4, calculation of those diagrams is equivalent to perturbative solution of classical Yang-Mills equations^{6,7}

$$D^\nu F_{\mu\nu}^a = \sum_f g \bar{\psi}^f t^a \gamma_\mu \psi^f, \quad (P - m_f) \psi^f = 0
 \tag{6}$$

with boundary conditions

$$\begin{aligned}
 A_\mu(x) \stackrel{x_* \rightarrow -\infty}{\cong} \bar{A}_\mu(x_\bullet, x_\perp), & \quad \psi(x) \stackrel{x_* \rightarrow -\infty}{\cong} \psi_a(x_\bullet, x_\perp) \\
 A_\mu(x) \stackrel{x_\bullet \rightarrow -\infty}{\cong} \bar{B}_\mu(x_*, x_\perp), & \quad \psi(x) \stackrel{x_\bullet \rightarrow -\infty}{\cong} \psi_b(x_*, x_\perp)
 \end{aligned}
 \tag{7}$$

reflecting the fact that at $t \rightarrow -\infty$ we have only incoming hadrons with “A” and “B” fields.

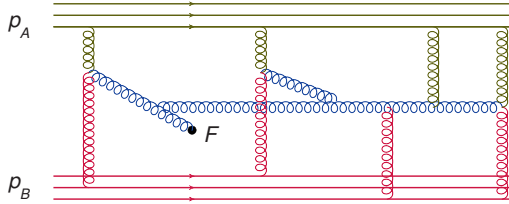


Figure 3 – Feynman diagrams with retarded propagators \Leftrightarrow perturbative solution of classical YM equations.

The solution of YM equations (6) in general case is yet unsolved problem, especially important for scattering of two heavy nuclei in semiclassical approximation. Fortunately, for our case of particle production with $\frac{q}{Q} \ll 1$ we can construct the approximate solution of (6) as a series in this small parameter.

The main idea is as follows. Let us expand quark and gluon propagators in powers of background fields, then we get a set of diagrams shown in Fig. 4. The typical bare gluon propagator in Fig. 4 is

$$\frac{1}{p^2 + i\epsilon p_0} = \frac{1}{\alpha\beta s - p_\perp^2 + i\epsilon(\alpha + \beta)} \quad (8)$$

Since we do not consider loops of C -fields in this paper, the transverse momenta in tree diagrams are determined by further integration over projectile (“A”) and target (“B”) fields which converges on either q_\perp or m . On the other hand, the integrals over α converge on either α_q or $\alpha \sim 1$ and similarly the characteristic β 's are either β_q or ~ 1 . Since $\alpha_q\beta_qs = Q_\parallel^2 \gg Q_\perp^2$, one can expand gluon and quark propagators in powers of $\frac{p_\perp^2}{\alpha\beta s}$

$$\begin{aligned} \frac{1}{p^2 + i\epsilon p_0} &= \frac{1}{s(\alpha + i\epsilon)(\beta + i\epsilon)} \left(1 + \frac{p_\perp^2/s}{(\alpha + i\epsilon)(\beta + i\epsilon)} + \dots \right) \\ \frac{\not{p}}{p^2 + i\epsilon p_0} &= \frac{1}{s} \left(\frac{\not{p}_\perp}{\beta + i\epsilon} + \frac{\not{p}_\perp}{\alpha + i\epsilon} + \frac{\not{p}_\perp}{(\alpha + i\epsilon)(\beta + i\epsilon)} \right) \left(1 + \frac{p_\perp^2/s}{(\alpha + i\epsilon)(\beta + i\epsilon)} + \dots \right) \end{aligned} \quad (9)$$

After the expansion (9), the dynamics in the transverse space effectively becomes trivial: all background fields stand either at x or at 0.

In this approximation we get

$$\begin{aligned} g^4 F^2(x) F^2(0) &= \frac{64}{s^2} U_*^{mi}(x) V_{\bullet i}^m(x) U_*^{nj}(0) V_{\bullet j}^n(0) \\ &\quad + \frac{16}{s} f^{mac} f^{mbd} \Delta^{ij,kl} [U_i^a(x) U_j^b(x) V_k^c(x) V_l^d(x) U_*^{nr}(0) V_{\bullet r}^n(0) \\ &\quad \quad \quad + U_*^{nr}(x) V_{\bullet r}^n(x) U_i^a(0) U_j^b(0) V_k^c(0) V_l^d(0)] \end{aligned} \quad (10)$$

where the first term is the leading order and the second is the higher-twist correction.

Substituting our approximation (10) to Eq. (4) and promoting background fields to operators, we get (note that $\alpha_q\beta_qs = Q_\parallel^2 \simeq Q^2$):⁸

$$\begin{aligned} W(p_A, p_B, q) &= \frac{64/s^2}{N_c^2 - 1} \int d^2 x_\perp \frac{2}{s} \int dx_\bullet dx_* \cos(\alpha_q x_\bullet + \beta_q x_* - (q, x)_\perp) \\ &\quad \times \left\{ \langle p_A | \hat{U}_*^{mi}(x_\bullet, x_\perp) \hat{U}_*^{mj}(0) | p_A \rangle \langle p_B | \hat{V}_{\bullet i}^n(x_*, x_\perp) \hat{V}_{\bullet j}^n(0) | p_B \rangle \right. \\ &\quad - \frac{4N_c^2}{N_c^2 - 4} \frac{\Delta^{ij,kl}}{Q^2} \frac{2}{s} \int_{-\infty}^{x_\bullet} dx'_\bullet d^{abc} \langle p_A | \hat{U}_{*i}^a(x_\bullet, x_\perp) \hat{U}_{*j}^b(x'_\bullet, x_\perp) \hat{U}_{*r}^c(0) | p_A \rangle \\ &\quad \quad \quad \times \left. \frac{2}{s} \int_{-\infty}^{x_*} dx'_* d^{mpq} \langle p_B | \hat{V}_{\bullet k}^m(x_*, x_\perp) \hat{V}_{\bullet l}^p(x'_*, x_\perp) \hat{V}_{\bullet r}^{qr}(0) | p_B \rangle \right\} \end{aligned} \quad (11)$$

where

$$\begin{aligned} \hat{U}_*^{ai}(x_\bullet, x_\perp) &= \hat{F}_*^{mi}(x_\bullet, x_\perp) \text{Pexp} \left\{ ig \frac{2}{s} \int_{-\infty}^{x_\bullet} dz_\bullet A_\bullet(z_\bullet, x_\perp) \right\}^{ma} \\ \hat{V}_{\bullet i}^a(x_*, x_\perp) &= \hat{F}_{\bullet}^{ni}(x_*, x_\perp) \text{Pexp} \left\{ ig \frac{2}{s} \int_{-\infty}^{x_*} dz_* A_\bullet(z_*, x_\perp) \right\}^{ma} \end{aligned} \quad (12)$$

Since an extra U_{*k} (or $V_{\bullet k}$) brings $s \frac{x_i}{x_\perp^2}$ we see that the higher-twist correction in the r.h.s of Eq. (11) is $\sim \frac{q_\perp^2}{Q^2}$ so it gives the leading power correction in the region $s \gg Q^2 = m_\Phi^2 \gg q_\perp^2 \gg m^2$. Unfortunately, matrix elements of the twist-3 gluon operators are not known even at $x_\perp = 0$ (which corresponds to DIS).

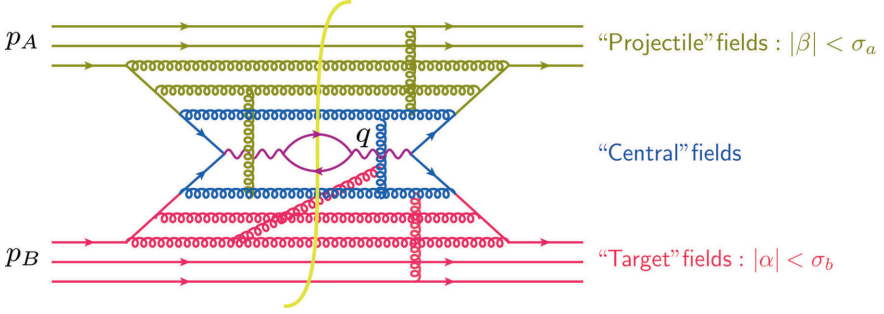


Figure 4 – Rapidity factorization for Z -boson production

3 Power corrections to Z -boson production

In a similar way one can calculate power corrections to Z -boson production.

Technically, the difference is that we need to find the approximate solution of YM equations for quarks rather than gluons. Typical terms look like

$$\begin{aligned}\Psi_A &= \psi_A - \frac{g}{s} \not{p}_2 \gamma^i B_i \frac{1}{\alpha + i\epsilon} \psi_A + \dots, \\ \Psi_B &= \psi_B - \frac{g}{s} \not{p}_1 \gamma^i A_i \frac{1}{\beta + i\epsilon} \psi_B + \dots,\end{aligned}\quad (13)$$

To estimate the order of magnitude of power corrections, one can assume that $\frac{1}{N_c}$ is a good parameter and get⁹

$$\begin{aligned}W(p_A, p_B, q) &= -\frac{e^2}{8s_W^2 c_W^2 N_c} \int d^2 k_\perp \left[\left\{ (1 + a_u^2) \left[1 - 2 \frac{(k, q - k)_\perp}{Q^2} \right] \right. \right. \\ &\quad \times f_{1u}(\alpha_z, k_\perp) \bar{f}_{1u}(\beta_z, q_\perp - k_\perp) + 2(a_u^2 - 1) \frac{k_\perp^2 (q - k)_\perp^2}{m_N^2 Q^2} h_{1u}^\perp(\alpha_z, k_\perp) \bar{h}_{1u}^\perp(\beta_z, q_\perp - k_\perp) \\ &\quad \left. \left. + (\alpha_z \leftrightarrow \beta_z) \right\} + \{u \leftrightarrow c\} + \{u \leftrightarrow d\} + \{u \leftrightarrow s\} \right] + O\left(\frac{m_s^8}{s}\right) + O\left(\frac{1}{N_c^2}\right).\end{aligned}\quad (14)$$

The eq. (14) is a tree-level formula and for an estimate we should specify the rapidity cutoffs for f_1 's and h_1^\perp 's. As we discussed above, the rapidity cutoff for $f_1(\alpha_z, k_\perp^2)$ is σ_a and for $f_1(\alpha_z, k_\perp^2)$ σ_b , where σ_a and σ_b are rapidity bounds for central fields. Since we calculated only tree diagrams made of C -fields we have $\sigma_a = \beta_z$ and $\sigma_b = \alpha_z$ in eq. (14).^b

Next, power corrections become sizable at $q_\perp^2 \gg m_N^2$ where we probe the perturbative tails of TMD's $f_1 \sim \frac{1}{k_\perp^2}$ and $h_1^\perp \sim \frac{1}{k_\perp^4}$ ¹⁰. So, as long as $k_\perp^2 \leq \alpha_z \sigma_a s = Q^2$ we can approximate

$$f_1(\alpha_z, k_\perp^2) \simeq \frac{f(\alpha_z)}{k_\perp^2}, \quad h_1^\perp(\alpha_z, k_\perp^2) \simeq \frac{m_N^2 h(\alpha_z)}{k_\perp^4}, \quad \bar{f}_1 \simeq \frac{\bar{f}(\alpha_z)}{k_\perp^2}, \quad \bar{h}_1^\perp \simeq \frac{m_N^2 \bar{h}(\alpha_z)}{k_\perp^4} \quad (15)$$

(up to logarithmic corrections). Similarly, for the target we can use the estimate

$$f_1(\beta_z, k_\perp^2) \simeq \frac{f(\beta_z)}{k_\perp^2}, \quad h_1^\perp(\beta_z, k_\perp^2) \simeq \frac{m_N^2 h(\beta_z)}{k_\perp^4}, \quad \bar{f}_1 \simeq \frac{\bar{f}(\beta_z)}{k_\perp^2}, \quad \bar{h}_1^\perp \simeq \frac{m_N^2 \bar{h}(\beta_z)}{k_\perp^4} \quad (16)$$

as long as $k_\perp^2 \leq \beta_z \sigma_b s = Q^2$.

^bIn general, we should integrate over C -fields in the leading log approximation and match the logs to the double-log and/or single-log evolution of TMDs.

Substituting this to eq. (14) we get the following estimate of the strength of power corrections for Z-boson production⁹

$$\begin{aligned}
W(p_A, p_B, q) &= -\frac{e^2}{8s_W^2 c_W^2 N_c} \int d^2 k_\perp \frac{1}{k_\perp^2 (q-k)_\perp^2} \\
&\times \left[\left\{ (1+a_u^2) \left[1 - 2 \frac{(k, q-k)_\perp}{Q^2} \right] [f_u(\alpha_z) \bar{f}_u(\beta_z) + \bar{f}_u(\alpha_z) f_u(\beta_z)] \right. \right. \\
&+ 2(a_u^2 - 1) [h_u(\alpha_z) \bar{h}_u(\beta_z) + \bar{h}_u(\alpha_z) h_u(\beta_z)] \frac{m_N^2}{Q^2} \left. \left. \right\} + \{u \leftrightarrow c\} + \{u \leftrightarrow d\} + \{u \leftrightarrow s\} \right] \\
&\simeq -\frac{e^2}{8s_W^2 c_W^2 N_c} \int d^2 k_\perp \frac{1}{k_\perp^2 (q-k)_\perp^2} \left[1 - 2 \frac{(k, q-k)_\perp}{Q^2} \right] \\
&\times \left[\left\{ (1+a_u^2) [f_u(\alpha_z) \bar{f}_u(\beta_z) + \bar{f}_u(\alpha_z) f_u(\beta_z)] \right\} + \{u \leftrightarrow c\} + \{u \leftrightarrow d\} + \{u \leftrightarrow s\} \right].
\end{aligned} \tag{17}$$

Here we used the fact that due to the ‘‘positivity constraint’’ $h_\perp^\perp(x, k_\perp^2) \leq \frac{m_N}{|k_\perp|} f_\perp^\perp(x, k_\perp^2)$?, we can safely assume that the numbers $f(x)$ and $h(x)$ in eqs. (15) and (16) are of the same order of magnitude so the last term in the third line in eq. (17) $\sim \frac{m_N^2}{Q^2}$ can be neglected. Thus, the relative weight of the leading term and power correction is determined by the factor $1 - 2 \frac{(k, q-k)_\perp}{Q^2}$. The integrals over k_\perp are logarithmic and should be cut from below by m_N^2 and from above by Q^2 so we get an estimate

$$\begin{aligned}
W(p_A, p_B, q) &= -\frac{\pi e^2}{4s_W^2 c_W^2 N_c} \left[\frac{1}{q_\perp^2} \ln \frac{q_\perp^2}{m_N^2} + \frac{1}{Q^2} \ln \frac{Q^2}{q_\perp^2} \right] \\
&\times \left[\left\{ (1+a_u^2) [f_u(\alpha_z) \bar{f}_u(\beta_z) + \bar{f}_u(\alpha_z) f_u(\beta_z)] \right\} + \{u \leftrightarrow c\} + \{u \leftrightarrow d\} + \{u \leftrightarrow s\} \right],
\end{aligned} \tag{18}$$

where we assumed that the first term is determined by the logarithmical region $q_\perp^2 \gg k_\perp^2 \gg m_N^2$ and the second by $Q^2 \gg k_\perp^2 \gg q_\perp^2$. By this estimate, the power correction reaches the level of few percent at $q_\perp \geq 20$ GeV. Of course, when q_\perp^2 increases, the correction becomes bigger, but the validity of the approximation $\frac{q_\perp^2}{Q^2} \ll 1$ worsens. Moreover, we have ignored all logarithmic (and double-log) evolutions which can significantly change the relative strength of power corrections. Still, we hope that our estimate (18) reflects the correct order of magnitude for power corrections to TMD factorization.

Acknowledgments

This work was supported by DOE contract DE-AC05-06OR23177 and by the grant DE-FG02-97ER41028.

References

1. J.C. Collins, *Foundations of perturbative QCD*, Cambridge University Press, 2013
2. J.C. Collins and D.E. Soper, NPB **194**, 445 (1982)
3. J.C. Collins, D.E. Soper, and G.F. Sterman, *Nucl. Phys. B* **250**, 199 (1985).
4. Xiang-dong Ji, Jian-ping Ma, and F. Yuan, *Nucl. Phys. B* **71**, 034005 (2005).
5. J.C. Collins and T. Rogers, *Phys. Rev. D* **91**, 074020 (2015).
6. F. Gelis and R. Venugopalan, *Phys. Rev. D* **69**, 014019 (2004)
7. F. Gelis and R. Venugopalan, *Nucl. Phys. A* **776**, 135 (2006)
8. I. Balitsky and A.V. Tarasov, *JHEP* **1707**, 095 (2017).
9. I. Balitsky and A.V. Tarasov, *JHEP* **1805**, 150 (2018).
10. J. Zhou, F. Yuan, and Z-T. Liang, *Phys. Rev. D* **78**, 114008 (2008)

Angular ordering effects in TMD parton distribution functions and Drell-Yan q_\perp spectra

Aleksandra Lelek

University of Antwerp (UAntwerp)

We present new results of our studies of soft-gluon angular ordering effects on the evolution of both collinear and transverse momentum dependent (TMD) parton distribution functions, and discuss their implications for precision predictions of Drell-Yan transverse momentum spectra at the LHC. Our method is based on the parton branching (PB) approach. We compare this with the implementation of angular ordering in the Kimber-Martin-Ryskin-Watt (KMRW) approach and with the Collins-Soper-Sterman (CSS) approach. We illustrate numerically the effects of different ordering scenarios (p_\perp , angular ordering), including definitions of the soft-gluon resolution scale and scale in the running coupling, on the theoretical accuracy of predictions in the low transverse momentum region of Drell-Yan spectra measured at the LHC.

1 Motivation

One of the uncertainty sources in obtaining QCD predictions for collider measurements comes from the assumption that partons are collinear with the hadron they build. The collinear factorization theorem¹ successfully predicts a large number of processes. However, it was realised a long time ago that for certain observables also the parton's transverse momentum needs to be taken into account in order to obtain sufficient precision. This is accomplished via transverse momentum dependent (TMD) factorization theorems, like high energy k_\perp -factorization^{2,3} or Collins-Soper-Sterman⁴ formalism. An overview of the field is given in.⁵

In the following sections we present new results from the Parton Branching (PB) method⁶⁻⁹ to obtain TMD parton distribution functions (PDFs), referred to as TMDs. We concentrate especially on the proper treatment of soft gluons emissions via the angular ordering condition and on the comparison of PB with other existing approaches, as Marchesini's and Webber's prescription,¹¹ Kimber-Martin-Ryskin-Watt (KMRW) approach^{12,13} and Collins-Soper-Sterman⁴ formalism.

2 TMDs from PB method

2.1 TMD evolution equation

The PB TMDs are obtained by constructing and solving using MC techniques an evolution equation which takes into account not only the collinear evolution but also the transverse momentum at each branching. The proposed equation has the following form⁷

$$\begin{aligned} \tilde{A}_a(x, k_\perp, \mu^2) &= \Delta_a(\mu^2, \mu_0^2) \tilde{A}_a(x, k_\perp, \mu_0^2) + \sum_b \int \frac{d^2\mu'_\perp}{\pi\mu'^2} \Theta(\mu^2 - \mu'^2) \Theta(\mu'^2 - \mu_0^2) \times \\ &\times \Delta_a(\mu^2, \mu'^2) \int_x^{z_M} dz P_{ab}^R(z, \alpha_s(a(z)^2\mu'^2)) \tilde{A}_b\left(\frac{x}{z}, k_\perp + a(z)\mu_\perp, \mu'^2\right) \end{aligned} \quad (1)$$

where $\tilde{A}_a(x, k_\perp, \mu^2) = xA_a(x, k_\perp, \mu^2)$ is the momentum weighted TMD for a parton species and flavour a , carrying the fraction x of the proton's momentum and having the transverse momentum k_\perp at the evolution scale μ , P_{ab}^R is the real-emission part of the splitting function for a parton b splitting into a parton a which propagates towards the hard scattering, $z = x_a/x_b$ is the splitting variable, $|\mu_\perp| \equiv \mu'$ is the scale at which the branching happens, μ_0 is the initial evolution scale. $\Delta_a(\mu^2, \mu_0^2) = \exp\left[-\int_{\mu_0^2}^{\mu^2} \frac{d\mu'^2}{\mu'^2} \sum_b \int_0^{z_M} dz z P_{ba}^R(z, \alpha_s(a(z)^2 \mu'^2))\right]$ is the Sudakov form factor. The function $a(z)$ expresses the relation between the scale of the branching and the transverse momentum of the emitted and propagating parton. For p_\perp -ordering condition, $a(z) = 1$, i.e. the scale of the branching is associated with the transverse momentum of the emitted parton $q_\perp^2 = \mu'^2$. For angular ordering condition, $a(z) = 1 - z$, i.e. the scale of the branching is associated with energy times the angle of the emitted parton with respect to the beam direction $q_\perp^2 = (1 - z)^2 \mu'^2$. The soft gluon resolution scale parameter z_M is fixed to a value very close to 1 for p_\perp -ordering or it is defined as $z_M = 1 - \frac{q_0}{\mu'}$ for angular ordering where q_0 is the minimum transverse momentum of the emitted parton with which it can be resolved. The PB method allows one to select the definition of z_M , α_s and the way the transverse momentum is related to the branching scale independently^b.

In the PB method the transverse momentum of the propagating parton is a sum of the transverse momentum of all the emitted partons $k_\perp = -\sum_i q_{\perp,i}$. After integrating eq. (1) over the transverse momentum k_\perp one obtains collinear PDF. In the limit of $z_M \rightarrow 1$ and with $\alpha_s(\mu'^2)$ the Dokshitzer-Gribov-Lipatov-Altarelli-Parisi (DGLAP) evolution equation¹⁴⁻¹⁷ is reproduced.

2.2 Highlights

The key observation was that if one relates the transverse momentum and the scale of the branching according to the angular ordering condition, stable, z_M independent (as long as $z_M \approx 1$) TMD is obtained whereas with p_\perp ordering it is not possible.^{6,7} Based on this result, fits of TMDs to precision measurements of deep inelastic scattering (DIS) cross sections at HERA were performed using `xFitter`¹⁰ for angular ordering ($q_\perp^2 = (1 - z)^2 \mu'^2$) in two scenarios: with $\alpha_s(\mu'^2)$ and $\alpha_s(q_\perp^2)$.⁸ A very good description of the Z boson p_\perp spectrum measured by ATLAS experiment at 8 TeV¹⁸ was obtained with $\alpha_s(q_\perp^2)$ which is shown in the left panel of fig. 1.⁸

3 PB and other approaches

3.1 Marchesini and Webber

Eq. (1) with angular ordering condition, once integrated over transverse momentum, gives the following evolution formula for the collinear distribution

$$\begin{aligned} \tilde{f}_a(x, \mu^2) &= \tilde{f}_a(x, \mu_0^2) \Delta_a(\mu^2, \mu_0^2) \\ &+ \int_{\mu_0^2}^{\mu^2} \frac{d\mu'^2}{\mu'^2} \Delta_a(\mu^2, \mu'^2) \sum_b \int_x^{1-\frac{q_0}{\mu'}} dz P_{ab}^R(\alpha_s((1-z)^2 \mu'^2), z) \tilde{f}_b\left(\frac{x}{z}, \mu'^2\right). \end{aligned} \quad (2)$$

This coincides with the evolution formula of Marchesini and Webber^{11 c}.

3.2 Kimber-Martin-Ryskin-Watt

In this section we compare the PB formula with the KMRW approach.^{12,13} To this end, we rewrite the PB formula for angular ordering eq. (2) in terms of integral over the transverse

^aFor a given 4-vector $k = (k^0, k^1, k^2, k^3) = (E_k, k_\perp, k^3)$, where $k_\perp = (k^1, k^2)$. Analogously $\mu'_\perp = (\mu'^1, \mu'^2)$.

^bE.g. one can select angular ordered way of relating q_\perp and μ' but keeping z_M fixed and $\alpha_s(\mu'^2)$ as in p_\perp -ordering to study the effect of each piece of the ordering definition.

^cNote, that Marchesini and Webber studied the coherent branching with LO splitting functions and α_s whereas we are using them at NLO.

momentum q_{\perp}^2 instead of the branching scale μ'^2

$$\begin{aligned} \tilde{f}_a(x, \mu^2) &= \tilde{f}_a(x, \mu_0^2) \Delta_a(\mu^2, \mu_0^2) \\ &+ \int_{q_0^2}^{(1-x)^2 \mu^2} \frac{dq_{\perp}^2}{q_{\perp}^2} \int_x^{1-\frac{q_{\perp}}{\mu}} dz \Delta_a\left(\mu^2, \frac{q_{\perp}^2}{(1-z)^2}\right) \sum_b P_{ab}^R(\alpha_s(q_{\perp}^2), z) \tilde{f}_b\left(\frac{x}{z}, \frac{q_{\perp}^2}{(1-z)^2}\right). \end{aligned} \quad (3)$$

The KMRW angular ordered evolution equation has the following form

$$\begin{aligned} \tilde{f}_a(x, \mu^2) &= \tilde{f}_a(x, \mu_0^2) \Delta_a(\mu^2, \mu_0^2) \\ &+ \int_{q_0^2}^{\mu^2 \left(\frac{1-x}{x}\right)^2} \frac{dq_{\perp}^2}{q_{\perp}^2} \left(\Delta_a(\mu^2, q_{\perp}^2) \sum_b \int_x^{1-\frac{q_{\perp}}{q_{\perp}+\mu}} dz P_{ab}^R(\alpha_s(q_{\perp}^2), z) \tilde{f}_b\left(\frac{x}{z}, q_{\perp}^2\right) \right) \end{aligned} \quad (4)$$

where the expression $\tilde{f}(x, \mu^2, q_{\perp}^2) = \Delta_a(\mu^2, q_{\perp}^2) \sum_b \int_x^{1-\frac{q_{\perp}}{q_{\perp}+\mu}} dz P_{ab}^R(\alpha_s(q_{\perp}^2), z) \tilde{f}_b\left(\frac{x}{z}, q_{\perp}^2\right)$ defines the TMD (called *unintegrated PDF* there). KMRW is *one-step* evolution: it generates the second scale only in the last step of the evolution in contrast to PB method where both k_{\perp} and μ' (or equivalently q_{\perp}) are calculated at each branching. Nevertheless, it is interesting to compare the formulas eq. (3) and eq. (4). First, we notice that in KMRW and PB the integration limits differ. Moreover, PB and KMRW use different scales in parton densities \tilde{f}_b and Sudakov form factors Δ_a . Both formalisms use q_{\perp} as the scale in α_s . The TMD sets obtained according to KMRW angular ordering prescription are included in TMDlib and TMDplotter¹⁹ under the name MRW-CT10nlo.²⁰ Despite many differences, PB and KMRW are similar in the middle k_{\perp} range compared to the scale μ which is illustrated in the middle and right panels of fig. 1^e. They differ in the low k_{\perp} region where for KMRW we see the intrinsic k_{\perp} constant parametrization whereas for PB the Gaussian intrinsic k_{\perp} is smeared during the evolution process. PB and KMRW differ also in the large k_{\perp} region: KMRW has a very large k_{\perp} tail coming from their treatment of the Sudakov form factor for $k_{\perp} > \mu$.

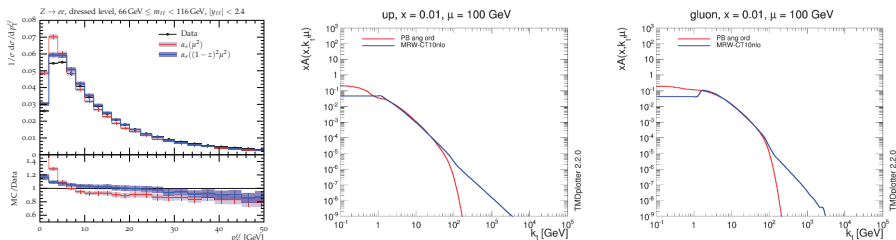


Figure 1 – Prediction for Z boson p_{\perp} spectrum obtained with PB TMDs from the fit compared to 8 TeV ATLAS measurement (left). Comparison of KMRW and PB TMD (middle and right).

3.3 Collins-Soper-Sterman

The PB Sudakov form factor written in terms of virtual pieces of the splitting functions and with angular ordering has the form $\Delta_a(\mu^2, \mu_0^2) = \exp\left(-\int_{\mu_0^2}^{\mu^2} \frac{dq_{\perp}^2}{q_{\perp}^2} \alpha_s(q_{\perp}) \left(\int_0^{1-\frac{q_{\perp}}{\mu}} dz \left(k_{a\frac{1}{1-z}} - d_a\right)\right)\right)$. By comparing the coefficients k_q and d_q ⁷ in the PB Sudakov with A_1 (giving leading logarithmic (LL) contributions), B_1 and A_2 (giving together with C_1 next-to-leading logarithmic (NLL) contributions) coefficients of the CSS formalism for Drell-Yan (DY) cross section⁴ we find that they are exactly the same. The fact that coherent branching algorithms should reproduce correctly LL and NLL behavior for DY and DIS was discussed in.²¹

⁷We neglect the difference between μ_0 and q_0 .

^ePB TMDs were obtained with $q_0 = 1\text{ GeV}$ and cut in α_s forbidding the renormalization scale to go below the initial evolution scale. The starting distribution is ct10nlo.

It was realised²² that Sudakov form factor is process dependent what can be explained by renormalization group equation and resummation scheme dependence. We find a difference between B_2 CSS coefficient (giving together with A_3 and C_2 next-to-next-to leading (NNLL) logarithmic contribution) and the $2d_q^1$ coefficient in PB Sudakov being $\pi\beta_0 16 \left(\frac{\pi^2}{6} - 1\right)$ where β_0 is the first coefficient of the expansion of the QCD β function.

4 Conclusions

PB method allows to obtain collinear and TMD PDFs by calculating the kinematics at each branching and to study different ordering definitions. We have shown that angular ordering definition leads to stable, z_M -independent TMDs and good description of Z boson p_\perp spectrum.

We showed that PB method agrees with Marchesini's and Webber's prescription. We discussed the differences and similarities of PB and KMRW approach. We illustrated that PB includes the same LL and NLL coefficients in the Sudakov form factor as CSS formalism. The differences between NNLL coefficients in the Sudakov form factors of these two methods come from the resummation scheme dependence.

5 Acknowledgments

The results presented in this article were obtained in collaboration with Francesco Hautmann, Hannes Jung, Aron Mees van Kampen and Lissa Keersmaekers.

References

1. J. C. Collins, D. E. Soper and G. F. Sterman, Adv.Ser. Direct. High Energy Phys. **5** (1989) 1
2. S. Catani, M. Ciafaloni and F. Hautmann, Phys. Lett. B **242** (1990) 97
3. S. Catani, M. Ciafaloni and F. Hautmann, Nucl. Phys. B **366** (1991) 135
4. J. C. Collins, D. E. Soper and G. F. Sterman, Nucl. Phys. B **250** (1985) 199
5. R. Angeles-Martinez *et al.*, Acta Phys. Polon. B **46** (2015) no.12, 2501
6. F. Hautmann, H. Jung, A. Lelek, V. Radescu and R. Zlebcik, Phys. Lett. B **772** (2017) 446
7. F. Hautmann, H. Jung, A. Lelek, V. Radescu and R. Zlebcik, JHEP **1801** (2018) 070
8. A. Bermudez Martinez, P. Connor, H. Jung, A. Lelek, R. Zlebcik, F. Hautmann and V. Radescu, Phys. Rev. D **99** (2019) no.7, 074008
9. A. Lelek, doi:10.3204/PUBDB-2018-02949
10. S. Alekhin *et al.*, Eur. Phys. J. C **75** (2015) no.7, 304
11. G. Marchesini and B. R. Webber, Nucl. Phys. B **310** (1988) 461
12. M. A. Kimber, A. D. Martin and M. G. Ryskin, Eur. Phys. J. C **12** (2000) 655
13. A. D. Martin, M. G. Ryskin and G. Watt, Eur. Phys. J. C **66** (2010) 163
14. V. N. Gribov and L. N. Lipatov, Sov. J. Nucl. Phys. **15** (1972) 438
15. L. N. Lipatov, Sov. J. Nucl. Phys. **20** (1975) 94
16. G. Altarelli and G. Parisi, Nucl. Phys. B **126** (1977) 298
17. Y. L. Dokshitzer, Sov. Phys. JETP **46** (1977) 641
18. G. Aad *et al.* [ATLAS Collaboration], Eur. Phys. J. C **76** (2016) no.5, 291
19. F. Hautmann, H. Jung, M. Krmer, P. J. Mulders, E. R. Nocera, T. C. Rogers and A. Signori, Eur. Phys. J. C **74** (2014) 3220
20. M. Bury, A. van Hameren, H. Jung, K. Kutak, S. Sapeta and M. Serino, Eur. Phys. J. C **78** (2018) no.2, 137
21. S. Catani, B. R. Webber and G. Marchesini, Nucl. Phys. B **349** (1991) 635
22. S. Catani, D. de Florian and M. Grazzini, Nucl. Phys. B **596** (2001) 299

DETERMINATION OF PARTON DISTRIBUTION FUNCTIONS IN PION USING XFITTER

IVAN NOVIKOV

on behalf of `xFitter` developers

Joint Institute for Nuclear Research

Joliot-Curie 6, Dubna, Moscow region, Russia, 141980



Parton distribution functions (PDFs) remain a crucial component for description of hadron collisions. While PDFs of proton and related particles: antiproton, neutron, have been determined with high precision, PDFs of light mesons: pion and kaon, are experimentally poorly studied. On the other hand, light mesons are currently a topic of interest from theoretical side, with several nonperturbative models predicting their properties. We approach PDFs of charged pion from a phenomenological perspective, and extract them from the currently available experimental data using `xFitter`.¹ The preliminary results of pion PDF determination are presented.

1 Introduction

Our analysis is based on Drell-Yan data from [E615](#)² and [NA10](#)³ experiments and prompt photon production data from [WA70](#)⁴ experiment. We choose to parameterise π^- PDF at initial scale $Q_0^2 = 1.9 \text{ GeV}^2$, just below the charm mass threshold. Neglecting electroweak corrections and quark masses, we assume charge symmetry: $d = \bar{u}$, and SU(3)-symmetric sea: $u = \bar{d} = s = \bar{s}$. Under these assumptions, pion PDFs are reduced to three distributions: valence v , sea s , and gluon g ; which we parameterise using the generic form $xq_i(x, Q_0^2) = A_i x^{B_i} (1-x)^{C_i}$:

$$\begin{aligned}
 v &:= \frac{(d - \bar{d}) - (u - \bar{u})}{2} = d - u & xv(x) &= A_v x^{B_v} (1-x)^{C_v} \\
 s &:= \frac{u + \bar{d}}{2} = u & xs(x) &= A_s x^{B_s} (1-x)^{C_s} \\
 g &:= g & xg(x) &= A_g x^{B_g} (1-x)^{C_g}
 \end{aligned}
 \tag{1}$$

Quark-counting and momentum sum rules have the following form for π^- :

$$\int_0^1 v(x) dx = 1 \qquad \int_0^1 x(2v(x) + 6s(x) + g(x)) dx = 1
 \tag{2}$$

The sum rules are enforced by constraining the normalization parameters A_v and A_g .

Table 1: Fitted parameter values and χ^2 . Parameters C_s, C_g are fixed. The first column corresponds to the fit using the parameterisation of Eq.1. Second column shows the final fit with an additional free parameter D_v (Eq.3). The change in C_v between the two columns shows that the data do not constrain the derivative of $v(x)$ at $x = 1$.

χ^2/N_{DoF}	450/374=1.20	445/373=1.19
B_v	0.89±0.03	0.79±0.05
C_v	0.96±0.03	0.37±0.12
D_v	0	-0.86±0.08
A_s	6.4±1.9	7.4±2.2
B_s	1.35±0.16	1.39±0.16
C_s	8	8
B_g	6.3±1.3	6.3±1.3
C_g	5	5

2 Cross-section calculation

PDFs are evolved up from the starting scale Q_0^2 by solving DGLAP equations numerically using QCDNUM⁵. Predicted cross-sections are calculated as a convolution of evolved pion PDFs with a precomputed grid and PDF of proton or tungsten target, using the APPLgrid⁶ package. The grids were generated using the MCFM⁷ generator. For tungsten and proton targets we use nuclear PDF set nCTEQ15.⁸ Both evolution and cross-section calculations are performed at next-to-leading order (NLO).

3 Results

An initial fit with free parameters had good fit quality with $\chi^2/N_{\text{DoF}} = 1.18$ and found valence parameters to be well-determined. However, without additional assumptions, the considered data are not sensitive enough to unambiguously determine all sea and gluon parameters, and only constrain some combination of them (Figure 1).

In the following we arbitrarily fix $C_s = 8, C_g = 5$. These values are chosen to be similar to corresponding parameters in proton PDF set HERAPDF2.0⁹. The choice maintains good χ^2 (Table 1, column 1). To address the arbitrariness of this parameter fixing we vary values of fixed parameters C_s, C_g by a factor of 2 up and down and treat the resulting change in extracted PDFs as an additional parameterisation uncertainty.

Correlated uncertainties are taken into account using nuisance parameters. These uncertainties include overall normalizations of the datasets, uncertainty in strong coupling constant $\alpha_S = 0.118 \pm 0.001$, and uncertainty of nuclear PDFs.

The uncertainty of perturbative calculation is estimated by varying renormalization scale μ_R by a factor of 2 up and down. We observe a significant dependence of predicted cross-sections on μ_R , indicating that missing higher order corrections may be significant.

The impact of including additional free parameters has been considered. It has been found that adding the D_v term in the following way:

$$xv(x) = A_v x^{B_v} (1-x)^{C_v} (1 + D_v x^{\frac{5}{2}}) \quad (3)$$

improves the χ^2 significantly (Table 1, column 2). For the parameterisation uncertainties, the impact of varying the input parameterisation scale Q_0^2 up and down by 0.1 GeV² is considered as well.

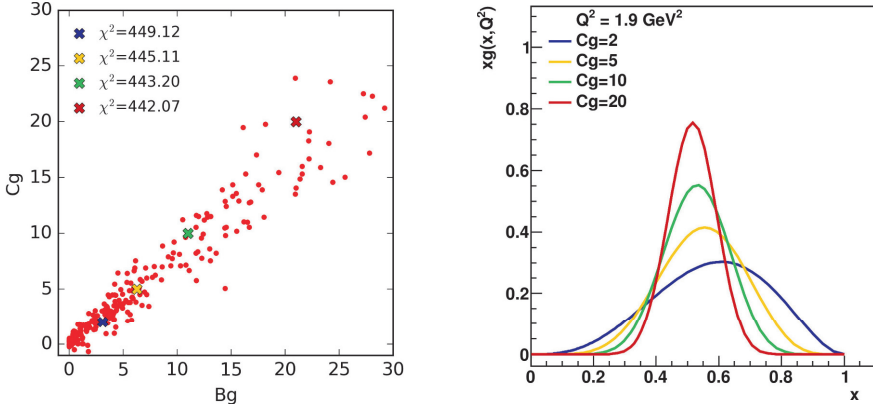


Figure 1 – The left plot shows degeneracy in sensitivity of the data and correlation between parameters B_g and C_g . The red points were obtained in Monte-Carlo sensitivity study with central values based on theory predictions and magnitude of random fluctuations based on experimental uncertainty. One can see that optimal parameter values for different instances are scattered around a line in parameter space. The plot on the right shows how gluon distribution changes when moving along the correlation line. Crosses of different colors on the left plot correspond to gluon distributions on the right plot, plotted with the same color. These gluon distributions were obtained in fits with C_g fixed to 2, 5, 10, 20, without MC variation.

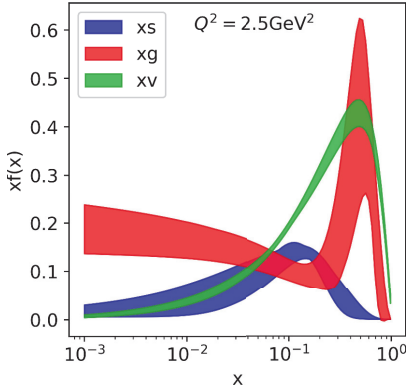


Figure 2 – The extracted distributions and their uncertainties. The valence is well-constrained. The large error bands on x_s and x_g come mainly from variation of values of fixed parameters C_g, C_s .

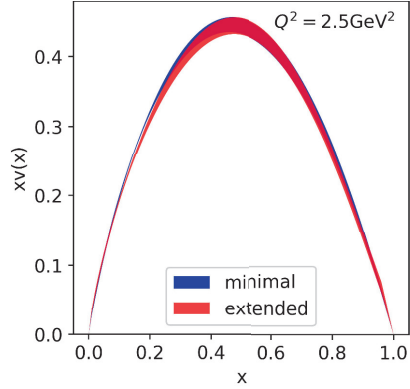


Figure 3 – Valence distribution when using minimal parameterisation (Eq. 1) and the one extended with an additional free parameter D_v (Eq. 3). High- x behavior is linear in $(1-x)$.

The extracted value of parameter C_v is consistent with 1, meaning that $v(x) \sim (1-x)$ as $x \rightarrow 1$ (Figure 3). However, the data are only sensitive to some region $x < 1$ and do not constrain the derivative of $v(x)$ at $x = 1$. The behavior $v(x) \sim (1-x)$ is favored by Nambu-Jona-Lasinio models¹⁰ and is in conflict with approaches based on Dyson-Schwinger equations,^{11,12} which predict $v(x) \sim (1-x)^2$.

We evaluate fractions of momentum carried by valence, sea and gluon PDFs (Figure 4). One can see that in pion, in comparison to proton, valence carries more momentum.

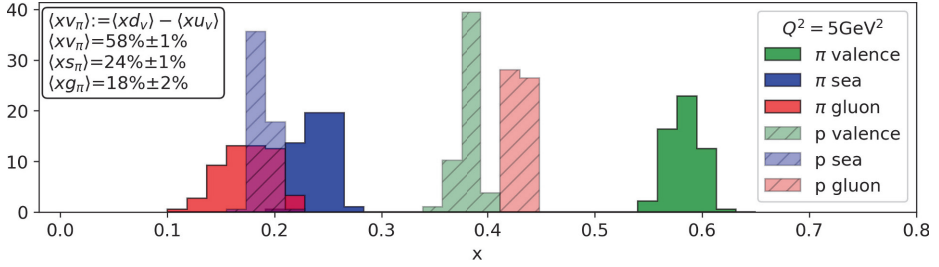


Figure 4 – Momentum fractions in pion in comparison to proton. The histograms were built from MC replicas with experimental data randomly varied according to their uncertainties, and repeating the fit. Parameters C_g , C_s were fixed.

Conclusions

We re-analysed currently available Drell-Yan and prompt photon production data using modern tools. We find that while valence distribution is well-constrained, the considered data are not sensitive enough to determine sea and gluon distributions. While the data are reasonably well-described by NLO QCD, the sensitivity to μ_R indicates that missing higher order corrections are significant. Valence distribution behaves as $v \sim (1-x)$ as $x \rightarrow 1$ in the experimentally accessible region, although the considered data do not constrain its derivative at $x = 1$. Valence momentum fraction in pion is found to be large in comparison to proton. In the future, new data from COMPASS++/AMBER¹³ experiment may constrain pion PDF.

References

1. S. Alekhin et al. HERAFitter. *Eur. Phys. J.*, C75(7):304, 2015.
2. J. S. Conway et al. Experimental Study of Muon Pairs Produced by 252-GeV Pions on Tungsten. *Phys. Rev.*, D39:92–122, 1989.
3. B. Betev et al. Differential Cross-section of High Mass Muon Pairs Produced by a 194-GeV/c π^- Beam on a Tungsten Target. *Z. Phys.*, C28:9, 1985.
4. M. Bonesini et al. High Transverse Momentum Prompt Photon Production by π^- and π^+ on Protons at 280-GeV/c. *Z. Phys.*, C37:535, 1988.
5. M. Botje. QCDNUM: Fast QCD Evolution and Convolution. *Comput. Phys. Commun.*, 182:490–532, 2011.
6. Tancredi Carli, Dan Clements, Amanda Cooper-Sarkar, Claire Gwenlan, Gavin P. Salam, Frank Siegert, Pavel Starovoitov, and Mark Sutton. A posteriori inclusion of parton density functions in NLO QCD final-state calculations at hadron colliders: The APPLGRID Project. *Eur. Phys. J.*, C66:503–524, 2010.
7. John M. Campbell and Richard Keith Ellis. An Update on vector boson pair production at hadron colliders. *Phys. Rev.*, D60:113006, 1999.
8. Karol Kovarik et al. nCTEQ15 - Global analysis of nuclear parton distributions with uncertainties in the CTEQ framework. *Phys. Rev.*, D93(8):085037, 2016.
9. H. Abramowicz et al. Combination of measurements of inclusive deep inelastic $e^\pm p$ scattering cross sections and QCD analysis of HERA data. *Eur. Phys. J.*, C75(12):580, 2015.
10. Roy J. Holt and Craig D. Roberts. Distribution Functions of the Nucleon and Pion in the Valence Region. *Rev. Mod. Phys.*, 82:2991–3044, 2010.
11. Chao Shi, Cdric Mezrag, and Hong-shi Zong. Pion and kaon valence quark distribution functions from Dyson-Schwinger equations. *Phys. Rev.*, D98(5):054029, 2018.
12. Kyle D. Bednar, Ian C. Clot, and Peter C. Tandy. Distinguishing Quarks and Gluons in Pion and Kaon PDFs. arXiv:1811.12310, 2018.
13. B. Adams et al. Letter of Intent: A New QCD facility at the M2 beam line of the CERN SPS (COMPASS++/AMBER). arXiv:1808.00848, 2018.

Forward-Backward Drell-Yan Asymmetry and PDF Determination ^a

H Abdolmaleki, E Accomando, V Bertone, J Fiaschi, F Giuli, A Glazov,
F Hautmann, A Luszczak, S Moretti, I Novikov, F Olness, O Zenaiev

We investigate the impact of high-statistics Drell-Yan (DY) measurements at the LHC on the study of non-perturbative QCD effects from parton distribution functions (PDF). We present the results of a PDF profiling analysis based on the neutral-current DY forward-backward asymmetry, using the open source fit platform `xFitter`.

The high statistics at the Large Hadron Collider (LHC) Run II and the forthcoming Run III and high-luminosity HL-LHC open the way to precision measurements at the TeV scale, which will be used both for studies of the Standard Model (SM) and for searches for beyond-Standard-Model (BSM) physics. In order to keep up with the increasing statistical precision of experimental measurements, an impressive effort is being made on the theoretical side to provide higher-order perturbative QCD calculations — see e.g. ¹. With improving perturbative accuracy, nonperturbative QCD contributions such as parton distribution functions (PDF) more and more become a crucial limiting factor in the theoretical systematics affecting both precision SM studies and BSM searches. An important part of the physics program to be carried out with current and upcoming collider data is thus to identify which measurements can be most helpful in placing constraints on the nonperturbative PDF and their uncertainties.

In the Drell-Yan (DY) production channel, measurements of differential distributions in mass and rapidity and of the charged-current (CC) asymmetry have long been used to constrain PDFs (see e.g. ^{2,3,4,5,6,7} for recent results), while measurements of the neutral current (NC) forward-backward asymmetry (henceforth denoted as A_{FB}) have traditionally been used for determinations of the weak mixing angle θ_W (see e.g. ^{8,9,10,11,12,13}). In ^{14,15} it was observed that A_{FB} measurements in NC processes at the LHC can usefully be employed for PDF determinations. Ref. ¹⁶ investigates the impact of A_{FB} data on PDF extractions by using the open source fit platform `xFitter`¹⁷, considering different scenarios for luminosities (from Runs II, III to the HL-LHC stage¹⁸) and performing PDF profiling to analyze quantitatively the effect of A_{FB} on PDF uncertainties. In this article we report on this study.

The five-fold differential DY cross section in the vector boson mass, rapidity, transverse momentum and lepton decay angles may be written in terms of angular coefficients A_k as

$$\begin{aligned} \frac{d\sigma}{dM_{\ell\ell}dY_{\ell\ell}dP_{\ell\ell}^{\perp}d\cos\theta d\phi} &= \frac{d\sigma^{(\text{U})}}{dM_{\ell\ell}dY_{\ell\ell}dP_{\ell\ell}^{\perp}} \frac{3}{16\pi} \left[1 + \cos^2\theta + \frac{1}{2}A_0(1 - 3\cos^2\theta) \right. \\ &+ A_1 \sin 2\theta \cos\phi + \frac{1}{2}A_2 \sin^2\theta \cos 2\phi + A_3 \sin\theta \cos\phi \\ &\left. + A_4 \cos\theta + A_5 \sin^2\theta \sin 2\phi + A_6 \sin 2\theta \sin\phi + A_7 \sin\theta \sin\phi \right]. \end{aligned} \quad (1)$$

^aCERN-TH-2019-116

The azimuthally integrated cross section is given by

$$\frac{d\sigma}{dM_{\ell\ell}dY_{\ell\ell}dP_{\ell\ell}^{\perp}d\cos\theta} = \frac{d\sigma^{(U)}}{dM_{\ell\ell}dY_{\ell\ell}dP_{\ell\ell}^{\perp}} \frac{3}{8} \left[1 + \cos^2\theta + \frac{1}{2}A_0(1 - 3\cos^2\theta) + A_4\cos\theta \right], \quad (2)$$

where the A_4 term is responsible for the forward-backward asymmetry. This may be defined as

$$A_{\text{FB}} = \frac{\sigma_F - \sigma_B}{\sigma_F + \sigma_B} \quad \text{where} \quad \sigma_F = \int_0^1 \frac{d\sigma}{d\cos\theta} d\cos\theta, \quad \sigma_B = \int_{-1}^0 \frac{d\sigma}{d\cos\theta} d\cos\theta. \quad (3)$$

At leading order (LO) in α_s , $A_0 = 0$, $A_4 \neq 0$. The LO triple differential cross section may be written as

$$\frac{d\sigma}{dM_{\ell\ell}dY_{\ell\ell}d\cos\theta} = \frac{\pi\alpha^2}{3M_{\ell\ell}s} \sum_q H_q [f_q f_{\bar{q}} + \{q \leftrightarrow \bar{q}\}], \quad (4)$$

where f is the PDF and H_q is given in terms of the vector and axial couplings v and a and electric charges e by

$$\begin{aligned} H_q = & e_{\ell}^2 e_q^2 (1 + \cos^2\theta) \\ & + e_{\ell} e_q \frac{2M_{\ell\ell}^2 (M_{\ell\ell}^2 - M_Z^2)}{\sin^2\theta_W \cos^2\theta_W [(M_{\ell\ell}^2 - M_Z^2)^2 + \Gamma_Z^2 M_Z^2]} [v_{\ell} v_q (1 + \cos^2\theta) + 2a_{\ell} a_q \cos\theta] \\ & + \frac{M_{\ell\ell}^4}{\sin^4\theta_W \cos^4\theta_W [(M_{\ell\ell}^2 - M_Z^2)^2 + \Gamma_Z^2 M_Z^2]} \\ & \times [(a_{\ell}^2 + v_{\ell}^2)(a_q^2 + v_q^2)(1 + \cos^2\theta) + 8a_{\ell} v_{\ell} a_q v_q \cos\theta]. \end{aligned} \quad (5)$$

The A_{FB} is dominated by the Z/γ interference $\cos\theta$ term in the second line of Eq. (5), proportional to $e_{\ell} e_q a_{\ell} a_q$, with $a_q = T_q^3/2$, where T_q^3 is the third component of weak isospin. It is thus primarily sensitive to the charge-weighted PDF linear combination $(2/3)u + (1/3)d$.

To carry out the PDF profiling analysis, the A_{FB} is implemented in `xFitter`, and NLO QCD corrections to DY are included via NLO grids obtained with `MadGraph5_aMC@NLO`¹⁹, interfaced to `APPLgrid`²⁰ through `aMCfast`²¹. At LO the angle θ may be reconstructed using the direction of the boost of the di-lepton system^{22,23,24,25,26}, while in general we use the definition of angle θ in the CS frame²⁷. The cross sections are computed in the detector fiducial region using the acceptance cuts of²⁸. Suitable datafiles with pseudodata are generated for the profiling analysis as described in¹⁶.

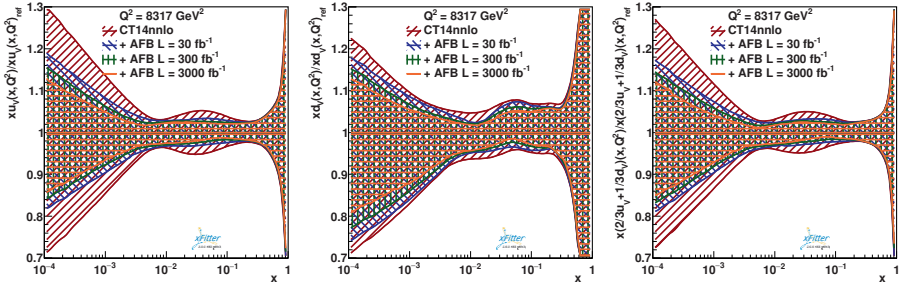


Figure 1 – Original (red) and profiled curves distributions for the normalised distribution of the ratios of (left to right) u -valence, d -valence and $((2/3)u + (1/3)d)$ -valence of the CT14nnlo PDF set, using A_{FB} pseudodata corresponding to integrated luminosities of 30 fb^{-1} (blue), 300 fb^{-1} (green) and 3000 fb^{-1} (orange).

Figs. 1 and 2 show results from the profiling analysis¹⁶, illustrating the reduction of PDF uncertainties for various scenarios of A_{FB} pseudodata and various PDF sets. In Fig. 1 the role

of different integrated luminosities is illustrated for the case of valence quark distributions in the CT15nnlo set³. In Fig. 2 the cases of valence and sea quark distributions are illustrated for NNPDF3.1nnlo⁴, MMHT2014nnlo⁶, ABMP16nnlo⁵ and HERAPDF2.0nnlo⁷, using A_{FB} pseudodata corresponding to an integrated luminosity of 300 fb^{-1} . The largest effects are observed for u -valence and d -valence distributions in the region of intermediate and low momentum fraction x , and for ABMP16nnlo and HERAPDF2.0nnlo sets. Sea quark determinations show a moderate improvement¹⁶, progressively increasing with the integrated luminosity. For PDF sets with Hessian eigenvectors, it is shown explicitly in¹⁶ by eigenvector reparameterization that u -valence and d -valence eigenvectors are highly correlated and A_{FB} data constrain their charge-weighted sum $(2/3)u_V + (1/3)d_V$.

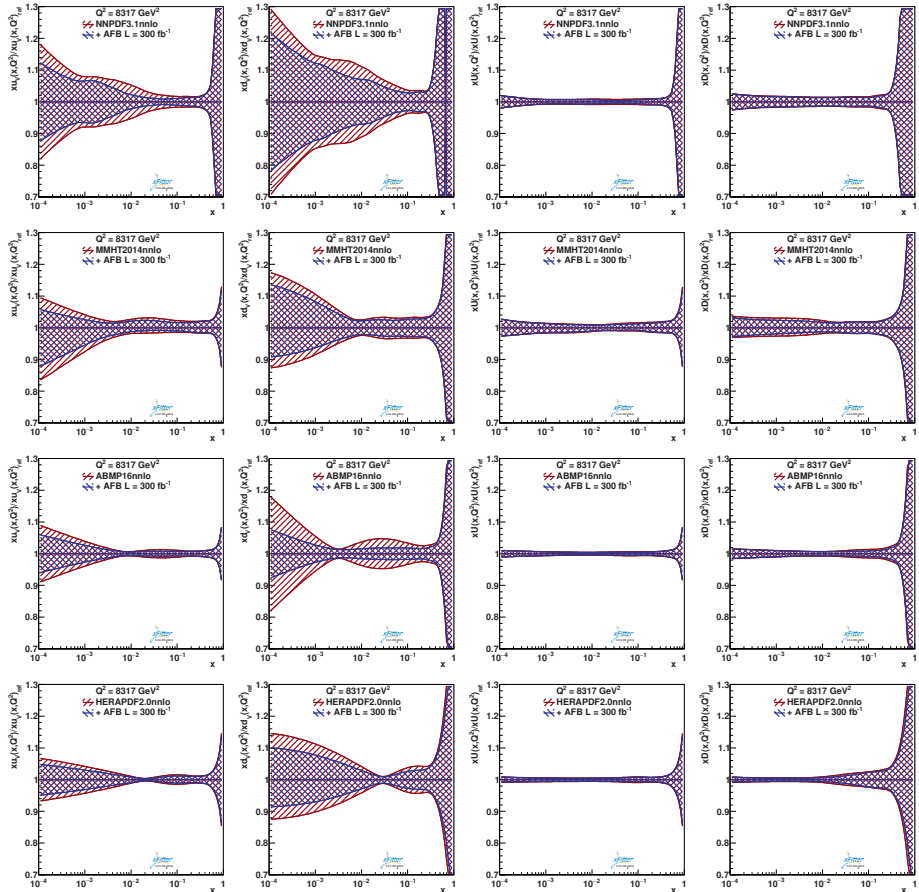


Figure 2 – Original (red) and profiled (blue) distributions for the normalised distribution of the ratios of (left to right) u -valence, d -valence, u -sea and d -sea quarks. The profiled curves are obtained using A_{FB} pseudodata corresponding to an integrated luminosity of 300 fb^{-1} . Distributions are shown for (rows top to bottom) NNPDF3.1nnlo, MMHT2014nnlo, ABMP16nnlo and HERAPDF2.0nnlo.

Ref.¹⁶ also studies different scenarios corresponding to different selection cuts on the dilepton rapidity. By increasing the rapidity cut, enhanced sensitivity is obtained to quark distributions in the high x region. In this case the high statistics of the HL-LHC is crucial to achieve

sufficient precision in the measurement of the A_{FB} .

In summary, the study reported in this article shows that neutral-current DY data from Run II, III and HL-LHC can be exploited to constrain nonperturbative QCD effects from PDFs, and thus to reduce the theoretical systematics affecting both precision SM studies and BSM searches. The A_{FB} , in particular, plays a complementary role to the lepton charge asymmetry of the DY charged-current channel, which has long been used in PDF global fits. Traditionally the A_{FB} has been used for determinations of the weak mixing angle θ_W . We have found that new PDF sensitivity arises from the di-lepton mass and rapidity spectra of the A_{FB} , which encodes information on the lepton polar angle, or pseudorapidity. We have presented quantitative results on PDF uncertainties based on PDF profiling calculations in `xFitter`. The results strongly support using DY data for combined determinations of θ_W and PDFs.

Acknowledgments

Many thanks to the Moriond organizers and staff for the invitation and for the pleasant atmosphere at this very interesting conference.

References

1. D. Wackerroth, arXiv:1906.09138 [hep-ph].
2. M. Aaboud et al. (ATLAS), Eur. Phys. J. C77, 367 (2017).
3. S. Dulat et al., Phys. Rev. D93, 033006 (2016).
4. R. D. Ball et al. (NNPDF), Eur. Phys. J. C77, 663 (2017).
5. S. Alekhin, J. Bluemlein, S. Moch and R. Placakyte, Phys. Rev. D96, 014011 (2017).
6. L. A. Harland-Lang et al., Eur. Phys. J. C75, 204 (2015).
7. H. Abramowicz et al. (ZEUS, H1), Eur. Phys. J. C75, 580 (2015).
8. CMS Coll., Eur. Phys. J. C78, 701 (2018).
9. ATLAS Coll., ATL-CONF-2018 037.
10. A. Bodek, J. Han, A. Khukhunaishvili and W. Sakumoto, Eur. Phys. J. C76, 115 (2016).
11. G. Aad et al. (ATLAS), JHEP 09, 049 (2015).
12. S. Chatrchyan et al. (CMS), Phys. Rev. D84, 112002 (2011).
13. R. Aaij et al. (LHCb), JHEP 11, 190 (2015).
14. E. Accomando, J. Fiaschi, F. Hautmann and S. Moretti, Eur. Phys. J. C78, 663 (2018).
15. E. Accomando, J. Fiaschi, F. Hautmann and S. Moretti, Phys. Rev. D98, 013003 (2018).
16. E. Accomando et al., preprint CERN-TH-2019-110, DESY 19-127.
17. S. Alekhin et al., Eur. Phys. J. C75, 304 (2015).
18. P. Azzi et al. (HL-LHC, HE-LHC Working Group), arXiv:1902.04070 [hep-ph].
19. J. Alwall et al., JHEP 07, 079 (2014).
20. T. Carli et al., Eur. Phys. J. C66, 503 (2010).
21. V. Bertone et al., JHEP 08, 166 (2014).
22. M. Dittmar, Phys. Rev. D55, 161 (1997).
23. T. G. Rizzo, JHEP 08, 082 (2009).
24. E. Accomando et al., Phys. Rev. D95, 035014 (2017).
25. E. Accomando et al., Phys. Lett. B770, 1 (2017).
26. E. Accomando et al., JHEP 01, 127 (2016).
27. J. C. Collins and D. E. Soper, Phys. Rev. D 16, 2219 (1977).
28. M. Aaboud et al. (ATLAS), JHEP 12, 059 (2017).

5. Heavy Ion

COLLECTIVITY IN RHIC GEOMETRY SCAN AS SEEN BY PHENIX

T. Novák for the PHENIX Collaboration

EKU KRC

Gyöngyös, Mátrai út 36, Hungary

In this paper we show azimuthal particle correlations in three different small-system collisions with different intrinsic initial geometries. The simultaneous constraints of v_2 and v_3 in $p/d/{}^3\text{He}+\text{Au}$ collisions definitively demonstrate that the v_n 's are correlated to the initial geometry. In addition, we find that hydrodynamical models which include QGP formation describe simultaneously the elliptic and triangular flow data in a statistically acceptable manner in all three systems.

1 Introduction

One of the key discoveries at RHIC is the identification of quark-gluon plasma (QGP) and its characterization as a near-perfect fluid via its collective flow.¹⁻⁵ One of the first observations of collective longitudinal and radial flow and their hydrodynamical coupling in the invariant momentum distribution and Bose-Einstein correlations was made by the EHS/NA22 experiment⁶ in $h+p$ collisions at CERN SPS at the beam momentum of 250 GeV/c, corresponding to $\sqrt{s} \approx 22$ GeV. As one of the first results of the d+Au beam energy scan at RHIC, PHENIX observed collective hydrodynamical behaviour of elliptic flow in d+Au collisions,^{7,8} providing evidence for collectivity in d+Au collisions from $\sqrt{s_{NN}} = 20$ GeV to 200 GeV. The LHC experiments observed similar features in small-system collisions.⁹⁻¹² These results not only broaden the domain of the applicability of the hydrodynamical paradigm to a previously unexpected domain, but also raise several fundamental questions as well. Is it due to the appearance of sQGP (i.e. a strongly coupled fluid)? If yes, how much time is spent in the QGP phase? What is the origin of final state collectivity? Is it due to initial geometry and hydrodynamics? Is the initial state geometry the primary driver of final state momentum correlations in small systems?

In order to test and answer these questions RHIC performed not only beam energy scan but also geometry scan measurements which allows for the investigation of the phase diagram of QCD matter by varying the beam energy in the region where the change from crossover to first order phase transition is suggested to occur. The beam-energy-scan program found real-valued v_2 in d+Au at all collision energies, providing evidence for collectivity in d+Au at all energies. Applying the unique capabilities of RHIC a projectile geometry scan¹³ was utilized in order to discriminate between hydrodynamical models that couple to the initial geometry and initial-state momentum correlation models that do not.

To characterize the fluidity of QGP, the azimuthal distribution of each event's final-state particles, $\frac{dN}{d\phi}$, is decomposed into a Fourier series as follows: $\frac{dN}{d\phi} \propto 1 + \sum_n 2v_n(p_T) \cos(n(\phi - \psi_n))$, where p_t and ϕ are the transverse momentum and the azimuthal angle of a particle relative to the beam direction, respectively, and ψ_n is the orientation of the n^{th} order symmetry plane of the produced particles. The second (v_2) and third (v_3) Fourier coefficients represent the amplitude of elliptic and triangular flow, respectively.

Varying the collision system from p +Au, to d +Au, to ${}^3\text{He}$ +Au changes the initial geometry from dominantly circular, to elliptical, and to triangular configurations, as characterized by the 2nd and 3rd order spatial eccentricities, which correspond to ellipticity and triangularity, respectively. The mean ε_2 and ε_3 values for small impact parameter $p/d/{}^3\text{He}$ +Au collisions are shown in Fig. 1a. The definition of the n^{th} order spatial eccentricity of the system, ε_n , is $\varepsilon_n = \frac{\sqrt{\langle r^n \cos(n\phi) \rangle^2 + \langle r^n \sin(n\phi) \rangle^2}}{\langle r^n \rangle}$, where r and ϕ are the polar coordinates of participating nucleons.¹⁴ Based on the calculation from a MC Glauber model, the average second and third order spatial eccentricities (ε_2 and ε_3) are shown as columns in Fig. 1a. The second and third order spatial eccentricities are called ellipticity and triangularity, respectively.

Hydrodynamical models begin with an initial spatial energy-density distribution with a given temperature that evolves in time following the laws of relativistic viscous hydrodynamics using an equation of state determined from lattice QCD.¹⁵ Examples of this temperature evolution are shown for $p/d/{}^3\text{He}$ +Au collisions in Fig. 1b using the hydrodynamical model SONIC.¹⁶ Based on hydrodynamical models a clear prediction for the ordering of the experimentally accessible v_2 and v_3 can be given, namely

$$v_2^{p+\text{Au}} < v_2^{d+\text{Au}} \approx v_2^{{}^3\text{He}+\text{Au}}, \quad v_3^{p+\text{Au}} \approx v_3^{d+\text{Au}} < v_3^{{}^3\text{He}+\text{Au}}. \quad (1)$$

This ordering assumes that hydrodynamics can efficiently translate the initial geometric ε_n into dynamical v_n , which is indeed seen in hydrodynamical simulations with small values of specific shear viscosity, as indicated on Fig. 1.

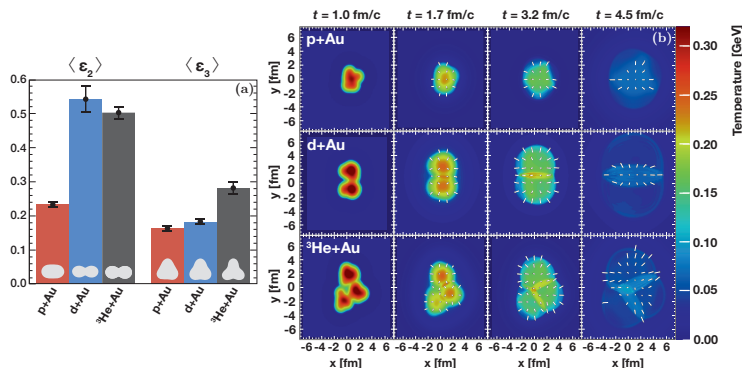


Figure 1 – Average ε_n from a MC Glauber model and hydrodynamic evolution of small systems.

There exist a class of alternative explanations where v_n is not generated via flow, but rather is created at the earliest time in the collision process as described by so-called color glass condensate or initial momentum space correlation models.¹⁷ The expectation from models based on initial-state momentum domain correlations for the ordering of the magnitude of the v_2 and v_3 coefficients is:

$$v_n^{p+\text{Au}} > v_n^{d+\text{Au}} > v_n^{{}^3\text{He}+\text{Au}}, \quad (2)$$

while the MSTV model in which gluons from the Au target do not resolve the individual color domains in the projectile $p/d/{}^3\text{He}$ does not follow Eq. (2).^a

^aPlease see the Note Added in Proof at the end of this manuscript for an important update regarding the MSTV calculation.

2 Models vs. data

Fig. 2 summarizes the results of elliptic and triangular flow measurements in the RHIC $p/d/{}^3\text{He}+\text{Au}$ geometry scan. The data points follow a geometrical ordering in a qualitative agreement with expectations from hydrodynamics.

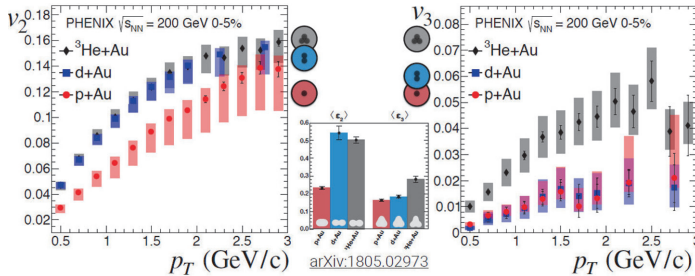


Figure 2 – PHENIX results for $v_2(p_T)$ and $v_3(p_T)$ in the RHIC geometry scan at $\sqrt{s_{NN}} = 200$ GeV.

Fig. 3 compares quantitatively the PHENIX elliptic and triangular flow measurements for $p/d/{}^3\text{He}+\text{Au}$ collisions with the results of numerical simulations. Two of these, SONIC and iEBE-VISHNU indicate predictions from numerical solutions of 2d+1 relativistic hydrodynamics with lattice QCD equation of state. The third model MSTV is on the other hand is based on initial state correlations and a color glass condensate initial state. Hydrodynamical models are consistent with the v_n data in all three systems, however, they tend to diverge at higher p_T in case of v_3 , which may be more sensitive to the hadronic scattering. Focusing on the MSTV, Fig. 3 shows that this model does a fair job in case of v_2 , but fails in case of v_3 .

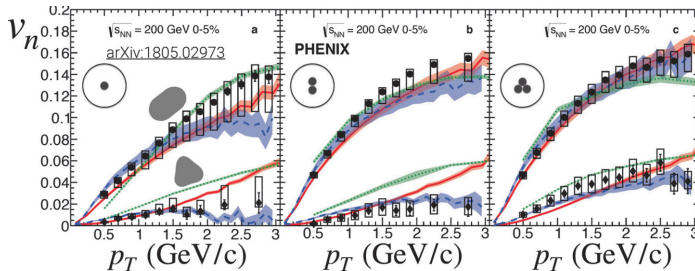


Figure 3 – Elliptic and triangular flows as a function of p_T in the RHIC geometry scan. Panel a) shows results for $p+\text{Au}$, panel b) for $d+\text{Au}$ and panel c) for ${}^3\text{He}+\text{Au}$ collisions at $\sqrt{s_{NN}} = 200$ GeV in 0-5% centrality class, as compared to SONIC (solid red), VISHNU (dashed blue) predictions and MSTV (solid green) postdictions.

In order to distinguish these models, a statistical significance test was made and provided a p -value for the MSTV calculations of v_2 and v_3 for the three collision systems of effectively zero, in contradiction to the robust values found for the hydrodynamical models.

The MSTV paper made a clear prediction that the v_2 will be identical between systems when selecting on the same event multiplicity. Shown in Fig. 4 are the previously published $d+\text{Au}(20-40\%)$ and $p+\text{Au}(0-5\%)$ v_2 where the measured mean charged particle multiplicities ($dN_{ch}/d\eta$) match.¹⁸ Our results contradict to this MSTV prediction, as they indicate clear differences between the v_2 of $d+\text{Au}$ and $p+\text{Au}$ collisions even if they are measured in the same multiplicity class, as indicated by Fig. 4. The results are however in a reasonable qualitative agreement with hydrodynamical predictions.

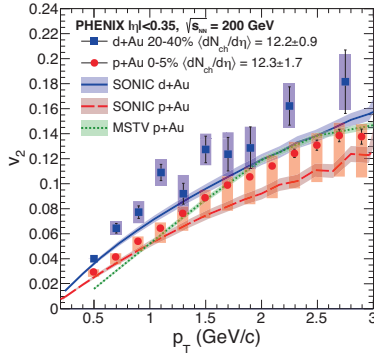


Figure 4 – Measured $v_2(p_T)$ in $p+Au$ and $d+Au$ collisions at the same event multiplicity, as compared to hydrodynamical calculations with SONIC and MVST color glass condensate calculations (note that these calculations predict the same green line for $p+Au$ and $d+Au$ collisions).

Note Added in Proof

Subsequent to the preparation of this manuscript we were made aware that there is an issue in the MSTV calculation and that the calculation no longer agrees with the PHENIX data when the issue is corrected. For details see http://www.int.washington.edu/talks/WorkShops/int_19_1b/People/Mace_M/Mace.pdf.

Acknowledgments

The author is grateful for the support of EFOP 3.6.1-16-2016-0001, and NKFIH grant FK 123842 - 123959 (Hungary), as well as to the full list of [PHENIX funding agencies](#).

References

1. Arsene, I. *et al.* Nucl. Phys. A **757**, 1 (2005).
2. Back, B. B. *et al.* Nucl. Phys. A **757**, 28 (2005).
3. Adams, J. *et al.* Nucl. Phys. A **757**, 102 (2005).
4. Adcox, K. *et al.* Nucl. Phys. A **757**, 184 (2005).
5. Heinz, U. & Snellings, R. Ann. Rev. Nucl. Part. Sci. **63**, 123 (2013).
6. N. M. Agababyan *et al.* [EHS/NA22 Collaboration], Phys. Lett. B **422**, 359 (1998)
7. C. Aidala *et al.* [PHENIX Collaboration], Phys. Rev. C **96**, no. 6, 064905 (2017)
8. C. Aidala *et al.* [PHENIX Collaboration], Phys. Rev. Lett. **120**, no. 6, 062302 (2018)
9. Khachatryan, V. *et al.* J. High Energy Phys. **09**, (0)91 (2010).
10. Chatrchyan, S. *et al.* Phys. Lett. B **718**, 795 (2013).
11. Abelev, B. *et al.* Phys. Lett. B **719**, 29 (2013).
12. Aad, G. *et al.* Phys. Rev. Lett. **110**, 182302 (2013).
13. Nagle, J. L. *et al.* Phys. Rev. Lett. **113**, 112301 (2014).
14. Alver, B. & Roland, G. Phys. Rev. C **81**, 054905 (2010).
15. Gale, C., Jeon, S. & Schenke, B. Int. J. Mod. Phys. A **28**, 1340011 (2013).
16. Habich, M., Nagle, J. L. & Romatschke, P. Eur. Phys. J. C **75**, 15 (2015).
17. Mace, M., Skokov, V. V., Tribedy, P. & Venugopalan, R. Phys. Rev. Lett. **121**, 052301 (2018).
18. Adare, A. *et al.* 1807.11928 (2018).

Studying Parton Dynamics via Single-Spin Asymmetries and Two-Particle Correlations at PHENIX

Nicole Lewis on behalf of the PHENIX Collaboration
University of Michigan Physics Department 450 Church St, Ann Arbor, MI 48109

The experimental observations of striking Transverse Single-Spin Asymmetries (TSSAs) opened a window into the parton dynamics present in hadronic collisions, revealing large spin-momentum correlations within nucleons and the process of hadronization. The Relativistic Heavy Ion Collider (RHIC) is the only collider in the world that can run polarized proton beams, allowing for these asymmetries to be measured at high energies, from $\sqrt{s} = 60$ to 500 GeV. In 2015 transversely polarized proton beams were collided with nuclear beams for the first time, enabling the exploration of the nuclear dependence of these asymmetries. Nonperturbative parton dynamics can also be studied in nearly back-to-back particle production by using the out-of-plane momentum component between the two particles, which is sensitive to the partonic transverse momentum in the proton and in fragmentation. Studying these correlations in both $p + p$ and $p + A$ collisions provides information on the modification of these nonperturbative parton dynamics in the presence of a nucleus. Recent results from the PHENIX experiment of polarized and polarization-averaged $p + p$, $p + \text{Al}$, and $p + \text{Au}$ collision data at $\sqrt{s_{NN}} = 200$ GeV will be shown.

1 Transverse Single-Spin Asymmetries

Transverse Single-Spin Asymmetries (TSSAs) are measured in high energy collisions where one transversely polarized particle collides with another unpolarized particle. The asymmetry measures the difference in yields of a particular outgoing particle traveling to the left versus the right of the direction that the colliding upward polarized particle was traveling:

$$A_N = \frac{\sigma_L - \sigma_R}{\sigma_L + \sigma_R} \quad (1)$$

Theoretical predictions have shown that if these asymmetries were only caused by perturbative QCD effects, they would be less than one percent¹, but TSSAs have been measured in proton-proton collisions to be as large as 40% for forward pions and have persisted for forward neutral pions in $\sqrt{s} = 500$ GeV proton-proton collisions with transverse momentum up to 7 GeV/c². Because the perturbative part of the scattering cross section cannot account for the measured large spin-momentum correlations, we must reexamine the nonperturbative part. One theoretical framework that developed to explain these large spin-momentum correlations is Transverse Momentum Dependent (TMD) functions, a set of PDFs and Fragmentation Functions that explicitly depend on the nonperturbative transverse momentum of partons. Thus in order to directly measure these two-scale functions, measurements need to be sensitive to both the hard scale and soft scale energies. In contrast twist-3 collinear correlation functions are multiparton correlations that have no explicit dependence on parton nonperturbative transverse momentum and so direct access only requires sensitivity to the hard scale energy. Twist-3 collinear correlation functions calculate the effects from the quantum interference of interacting with one

parton versus interacting with two partons of the same Bjorken x , for example the quantum interference between scattering off of one up quark in a proton versus scattering off of an up quark and a gluon. They can also be used to express spin-momentum correlations in the process of hadronization. The current understanding is that these two theoretical frameworks are not in conflict, but simply different ways of calculating the effects of the same physical processes³.

The PHENIX experiment is one of the experiments located on the ring of the Relativistic Heavy Ion Collider (RHIC). In addition to producing high energy collisions between a wide variety of heavy ions, RHIC is also the only collider in the world that can run polarized proton beams. In 2015 RHIC collided a polarized proton beam on proton, aluminum, and gold beams at $\sqrt{s_{NN}} = 200$ GeV. This unique data set provides a novel opportunity to study how nuclear structure affects parton dynamics in both the initial and final state.

PHENIX measured the forward neutron TSSA in $p + p$, $p + \text{Al}$ and $p + \text{Au}$ collisions and Figure 1 shows a very clear increase in the asymmetry as a function of A . The ‘‘ZDC inclusive’’ asymmetry (red circles) was calculated using all of the neutrons detected in the very far forward ($6.8 \leq \eta \leq 8.8$) Zero Degree Calorimeter (ZDC), the ‘‘ZDC \otimes BBC-tag’’ (green squares) used only neutrons from events where there was activity in either the forward or backward Beam Beam Counters (BBCs) and the ‘‘ZDC \otimes BBC-veto’’ asymmetries (blue triangles) were calculated using neutrons from events in which there were no hits in either of the BBCs, indicating that these might have come from diffractive and ultraperipheral events. The asymmetry even changes sign for both the inclusive and the BBC-veto data⁴.

In contrast, the TSSA for forward rapidity positively charged hadrons clearly decreases as a function of A , as shown in Figure 2 where the asymmetry is for $1.8 < p_T < 7.0$ GeV/ c , $0.1 < x_F < 0.2$ and $1.4 < \eta < 2.4$. The left panel shows a functional fit of $A_N^0/(A^{1/3})^\alpha$ where the best fit value for function was found to be $\alpha = 1.21^{+1.00(\text{stat})+0.09(\text{sys})}_{-0.42(\text{stat})-0.07(\text{sys})}$, again clearly favoring an A dependence. The right panel breaks these asymmetries into bins of centrality and shows the TSSA as a function of $N_{\text{coll}}^{\text{ave}}$, the average number of nucleon-nucleon collisions, where the best value for the displayed fit function was found to be $\beta = 1.19^{+0.68(\text{stat})+0.11(\text{sys})}_{-0.39(\text{stat})-0.08(\text{sys})}$, again clearly favoring a dependence on $N_{\text{coll}}^{\text{ave}}$ ⁵.

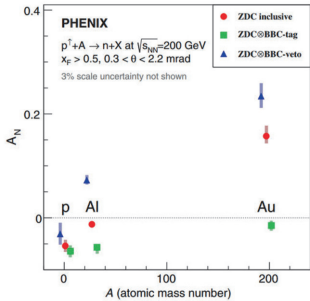


Figure 1 – Forward neutron TSSA⁴

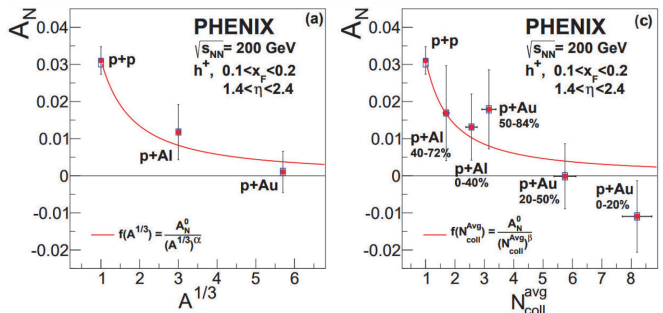


Figure 2 – Forward positively charged hadron TSSA⁵

Figure 3 shows both the forward and backward J/ψ TSSA asymmetry for $p + p$, $p + \text{Al}$ and $p + \text{Au}$ in two bins of p_T . This result is too statistically limited to show an obvious dependence on A , but with more data could provide insight into nuclear effects on gluon spin-momentum correlations. This is because at RHIC energies J/ψ production is dominated by gluon-gluon fusion. In $p + \text{Au}$ collisions the asymmetry is consistent with zero for the higher p_T bin, but the lower p_T bin is consistent with a negative A_N at the 2σ level in both the forward and backward directions⁶. Although the forward π^0 asymmetry has been measured to be nonzero,

the midrapidity π^0 TSSA has been shown to be consistent with zero to within 10^{-4} at low p_T . Figure 4 shows this asymmetry is also zero in $p + \text{Al}$ and $p + \text{Au}$ collisions⁷.

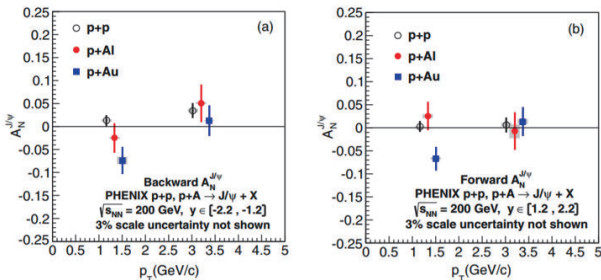


Figure 3 – Forward and backward J/ψ TSSA⁶

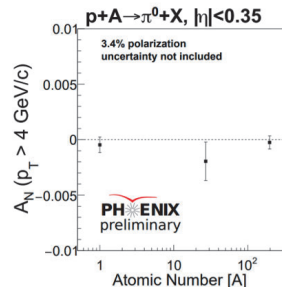


Figure 4 – Midrapidity π^0 TSSA⁷

2 Two-Particle Correlations

Most of the transverse single-spin asymmetries shown in this document are most easily analyzed in the twist-3 collinear framework as compared to transverse momentum dependent functions (provided they are at high enough p_T). This is because they only measure one outgoing hadron ($p + p(A) \rightarrow h + X$) and so while p_T is used as a proxy for the hard scale, there is no way of accessing a nonperturbative parton transverse momentum scale. In order to do this, we need to collect more information from the event such as measuring two-particle correlations. Figure 5 shows a schematic of this two-particle correlation, which in this case is performed on trigger π^0 with $5 < p_T^{\text{trig}} < 9$ GeV/c and another associated charged hadron with p_T^{assoc} in the same event. The red arrows indicate the transverse momenta of the outgoing partons, which cannot be measured and are also not back-to-back because of the nonperturbative initial-state partonic transverse momenta k_T . The black arrows represent the p_T of the measured hadrons, which are not collinear with the outgoing parton transverse momentum because of nonperturbative fragmentation transverse momentum j_T . Instead of measuring the correlations between these two particles as a function of the angle between them in the plane transverse to the beam $\Delta\phi$, the charged hadron yields are measured as a function of p_{out}

$$p_{\text{out}} = |\mathbf{p}_T^{\text{assoc}}| \sin \Delta\phi \quad (2)$$

This serves as our proxy for the soft scale momentum. The correlations can then be binned in x_E , which serves as our proxy for the fragmentation fraction z ⁸.

$$x_E = -\frac{\mathbf{p}_T^{\text{trig}} \cdot \mathbf{p}_T^{\text{assoc}}}{|\mathbf{p}_T^{\text{trig}}|^2} = -\frac{|\mathbf{p}_T^{\text{assoc}}|}{|\mathbf{p}_T^{\text{trig}}|} \cos \Delta\phi \quad (3)$$

These charged hadron yields are measured as a function p_{out} for both the away-side ($\frac{2\pi}{3} < \Delta\phi < \frac{4\pi}{3}$) and the near-side ($-\frac{\pi}{2} < \Delta\phi < \frac{\pi}{2}$). In a high p_T back-to-back two-jet event topology, which describes the majority of events at RHIC energies, the away-side corresponds to sampling the jet on the opposite side of the detector from the trigger π^0 , which makes it sensitive to both k_T and j_T effects. The near-side corresponds to sampling the jet around the trigger π^0 and is only sensitive to j_T effects. The charged particle p_{out} distributions show a very clear transition from a low p_{out} Gaussian behavior and a more power-law-like behavior at higher p_{out} . From these distributions, the width of these Gaussians at low p_{out} is extracted for both the $p + p$ and

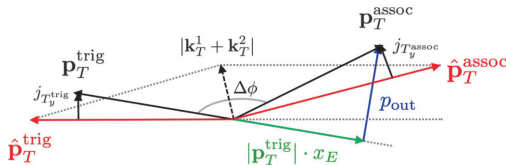


Figure 5 – A schematic diagram of a dihadron correlation in the transverse plane⁸

$p + A$ collisions. The left plot of Figure 6 shows the squared difference of the Gaussian widths for $p + A$ vs $p + p$ data. In the near-side there is no significant difference for either $p + \text{Al}$ or $p + \text{Au}$ collisions. For the away side, there might be some hint of a difference in width for $p + p$ vs $p + \text{Al}$ collisions, but for the $p + \text{Au}$ panel there is a clear difference in the away side widths. This trend continues when the away-side data is split into bins of N_{Coll} , the number of binary nucleon-nucleon collisions in a given event class, as shown in the right plot of Figure 6. For both x_E bins, the difference in widths shows a clear positive dependence on N_{Coll} , suggesting transverse momentum broadening in $p + A$ vs $p + p$ collisions⁸.

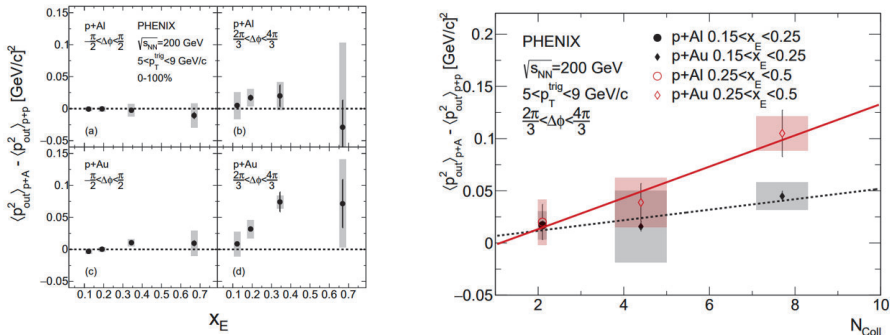


Figure 6 – The difference between the Gaussian widths of two-particle correlations in $p + p$ vs. $p + A$ collisions⁸

We still have much to learn about parton dynamics in bound states, the process of hadronization, and even hadronic interactions. Spin-momentum correlation and two-particle correlation measurements provide access to both initial- and final-state effects, where typically multiscale processes are involved. Because RHIC is the the most versatile hadronic collider in the world, it allows us to explore parton dynamics in both protons and nuclei in a wide variety of ways.

References

1. G.L. Kane, J. Pumplin, and W. Repko, *Phys. Rev. Lett.* **41**, 1689 (1978).
2. Yuxi Pan for the STAR Collaboration, *International Journal of Modern Physics: Conference Series* **40**, 1660037 (2016)
3. X. Ji, J-W Qiu, W. Vogelsang, and F. Yuan, *Phys. Rev. Lett.* **97**, 082002 (2006)
4. C. Aidala *et al.* (PHENIX Collaboration), *Phys. Rev. Lett.* **120**, 022001 (2018).
5. C. Aidala *et al.* (PHENIX Collaboration) (2019). arXiv:1903.07422 [hep-ex].
6. C. Aidala *et al.* (PHENIX Collaboration), *Phys. Rev. D* **98**, 012006 (2018).
7. N. Novitzky for the PHENIX Collaboration, presentation, 22nd International Spin Symposium (2016).
8. C. Aidala *et al.* (PHENIX Collaboration), *Phys. Rev. C* **99**, 044912 (2019).

RESULTS FROM PROTON-LEAD AND FIXED-TARGET COLLISIONS AT LHCb

DANIELE MARANGOTTO on behalf of the LHCb Collaboration
INFN Milano & Università degli Studi di Milano, Italy

The latest results obtained by the LHCb collaboration from proton-lead and proton-gas fixed-target collisions are presented. Results related to charm and beauty flavour hadron and quarkonia production in proton-lead collisions, being clean probes for Cold Nuclear Matter effects, are compatible to predictions based on initial-state effects. Indications of significant final-state effects in excited $\Upsilon(nS)$ resonances production are reported. The first cross-section measurement of $c\bar{c}$ and antiproton production in fixed-target proton-helium collisions at 100 GeV energy scale are also presented. More results will come from the latest Run 2 and future Run 3 data.

1 Introduction

The LHCb detector, mainly designed to study flavour physics in proton-proton collisions, is the only LHC experiment fully instrumented in the forward pseudorapidity region $2 < \eta < 5$, providing complementary coverage with respect to the other LHC experiments. LHCb features excellent tracking performances, momentum resolution and particle identification capabilities.

Besides proton-proton collisions, LHCb also recorded proton-lead and lead-lead collisions. In asymmetric proton-lead collisions, LHCb is able to probe both forward and backward nucleon-nucleon centre-of-mass rapidity (y^*) by exchanging the proton and lead beam directions: LHCb covers the forward $1.5 < y^* < 4.0$ rapidity region when the proton beam goes towards the detector, and the backward $-5.0 < y^* < 2.5$ range when the lead beam is directed towards LHCb.

LHCb studied the production of charm and beauty quarks in proton-lead collisions, which is a clean probe for Cold Nuclear Matter (CNM) effects, comprising the modification of nuclear partonic distributions (nPDFs), initial-state radiation or coherent energy loss of the heavy quark, gluon saturation (described by the Colour Glass Condensate theory, CGC) and final-state hadronic rescatterings. The quantitative understanding of CNM effects is crucial for a correct interpretation of Quark Gluon Plasma (QGP) signatures in lead-lead collisions, where heavy quarks constitute special probes for QGP properties. LHCb provides measurements for CNM effects at low transverse momentum (p_T) and forward/backward rapidity, down to very small parton momentum fraction (Björken $x \sim 10^{-5} - 10^{-6}$), where nPDFs are poorly constrained.

LHCb is also the only LHC experiment able to collect proton-gas fixed-target collisions thanks to its internal gas target, SMOG, which injects noble gases at $10^{-7} - 10^{-6}$ mbar pressures into the beampipe, and designed to perform precise luminosity measurements¹. SMOG allows LHCb to explore fixed-target collisions at the unprecedented $\sqrt{s_{NN}} = 100$ GeV nucleon-nucleon centre-of-mass energy scale.

2 Observables and theoretical predictions

Besides total and differential cross-sections, heavy quark production is studied by defining cross-section ratios as a function of p_T and y^* , less sensitive to systematic uncertainties and more easily comparable to theoretical predictions. The nuclear modification factor R_{pPb} describe differences in heavy quark production between proton-lead and proton-proton collisions,

$$R_{pPb}(p_T, y^*) \equiv \frac{1}{208} \frac{d^2\sigma_{pPb}(p_T, y^*)/dp_T dy^*}{d^2\sigma_{pp}(p_T, y^*)/dp_T dy^*}, \quad (1)$$

which is sensitive to the effects of nuclear interactions. The forward-to-backward ratio describes differences in heavy quark production for equal but opposite rapidity,

$$R_{FB}(p_T, y^*) \equiv \frac{d^2\sigma(p_T, +y^*)/dp_T dy^*}{d^2\sigma(p_T, -y^*)/dp_T dy^*}. \quad (2)$$

LHCb also measured baryon-to-meson ratios, which are sensitive to the heavy quark hadronisation mechanism,

$$R_{B/M}(p_T, y^*) \equiv \frac{d^2\sigma_B(p_T, y^*)/dp_T dy^*}{d^2\sigma_M(p_T, y^*)/dp_T dy^*}. \quad (3)$$

Measured ratios are compared to different theoretical predictions. Predictions based on initial-state (nPDFs) effects are obtained using the HELAC-Onia generator for collinear factorisation² or a perturbative QCD calculation at fixed-order next-to-leading log (FONLL)³, based on different nPDF sets: EPS09 at LO/NLO⁴, nCTEQ15⁵ and CT14NLO⁶. Where applicable, predictions from CGC effective field theory in dilute-dense approximation⁷ and coherent energy loss from soft gluon radiation⁸ are employed.

3 Heavy quark production in proton-lead collisions

LHCb studied the J/ψ production at nucleon-nucleon centre-of-mass energy of $\sqrt{s_{NN}} = 5.02$ and 8.16 TeV energies, separating prompt quarkonia produced in the proton-lead interaction from displaced ones coming from b quark decays⁹. A strong suppression of the nuclear modification factor (down to 0.6) is observed for prompt J/ψ at low p_T and forward y^* , while it is much less pronounced for backward rapidity. No significant suppression for J/ψ from b decays is seen. Predictions from nPDF effects, CGC and coherent energy loss follow the observed ratios, but on average they tend to overestimate data, indicating less anti-shadowing than expected. The forward-to-backward ratio is found to rise with p_T , especially for prompt J/ψ , while a flat rapidity dependence is seen.

The production of the Λ_c^+ charm baryon is studied at $\sqrt{s_{NN}} = 5.02$ TeV¹⁰. The forward-to-backward ratio is found consistent with HELAC-Onia predictions. The baryon-to-meson ratio $R_{\Lambda_c^+/D^0}$ agrees with results from proton-proton data but for forward rapidity and high p_T , where the Λ_c^+ baryon production seems suppressed.

LHCb studied open beauty hadron production at $\sqrt{s_{NN}} = 8.16$ TeV¹¹, reconstructing beauty hadrons in the exclusive decay modes $B^+ \rightarrow \bar{D}^0\pi^+$, $B^+ \rightarrow J/\psi K^+$, $B^0 \rightarrow D^-\pi^+$ and $\Lambda_b^0 \rightarrow \Lambda_c^+\pi^-$. This is the first measurement in nuclear collisions down to very low p_T . The measured nuclear modification factor confirms the suppression pattern seen in J/ψ from b decays production and the Λ_b^0 -to-meson ratio is consistent with proton-proton data results.

The production of the three $\Upsilon(nS)$ states is studied at $\sqrt{s_{NN}} = 8.16$ TeV¹². Thanks to the performances of the LHCb detector the three $\Upsilon(nS)$ are clearly resolved in the reconstructed $\mu^+\mu^-$ invariant mass. The suppression of nuclear modification factors for excited $\Upsilon(2S)$, $\Upsilon(3S)$ resonances is expected to be larger than the $\Upsilon(1S)$ state according to the ‘‘comover model’’ final-state effects¹⁶, especially for backward rapidities. This model predicts the production of excited $\Upsilon(nS)$ resonances to be reduced due to the interaction of comoving particles, a

possible explanation for the $\Upsilon(nS)$ suppression observed in lead-lead collisions. The measured nuclear modification factors show indeed a larger suppression for excited $\Upsilon(nS)$ quarkonia states, compatible with the “comover” model predictions, Fig. 1.

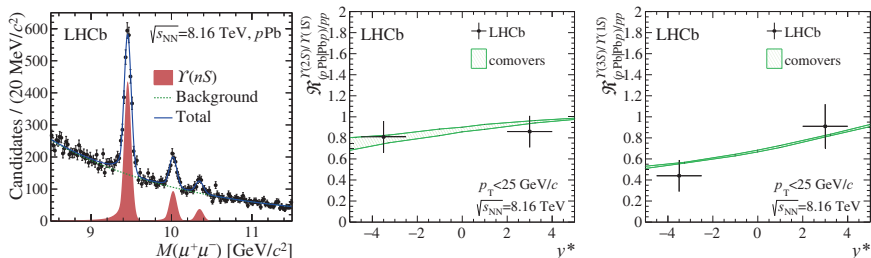


Figure 1 – (left) Reconstructed $\Upsilon(nS) \rightarrow \mu^+\mu^-$ invariant mass and nuclear modification factor for (center) $\Upsilon(2S)$ and (right) $\Upsilon(3S)$ states normalized to the $\Upsilon(1S)$ one.

4 Fixed-target p-gas collisions studies

LHCb collected the first charm (J/ψ and D^0) samples in proton-argon and proton-helium collisions at $\sqrt{s_{NN}} = 110$ and 87 GeV energy, respectively¹³. The first $c\bar{c}$ cross-section measurement is performed using the proton-helium dataset, Fig. 2, for which the integrated luminosity was determined from the yield of elastically scattered electrons off the target helium atoms¹⁴. Predictions from HELAC-Onia generator follow the shape of the measured differential cross-sections but underestimate the total by a factor 1.5-1.8. Results are also compared to linear and logarithmic interpolations from cross-section results at the closest energy available. From the measured differential cross-section it is possible to infer that there is no evidence for a significant c quark content in the nPDF functions in the kinematic region probed by LHCb.¹⁷

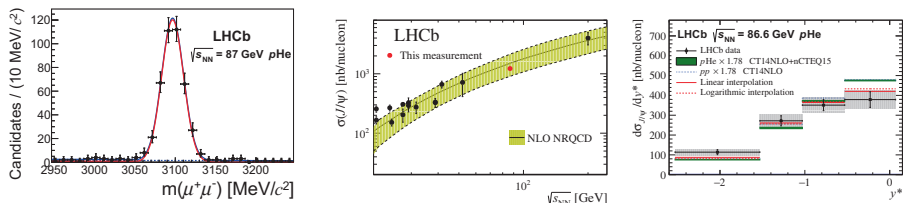


Figure 2 – (left) Reconstructed $J/\psi \rightarrow \mu^+\mu^-$ invariant mass and (center) total and (right) differential J/ψ cross-sections, obtained from the proton-helium dataset at $\sqrt{s_{NN}} = 87 \text{ GeV}$.

Space-based high-energy cosmic ray experiments AMS-02 and PAMELA have observed an excess of the antiproton-to-proton (\bar{p}/p) ratio at the 100 GeV energy scale¹⁸. An enhancement of the \bar{p}/p ratio can be an indirect signal of dark matter, however the significance of the result is limited by the large uncertainties related to antiproton production predictions. In particular, the antiproton production cross-sections in proton-hydrogen and proton-helium collisions are poorly known. LHCb performed the first measurement of antiproton production in proton-helium collisions at $\sqrt{s_{NN}} = 110 \text{ GeV}$ ¹⁴, providing precious information for more precise \bar{p}/p ratio predictions. The measured total and differential cross-sections have been compared to predictions from different generators¹⁹. The absolute antiproton yield is found to be underestimated by predictions up to a factor two, a result tending to disfavour the hypothesis of a dark

matter origin of the measured \bar{p}/p ratio excess in cosmic rays. Generators are able to reproduce the shape of the measured proton-helium differential cross-section, but for low momentum antiproton production is found to be lower than expected.

5 Prospects

The presented studies are just the beginning of the LHCb physics program with heavy ion and fixed-target collisions. Much more analyses are to come, like Drell-Yan and vector boson production studies, the investigation of more quarkonia states and dihadron correlations, Bose-Einstein condensates and flow studies. The latest LHC Run 2 samples of proton-neon, lead-lead and lead-neon collisions, the LHCb datasets with higher statistics in their respective configurations, are being analysed. At least a factor ten more integrated luminosity of proton-lead and lead-lead collisions is planned for the LHC Run 3 data-taking, to be recorded with an upgraded LHCb detector. The LHCb Collaboration is considering the installation of an upgraded gas injection system, SMOG2, aiming at increasing the injected gas pressure, therefore the luminosity of fixed-target collisions, by a factor 100. SMOG2 would also allow to inject more gas species (not only noble gases) with a precise density control. The LHCb Collaboration is also considering a Phase II upgrade of the LHCb detector for the LHC Run 5, for which a detailed physics case has been presented¹⁵.

A rich physics program with heavy ions and fixed-target is ahead for the LHCb experiment.

References

1. LHCb Collaboration, *JINST* **9**, P12005 (2014).
2. Hua-Sheng Shao, *Comput. Phys. Commun.* **198**, 238259 (2016).
3. M. Cacciari, M. Greco, P. Nason, *JHEP* **05**, 007 (1998).
4. K. J. Eskola, H. Paukkunen, C. A. Salgado, *JHEP* **04**, 065 (2009).
5. K. Kovarik *et al*, *Phys. Rev. D* **93**, 085037 (2016).
6. S. Dulat *et al*, *Phys. Rev. D* **93**, 033006 (2016).
7. B. Ducloué, T. Lappi, H. Mäntysaari, *Phys. Rev. D* **94**, 074031 (2016).
8. F. Arleo, S. Peigne, *JHEP* **03**, 122 (2013).
9. LHCb Collaboration, *Phys. Lett. B* **774**, 159-178 (2017).
10. LHCb Collaboration, *JHEP* **02**, 102 (2019).
11. LHCb Collaboration, *Phys. Rev. D* **99**, 052011 (2019).
12. LHCb Collaboration, *JHEP* **11**, 194 (2018).
13. LHCb Collaboration, *Phys. Rev. Lett.* **122**, 132002 (2019).
14. LHCb Collaboration, *Phys. Rev. Lett.* **121**, 222001 (2018).
15. LHCb Collaboration, arXiv:1808.08865.
16. E.G. Ferreira, J. Lansberg *JHEP* **10**, 094 (2018).
17. J. Pumplin, H. L. Lai, W. K. Tung, *Phys. Rev. D* **75**, 054029 (2007).
18. AMS Collaboration *Phys. Rev. Lett.* **117**, 091103 (2016).
19. T. Pierog *et al*, *Phys. Rev. C* **92**, 034906 (2015); T. Pierog, K. Werner, *Nucl. Phys. Proc. Suppl.* **196**, 102-105 (2009); S. Ostapchenko, *Phys. Rev. D* **83**, 014018 (2011); M. Kachelriess, I. V. Moskalenko, S. Ostapchenko, *Astrophys. J.* **803**, 54 (2015); M. Gyulassy and X. Wang *Comput. Phys. Commun.* **83**, 307-331 (1994); T. Sjöstrand, S. Mrenna, P. Skands, *JHEP* **05**, 026 (2006).

Heavy ion physics at CMS and ATLAS: hard probes

Gábor I. Veres on behalf of the CMS and ATLAS Collaborations
*Eötvös Loránd University, Department of Atomic Physics,
Pázmány Péter sétány, 1111 Budapest, Hungary*



Hard probes are indispensable tools to study the hot and dense quark-gluon matter created in ultra-relativistic heavy ion collisions. These probes are created in the collision itself with a small cross section, and they serve as indicators of various properties of the medium, such as temperature, viscosity, energy density, transport coefficients. Hard probes measured by the CMS and ATLAS experiments at the LHC include highly energetic jets and charged particles, quarkonium states, and electroweak gauge bosons. An overview of those recent experimental results will be given that represent the path towards high-precision measurements, even in the challenging, high-multiplicity environment created by colliding heavy ions.

1 Transport properties, parton energy loss

In heavy ion physics it is common to compare A+A and p+p interactions in order to isolate physical phenomena unique to large colliding systems. For the interpretation of such comparisons, it is necessary to quantify the modification of parton distribution functions in nuclei, including gluon saturation at low x . Nuclei can be probed with p+Pb collisions at the LHC, and recent results in this area include high-energy photons and dijets with a large rapidity separation.

The ATLAS collaboration¹ has recently measured the nuclear modification factors, R_{pA} , of isolated photons in p+Pb collisions, and concluded that the data disfavor a large amount of (initial state) energy loss, and impose constraints on the nuclear PDFs³. Dijets measured in p+Pb collisions with a large rapidity separation can probe partons at low x (between $10^{-4} - 10^{-5}$). No broadening was observed in the azimuthal angle correlations for such dijets. Jet pairs, where both jets had a high rapidity in the proton-going direction (i.e. sampling low- x partons in the Pb nucleus) were found to be suppressed with respect to p+p collisions⁴.

Departing from the baseline of nPDFs, one can study final state suppression using the nuclear modification factors in Pb+Pb and Xe+Xe collisions, as measured by the CMS collaboration² for charged hadrons⁵. On the left panel of Fig. 1 the charged-particle R_{AA} is shown for Xe+Xe collisions at $\sqrt{s_{NN}} = 5.44$ TeV for the 5% most central collisions, together with earlier data on R_{AA} in Pb+Pb collisions at 5.02 TeV. The data may indicate a slight difference in suppression at

Copyright 2019 CERN for the benefit of the ATLAS and CMS Collaborations. CC-BY-4.0 license.

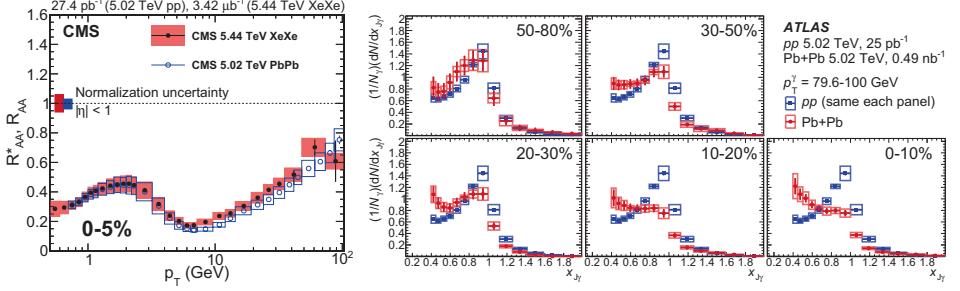


Figure 1 – Left: The charged-particle R_{AA} for Xe+Xe collisions at $\sqrt{s_{NN}} = 5.44$ TeV for the 5% most central collisions⁵, together with an earlier measurement of R_{AA} in Pb+Pb collisions at 5.02 TeV. Right: photon-jet p_T -balance distributions⁷ in Pb+Pb events (red circles) in different centrality bins compared to that in p+p events (blue squares) for $p_T^\gamma = 79.6$ -100 GeV, where $x_{J\gamma} = p_T^{\text{jet}}/p_T^\gamma$.

high p_T . Comparing R_{AA} values at the same number of participating nucleons, there is a hint of a greater suppression in Xe+Xe collisions, probably due to a geometrical effect.

The final state suppression of jets was also measured by the ATLAS experiment with an unprecedented precision recently, showing that the nuclear modification factor increases from low to high p_T and from central to peripheral Pb+Pb collisions⁶. Since photons are not affected by final state interactions, the energy loss of jets can be more precisely characterized by selecting photon-jet events. The recent data published by the ATLAS collaboration⁷ is corrected for accidental pairings and unfolded for energy resolution. The result can be seen on the right panel of Fig. 1, in terms of the distribution of the photon-jet p_T -balance distributions in different centrality bins, where $x_{J\gamma} = p_T^{\text{jet}}/p_T^\gamma$. One can conclude that while many of the jets lose a significant amount of energy in the most central Pb+Pb collisions, there still remain some relatively symmetric photon-jet pairs, producing a peak-like structure close to unity in $x_{J\gamma}$.

2 Medium temperature, quarkonium states, heavy flavor

Quarkonium production is a sensitive gauge of the temperature in the colored medium created in heavy ion collisions. These heavy mesons have a modest binding energy and a large radius, and the Debye-screening in the quark-gluon matter may cause their dissociation. The weakly bound states (like $\Upsilon(2S)$ and $\Upsilon(3S)$) are expected to suffer a stronger suppression, in comparison to p+p collisions, than more tightly bound ones, like $\Upsilon(1S)$. The dissociation temperatures are predicted to be at $2T_c$, $1.2T_c$ and T_c for these three mesons, where T_c is the critical temperature.

Indeed, this successive suppression of the Υ states, measured in their dimuon decay channel was observed by the CMS collaboration using a high-statistics data set of Pb+Pb collisions⁸. The invariant dimuon mass spectrum can be seen on the left panel of Fig. 2. The result of the fit to the data including the three Υ states and the non-resonant background is shown as a solid blue line. The dashed red line represents the result of the same fit, but with the Υ yield for each state respectively divided by their measured R_{AA} value (i.e. their measured suppression with respect to p+p collisions recorded at the same center-of-mass energy). The suppression is also found to be gradually strengthening with increasing collision centrality. It was also shown by the recent analysis of the CMS collaboration that the excited prompt $\Psi(2S)$ is more suppressed in Pb+Pb collisions than the J/Ψ ground state⁹.

The J/Ψ mesons also constitute an important tool to characterize the b-quark energy loss, since b-decays to J/Ψ can be measured separately from prompt J/Ψ production making use of the long lifetime of the b quark. The ATLAS collaboration has measured the nuclear modification factors of prompt and non-prompt J/Ψ particles at high p_T , and found a strong suppression in both cases¹⁰, as can be seen on the right panel of Fig. 2. Prompt J/Ψ mesons are suppressed to a similar

extent as inclusive charged particles, while the non-prompt states experience less suppression in the $p_T < 20$ GeV range, owing to the more modest energy loss of b-quarks compared to light quarks. A further confirmation of this phenomena is that the suppression of non-prompt $\Psi(2S)$ and non-prompt J/Ψ states, both originating from b-decays, were found to be equal. A similar conclusion can be drawn from a recent analysis of muons originating from heavy quark decays by the ATLAS experiment¹¹, and from the CMS measurement of the non-prompt $D^0 \rightarrow K^- \pi^+$ mesons (coming from b-hadron decays), which exhibit significantly less suppression at low p_T compared to charged hadrons¹².

It is also interesting to measure the B_s^0 state in Pb+Pb collisions to test if beauty and strange quarks can coalesce in the environment abundant in s quarks, possibly leading to an increase of the B_s^0/B^+ ratio. The CMS collaboration has published the first result on that recently in the $B_s^0 \rightarrow \mu^+ \mu^- K^+ K^-$ decay channel, with a possible indication of such an increase¹³.

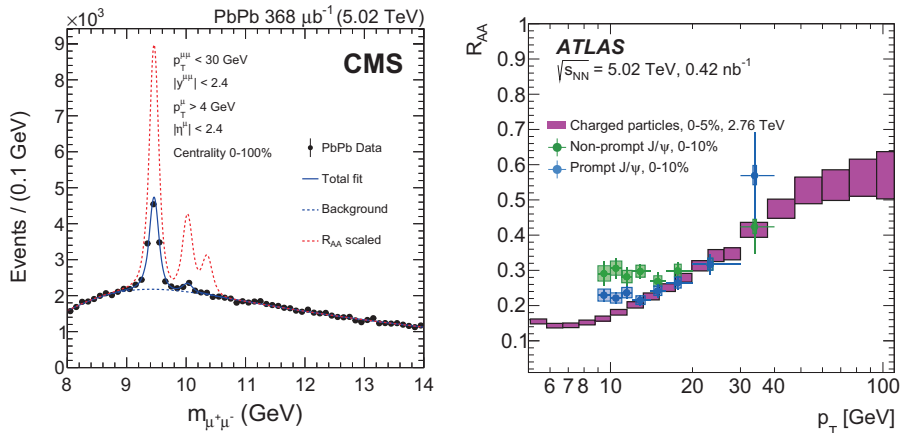


Figure 2 – Quarkonium results in Pb+Pb collisions at $\sqrt{s_{NN}} = 5.02$ TeV. Left: invariant mass distribution of muon pairs⁸ for the kinematic range $p_T^{\mu^+\mu^-} < 30$ GeV and $|y^{\mu^+\mu^-}| < 2.4$. The result of the fit to the data is shown as a solid blue line. The dashed red line is also the result of the same fit but with the Υ yield for each state divided by the measured R_{AA} . Right: Comparison of prompt and non-prompt J/Ψ R_{AA} with the R_{AA} of charged particles¹⁰.

3 Jet substructure

After considering the spectacular jet quenching (parton energy loss) results obtained from heavy ion data, the next immediate question to ask is about the possible changes of the jet structure with respect to p+p collisions.

The CMS experiment has measured the transverse shape (energy density) of jets tagged by isolated photons, as a function of the distance r from the jet axis for various centrality categories¹⁴, as shown on the left panel of Fig. 3. A jet broadening can be observed for central Pb+Pb collisions in these photon-jet events, while no depletion is visible in the $0.1 < r < 0.2$ region, as opposed to inclusive jets. The longitudinal structure of jets, the fragmentation functions, were published by the ATLAS experiment¹⁵, and show that there is an enhancement of particles with a small or very large fraction of the jet momentum, and a suppression of particles with an intermediate momentum fraction. The jet fragmentation functions were also measured in photon-tagged jets¹⁶, and a ratio with respect to those in p+p collisions are shown on the right panel of Fig. 3. The jets with a photon partner, dominated by quark jets (blue data points), and inclusive jets (red points) are modified in a different way in central Pb+Pb events, although the interpretation of the data is complicated due to the different selection biases.

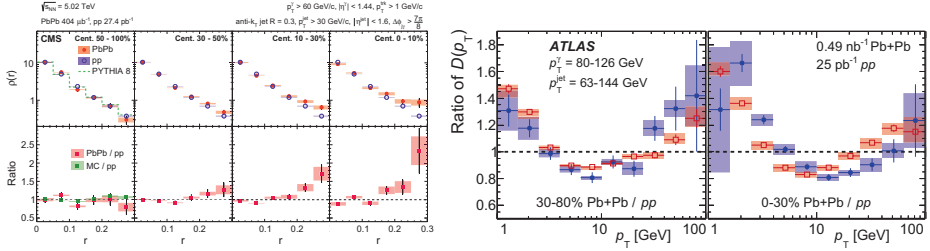


Figure 3 – Left panel, upper plots: the differential jet shape, $\rho(r)$, for jets associated with an isolated photon for (from left to right) 50-100%, 30-50%, 10-30%, 0-10% Pb+Pb (full circles), and p+p (open circles) collisions and from PYTHIA simulation (histogram). Left panel, lower plots: the ratios of the fragmentation function in jets azimuthally balanced by a high- p_T photon: 30-80% Pb+Pb collisions to p+p collisions (left panel) and 0-30% Pb+Pb collisions to p+p collisions (right panel). Results are shown as a function of charged-particle transverse momentum p_T , for γ -tagged jets (this measurement, full markers) and for inclusive jets in 2.76 TeV Pb+Pb collisions (open markers)¹⁶.

Finally, the CMS experiment has employed the jet grooming technique to remove large-angle, soft radiation, and extract the hard subjets. Since the opening angle between those subjets is sensitive to medium induced modifications, the distribution of the jet mass of these groomed jets is an important observable. These results indicate that available model calculations overestimate the yield of jets with a large groomed mass relative to the jet p_T ¹⁷.

In summary, the heavy ion research program at the LHC provides a precise and detailed set of experimental data, challenging many of the phenomenological models concerning jet substructure modifications, and supporting various expectations about nuclear PDFs, energy loss of light and heavy quarks and quarkonium dissociation.

Acknowledgments

The author is grateful for the support of the MTA Momentum program LP 2015-7/2015 and the support by the grants NKFI K.18 128713, NKFI K.17 124845 and NKFI FK.17 123842.

References

1. ATLAS Collaboration *JINST* **3** S08003 (2008).
2. CMS Collaboration *JINST* **3** S08004 (2008).
3. ATLAS Collaboration, submitted to *Phys. Lett. B*, arXiv:1903.02209 (2019).
4. ATLAS Collaboration, submitted to *Phys. Rev. C*, arXiv:1901.10440 (2019).
5. CMS Collaboration *JHEP* **10** 138 (2018).
6. ATLAS Collaboration *Phys. Lett. B* **790** 108 (2019).
7. ATLAS Collaboration *Phys. Lett. B* **789** 167 (2019).
8. CMS Collaboration *Phys. Lett. B* **790** 270 (2019).
9. CMS Collaboration *Eur. Phys. J. C* **78** 509 (2018).
10. ATLAS Collaboration *Eur. Phys. J. C* **78** 762 (2018).
11. ATLAS Collaboration *Phys. Rev. C* **98** 044905 (2018).
12. CMS Collaboration, submitted to *Phys. Rev. Lett.*, arXiv:1810.11102 (2018).
13. CMS Collaboration, submitted to *Phys. Lett. B*, arXiv:1810.03022 (2018).
14. CMS Collaboration *Phys. Rev. Lett.* **122** 152001 (2019).
15. ATLAS Collaboration *Phys. Rev. C* **98** 024908 (2018).
16. ATLAS Collaboration, submitted to *Phys. Rev. Lett.*, arXiv:1902.10007 (2019).
17. CMS Collaboration *JHEP* **10** 161 (2018).

**Heavy ion physics at ATLAS and CMS:
flow harmonics across systems (pp , $p+Pb$, $Xe+Xe$, $Pb+Pb$)**

Krzysztof W. Woźniak on behalf of the ATLAS and CMS Collaborations
*Institute of Nuclear Physics, PAS,
ul. Radzikowskiego 152, 31-342 Krakow, Poland*

The collective flow of produced particles is one of the signatures of the creation of the Quark-Gluon Plasma (QGP) in heavy ion collisions. However, similar long-range azimuthal correlations are observed at the LHC energies also in proton-lead and even proton-proton collisions. Extensive and detailed studies of flow harmonics are performed by the ATLAS and the CMS experiments in order to understand mechanisms responsible for these correlations.

Long-range azimuthal correlations of particles produced in heavy ion collisions at high energies can be explained as a consequence of the asymmetry of the overlap area of colliding nuclei leading to differences in the pressure gradients in QGP which affect the particle production. The distribution of azimuthal angles, ϕ , of charged particles with respect to the event plane features a cosine-like modulation¹, which in the case of single events can be described by a complete Fourier series:

$$\frac{dN}{d\eta} \sim 1 + 2 \sum_{n=1}^{\infty} v_n \cos [n(\phi - \Phi_n)], \quad (1)$$

where Φ_n is the event plane angle and v_n parameters are called flow harmonics. These harmonics can be calculated not only using the Event Plane method, based on Eq. 1, but also from two- or multi-particle correlations, for example using the Scalar Product method, the standard cumulants method or the subevent cumulants method.

The importance of proper removal of non-flow effects in the calculations of flow harmonics, especially in pp collisions, is evident in the studies of cumulants². In the absence of non-flow effects the four-particle cumulants

$$c_n\{4\} = \langle\langle e^{in(\phi_1+\phi_2-\phi_3-\phi_4)} \rangle\rangle - 2 \langle\langle e^{in(\phi_1-\phi_2)} \rangle\rangle^2 \quad (2)$$

should be negative as $c_n\{4\}_{\text{flow}} = -v_n^4$. In Fig. 1 the standard cumulants calculated using all quadruplets of particles are positive and only in the three-subevent method, where particles compared are from different η regions, $c_n\{4\}$ is negative in a wide multiplicity interval². Obviously, the standard cumulants are sensitive to correlations between particles from jets.

The elliptic flow, v_2 , is expected to reflect the geometry of collisions. In Fig. 2 the values of v_2 for pp , $p+Pb$ and low-multiplicity $Pb+Pb$ collisions³ are shown as a function of multiplicity, N_{ch} . For pp collisions v_2 is constant, it increases with N_{ch} for two other systems and is the largest in $Pb+Pb$ collisions, in which the overlap of these nuclei has the most elongated shape.

The subtle differences in the geometry are visible even in the comparison of harmonics for $Xe+Xe$ and $Pb+Pb$ collisions^{4,5}, as indicated by the ratios of harmonics shown in Fig. 3. Fluctuations of the shape of the overlap of nuclei are larger for $Xe+Xe$ than for $Pb+Pb$ collisions.

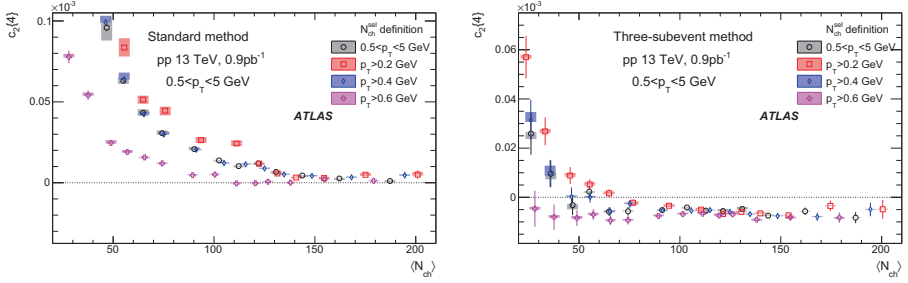


Figure 1 – The cumulant $c_2\{4\}$ values calculated for charged particles with $0.5 < p_T < 5$ GeV with (left) the standard cumulant method and (right) the three-subevent cumulant method using the 13 TeV pp data².

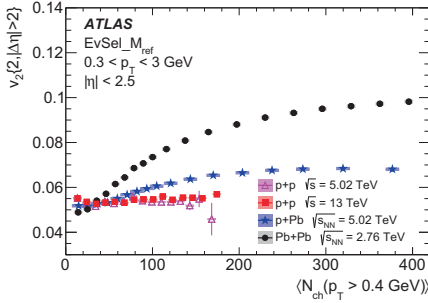


Figure 2 – Comparison of $v_2\{2, |\Delta\eta| > 2\}$, calculated for reference particles with $0.3 < p_T < 3$ GeV, shown as a function of $\langle N_{ch}(p_T > 0.4\text{GeV}) \rangle$ for pp collisions at $\sqrt{s} = 5.02$ and 13 TeV, $p+Pb$ collisions at $\sqrt{s_{NN}} = 5.02$ TeV and low-multiplicity $Pb+Pb$ collisions at $\sqrt{s_{NN}} = 2.76$ TeV³.

This causes that in the most central collisions v_2 and v_3 are larger in the first system. Contrary, in peripheral Xe+Xe collisions all harmonics are smaller than in Pb+Pb collisions as in this case fluctuations usually lead to smaller initial eccentricity.

In $p+Pb$ collisions, an asymmetry in particle production in proton-going and lead-going direction is observed. This could influence also the ratio of flow harmonics at the same absolute pseudorapidity⁶, shown in Fig. 4. All standard methods of elliptic flow calculations give smaller values in p -going than in Pb -going direction. However, they do not account for decorrelations (flow fluctuations along η), and once appropriate corrections are applied in calculations of $v_2\{SP; \eta_C = \eta_{ROI}\}$ the differences between p -going and Pb -going sides largely disappear⁶. Detailed studies of flow decorrelations in $Pb+Pb$ collisions⁷ show that flow magnitude and event

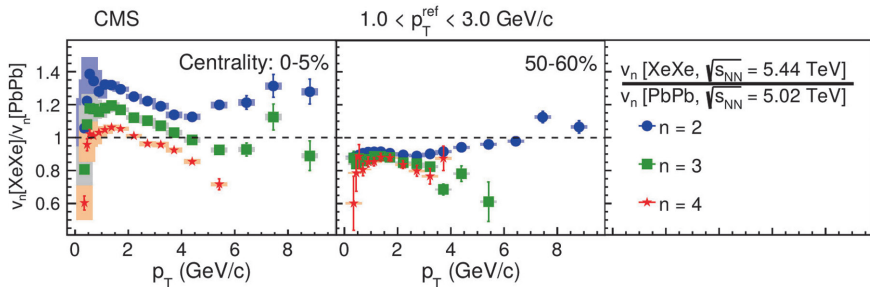


Figure 3 – Ratios of the v_2 , v_3 , and v_4 harmonic coefficients from two-particle correlations in Xe+Xe and Pb+Pb collisions as functions of p_T in two example centrality intervals⁴.

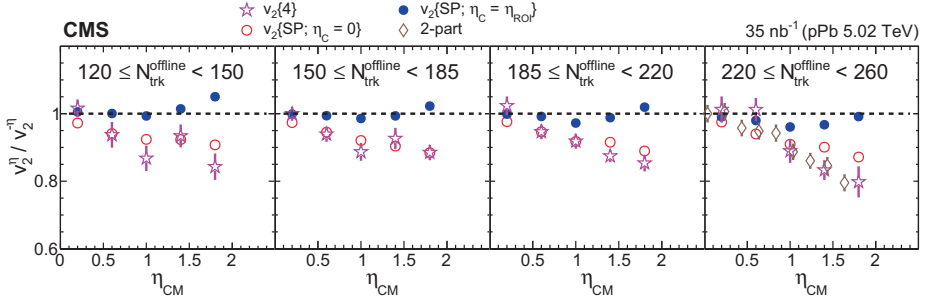


Figure 4 – Ratio of the p - to Pb-going side v_2 coefficients at comparable η_{CM} values for p +Pb collisions⁶.

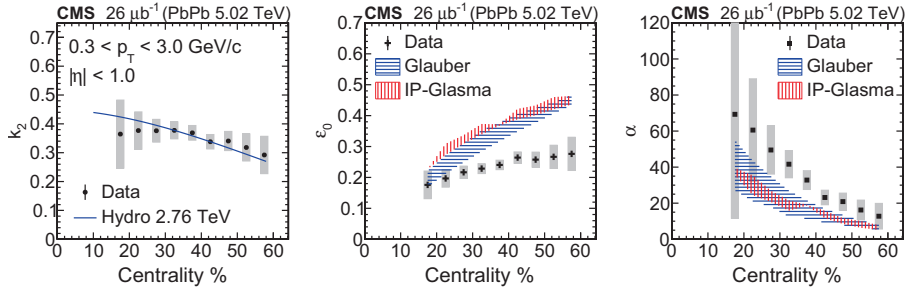


Figure 5 – Centrality dependence of the parameters extracted from elliptic power function fits to the unfolded $p(v_2)$ distributions⁸.

plane rotation (twist) fluctuations are of similar order and increase approximately linearly with pseudorapidity.

Deeper insight into the properties of the initial eccentricity, ϵ_n , is possible in the studies of event-by-event flow fluctuations by measuring the probability function $p(v_n)$. Under some model assumptions, including emission of particles from N sources and a linear response of v_n to the initial eccentricity: $v_n = k_n \epsilon_n$, $p(v_n)$ can be described by the elliptic power function⁸, parameters of which are shown in Fig. 5. Lower values of parameter ϵ_0 than predicted by theoretical models may indicate that the assumption of linear response is not valid.

The flow fluctuations are sensitive to the number of sources of particles, N_s . It is thus possible to estimate N_s using the ratio of $v_2\{2\}$ from two-particle correlations to $v_2\{4\}$ obtained from cumulants², as shown in Fig. 6. Results for pp and p +Pb collisions are compatible and N_s increases with mean multiplicity.

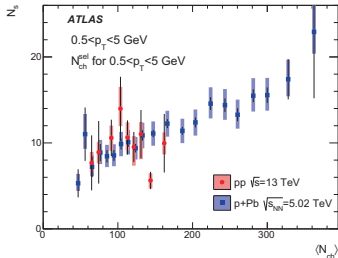


Figure 6 – The number of sources: $N_s = 4(v_2\{2\}/v_2\{4\})^4 - 3$, inferred from $v_2\{2\}$ and $v_2\{4\}$ measurements via the model framework in 13 TeV pp and 5.02 TeV p +Pb collisions², for charged particles with $0.5 < p_T < 5$ GeV.

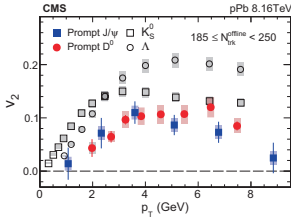


Figure 7 – Comparison of the v_2 results of the prompt J/ψ mesons, as a function of p_T for p +Pb collisions at $\sqrt{s_{NN}} = 8.16$ TeV with those for for K_0^S , Λ hadrons and D^0 mesons⁹.

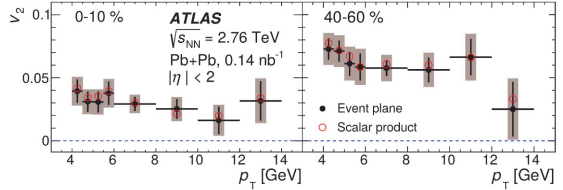


Figure 8 – The p_T dependence of the Pb+Pb heavy-flavor muon v_2 for two centralities obtained from the Event Plane and the Scalar Product methods¹⁰.

Flow harmonics are measured also for specific classes of particles. In Fig. 7 values of elliptic flow are shown for particles containing strange or charm quarks found in p +Pb collisions⁹. While v_2 as a function of p_T has similar shape for both quark flavours, lower v_2 values indicate weaker collective behaviour of particles containing heavy quarks. The same conclusion can be drawn from the measurements of the flow of muons from heavy-flavour decays¹⁰ shown in Fig. 8.

The results presented here on flow harmonics from ATLAS and CMS are not complete. There are several other studies, most recent of which include measurements of elliptic flow in Z boson-tagged events¹¹, elliptic flow of high- p_T particles¹² and mixed flow harmonics¹³.

In summary, long range azimuthal correlations are present in all types of collisions available at the LHC and studied using ATLAS¹⁴ and CMS¹⁵ detectors. The flow harmonics magnitude depends on the type of collision, but similar general properties are observed in p +Pb, Xe+Xe and Pb+Pb collisions, while larger differences are found for pp collisions. In the recent studies many different methods are used to remove contributions from non-flow effects. Their results allow better understanding of flow properties and relations to the initial conditions. Analyses of harmonics for different types of particles or specific classes of events provide additional information which can be used to test theoretical models.

Acknowledgments

This work was supported in part by the National Science Centre, Poland grant 2016/23/B/ST2/00702 and by PL-Grid Infrastructure.

References

1. ATLAS Collaboration, Phys. Lett. B **707** (2029) 330.
2. ATLAS Collaboration, Phys. Rev. C **97** (2018) 024904.
3. ATLAS Collaboration, Eur. Phys. J. C **77** (2017) 428.
4. CMS Collaboration, arXiv:1901.07997 [hep-ex].
5. ATLAS Collaboration, ATLAS-CONF-2018-011.
6. CMS Collaboration, Phys. Rev. C **98** (2018) 044902.
7. ATLAS Collaboration, Eur. Phys. J. C **76** (2018) 142.
8. CMS Collaboration, Phys. Lett. B **789** (2019) 643.
9. CMS Collaboration, Phys. Rev. Lett. **121** (2018) 082301.
10. ATLAS Collaboration, Phys. Rev. C **98** (2018) 044905.
11. ATLAS Collaboration, ATLAS-CONF-2017-068.
12. CMS Collaboration, Phys. Lett. B **776** (2017) 195.
13. ATLAS Collaboration, Phys. Lett. B **789** (2019) 444.
14. ATLAS Collaboration, JINST **3** (2008) S08003.
15. CMS Collaboration, JINST **3** (2008) S08004.

PROBING OF MULTIQUARK STRUCTURE IN HADRON AND HEAVY ION COLLISIONS

M.Yu. Barabanov¹, S. L. Olsen²

¹ *Joint Institute for Nuclear Research Joliot-Curie 6 Dubna Moscow region 141980, Russia*

² *University of the Chinese Academy of Science, Beijing 100039, People's Republic of China*

The possibility of selected study of heavy charmonium-like hadrons is discussed. The topic includes detailed analysis of their strong, weak and electromagnetic decays containing pair, physics simulation and events reconstruction at NICA facility. These provide a good tool for testing theories of the strong interactions including both perturbative and non-perturbative QCD, lattice QCD, potential and other phenomenological models.

1 Introduction

The analysis of multi-quark states is of great importance. Their predictions are closely linked to existing and forthcoming data of running and planned experiments like Belle, BaBar, BES, LHCb, NICA, PANDA, etc. Given the existing experience of model calculation, physics simulation and event reconstruction, the detailed analysis of their structure is performed. This can be realized by using well known methods based on QCD principles as well as new proposed phenomenological approaches, which allow describing the structure of bound state of hadrons and exotics. The obtained results will shed light on the nature of X, Y, Z exotics, which are one of the most mysterious states in modern particle physics.¹⁻⁴ Charmonium-like spectroscopy represents a good testing tool for the theories of strong interactions, including: QCD in both the perturbative and non-perturbative regimes, LQCD, potential models and phenomenological models. The experiments planned at NICA are well suited for testing these states. The facility will allow colliding heavy-ion beams with the luminosity $10^{27} \text{cm}^{-2} \text{s}^{-1}$ and \sqrt{s} up to 11 GeV and proton-proton beams with the luminosity up to $10^{32} \text{cm}^{-2} \text{s}^{-1}$ and \sqrt{s} up to 26 GeV.⁵

2 Heavy flavour study

Good tracking and particle identification performance of NICA over significant fraction of the final state phase space can provide a good opportunity to extend its ambitious physics program to studies of heavy charmed objects via their decays to electrons, hadrons or photons. It can be illustrated by the PYTHIA8⁶ simulated data on heavy quarkonia production in p-p collisions at $\sqrt{s} \sim 26$ GeV. One can see from Fig. 1 that the detector acceptance for electron-positron pairs from $J\psi$ decays is quite high (80% for $|\eta| < 1.5$). The detector acceptance for photons from electromagnetic decays of heavy quarkonia can be seen in Fig. 2. It exceeds 80% for χ_{c1} and χ_{c2} decays. The momentum resolution for electrons and photons is presented in Figs. 3 and 4. One can see that it will be possible to combine momentum measurement of electrons in tracking detectors with energy measurement in the electromagnetic calorimeter to obtain better accuracy for fast particles. Signal reconstruction performance of the detector for $J\psi \rightarrow e^+e^-$

decays was evaluated using full simulation/reconstruction chain. As can be seen in Fig. 5, $J\psi$ invariant mass peak is clearly visible.

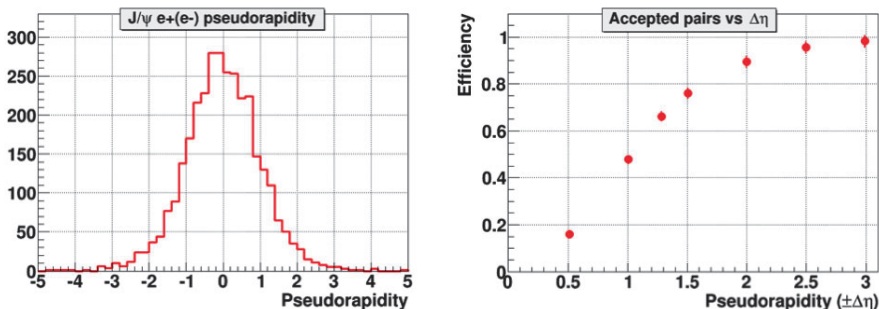


Figure 1 – Left: Pseudorapidity distribution of electrons and positrons from $J\psi$ decays; Right: percentage of $J\psi \rightarrow e^+e^-$ decays with both the electron and positron within the pseudorapidity window of $\pm\Delta\eta$.

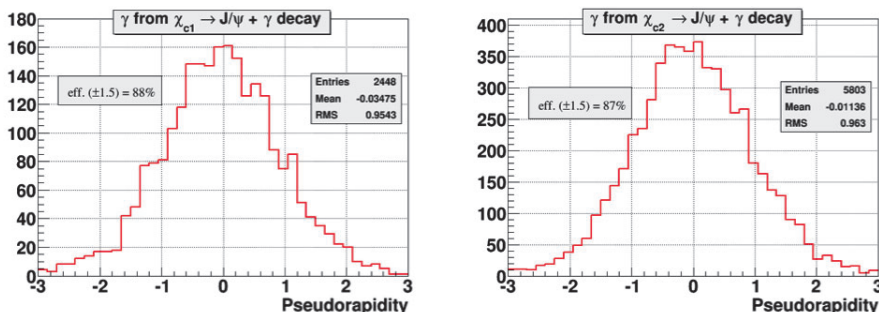


Figure 2 – Pseudorapidity distributions of the photons from charmonia decays: χ_{c1} (left), χ_{c2} (right).

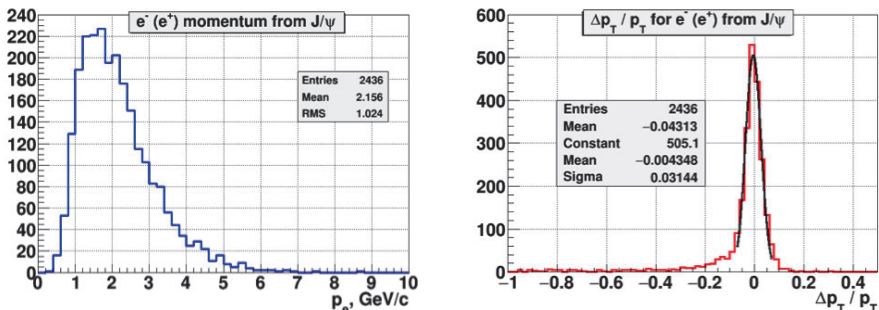


Figure 3 – Left: momentum spectrum of electrons and positrons with $|\eta| < 1.5$ from $J\psi$ decays; Right: $\Delta p_T / p_T$ distribution for decay products, where Δp_T is the difference between reconstructed and true transverse momentum.

3 Reconstruction of X(3872)

The exotic state X(3872) was simulated in PYTHIA8 under the assumption that it is a charmonium state and the branching ratio to $J\psi + \rho^0$ was taken to be 5%.⁷ As a result, the $e^+e^-\pi^+\pi^-$

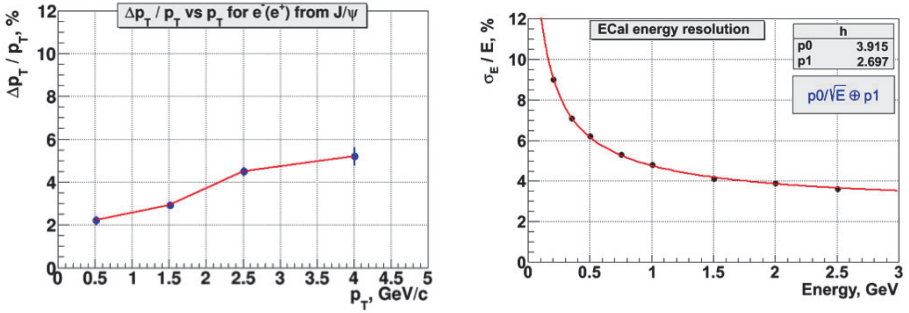


Figure 4 – Left: $\Delta p_T / p_T$ versus p_T for electrons and positrons with $|\eta| < 1.5$ from $J\psi$ decays; Right: energy resolution (σ_E/E) of the electromagnetic calorimeter for photons and electrons as a function of their energy.

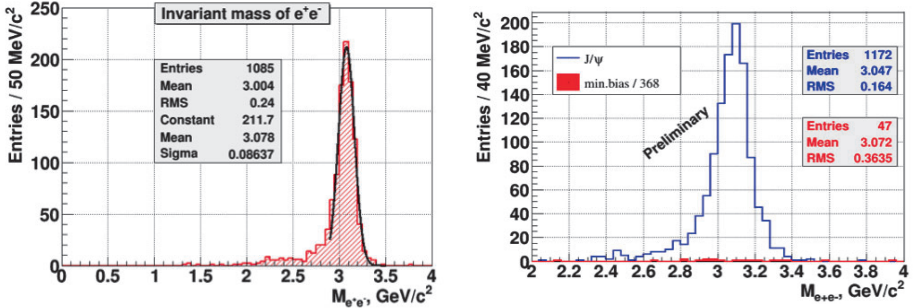


Figure 5 – Left: reconstructed invariant mass of electron-positron pairs from $J\psi$ decays (signal); Right: the same and minimum bias events (background), remaining after applying selection cuts (red). Note that only 1/368 part of all the minimum bias statistics was processed.

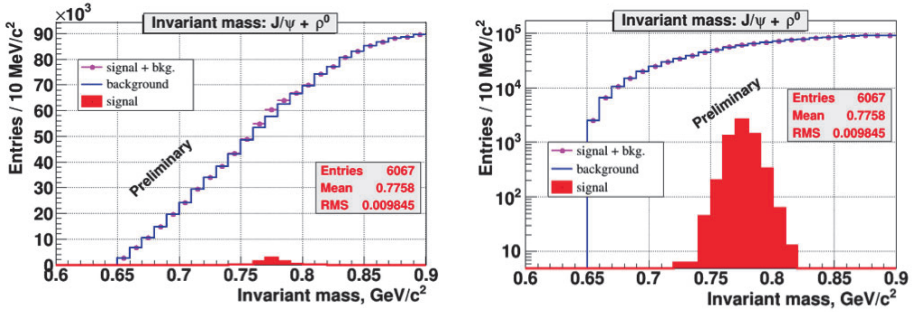


Figure 6 – Invariant mass combination $M_{e^+e^-\pi^+\pi^-} - M_{e^+e^-}$.

final state branching ratio $\sim 3 \times 10^{-3}$ gives the cross section for this channel of 12.2 pb or ~ 10 days of running time at the luminosity of $10^{32} \text{cm}^{-2} \text{s}^{-1}$ to produce ~ 1000 events. To better distinguish the signal peak from the background, it is better to use the invariant mass combination $M_{e^+e^-\pi^+\pi^-} - M_{e^+e^-}$ due to its smaller width (~ 10 MeV in our case as can be seen in Fig. 6). Figure 6 also shows the background from events with charmonia production. The plots correspond to statistics collected during 10 months at luminosity of $10^{32} \text{cm}^{-2} \text{s}^{-1}$. After fitting the background to the polynomial function using side bands of invariant mass distribution and sub-

tracting it from the original distribution it is possible to observe a clear peak from the X(3872) decay (Fig. 7). As an extension of this topic one can consider looking at other decay modes X(3872). Since the branching ratio of X(3872) to pairs of D-mesons is much higher (D^+D^- is $\sim 40\%$ and $D^{(0)}\bar{D}^{(*)0}$ is $\sim 55\%$), one should try to evaluate the possibility to reconstruct this state from hadronic decays of D-meson pairs. For such a study, the ability to tag the D-meson decays using the silicon microvertex detector should be very important. Thus, this physics topic becomes synergetic to the heavy ion charm program of NICA.

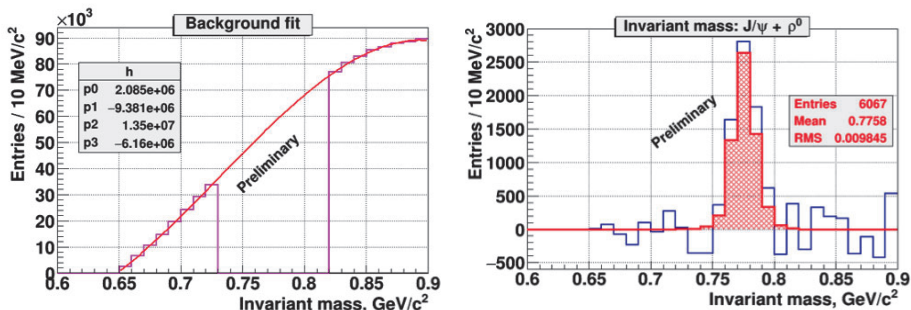


Figure 7 – Left: Background estimation using the polynomial fit of the side bands of Fig. 6 (left); Right: background - subtracted invariant mass combination from Fig. 6 (left) (blue line) and true X(3872) histogram (red line).

4 Conclusion

- Many observed states remain puzzling and can't be explained for many years. This stimulates and motivates for new searches and ideas to obtain the nature of multiquark states.
- Physics analysis for the proton-proton and proton-nuclear collisions is in progress nowadays. The preliminary results have been obtained.
- The experiments with pp and pA collisions can obtain some valuable information on charm production.
- Measurements of charmonium-like states are possible to consider as one of the “pillar” of pp and pA program.

References

1. N. Brambilla et al., European Physical Journal C 71:1534, (2011) 1 (World Scientific, Singapore, 1988).
2. C. Patrignani et al. (Particle Data Group), Chin. Phys. C, 40, 100001 (2016) and 2017 update
3. M.Yu. Barabanov, A.S. Vodopyanov, S.L. Olsen, Physics of Atomic Nuclei, V.77, N.1, (2014) 126
4. M.Yu. Barabanov, A.S. Vodopyanov, S.L. Olsen, A.I. Zinchenko, Physics of Atomic Nuclei, V.79, N 1 (2016) 126
5. http://nica.jinr.ru/files/NICA_CDR.pdf
6. <http://home.thep.lu.se/~torbjorn/Pythia.html/>
7. R. Aaij et al., LHCb Collaboration, Eur. Phys. J. C73, 2462 (2013)

TRANSPORT ANOMALIES NEAR THE QCD PHASE TRANSITION AT FINITE DENSITY

B.O. Kerbikov

A.I. Alikhanov Institute for Theoretical and Experimental Physics, Moscow 117218, Russia

Lebedev Physical Institute, Moscow 119991, Russia

Moscow Institute of Physics and Technology, Dolgoprudny 141700, Moscow Region, Russia

We show that at finite density pressure-pressure and current-current correlators exhibit divergences at T_c owing to the fluctuations of the diquark field. Specifically, this leads to a significant excess of the soft photon production rate near T_c .

A large body of experimental data on heavy ion collisions obtained at RHIC and LHC has lead to a revolutionary change in our view on the properties of QCD matter at finite temperature and density. These properties depend on the location of the system in the QCD phase diagram, i.e. on the values of the temperature and the chemical potential. At present the most intriguing is the regime of finite density and low or moderate temperature. On the theoretical side we understand much better what happens to quark-gluon matter at high temperature and zero or small μ since this domain of the phase diagram is accessible to lattice calculations. At nonzero density one has to resort to effective theories or models like NJL. At this point necessary to mention the new emerging approach to quark-gluon thermodynamic at finite density¹.

Our focus in the present talk is on the finite density pre-critical fluctuation region with $T \rightarrow T_c$ from above. Comprehensive study has shown that at high density and low temperature the ground state of QCD is color superconductor^{2,3}. We consider the 2SC color superconducting phase when u - and d - quarks participate in pairing but the density is not high enough to involve the heavier s - quark in pairing. The value of the quark chemical potential under consideration is $\mu \simeq 200$ -300 MeV and the critical temperature $T_c \simeq 40$ MeV. The corresponding density is two to three times the normal nuclear matter density. Both numbers should be considered as an educated guess since they rely on model calculations.

An important difference of color superconductor from the BCS one is that instead of an almost sharp border in BCS between the normal and superconducting phases the transition in color superconductor is significantly smeared⁴. The fluctuation contribution to the physical quantities is characterized by the Ginzburg-Levanyuk number Gi which for the quark matter can be estimated as⁴

$$Gi \simeq \frac{\delta T}{T_c} \simeq \left(\frac{T_c}{\mu} \right)^4 \lesssim 10^{-3}, \quad (1)$$

where δT is the width of the fluctuation region. Note that for BCS superconductor $Gi \sim 10^{-12}$ - 10^{-14} .

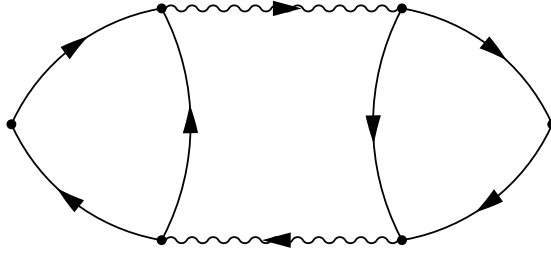


Figure 1 – Feynman diagram for the AL polarization operator.

We want to investigate the pressure and the electromagnetic response of the above fluctuation state, i.e. the temperature dependence of the energy-momentum and current-current correlators. It is known that these correlators, or the related response operators, can be evaluated only in perturbation theory. The related physical observables are: (i) bulk viscosity and sound attenuation, (ii) electrical conductivity and soft photon emissivity. It will be conjectured that these observables diverge at $T \rightarrow T_c$ as $(T - T_c)^{-3/2}$ for (i) and as $(T - T_c)^{-1/2}$ for (ii).

The dynamical origin of fluctuations is the soft mode of the diquark field. In the vicinity of T_c non-equilibrium quark pairs are formed with the characteristic Ginzburg-Landau life time $\tau_{GL} \sim (T - T_c)^{-1}$. Precursor pair fluctuations above T_c give the dominant contribution to the quark transport coefficients. The leading diagram defining the retarded response operator is the Aslamazov-Larkin (AL) ^{5,6} one shown in Fig.1. It includes two singular at T_c fluctuation propagators (FP) of the diquark field depicted by wavy lines. The solid lines are quark Matsubara propagators, the in- and out- vertices stand for quark-phonon and quark-photon interactions. Quark pairs formation like Cooper pairs formation is a non-perturbative process. In this sense the AL diagram is a non-perturbative one.

Relativistic FP has been evaluated using either Dyson equation ⁷, or time-dependent Landau-Ginzburg equation with stochastic Langevin forces ⁸. It reads

$$L(\mathbf{k}, \omega) = -\frac{1}{\nu \varepsilon + \frac{\pi}{8T_c} (-i\omega + D\mathbf{k}^2)}. \quad (2)$$

Here $\nu = \frac{p_0 \mu}{2\pi^2}$ is relativistic density of states at the Fermi surface with p_0 being the Fermi momentum, $\varepsilon = (T - T_c)T_c^{-1}$, D is the diffusion coefficient. The two FP-s entering into the AL diagram lead to the divergence of the transport coefficients at $T \rightarrow T_c$.

The finite-temperature retarded response function can be symbolically written as ^{7,8}

$$\Pi = -4Q^2 T \sum \int BLBL, \quad (3)$$

where summation goes over the internal Matsubara frequencies and integration is over the internal momenta. The coupling is $Q^2 = \frac{5}{9}e^2$ for the electromagnetic mode with two flavors and $Q^2 = g^2$ for the sound mode. The FP L is defined by (2), $B \sim GGG$ is the block of three Matsubara propagators shown in Fig.1. Different character of coupling of the two modes (vector and scalar) induces important difference into the factors B . To get nonzero B_s for the sound mode one has to take into account the energy dependence of the density of states at the Fermi surface and to introduce the ultraviolet cutoff Λ so that $B_s \sim \log(\Lambda/2\pi T_c)$ ^{5,8,9}. Keeping only linear in the external frequency ω terms one arrives at

$$\Pi_{em} = -i\omega \frac{B_{em}}{12\nu^2} \int \frac{d\mathbf{q}}{(2\pi)^3} \frac{\mathbf{q}^2}{(\varepsilon + \frac{\pi}{8T_c} D\mathbf{q}^2)^3} \quad (4)$$

$$\Pi_s = -i\omega \frac{B_s}{\nu^2} \int \frac{d\mathbf{q}}{(2\pi)^3} \frac{1}{\left(\varepsilon + \frac{\pi}{8T_c} D\mathbf{q}^2\right)^3} \quad (5)$$

For the electrical conductivity σ and the sound attenuation coefficient γ this yields

$$\sigma = -\frac{1}{\omega} \text{Im} \Pi_{em} = \frac{e^2}{16} \left(\frac{\pi D}{8T_c}\right)^{-1/2} \left(\frac{T-T_c}{T_c}\right)^{-1/2}, \quad (6)$$

$$\gamma = \omega^2 g^2 A \log^2 \frac{\Lambda}{2\pi T_c} \left(\frac{T-T_c}{T_c}\right)^{-3/2}, \quad (7)$$

where $A = m^2(2p_0)^{-4}\kappa^{-3}$, $\kappa^2 = \frac{\pi D}{8T_c}$. The sound attenuation per wavelength is $\alpha = \gamma\lambda \sim \omega\varepsilon^{-3/2}$. The rise of the acoustic attenuation near T_c results in strongly divergent bulk viscosity $\zeta(T) \sim \varepsilon^{-3/2}$. This temperature dependence is rather close to the scaling law $\zeta \sim \xi^{z-\alpha/\nu}$ ^{10,11}, where ξ is the correlation length, $z \simeq 3$ is the dynamical critical exponent, $\nu \simeq 0.6$ is the correlation length critical exponent, $\alpha \simeq 0.11$ is the critical exponent of the heat capacity.

Along with the electromagnetic conductivity the current-current correlator gives rise to the photon emissivity which is expressed through the imaginary part of the retarded photon self-energy as¹²

$$\omega \frac{dR}{d^3p} = -\frac{2}{(2\pi)^3} \text{Im} \Pi_{em} \frac{1}{e^{\omega/T} - 1}, \quad (8)$$

where Π_{em} is given by the diagram shown in Fig.1. This diagram defines the electrical conductivity and the photon emissivity to the order α in the electromagnetic sector and non-perturbatively in strong interactions since pair formation in the vicinity of the Fermi surface is not calculable in perturbation theory. Comparing (6) and (8) we find

$$\lim_{\omega \rightarrow 0} \omega \frac{dR}{d^3p} = \frac{1}{4\pi^3} T\sigma. \quad (9)$$

As an illustration we present a numerical estimate of the photon emissivity. We take $T_c = 40$ MeV and $Gi \simeq \varepsilon = 10^{-3}$. Note that the linear fluctuation theory breaks down at some small value of ε which is difficult to estimate. We also need the diffusion coefficient equal to $D = \frac{1}{3}v^2\tau \simeq 0.17$ fm under the assumption $v = 1$, $\tau = 0.5$ fm.

With the above set of parameters we obtain

$$\sigma \simeq 0.18 \text{ fm}^{-1}, \quad \lim_{\omega \rightarrow 0} \omega \frac{dR}{d^3p} \simeq 0.73 \cdot 10^{-2} \text{ fm}^{-4} \text{ GeV}^{-2}. \quad (10)$$

According to (6) and (9) the soft photon production is enhanced in the vicinity of T_c which may be a tentative suggestion for the FAIR/NICA investigation.

Acknowledgments

This work has been supported by a grant from the RFBR number 18-02-40054. The author's participation in Rencontres de Moriond QCD 2019 Conference was a part of MIPT "5-100" Program.

References

1. M.A. Andreichikov, M.S. Lukashov, and Yu.A. Simonov, *Int. J. Mod. Phys. A* **33**, 1850043 (2018).
2. M.G. Alford, K. Rajagopal, T. Schafer, A. Schmitt, *Rev. Mod. Phys.* **80**, 1455 (2008).
3. M. Buballa, *Phys. Rept.* **407**, 205 (2005).

4. B.O. Kerbikov and E.V. Lushevskaya, *Phys. Atom. Nucl.* **71**, 364 (2008).
5. L.G. Aslamazov and A.I. Larkin, *Sov. Phys. Solid State* **10**, 875 (1968).
6. A.I. Larkin and A.A. Varlamov, *Theory of Fluctuations in Superconductors* (Clarendon Press, Oxford, 2005).
7. B.O. Kerbikov and M.A. Andreichikov, *Phys. Rev. D* **91**, 074010 (2015).
8. B.O. Kerbikov and M.S. Lukashov, *Mod. Phys. Lett. A* **31**, 1650179 (2016).
9. L.G. Aslamazov and A.A. Varlamov, *Sov. Phys. JETP* **50**, 1164 (1979).
10. G.D. Moore and O. Saremi, *JHEP* **0809**, 015 (2008).
11. N.G. Antoniou, F.K. Diakonou, and A.S. Kapoyannis, *Nucl. Phys. A* **967**, 816 (2017).
12. J. Kapusta, P. Lichard, and D. Seibert, *Phys. Rev. D* **44**, 2774 (1991).

RADIATIVE QUARK p_{\perp} -BROADENING IN A QUARK-GLUON PLASMA AT RHIC AND LHC ENERGIES

B.G. ZAKHAROV

*L.D. Landau Institute for Theoretical Physics, GSP-1, 117940,
Kosygina Str. 2, 117334 Moscow, Russia*

We study the radiative correction to p_{\perp} -broadening of a fast quark in a quark-gluon plasma beyond the soft gluon approximation. We find that the radiative contribution to quark $\langle p_{\perp}^2 \rangle$ for RHIC and LHC conditions is negative.

1. Parton transverse momentum broadening in a quark-gluon plasma (QGP) is usually characterized by the transport coefficient \hat{q} ¹: the mean squared transverse momentum of a fast parton passing through a uniform QGP of thickness L is $\langle p_{\perp}^2 \rangle = \hat{q}L$. This is a leading order formula which includes only p_{\perp} -broadening due to multiple scattering on the QGP constituents. The radiative processes can give an additional contribution to p_{\perp} -broadening. In the soft gluon approximation the radiative contribution to $\langle p_{\perp}^2 \rangle$ has been addressed in^{2,3,4}. In³ it has been shown that radiative p_{\perp} -broadening is dominated by the double logarithmic contribution with $\langle p_{\perp}^2 \rangle_{rad} \sim \frac{\alpha_s N_c \hat{q} L}{\pi} \ln^2(L/l_0)$ (where l_0 is about the QGP Debye radius), and may be rather large.

In this talk we consider radiative p_{\perp} -broadening beyond the soft gluon and logarithmic approximations. The analysis is based on the light-cone path integral (LCPI)^{5,6,7} approach. In the LCPI diagram technique of⁶ the spectrum of a $a \rightarrow bc$ process in the Feynman variable x and the transverse momentum of particle b is described by the diagram Fig. 1a. For analysis of radiative p_{\perp} -broadening when $a = b$ one should also account for the virtual process $a \rightarrow bc \rightarrow a$ described by the diagram Fig. 1b. We perform calculations for $q \rightarrow qq$ process, i.e., for $a = b = q$ and $c = g$.

2. We consider a fast quark with energy E produced at $z = 0$ (we choose the z -axis along the initial quark momentum) traversing a uniform medium of thickness L . We neglect collisional energy loss (which is relatively small⁸), then the energy of the final quark without gluon emission equals E , for the two-parton final state the total energy also equals E . However, medium modifies the relative fraction of the one-parton state and its transverse momentum distribution, and for the two-parton channel medium modifies both the x and the transverse momentum distributions.

In the approximation of single gluon emission the radiative contribution to $\langle p_{\perp}^2 \rangle$ reads

$$\langle p_{\perp}^2 \rangle_{rad} = \int dx_q d\mathbf{p}_{\perp} \mathbf{p}_{\perp}^2 \left[\frac{dP}{dx_q d\mathbf{p}_{\perp}} + \frac{d\tilde{P}}{dx_q d\mathbf{p}_{\perp}} \right], \quad (1)$$

where $\frac{dP}{dx_q d\mathbf{p}_{\perp}}$ is the distribution for real splitting $q \rightarrow qq$ in the transverse momentum of the final quark and its fractional longitudinal momentum x_q (it corresponds to diagram Fig. 1a), $\frac{d\tilde{P}}{dx_q d\mathbf{p}_{\perp}}$ is the distribution for the virtual process $q \rightarrow qq \rightarrow q$ (it corresponds to diagram Fig. 1b). In the latter case x_q means the quark fractional momentum in the intermediate qq system, but \mathbf{p}_{\perp} , as

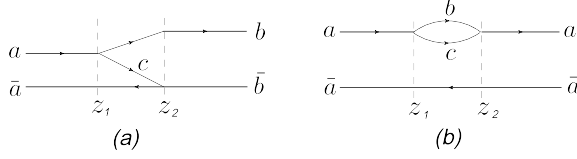


Figure 1 – Diagrammatic representation of $dP/dx_b d\mathbf{p}_\perp$ ($a \rightarrow bc$ process) (a) and of its virtual counterpart $d\tilde{P}/dx_b d\mathbf{p}_\perp$ ($a \rightarrow bc \rightarrow a$ process) (b). There are more two graphs with interexchange of vertices between the upper and lower lines.

for the real process, corresponds to the final quark. The x_q -integration in (1) can equivalently be written in terms of the gluon fractional momentum $x_g = 1 - x_q$.

Let us consider the real splitting. The distribution in the transverse momentum and the longitudinal fractional momentum of the particle b for $a \rightarrow bc$ transition corresponding to the graph of Fig. 1a has the form⁶

$$\frac{dP}{dx_b d\mathbf{p}_\perp} = \frac{1}{(2\pi)^2} \int d\boldsymbol{\tau}_f \exp(-i\mathbf{p}_\perp \boldsymbol{\tau}_f) F(\boldsymbol{\tau}_f), \quad (2)$$

where

$$F(\boldsymbol{\tau}_f) = 2\text{Re} \int_0^\infty dz_1 \int_{z_1}^\infty dz_2 \Phi_f(\boldsymbol{\tau}_f, z_2) \hat{g} K(\boldsymbol{\rho}_2, z_2 | \boldsymbol{\rho}_1, z_1) \Phi_i(\boldsymbol{\tau}_i, z_1) \Big|_{\boldsymbol{\rho}_2 = \boldsymbol{\tau}_f, \boldsymbol{\rho}_1 = 0}, \quad (3)$$

$$\Phi_i(\boldsymbol{\tau}_i, z_1) = \exp \left[-\frac{\sigma_{a\bar{a}}(\boldsymbol{\tau}_i)}{2} \int_0^{z_1} dz n(z) \right], \quad \Phi_f(\boldsymbol{\tau}_f, z_2) = \exp \left[-\frac{\sigma_{b\bar{b}}(\boldsymbol{\tau}_f)}{2} \int_{z_2}^\infty dz n(z) \right], \quad (4)$$

$\boldsymbol{\tau}_i = x_b \boldsymbol{\tau}_f$, $n(z)$ is the number density of the medium, $\sigma_{a\bar{a}}$ and $\sigma_{b\bar{b}}$ are the dipole cross sections for the $a\bar{a}$ and $b\bar{b}$ pairs, \hat{g} is the vertex operator, K is the Green function for the Hamiltonian

$$H = \frac{\mathbf{q}^2 + \epsilon^2}{2M} - \frac{in(z)\sigma_{\bar{a}bc}(\boldsymbol{\tau}_i, \boldsymbol{\rho})}{2}, \quad (5)$$

where $\mathbf{q} = -i\partial/\partial\boldsymbol{\rho}$, $M = E_a x_b x_c$, $\epsilon^2 = m_b^2 x_c + m_c^2 x_b - m_a^2 x_b x_c$ with $x_c = 1 - x_b$, and $\sigma_{\bar{a}bc}$ is the cross section for the three-body $\bar{a}bc$ system. The relative transverse parton positions for the $\bar{a}bc$ state read: $\boldsymbol{\rho}_{b\bar{a}} = \boldsymbol{\tau}_i + x_c \boldsymbol{\rho}$, $\boldsymbol{\rho}_{c\bar{a}} = \boldsymbol{\tau}_i - x_b \boldsymbol{\rho}$. The vertex operator in (3) is

$$\hat{g} = \frac{\alpha_s P_a^b(x_b) g(z_1) g(z_2)}{2M^2} \frac{\partial}{\partial \boldsymbol{\rho}_1} \cdot \frac{\partial}{\partial \boldsymbol{\rho}_2}, \quad (6)$$

where $P_a^b(x_b)$ is the $a \rightarrow b$ splitting function. Because the z -integrations in (3) extend up to infinity, and the adiabatically vanishing at $z \rightarrow \infty$ coupling $g(z)$ should be used. The three-body cross section can be written via the dipole cross section $\sigma_{q\bar{q}}$ of the $q\bar{q}$ system. We will use the quadratic approximation $\sigma_{q\bar{q}}(\boldsymbol{\rho}) = C\rho^2$ with $C = \hat{q}/2n$. In this case the Hamiltonian (5) takes the oscillator form, and one can use analytical formula for the Green function.

To separate in (3) the contribution of the vacuum decay it is convenient to write the product $\Phi_f(\boldsymbol{\tau}_f, z_2) \hat{g} K(\boldsymbol{\rho}_2, z_2 | \boldsymbol{\rho}_1, z_1) \Phi_i(\boldsymbol{\tau}_i, z_1)$ in the integrand on the right-hand side of (3) as (we denote $\hat{g}K$ as \mathcal{K} and omit arguments for notational simplicity)

$$\Phi_f \mathcal{K} \Phi_i = \Phi_f (\mathcal{K} - \mathcal{K}_0) \Phi_i + (\Phi_f - 1) \mathcal{K}_0 \Phi_i + \mathcal{K}_0 (\Phi_i - 1) + \mathcal{K}_0, \quad (7)$$

where $\mathcal{K}_0 = \hat{g}K_0$, and K_0 is the vacuum Green function. The last term \mathcal{K}_0 in (7) can be omitted because it does not contain medium effects.

The $\langle p_\perp^2 \rangle_{rad}$ given by (1) may be written via the Laplacian ∇^2 at $\boldsymbol{\tau}_f = 0$ of the function F and its counterpart \tilde{F} for the virtual diagram Fig. 1b. The result reads

$$\langle p_\perp^2 \rangle_{rad} = I_1 + I_2 + I_3, \quad (8)$$

$$I_1 = 2\text{Re} \int dx_q \int_0^L dz_1 \int_0^\infty d\Delta z \nabla^2 [(\mathcal{K} - \mathcal{K}_0) - (\tilde{\mathcal{K}} - \tilde{\mathcal{K}}_0)], \quad (9)$$

$$\begin{aligned} I_2 &= 2\text{Re} \int dx_q \int_0^L dz_1 \int_0^\infty d\Delta z [(\mathcal{K} - \mathcal{K}_0) \nabla^2 \Phi_i - (\tilde{\mathcal{K}} - \tilde{\mathcal{K}}_0) \nabla^2 \tilde{\Phi}_i] \\ &= -2\langle p_\perp^2 \rangle_0 \text{Re} \int dx_q f(x_q) \int_0^L dz_1 \frac{z_1}{L} \int_0^\infty d\Delta z (\mathcal{K} - \mathcal{K}_0), \end{aligned} \quad (10)$$

$$\begin{aligned} I_3 &= 2\text{Re} \int dx_q \int_0^\infty dz_1 \int_0^\infty d\Delta z [\mathcal{K}_0 \nabla^2 \Phi_i - \tilde{\mathcal{K}}_0 \nabla^2 \tilde{\Phi}_i] \\ &= -2\text{Re} \int dx_q f(x_q) \int_0^\infty dz_1 \int_0^\infty d\Delta z \mathcal{K}_0 \nabla^2 \tilde{\Phi}_i \end{aligned} \quad (11)$$

with $f(x_q) = 1 - x_q^2$, and $\Delta z = z_2 - z_1$. In (9)–(11) all functions in the integrands should be calculated at $\tau_f = 0$ (as in (7), we omit arguments for simplicity). In (10), (11) we used that at $\tau_f = 0$ $\mathcal{K} = \tilde{\mathcal{K}}$, $\mathcal{K}_0 = \tilde{\mathcal{K}}_0$, $\nabla^2 \Phi_i = x_q^2 \nabla^2 \tilde{\Phi}_i$, and $\nabla^2 \tilde{\Phi}_i$ equals $-\langle p_\perp^2 \rangle_0 z_1 / L$, where $\langle p_\perp^2 \rangle_0$ corresponds to nonradiative p_\perp -broadening. The integration over z_1 in (11) is unconstrained, and should be performed for an adiabatically vanishing coupling $g(z)$ in (6). We use $g(z) \propto \exp(-\delta z)$. Taking the limit $\delta \rightarrow 0$ after calculations for a finite δ we obtain for I_3

$$I_3 = -\langle p_\perp^2 \rangle_0 \int dx_q f(x_q) \frac{dP_0}{dx_q}, \quad (12)$$

where

$$\frac{dP_0}{dx_q} = \int d\mathbf{p}_\perp \frac{dP_0}{dx_q d\mathbf{p}_\perp} \quad (13)$$

is the \mathbf{p}_\perp -integrated vacuum spectrum. The \mathbf{p}_\perp -integral in (13) is logarithmically divergent. This occurs because we work in the small angle approximation⁶, which ignores the kinematic limits. We regulate (13) by restricting the integration region to $p_\perp < p_\perp^{max} = E \min(x_q, (1 - x_q))$.

The Δz -integral in (9) is also logarithmically divergent, because the integrand is $\propto 1/\Delta z$ as $\Delta z \rightarrow 0$. It is reasonable to regulate the Δz -integral in (9) by using the lower limit $\Delta z \sim 1/m_D$. This prescription has been used in³ for calculation in the logarithmic approximation of the contribution corresponding to our I_1 (9). The contributions from I_2 and I_3 terms have not been included in³.

3. In numerical calculations we use the quasiparticle masses $m_q = 300$ and $m_g = 400$ MeV⁹, that have been used in our previous analyses^{10,11} of the RHIC and LHC data on the nuclear modification factor R_{AA} . The calculations of^{10,11} have been performed for a more sophisticated model with running α_s for the QGP with Bjorken's longitudinal expansion, which corresponds to $\hat{q} \propto 1/\tau$. In the present work, as in³, we use constant \hat{q} and α_s . To make our estimates more realistic we adjusted \hat{q} to reproduce the quark energy loss ΔE for running α_s in the model of¹¹ with the Debye mass from the lattice calculations¹². We obtained $\hat{q} \approx 0.12$ GeV³ at $E = 30$ GeV for Au+Au collisions at $\sqrt{s} = 0.2$ TeV and $\hat{q} \approx 0.14$ GeV³ at $E = 100$ GeV for Pb+Pb collisions at $\sqrt{s} = 2.76$ TeV. As in³, we take $\alpha_s = 1/3$ and $L = 5$ fm.

We have taken into account that the transport coefficient that describes the Glauber factors Φ_i and $\tilde{\Phi}_i$ in the formulas for $I_{2,3}$ may differ from \hat{q} that controls the Green functions in $I_{1,2}$. For the Glauber factors \hat{q} should be calculated at the energy of the initial quark E , but for the Green functions it is reasonable to use the transport coefficient at the typical energy of the radiated gluon $\bar{\omega}$. The above adjusted values of \hat{q} correspond just to the transport coefficients for gluons with energy $\sim \bar{\omega}$. We denote the transport coefficient for the Glauber factors \hat{q}' . Since $E \gg \bar{\omega}$, the ratio $r = \hat{q}'/\hat{q}$ may differ significantly from unity. Using the Debye mass from¹² and running α_s parametrized as in our previous jet quenching analysis¹¹ we obtained $r \approx 1.94(2.13)$ at $E = 30(100)$ GeV for quark jets for RHIC(LHC) conditions.

In numerical calculations in (9)–(11) we integrate over x_q from $x_q^{min} = m_q/E$ to $x_q^{max} = 1 - m_q/E$. As in ³, for the cutoff in the Δz -integration we use $\Delta z_{min} = 1/m$ with $m = 300$ MeV. With these parameters we obtained at $E = 30$ GeV for the RHIC conditions

$$[I_1, I_2, I_3]/\langle p_{\perp}^2 \rangle_0 \approx [0.417/r, -0.213, -0.601], \quad (14)$$

and at $E = 100$ GeV for the LHC conditions

$$[I_1, I_2, I_3]/\langle p_{\perp}^2 \rangle_0 \approx [0.823/r, -0.107, -0.908]. \quad (15)$$

From (8), (14) and (15) for our RHIC(LHC) versions we obtain

$$\langle p_{\perp}^2 \rangle_{rad}/\langle p_{\perp}^2 \rangle_0 \approx -0.598(-0.629), \quad r = 1.94(2.13). \quad (16)$$

And if we take $r = 1$

$$\langle p_{\perp}^2 \rangle_{rad}/\langle p_{\perp}^2 \rangle_0 \approx -0.397(-0.192), \quad r = 1(1). \quad (17)$$

Thus, in all the cases the radiative contribution is negative. We have checked that under variations of parton masses by a factor of ~ 2 the value of $\langle p_{\perp}^2 \rangle_{rad}$ remains negative. Our predictions differ drastically from $\langle p_{\perp}^2 \rangle_{rad} \approx 0.75\hat{q}L$ obtained in ³. The negative values of $\langle p_{\perp}^2 \rangle_{rad}$ in our calculations are due to large negative values of $I_{2,3}$. Since these terms have not been accounted for in ³, it is interesting to compare prediction of ³ with our results for I_1 term alone. From (14) and (15) one can see that our $\langle p_{\perp}^2 \rangle_{rad}|_{I_1}$ agrees qualitatively with $\langle p_{\perp}^2 \rangle_{rad}$ from ³.

4. In summary, we have studied within the LCPI ^{5,6,7} approach the radiative contribution to p_{\perp} -broadening of fast quarks in the QGP. The analyses is performed beyond the soft gluon approximation. We have found that for RHIC and LHC conditions the radiative contribution to quark $\langle p_{\perp}^2 \rangle$ may be negative. This seems to be supported by the recent STAR measurement of the hadron-jet correlations ¹³, in which no evidence for large-angle jet scattering in the medium has been found.

Acknowledgments

This work was partly supported by the RFBR grant 18-02-40069mega.

References

1. R. Baier, Y.L. Dokshitzer, A.H. Mueller, S. Peigné and D. Schiff, Nucl. Phys. B**483**, 291 (1997) [hep-ph/9607355]; *ibid.* B**484**, 265 (1997) [hep-ph/9608322].
2. B. Wu, JHEP **1110**, 029 (2011) [arXiv:1102.0388].
3. T. Liou, A.H. Mueller and B. Wu, Nucl. Phys. A**916**, 102 (2013) [arXiv:1304.7677].
4. J.-P. Blaizot and Y. Mehtar-Tani, Nucl. Phys. A**929**, 202 (2014) [arXiv:1403.2323].
5. B.G. Zakharov, JETP Lett. **63**, 952 (1996) [hep-ph/9607440]; Phys. Atom. Nucl. **61**, 838 (1998) [hep-ph/9807540].
6. B.G. Zakharov, JETP Lett. **70**, 176 (1999) [hep-ph/9906536].
7. B.G. Zakharov, Nucl. Phys. Proc. Suppl. **146**, 151 (2005) [hep-ph/0412117].
8. B.G. Zakharov, JETP Lett. **86**, 444 (2007) [arXiv:0708.0816].
9. P. Lévai and U. Heinz, Phys. Rev. C**57**, 1879 (1998).
10. B.G. Zakharov, J. Phys. G**40**, 085003 (2013) [arXiv:1304.5742].
11. B.G. Zakharov, J. Phys. G**41**, 075008 (2014) [arXiv:1311.1159].
12. O. Kaczmarek and F. Zantow, Phys. Rev. D**71**, 114510 (2005) [hep-lat/0503017].
13. L. Adamczyk *et al.* [STAR Collaboration], Phys.Rev. C**96**, 024905 (2017) [arXiv:1702.01108].

Particle production in high energy p-p collisions

A.V.Koshelkin

General Physics Department, National Research Nuclear University, Kashirskoye shosse, 31, Moscow, Russia

Based on the compactification of the standard (3+1) chromodynamics into $QCD_{xy} + QCD_{zt}$, the rate of hadron production with respect to both the rapidity and p_T distributions is derived in the flux tube approach. In the case of the pion production in pp collisions we obtain good agreement to the experimental results on the pion yield with respect to both the rapidity and p_T distributions.

1 Introduction

The hadronization of the deconfined matter arising in high-energy particle collisions is an important problem in the physics of the strong interaction. It plays a key role in hadron productions in pp , pA and AA collisions. Such a problem is however an extremely complicate to be solved in the unified approach, starting from the fundamental theory of QCD. Therefore, various models have been developed to describe the hadronization of the deconfined matter which applicability essentially depends on the energies of colliding particles. One of them is the color flux tube approach we will follow in the present consideration.

2 Hadron production in high energy collisions in the flux tube approach

Then, the number of the hadrons generated in the unit volume of the momentum space, dN_h/d^3p , is determined by a formula

$$\frac{E(\mathbf{p})dN_h}{d^3p} = \sum_{a=1}^N \int \frac{d^3p_1 d^3p_2}{(2\pi)^6} \left\{ \varrho_a(\mathbf{p}, \mathbf{p}_1 - \mathbf{p}_2) \left\langle \left(\Psi_{q_a}^\dagger(\mathbf{p}_1) \Psi_{q_a}(\mathbf{p}_1) \right) \left(\Psi_{\bar{q}_a}^\dagger(\mathbf{p}_2) \Psi_{\bar{q}_a}(\mathbf{p}_2) \right) \right\rangle \right\}, \quad (1)$$

where $E(\mathbf{p}) = \sqrt{\mathbf{p}^2 + m_h^2}$ and $\mathbf{p} = \mathbf{p}_1 + \mathbf{p}_2$ are the energy and momentum of the on-shell hadron whose mass is m_h , $\Psi_{q_a, \bar{q}_a}(\mathbf{p}_i)$ is the wave function of quarks and antiquarks in the a -th flux tube, which momenta are \mathbf{p}_i . The function $\varrho_a(\mathbf{p}, \mathbf{p}_1 - \mathbf{p}_2)$ denotes the probability to create a hadron with the four-momentum $p = (E(\mathbf{p}), \mathbf{p})$, which is generally governed by the hadron-parton vertex, and is phenomenologically incorporated in the developed consideration. The index a numerates N equivalent non-interacting tubes, whereas the angle brackets means averaging with respect to the vacuum of partons which are bosonized in a hadron.

In terms of the rapidities y_i and transverse momenta $\mathbf{p}_{i\perp}$ of the mentioned particle Eq.(1) takes the following form

$$\frac{dN_h}{d^2p_T dy} = \sum_{a=1}^N \int \frac{d^2p_{1\perp} d^2p_{2\perp} dy_1 dy_2}{(2\pi)^6} m_q m_{\bar{q}} \cosh y_1 \cosh y_2 \left\{ \varrho_a(\mathbf{p}_T, y; \mathbf{p}_{1\perp} - \mathbf{p}_{2\perp}, y_2 - y_1) \right. \\ \left. \left\langle \left(\Psi_{q_a}^\dagger(\mathbf{p}_{1\perp}, y_1) \Psi_{q_a}(\mathbf{p}_{1\perp}, y_1) \right) \left(\Psi_{\bar{q}_a}^\dagger(\mathbf{p}_{2\perp}, y_2) \Psi_{\bar{q}_a}(\mathbf{p}_{2\perp}, y_2) \right) \right\rangle \right\}. \quad (2)$$

where

$$y = \frac{1}{2} \ln \left(\frac{E(\mathbf{p}) + p_z}{E(\mathbf{p}) - p_z} \right), \quad y_i = \frac{1}{2} \ln \left(\frac{\varepsilon_{q,\bar{q}}(\mathbf{p}_i) + p_{iz}}{\varepsilon_{q,\bar{q}}(\mathbf{p}_i) - p_{iz}} \right), \\ E(\mathbf{p}) = \sqrt{\mathbf{p}^2 + m_h^2}; \varepsilon_{q,\bar{q}}(\mathbf{p}_i) = \sqrt{m_{q,\bar{q}}^2 + p_{iz}^2} \quad (3)$$

where $\varepsilon_{q,\bar{q}}(\mathbf{p}_i)$ is the energy of a quark or antiquark with a mass $m_{q,\bar{q}}$ in the a -th tube.

We assume that the probability $\varrho(p, q)$ to create an on-shell hadron is governed by the equilibrium phase transition of the first kind, whereas quarks and antiquarks are massless. Then, we have

$$\varrho_a(\mathbf{p}_T, y; \mathbf{p}_{1\perp} - \mathbf{p}_{2\perp}, y_2 - y_1) = A \exp \left(-\frac{E_T}{T} \right) \delta(y - y_c) \delta(y_2 - y_1), \quad (4)$$

where E_T is the transverse energy of a hadron, $y_c = (y_2 + y_1)/2$.

In the concept of the longitudinal dominance and transverse confinement the Ψ -functions in Eq.(2) appear to be factorized with respect to $\mathbf{p}_{i\perp}$ and y_i . In this way, according to the compactified (1 + 1) QCD¹ the transverse motion of a quark is governed by an equation

$$(p_1 + ip_2) \Psi_+(\mathbf{r}_\perp) = (m(\mathbf{r}_\perp) + E_\nu^2) \Psi_-(\mathbf{r}_\perp), \\ (p_1 - ip_2) \Psi_-(\mathbf{r}_\perp) = (E_\nu^2 - m(\mathbf{r}_\perp)) \Psi_+(\mathbf{r}_\perp), \quad (5)$$

where E_ν^2 is the energy related to the transverse motion, \mathbf{r}_\perp is a radius-vector in the plane being orthogonal to the z -axis; $m(\mathbf{r}_\perp)$ is the transverse confinement potential, whereas

$$p_1 \mp ip_2 = e^{\mp i\varphi} \left(i \frac{d}{dr_\perp} \pm \frac{1}{r_\perp} \frac{d}{d\varphi} \right), \quad (6)$$

where r_\perp and φ are the polar radius and azimuth angle.

As for the longitudinal motion of quarks it is controlled the by the (1 + 1) Dirac equation¹ which is reduced to the corresponding Klein- Gordon equation

$$\partial_z^2 \psi(t, z) - \partial_t^2 \psi(t, z) = m_{qT}^2 \psi(t, z), \quad (7)$$

where m_{qT} is the effective mass of a quark.

In the massless case the solutions (7) take a form

$$\psi_\pm(\tau, \eta) = \frac{1}{\sqrt{\sigma\pi^{1/2}}} \exp \left(-\frac{(\eta \mp \ln(\tau/\tau_0))^2}{2\sigma^2} \right), \quad (8)$$

where σ is some constant.

We should note here that in the Lund fragmentation mode², we will follow below, the kinematic rapidity η coincides with the pion rapidity $y = 1/2 \ln(p_+/p_-)$, whereas τ is proportional to the invariant mass M of a quark-antiquark pair^{2,3}.

Due to the longitudinal dominance the integration over the transverse variables is found to be independent on rapidities in Eqs.(2), (4), and to lead to some constant Σ_a in each flux tube. As a result, we derive from Eq.(2), taking into account Eq.(4)

$$\frac{dN_h}{dyd^2p_\perp} = \frac{N_f N_c^2 \theta(T_c - T)}{512\pi^8 m_h T K_1(m_h/T)} \exp\left(-\frac{E_T}{T}\right) \sum_{a=1}^N \sum_{\xi=\pm} \frac{\Sigma_a^2}{\sigma_a^2} \exp\left(-\frac{2(y - \xi \cdot y_a)^2}{\sigma_a^2}\right). \quad (9)$$

where m_h is a hadron mass, N_f and N_c are the numbers of flavors and colors, respectively. Two terms in last equation have arisen due to the quarks which move parallel to the line of particle collision into opposite directions with respect to the collision point in the LUND model².

Integrating Eq.(9) over the transverse momenta, we go the rapidity distribution

$$\frac{dN_h}{dy} = \frac{N_f N_c^2 \theta(T_c - T)(1 + (T/m_h))}{256\pi^7 K_1(m_h/T) \exp(m_h/T)} \sum_{a=1}^N \sum_{\xi=\pm} \frac{\Sigma_a^2}{\sigma_a^2} \exp\left(-\frac{2(y - \xi \cdot y_a)^2}{\sigma_a^2}\right). \quad (10)$$

3 Relation to the experimental results

To compare with the experimental results⁴ we firstly need to specify the developed model. We assume that the flux tubes arisen in high energy pp collisions are equivalent. Taking $\Sigma_a = \Sigma$ and $\sigma_a = \sigma$, and rewriting Eqs.(9), (10) in terms of the pion multiplicity $\langle N_{ch}(s) \rangle$, we have

$$\frac{dN_h}{dyd^2p_\perp} = \frac{\langle N_{ch}(s) \rangle \exp(m_h/T)}{(2\pi)^{3/2} \sigma m_h T (1 + (T/m_h))} \exp\left(-\frac{E_T}{T}\right) \sum_{\xi=\pm} \exp\left(-\frac{2(y - \xi \cdot y_0)^2}{\sigma^2}\right). \quad (11)$$

$$\frac{dN_h}{dy} = \frac{\langle N_{ch}(s) \rangle}{(2\pi)^{1/2} \sigma} \left\{ \exp\left(-\frac{2(y - y_0)^2}{\sigma^2}\right) + \exp\left(-\frac{2(y + y_0)^2}{\sigma^2}\right) \right\}. \quad (12)$$

Then, setting $T = T_c = 160MeV$ and $m_\pi = 140MeV$ in Eqs.(11), (12), we obtain the p_T and rapidity distributions of pions which are presented in Fig.1,2.

References

1. A.V.Koshelkin, C.-Y.Wong, Phys. Rev. **D86** 125026 (2012).
2. B. Andersson, G. Gustafson, T. Sjöstrand, Zeit. für Phys. **C20**, 317 (1983); B. Andersson, G. Gustafson, G. Ingelman, T. Sjöstrand, Phys. Rep. **97**, 31 (1983).
3. C. Y. Wong, *Introduction to High-Energy Heavy-Ion Collisions*, World Scientific Publisher, 1994.
4. N.Abgrall et al, Eur.Phys.J. **C74**, 2794 (2014).

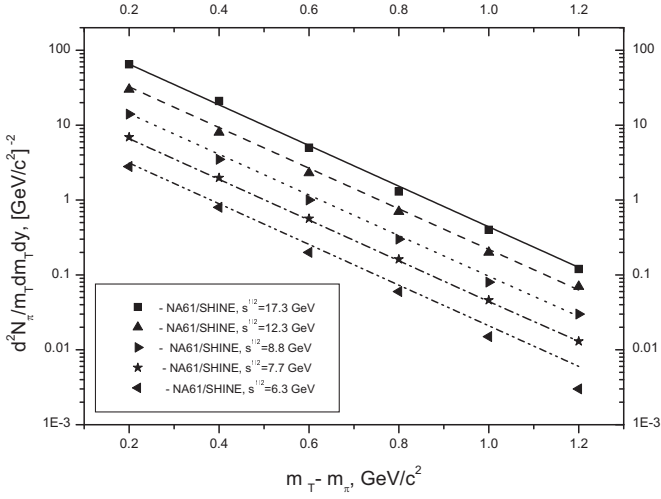


Figure 1 – The lines of various types are the p_T distributions of pions which are given by Eq.(11) at $T_c = 160MeV$ and $\kappa = 1GeV/F$, $y = 0$, which are normalized by the experimental value of the pion rate at $(m_T - m_\pi) = 0.2GeV/c$ v.s. the pion rate in $p - p$ collisions (the scattered symbols) at the same projectile energies, $m_T \equiv E_T$.

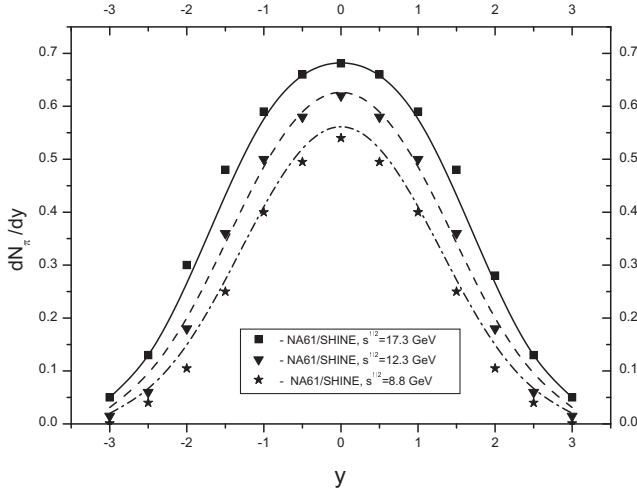
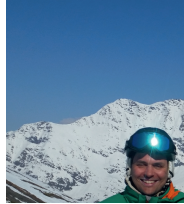


Figure 2 – The rapidity distributions given by Eq.(12) at $\sqrt{s} = 17,3GeV$ (solid lines), $\sqrt{s} = 12,3GeV$ (dashed line), $\sqrt{s} = 8,8GeV$ (dot-dashed line), and at $T_c = 160MeV$ v.s. the rapidity distributions in $p - p$ collisions.

Hadron interactions at ultra-high energies measured by the Pierre Auger Observatory

Ralf Ulrich for the Pierre Auger Collaboration

Institute for Nuclear Physics, Karlsruhe Institute of Technology, 76131 Karlsruhe, Germany



1 Introduction

The Pierre Auger Observatory, located in Malargüe, Argentina, has a surface area of about 3000 km² and provides the largest-ever instrumented area for the detection of individual particles. The observatory was built to reveal the nature and the sources of ultra-high energy cosmic ray particles with energies of up to a few 10²⁰ eV. Besides fundamental questions of cosmic ray astrophysics, the observatory is also sensitive to particle physics at very extreme energies – much beyond what even LHC can achieve.

2 The Pierre Auger Observatory

The Pierre Auger Observatory² is built of two main components: the surface detector array with about 1600 water-Cherenkov tanks distributed on a triangular grid with a spacing of 1.5 km, and 27 fluorescence telescopes² overlooking the huge ground array. In Fig. ??, a typical event and its reconstruction are illustrated.

The surface detector operates with a duty cycle of close to 100% and measures the footprint of air showers on ground level with water-Cherenkov tanks. These tanks are sensitive to electromagnetic particles and muons. The size of the shower signal at a distance of 1000 m from the shower core on the ground level, S_{1000} , is used to construct an estimator for the shower energy. The number of muons at the ground, N_μ , depends logarithmically on the cosmic ray primary mass. Currently, N_μ can only be indirectly inferred², furthermore, N_μ is the air shower observable with the largest modelling uncertainties².

The fluorescence detector can operate only in dark, clear and moonless nights. The duty cycle is, thus, on the order of 10%. The signal measured by the telescopes is directly proportional to the energy deposit, dE/dX , of the air shower in the atmosphere². The integral over the energy loss of an air shower corresponds to a calorimetric energy determination. The location of the shower maximum, X_{\max} , measured as atmospheric column density in units of g/cm², depends

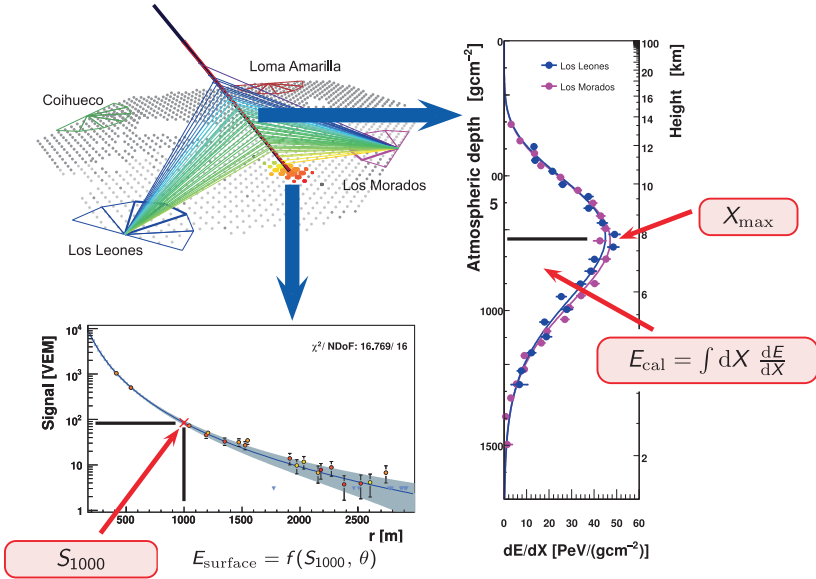


Figure 1 – View of one reconstructed stereo event of the Pierre Auger Observatory. Top left: each black marker is one active surface tank; the four telescope sites are at the border of the array; the air shower event is seen by the array and two telescopes; the colors from blue to red indicate time. Right side: the longitudinal energy deposit profiles. Bottom: the reconstructed lateral signal measured at ground level. The most important observables are introduced in red boxes.

logarithmically on the primary particle mass. It is interesting to note that X_{\max} is the air shower observable that can be measured and modelled with the smallest uncertainties.

3 Energy measurement, invisible energy and muons

Due to the enormous exposure, it is the surface array that can measure energy fluxes up to the very highest energies. The exact shape of the flux suppression above $10^{19.5}$ eV was determined to high precision with data of the surface detector².

It is one of the major advantages that the observable S_{1000} is experimentally cross-calibrated to the calorimetric energy scale of the fluorescence telescopes. Thus, for the determination of the primary cosmic ray energy, there remains only the correction for *invisible* energy, E_{inv} , which is the fraction of the energy that does not lead to the emission of fluorescence light. This happens in analogy to non-compensation in hadron calorimeters via the breakup of nuclei, production of neutrons, muons and neutrinos, etc. The determination of E_{inv} depends on air shower physics and in particular on the muon production, which is not very well understood. In Fig. ?? (left) the current discrepancy in describing the air shower muon data is illustrated.

Thus, the Pierre Auger Observatory has developed a method to estimate E_{inv} from the data itself. The approach relies on the phenomenological assumption that $E_{\text{inv}} \propto N_{\mu}$, which is shown in Fig. ?? (right). This is combined with the fact that $N_{\mu} \propto E^{\beta}$, with $\beta \approx 0.9$, and $E \propto S_{1000}$. Furthermore, there are first-order corrections for different shower geometries (zenith angles) as well as residual corrections of observed deviations between data and simulations². This approach does not rely on the absolute predictions of simulations and provides an estimate of

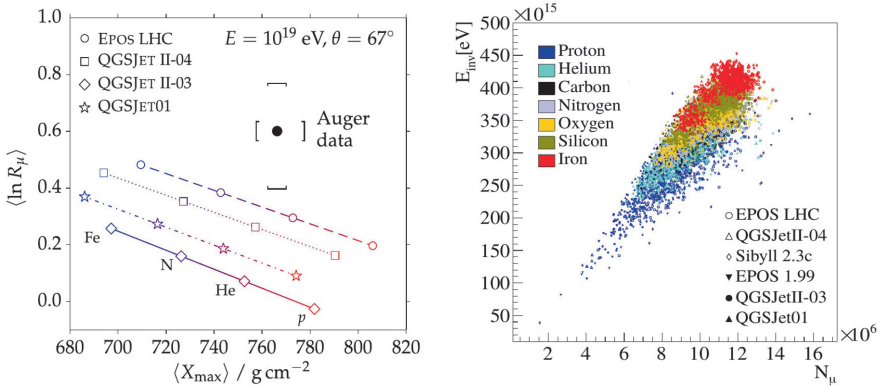


Figure 2 – Left panel: Combined measurement of the depth of the average shower maximum and the abundance of muons at ground level[?]. The data is not compatible with the simulations and cannot be made compatible either by changing the model, or by modifying the primary mass composition. Right panel: Correlation between E_{inv} and N_μ determined from simulations[?]. The predictions of many different primary mass particles are all lining up along one direction.

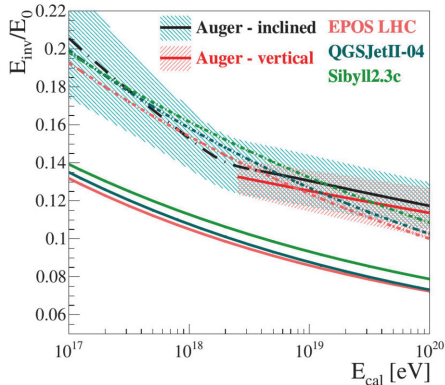


Figure 3 – The invisible energy as determined from data for vertical and inclined events with uncertainties compared to simulations with protons (bottom, solid) and iron (top, dashed) predictions[?].

E_{inv} that is based on data itself with much smaller uncertainties compared to purely simulation-based methods. The resulting E_{inv} is shown in Fig. ???. The data-driven results are shown with uncertainty bands. The data is also overlayed with predictions from simulations. The data is very compatible with the iron simulations over the whole energy interval, while the proton simulations are significantly lower. This is remarkable since there are indications that the primary mass composition in the energy range 10^{18} – $10^{18.5}$ eV is indeed dominated by protons[?].

4 Average longitudinal development

The average longitudinal air shower profiles are measured to very high precision[?] in two energy bins. The data, in general, is found to be well reproduced by a Gaisser-Hillas functional form. However, the parameters of the normal Gaisser-Hillas function (λ , X_0) are highly correlated. Thus, it is a better choice to introduce the following transformations, $X'_0 = X_0 - X_{\text{max}}$, $R = \sqrt{\lambda/|X'_0|}$ and $L = \sqrt{|X'_0|\lambda}$, in order to yield the uncorrelated parameters R and L [?].

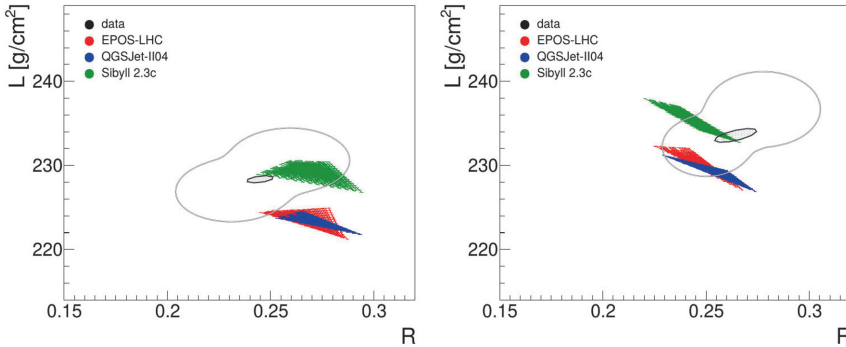


Figure 4 – Representation of the measured parameters of the shape of the average longitudinal profile at two different energies². Left panel: 10^{18} – $10^{18.2}$ eV, Right panel: $10^{18.8}$ – $10^{19.2}$ eV. The data is shown with confidence levels, while the simulations indicate the areas allowed by different mass composition mixtures.

The parameters R and L are determined from Auger data and compared to model predictions of all possible primary mass mixtures and several different interaction models in Fig. ???. The data is demonstrated to be sensitive to the primary mass as well as for testing hadronic interaction models². When the experimental uncertainties can be further improved, this will add another important experimental handle.

5 Conclusion

Some of the results of the Pierre Auger Observatory have been reviewed with a slight focus on air shower physics and hadronic interactions at ultra-high energies. Currently, one of the most puzzling observation yet to be explained in particle physics is the discrepancy in muon content of air showers on ground level with energies at and above 10^{19} eV.

References

1. A. Aab *et al.* [Pierre Auger Collaboration], Nucl. Instrum. Meth. A **798** (2015) 172 doi:10.1016/j.nima.2015.06.058, arXiv:1502.01323 [astro-ph.IM].
2. J. Abraham *et al.* [Pierre Auger Collaboration], Nucl. Instrum. Meth. A **620** (2010) 227 doi:10.1016/j.nima.2010.04.023, arXiv:0907.4282 [astro-ph.IM].
3. A. Aab *et al.* [Pierre Auger Collaboration], Phys. Rev. D **91** (2015) no.3, 032003 Erratum: [Phys. Rev. D **91** (2015) no.5, 059901] doi:10.1103/PhysRevD.91.059901, 10.1103/PhysRevD.91.032003, arXiv:1408.1421 [astro-ph.HE].
4. R. Ulrich, R. Engel and M. Unger, Phys. Rev. D **83** (2011) 054026 doi:10.1103/PhysRevD.83.054026, arXiv:1010.4310 [hep-ph].
5. M. Unger, B. R. Dawson, R. Engel, F. Schussler and R. Ulrich, Nucl. Instrum. Meth. A **588** (2008) 433 doi:10.1016/j.nima.2008.01.100, arXiv:0801.4309 [astro-ph].
6. J. Abraham *et al.* [Pierre Auger Collaboration], Phys. Rev. Lett. **101** (2008) 061101 doi:10.1103/PhysRevLett.101.061101, arXiv:0806.4302 [astro-ph].
7. Pierre Auger Collaboration, submitted to PRD (2019), arXiv:1901.08040 [astro-ph.HE].
8. A. Aab *et al.* [Pierre Auger Collaboration], Phys. Rev. D **96** (2017) no.12, 122003 doi:10.1103/PhysRevD.96.122003, arXiv:1710.07249 [astro-ph.HE].
9. A. Aab *et al.* [Pierre Auger Collaboration], JCAP **03** (2019) no.03, 018 doi:10.1088/1475-7516/2019/03/018, arXiv:1811.04660 [astro-ph.HE].
10. S. Andringa, R. Conceicao and M. Pimenta, Astropart. Phys. **34** (2011) 360. doi:10.1016/j.astropartphys.2010.10.002

6. Closing

6.1

Summaries

QCD AND HIGH ENERGY INTERACTIONS: EXPERIMENTAL SUMMARY

Vincenzo M. Vagnoni
*Istituto Nazionale di Fisica Nucleare, Sezione di Bologna,
via Irnerio 46, 40126 Bologna, Italy*



The conference included about 90 talks covering a plethora of different sectors, like Higgs physics, electroweak physics, top physics, BSM physics, soft QCD, jets, PDFs, heavy ions, heavy flavours, spectroscopy, etc. A few experimental results are here highlighted.

1 Introduction

The Standard Model of particle physics (SM) has been working beautifully, up to a few hundred GeV so far, yet we know that it must be an effective theory valid up to some energy scale. There are many compelling reasons to believe that the SM is an incomplete theory; we can mention the hierarchy problem, the lack of a dark matter candidate, the unification of gauge couplings, the need for new sources of CP violation to explain the dynamical generation of the baryon asymmetry in the universe, the reason for the existence of three generations of quarks and leptons, the origins of mass and CKM hierarchies, etc. The SM has proven to be very solid, well beyond any expectation, but we have powerful tools to go on with the investigations. For example, despite some operational issues, the LHC reached a performance record in 2018, with a peak luminosity steadily at about $2 \times 10^{34} \text{ cm}^{-2}\text{s}^{-2}$, that is two times larger than the design value.

2 Higgs physics

Although it seems with us since ages, we have not to forget that the discovery of the Higgs boson took place only seven years ago. Measurements of Higgs properties with increasing precision are now a formidable tool to look for new-physics manifestations. A framework for cross-section measurements with reduced model dependence targeting Higgs production, namely simplified template cross-sections (STXS), has been developed and deployed. Within this framework, Higgs production is split into the main production modes and further into fine-grain kinematic regions of phase space.

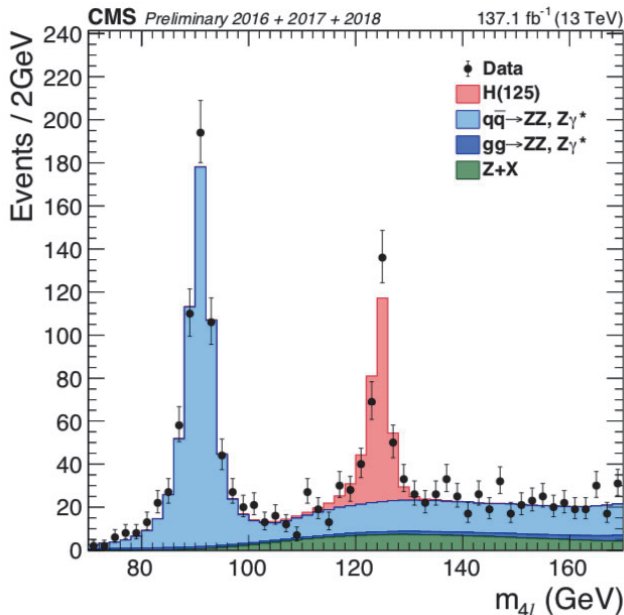


Figure 1 – Distribution of the reconstructed four-lepton invariant mass with 2018 data³.

The associated production of $H \rightarrow b\bar{b}$ and W or Z bosons decaying into leptons as a function of $p_T(W/Z)$ with STXS has been measured, using a data sample corresponding to 80 fb^{-1} at 13 TeV ¹. Cross-sections are used to constrain parameters in an effective Lagrangian framework. Another relevant measurement is that of the Higgs coupling to the top quark using $H \rightarrow \gamma\gamma$ decays. A simultaneous fit in seven signal-enriched event categories is performed, and $t\bar{t}H$ production is observed at 4.9σ , using 140 fb^{-1} of data at 13 TeV ².

Several new measurements in the four-lepton final state have been performed. All main production modes have been studied, *i.e.* ggH , vector-boson fusion, associated production of gauge bosons and $t\bar{t}H$. There is little sensitivity to $b\bar{b}H$ or tH , but these processes have been also considered explicitly. Differential cross-sections have been measured as a function of the Higgs p_T and y , the number of associated jets, and the p_T of the leading associated jet, using 137 fb^{-1} of data at 13 TeV ³. The distribution of the reconstructed four-lepton invariant mass with 2018 data is shown in Fig. 1.

With more and more statistics, searches for Higgs rare decays are becoming increasingly important. Exclusive decays of the Higgs boson to mesons, such as $H \rightarrow J/\psi J\psi$ or $\Upsilon\Upsilon$, recently measured using 37.5 fb^{-1} at 13 TeV ⁴, are interesting to study Yukawa couplings to quarks and for beyond-the-SM (BSM) searches. New physics could affect direct $Hq\bar{q}$ couplings or enter through loops, and modify interference patterns between the various amplitudes. However, SM predictions are very small and uncertain.

We have not yet found evidence for non-SM behaviour of the Higgs particle. But the transition from observation to detailed measurements has only started, and now also in the STXS framework with finer granularity to probe deviations from the SM. Several new Higgs results have been presented at winter conferences, many with partial Run-2 statistics and only a few with full Run-2 statistics. Significant improvements with the full set of analyses and the full Run-2 data set are anticipated.

3 Top physics

The LHC is also a powerful top factory. Top quarks are produced predominantly in pairs, with $\sigma(t\bar{t}) \simeq 0.8$ nb at 13 TeV. Single-top production via electroweak interactions is rarer, but theoretically very clean. The top quark is the heaviest known fundamental particle by far, with a mass of about 173 GeV. An interesting question is whether the similarity in mass scale to H , W and Z is related to electroweak symmetry breaking. Due to the short lifetime, order of 10^{-25} s, the top decays before hadronisation. For this reason it provides a unique opportunity to study a quasi-free quark. Furthermore, spin decorrelation time is much longer, and then one can study spin correlation via decay products⁵. The top quark decays almost exclusively to Wb in the SM. Events are categorised by the decays of the W boson: all hadronic, lepton plus jets and di-lepton.

The mass of the Higgs at 125 GeV is close to the minimum value that ensures absolute vacuum stability within the SM. Precise top-mass measurements are very relevant, and several different techniques are adopted

- ideogram method, measured with 35.9 fb^{-1} at 13 TeV⁶;
- all-jets final state, 35.9 fb^{-1} at 13 TeV⁷;
- differential cross-section, 35.9 fb^{-1} at 13 TeV⁸;
- inclusive cross-section, 35.9 fb^{-1} at 13 TeV⁸.

Concerning associated production of $t\bar{t}$ pairs with W and Z bosons, these are rare processes with cross-sections of about 1 pb at 13 TeV. Such measurements are very useful to test QCD predictions, as deviations might indicate the presence of new physics, like vector-like quarks, strongly coupled Higgs bosons, exotic quarks with charge $-4/3$ and anomalous dipole moments of the top quark. Several measurements have been performed recently, *e.g.* by ATLAS with 36.1 fb^{-1} at 13 TeV⁹, and by CMS with 35.9 fb^{-1} and 77.5 fb^{-1} at 13 TeV^{10,11}. Results are in line with NLO predictions. The CMS result on $t\bar{t}Z$ has better precision than NLO, but resummed calculations are now reaching NNLL+NLO accuracy.

An interesting search is that of four-top production. This is a very rare process, with a cross-section of about 10 fb at 13 TeV. Events are characterised by very large jets, b-jet multiplicities and hadronic activity. The latest search by CMS is for same-sign di-lepton and multi-lepton events using 137 fb^{-1} at 13 TeV¹². A multivariate analysis yields a significance of 2.6σ relative to the background-only hypothesis, and a cross-section of $12.6_{-5.2}^{+5.8}$ fb. The results are used to constrain the top Yukawa coupling with respect to the SM value.

The top quark is also a tool to look directly for BSM physics. In FCNC processes the top quark can couple to a light quark (up or charm) and a neutral boson (γ , Z , H , g). These processes are forbidden at tree-level in the SM, and not observable with present data unless new physics is at play. Observation of FCNC would be indicative of new physics. A recent measurement by ATLAS in $t \rightarrow uH$ and $t \rightarrow cH$, using 36.1 fb^{-1} at 13 TeV¹³, did not find evidence for these processes. Combining the search with other ATLAS searches in di-photon and multi-lepton final states, at 95% C.L. one gets $BR(t \rightarrow uH) < 1.1 \times 10^{-3}$ and $BR(t \rightarrow cH) < 1.2 \times 10^{-3}$. There is nothing unexpected in exotic physics with top quarks yet, but the full Run-2 data set has still to be analysed.

To conclude this section, a peculiar measurement of top production that is also worth mentioning is that performed by LHCb, using 1.9 fb^{-1} at 13 TeV¹⁴. The forward acceptance of the LHCb detector allows measurements in a phase space inaccessible to ATLAS and CMS. In this analysis, events containing a high- p_T muon and electron of opposite charge in addition to a high- p_T jet have been selected. No discrepancy from the SM expectation has been found.

4 Electroweak physics

In the SM, three parameters define the electroweak sector, namely U(1) and SU(2) couplings and vacuum expectation value. The electroweak sector of the SM is over-constrained and the strength of global fits can be exploited to predict key observables, such as the W mass and the effective electroweak mixing angle, with a precision exceeding that of direct measurements.

The W mass is sensitive to the Higgs and top masses via radiative corrections. The precise determination of the W mass is of great importance in testing the internal consistency of the SM. The global electroweak fit yields the mass of the W with an uncertainty of 8 MeV, to be compared with the experimental precision of 15 MeV. Therefore there is the need to improve the experimental uncertainty. The only W mass measurement at the LHC to date has been performed by ATLAS: $M_W = 80370 \pm 7$ (stat.) ± 11 (exp.syst.) ± 14 (mod.syst.) MeV. The dominating uncertainty stems from theory. This lone ATLAS measurement competes with the Tevatron combination. It is worth reminding that the measurement at the LHC is affected by PDF uncertainties more than at the Tevatron.

In the SM, ZZ production proceeds mainly through quark-antiquark t - and u -channel scattering diagrams. At higher orders in QCD also gg fusion contributes via box diagrams with quark loops. There has been a recent CMS study of four-lepton production, $pp \rightarrow (Z/\gamma^*)(Z/\gamma^*) \rightarrow 4l$, where $l = e$ or μ , using 101 fb^{-1} at 13 TeV¹⁵. By combining with the 2016 results, the measured cross-section value is found to be consistent with the SM prediction.

5 BSM searches

BSM searches are amongst the most important (and challenging) analyses at the LHC. As first searches, BSM models predict new resonances decaying to a pair of objects, *i.e.* two-body resonances like di-photons, di-leptons, di-bosons, di-jets. When the multiplicity of the final states gets larger, or one goes for exotic signatures like long-lived particles (LLPs), analyses become increasingly more complex and model-dependent, requiring better understanding of the underlying physics models being tested and of the detector response. Many signatures have been probed already with full Run-2 statistics. First analyses did not reveal evidence for new physics yet, but a lot of phase space has still to be explored. In the following, a few examples of recent analyses presented during the conference will be highlighted.

A recent search for new resonances decaying to electron and muon pairs has been performed by ATLAS using 139 fb^{-1} of data at 13 TeV¹⁶. The background fit with a parametric function exhibits an excellent description of the di-lepton spectra up to several TeV. The distributions of the di-electron and di-muon invariant masses are shown in Fig. 2. No significant excess over the SM expectation is found. Cross-section limits are set for generic resonances with a relative natural width between zero and 10%.

New heavy particles that decay to partons are predicted in many BSM models. For example, excited quarks are predicted in compositeness models and are a typical benchmark used in many di-jet searches. Partons shower and hadronise, creating collimated jets. BSM phenomena may produce a di-jet signal up to masses that are a significant fraction of the total collision energy. Two recent searches for new resonances in the di-jet invariant mass by ATLAS (with 139 fb^{-1} at 13 TeV¹⁷) and CMS (with 77.8 fb^{-1} at 13 TeV¹⁸) show no significant excess from the SM expectation. Moving to a more complex analysis, with three or more electrons and muons in the final state, one looks for non-resonant excesses in the tails of the sum of lepton p_T plus missing transverse momentum (with 137 fb^{-1} at 13 TeV¹⁹). Observed data are consistent with the SM expectation.

While the phase space for an easy discovery is reducing, growing interest is emerging for new-physics searches with unconventional signatures, like emerging jets, heavy charged LLPs, delayed jets, displaced jets, disappearing tracks, displaced muons. A community white paper has been released recently²⁰. At low energy, a search for a spin-0 boson using prompt decays

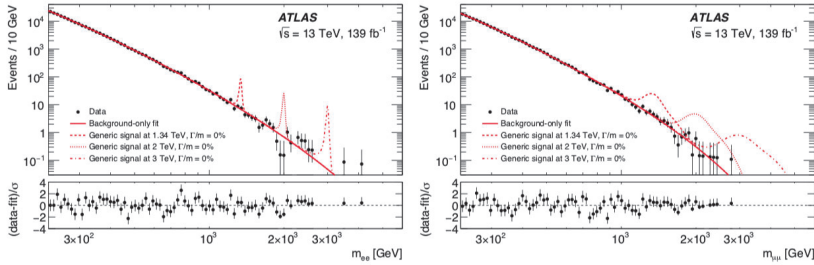


Figure 2 – Distributions of the (left) di-electron and (right) di-muon invariant masses. Zero-width signal shapes, scaled to 20 times the value of the corresponding expected upper limit at 95% CL on the fiducial cross-section times branching ratio, are superimposed¹⁶.

to $\mu^+\mu^-$ has been performed by LHCb, with 3 fb^{-1} of data at 7 and 8 TeV²¹. The LHCb detector has good sensitivity to light spin-0 particles due to its high-precision spectrometer and its capability of triggering on objects with small transverse momenta. No evidence for a signal is observed and limits are placed.

In conclusion, BSM searches are very challenging as they look for corners and tails of SM physics. The community working in the sector is continuously developing new techniques and adding new models, phase-space regions and correlations with SM backgrounds. Many results are anticipated to come out soon with Run-2 statistics, while preparing for Run 3. The phase space has been narrowed down for some models, but there are many others to study, and the end of the searches is still very far to come.

6 (Some) hard and soft QCD processes

Genuine QCD measurements at the LHC are important for the good modelling of hadronic collisions and obviously to test our understanding of QCD: probing PDFs and NLO predictions; studying event topologies in interesting phase space regions, *i.e.* multi-jet production, di-jet decorrelations, and very forward region; studying jet substructure; understanding backgrounds for electroweak analyses, BSM searches, etc.; studying multiple parton interactions, *e.g.* double parton scattering (DPS); etc. In addition, accurate knowledge is crucial for the development of future projects, like ATLAS and CMS phase-2 upgrades. Several recent measurements have been performed by ATLAS and CMS, the latter also using CASTOR to study very forward energy flow and jets.

A measurement of simultaneous Drell-Yan production with four leptons in the final state has been performed using 20.2 fb^{-1} of data at 8 TeV²². The process is particularly relevant as a background in the Higgs analysis with four-lepton decays. A simplified model for a DPS cross-section can be written as $\sigma_{AB}^{\text{DPS}} \simeq \sigma_A \sigma_B / \sigma_{\text{eff}}$, where σ_{eff} is assumed to be process- and energy-independent. No signal of DPS is observed. The upper limit on the fraction of the DPS contribution to the inclusive four-lepton final state translates into a lower limit of 1.0 mb on the effective cross-section.

Another DPS measurement has been performed by looking for same sign WW production with 77 fb^{-1} of data at 13 TeV²³. This is an important channel to test DPS predictions. Both hard scatterings lead to the production of a W boson, and particularly interesting is the final state with two same-charge W bosons. The W decay provides a relatively clean signal, with well-understood background processes. In particular, WZ production constitutes the main background. A fit is performed in different flavour-sign categories separately, $\mu^\pm\mu^\pm$ and $e^\pm e^\pm$. This result represents the first experimental evidence of the DPS WW process.

Production of prompt photons in $pp \rightarrow \gamma X$ allows pQCD tests with a hard colourless probe.

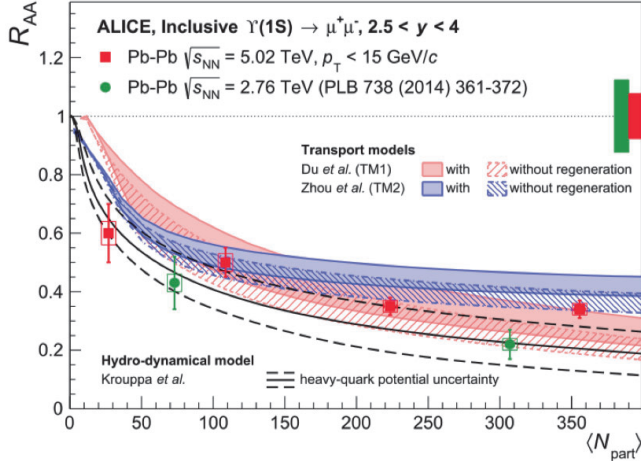


Figure 3 – Nuclear modification factor for Υ production as a function of centrality²⁵.

The dominant production mechanism at the LHC is $qg \rightarrow q\gamma$. The cross-section is sensitive to the gluon density in the proton. An isolation cut is needed to reduce background from neutral-hadron decays and from fragmentation where the emitted photon is close to a jet. An analysis of 20.2 fb^{-1} and 3.2 fb^{-1} of data at 8 and 13 TeV has been performed²⁴. The ratio between cross-sections at 13 and 8 TeV is measured as a function of the energy of the photon in different photon pseudorapidity ranges. Predictions using several PDFs agree well with data.

7 Heavy ions

Hard probes are one of the pillars to study hot and dense QCD matter created in heavy ion collisions. Perturbative processes take place before the QGP forms, *e.g.* heavy-quark production. On the other hand, heavy quarks decay weakly such that their lifetime is greater than that of the QGP and so they experience the full system evolution. In addition, quarkonium states have binding energies of the order of a few hundred MeV, and interactions with hard gluons in a QGP can overcome this threshold breaking the quarkonium system. The modification of the jet structures while traversing the hot medium is also another relevant example (jet quenching).

The production of J/ψ mesons at high p_T is strongly suppressed in PbPb with respect to pp collisions. The suppression increases as a function of the centrality of the collision. Also strong Υ suppression is observed (see Fig. 3), and higher Υ states are even more suppressed: $R_{AA}(\Upsilon(2S))/R_{AA}(\Upsilon(1S)) = 0.28 \pm 0.12 \text{ (stat.)} \pm 0.06 \text{ (syst.)}$, as measured by ALICE²⁵. Also CMS observes a similar spectacular behaviour. The R_{AA} of the $\Upsilon(3S)$ state is measured to be below 0.096 at 95% C.L.²⁶. This is the strongest suppression observed for a quarkonium state in heavy ion collisions to date. By contrast, at low p_T , smaller J/ψ suppression at the LHC than at RHIC is found, owing to measurements by ALICE, PHENIX and STAR. New regenerated J/ψ mesons are produced by recombination of charm quarks, with larger regeneration occurring at higher $c\bar{c}$ pair density and higher energy density.

The ratio of Λ_c to D^0 production has been measured by ALICE in pp , pPb , and PbPb collisions²⁷. A similar ratio in pp and pPb collisions is found, whereas enhanced production of Λ_c baryons with respect to D^0 mesons is observed in PbPb collisions. The measurement is still limited in precision, but appears to be intriguing. Also STAR seems to observe a larger Λ_c to D^0 ratio in AuAu collisions. In the forward region, as a dedicated heavy-flavour experiment, LHCb

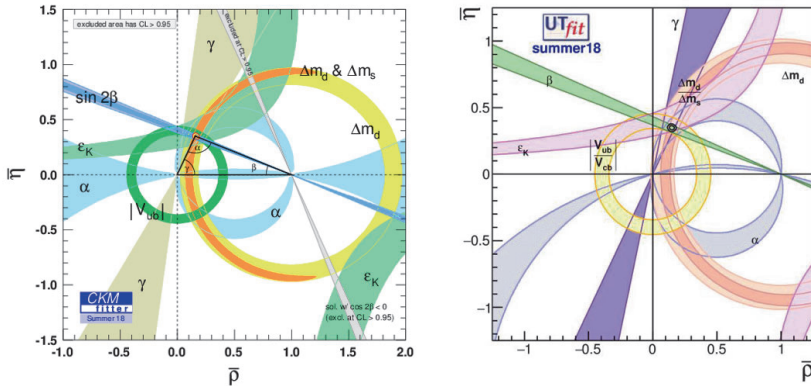


Figure 4 – Results of global CKM fits from (left) CKMfitter and (right) UTfit groups.

has obvious advantages in measuring b -hadron decays (at pPb event multiplicities). Beauty hadrons are cleanly reconstructed in exclusive decay modes²⁸. First measurements in nuclear collisions are made down to very low p_T values. The R_{pPb} suppression pattern seen in J/ψ from b is confirmed. LHCb can also inject gas into the beam pipe to measure cross-sections in fixed-target mode, see e.g. antiproton production in pHe²⁹ or charm production in pAr and pHe³⁰ collisions.

ATLAS measured the flow of muons from heavy flavour decays in pp and PbPb collisions at 2.76 TeV³¹. The value of R_{AA} is found to be less than unity, hence observing suppressed production of heavy-flavour muons in PbPb collisions. In particular, for the 10% most central PbPb events, R_{AA} is about 0.35. Furthermore, lower values of the elliptic flow are found for particles with heavy quarks than with the lighter quarks. This is a useful information for the analysis of quark interactions in the medium. Charged hadron production in PbPb and XeXe collisions has been studied at 5.02 and 5.44 TeV by ALICE. The production of (most of) light-flavour hadrons in PbPb at 5.02 TeV is described by the thermal model. The differences between protons and the strangeness sector are confirmed. Hydrodynamic properties are studied with spectral shape and azimuthal anisotropy. Hydrodynamics works at low p_T for central collisions, with the agreement worsening towards peripheral collisions.

In recent years, momentum anisotropies have been measured in pp and pA collisions, despite expectations that the volume and lifetime of the medium would be too small. PHENIX observed elliptic and triangular flow patterns in pAu , dAu and 3HeAu collisions³². The three initial geometries and two flow patterns provide powerful model discrimination. In the PHENIX analysis, hydrodynamic models, based on the formation of short-lived QGP droplets, provide the best simultaneous description of the measurements.

8 Heavy flavours

The present consistency of global CKM fits is displayed in Fig. 4. Each coloured band defines the allowed region of the apex of the unitarity triangle, according to the measurement of a specific process. Such a consistency represents a tremendous success of the CKM paradigm in the SM: all of the available measurements agree in a highly profound way. In presence of BSM physics affecting the measurements, the various contours would not cross each other into a single point. Hence the quark-flavour sector is generally very well described by the CKM mechanism, and one must look for small discrepancies.

In the charm sector, using 6 fb^{-1} at 13 TeV³³, LHCb measured the difference ΔA_{CP} of

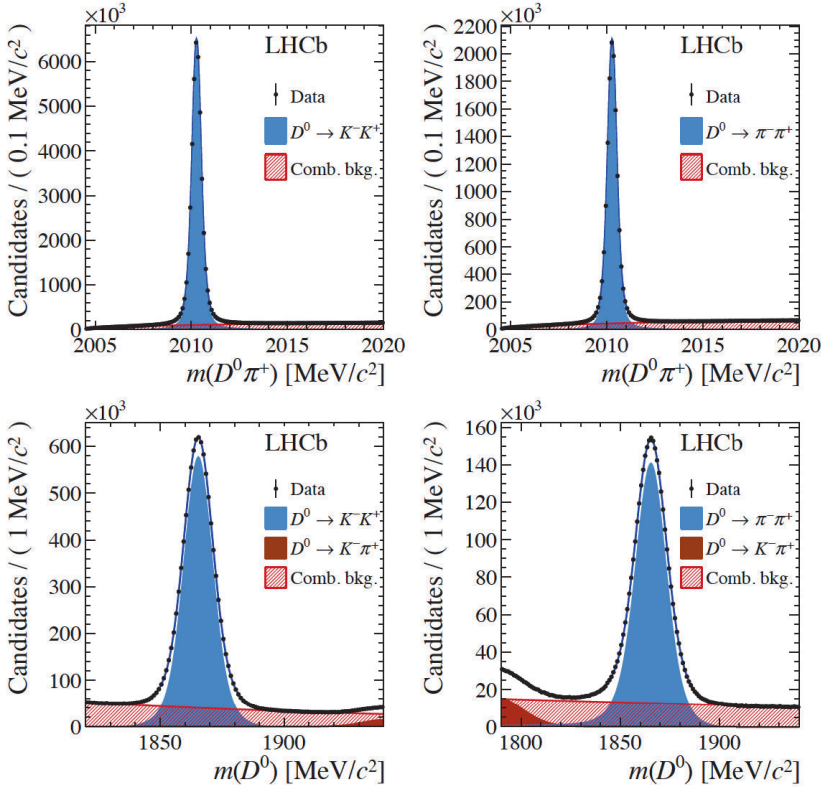


Figure 5 – Mass distributions of selected (top) π^\pm -tagged and (bottom) μ^\pm -tagged candidates for (left) K^+K^- and (right) $\pi^+\pi^-$ final states of the D^0 -meson decays, with fit projections overlaid³³.

the CP -violating asymmetries in the decays $D^0 \rightarrow K^-K^+$ and $D^0 \rightarrow \pi^-\pi^+$. To perform the measurement, the flavour of the D^0 meson is tagged either by using the charge of the pion in $D^{*+} \rightarrow D^0\pi^+$ decays, or the charge of the muon in $B \rightarrow D^0\mu\nu X$ decays. The invariant-mass distributions are shown in Fig. 5. Run-2 results are well compatible with previous LHCb results and the world average. The combination of Run-1 and Run-2 data gives $\Delta A_{CP} = (-15.4 \pm 2.9) \times 10^{-4}$, resulting in the first observation of CP violation in the charm sector, with a significance of 5.3σ . The result is roughly compatible with the SM, whose prediction however is way more uncertain than data.

The golden mode $B_s^0 \rightarrow J/\psi\phi$ is the B_s^0 analogue of $B^0 \rightarrow J/\psi K_S^0$, and one measures the interference between B_s^0 mixing and decay graphs through the phase-difference ϕ_s between the two processes, precisely predicted in the SM to be $\phi_s = -37.4 \pm 0.7$ mrad. This is very small, but can receive sizeable contributions from new physics. New measurements by ATLAS (with 80.5 fb^{-1} at 13 TeV³⁴) using $B_s^0 \rightarrow J/\psi\phi$ and LHCb (with 1.9 fb^{-1} at 13 TeV^{35,36}) using $B_s^0 \rightarrow J/\psi\phi$ and $B_s^0 \rightarrow J/\psi\pi\pi$ decays have been performed. The combination of Run-1 and Run-2 data gives $\phi_s = -0.076 \pm 0.034$ (stat) ± 0.019 (syst) rad for ATLAS and $\phi_s = -0.040 \pm 0.025$ (stat + syst) rad for LHCb. The new world average provided by HFLAV is $\phi_s = -0.0544 \pm 0.0205$ rad. The experimental precision is quickly approaching the sensitivity to observe a nonzero SM value. For this reason, the ATLAS and LHCb analyses with full Run-2 statistics and Run-2 CMS results are now eagerly awaited.

Another recent measurement is that of the radiative decay $B_s^0 \rightarrow \phi\gamma$, performed by LHCb with 3 fb^{-1} of data at 7 and 8 TeV³⁷. The chiral structure of the W boson leads to a photon polarisation mostly left-handed in the SM, with a small right-handed component. New physics might significantly alter the contribution of the right-handed component to the total amplitude. LHCb has measured now for the first time direct and mixing-induced CP violation in $B_s^0 \rightarrow \phi\gamma$ decays, with values compatible with the SM, albeit with large uncertainties.

Moving to rare B decays, $B \rightarrow \mu^+\mu^-$ decays are FCNC- and helicity-suppressed, proceeding via Z penguin and W box diagrams. The value of the branching fraction is particularly sensitive to new-physics scalar contributions, such as extra Higgs doublets. CMS and LHCb performed in 2015 a combined fit to their full Run-1 data sets, observing the $B_s^0 \rightarrow \mu^+\mu^-$ decay for the first time at 6.2σ ³⁸. In 2016 ATLAS published with Run-1 data³⁹ and in 2017 LHCb performed the first measurement using Run-2 data⁴⁰. A new measurement by ATLAS, using 26.3 fb^{-1} at 13 TeV, has been published recently⁴¹. By combining Run-1 and Run-2 results, the branching fractions are found to be compatible with the SM at 2.4σ . The analysis of 2016 and 2017 data by CMS is in preparation. In total, 433 B_s^0 and 54 B^0 candidates are expected with full Run-2 statistics.

The sector of lepton-flavour universality (LFU) tests has received great attention during the last few years. Focusing on $b \rightarrow sl^+l^-$ transitions, one measure the ratios $R_K = \text{BR}(B^+ \rightarrow K^+\mu^+\mu^-)/\text{BR}(B^+ \rightarrow K^+e^+e^-)$ and $R_{K^*} = \text{BR}(B^0 \rightarrow K^{*0}\mu^+\mu^-)/\text{BR}(B^0 \rightarrow K^{*0}e^+e^-)$. The theoretical predictions of such ratios are very clean, hence an observation of non-LFU would be a clear sign of new physics. The measurements are presently at about 3σ from the SM, complementing a range of other anomalies in $b \rightarrow sl^+l^-$ transitions, namely branching fractions in various decays and the angular analysis of $B \rightarrow K^*\mu\mu$ decays. A new measurement of R_K has been performed by LHCb, adding 2 fb^{-1} of Run-2 data to 3 fb^{-1} of Run-1 data⁴². The statistics has been doubled with respect to the previous measurement, and the result is $R_K = 0.846_{-0.054}^{+0.060+0.016}_{-0.014}$. In practice, the significance of the discrepancy from the SM is unchanged after the new measurement, as the uncertainty has been reduced but the central value has moved closer to the SM. The outlook is to include also 2017 and 2018 data, for further doubling the statistics, and to add more channels, first to measure R_{K^*} with full Run-2 statistics, but also to provide first measurements with B_s^0 and Λ_b channels.

LFU tests are also performed with semitaonic $B \rightarrow D^{(*)}\tau\nu$ decays. Here one measures the ratios $R_{D^{(*)}} = \text{BR}(B \rightarrow D^{(*)}\tau\nu)/\text{BR}(B \rightarrow D^{(*)}\mu\nu)$, sensitive to new physics at tree level. Measurements of R_D and R_{D^*} have been performed by BaBar, Belle and LHCb. The overall average shows a discrepancy from the SM by about 3.8σ . LHCb can also perform measurements with other b hadrons: *e.g.* B_s^0 , B_c and Λ_b decays will help better understand the global picture. A new measurement from Belle has been performed recently, reporting the most precise determination of $R(D)$ and $R(D^*)$ to date, and in particular the first $R(D)$ measurement realised using the semileptonic tag. The new results are compatible with the SM at 1.2σ . The $R(D) - R(D^*)$ Belle average is now at 2σ from the SM prediction, and the overall tension with the SM expectation decreases to about 3.1σ .

Concerning the upcoming future, Belle II has concluded successfully the phase-2 pilot run. The basic detector performance is as good as expected, and the nano-beam scheme of the collision point has been tested with encouraging results. The target for phase 3 is to have a full physics run and collect 20 fb^{-1} of luminosity by summer 2019. These are crucial years to demonstrate the capability of the machine to provide the required luminosity while keeping background under control.

9 Kaon physics

While waiting for the measurement of $\text{BR}(K^+ \rightarrow \pi^+\nu\nu)$, NA62 performed a measurement using the kaon beam as a source of π^0 s to search for an invisible massive dark photon, A' ⁴³.

No significant excess is detected, using only 1% of the available statistics collected in 2016–2018. Upper limits are set at 90% C.L., compatible with fluctuations from the background-only hypothesis. The analysis improves on previous limits over the mass range 60–110 MeV/ c^2 .

Another new measurement in the kaon sector has been performed by NA48 with the $K^\pm \rightarrow \pi^\pm \pi^0 e^+ e^-$ decay⁴⁴. This is a rare decay proceeding through virtual photon exchange. The first observation has been achieved, and the branching fraction determined to be $(4.237 \pm 0.063 \text{ (stat.)} \pm 0.033 \text{ (syst.)} \pm 0.126 \text{ (ext.)}) \times 10^{-6}$. Several CP -violating asymmetries and a long-distance P -violating asymmetry have been measured and found to be consistent with zero.

10 Muon magnetic anomaly

In the SM, the theoretical uncertainty on a_μ is dominated by hadron vacuum polarisation and hadronic light-by-light scattering. E821 measured a_μ with a precision of 550 ppb, observing a (statistically dominated) discrepancy from the SM expectation at 3.7σ . E989 is now taking data to reduce the experimental uncertainty to 140 ppb. With such an experimental precision, the reduction of the hadronic theoretical uncertainties will become mandatory. The contribution of hadron vacuum polarisation to a_μ is calculated through a dispersion relation using the experimental information on the cross-section $\sigma(e^+e^-) \rightarrow \text{hadrons}$, as the relevant energy scale is too low for applying perturbative QCD. A reduction of about 20% in the uncertainty has been achieved since 2013, mostly owing to results from BaBar and VEPP-2000. By contrast, the hadronic light-by-light scattering contribution remains as an open issue, and can be determined with lattice QCD calculations or via further experimental measurements like the proposed MUonE, which aims at measuring the elastic reaction $\mu e \rightarrow \mu e$ to constrain a_μ^{HLO} from data. Additional physics motivations for light-resonance spectroscopy are the study of hadronic decays of charmonium, via $e^+e^- \rightarrow \gamma\psi(\rightarrow \text{hadrons})$, the study of other hadronic resonances, searches for dark-photon decays, etc.

11 Spectroscopy

A renaissance of QCD in the non-perturbative regime has been taking place during the last decade. A recent measurement with the observation of excited B_c mesons has been performed by CMS, using 140 fb $^{-1}$ of data at 13 TeV⁴⁵. Two excited B_c states have been observed in the $B_c\pi\pi$ final state, with $B_c \rightarrow J/\psi(\mu\mu)\pi$ (see Fig. 6). The result has been also confirmed by LHCb, with an analysis on 8.5 fb $^{-1}$ of data at 7, 8 and 13 TeV⁴⁶.

One of the most active experiments in spectroscopy measurements with charm quarks is BESIII. BESIII is a dedicated e^+e^- open charm and charmonium factory at BEPC. A plethora of spectroscopy measurements have been performed through the years, notably including tetraquark states. For example, the observation of $X(3872) \rightarrow \omega J/\psi$ has been recently reported⁴⁷. Furthermore, the cross-section measurement of $\gamma X(3872)$ suggests a connection between $X(3872)$ and $Y(4260)$. BESIII is also very active in searching for and studying glueball candidates.

Also LHCb is extremely active, with novel spectroscopy measurements being performed at an impressive rate. LHCb has observed recently a new state, likely to be $\psi(1^3D_3)$, *i.e.* achieving the first observation of a spin-3 charmonium state⁴⁸. LHCb has also got relevant news on pentaquarks. First pentaquarks were observed by LHCb four years ago using $\Lambda_b \rightarrow J/\psi p K$ decays as a proxy. Two charged states were determined: one narrow, dubbed $P_c(4450)$, and one broader, dubbed $P_c(4380)$, both decaying into $J/\psi p$. The measurement triggered great theoretical interest to understand the nature of the new resonances, *i.e.* whether they are tightly bound or molecular states. LHCb has now updated the same pentaquark analysis using 9 fb $^{-1}$ of data at 7, 8 and 13 TeV⁴⁹. The overall statistics has increased by a factor nine with respect to the the Run-1 analysis. Only a narrow bump-hunting analysis with empirical background

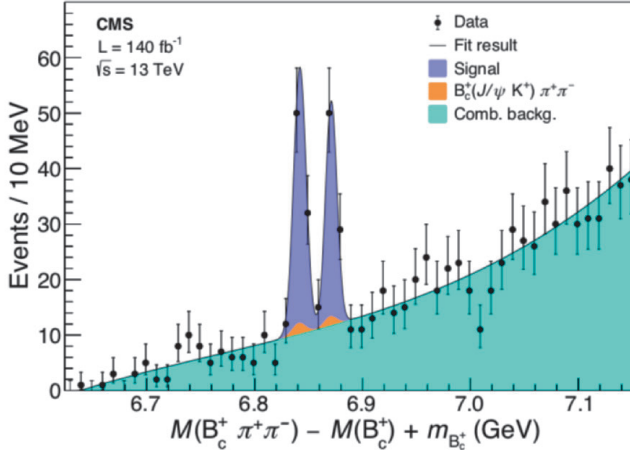


Figure 6 – Invariant $B_c \pi \pi$ mass showing two peaks of excited B_c states⁴⁵.

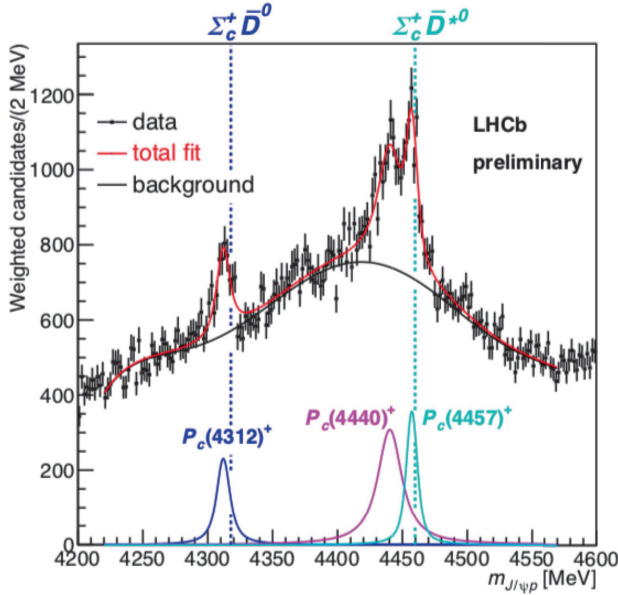


Figure 7 – Invariant $J/\psi p$ mass with the three pentaquark states observed by LHCb⁴⁹.

shape has been performed so far. As shown in Fig. 7, the previously found $P_c(4450)$ reveals a finer structure with two close peaks, and a new peak is found at 4312 MeV. This constitutes an important novel input to shed light into the nature of pentaquarks. A full amplitude analysis is ongoing, especially needed to confirm the $P_c(4380)$ state.

12 Conclusions

Despite the formidable attempts performed so far by high-energy physics experiments, the Standard Model of particle physics still proves to be unbreakable. In the current state of fundamental physics, it is of paramount importance to maintain and further develop a diversified programme, ranging from the high-energy frontier to the intensity frontier, from astrophysics and cosmology to dark matter detection. We know that the Standard Model will capitulate in the end, the only question is when and how. Meanwhile, long live Rencontres de Moriond!

Acknowledgments

I wish to express my cordial thanks to the organisers of the conference for the kind invitation and for the pleasant environment.

References

1. M. Aaboud *et al.* [ATLAS Collaboration], “Measurement of VH , $H \rightarrow b\bar{b}$ production as a function of the vector-boson transverse momentum in 13 TeV pp collisions with the ATLAS detector”, JHEP **1905** (2019) 141, arXiv:1903.04618 [hep-ex].
2. [ATLAS Collaboration], “Measurement of Higgs boson production in association with a $t\bar{t}$ pair in the diphoton decay channel using 139 fb^{-1} of LHC data collected at $\sqrt{s} = 13 \text{ TeV}$ by the ATLAS experiment”, ATLAS-CONF-2019-004.
3. [CMS Collaboration], “Measurements of properties of the Higgs boson in the four-lepton final state in proton-proton collisions at $\sqrt{s} = 13 \text{ TeV}$ ”, CMS-PAS-HIG-19-001.
4. [CMS Collaboration], “Search for Higgs and Z boson decays to J/ψ or Υ pairs in proton-proton collisions at $\sqrt{s} = 13 \text{ TeV}$ ”, CMS-PAS-HIG-18-025.
5. M. Aaboud *et al.* [ATLAS Collaboration], “Measurements of top-quark pair spin correlations in the $e\mu$ channel at $\sqrt{s} = 13 \text{ TeV}$ using pp collisions in the ATLAS detector”, arXiv:1903.07570 [hep-ex].
6. A. M. Sirunyan *et al.* [CMS Collaboration], “Measurement of the top quark mass with lepton+jets final states using pp collisions at $\sqrt{s} = 13 \text{ TeV}$ ”, Eur. Phys. J. C **78** (2018) 891, arXiv:1805.01428 [hep-ex].
7. A. M. Sirunyan *et al.* [CMS Collaboration], “Measurement of the top quark mass in the all-jets final state at $\sqrt{s} = 13 \text{ TeV}$ and combination with the lepton+jets channel”, Eur. Phys. J. C **79** (2019) 313, arXiv:1812.10534 [hep-ex].
8. A. M. Sirunyan *et al.* [CMS Collaboration], “Measurement of the $t\bar{t}$ production cross section, the top quark mass, and the strong coupling constant using dilepton events in pp collisions at $\sqrt{s} = 13 \text{ TeV}$ ”, Eur. Phys. J. C **79** (2019) 368, arXiv:1812.10505 [hep-ex].
9. M. Aaboud *et al.* [ATLAS Collaboration], “Measurement of the $t\bar{t}Z$ and $t\bar{t}W$ cross sections in proton-proton collisions at $\sqrt{s} = 13 \text{ TeV}$ with the ATLAS detector”, Phys. Rev. D **99** (2019) 072009, arXiv:1901.03584 [hep-ex].
10. A. M. Sirunyan *et al.* [CMS Collaboration], “Measurement of the cross section for top quark pair production in association with a W or Z boson in proton-proton collisions at $\sqrt{s} = 13 \text{ TeV}$ ”, JHEP **1808** (2018) 011, arXiv:1711.02547 [hep-ex].
11. [CMS Collaboration], “Measurement of top quark pair production in association with a Z boson in proton-proton collisions at $\sqrt{s} = 13 \text{ TeV}$ ”, CMS-PAS-TOP-18-009.
12. [CMS Collaboration], “Search for standard model production of four top quarks in final states with same-sign and multiple leptons in proton-proton collisions at $\sqrt{s} = 13 \text{ TeV}$ ”, CMS-PAS-TOP-18-003.
13. M. Aaboud *et al.* [ATLAS Collaboration], “Search for top-quark decays $t \rightarrow Hq$ with 36 fb^{-1} of pp collision data at $\sqrt{s} = 13 \text{ TeV}$ with the ATLAS detector”, JHEP **05** (2019) 123, arXiv:1812.11568 [hep-ex].

14. R. Aaij *et al.* [LHCb Collaboration], “Measurement of forward top pair production in the dilepton channel in pp collisions at $\sqrt{s} = 13$ TeV”, *JHEP* **08** (2018) 174, arXiv:1803.05188 [hep-ex].
15. [CMS Collaboration], “Measurement of the $pp \rightarrow ZZ$ production cross section at $\sqrt{s} = 13$ TeV with the Run 2 data set”, CMS-PAS-SMP-19-001.
16. G. Aad *et al.* [ATLAS Collaboration], “Search for high-mass dilepton resonances using 139 fb⁻¹ of pp collision data collected at $\sqrt{s} = 13$ TeV with the ATLAS detector”, arXiv:1903.06248 [hep-ex].
17. [ATLAS Collaboration], “Search for New Phenomena in Dijet Events using 139 fb⁻¹ of pp collisions at $\sqrt{s} = 13$ TeV collected with the ATLAS Detector”, ATLAS-CONF-2019-007.
18. [CMS Collaboration], “Searches for dijet resonances in pp collisions at $\sqrt{s} = 13$ TeV using the 2016 and 2017 datasets”, CMS-PAS-EXO-17-026.
19. [CMS Collaboration], “Search for new physics in multilepton final states in pp collisions at $\sqrt{s} = 13$ TeV”, CMS-PAS-EXO-19-002.
20. J. Alimena *et al.*, “Searching for long-lived particles beyond the Standard Model at the Large Hadron Collider”, arXiv:1903.04497 [hep-ex].
21. R. Aaij *et al.* [LHCb Collaboration], “Search for a dimuon resonance in the Υ mass region”, *JHEP* **09** (2018) 147, arXiv:1805.09820 [hep-ex].
22. M. Aaboud *et al.* [ATLAS Collaboration], “Study of the hard double-parton scattering contribution to inclusive four-lepton production in pp collisions at $\sqrt{s} = 8$ TeV with the ATLAS detector”, *Phys. Lett. B* **790** (2019) 595, arXiv:1811.11094 [hep-ex].
23. [CMS Collaboration], “Evidence for WW production from double-parton interactions in proton-proton collisions at $\sqrt{s} = 13$ TeV”, CMS-PAS-SMP-18-015.
24. M. Aaboud *et al.* [ATLAS Collaboration], “Measurement of the ratio of cross sections for inclusive isolated-photon production in pp collisions at $\sqrt{s} = 13$ and 8 TeV with the ATLAS detector”, *JHEP* **1904** (2019) 093, arXiv:1901.10075 [hep-ex].
25. S. Acharya *et al.* [ALICE Collaboration], “ Υ suppression at forward rapidity in Pb-Pb collisions at $\sqrt{s_{NN}} = 5.02$ TeV”, *Phys. Lett. B* **790** (2019) 89, arXiv:1805.04387 [nucl-ex].
26. A. M. Sirunyan *et al.* [CMS Collaboration], “Measurement of nuclear modification factors of $\Upsilon(1S)$, $\Upsilon(2S)$, and $\Upsilon(3S)$ mesons in PbPb collisions at $\sqrt{s_{NN}} = 5.02$ TeV”, *Phys. Lett. B* **790** (2019) 270, arXiv:1805.09215 [hep-ex].
27. S. Acharya *et al.* [ALICE Collaboration], “ Λ_c^+ production in Pb-Pb collisions at $\sqrt{s_{NN}} = 5.02$ TeV”, *Phys. Lett. B* **793** (2019) 212, arXiv:1809.10922 [nucl-ex].
28. R. Aaij *et al.* [LHCb Collaboration], “Measurement of B^+ , B^0 and Λ_b^0 production in pPb collisions at $\sqrt{s_{NN}} = 8.16$ TeV”, *Phys. Rev. D* **99** (2019) 052011, arXiv:1902.05599 [hep-ex].
29. R. Aaij *et al.* [LHCb Collaboration], “Measurement of Antiproton Production in pHe Collisions at $\sqrt{s_{NN}} = 110$ GeV”, *Phys. Rev. Lett.* **121** (2018) 222001, arXiv:1808.06127 [hep-ex].
30. R. Aaij *et al.* [LHCb Collaboration], “First Measurement of Charm Production in its Fixed-Target Configuration at the LHC”, *Phys. Rev. Lett.* **122** (2019) 132002, arXiv:1810.07907 [hep-ex].
31. M. Aaboud *et al.* [ATLAS Collaboration], “Measurement of the suppression and azimuthal anisotropy of muons from heavy-flavor decays in Pb+Pb collisions at $\sqrt{s_{NN}} = 2.76$ TeV with the ATLAS detector”, *Phys. Rev. C* **98** (2018) 044905, arXiv:1805.05220 [nucl-ex].
32. C. Aidala *et al.* [PHENIX Collaboration], “Creation of quarkgluon plasma droplets with three distinct geometries”, *Nature Phys.* **15** (2019) 214, arXiv:1805.02973 [nucl-ex].
33. R. Aaij *et al.* [LHCb Collaboration], “Observation of CP violation in charm decays”, *Phys. Rev. Lett.* **122** (2019) 211803, arXiv:1903.08726 [hep-ex].
34. [ATLAS Collaboration], “Measurement of the CP violation phase ϕ_s in $B_s \rightarrow J/\psi\phi$ decays in ATLAS at 13 TeV”, ATLAS-CONF-2019-009.

35. R. Aaij *et al.* [LHCb Collaboration], “Search for lepton-universality violation in $B^+ \rightarrow K^+ \ell^+ \ell^-$ decays”, *Phys. Rev. Lett.* **122** (2019) 191801, arXiv:1903.09252 [hep-ex].
36. R. Aaij *et al.* [LHCb Collaboration], “Measurement of the CP -violating phase ϕ_s from $B_s^0 \rightarrow J/\psi \pi^+ \pi^-$ decays in 13 TeV pp collisions”, arXiv:1903.05530 [hep-ex].
37. R. Aaij *et al.* [LHCb Collaboration], “Measurement of CP -violating and mixing-induced observables in $B_s^0 \rightarrow \phi \gamma$ decays”, arXiv:1905.06284 [hep-ex].
38. V. Khachatryan *et al.* [CMS and LHCb Collaborations], “Observation of the rare $B_s^0 \rightarrow \mu^+ \mu^-$ decay from the combined analysis of CMS and LHCb data”, *Nature* **522** (2015) 68, arXiv:1411.4413 [hep-ex].
39. M. Aaboud *et al.* [ATLAS Collaboration], “Study of the rare decays of B_s^0 and B^0 into muon pairs from data collected during the LHC Run 1 with the ATLAS detector”, *Eur. Phys. J. C* **76** (2016) 513, arXiv:1604.04263 [hep-ex].
40. R. Aaij *et al.* [LHCb Collaboration], “Measurement of the $B_s^0 \rightarrow \mu^+ \mu^-$ branching fraction and effective lifetime and search for $B^0 \rightarrow \mu^+ \mu^-$ decays”, *Phys. Rev. Lett.* **118** (2017) 191801, arXiv:1703.05747 [hep-ex].
41. M. Aaboud *et al.* [ATLAS Collaboration], “Study of the rare decays of B_s^0 and B^0 mesons into muon pairs using data collected during 2015 and 2016 with the ATLAS detector”, *JHEP* **1904** (2019) 098, arXiv:1812.03017 [hep-ex].
42. R. Aaij *et al.* [LHCb Collaboration], “Search for lepton-universality violation in $B^+ \rightarrow K^+ \ell^+ \ell^-$ decays”, *Phys. Rev. Lett.* **122** (2019) 191801, arXiv:1903.09252 [hep-ex].
43. E. Cortina Gil *et al.* [NA62 Collaboration], “Search for production of an invisible dark photon in π^0 decays”, arXiv:1903.08767 [hep-ex].
44. J. R. Batley *et al.* [NA48/2 Collaboration], “First observation and study of the $K^\pm \rightarrow \pi^\pm \pi^0 e^+ e^-$ decay”, *Phys. Lett. B* **788** (2019) 552, arXiv:1809.02873 [hep-ex].
45. A. M. Sirunyan *et al.* [CMS Collaboration], “Observation of Two Excited B_c^+ States and Measurement of the $B_c^+(2S)$ Mass in pp Collisions at $\sqrt{s} = 13$ TeV”, *Phys. Rev. Lett.* **122** (2019) 132001, arXiv:1902.00571 [hep-ex].
46. R. Aaij *et al.* [LHCb Collaboration], “Observation of an excited B_c^+ state”, arXiv:1904.00081 [hep-ex].
47. M. Ablikim *et al.* [BESIII Collaboration], “Study of $e^+ e^- \rightarrow \gamma \omega J/\psi$ and Observation of $X(3872) \rightarrow \omega J/\psi$ ”, arXiv:1903.04695 [hep-ex].
48. R. Aaij *et al.* [LHCb Collaboration], “Near-threshold $D\bar{D}$ spectroscopy and observation of a new charmonium state”, arXiv:1903.12240 [hep-ex].
49. R. Aaij *et al.* [LHCb Collaboration], “Observation of a narrow pentaquark state, $P_c(4312)^+$, and of two-peak structure of the $P_c(4450)^+$ ”, arXiv:1904.03947 [hep-ex].

QCD AND HIGH ENERGY INTERACTIONS: MORIOND 2019 THEORY SUMMARY

D. WACKEROTH

*Department of Physics, University at Buffalo, 239 Fronczak Hall,
Buffalo, NY 14221, U.S.A.*



Highlights of recent theory developments are summarized relevant to precision Standard Model (SM) studies and searches for Beyond-the-SM (BSM) phenomena at present and future high-energy pp and e^+e^- colliders, and B -factories, as well as to selected topics in heavy ion collisions.

1 Introduction

We live in exciting times where a wealth of data from a wide range of experiments (see, e.g., the experimental summary by V. Vagnoni¹) allows us to probe all aspects of the SM and the computational framework of Quantum Field Theory, often at an unprecedented level of precision, and to perform new and increasingly sensitive searches for BSM physics. At this conference, we were treated to an impressive line-up of talks on recent theory developments in a wide range of topics. In the following, I will provide a brief summary of the presented results and studies and I refer to the corresponding publications and contributions to these proceedings for more details.

2 BSM searches in flavor-changing processes in B meson decays

Flavor-changing processes in the quark and lepton sectors provide an indirect window to BSM physics, which have the potential to probe high energy scales of new physics (NP) complementary to direct searches for new particles at the LHC. Several measurements of flavor observables in B meson decays by the ATLAS, CMS, LHCb, Belle and BABAR show tensions with the SM predictions (see, e.g., Ref.¹ for a recent overview). While it can well be that these *flavor anomalies* are statistical fluctuations, underestimated experimental systematics or theoretical uncertainties, it is still interesting to confront them with specific NP scenarios or in a model-independent effective field theory (EFT) approach, to see whether a consistent picture emerges. Before presenting the highlights of some of these studies, let's first discuss an example of how

theory uncertainties can be further reduced, for instance by new ideas for a precision, model-independent extraction of the CKM mixing matrix element V_{cb} from data presented in². V_{cb} is not only an important input parameter for heavy flavor observables but also a sensitive probe of NP, for example NP may not obey the SM CKM unitarity relation. An extraction of V_{cb} from inclusive $B \rightarrow X_c l \bar{\nu}$ decays relies on Heavy Quark Expansion (HQE) (see, e. g., Ref.³ for a review), which allows the moments of kinematic distributions to be written as a series in α_s and Λ_{QCD}/m_b . The series involves non-perturbative HQE parameters, which need to be extracted from data. However, the higher the order in α_s and $1/m_b$, the higher the number of HQE parameters, e. g., at $\mathcal{O}(1/m_b^4)$ there are 9 and 13 parameters at tree-level and $\mathcal{O}(\alpha_s)$, respectively. The current method can handle up to $\mathcal{O}(1/m_b^3)$ but for further improvements in the theory uncertainty $\mathcal{O}(1/m_b^4)$ should be included as well. In making use of a known reparametrization invariance, which links the HQE parameters at different orders and thus can reduce the number of independent parameters, an alternative model-independent extraction of V_{cb} from data is proposed in². This promising approach based on using the moments of the leptonic invariant mass spectrum can be already tested with existing BARBAR and Belle data.

Among the flavor anomalies the ones observed in the precisely measured (by LHCb⁴) lepton flavor universal (LFU) ratios R_M of flavor changing neutral current (FCNC) processes $b \rightarrow sl^+l^-$ ($M = K, K^*$ and $q^2 = m_{ll}^2, l = e, \mu$):

$$R_M[q_{min}^2; q_{max}^2] = \frac{\int_{q_{min}^2}^{q_{max}^2} dq^2 d\Gamma(B \rightarrow M\mu^+\mu^-)/dq^2}{\int_{q_{min}^2}^{q_{max}^2} dq^2 d\Gamma(B \rightarrow Me^+e^-)/dq^2} \quad (1)$$

are especially interesting probes of NP: the theoretical uncertainties are under such good control that a deviation from unity larger than about 1%⁵ could be interpreted as a signal of LFU violating (LFUV) NP. In⁶, the impact of R_M together with other anomalies observed in $b \rightarrow sl^+l^-$ transitions was studied by performing a global fit in a model-independent approach based on the effective Hamiltonian^{7,8}:

$$\mathcal{H}_{eff}(b \rightarrow s\gamma^*) = -\frac{4G_F}{\sqrt{2}} V_{ts}^* V_{tb} \sum_i C_i \mathcal{O}_i \quad (2)$$

Here the heavy degrees of freedom above the electroweak scale (t, H, W, Z and possible NP) have been integrated out in short-distance Wilson coefficients C_i . NP can either modify the ten main SM Wilson coefficients or introduce additional operators. In the global fit to $b \rightarrow sl^+l^-$ data of⁹ many different NP scenarios considering both LFU NP and LFU violating (LFUV) NP have been found to be in good agreement with the data. With more precise measurements these EFT results can serve as guidance for the construction of specific NP models.

Naturally the NP scenarios consistent with B meson decay observables also need to be confronted with other flavor observables or electroweak precision observables, which can consistently be done in a model-independent way by performing a global fit in the SM EFT (SMEFT) approach¹⁰ (and proper matching to the aforementioned low-energy EFT valid at scales smaller than the electroweak scale). SMEFT assumes that the UV-complete NP model is beyond the reach of direct observation and thus only manifests itself in form of higher-dimensional operators built from SM fields (it is also assumed that the SM gauge symmetry is preserved). For a recent SMEFT global fit to flavor data see, e. g., Ref.¹¹. Within SMEFT, NP contributions in the extraction of SM input parameters can be consistently taken into account, as discussed in¹² on the example of CKM mixing matrix elements V_{ij} extracted from a suggested subset of four flavor observables. The proposed procedure in¹² allows for a separation of NP effects originating from the extraction of V_{ij} and those affecting the flavor observables included in the global fit.

Examples of specific NP models, which already contribute at tree-level and are consistent with B anomalies, are models with an extra Z' boson, Lepto-Quarks (LQ), and a charged Higgs boson. A specific SM extension consistent with R_M and which has the added benefit that it

could explain the hierarchy of fermion masses and mixing, is a flavor-dependent, spontaneously broken, anomaly-free $U(1)_F$ extension of the SM studied in ¹³. There, it is assumed that the heavy $U(1)_F$ gauge boson Z' only couples to the third family (which is also motivated by the fact that there are no deviations from SM predictions in the decay of lighter mesons), where its couplings are fixed by gauge anomaly cancellation conditions. In this model, R_M is affected via tree-level exchange of a Z' with couplings to $b_L \bar{s}_L, \mu_L^+ \mu_L^-$ due to mixing with the SM Z boson. Among the considered observables apart from R_M , are LFU tests at LEP, direct searches for the Z' boson at the LHC, and $B_s - \bar{B}_s$ mixing, and interesting bounds on the parameters space of the model are extracted as well as the prospects for a full coverage at the HL-LHC are discussed ¹⁴.

A minimal Z' model where the Z' does not have significant couplings to the muon and the implications for the model parameters $C_{1q}^C, q = u, d$ from both B anomalies (see also, e.g., ¹⁵) and the weak charge of the Caesium Q_W^{CS} atom and the proton Q_W^p has been considered in ¹⁶. Interestingly, there is only a small overlap between bounds from B anomalies and $Q_W^{CS,p}$ and including the former can provide additional discriminating information.

Another intriguing NP explanation for the observed B anomalies is a vector LQ $SU(2)_L$ singlet (V_μ^1) with hypercharge $-4/3$ arising in the Pati-Salam model ¹⁷, which affects both the charged current $b \rightarrow c\tau\nu_\tau$ and FCNC $b \rightarrow s\mu\mu$ transitions via tree-level exchange of a vector LQ ^{18,19}. As discussed in ¹⁸, in this model there are only loop-suppressed effects in flavor observables, which agree with SM predictions such as $b \rightarrow s\gamma$, but one can strongly enhance $b \rightarrow s\tau\tau$ transitions and can induce large loop effects in $b \rightarrow s\mu\mu$. Figure 1 shows the allowed parameter space of the couplings $\kappa_{f_i}^L$ of the LQ to SM particles described by the Lagrangian $\mathcal{L} = \kappa_{f_i}^L \bar{Q}_f \gamma^\mu L_i V_\mu^{1\dagger}$ ¹⁹.

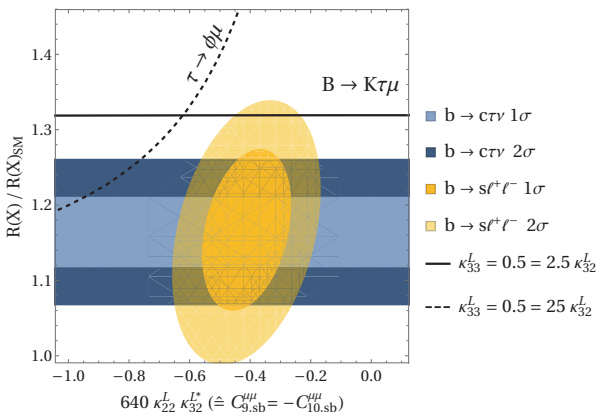


Figure 1 – Allowed (colored) regions in the $R(X)/R(X)_{SM} - \kappa_{22}^L \kappa_{32}^{L*}$ plane ($X = D, D^*$) at the 1σ and 2σ level. Taken from ¹⁹.

The $b \rightarrow c\tau\nu$ transitions can also be affected by tree-level exchanges of a scalar LQ or a charged Higgs boson. Combinations of Wilson coefficients corresponding to these scenarios have been considered in fits to taonic B decay observables in ^{20,21}. While predictions for individual decay rates come with large theoretical uncertainties due to their dependence on hadronic form factors and V_{ij} parameters, in the branching fraction ratios $R(D^{(*)}) = \text{BR}(B \rightarrow D^{(*)}\tau\nu)/\text{BR}(B \rightarrow D^{(*)}l\nu)$ the V_{ij} cancel and the uncertainties originating from the form factors are reduced. They are thus sensitive probes of NP and the inclusion of the tau polarization asymmetry $P_\tau(D^*)$ measured by Belle could help to distinguish between different NP scenarios ²⁰. Apart from theoretically well controlled observables such as ratios R_M , very rare B meson decays, which are strongly suppressed in the SM, are also ideal for the search for indirect signals of NP.

An example is the doubly weak transition $b \rightarrow dd\bar{s}$ due to a box diagram in the SM, studied in²² in the exclusive wrong-sign weak decay $\bar{B}^0 \rightarrow K^+\pi^-$. An enhancement of up to six orders of magnitude over the SM prediction for the decay rate is found in two variants of the Randall-Sundrum model for a wide range of model parameters, which could push future NP searches in this decay at Belle-II and LHCb into the range of observability²².

3 BSM searches at the LHC beyond simplified models

Direct searches for SUSY particles and their interpretation in terms of bounds on the SUSY parameter space at the LHC may rely on phenomenological versions of the minimal supersymmetric SM (MSSM) with a reduced set of parameters or more often on so-called simplified models (see, e.g., the review *SUSY: experiment* in²³). Exploring LHC data beyond these simplifications is becoming increasingly important and may reveal something unexpected. For instance, an interpretation of LHC searches in the full neutralino and chargino sector of the MSSM has been performed within the GAMBIT framework in^{24,25} and it turns out that a light SUSY scenario is preferred by the global fit with the masses of the lightest (heaviest) bino-like neutralino to be about 200(700) GeV. Furthermore, non-minimal realizations of SUSY as the one studied in²⁶ can have very distinct signatures which have not yet been probed by LHC searches. Ref.²⁶ investigates the phenomenological consequences of the Minimal Dirac Gaugino MSSM (MDMSSM), which allows for Dirac masses for gauginos, and after SUSY breaking contains a scalar and pseudo-scalar sgluon. An interesting feature of the MDMSSM is that gluino(squark)-pair production cross sections are significantly enhanced(reduced) compared to the MSSM. The impact on existing bounds on squark or gluino masses can be studied by recasting LHC analyses done in the context of simplified model, and significant effects have been found in a number of benchmark scenarios²⁶. Another non-minimal extension of SUSY is studied in²⁷, where the MSSM is extended in such a way that a right-handed sneutrino emerges as a viable dark matter candidate, either by adding a gauged $(B - L)$ symmetry (BLSSM)²⁸, or by supersymmetrizing the SM extended by three heavy neutrinos. These models have the attractive feature that they address the origin of both DM and neutrino masses. Again existing searches can be recast to obtain bounds on the parameter space of these models as discussed in²⁷, where it has been also found that sneutrino DM can be better accommodated by relic density limits than MSSM neutralino DM.

4 Precision calculations for SM and BSM studies at the LHC

Studies of the properties of the Higgs boson at the 13 TeV LHC are well under way, and we can look forward to a rich program of precision exploration of the Higgs sector at the HL-LHC and HE-LHC (see, e.g., Ref.^{29,30} for a review), provided predictions for the relevant observables are well under control. Given the importance of Higgs production in gluon-gluon fusion via a heavy quark loop, which is the dominant SM Higgs production mode at the LHC, significant theory effort went into improving predictions for both the total rate and kinematic distributions. Recently, two independent calculations of the Higgs rapidity distribution in $gg \rightarrow H$ production at next-to-next-to-next-to-leading order (N³LO) in perturbative QCD became available^{31,32}. They employ very different methods and their agreement provides a powerful and important cross-check. In³¹, an expansion about the Higgs production threshold is used and the missing terms have been fixed so that the known, inclusive all-order result is reproduced. In^{33,32} for the first time the transverse momentum (q_T) subtraction formalism is extended to a N³LO calculation, making use of the fact that N³LO specific singularities only arise in the $q_T \rightarrow 0$ limit which are known analytically. The impressive reduction of the theoretical uncertainty from the variation of the renormalization and factorization scale when including higher-orders in QCD is shown in Fig. 2.

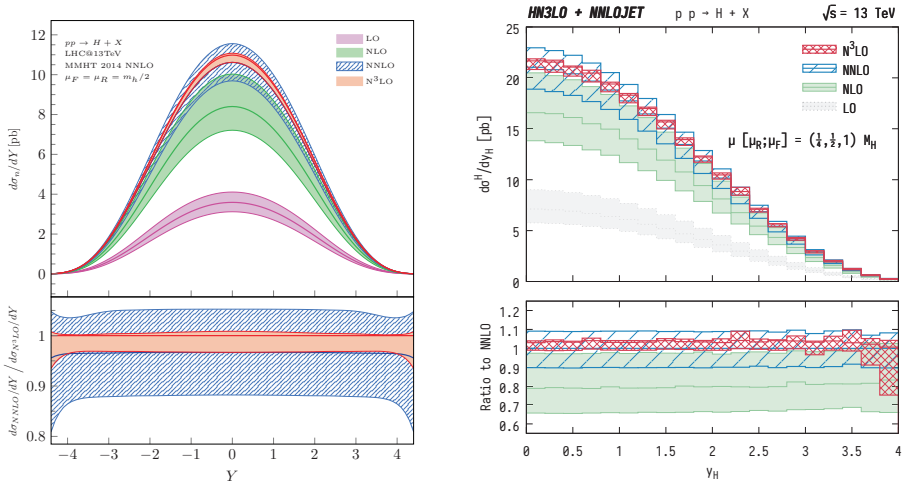


Figure 2 – Predictions for the SM Higgs boson rapidity distribution at LO, NLO, NNLO and $N^3\text{LO}$ at the 13 TeV LHC. The lower panel shows the $N^3\text{LO}$ and NNLO predictions normalized to the $N^3\text{LO}$ prediction. Taken from ³¹ (left) and from ³² (right).

The study of the production of a pair of Higgs bosons is one of the main goals of the HL-LHC ²⁹, since it directly probes the trilinear Higgs self interaction and thus the shape of the Higgs potential. Di-Higgs production in vector boson fusion (VBF), $pp \rightarrow HHjj$, is the second largest di-Higgs production cross section and is now also available at $N^3\text{LO}$ QCD ³⁴ in the public code PROVBFFH. This represents the first $N^3\text{LO}$ calculation for a $2 \rightarrow 4$ process. The calculation of the inclusive cross section is based on the structure function approach where all radiation is integrated over. The differential distributions are obtained by using the projection-to-Born method ³⁵ where the inclusive $N^3\text{LO}$ calculation is combined with the differential NNLO calculation of di-Higgs production in association with three jets presented in ³⁶. The $N^3\text{LO}$ QCD corrections to differential distributions studied in ³⁴ show a remarkable stability against scale variations and also against deviations of the trilinear coupling from the SM value.

While $N^3\text{LO}$ QCD predictions for the LHC are still few and far between, state-of-the-art predictions for SM precision physics at the LHC are processes with up to two colored particles in the final state at next-to-next-to-leading order (NNLO) in QCD and $2 \rightarrow 6$ fermions processes at next-to-leading-order (NLO) in EW theory (see, e.g., ³⁷ for a recent review). For instance, the MATRIX framework ³⁸ provides automated NNLO QCD calculations of fully differential cross sections for the LHC based on the q_T subtraction formalism. The long list of available processes includes single electroweak (EW) gauge and Higgs boson production, di-boson and $t\bar{t}$ production. In ³⁹ results from a combination of NNLO QCD and NLO EW predictions for differential distributions in VV ($V = Z, W$) production processes (including decays into fermion pairs) show the large reduction of differential cross sections due to NLO EW corrections, especially at high transverse momenta or invariant masses. Good theoretical control of di-EW boson (and tri-EW boson) production especially in these kinematic regions is essential for precision tests of EW triple (and quartic couplings) thereby searching for indirect signals of NP. Another recent improvement provided in the MATRIX framework is the consistent combination of the NNLO QCD contribution to ZZ production in the $q\bar{q}$ annihilation channel with the NLO corrections to the loop-induced $gg \rightarrow ZZ$ channel ⁴⁰. This also requires the inclusion of the qg channel and allows for the construction of an approximate $N^3\text{LO}$ prediction.

An important hadron collider observable which provides a sensitive test of perturbative QCD

and direct access to the gluon distribution inside the hadron is the transverse momentum of the photon p_T^γ at large p_T^γ in isolated photon and photon+jet production. A new calculation of the p_T^γ distribution at NNLO in QCD with emphasis on studying different prescription for photon isolation has been presented in ^{41,42} (and compared to ⁴³). Photon isolation criteria need to be applied to be able to define a cross section which only depends on the perturbatively calculable direct photon production and not on the non-perturbative fragmentation of a quark or gluon into a photon (see, e.g., ⁴⁴). In ⁴² a hybrid approach ⁴⁵ is found to be closer to the experimental treatment and to open new ways for perturbative QCD test of this procedure. Figure 3 shows the impressive agreement of the p_T^γ distribution at NNLO QCD with ATLAS data at the few percent level.

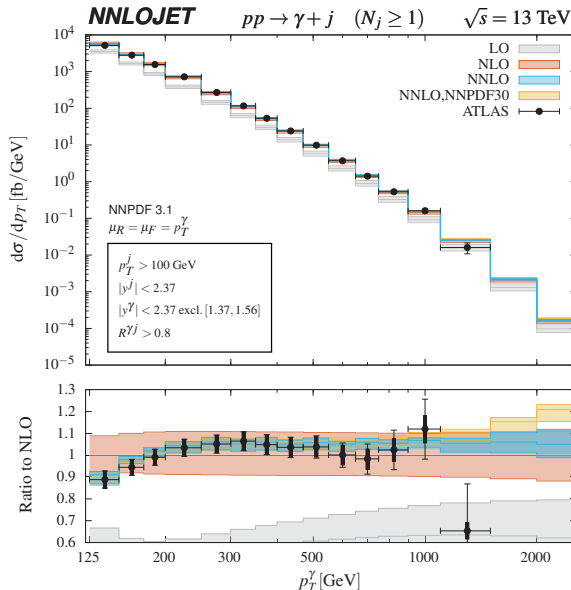


Figure 3 – Predictions for the p_T^γ distribution of the photon in γ +jet production, at LO, NLO and NNLO QCD compared to ATLAS data. Taken from ⁴².

To take full advantage of the ever increasing experimental precision at the LHC, continued advances in performing multi-loop QCD calculations are needed. For instance, knowledge of the 3-jet production cross section at NNLO QCD would allow for a precision measurement of the strong coupling constant $\alpha_s(Q^2)$ at high energy scale Q^2 when extracted from the ratio of 3-jet and 2-jet rates. One of the challenges in achieving this goal is the analytic calculation of five-parton scattering amplitudes at 2-loop order. Only recently the previously unknown massless non-planar master integrals (MI) became available in terms of Goncharov polylogarithms ⁴⁶ “thanks to nice mathematics” ^{47,48}, which completes the full set of master integrals needed for the analytic calculation of the five-parton scattering amplitude. How the latter can be assembled was shown in ^{49,50} on the example of a $N = 4$ super Yang-Mills theory and is based on the idea of rational reconstruction ⁵¹, which combines 2-loop numerical unitarity results for the MI coefficients with analytic results for the MI. These advances in multi-loop calculations also crucially rely on a systematic understanding of special functions appearing in Feynman integrals such as the Goncharov polylogarithms. As discussed in ⁵² in NNLO calculations for processes involving massive particles in the loops such as $t\bar{t}$ production at NNLO QCD or

mixed 2-loop QCD-EW corrections, integrals appear whose analytic calculation requires elliptic multiple polylogarithms (eMPL). While MPLs are obtained by integrating rational functions on a Riemann sphere, eMPLs arise as integrals on a torus. Much effort is now under way to express these complex two-loop scattering amplitudes in terms of eMPLs and to find a formulation of eMPLs suitable for use in these calculations⁵².

Apart from improvements in fixed-order calculations, advances are also needed in the identification and all-order resummation of large logarithms as well as in the consistent combination of fixed-order and resummed calculations. Large logarithms appear in processes involving very different energy scales in certain regions of phase space and may spoil the perturbative convergence. The combination is especially useful for reducing the theory uncertainty due to scale variation for processes where performing a higher fixed-order calculation is currently out of reach. For example, the production of a Higgs boson in association with a $t\bar{t}$ pair ($t\bar{t}H$) is an important SM Higgs production process, since it allows for direct measurement of the top-quark Yukawa coupling. Although only recently being discovered by CMS⁵³ and ATLAS⁵⁴, it is already clear that the NLO QCD prediction for the total cross section needs to be improved given its large uncertainty due to scale variation. As shown in⁵⁵, combining the NLO QCD prediction for $t\bar{t}H$ production at the LHC with threshold-resummed logarithmic contributions from soft gluon emission at next-to-next-to-leading logarithmic (NNLL) accuracy considerably reduces the scale uncertainty compared to the NLO result. It is interesting to note that the aforementioned MATRIX framework also provides NNLO+NNLL predictions for VV production⁵⁶.

The current state-of-the-art for resummation (of global logarithms) is N^3LL accuracy for hadronic inclusive cross sections and event shapes, but there are observables which exhibit more complicated radiation patterns resulting in the occurrence of non-global logarithms⁵⁷. Non-global observables are sensitive to radiation in only part of the phase space, such as the jet mass discussed in⁵⁸. In Soft-Collinear EFT (SCET) a factorization theorem for non-global observables allows for resummation of the non-global logarithms at NLL' accuracy. It is interesting to note that the renormalization group evolution (RGE) equation for the Wilson coefficients in the SCET formulation is equivalent to a parton shower equation, and a comparison of the jet observable at NLL+LO with PYTHIA is shown in⁵⁸.

Large logarithms can also appear in higher-order BSM predictions for large NP energy scales, which need to be resummed. For example, in⁵⁹, large logarithms appearing in radiative corrections to the MSSM Higgs masses for $M_{SUSY} \gg m_{top}$ are resummed up to partial N^3LL accuracy in a SM EFT approach (SUSY particles are integrated out). The resummed result is then combined with fixed-order calculations to obtain precise predictions also for intermediate values of M_{SUSY} . Its implementation in FEYNHIGGS⁶⁰ is then used to define new MSSM Higgs benchmark scenarios. In Ref.⁶¹ SCET is used to describe a NP scenario with a new gauge-singlet heavy spin-0 particle with mass M_S far above the EW scale v , which allows for the resummation of large logarithms of M_S/v via RGE in predictions for its decay width to SM particles (see also⁶²).

5 PDFs, BFKL dynamics, TMD factorization and evolution, and hadronization

Parton distribution functions (PDF) are an essential component of predictions for hadron collisions, and PDF uncertainties can be a limiting factor in high-precision studies of key SM processes and observables. For example, the PDF uncertainty in the first W boson mass measurement at the LHC by ATLAS⁶³ is quoted to be 9 MeV (see, e. g.,⁶⁴ for a recent study) compared to an experimental systematic uncertainty of 11 MeV. It is therefore of the utmost importance to further improve our knowledge of the PDFs of the proton, for instance by including new data in global PDF fits. Lepton-pair production via the Drell-Yan (DY) process at the LHC, $pp \rightarrow l^+l^-X$ (neutral current (NC)) and $pp \rightarrow l\nu X$ (charged current (CC)) ($l = e, \mu$), is an excellent probe of the structure of the proton. A study in⁶⁵ of the impact of including the forward-backward asymmetry A_{FB} in the NC DY process at the LHC and HL-LHC on different

NNLO PDF sets shows that indeed A_{FB} has the potential to further constrain the quark PDF. In ⁶⁵, it is also proposed to apply a high rapidity cut in order to suppress the $d\bar{d}$ -quark luminosity and increase sensitivity to the up-type (anti)-quark PDFs. This study was done by using xFITTER ⁶⁶, which is a framework for performing PDF fits, studying the impact of including data in the fits, and a variety of QCD and PDF studies. For instance, in ⁶⁷ xFITTER is used to determine the pion PDF from NA10, E615, and WA70 data.

The DY process also offers the possibility of testing the description of the high-energy behavior of the scattering of hadrons in QCD ⁶⁸ according to Balitsky, Fadin, Kuraev and Lipatov (BFKL) and the QCD factorization formula for transverse momentum dependent parton densities (TMD) ⁶⁹. In ⁶⁸, the forward production of a lepton pair in association with a backward jet is proposed to probe the resummation of large logarithms due to QCD radiation at high energies via the BFKL formalism. Especially the angular coefficients A_i , $i = 0, 1, 2$ of the DY lepton pair offer sensitive tests of the BFKL dynamics in this process. Moreover, the combination $A_0 - A_2$ is sensitive to the TMD of the gluon ⁶⁸. Unlike collinear PDFs, TMDs include non-perturbative information about partonic transverse momentum and polarization degrees of freedom, and a classic example for their application is the description of the transverse momentum q_T distribution of the EW gauge boson in DY production at small q_T . TMD factorization allows to express differential cross sections of DY processes at small q_T ($q_T^2 \ll Q^2$, where Q is the high-mass scale of the hard scattering) as a convolution of the partonic, hard scattering cross section with TMDs up to large q_T corrections ⁷⁰ (for $q_T \approx Q^2$, TMD \rightarrow collinear factorization). It is therefore important to quantify at which q_T these corrections become important. In ⁶⁹ the higher-twist power corrections to the NC DY process for $s \gg Q^2 \gg q_T^2$ have been calculated and estimated to be a few percent of the leading twist result at $q_T \approx Q/4$. In ⁷¹ TMDs are constructed from QCD evolution equations in the Parton Branching (PB) method at NLO QCD. The PB method has the feature that the splitting kinematics at each branching can be calculated, similarly to a parton shower. These TMDs depend on the ordering variable in the branching and their impact on DY q_T spectra have also been studied in Ref. ^{71,72}.

Another crucial non-perturbative aspect of hadron collider physics is the formation of hadrons from quarks and gluons. Predictions for hadron production rely on models with tunable parameters implemented in Monte Carlo event generators (see, e.g. ⁷³ for a review), such as the Lund string model in PYTHIA. In a simple string or flux tube model $q\bar{q}$ pairs are created in the strong color field in the flux tube which then combine to color singlet hadrons. Ref. ⁷⁴ considers the extension of a one-dimensional string model which cannot describe transverse dynamics to a 2-dim. flux tube. It is based on a compactification of 3 + 1-dim. QCD to 1 + 1-dim. QCD assuming longitudinal dominance and transverse confinement. Predictions for p_T and rapidity distributions in this approach have been derived and compared to NA61 pion production data ⁷⁵. The modeling of baryon production in the cluster model (see, e.g., ⁷⁶), in particular the role of baryon number in formations of pre-confined baryonic clusters has been discussed in ⁷⁷.

6 Heavy Ion Collision

In high-energy heavy ion collisions at the LHC and RHIC, a new form of matter is produced with unexpected properties. This Quark-Gluon Plasma (QGP) is understood to be a strongly interacting near perfect liquid. The study of QGP properties in heavy-ion collisions is a vast and exciting field of experimental and theoretical exploration, and for a recent review see, e. g., Ref. ⁷⁸. Here a brief summary will be given of calculations for jet p_\perp broadening and Higgs boson production in a QGP, and for some interesting phenomena observed near T_c , i. e. the temperature where the QCD phase transition between the confined and QGP phase occurs.

High-energy quarks and gluons traversing the QGP experience a broadening of the transverse momentum (p_\perp) distributions originating from radiative energy loss in multiple parton scattering and from QCD radiative corrections. While Ref. ⁷⁹ considers the NLO QCD corrections to quark

p_{\perp} broadening in the soft gluon approximation, Ref.⁸⁰ goes beyond this approximation and finds large negative contributions not included in⁷⁹. Interestingly this finding seems to be supported by the recent STAR measurement of the hadron-jet correlations as stated in⁸⁰.

Properties of the QGP such as bulk viscosity ($\zeta/s(T)$), speed of sound $C_s(T)$ and electric conductivity $\sigma_{el}(T)$ are expected to exhibit interesting behaviors for $T \rightarrow T_c$, i.e. ζ/s quickly rises, C_s is at its minimum, and σ_{el} decreases. In^{81,82} it is shown that for quark matter at moderate density ($\approx 300 - 400$ MeV) and temperature ($T \rightarrow T_c$ from above, ~ 20 MeV) all these phenomena can be traced back to a common dynamical origin namely the interaction of phonons(photons) with the soft collective mode of the di-quark field. This result is derived from the time-dependent Ginzburg-Landau functional with random Langevin forces.

Finally, the prospect of observing the SM Higgs boson in high-energy heavy ion collisions is studied in^{83,84}, and the enhancements of the Higgs production cross sections in $PbPb$ and pPb collisions over the ones in pp collisions at the LHC, HE-LHC and FCC is shown in Fig. 4. It is also interesting to note that the effect of the medium on the Higgs decay widths to a gluon or light quark pair only introduces an additional correction of $\mathcal{O}(\alpha_s(T/M_H)^4)$ times the vacuum branching ratios⁸⁵.

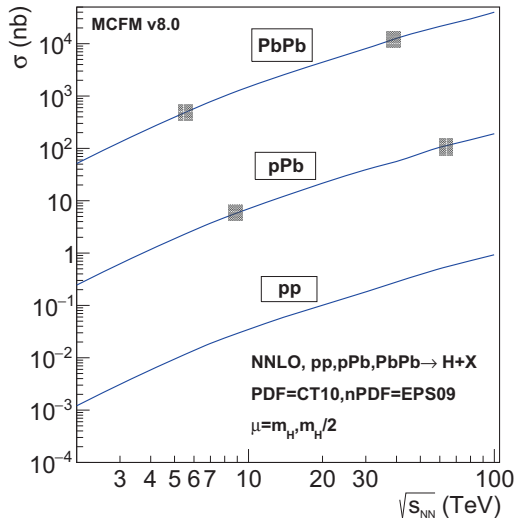


Figure 4 – Total production cross sections for the Higgs boson at NNLO in pp, pPb and $PbPb$ collisions as a function of the center-of-mass energy $\sqrt{s_{nn}}$ (the shaded boxes indicate the nominal LHC and FCC energies). Taken from⁸³.

Acknowledgments

I would like to thank the organizers for the invitation, and a perfectly organized, inspiring conference, featuring excellent presentations over a wide range of interesting and relevant topics in QCD and high-energy interactions. I am grateful to the many speakers, who patiently answered my questions and provided me with additional information and explanations. I also gratefully acknowledge support by the U.S. National Science Foundation under award no. PHY-1719690.

References

1. Vincenzo M. Vagnoni. Experimental summary: QCD session of the 54th Rencontres de Moriond (Moriond QCD 2019). In *54th Rencontres de Moriond on QCD and High Energy Interactions (Moriond QCD 2019) La Thuile, Italy, March 23-30, 2019*, 2019.
2. Matteo Fael, Thomas Mannel, and K. Keri Vos. V_{cb} determination from inclusive $b \rightarrow c$ decays: an alternative method. *JHEP*, 02:177, 2019.
3. Aneesh V. Manohar and Mark B. Wise. Heavy quark physics. *Camb. Monogr. Part. Phys. Nucl. Phys. Cosmol.*, 10:1–191, 2000.
4. Roel Aaij et al. Search for lepton-universality violation in $B^+ \rightarrow K^+\ell^+\ell^-$ decays. *Phys. Rev. Lett.*, 122(19):191801, 2019.
5. Marzia Bordone, Gino Isidori, and Andrea Pattori. On the Standard Model predictions for R_K and R_{K^*} . *Eur. Phys. J.*, C76(8):440, 2016.
6. Marcel Algueró, Bernat Capdevila, Sébastien Descotes-Genon, Pere Masjuan, and Joaquim Matias. What R_K and Q_5 can tell us about New Physics in $b \rightarrow s\ell\ell$ transitions? 2019.
7. Benjamin Grinstein, Roxanne P. Springer, and Mark B. Wise. Effective Hamiltonian for Weak Radiative B Meson Decay. *Phys. Lett.*, B202:138–144, 1988.
8. Gerhard Buchalla, Andrzej J. Buras, and Markus E. Lautenbacher. Weak decays beyond leading logarithms. *Rev. Mod. Phys.*, 68:1125–1144, 1996.
9. Marcel Algueró, Bernat Capdevila, Andreas Crivellin, Sébastien Descotes-Genon, Pere Masjuan, Joaquim Matias, and Javier Virto. Emerging patterns of New Physics with and without Lepton Flavour Universal contributions. 2019.
10. W. Buchmuller and D. Wyler. Effective Lagrangian Analysis of New Interactions and Flavor Conservation. *Nucl. Phys.*, B268:621–653, 1986.
11. Jason Aebischer, Wolfgang Altmannshofer, Diego Guadagnoli, MÉRIL Reboud, Peter Stangl, and David M. Straub. B -decay discrepancies after Moriond 2019. 2019.
12. Sébastien Descotes-Genon, Adam Falkowski, Marco Fedele, Martín González-Alonso, and Javier Virto. The CKM parameters in the SMEFT. 2018.
13. Joe Davighi. Connecting neutral current B anomalies with the heaviness of the third family. In *54th Rencontres de Moriond on QCD and High Energy Interactions (Moriond QCD 2019) La Thuile, Italy, March 23-30, 2019*, 2019.
14. B. C. Allanach and Joe Davighi. Deforming the Third Family Hypercharge Model for Neutral Current B -Anomalies. 2019.
15. Guido D’Amico, Marco Nardecchia, Paolo Panci, Francesco Sannino, Alessandro Strumia, Riccardo Torre, and Alfredo Urbano. Flavour anomalies after the R_{K^*} measurement. *JHEP*, 09:010, 2017.
16. G. D’Ambrosio, A. M. Iyer, F. Piccinini, and A. D. Polosa. Confronting B anomalies with atomic physics. 2019.
17. Jogesh C. Pati and Abdus Salam. Lepton Number as the Fourth Color. *Phys. Rev.*, D10:275–289, 1974. [Erratum: *Phys. Rev.*D11,703(1975)].
18. Andreas Crivellin, Christoph Greub, Dario Müller, and Francesco Saturnino. Importance of Loop Effects in Explaining the Accumulated Evidence for New Physics in B Decays with a Vector Leptoquark. *Phys. Rev. Lett.*, 122(1):011805, 2019.
19. Andreas Crivellin and Francesco Saturnino. Explaining the Flavor Anomalies with a Vector Leptoquark (Moriond 2019 update). In *54th Rencontres de Moriond on QCD and High Energy Interactions (Moriond QCD 2019) La Thuile, Italy, March 23-30, 2019*, 2019.
20. Monika Blanke, Andreas Crivellin, Stefan de Boer, Teppei Kitahara, Marta Moscati, Ulrich Nierste, and Ivan Nišandžić. Impact of polarization observables and $B_c \rightarrow \tau\nu$ on new physics explanations of the $b \rightarrow c\tau\nu$ anomaly. *Phys. Rev.*, D99(7):075006, 2019.
21. Monika Blanke, Andreas Crivellin, Teppei Kitahara, Marta Moscati, Ulrich Nierste, and Ivan Nišandžić. Addendum: ”Impact of polarization observables and $B_c \rightarrow \tau\nu$ on new physics explanations of the $b \rightarrow c\tau\nu$ anomaly”. 2019.

22. Faisal Munir Bhutta and Cai-Dian Lü. Search for New Physics Signals via Doubly Weak B Decays. In *54th Rencontres de Moriond on QCD and High Energy Interactions (Moriond QCD 2019) La Thuile, Italy, March 23-30, 2019*, 2019.
23. M. Tanabashi et al. Review of Particle Physics. *Phys. Rev.*, D98(3):030001, 2018.
24. Peter Athron et al. A global fit of the MSSM with GAMBIT. *Eur. Phys. J.*, C77(12):879, 2017.
25. Anders Kvellestad. Exploring light supersymmetry with GAMBIT. In *54th Rencontres de Moriond on QCD and High Energy Interactions (Moriond QCD 2019) La Thuile, Italy, March 23-30, 2019*, 2019.
26. Guillaume Chalons, Mark D. Goodsell, Sabine Kraml, Humberto Reyes-González, and Sophie L. Williamson. LHC limits on gluinos and squarks in the minimal Dirac gaugino model. *JHEP*, 04:113, 2019.
27. Luigi Delle Rose, Shaaban Khalil, Simon J. D. King, Suchita Kulkarni, Carlo Marzo, Stefano Moretti, and Cem S. Un. Sneutrino Dark Matter, Constraints and Perspectives. 2018.
28. Luigi Delle Rose, Shaaban Khalil, Simon J. D. King, Suchita Kulkarni, Carlo Marzo, Stefano Moretti, and Cem S. Un. Sneutrino Dark Matter in the BLSSM. *JHEP*, 07:100, 2018.
29. M. Cepeda et al. Higgs Physics at the HL-LHC and HE-LHC. 2019.
30. J. De Blas et al. Higgs Boson Studies at Future Particle Colliders. 2019.
31. Falko Dulat, Bernhard Mistlberger, and Andrea Pelloni. Precision predictions at N³LO for the Higgs boson rapidity distribution at the LHC. *Phys. Rev.*, D99(3):034004, 2019.
32. Leandro Cieri. The transverse-momentum subtraction method at N³LO applied to Higgs boson production at the LHC. In *54th Rencontres de Moriond on QCD and High Energy Interactions (Moriond QCD 2019) La Thuile, Italy, March 23-30, 2019*, 2019.
33. Leandro Cieri, Xuan Chen, Thomas Gehrmann, E. W. N. Glover, and Alexander Huss. Higgs boson production at the LHC using the q_T subtraction formalism at N³LO QCD. *JHEP*, 02:096, 2019.
34. Frédéric A. Dreyer and Alexander Karlberg. Vector-Boson Fusion Higgs Pair Production at N³LO. *Phys. Rev.*, D98(11):114016, 2018.
35. Matteo Cacciari, Frédéric A. Dreyer, Alexander Karlberg, Gavin P. Salam, and Giulia Zanderighi. Fully Differential Vector-Boson-Fusion Higgs Production at Next-to-Next-to-Leading Order. *Phys. Rev. Lett.*, 115(8):082002, 2015. [Erratum: *Phys. Rev. Lett.*120,no.13,139901(2018)].
36. Frédéric A. Dreyer and Alexander Karlberg. Fully differential Vector-Boson Fusion Higgs Pair Production at Next-to-Next-to-Leading Order. *Phys. Rev.*, D99(7):074028, 2019.
37. P. Azzi et al. Standard Model Physics at the HL-LHC and HE-LHC. 2019.
38. Massimiliano Grazzini, Stefan Kallweit, and Marius Wiesemann. Fully differential NNLO computations with MATRIX. *Eur. Phys. J.*, C78(7):537, 2018.
39. Stefan Kallweit. In *54th Rencontres de Moriond on QCD and High Energy Interactions (Moriond QCD 2019) La Thuile, Italy, March 23-30, 2019*, 2019.
40. Massimiliano Grazzini, Stefan Kallweit, Marius Wiesemann, and Jeong Yeon Yook. ZZ production at the LHC: NLO QCD corrections to the loop-induced gluon fusion channel. *JHEP*, 03:084, 2019.
41. X. Chen, T. Gehrmann, N. Glover, M. Höfer, and A. Huss. Isolated photon and photon+jet production at NNLO QCD accuracy and the ratio $R_{13/8}^7$. In *54th Rencontres de Moriond on QCD and High Energy Interactions (Moriond QCD 2019) La Thuile, Italy, March 23-30, 2019*, 2019.
42. Xuan Chen, Thomas Gehrmann, Nigel Glover, Marius Höfer, and Alexander Huss. Isolated photon and photon+jet production at NNLO QCD accuracy. *Submitted to: J. High Energy Phys.*, 2019.

43. John M. Campbell, R. Keith Ellis, and Ciaran Williams. Direct Photon Production at Next-to-Next-to-Leading Order. *Phys. Rev. Lett.*, 118(22):222001, 2017.
44. Stefano Frixione. Isolated photons in perturbative QCD. *Phys. Lett.*, B429:369–374, 1998.
45. Frank Siegert. A practical guide to event generation for prompt photon production with Sherpa. *J. Phys.*, G44(4):044007, 2017.
46. Alexander B. Goncharov. Multiple polylogarithms, cyclotomy and modular complexes. *Math. Res. Lett.*, 5:497–516, 1998.
47. Johannes Henn. In *54th Rencontres de Moriond on QCD and High Energy Interactions (Moriond QCD 2019) La Thuile, Italy, March 23-30, 2019*, 2019.
48. D. Chicherin, T. Gehrmann, J. M. Henn, P. Wasser, Y. Zhang, and S. Zoia. All master integrals for three-jet production at NNLO. 2018.
49. S. Badger, D. Chicherin, T. Gehrmann, G. Heinrich, J. M. Henn, T. Peraro, P. Wasser, Y. Zhang, and S. Zoia. Analytic form of the full two-loop five-gluon all-plus helicity amplitude. 2019.
50. Dmitry Chicherin, Thomas Gehrmann, Johannes M. Henn, Pascal Wasser, Yang Zhang, and Simone Zoia. The two-loop five-particle amplitude in $\mathcal{N} = 8$ supergravity. *JHEP*, 03:115, 2019.
51. S. Abreu, F. Febres Cordero, H. Ita, B. Page, and V. Sotnikov. Planar Two-Loop Five-Parton Amplitudes from Numerical Unitarity. *JHEP*, 11:116, 2018.
52. Johannes Broedel, Claude Duhr, Falko Dulat, Brenda Penante, and Lorenzo Tancredi. Elliptic polylogarithms and Feynman parameter integrals. *JHEP*, 05:120, 2019.
53. Albert M Sirunyan et al. Observation of $t\bar{t}H$ production. *Phys. Rev. Lett.*, 120(23):231801, 2018.
54. M. Aaboud et al. Observation of Higgs boson production in association with a top quark pair at the LHC with the ATLAS detector. *Phys. Lett.*, B784:173–191, 2018.
55. Anna Kulesza, Leszek Motyka, Daniel Schwartzländer, Tomasz Stebel, and Vincent Theeuwes. Associated top-pair production with a heavy boson production through NLO+NNLL accuracy at the LHC. In *54th Rencontres de Moriond on QCD and High Energy Interactions (Moriond QCD 2019) La Thuile, Italy, March 23-30, 2019*, 2019.
56. Massimiliano Grazzini, Stefan Kallweit, Dirk Rathlev, and Marius Wiesemann. Transverse-momentum resummation for vector-boson pair production at NNLL+NNLO. *JHEP*, 08:154, 2015.
57. M. Dasgupta and G. P. Salam. Resummation of nonglobal QCD observables. *Phys. Lett.*, B512:323–330, 2001.
58. Marcel Balsiger, Thomas Becher, and Ding Yu Shao. Non-global logarithms in jet and isolation cone cross sections. *JHEP*, 08:104, 2018.
59. Henning Bahl. Constraining the MSSM Higgs sector using precise Higgs mass predictions. In *54th Rencontres de Moriond on QCD and High Energy Interactions (Moriond QCD 2019) La Thuile, Italy, March 23-30, 2019*, 2019.
60. H. Bahl, T. Hahn, S. Heinemeyer, W. Hollik, S. Paßehr, H. Rzehak, and G. Weiglein. Precision calculations in the MSSM Higgs-boson sector with FeynHiggs 2.14. 2018.
61. Matthias König. Effective Field Theory after a New-Physics Discovery. In *54th Rencontres de Moriond on QCD and High Energy Interactions (Moriond QCD 2019) La Thuile, Italy, March 23-30, 2019*, 2019.
62. Stefan Alte, Matthias König, and Matthias Neubert. Effective Theory for a Heavy Scalar Coupled to the SM via Vector-Like Quarks. *Eur. Phys. J.*, C79(4):352, 2019.
63. Morad Aaboud et al. Measurement of the W -boson mass in pp collisions at $\sqrt{s} = 7$ TeV with the ATLAS detector. *Eur. Phys. J.*, C78(2):110, 2018. [Erratum: *Eur. Phys. J.* C78,no.11,898(2018)].
64. Moh'd Hussein, Joshua Isaacson, and Joey Huston. A Study of the PDF uncertainty on the LHC W -boson mass measurement. 2019.

65. Elena Accomando, Juri Fiaschi, Francesco Hautmann, and Stefano Moretti. Neutral current forward-backward asymmetry: from θ_W to PDF determinations. *Eur. Phys. J.*, C78(8):663, 2018.
66. S. Alekhin et al. HERAFitter. *Eur. Phys. J.*, C75(7):304, 2015.
67. Ivan Novikov. In *54th Rencontres de Moriond on QCD and High Energy Interactions (Moriond QCD 2019) La Thuile, Italy, March 23-30, 2019*, 2019.
68. Krzysztof Golec-Biernat, Leszek Motyka, and Tomasz Stebel. Forward Drell-Yan and backward jet production as a probe of the BFKL dynamics. *JHEP*, 12:091, 2018.
69. I. Balitsky and A. Tarasov. Power corrections to TMD factorization for Z-boson production. *JHEP*, 05:150, 2018.
70. John Collins. Foundations of perturbative QCD. *Camb. Monogr. Part. Phys. Nucl. Phys. Cosmol.*, 32:1–624, 2011.
71. F. Hautmann, H. Jung, A. Lelek, V. Radescu, and R. Zlebcik. Collinear and TMD Quark and Gluon Densities from Parton Branching Solution of QCD Evolution Equations. *JHEP*, 01:070, 2018.
72. A. Bermudez Martinez et al. Production of Z-bosons in the parton branching method. 2019.
73. Torbjörn Sjöstrand. Status and developments of event generators. *PoS*, LHCP2016:007, 2016.
74. Andrew V. Koshelkin and Cheuk-Yin Wong. Dynamics of Quarks in a 2D Flux Tube. *EPJ Web Conf.*, 90:01004, 2015.
75. Andrew V. Koshelkin. In *54th Rencontres de Moriond on QCD and High Energy Interactions (Moriond QCD 2019) La Thuile, Italy, March 23-30, 2019*, 2019.
76. Stefan Gieseke, Patrick Kirchgaesser, and Simon Plätzer. Baryon production from cluster hadronisation. *Eur. Phys. J.*, C78(2):99, 2018.
77. Shi-Yuan Li. In *54th Rencontres de Moriond on QCD and High Energy Interactions (Moriond QCD 2019) La Thuile, Italy, March 23-30, 2019*, 2019.
78. Wit Busza, Krishna Rajagopal, and Wilke van der Schee. Heavy Ion Collisions: The Big Picture, and the Big Questions. *Ann. Rev. Nucl. Part. Sci.*, 68:339–376, 2018.
79. Tseh Liou, A. H. Mueller, and Bin Wu. Radiative p_{\perp} -broadening of high-energy quarks and gluons in QCD matter. *Nucl. Phys.*, A916:102–125, 2013.
80. B. G. Zakharov. Radiative Quark p_{\perp} -Broadening in a Quark-Gluon Plasma beyond the Soft Gluon Approximation. *Pisma Zh. Eksp. Teor. Fiz.*, 108(8):541–542, 2018. [JETP Lett.108,no.8,508(2018)].
81. Boris O. Kerbikov. Critical acoustics and singular bulk viscosity of quark matter. In *53rd Rencontres de Moriond on QCD and High Energy Interactions (Moriond QCD 2018) La Thuile, Italy, March 17-24, 2018*, 2018.
82. Boris O. Kerbikov. In *54th Rencontres de Moriond on QCD and High Energy Interactions (Moriond QCD 2019) La Thuile, Italy, March 23-30, 2019*, 2019.
83. David d’Enterria. Top-quark and Higgs boson perspectives at heavy-ion colliders. *Nucl. Part. Phys. Proc.*, 289-290:237–240, 2017.
84. David d’Enterria, Daniel E. Martins, and Patricia Rebello Teles. Higgs boson production in photon-photon interactions with proton, light-ion, and heavy-ion beams at current and future colliders. 2019.
85. Jacopo Ghiglieri and Urs Achim Wiedemann. Thermal width of the Higgs boson in hot QCD matter. *Phys. Rev.*, D99(5):054002, 2019.



6.2
Common Session
with the
Gravitation conference

SEARCHING FOR NEW PHYSICS WITH PRECISION LOW TEMPERATURE EXPERIMENTS

M.E. TOBAR

ARC Centre of Excellence For Engineered Quantum Systems, Department of Physics, School of Physics, Mathematics and Computing, University of Western Australia, 35 Stirling Highway, Crawley WA 6009, Australia.



Major unsolved problems in physics include the nature of Dark Matter, Dark Energy and the unification of Quantum Mechanics with General Relativity to determine a unified theory of Quantum Gravity. At the University of Western Australia we are undertaking a series of low temperature precision experiments to search for new physics that could shed light on these important problems. These experiments include measurements with photons, phonons and spins as well as hybridised quasi-particles. In this article the research program and experimental result to date are summarised.

1 Some Tools for Precision Measurements

At the University of Western Australia, the Frequency and Quantum Metrology research group within the Department of Physics has a rich history of developing precision tools for both fundamental physics and industrial applications. This includes the development of high-Q resonant photonic cavities based on whispering gallery modes,¹ layered Bragg structures,²⁻⁶ low loss crystals⁷ and re-entrant cavities.⁸⁻¹⁰ These types of cavities have been used in a range of applications, including highly stable low noise classical¹¹⁻¹⁶ and atomic^{17,18} oscillators, low noise readout and measurement systems,¹⁹⁻²¹ high sensitivity displacement sensors,^{22,23} high precision electron spin resonance spectroscopy,^{24,25} high precision measurement of material properties²⁶⁻²⁸ and high-Q hybrid quantum systems strongly coupled to form quasi-particles.²⁹⁻³²

Over the years we have applied these precision measurement tools and techniques to testing core aspects of fundamental physics, such as searches for Lorentz invariance violations in the photon, phonon and gravity sectors,³³⁻⁴⁰ variations in fundamental constants⁴¹⁻⁴³ and searching for ultra-light dark matter (ULDM) and weakly interacting sub-eV particle (WISP) dark matter.⁴⁴⁻⁵² We have also studied modified Maxwell's equations and as a result have developed new experiments to test for Lorentz invariance violations,³⁴ dark matter axions^{44-48,53} and hidden sector photons.⁴⁹⁻⁵² We continue to follow this tradition and recently gained funding to apply our expertise to new directions in fundamental physics with particular focus on detecting ULDMs and axions.

2 Searching for Axion Dark Matter with Precision Measurement

In general, the physics community is searching for two types of dark matter, Weakly Interacting Massive Particles (WIMPs) and the low mass particles. The former are typically large mass or high energy (order of 100 GeV), which requires large-scale well-funded mega-projects. However, recent null results from direct detection experiments including LUX and SuperCDMS, along with the failure to produce evidence of supersymmetry in the Large Hadron Collider have cast doubts on the simplest WIMP hypothesis.^{54,55} In contrast, WISP experiments search for lighter mass particles of $1eV$ or lower, allowing more "table-top" type low-energy high-precision experiments. These factors have seen a renaissance in experiments to search for axions, ALPs and ULDMs in the laboratory. Experiments are gaining momentum around the world with recent funded proposals searching for interactions with Standard Model particles. For example, current funded experimental programs include; ADMX ($1 - 10\mu eV$ photon interaction),^{56,57} ADMX-HF⁵⁸ ($10 - 40\mu eV$ photon interaction), ARIADNE ($1\mu eV - 1meV$ nuclear spin interaction),⁵⁹ ABRACADABRA ($10^{-14} - 10^{-6}eV$ magnetometer),⁶⁰ CASPRr Electric, CASPER Wind ($10^{-9} - 1\mu eV$ via nuclear spin interactions),⁶¹ QUAX⁶² ($200\mu eV$ electron spin interaction), CULTASK ($20\mu eV$ photon interactions),⁶³ MADMAX($40\mu eV - 400\mu eV$)⁶⁴ and finally our experiment at UWA, the Oscillating Resonant Group AxioN, ORGAN($60\mu eV - 210\mu eV$), which recently completed a path finding run⁴⁶ and has been funded with a new dilution refrigerator and 14 T magnet. It has also been suggested that successful detection could lead to a whole new era of "axion astronomy",⁶⁵ with further suggestions of varied axion signals shapes from a class of galaxies encompassing the Milky Way.⁶⁶ Furthermore a recent proposal highlights that axion sensitivity may be enhanced through a network of detectors positioned around the world.⁶⁷ This network of detectors would detect streaming dark matter axions, whose flux might get temporarily enormously enhanced due to gravitational lensing. This may occur if the Sun, Moon or some planet is found along the direction of a DM stream propagating towards the Earth location.⁶⁶ The UWA program is the only such effort in the Southern Hemisphere and is uniquely positioned to take full advantage of its location.

2.1 Photon-Cavities

The current most common way to search for galactic halo dark matter axions is the Sikivie haloscope technique⁶⁸ pioneered by ADMX.^{56,57} In a typical detector, the particles interact with the DC magnetic field, or virtual photons, to produce real photons whose frequency corresponds to the mass of the axions. This scheme employs one or several tuneable microwave cavities, serving as resonant antennas, with the output coupled to the lowest noise amplifiers so generated photons may be detected as sensitively as possible. Along these lines, we are currently constructing ORGAN at UWA.⁴⁶ The goal of ORGAN is to search for the range of masses proposed by the SMASH model.⁶⁹ The experiment will operate in a new dedicated BlueFors-XLD1000 dilution refrigerator with a base temperature of $7mK$ and a $14T$ superconducting solenoid. Both have been ordered and will arrive in October 2019. Cavity research and development builds on our work on tunable super-mode dielectric resonators.⁴⁴ These resonators can be designed to have scan rates improved by 1 to 2 orders of magnitude over traditionally tuned haloscope resonators.

Another alternative is to utilise RF, microwave or optical fields instead of static ones. Indeed, the Primakoff process works equally well with real photons instead of virtual ones.⁷⁰ Prior work has considered a single pumped cavity as a source of real photons, which interact with axions to generate a small signal in the orthogonal polarized mode. Our approach is totally new, we consider pumping both polarizations (AC scheme). Despite the similarity between the DC and AC detection schemes, they belong to a different class of detectors. Since virtual photons or static fields carry no phase, the Sikivie detectors belong to the class of phase insensitive systems. On the other hand, the AC scheme considered here relies on pumping signals carrying relative phase as well as separate phases relative to the axion signal. Thus, the detected signal as well as

the overall result would have a footprint of these phases. This fact draws analogies with existing amplifiers that can be grouped into DC (phase insensitive) amplifiers, where energy is drawn from static power supply, and parametric (phase sensitive) amplifiers, where energy comes from oscillating fields. The second type gives more freedom allowing improved amplification/detection schemes based on quadrature squeezing. Thus, we have expanded investigations into a novel class of axion detectors employing the phase sensitive approach.⁷¹

We have studied axion electrodynamics for this case and made the following discoveries. The two-mode axion electrodynamics predicts interaction with axions of two different masses: 1) A high-mass axion, where the mass is down-converted to two photons of lower energy and the sum frequency, $\omega_2 + \omega_1$, is equal to the axion mass. 2) A low-mass axion, where the mass is up-converted to two photons of higher energy and the difference frequency, $\omega_2 - \omega_1$, is equal to the axion mass. This means this new technique can scan two mass ranges at once, in completely different mass ranges to traditional haloscope experiments. In the advent of detection, one needs to determine if the axion comes from the higher or lower mass range, but this would be almost trivial to verify. A simple version of this experiment is a cylindrical cavity excited with a TE and TM mode simultaneously, with a tuning plunger changing the length of the cavity. The frequency of the TE mode will tune but the TM mode would not allowing both sum and difference frequencies to be tuned. Two high power oscillators can be configured and a sensitive experiment can be set up by using cross correlation to measure the correlated phase or amplitude signals in both oscillators. Perturbations in the oscillators phase, amplitude and frequency will occur if an axion exists at either the sum or difference frequencies.

By implementing modified axion electrodynamics⁵³ we have also investigated using the induced electric field as a broadband low mass detector for axions.⁷² For such an experiment an electric sensor such as a capacitor with the plates aligned perpendicular to an applied B_z field from a solenoid connected to a low noise amplifier cooled to low temperatures that becomes a sensitive detector. Due to the Primakoff effect the mass of the axion will generate an oscillating electric field in the capacitor at the equivalent frequency, and the voltage across it will induce a current in the SQUID amplifier readout. We assume a broadband capacitive measurement from $1kHz$ to $1MHz$ (4×10^{-12} to 4×10^{-9} eV), only limited by SQUID in terms of mass range. For these calculations we make the following assumptions: 1) Axions comprise the dark matter halo ($0.45 GeV/cm^3$). 2) Axion effective quality factor is 10^6 (generally accepted due to Doppler shifts induced by the Earth's motion through the galaxy). 3) The SQUID rms current fluctuation noise floor is $0.5pA/\sqrt{Hz}$. The diameter of the capacitor is order $10cm$ (size of the magnet bore). Preliminary results constrain $g_{a\gamma\gamma} > \sim 2.35 \times 10^{-12} GeV^{-1}$ in the mass range of 2.08×10^{-11} to 2.2×10^{-11} eV, and demonstrate potential sensitivity to axion-like dark matter with masses in the range of 10^{-12} to 10^{-8} eV.⁷²

2.2 Magnon-Photon Polaritons

Searching for axions through coupling with electron spins was first proposed in 1985 by Kraus et al.⁷³ They showed that DFSZ axions would interact with aligned electrons and act as a catalyst for axion-photon conversion, unlike KSVZ axions, which are insensitive to spin interactions. This led to proposed schemes using magnons,⁷⁴ which have a higher density of oscillating electron spins than any other system, $10^{28}/m^3$. Interactions with axions change the effective magnetization and can be treated as an effective magnetic field oscillating at a frequency related to the mass of the axion. This allows an easily tuneable system to be engineered to scan different values of axion mass, as the bulk ferromagnetic resonance, or Kittel mode in a magnetic sphere may be easily tuned by a DC magnetic field. Recently this experiment was revived, with a current proposal and first measurement, which utilises more modern technology.^{62,75} Because it is possible that axions interact with spins rather than photons it is imperative that we develop experiments to test both interactions, which will also help determine the correct axion model. At UWA we have significant experience working with ferri/ferromagnetic systems at low tem-

peratures²⁹⁻³¹ as it is possible to engineer a huge dispersive regime over tens of GHz with the UWA design²⁹⁻³² avoiding mechanical tuning of the resonant frequency, required for the photon haloscope experiments. This is achieved through ultra-strong coupling between the photon and the magnon to create a cavity-magnon polariton, recently we have engineered such a system to enhance the bandwidth of a ferromagnetic haloscope,⁷⁶ setting first laboratory limits on the axion-electron coupling strength of $g_{a\gamma\gamma} > 3.7 \times 10^{-9}$ in the range $33.79\mu\text{eV} < m_a < 33.94\mu\text{eV}$ with 95% confidence.

3 Searching For Lorentz Invariance Violations

3.1 Photon-Cavities

We have built continuously operating cryogenic sapphire oscillators at UWA^{15,77} with frequency stability of parts in 10^{16} , and are based on very high-Q whispering gallery modes propagating in a low loss cylindrical sapphire crystal. Two co-rotating systems with the resonators set in an orthogonal way, have put the best limits on some photon sector coefficients,³⁵ Data from the experiment was analysed for Lorentz invariance violations (LIV) with a sensitivity > 100 times than previous results. This work is unequivocally the most sensitive lab test of LIV of the photon ever undertaken at parts in 10^{18} for even parity coefficients, parts in 10^{14} for odd parity coefficients, and parts in 10^{10} for the scalar coefficient.³⁵ We have also put new limits on higher order LIV photon sector coefficients from an asymmetric optical ring resonator experiment.³⁶

Research at UWA continues into improving cryogenic sapphire oscillator technology. We identified current limitation due to power sensitivities and we have identified ways to further improve these oscillators.⁷⁷ It is our goal in this research program to obtain a further significant improvement, which would benefit clock technology and future tests on fundamental physics.

3.2 Phonon-Cavities

Quartz Bulk Acoustic Wave (BAW) resonators have a higher $Q \cdot f$ product than any other acoustic system currently available.⁷⁸⁻⁸¹ Thus, we have previously implemented such oscillators for a high precision test of Lorentz Invariance.³⁷ The first experiment utilised oscillators inferior to the best available, and we have began a second generation of Lorentz Invariance experiment based on the best available oscillators with technological improvements in the rotation set up.⁸² In this experiment, room temperature oscillators with state-of-the-art phase noise are continuously compared on a platform that rotates at a rate of order of a cycle per second. Improvements in noise measurement techniques, data acquisition, and data processing have been made and are detailed in.⁸² Preliminary results of the second generation of such tests indicate that standard model extension coefficients in the matter sector can be measured at a precision of order 10^{-16} GeV after taking a year's worth of data. This is equivalent to an improvement of two orders of magnitude over the prior acoustic phonon sector experiment.³⁷ Currently the experiment has been running for nearly a year, and soon in the future we will put limits on SME coefficients in the non-minimal and higher dimensional matter sector.

4 Macroscopic Acoustic Oscillators to Test Fundamental Physics

Rather than oscillators as discussed previously, macroscopic acoustic oscillators with a low noise readout also make good test beds for many fundamental physics tests. The original high precision measurement of this type was the resonant-mass gravitational wave detector.⁸³ Since this time the quantum information discipline has further pushed this technology and there have been many other ideas and systems proposed. Such systems can now operate at the quantum limit and surpass this limit in sensitivity. In particular we have built such experiments based on

high-Q modes in sapphire⁸⁴ and quartz⁷⁹ and we are using such set ups to also test quantum gravity.⁸⁵

4.1 Search for High Frequency Gravity Waves

For this experiment we harness phonons by implementing phonon-trapping BAW resonator technology.⁸⁶ Extremely sensitive experiments are possible due to the extremely high Q-factors at cryogenic temperatures, $Q \approx 10^{10}$, for frequencies ranging from 5 MHz to nearly a GHz, which is beyond the capability of any other technology. We have shown that a new highly sensitive GW search is possible over this frequency range, where no prior search has been undertaken before. The experiment consists of a BAW resonator coupled to a SQUID amplifier, with two independent cryogen-free cooled experiments initially at 4K.⁷⁹ Two independent systems are needed to look for the signal correlations necessary to confirm the existence of GWs, in a similar way that the two LIGO detectors operate. Furthermore, we propose in the future to have two BAW resonators oriented orthogonally in each experiment, so we can reject spurious signals originating from within each cryogen free system, this will reduce the background and improve detection confidence.

This is a low cost experiment, with high potential gain and no risk. A first-detection would be of major scientific importance and a null result will still attract large interest, as there are a number of theoretical predictions for astrophysical and cosmological objects at these frequencies, which this experiment can either verify or rule out.⁸⁶ The aim is to do the first search in a 4 K environment with sensitivity of $10 - 21/\sqrt{Hz}$ per mode (in the future a more sensitive mK experiment is possible).

4.2 Search for Scalar Dark matter

The same set up to search for GWs is also sensitive to scalar dark mater, as shown by Arvanitaki et al, "Sound of Dark Matter: Searching for Light Scalars with Resonant-Mass Detectors".⁸⁷ Scalar fields called moduli determine the fine-structure constant and electron mass in string theory. They show that our quartz GW experiment can put limits dark matter if it takes on the form of such a light modulus, and will oscillates with a frequency equal to its mass and amplitude determined by the local dark-matter density. This translates into an oscillation of the size of a solid that can be observed by resonant-mass GW antennas, and hence the phonon modes in quartz BAW resonators. The data analysis required to put limits on such oscillations, is very similar to searching for a coherent source of GWs.

Acknowledgments

This work was funded by Australian Research Council grant numbers DP190100071 and CE170100009. We acknowledge that this is a summary of extensive work by many researchers from the Frequency and Quantum Metrology research group at the University of Western Australia.

References

1. Daniel L. Creedon, Yarema Reshitnyk, Warrick Farr, John M. Martinis, Timothy L. Duty, and Michael E. Tobar. High q-factor sapphire whispering gallery mode microwave resonator at single photon energies and millikelvin temperatures. *Applied Physics Letters*, 98(22):222903, 2011.
2. M. E. Tobar, J. M. Le Floch, D. Cros, J. Krupka, J. D. Anstie, and J. G. Hartnett. Spherical bragg reflector resonators. *IEEE Transactions on Ultrasonics, Ferroelectrics, and Frequency Control*, 51(9):1054–1059, 2004.

3. Jean-Michel le Floch, Michael E. Tobar, Dominique Cros, and Jerzy Krupka. Low-loss materials for high q-factor bragg reflector resonators. *Applied Physics Letters*, 92(3):032901, 2008.
4. J. Krupka, A. Cwikla, M. Mrozowski, R. N. Clarke, and M. E. Tobar. High q-factor microwave fabry-perot resonator with distributed bragg reflectors. *IEEE Transactions on Ultrasonics, Ferroelectrics, and Frequency Control*, 52(9):1443–1451, 2005.
5. Jean-Michel le Floch, Michael E. Tobar, David Mouneyrac, Dominique Cros, and Jerzy Krupka. Discovery of bragg confined hybrid modes with high q factor in a hollow dielectric resonator. *Applied Physics Letters*, 91(14):142907, 2007.
6. N. C. Carvalho, Y. Fan, J-M. Le Floch, and M. E. Tobar. Piezoelectric voltage coupled reentrant cavity resonator. *Rev. Sci. Instrum.*, 85:104705, 2014.
7. Michael Edmund Tobar, Jerzy Krupka, Eugene Nicolay Ivanov, and Richard Alex Woode. Anisotropic complex permittivity measurements of mono-crystalline rutile between 10 and 300 k. *Journal of Applied Physics*, 83(3):1604–1609, 1998.
8. Michael E. Tobar, Eugene N. Ivanov, and David G. Blair. Parametric transducers for the advanced cryogenic resonant-mass gravitational wave detectors. *General Relativity and Gravitation*, 32(9):1799–1821, Sep 2000.
9. J-M. Le Floch, Y. Fan, M. Aubourg, D. Cros, N. C. Carvalho, Q. Shan, J. Bourhill, E. N. Ivanov, G. Humbert, V. Madrangeas, and M. E. Tobar. Rigorous analysis of highly tunable cylindrical transverse magnetic mode re-entrant cavities. *Review of Scientific Instruments*, 84(12):125114, 2013.
10. M. Goryachev and M. E. Tobar. Creating tuneable microwave media from a two-dimensional lattice of re-entrant posts. *Journal of Applied Physics*, 118(20):204504, 2015.
11. M. E. Tobar and D. G. Blair. Phase noise analysis of the sapphire loaded superconducting niobium cavity oscillator. *IEEE Transactions on Microwave Theory and Techniques*, 42(2):344–347, Feb 1994.
12. M. E. Tobar, A. J. Giles, S. Edwards, and J. H. Searls. High-q thermoelectric-stabilized sapphire microwave resonators for low-noise applications. *IEEE Transactions on Ultrasonics, Ferroelectrics, and Frequency Control*, 41(3):391–396, May 1994.
13. E. N. Ivanov and M. E. Tobar. Low phase-noise microwave oscillators with interferometric signal processing. *IEEE Transactions on Microwave Theory and Techniques*, 54(8):3284–3294, 2006.
14. E. N. Ivanov and M. E. Tobar. Low phase-noise sapphire crystal microwave oscillators: current status. *IEEE Transactions on Ultrasonics, Ferroelectrics, and Frequency Control*, 56(2):263–269, 2009.
15. C. R. Locke, E. N. Ivanov, J. G. Hartnett, P. L. Stanwix, and M. E. Tobar. Invited article: Design techniques and noise properties of ultrastable cryogenically cooled sapphire-dielectric resonator oscillators. *Review of Scientific Instruments*, 79(5):051301, 2008.
16. R. A. Woode, M. E. Tobar, E. N. Ivanov, and D. G. Blair. An ultralow noise microwave oscillator based on a high-q liquid nitrogen cooled sapphire resonator. *IEEE Transactions on Ultrasonics, Ferroelectrics, and Frequency Control*, 43(5):936–941, Sept 1996.
17. P.-Y. Bourgeois, N. Bazin, Y. Kersalé, V. Giordano, M. E. Tobar, and M. Oxborrow. Maser oscillation in a whispering-gallery-mode microwave resonator. *Applied Physics Letters*, 87(22):224104, 2005.
18. J. Bourhill, K. Benmessai, M. Goryachev, D. L. Creedon, W. Farr, and M. E. Tobar. Spin bath maser in a cryogenically cooled sapphire whispering gallery mode resonator. *Phys. Rev. B*, 88:235104, Dec 2013.
19. E. N. Ivanov, M. E. Tobar, and R. A. Woode. Microwave interferometry: application to precision measurements and noise reduction techniques. *IEEE Transactions on Ultrasonics, Ferroelectrics, and Frequency Control*, 45(6):1526–1536, Nov 1998.
20. Eugene N. Ivanov and Michael E. Tobar. Microwave phase detection at the level of 10^{-11}

- rad. *Review of Scientific Instruments*, 80(4):044701, 2018/03/19 2009.
21. Ben T. McAllister, Stephen R. Parker, Eugene N. Ivanov, and Michael E. Tobar. Cross-correlation signal processing for axion and wisp dark matter searches. *IEEE Transactions on Ultrasonics, Ferroelectrics, and Frequency Control*, 66(1):236–243, 2019.
 22. B. D. Cuthbertson, M. E. Tobar, E. N. Ivanov, and D. G. Blair. Parametric backaction effects in a high-q cryogenic sapphire transducer. *Review of Scientific Instruments*, 67(7):2435–2442, 1996.
 23. C R Locke, M E Tobar, and E N Ivanov. Properties of a monolithic sapphire parametric transducer: prospects of measuring the standard quantum limit. *Classical and Quantum Gravity*, 19(7):1877, 2002.
 24. Warrick G. Farr, Daniel L. Creedon, Maxim Goryachev, Karim Benmessai, and Michael E. Tobar. Ultrasensitive microwave spectroscopy of paramagnetic impurities in sapphire crystals at millikelvin temperatures. *Phys. Rev. B*, 88:224426, Dec 2013.
 25. Maxim Goryachev, Warrick G. Farr, Daniel L. Creedon, and Michael E. Tobar. Spin-photon interaction in a cavity with time-reversal symmetry breaking. *Phys. Rev. B*, 89:224407, Jun 2014.
 26. J. Krupka, K. Derzakowski, A. Abramowicz, M. E. Tobar, and R. G. Geyer. Use of whispering-gallery modes for complex permittivity determinations of ultra-low-loss dielectric materials. *IEEE Transactions on Microwave Theory and Techniques*, 47(6):752–759, 1999.
 27. Jerzy Krupka, Krzysztof Derzakowski, Michael Tobar, John Hartnett, and Richard G Geyer. Complex permittivity of some ultralow loss dielectric crystals at cryogenic temperatures. *Measurement Science and Technology*, 10(5):387, 1999.
 28. N. C. Carvalho, M. Goryachev, J. Krupka, P. Bushev, and M. E. Tobar. Low-temperature microwave properties of biaxial YAlO_3 . *Phys. Rev. B*, 96:045141, Jul 2017.
 29. Maxim Goryachev, Warrick G. Farr, Daniel L. Creedon, Yaohui Fan, Mikhail Kostylev, and Michael E. Tobar. High-cooperativity cavity qed with magnons at microwave frequencies. *Phys. Rev. Applied*, 2:054002, Nov 2014.
 30. J. Bourhill, N. Kostylev, M. Goryachev, D. L. Creedon, and M. E. Tobar. Ultrahigh cooperativity interactions between magnons and resonant photons in a yig sphere. *Phys. Rev. B*, 93:144420, Apr 2016.
 31. Maxim Goryachev, Stuart Watt, Jeremy Bourhill, Mikhail Kostylev, and Michael E. Tobar. Cavity magnon polaritons with lithium ferrite and three-dimensional microwave resonators at millikelvin temperatures. *Physical Review B*, 97(15):155129–, 04 2018.
 32. Graeme Flower, Jeremy Bourhill, Maxim Goryachev, and Michael E. Tobar. Experimental implementations of cavity optomagnonic systems: from ultra strong coupling to applications in precision measurement. *arXiv:1905.04002 [quant-ph]*, 2019.
 33. Paul L. Stanwix, Michael E. Tobar, Peter Wolf, Mohamad Susli, Clayton R. Locke, Eugene N. Ivanov, John Winterflood, and Frank van Kann. Test of lorentz invariance in electrodynamics using rotating cryogenic sapphire microwave oscillators. *Phys. Rev. Lett*, 95(4):040404–, 07 2005.
 34. Michael Edmund Tobar, Peter Wolf, Alison Fowler, and John Gideon Hartnett. New methods of testing lorentz violation in electrodynamics. *Phys. Rev. D*, 71(2):025004–, 01 2005.
 35. Moritz Nagel, Stephen R. Parker, Evgeny V. Kovalchuk, Paul L. Stanwix, John G. Hartnett, Eugene N. Ivanov, Achim Peters, and Michael E. Tobar. Direct terrestrial test of lorentz symmetry in electrodynamics to 10^{-18} . *Nature Communications*, 6:8174 EP, 09 2015.
 36. Stephen R. Parker, Matthew Mewes, Fred N. Baynes, and Michael E. Tobar. Bounds on higher-order lorentz-violating photon sector coefficients from an asymmetric optical ring resonator experiment. *Physics Letters A*, 379(42):2681 – 2684, 2015.

37. Anthony Lo, Philipp Haslinger, Eli Mizrachi, Loïc Anderegg, Holger Müller, Michael Hohensee, Maxim Goryachev, and Michael E. Tobar. Acoustic tests of lorentz symmetry using quartz oscillators. *Physical Review X*, 6(1):011018–, 02 2016.
38. Cheng-Gang Shao, Ya-Fen Chen, Yu-Jie Tan, Shan-Qing Yang, Jun Luo, Michael Edmund Tobar, J. C. Long, E. Weisman, and V. Alan Kostelecký. Combined search for a lorentz-violating force in short-range gravity varying as the inverse sixth power of distance. *Phys. Rev. Lett.*, 122:011102, Jan 2019.
39. Cheng-Gang Shao, Yu-Jie Tan, Wen-Hai Tan, Shan-Qing Yang, Jun Luo, Michael Edmund Tobar, Quentin G. Bailey, J. C. Long, E. Weisman, Rui Xu, and V. Alan Kostelecký. Combined search for lorentz violation in short-range gravity. *Phys. Rev. Lett.*, 117:071102, Aug 2016.
40. Cheng-Gang Shao, Yu-Jie Tan, Wen-Hai Tan, Shan-Qing Yang, Jun Luo, and Michael Edmund Tobar. Search for lorentz invariance violation through tests of the gravitational inverse square law at short ranges. *Phys. Rev. D*, 91:102007, May 2015.
41. Michael Edmund Tobar, Peter Wolf, Sébastien Bize, Giorgio Santarelli, and Victor Flambaum. Testing local lorentz and position invariance and variation of fundamental constants by searching the derivative of the comparison frequency between a cryogenic sapphire oscillator and hydrogen maser. *Phys. Rev. D*, 81:022003, Jan 2010.
42. M. E. Tobar, P. L. Stanwix, J. J. McFerran, J. Guéna, M. Abgrall, S. Bize, A. Clairon, Ph. Laurent, P. Rosenbusch, D. Rovera, and G. Santarelli. Testing local position and fundamental constant invariance due to periodic gravitational and boost using long-term comparison of the syrté atomic fountains and h-masers. *Phys. Rev. D*, 87:122004, Jun 2013.
43. J. Guéna, M. Abgrall, D. Rovera, P. Rosenbusch, M. E. Tobar, Ph. Laurent, A. Clairon, and S. Bize. Improved tests of local position invariance using ^{87}Rb and ^{133}Cs fountains. *Phys. Rev. Lett.*, 109:080801, Aug 2012.
44. Ben T. McAllister, Graeme Flower, Lucas E. Tobar, and Michael E. Tobar. Tunable supermode dielectric resonators for axion dark-matter haloscopes. *Phys. Rev. Applied*, 9:014028, Jan 2018.
45. Maxim Goryachev, Ben T. Mcallister, and Michael E. Tobar. Axion detection with negatively coupled cavity arrays. *Physics Letters A*, 382:2199–2204, 2018.
46. Ben T. McAllister, Graeme Flower, Eugene N. Ivanov, Maxim Goryachev, Jeremy Bourhill, and Michael E. Tobar. The organ experiment: An axion haloscope above 15 ghz. *Physics of the Dark Universe*, 18:67 – 72, 2017.
47. Ben T. McAllister, Stephen R. Parker, and Michael E. Tobar. Axion dark matter coupling to resonant photons via magnetic field. *Phys. Rev. Lett.*, 116(16):161804, 2016. [Erratum: *Phys. Rev. Lett.* 117, no. 15, 159901 (2016)].
48. Ben T. McAllister, Stephen R. Parker, and Michael E. Tobar. 3D Lumped LC Resonators as Low Mass Axion Haloscopes. *Phys. Rev.*, D94(4):042001, 2016.
49. Stephen R. Parker, John G. Hartnett, Rhys G. Povey, and Michael E. Tobar. Cryogenic resonant microwave cavity searches for hidden sector photons. *Phys. Rev. D*, 88:112004, Dec 2013.
50. Stephen R. Parker, Gray Rybka, and Michael E. Tobar. Hidden sector photon coupling of resonant cavities. *Phys. Rev. D*, 87:115008, Jun 2013.
51. Rhys G. Povey, John G. Hartnett, and Michael E. Tobar. Microwave cavity light shining through a wall optimization and experiment. *Phys. Rev. D*, 82:052003, Sep 2010.
52. Rhys G. Povey, John G. Hartnett, and Michael E. Tobar. Microwave cavity hidden sector photon threshold crossing. *Phys. Rev. D*, 84:055023, Sep 2011.
53. Michael E. Tobar, Ben T. McAllister, and Maxim Goryachev. Modified axion electrodynamics as impressed electromagnetic sources through oscillating background polarization and magnetization. *arXiv:1809.01654 [hep-ph]*, 2018.

54. Patrick J. Fox, Gabriel Jung, Peter Sorensen, and Neal Weiner. Dark matter in light of the lux results. *Phys. Rev. D*, 89:103526, May 2014.
55. Junjie Cao, Chengcheng Han, Lei Wu, Peiwen Wu, and Jin Min Yang. A light susy dark matter after cdms-ii, lux and lhc higgs data. *Journal of High Energy Physics*, 2014(5):56, May 2014.
56. S. J. Asztalos, G. Carosi, C. Hagmann, D. Kinion, K. van Bibber, M. Hotz, L. J Rosenberg, G. Rybka, J. Hoskins, J. Hwang, P. Sikivie, D. B. Tanner, R. Bradley, and J. Clarke. Squid-based microwave cavity search for dark-matter axions. *Phys. Rev. Lett.*, 104:041301, Jan 2010.
57. J. Hoskins, J. Hwang, C. Martin, P. Sikivie, N. S. Sullivan, D. B. Tanner, M. Hotz, L. J Rosenberg, G. Rybka, A. Wagner, S. J. Asztalos, G. Carosi, C. Hagmann, D. Kinion, K. van Bibber, R. Bradley, and J. Clarke. Search for nonvirialized axionic dark matter. *Phys. Rev. D*, 84:121302, Dec 2011.
58. B. M. Brubaker, L. Zhong, Y. V. Gurevich, S. B. Cahn, S. K. Lamoreaux, M. Simanovskaia, J. R. Root, S. M. Lewis, S. Al Kenany, K. M. Backes, I. Urdinaran, N. M. Rapisdi, T. M. Shokair, K. A. van Bibber, D. A. Palken, M. Malnou, W. F. Kindel, M. A. Anil, K. W. Lehnert, and G. Carosi. First results from a microwave cavity axion search at $24\mu\text{eV}$. *Phys. Rev. Lett.*, 118:061302, Feb 2017.
59. Asimina Arvanitaki and Andrew A. Geraci. Resonantly detecting axion-mediated forces with nuclear magnetic resonance. *Phys. Rev. Lett.*, 113:161801, Oct 2014.
60. Yonatan Kahn, Benjamin R. Safdi, and Jesse Thaler. Broadband and Resonant Approaches to Axion Dark Matter Detection. *Phys. Rev. Lett.*, 117(14):141801, 2016.
61. Dmitry Budker, Peter W. Graham, Micah Ledbetter, Surjeet Rajendran, and Alexander O. Sushkov. Proposal for a cosmic axion spin precession experiment (casper). *Phys. Rev. X*, 4:021030, May 2014.
62. R. Barbieri, C. Braggio, G. Carugno, C.S. Gallo, A. Lombardi, A. Ortolan, R. Pengo, G. Ruoso, and C.C. Speake. Searching for galactic axions through magnetized media: The quax proposal. *Physics of the Dark Universe*, 15:135 – 141, 2017.
63. J. Choi, H. Themann, M. J. Lee, B. R. Ko, and Y. K. Semertzidis. First axion dark matter search with toroidal geometry. *Phys. Rev. D*, 96:061102, Sep 2017.
64. Allen Caldwell, Gia Dvali, Béla Majorovits, Alexander Millar, Georg Raffelt, Javier Redondo, Olaf Reimann, Frank Simon, and Frank Steffen. Dielectric haloscopes: A new way to detect axion dark matter. *Phys. Rev. Lett.*, 118:091801, Mar 2017.
65. Ciaran A. J. O’Hare and Anne M. Green. Axion astronomy with microwave cavity experiments. *Phys. Rev. D*, 95:063017, Mar 2017.
66. Erik W. Lentz, Thomas R. Quinn, Leslie J. Rosenberg, and Michael J. Tremmel. A new signal model for axion cavity searches from n-body simulations. *The Astrophysical Journal*, 845(2):121, aug 2017.
67. K. Zioutas et al. Search for axions in streaming dark matter. 2017.
68. P. Sikivie. Experimental tests of the "invisible" axion. *Phys. Rev. Lett.*, 51:1415–1417, Oct 1983.
69. Guillermo Ballesteros, Javier Redondo, Andreas Ringwald, and Carlos Tamarit. Unifying inflation with the axion, dark matter, baryogenesis and the seesaw mechanism. *Phys. Rev. Lett.*, 118:071802, 2017.
70. Pierre Sikivie. Superconducting radio frequency cavities as axion dark matter detectors. *arXiv:1009.0762 [hep-ph]*, 2010.
71. M. Goryachev, B. McAllister, and M.E. Tobar. Axion detection with precision frequency metrology. *arXiv*, page arXiv:1806.07141, 2018.
72. Ben T. McAllister, Maxim Goryachev, Jeremy Bourhill, Eugene N. Ivanov, and Michael E. Tobar. Broadband axion dark matter haloscopes via electric field sensing. *arXiv:1803.07755 [physics.ins-det]*, 2018.

73. Lawrence Krauss, John Moody, Frank Wilczek, and Donald E. Morris. Calculations for cosmic axion detection. *Phys. Rev. Lett.*, 55:1797–1800, Oct 1985.
74. R Barbieri, M Cerdonio, G Fiorentini, and S Vitale. Axion to magnon conversion. a scheme for the detection of galactic axions. *Physics Letters B*, 226(3):357 – 360, 1989.
75. N. Crescini, D. Alesini, C. Braggio, G. Carugno, D. Di Gioacchino, C. S. Gallo, U. Gambardella, C. Gatti, G. Iannone, G. Lamanna, C. Ligi, A. Lombardi, A. Ortolan, S. Pagano, R. Pengo, G. Ruoso, C. C. Speake, and L. Taffarello. Operation of a ferromagnetic axion haloscope at $m_a = 58\mu\text{ev}$. *The European Physical Journal C*, 78(9):703, Sep 2018.
76. Graeme Flower, Jeremy Bourhill, Maxim Goryachev, and Michael E. Tobar. Broadening frequency range of a ferromagnetic axion haloscope with strongly coupled cavity–magnon polaritons. *Physics of the Dark Universe*, 25:100306, 2019.
77. Nitin R. Nand, Stephen R. Parker, Eugene N. Ivanov, Jean-Michel le Floch, John G. Hartnett, and Michael E. Tobar. Resonator power to frequency conversion in a cryogenic sapphire oscillator. *Applied Physics Letters*, 103(4):–, 2013.
78. M. Goryachev, D.L. Creedon, E.N. Ivanov, S. Galliou, R. Bourquin, and M.E. Tobar. Extremely low-loss acoustic phonons in a quartz bulk acoustic wave resonator at millikelvin temperature. *Appl. Phys. Lett.*, 100(24):243504, 2012.
79. Maxim Goryachev, Eugene N. Ivanov, Frank van Kann, Serge Galliou, and Michael E. Tobar. Observation of the fundamental nyquist noise limit in an ultra-high q-factor cryogenic bulk acoustic wave cavity. *Applied Physics Letters*, 105(15):153505, 2014.
80. M. Goryachev, D.L. Creedon, S. Galliou, and M.E. Tobar. Observation of rayleigh phonon scattering through excitation of extremely high overtones in low-loss cryogenic acoustic cavities for hybrid quantum systems. *Phys. Rev. Lett*, 111(8):085502, 2013.
81. S. Galliou, M. Goryachev, R. Bourquin, Philippe Abbe, J.P. Aubry, and M.E. Tobar. Extremely low loss phonon-trapping cryogenic acoustic cavities for future physical experiments. *Nature: Scientific Reports*, 3(2132), 2013.
82. M. Goryachev, Z. Kuang, E. N. Ivanov, P. Haslinger, H. Müller, and M. E. Tobar. Next generation of phonon tests of lorentz invariance using quartz baw resonators. *IEEE Transactions on Ultrasonics, Ferroelectrics, and Frequency Control*, 65(6):991–1000, June 2018.
83. D. G. Blair, E. N. Ivanov, M. E. Tobar, P. J. Turner, F. van Kann, and I. S. Heng. High sensitivity gravitational wave antenna with parametric transducer readout. *Physical Review Letters*, 74(11):1908–1911, 1995.
84. J. Bourhill, E. Ivanov, and M. E. Tobar. Precision measurement of a low-loss cylindrical dumbbell-shaped sapphire mechanical oscillator using radiation pressure. *Physical Review A*, 92(2):023817, 2015.
85. P. A. Bushev, J. Bourhill, M. Goryachev, N. Kukharchyk, E. Ivanov, S. Galliou, M. E. Tobar, and S. Danilishin. Testing of quantum gravity with sub-kilogram acoustic resonators. *arXiv:1903.03346 [quant-ph]*, 2019.
86. Maxim Goryachev and Michael E. Tobar. Gravitational wave detection with high frequency phonon trapping acoustic cavities. *Phys. Rev. D*, 90(10):102005–, 11 2014.
87. Asimina Arvanitaki, Savas Dimopoulos, and Ken Van Tilburg. Sound of dark matter: Searching for light scalars with resonant-mass detectors. *Phys. Rev. Lett.*, 116:031102, Jan 2016.

Authors Index

Authors Index

Abdolmaleki, H.	Forward-backward Drell-Yan asymmetry and PDF determination	211
Abreu, S.	Analytic form of the planar two-loop five-parton scattering amplitudes in QCD	189
Abulaiti, Y.	Searches for new resonances (lepton, jets) at ATLAS and CMS	133
Accomando, E.	Forward-backward Drell-Yan asymmetry and PDF determination	211
Bahl, H.	Constraining the MSSM Higgs sector using precise Higgs mass predictions	21
Balitsky, I.	Power corrections to TMD factorization	197
Barabanov, M.	Probing of multiquark structure in hadron and heavy ion collisions	237
Beaceron, S.	CMS search highlights	121
Bertone, V.	Forward-backward Drell-Yan asymmetry and PDF determination	211
Bhutta, F. M.	Search for new physics signals via doubly weak B decays	59
Bossio Sola, J.	QCD with jets and photons at ATLAS and CMS	181
Brendlinger, K.	ATLAS Higgs physics results	3
Chen, X.	Isolated photon and photon+jet production at NNLO QCD accuracy and the ratio $R_{13/8}^\gamma$	185
Cieri, L. J.	The transverse momentum subtraction method at N ³ LO applied to Higgs boson production at the LHC	11
Crivellin, A.	Explaining the flavor anomalies with a vector leptoquark	85
d'Enterria, D.	Higgs boson production in partonic and electromagnetic interactions with heavy ions	25
Davighi, J.	Connecting neutral current B anomalies with the heaviness of the third family	91
Descotes-Genon, S.	The trouble with $R_{K^{(*)}}$ – updated global fits and future directions	81
Di Marco, E.	Inclusive and differential W and Z at CMS and ATLAS	159
Dormans, J.	Analytic form of the planar two-loop five-parton scattering amplitudes in QCD	189
Fael, M.	V_{cb} from inclusive $b \rightarrow c$ decays: an alternative method	69
Farinelli, R.	XYZ particles at BESIII	101
Fabres Cordeo, F.	Analytic form of the planar two-loop five-parton scattering amplitudes in QCD	189
Fiaschi, J.	Forward-backward Drell-Yan asymmetry and PDF determination	211
Fienberg, A.	The status and prospects of the muon $g - 2$ experiment at Fermilab	163
Flechl, M.	CMS Higgs physics results	7
Gehrmann, T.	Isolated photon and photon+jet production at NNLO QCD accuracy and the ratio $R_{13/8}^\gamma$	185
Giuli, F.	Forward-backward Drell-Yan asymmetry and PDF determination	211
Glazov, A.	Forward-backward Drell-Yan asymmetry and PDF determination	211
Glover, N.	Isolated photon and photon+jet production at NNLO QCD accuracy and the ratio $R_{13/8}^\gamma$	185
Höfer, M.	Isolated photon and photon+jet production at NNLO QCD accuracy and the ratio $R_{13/8}^\gamma$	185
Hautmann, F.	Forward-backward Drell-Yan asymmetry and PDF determination	211
Huss, A.	Isolated photon and photon+jet production at NNLO QCD accuracy and the ratio $R_{13/8}^\gamma$	185
Ita, H.	Analytic form of the planar two-loop five-parton scattering amplitudes in QCD	189
Iyer, A.	Confronting B anomalies with low energy parity violation experiments	95
König, M.	Effective field theory after a new-physics discovery	153
Kamenik, J. F.	Flavour physics in vogue	49
Kerbikov, B.	Transport anomalies near the QCD phase transition at finite density	241
Koshelkin, A.	Particle production in high energy p-p collisions	249
Kraml, S.	LHC constraints on extended SUSY	129
Kulesza, A.	Associated top-pair production with a heavy boson through NLO+NNLL accuracy at the LHC	39
Kulkarni, S.	Sneutrino dark matter - status and perspectives	149
Kvellestad, A.	Exploring light supersymmetry with GAMBIT	145
Lelek, A.	Angular ordering effects in TMD parton distribution functions and Drell-Yan q_\perp spectra	203
Lewis, N.	Studying parton dynamics via single-spin asymmetries and two-particle correlations at PHENIX	221
Li, S.-Y.	Baryon number fluctuation of preconfinement clusters and transverse momentum dependence of bottom baryon production	107
Lu, C.D.	Search for new physics signals via doubly weak B decays	59
Luszczak, A.	Forward-backward Drell-Yan asymmetry and PDF determination	211

Marangotto, D.	Results from proton-lead and fixed-target collisions at LHCb	225
Mirra, M.	Search for production of an invisible dark photon from π^0 decays at NA62	73
Moretti, S.	Forward-backward Drell-Yan asymmetry and PDF determination	211
Motyka, L.	Associated top-pair production with a heavy boson through NLO+NNLL accuracy at the LHC	39
Nišandžić, I.	Impact of polarization observables and $B_c \rightarrow \tau\nu$ on new physics explanations of the $b \rightarrow c\tau\nu$ anomaly	63
Novák, T.	Collectivity in RHIC geometry scan as seen by PHENIX	215
Novikov, I.	Determination of Parton Distribution Functions in pion using xFitter	207
Novikov, I.	Forward-backward Drell-Yan asymmetry and PDF determination	211
Oldeman, R.	Lepton Flavour Universality tests with heavy flavour decays at LHCb	77
Olness, F.	Forward-backward Drell-Yan asymmetry and PDF determination	211
Olsen, S. L.	Probing of multiquark structure in hadron and heavy ion collisions	237
Page, B.	Analytic form of the planar two-loop five-parton scattering amplitudes in QCD	189
Pedro, K.	Searches for new physics with unconventional signatures at ATLAS and CMS	137
Pinna, D.	Searches for dark matter at CMS and ATLAS	141
Remon Alepuz, C.	Rare, radiative, and electroweak penguin decays of heavy flavour hadrons at LHCb	55
Richter-Was, E.	LHC Higgs CP sensitive observables in $H \rightarrow \tau^+\tau^-; \tau^\pm \rightarrow (3\pi)^\pm\nu$ and machine learning benefits	15
Riu, I.	$t\bar{t} + X$ production at ATLAS and CMS	35
Schwartländer, D.	Associated top-pair production with a heavy boson through NLO+NNLL accuracy at the LHC	39
Skwarnicki, T.	Hadron spectroscopy and exotic states at LHCb	111
Solodov, E.	Recent results from the VEPP2000 e+e- collider	167
Sotnikov, V.	Analytic form of the planar two-loop five-parton scattering amplitudes in QCD	189
Stebel, T.	Associated top-pair production with a heavy boson through NLO+NNLL accuracy at the LHC	39
Ström, R.	News on the CLIC physics potential	171
Strobbe, N.	Strong SUSY at ATLAS and CMS	125
Tancredi, L.	Elliptic polylogarithms and pure functions	193
Theeuwes, V.	Associated top-pair production with a heavy boson through NLO+NNLL accuracy at the LHC	39
Tobar, M.	Searching for new physics with precision low temperature experiments	291
Ulrich, R.	Hadron interactions at ultra-high energies measured by the Pierre Auger Observatory	253
Vagnoni, V.	QCD and high energy interactions: experimental summary	261
van de Klundert, M.	Soft QCD at CMS and ATLAS	177
Verbeke, W.	Single top quark and rare top quark production at ATLAS and CMS	43
Veres, G.	Heavy ion physics at CMS and ATLAS: hard probes	229
Wackerroth, D.	QCD and high energy interactions: Moriond 2019 theory summary	275
Was, Z.	LHC Higgs CP sensitive observables in $H \rightarrow \tau^+\tau^-; \tau^\pm \rightarrow (3\pi)^\pm\nu$ and machine learning benefits	15
Woźniak, K.	Heavy ion physics at ATLAS and CMS: flow harmonics across systems (pp , p +Pb, Xe+Xe, Pb+Pb)	233
Zakharov, B.	Radiative quark p_\perp -broadening in a quark-gluon plasma at RHIC and LHC energies	245
Zenaiev, O.	Forward-backward Drell-Yan asymmetry and PDF determination	211

Participants List

Family name	First name	Home institution	Country	Email
Abreu	Samuel	CP3, UCLouvain	Belgium	samuel.abreu@uclouvain.be
Abulaiti	Yiming	CERN	Switzerland	yiming.abulaiti@cern.ch
Adam	Wolfgang	HEPHY-Vienna	Austria	wolfgang.adam@cern.ch
Augé	Étienne	Université Paris Sud	France	etienne.auge@u-psud.fr
Bahl	Henning	DESY Hamburg	Germany	henning.bahl@desy.de
Balitsky	Ian	JLab/ODU	USA	balitsky@jlab.org
Barabanov	Mikhail	JINR	Russia	barabanov@jinr.ru
Beauceron	Stephanie	IPN Lyon	France	stephanie.beauceron@ipnl.in2p3.fr
Becher	Thomas	University of Bern	Switzerland	becher@itp.unibe.ch
Bhattacharya	Soham	Tata Institute of Fundamental Research	India	soham.elessar@gmail.com
Bianchi	Livio	Università di Torino	Italy	Livio.Bianchi@cern.ch
Bielčik	Jaroslav	Czech Technical University in Prague	Czechia	jaroslav.bielcik@fffi.cvut.cz
Biino	Cristina	INFN Torino	Italy	cristina.biino@cern.ch
Bordry	Frederick	CERN	Switzerland	frederick.bordry@cern.ch
Bossio Sola	Jonathan David	McGill University	Canada	bossjonad@gmail.com
Bozzi	Giuseppe	Università di Pavia and INFN	Italy	giuseppe.bozzi@unipv.it
Brendlinger	Kurt	DESY Germany		kurt.brendlinger@cern.ch
Brost	Elizabeth	Northern Illinois University	USA	elizabeth.brost@cern.ch
Castillo Castellanos	Javier	CEA Saclay - Irfu/DPhN	France	Javier.Castillo@cea.fr
Cerri	Alessandro	University of Sussex	UK	a.cerri@sussex.ac.uk
Charles	Matthew	LPNHE/Sorbonne Université	France	matthew.john.charles@cern.ch
Cieri	Leandro Javier	INFN Milano Bicocca	Italy	lcieri@physik.uzh.ch
Contu	Andrea	INFN	Italy	andrea.contu@cern.ch
Crivellin	Andreas	PSI & UZH	Switzerland	andreas.crivellin@psi.ch
d'Enterria	David	CERN	Switzerland	dde@cern.ch
D'Eramo	Louis	LPNHE	France	lderamo@lpnhe.in2p3.fr
Davighi	Joseph	DAMTP	UK	joedavighi@gmail.com
Descotes-Genon	Sébastien	LPT Orsay	France	descotes@th.u-psud.fr
Di Marco	Emanuele	INFN - Sezione di Roma	Italy	emanuele.dimarco@roma1.infn.it
F. Kamenik	Jernej	Jozef Stefan Institute	Slovenia	jernej.kamenik@ijs.si
Fael	Matteo	University of Siegen	Germany	fael@physik.uni-siegen.de
Farinelli	Riccardo	INFN Ferrara	Italy	rfarinelli@fe.infn.it
Febres Cordero	Fernando	University of Freiburg	Germany	ffebres@physik.uni-freiburg.de
Fienberg	Aaron	University of Washington	USA	fienberg@uw.edu
Flechl	Martin	HEPHY Vienna	Austria	martin.flechl@cern.ch
Gangadharan	Dhevan	University of Heidelberg	Germany	dhevanga@gmail.com
Gonzalez-Alonso	Martin	CERN	Switzerland	martin.gonzalez.alonso@cern.ch
Hautmann	Francesco	U. of Oxford / U. of Antwerp	UK	francesco.hautmann@desy.de
Helary	Louis	Heidelberg Physikalisches Institut	Germany	louis.helary@cern.ch
Henn	Johannes	Max Planck Institute for Physics	Germany	henn@mpp.mpg.de
Hirschtühl	Dominic	University of Wuppertal	Germany	hirsch@physik.uni-wuppertal.de
Höfer	Marius	Physik-Institut Universität Zürich	Switzerland	mhoefer@physik.uzh.ch
Huang	Yanping	Institute of High Energy Physics	China	yanping.huang@cern.ch
Iyer	Abhishek	INFN Napoli	Italy	iyera@na.infn.it
Kallweit	Stefan	Università degli Studi di Milano-Bicocca	Italy	stefan.kallweit@cern.ch
Karlberg	Alexander	University of Zurich	Switzerland	karlberg@physik.uzh.ch
Kerbikov	Boris	MITP	Russia	bkerbikov@gmail.com
Klima	Boaz	Fermilab	USA	klima@fnal.gov
König	Matthias	University of Zurich	Switzerland	matthias.koenig@uzh.ch
Koshelkin	Andrew	MEPhI	Russia	and.kosh59@gmail.com
Kraml	Sabine	LPSC	France	sabine.kraml@lpsc.in2p3.fr
Krizka	Karol	Lawrence Berkeley National Laboratory	USA	kkrizka@gmail.com
Krokovny	Pavel	Novosibirsk State University	Russia	krokovny@gmail.com
Kulesza	Anna	ITP - University of Muenster	Germany	anna.kulesza@uni-muenster.de
Kulkarni	Suchita	HEPHY	Austria	suchita.kulkarni@oeaw.ac.at
Kvlestad	Anders	Imperial College London	UK	a.kvlestad@imperial.ac.uk

Landsberg Greg	Brown University USA	landsberg@hep.brown.edu
Lapidus Kirill	CERN Switzerland	kirill.lapidus@cern.ch
Lelek Aleksandra	University of Antwerp Belgium	aleksandra.lelek@uantwerpen.be
Lewis Nicole	University of Michigan USA	nialewis@umich.edu
Li Shiyuan	School of Physics, Shandong University China	lishy@sdu.edu.cn
Lu Cai-Dian	Institute of High Energy Physics China	lucd@ihep.ac.cn
Mahmoudi Nazila	Lyon University France	nazila@cern.ch
Malaescu Bogdan	LPNHE France	bogdan.malaescu@cern.ch
Marangotto Daniele	Università degli studi di Milano Italy	daniele.marangotto@mi.infn.it
Mirra Marco	Università degli Studi di Napoli Federico II Italy	marco.mirra@na.infn.it
Morgenstern Marcus	NIKHEF Netherlands	marcus.matthias.morgenstern@cern.ch
Motyka Leszek	Jagiellonian University Poland	leszekm@th.if.uj.edu.pl
Nišandžić Ivan	Karlsruher Institut für Technologie Germany	ivan.nisandzic@kit.edu
Novak Tamas	Eszterhazy Karoly University Hungary	novak.tamas@uni-eszterhazy.hu
Novikov Ivan	Joint Institute for Nuclear Research Russia	novivanya@yandex.ru
Oldeman Rudolf	Università degli Studi di Cagliari Italy	oldeman@unica.it
Pedro Kevin	Fermilab USA	pedrok@cern.ch
Pelloni Andrea	ETH Zürich Switzerland	apelloni@itp.phys.ethz.ch
Pietrzyk Bolek	LAPP France	bolek.pietrzyk@cern.ch
Pinna Deborah	Boston University USA	deborah.pinna@cern.ch
Remon Alepuz Clara	Instituto de Física Corpuscular (IFIC) Spain	Clarea@ific.uv.es
Richter-Was Elzbieta	Jagiellonian University Poland	Elzbieta.Richter-Was@cern.ch
Riu Imma	IFAE Barcelona Spain	imma.riu@cern.ch
Rizzi Chiara	CERN Switzerland	chiara.rizzi@cern.ch
Schoefbeck Robert	Institute for High Energy Physics Austria	robert.schoefbeck@cern.ch
Skwarnicki Tomasz	Syracuse University USA	tskwarni@syr.edu
Soffer Abner	Tel Aviv University Israel	asoffer@tau.ac.il
Solodov Evgeny	Budker INP Russia	solodov@inp.nsk.su
Strobbe Nadja	Fermilab USA	nadja.strobbe@cern.ch
Ström Rickard	CERN Switzerland	lars.rickard.stroem@cern.ch
Tamponi Umberto	INFN Torino Italy	tamponi@to.infn.it
Tancredi Lorenzo	CERN Theory Department Switzerland	lorenzo.tancredi@cern.ch
Ulrich Ralf	Karlsruhe Institute of Technology Germany	ralf.ulrich@cern.ch
Vagnoni Vincenzo	INFN Italy	Vincenzo.Vagnoni@cern.ch
Van Jean Tran Thanf	Rencontres du Vietnam France	jtrantv@gmail.com
van de Klundert Merijn	DESY Germany	mhfvandeklundert@gmail.com
Vázquez Doce Oton	TU - Munich Germany	oton.vazquez.doce@cern.ch
Verbeke Willem	Universiteit Gent Belgium	willem.verbeke@cern.ch
Veres Gabor	Eötvös Loránd University Hungary	vg@ludens.elte.hu
Volpe Giacomo	Università and INFN Italy	giacomo.volpe@cern.ch
Wackerroth Doreen	SUNY University at Buffalo USA	dw24@buffalo.edu
Wang Jianxiang	Institute of High Energy Physics China	jxwang@ihep.ac.cn
Was Zbigniew	ifj pan Poland	z.was@cern.ch
Wozniak Krzysztof	Institute of Nuclear Physics Poland	krzysztof.wozniak@ifj.edu.pl
Xiao Meng	Johns Hopkins University USA	meng.xiao@cern.ch
Ye Zhenyu	University of Illinois at Chicago USA	yezhenyu@uic.edu
Yook Jeong Yeon	University of Zurich, Physic-Institut Switzerland	jyook@physik.uzh.ch
Zakharov Bronislav	Landau Institute Russia	bgz@itp.ac.ru
Zoia Simone	Max Planck Institute for Physics Germany	zoia@mpp.mpg.de



Dépôt légal : octobre 2019
Achevé d'imprimer : octobre 2019

COPYMEDIA
www.copy-media.net
Avenue de Guitayne - 33610 CANÉJAN